Elena Ciappi · Sergio De Rosa ·
Francesco Franco · Stephen A. Hambric ·
Randolph C. K. Leung · Vincent Clair ·
Laurent Maxit · Nicolas Totaro *Editors*

Flinovia—Flow Induced Noise and Vibration Issues and Aspects-III

Springer

Flinovia—Flow Induced Noise and Vibration Issues and Aspects-III

Elena Ciappi · Sergio De Rosa · Francesco Franco ·
Stephen A. Hambric · Randolph C. K. Leung ·
Vincent Clair · Laurent Maxit · Nicolas Totaro
Editors

Flinovia—Flow Induced Noise and Vibration Issues and Aspects-III

Springer

Editors
Elena Ciappi
CNR-INM
Rome, Italy

Francesco Franco
Dipartimento di Ingegneria Industriale (DII)
University of Naples Federico II
Napoli, Italy

Randolph C. K. Leung
Department of Mechanical Engineering
Hong Kong Polytechnic University
Hung Hom, Kowloon, Hong Kong

Laurent Maxit
Univ Lyon, INSA Lyon, LVA, EA677
Villeurbanne, France

Sergio De Rosa
Dipartimento di Ingegneria Industriale (DII)
University of Naples Federico II
Napoli, Italy

Stephen A. Hambric
ARL, Pennsylvania State University
State College
PA, USA

Vincent Clair
Laboratoire de Mécanique des Fluides et d'Acoustique
École Centrale de Lyon
Écully, France

Nicolas Totaro
Univ Lyon, INSA Lyon, LVA, EA677
Villeurbanne, France

ISBN 978-3-030-64806-0 ISBN 978-3-030-64807-7 (eBook)
https://doi.org/10.1007/978-3-030-64807-7

This Springer imprint is published by the registered company Springer Nature Switzerland AG
The registered company address is: Gewerbestrasse 11, 6330 Cham, Switzerland

Organizing Committee

Supporting Institutions Committee

- CNR-INM, Institute of Marine Engineering, National Research Council, Rome, Italy, www.inm.cnr.it
- Pasta-Lab, Department of Industrial Engineering, Aerospace Section, University of Naples Federico II, Italy, www.pastalab.unina.it
- CELYA, Lyon Acoustics Center, University of Lyon, France, celya.universite-lyon.fr
- INSA Lyon, Institut National des Sciences Appliquées, Lyon, France, www.insa-lyon.fr
- ECL, Ecole Centrale de Lyon, Lyon, France, www.ec-lyon.fr.

International Organizing and Editors Committee

Elena Ciappi, CNR-INM, Institute of Marine Engineering, National Research Council, Rome, Italy.
Sergio De Rosa and Francesco Franco, Department of Industrial Engineering, Aerospace Section, University of Naples Federico II, Italy.
Stephen A. Hambric, Center for Acoustics and Vibration, Pennsylvania State University, University Park, PA, USA.
Randolph C. K. Leung, Department of Mechanical Engineering, The Hong Kong Polytechnic University, Hung Hom, Kowloon, Hong Kong.
Vincent Clair, Laboratoire de Mécanique des Fluides et d'Acoustique, Ecole Centrale de Lyon, Ecully Cedex, France.
Laurent Maxit and Nicolas Totaro, Univ Lyon, INSA Lyon, LVA, EA677, Villeurbanne, France.

Local Organizing Committee

Vincent Clair
Laurent Maxit and Nicolas Totaro.

Preface

This book documents the proceedings of the Third International Symposium on Flow Induced Noise and Vibration Issues and Aspects (FLINOVIA), held in Lyon, France 2–4 September 2019 at INSA Lyon, and co-sponsored by INSA-Lyon, the Lyon Centre for Acoustics (CeLyA), The French Naval Group, and Ecole Centrale de Lyon (ECL). The FLINOVIA series uses a novel approach

- invited papers only, with longer presentation times and no parallel talks;
- no registration fees;
- a limited audience (on the order of 100 attendees); and
- complimentary proceedings (the book you're reading now) to all attendees.

This method encourages more industry and government participants and maximizes discussion and interaction.

The first FLINOVIA was held in Rome, Italy in November 2013 at the Italian Consiglio Nazionale delle Ricerche (CNR), and the second was hosted at Penn State University by the Center for Acoustics and Vibration (CAV) in the United States 27–28 April 2017. Proceedings books for both are also available from Springer.

The papers in this volume (18 of the 26 presented at the symposium) are subdivided into four main groups:

- Source Modeling (4 papers)
- Experimental Techniques (4 papers)
- Analytical Developments (4 papers)
- Numerical Methods (5 papers).

The additional keynote paper by Daniel Juvé describes recent advances in measuring the wall pressure wavenumber spectra induced by Turbulent Boundary Layer (TBL) flow. Eleven of the papers also discuss TBL-induced vibration and noise, but other topics are also addressed, including tonal noise, noise due to ingested turbulence, fluid-structure interaction problems, and noise control techniques.

The third FLINOVIA was highly successful, with authors and attendees from Europe, Asia, and North America. Future meetings are being planned and will maintain the features described above—2–3 days of presentations with a small number of invited papers (no parallel sessions) with participation by industry and government strongly pursued to encourage transition of research. To monitor future developments please visit www.flinovia.org.

Rome, Italy — Elena Ciappi
Napoli, Italy — Sergio De Rosa
Napoli, Italy — Francesco Franco
State College, USA — Stephen A. Hambric
Hung Hom, Hong Kong — Randolph C. K. Leung
Écully, France — Vincent Clair
Lyon, France — Laurent Maxit
Lyon, France — Nicolas Totaro
Lyon, France — Jean-Louis Guyader
July 2020

Contents

Opening Lectures—Wall-Pressure Wavenumber-Frequency Spectra: Experimental Challenges and Recent Advances

Daniel Juvé, Simon L. Prigent, Edouard Salze, Pascal Souchotte, and Christophe Bailly

Abstract In the first part of this paper, the authors offer, based on their experience, a short review of the main difficulties encountered in measuring flow-induced wall-pressure fluctuations. Some recent advances are presented and illustrated with a focus on 2-point statistical quantities, spatial cross-correlations and wavenumber-frequency spectra. The second part describes three experiments conducted at Ecole centrale de Lyon on wall-pressure measurements and their use. The SONOBL experiment is devoted to the study of the influence of mean external pressure gradients on point-spectra and cross-spectra with the objective of identifying the acoustic contribution of a turbulent boundary layer (TBL). The CANOBLE experiment is focused on measurements of TBL wall-pressure fluctuations, induced vibrations of a representative side panel and acoustic transmission into a cavity performed on a full-scale mock-up of a business jet. The final objective is to predict flow-induced noise into an aircraft cockpit or cabin in cruise conditions. Finally measurements made inside the duct of a small turbofan used in aircraft ventilating systems are described, where array techniques involving MEMS microphones are used to extract the noise emitted by the fan from contaminating hydrodynamic wall-pressure fluctuations.

D. Juvé (✉) · S. L. Prigent · E. Salze · P. Souchotte · C. Bailly
University of Lyon, Ecole centrale de Lyon, LMFA UMR 5509,
36 Avenue Guy de Collongue, 69134 Ecully, France
e-mail: daniel.juve@ec-lyon.fr

S. L. Prigent
e-mail: simon.prigent@ec-lyon.fr

E. Salze
e-mail: edouard.salze@ec-lyon.fr

P. Souchotte
e-mail: pascal.souchotte@ec-lyon.fr

C. Bailly
e-mail: christophe.bailly@ec-lyon.fr

E. Ciappi et al. (eds.), *Flinovia—Flow Induced Noise and Vibration Issues and Aspects-III*, https://doi.org/10.1007/978-3-030-64807-7_1

1 A Short Review of the Interest of Wall-Pressure Measurements and of the Encountered Difficulties

The first part of this paper is devoted to a short personal overview of the importance of measuring wall-pressure fluctuations induced by turbulent flows, of the main difficulties encountered and of some recent improvements in microphone technology and data processing.

1.1 Why Measuring Wall-Pressure Fluctuations Induced by Turbulent Flows?

Wall-pressure fluctuations induced by unsteady flows are important in a variety of applications. Wall-pressure fluctuations can be due to flow separation around sharp edges and/or to random fluctuations in attached turbulent boundary layers (TBL); for the essential, this paper concentrates on TBL induced wall-pressure fluctuations. These fluctuations act as an unsteady loading on solid structures and they induce mechanical vibrations which in turn generate sound. The vast majority of applications is to be found in the transportation industry.

In aeronautics for example, the TBL is a major contributor to the noise radiated during cruise inside the cockpit and the cabin and this has important consequences on the nuisances for the pilots and on the perceived comfort for the passengers. In this case the noise radiated outside the aircraft by these mechanisms toward residents of airports is not an issue at all. In the automotive industry, the problem is slightly different. Flow induced interior noise is usually due to two different mechanisms: the first one is, as previously described, due to the unsteady loading of the side window (for example) and subsequent vibration and noise. A second contribution exists, associated with aeroacoustic sources in the unsteady wake behind the side mirror which generate acoustic waves impinging the side window which are then transmitted into the car. These two mechanisms are associated with different characteristics in terms of level and propagation speed (flow velocity vs speed of sound) and the filtering effect of the structure on these two kinds of excitation is different. The relative level of each contribution is thus of interest; it is frequency dependent and can significantly vary from car to car.

Besides these applications in air, similar problems are encountered in marine applications. Mach numbers are of course very different and the heavy loading due to water profoundly changes the vibration response of the structures. But the basic problem of transmission through the solid structure is the same. One classical application concerns sonars used to locate distant submarines by passively listening to their sound emission. The challenge here is to be able to detect distant acoustic waves in the presence of wall-pressure fluctuations induced by the TBL. This corresponds to a sort of filtering problem: the structure has to act as a filter to reject as much flow noise as possible while being more or less transparent to acoustic waves. Note that

for submarines for example, the noise generated by the flow, not only by the propeller but also by the TBL, is also critical for acoustic discretion. This corresponds to a different problem, that is not based on the structure's vibrations, but rather the direct noise radiation by (hydro)acoustic sources in the Lighthill sense.

This direct noise radiation is the mechanism at hand when dealing with the so-called self noise of airfoils and turbine blades. This self noise is due to the turbulent structures developing in the boundary layers along the chord of the blades; they are nearly silent due to the quadrupolar nature of their radiation unless they arrive at the trailing edge. The pressure fluctuations are then diffracted by the edge and, to first approximation, then radiate as stronger dipoles. The amplitude of the fluctuations together with their correlation length along the span are important parameters which control the intensity and frequency distribution of the radiated far-field noise. Reducing this noise is of course important in the aircraft industry but also for public acceptance of wind turbine farms. Considerable work has been done in recent years and continues to be done to reduce this noise by shaping the trailing edge of the blades in view of reducing the coherence of wall pressure fluctuations, typically by indentations of blades' edges, often called serrations, as explained by Oerlemans et al. [21].

The next question to be answered is that of the relevance of experimental measurements nearly 60 years after the first published experimental results. One could think that analytical models or numerical simulations should be sufficient, but generally speaking this is not the case. Regarding numerical simulations, the main difficulty is that simple statistical codes (of RANS type) do not give access even to such simple quantities as the rms value of pressure fluctuations along a surface, let alone more sophisticated quantities such as spectra and coherence lengths (see however promising attempts by Peltier and Hambric [24] or more recently by Grasso et al. [13] and Slama et al. [31]). Only unsteady codes (DNS or LES, see for example Cohen and Gloerfelt [7]) are able to provide the necessary information; but the use of these codes is usually limited to relatively low values of the Reynolds number and/or relatively simple geometries. Progress has been made in the recent years to overcome these limitations, for example with codes based on the Lattice Boltzmann Method (LBM), (see for example Casalino et al. [5]), but they are costly in terms of computation time and memory requirements and, at the moment, they do not properly cover the full range of frequencies necessary in real world applications.

Most of the available models are semi-empirical; several have been developed over the years and partially validated in canonical situations, typically a fully developed TBL along a flat rigid plate. This is the case for example of the Goody's model [10] for wall-pressure spectra, which is frequently used and is in good agreement with experimental data in the absence of external pressure gradients; the agreement is however not very good when, as is often the case in practice, pressure gradients are present, especially adverse ones. This model uses a number of coefficients which can be computed using standard RANS codes. The frequency spectrum $\Phi(\omega)$ is given by:

$$\frac{\Phi(\omega)U_\infty}{{\tau_w}^2\delta} = \frac{C_2\left(\omega\delta/U_\infty\right)^2}{\left[\left(\omega\delta/U_\infty\right)^{0.75}+C_1\right]^{3.7}+\left[C_3\left(\omega\delta/U_\infty\right)\right]^7} \tag{1}$$

In this formula, C_1, C_2 and C_3 are three empirical constants; by fitting a large number of experimental data, Goody obtained $C_1 = 0.5$, $C_2 = 3$ while connecting C_3 to a sort of Reynolds number R_T

$$C_3 = 1.1{R_T}^{-0.57};\ R_T = R_\tau\frac{u_\tau}{U_\infty}$$

$\omega = 2\pi f$ is the angular frequency, u_τ the friction velocity and R_τ the Reynolds number based on this friction velocity and on the boundary layer thickness δ. U_∞ is the external flow velocity and τ_w the wall shear stress ($\tau_w = \rho{u_\tau}^2$).

For 2-point quantities the situation is evidently more complex and a number of expressions have been proposed over the years, from the simple Corcos model [8] to the more elaborate ones by Chase [6]. Once again these models are all semi-empirical (or fully empirical) and not well validated. Precise measurements are still mandatory even in the simple case of a rigid flat plate. The expressions of the Corcos model for cross-spectra $S_{pp}(\mathbf{r},\omega)$ and wavenumber-frequency spectra $\widetilde{\Phi}_{pp}(\mathbf{k},\omega)$ are:

$$S_{pp}(\mathbf{r},\omega) = \Phi(\omega)\exp\left(-\alpha\frac{\omega\left|r_1\right|}{U_c}\right)\exp\left(-\beta\frac{\omega\left|r_2\right|}{U_c}\right)\exp\left(i\frac{\omega r_1}{U_c}\right) \tag{2}$$

$$\widetilde{\Phi}_{pp}(\mathbf{k},\omega) = \frac{1}{\pi^2}\frac{U_c^2}{\omega^2}\frac{\alpha\beta}{\left[\alpha^2+\left(U_ck_1/\omega-1\right)^2\right]\left[\beta^2+\left(U_ck_2/\omega\right)^2\right]} \tag{3}$$

where r_1 and r_2 denote the separations along the flow and in the transverse direction respectively, and the integral of the normalized wavenumber spectrum $\widetilde{\Phi}_{pp}$ over $\mathbf{k}$ is equal to 1. Classical values of the constants are $\alpha = 0.1$ and $\beta = 0.77$, but in practice they are generally chosen from a curve fit of experimental data, and then slightly different values are often encountered. Note also that the convection velocity U_c is a function of the frequency ω and should be provided by an external model.
The non-physical behavior of the Corcos wavenumber spectrum induced by the questionable hypothesis of separation of variables has been recognised for a long time and more appealing expressions have been given by Smol'yakov and Tkachenko [32] and Mellen [20]. The expression given by Mellen is now quite popular with its simple analytical expressions in both space and wavenumber domains; its formula for the wavenumber spectra reads:

$$\widetilde{\Phi}_{pp}(\mathbf{k},\omega) = \frac{1}{2\pi}\frac{U_c^2}{\omega^2}\frac{(\alpha\beta)^2}{\left[(\alpha\beta)^2+\beta^2\left(U_ck_1/\omega-1\right)^2+\left(\alpha U_ck_2/\omega\right)^2\right]^{3/2}} \tag{4}$$

The various models for the wavenumber-frequency spectrum due to Chase involve up to 7 adjustable coefficients when extrapolated to cover both the hydrodynamic (incompressible) region and the acoustic domain, see for example Howe [15]. Its form

limited to the hydrodynamic domain, depending on only 4 adjustable coefficients is:

$$\tilde{\Phi}_{pp}(\mathbf{k},\omega) = \frac{U_c^2}{\omega^2}\cdot\frac{1}{4\pi^2\Phi(\omega)}\cdot\frac{\rho^2U_\tau^3\delta^3}{\left[(k_+\delta)^2+1/b^2\right]^{5/2}} \cdot\left[C_M(k_1\delta)^2+C_T(k\delta)^2\frac{(k_+\delta)^2+1/b^2}{(k\delta)^2+1/b^2}\right] \tag{5}$$

where

$$k_+{}^2 = (\omega - U_c k_1)^2/(hu_\tau)^2 + k^2$$

$$M = U_\infty/c_0 \ll 1; k \gg \omega/c_0; \omega\delta/U_\infty > 1$$

The adjustable coefficients have been fixed by comparison with experiments and the recommended values are

$$b \approx 0.75,\ C_M \approx 0.1553,\ C_T \approx 0.0047,\ h \approx 3$$

C_M and C_T correspond to the contributions to wall pressure fluctuations of the shear and self terms respectively.

1.2 Which Characteristics Have to Be Measured or Modeled?

What we have to measure or model is of course function of the application considered, for instance the focus might be put on vibroacoustic or aeroacoustic matters. However beside the 1-point usual quantities, rms value of pressure fluctuations and frequency spectrum, in most of the applications it is mandatory to estimate 2-point quantities. Depending on the application it can be better to use one of the following quantities, which are theoretically equivalent: 2-point space-time correlations, 2-point space-frequency cross-spectra or wavenumber-frequency spectra. The relations between these quantities are reminded below (the brackets designate ensemble averaging, and statistical homogeneity is implied):

$$R_{pp}(\mathbf{r},\tau) = \langle p(\mathbf{x},t)\,.\,p(\mathbf{x}+\mathbf{r},t+\tau)\rangle\ ;\ \mathbf{r} = (r_1,r_2) \tag{6}$$

$$S_{pp}(\mathbf{r},\omega) = \frac{1}{2\pi}\int_{-\infty}^{+\infty} R_{pp}(\mathbf{r},\tau).\exp(i\omega\tau)\,d\tau \tag{7}$$

$$\Phi_{pp}(\mathbf{k},\omega) = \frac{1}{(2\pi)^2}\int_{-\infty}^{+\infty}\int_{-\infty}^{+\infty} S_{pp}(\mathbf{r},\omega).\exp(-i\mathbf{k}.\mathbf{r})\,d\mathbf{r} \tag{8}$$

The $2D$ wavenumber spectrum is usually obtained in this way as simultaneous measurements are not available on the whole plane; should it be the case, a $3D$ direct space-time Fourier Transform can be first performed, followed by ensemble (or time) averaging. Note than often only $1D$ arrays aligned with the flow direction are used. In such a case the $1D$ wavenumber-frequency spectrum is computed through a 1D Fourier transform along the stream-wise separation r_1; this 1D spectrum integrates the contributions of all transverse wavenumbers:

$$\Phi_{pp}(k_1, \omega) = \frac{1}{2\pi} \int_{-\infty}^{+\infty} S_{pp}(r_1, \omega). \exp(-ik_1.r_1)\, dr_1 = \int_{-\infty}^{+\infty} \Phi_{pp}(\mathbf{k}, \omega) dk_2 \quad (9)$$

This function is not to be confused with the cut along the longitudinal axis of the $2D$ spectrum, $\Phi_{pp}(k_1, k_2 = 0, \omega)$.

The three $2D$ expressions listed above share exactly the same information on the wall-pressure field but for modeling purpose or for numerical simulation one of these can be more suited than the others. Usually, the wavenumber-frequency spectrum is preferred for academic applications in vibroacoustics such as the excitation of a flat plate by a TBL for instance. The cross-spectrum, on the other hand, is often better suited for industrial applications since it enables to take into account a slightly non homogeneous load, at least in an approximate way. With the wavenumber-frequency approach, the influence of the characteristics of the vibrating structure (i.e. dispersion curve of bending waves or modal frequencies) and of the model of pressure fluctuations are clearly shown and we will follow this approach hereafter.

Let us first demonstrate the influence of choosing one model or another on the wavenumber-frequency spectra in the low wavenumber, or subconvective, region, that is for longitudinal wavenumbers much lower than the convective wavenumber $k_c = \omega / U_c$, U_c being the convection velocity which takes values in the range of 60 to 80% of the mean (external) flow velocity. The following characteristics are taken to match those of a flow regime experimentally studied at ECLyon during the SONOBL project: $U_\infty = 75\,\mathrm{m\,s^{-1}}$, $U_c = 0.75 U_\infty$, $\delta = 2.4\,\mathrm{cm}$ (see details on the SONOBL project in Sect. 2.1 below). Four models (by Corcos, Chase, Smol'yakov and Mellen) that do not take into account possible acoustic contributions around the acoustic wavenumber, are shown in Fig. 1. Around the convective peak, all models give similar results but on each side of this wavenumber (and especially in the low wavenumber region) they differ considerably, with differences up to 30 dB; as one can expect this will often induce very different responses of the flow-excited vibrating structures.

An example inspired by the work of Maxit [19] is chosen to illustrate this point. Figure 2 shows the frequency response (panel acceleration) of a simply supported plate subjected to TBL fluctuations modeled using Corcos and Chase approaches (in this case the Mellen formulation gives results close to those obtained with the Chase model; note that in order to facilitate reference to [19] in which a different definition of Fourier transforms has been used, the TBL spectra used in the computation have been multiplied by $4\pi^2$ relative to formulas (3) and (5). The plate characteristics

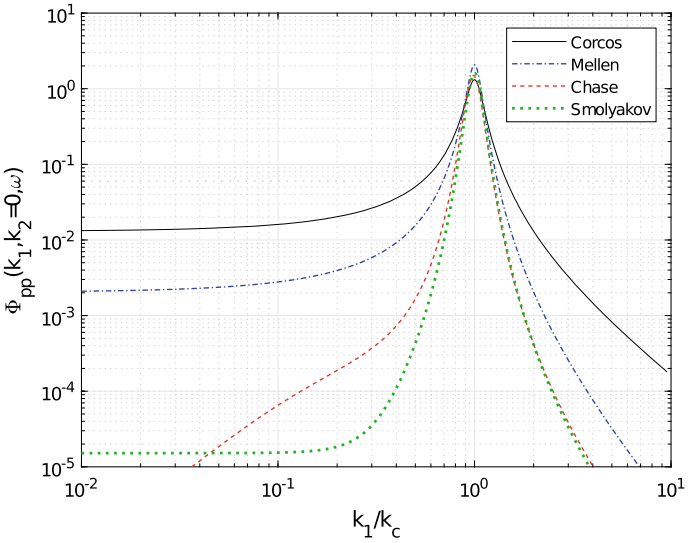

Fig. 1 Comparison of four 2D wavenumber-frequency spectra, cut along $k_2 = 0$, $\widetilde{\Phi}_{pp}(k_1, k_2 = 0, \omega)$. The spectra are plotted against the longitudinal wavenumber, non-dimensionalized on the convective wavenumber $k_c = \omega / U_c$

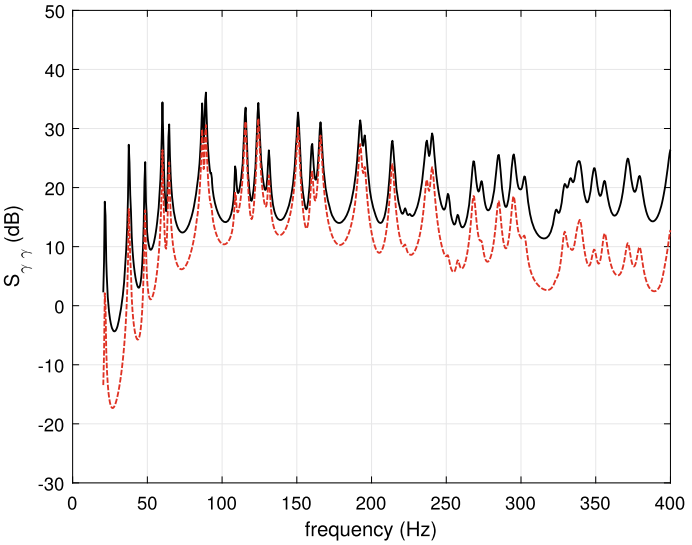

Fig. 2 Acceleration power spectral densities of a simply supported panel submitted to a TBL load simulated using the wavenumber-frequency spectra models due to Corcos (in plain) and Chase (in dashed)

are those used in [19], except for the plate's thickness taken here as 4 mm instead of 3 mm. Around the hydrodynamic coincidence frequency (the frequency for which the flexural wavenumber of the plate is equal to the turbulent convective wavenumber; in the present application $f_c \approx 65$ Hz), the curves are reasonably close but at lower frequencies and more clearly at higher frequencies, considerable differences are noted, the Corcos formulation giving results 10 dB higher than the other two models. This is due to the fact that the Corcos wavenumber spectrum is much higher than the other ones both in the subconvective and in the superconvective regions. It is common knowledge that the Corcos model does in fact strongly overestimates the levels in the subconvective region, which influences mostly the panel's response for frequencies greater than the hydrodynamic coincidence frequency. However there still is an open debate on what the correct spectral values are, especially in the subconvective region, and this justifies the continued efforts directed to developing new accurate measurements devices and numerical simulations for wall-pressure fluctuations.

1.3 How to Actually Measure These Quantities

Measuring wall-pressure fluctuations is still a challenge, even for 1-point measurements; one of the main difficulties is linked to the small turbulent wavelengths which have to be resolved by the sensors, whatever the technology used. The finite size of the sensor acts like a spatial low-pass filter and thus the high frequency part of the spectrum (associated to small turbulent structures) is difficult to measure precisely. This has been recognised for a long time and corrections have been first proposed by Corcos [8]. Figure 3 shows the Corcos correction which has to be applied when using a standard 1/8 in microphone and a remote sensor under pin-hole with a very small sensing surface ($D = 1$ mm) used in the SONOBL experiments. In this figure we also show the effect, on this correction, of the a priori choice made for the cross-correlation function (Corcos vs Mellen). Should one consider that acceptable correction requires that the difference be no more than $10 - 15$ dB and that the effect of the correlation model be negligible, the maximum reachable value of the dimensionless frequency would be around $\omega.r/U_c = 2.5$. In terms of dimensional frequencies, in a case taken from the SONOBL experiment ($U_\infty = 45\,\mathrm{m\,s^{-1}}$, $\delta = 3$ cm), spectra measured by a classical flush mounted 1/8 in microphone are thus limited to frequencies lower than 10 kHz (afterwards the influence of the a priori correlation model is important), while use of a the remote microphone permits an estimation of the spectrum up to 50 kHz. Therefore, the use of sensors with a very small sensing area is often mandatory; one drawback is the necessity of making a precise calibration of the device, which can be cumbersome when numerous sensors are used for array measurements. These small-size sensors also have a second utility: 2-point measurements with very small separation distances are only possible with such sensors, which is important to correctly estimate cross-correlations which rapidly decrease with the separation distance at medium and high frequency.

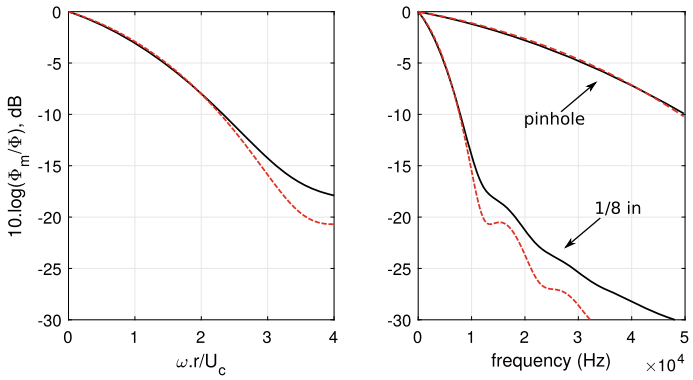

Fig. 3 Influence of the microphone diameter on its frequency response to TBL fluctuations. The difference in dB between the true value Φ, and the size-filtered one Φ_m is plotted as a function of the angular frequency ω normalized by the sensor radius r and the convection velocity U_c (at left) and as a function of frequency f at right for an experimental configuration studied in the SONOBL experiment (at right). Two diameters of sensors have been considered and the influence of the a priori choice of the TBL cross-correlation model (Corcos in plain and Mellen in dashed) is illustrated

Measuring 2-point quantities can be done with several techniques. The most simple one is to use only two microphones and progressively increase the distance between them along a line or two directions as done for example in Panton and Robert [23]. Arrays of sensors are now commonly used, although measurements are made along only one or two lines most of the time, typically along the mean flow direction and across it. The main difficulty is to resolve both short and long wavelengths; if both the hydrodynamic contribution and the acoustic contribution are to be measured at relatively low speeds, a large range of separations between sensors needs to be covered. Indeed, a typical acoustic wavelength is for example ten times larger than the most energetic hydrodynamic one when $U_c = 34\,\mathrm{m\,s^{-1}}$. This imposes the use of a very large number of sensors, and this in general precludes simultaneous measurements on a plane. For example, simultaneous measurements have been performed with transducers along a line which is then rotated to obtain the $2D$ quantities in a second step [2, 28] or using a spiral array which is also rotated to correctly discretise the measurement plane [18]. Note however that the advent of low cost MEMS microphones is changing the situation (permitting $2D$ simultaneous measurements and direct evaluation of wavenumber spectra) even if there are still issues linked to the relatively limited number of sensors, their size and dynamic range for high speed applications, see for example Bremner et al. [3].

In any case, the use of a periodic arrangement is not the best choice as this results in a large number of redundant distances between the sensors. The necessity to respect the Shannon-Nyquist criterion, that is choosing a distance between adjacent sensors lower than half the minimum energetic wavelength present in the flow to avoid wavenumber aliasing, would dramatically increase that number. Two important

indicators of array performance to look at are the maximum distance between sensors (normalized by the maximum wavelength of interest) and the size of its co-array. The former dictates the resolution of the array, i.e. the width of the main lobe of its Point Spread Function and the latter represents the number of different distances between all pairs of sensors of the array. When designing an array, a typical goal is to maximize this number for a fixed number of sensors by using an irregular arrangement; as a result a reasonably low level of secondary lobes can be obtained for a large frequency range, and this without any aliasing, see Underbrink [33]. Let us take the simple example of a 2D periodic square array containing 64 sensors; they are only 225 points in the associated co-array, while the maximum possible is 4033. Strategies to optimize array responses have been developed in the aeroacoustics community where spiral arrays are now very common; a 63-element Dougherty spiral array will for example permit to obtain the theoretical maximum value of 3907 points in the co-array. The SONOBL experiment [28] uses a line array of 63 unevenly placed remote microphones; the minimum distance is a little higher than 1 mm, and the maximum one is equal to 25 cm. For each angular position, one obtains 1711 different measurement points for estimating cross-correlations and then $2D$ wavenumber spectra via a spatial Fourier transform.

While classical pressure measurements using microphones are the norm, it should be noted that field methods using different physical principles can be used in specific applications. One of the most promising technique is uPSP (unsteady Pressure Sensitive Paint), see the review paper by Gregory et al. [12]. PSP measurements are based on an optical technique for determining surface pressure distributions: the painted surface is continuously illuminated and the intensity of light emitted by luminescent molecules in the paint is recorded. The response of fast PSP enables spatially resolved measurements at rates of several kilohertz. At the moment the use of uPSP is limited to applications in which the dynamic fluctuations are very high, typically flows at high Mach number. A very interesting example of the use of uPSP to obtain $2D$ wavenumber spectra on a launcher mock-up has recently been published by Panda et al. [22].

1.4 Deconvolution of Wavenumber Spectra

It is difficult to obtain good resolution of wavenumber spectra especially in the subconvective region and even more so in the acoustic domain. The size of the main lobe of an array is of the order of the inverse of its diameter; as an example, in the SONOBL experiment the disk diameter is $D = 25$ cm, which corresponds to the acoustic wavelength at a frequency of approximately 1.4 kHz. It is then clear that it will be very difficult to obtain detailed information on the acoustic part of the wavenumber spectrum below say 2 kHz by a direct exploitation of the Fourier transform of the measured cross-correlations. One possibility often used to enhance the low frequency resolution of arrays is to perform deconvolution, which roughly speaking, corresponds to the inversion of the PSF of the array. In the aeroacoustic community several methods

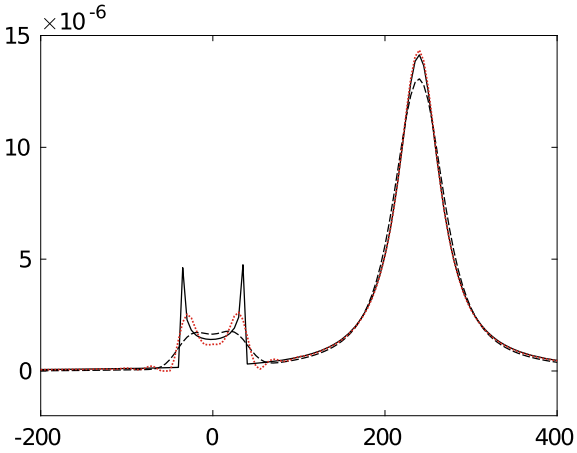

Fig. 4 Deconvolution of array response using the DAMAS2 algorithm. The theoretical array response for synthetic data combining a Corcos-type aerodynamic field with a diffuse acoustic field, computed for a frequency of 2 kHz, is plotted in continuous black line; the black dashed line shows the simulated SONOBL array response and the deconvolved response is plotted in dotted line. Levels are normalised by a unitary point spectra

are routinely used to improve the resolution of arrays used to localise distant acoustic sources, but application to surface arrays is rare. The first attempt seems to be due to Ehrenfried and Koop [9] and a recent detailed paper has been presented in the 2016 BeBec conference by Haxter [14]. As the wavenumber-frequency spectrum is a positive quantity by definition, use of the DAMAS algorithm introduced by Brooks et al. [4] or its variants is particularly adapted as it is based on a deconvolution algorithm with a positivity constraint. Figure 4 shows an example of applying DAMAS deconvolution on a synthetic field obtained by adding a diffuse acoustic field contribution to Corcos-type wall-pressure fluctuations, with the SONOBL array configuration, see Prigent et al. [26] for more details. At a frequency of 2 kHz, the cut at $k_2 = 0$ of the $2D$ wavenumber spectrum is clearly better defined in the acoustic domain with two distinct maxima at the acoustic wavenumber, $k_1 = \pm k_0$, than the curve resulting from the simple spatial Fourier transform, where only a broad hump around $k_1 = 0$ is visible; on the other hand, the convective peak is only marginally modified. Other examples together with a first application to experimental data are given in [26]. Of course the approach has limitations in part due to noisy data, but there is a hope this could enable a much better assessment of the subconvective and acoustic domains.

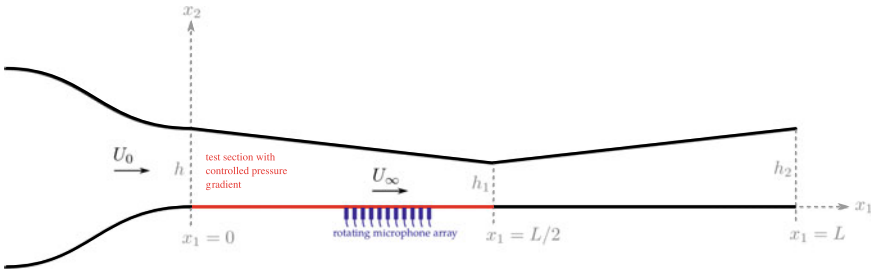

Fig. 5 Schematic sectional view of the SONOBL set-up. The flow speed at the position of the 63 microphones' array varies from a few $\mathrm{m\,s^{-1}}$ up to approximately $100\,\mathrm{m\,s^{-1}}$; the upper wall angle can be varied to obtain zero, adverse, and favorable gradients. Channel height and length are $h = 0.25\,\mathrm{m}$ and $L = 16\mathrm{h}$

2 A Short Description of Three Experiments Conducted at ECLyon and Illustration of Typical Results

In the second part of this paper, we present an illustration of experimental results obtained on wall-pressure measurements, mostly based on 1D or 2D array processing. A first experimental campaign was focused on the behavior of TBL submitted to external pressure gradients. In the second one measurements were performed on a full-scale mock-up of a business jet, while the third one was focused on the extraction of fan noise from wall-pressure measurements dominated by aerodynamic fluctuations.

2.1 The SONOBL Experiment

By SONOBL experiment we refer to an experimental set-up first developed during a project funded by the French National Agency for Research (ANR) and then frequently enhanced. The initial experimental set-up is fully described in Salze et al. [28]. The goal of the conducted experiments is to investigate the influence of an external mean pressure gradient on the wall-pressure wavenumber-frequency spectra induced by a TBL. Several values of the external pressure gradient are obtained by changing the ceiling angle of a rectangular channel flow. Wall-pressure spectra and cross-spectra are measured for zero-, adverse-, and favorable- pressure gradient TBL for a range of flow speeds extending up to a maximum Mach number of 0.3 (a recent modification will give access to higher flow speeds up to $M = 0.7 - 0.8$). An array of non-uniformly distributed pin-hole remote microphones is mounted on a rotating disk to give access to $2D$ wavevector-frequency spectra, with a view of separating TBL aerodynamic and acoustic contributions. A schematic description of the set-up is given in Fig. 5, while photos of the wind tunnel and the measurement disk are shown in Fig. 6.

Fig. 6 Different views of the SONOBL set-up; at left, overall view of the wind tunnel inside ECLyon anechoic room; at right, a photo of the rotating disk supporting *B&K* microphones and a line array of 63 irregularly distributed remote microphones; in the center, a bottom view of the disk is shown and the tubing used to eliminate any reflective waves is apparent

Typical results for point-spectra are displayed on Fig. 7 in a non-dimensional form, using external variables (external flow velocity, displacement thickness and wall shear stress). On the top part of the figure, spectra measured for zero pressure gradient and for velocities varying from 11 to 45 m s^{-1} are displayed. In dashed lines the prediction of the spectra using Goody's formula is also shown. The agreement is very satisfactory, except maybe for the lowest frequencies at the highest velocity. Note that with the external variables representation, a good collapse of the spectra is obtained for all velocities at low frequency. With internal variables, on the contrary, a good collapse would have been obtained at high frequency at the expense of a large dispersion at low frequency, see [28] for details. On the bottom part of the figure, the influence of the external pressure gradient is clearly shown; a favorable gradient reduces the level in the low frequency region without changing the high frequency slope, whereas an adverse pressure gradient both increases the low frequency content and completely changes the spectrum shape in the medium and high frequency range. Differences in friction velocities and displacement thicknesses used in the non-dimensional representation have only a slight influence and do not explain the large differences observed in the spectral shapes when the external gradient is varied. With an adverse pressure gradient, the predictions of the Goody's model are completely off, and while the Rozenberg model [27] does a better job, the agreement is far from being excellent, see for example Juvé et al. [16]. On-going work is currently performed to construct a large data base covering a larger range of parameters; it will offer the opportunity to construct an empirical model extending the existing ones and to test various models based on RANS computations or on unsteady numerical simulations.

As a final example of the results obtained in the SONOBL set-up, Fig. 8 shows the $2D$ wavenumber spectra of wall-pressure fluctuations, estimated at a velocity of 75 m s^{-1} and for a frequency of 3750 Hz, at left the raw data and at right after applying a DAMAS2 deconvolution, see details in [26]. The convective region is very well defined with a maximum around $k_1 = 420\,\mathrm{m}^{-1}$, which is associated with a convective velocity of the order of 75% of the mean flow velocity. More importantly, a significant contribution in the acoustic domain is also clearly seen for wavenumbers

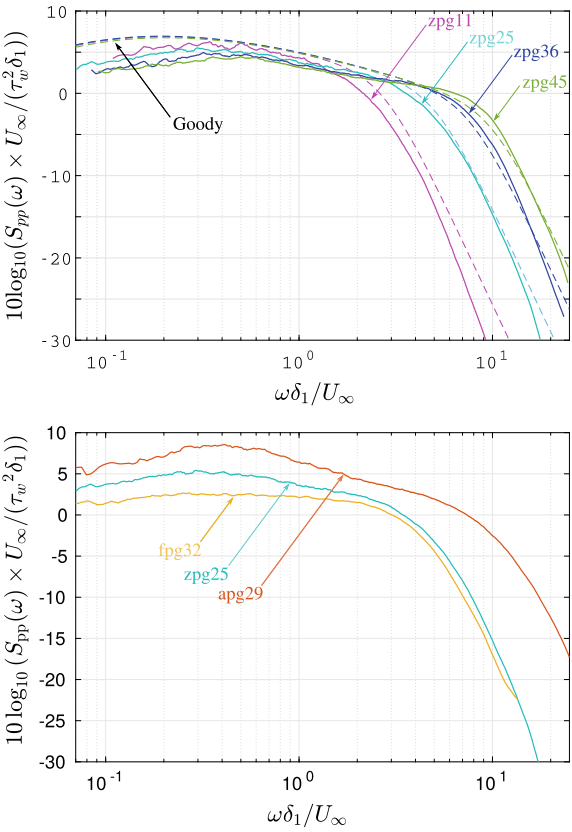

Fig. 7 Wall-pressure spectra measured during the SONOBL experiment. On top, non-dimensionalized spectra using external variables are shown for the zero pressure gradient case and velocities ranging from 11 to 45 m s^{-1}. These spectra are compared to the predictions of the Goody's model (dashed lines). On the bottom part we compare three spectra obtained for different values of the external mean pressure gradient (zero, favorable and adverse)

located inside the acoustic ellipse (corresponding to the acoustic dispersion relation with mean-flow effects taken into account). On the right hand side of the figure, the deconvolved wavenumber spectrum, while somewhat more noisy, permits a clearer view of the acoustic contribution with maximum values concentrated around the elliptic dispersion curve.

2.2 The CANOBLE Experiment

The CANOBLE project (a EU CleanSky2 program) is dedicated to the experimental evaluation of cabin noise induced by turbulent boundary layer excitation. A full-scale mock-up of a Dassault-Aviation business jet has been instrumented for wall-pressure and vibration measurements and installed in a large industrial wind tunnel. The Mach number studied are relatively low (up to $M = 0.2$), the aim being to first calibrate numerical codes in well-controlled conditions; in a second step these codes will

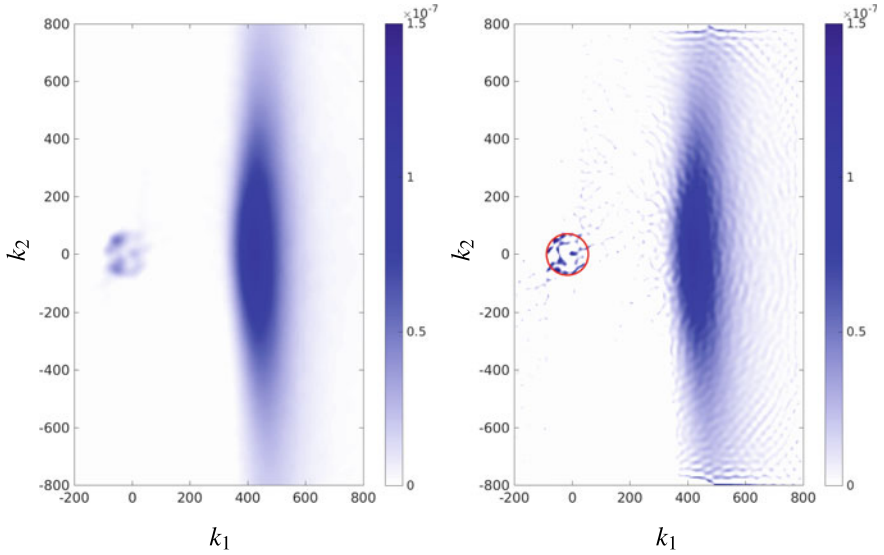

Fig. 8 2D wavenumber spectra measured at a frequency of 3750 Hz and a flow speed of 75 m s^{-1}. At left, the spectrum has been obtained through a classical Fourier transform of the cross-spectra. At right, the result of the deconvolution of the experimental data using DAMAS2 algorithm is shown. The acoustic contribution for wavenumbers inside the acoustic ellipse (red curve) is much better resolved

hopefully provide reliable information for the noise inside cabin and cockpit in cruise conditions. Measurements were conducted in the S2A aeroacoustic wind tunnel; the closed-loop tunnel opens to a semi-anechoic test room with an inlet section of 24 m^2. The mock-up is a full-scale fore part of a business jet; it is 10 m long in total, with the first 6 m true to the airplane geometry, the remainder serving as a tail to streamline the rear end. Static pressure sensors were fitted along some streamlines and two kinds of inserts were instrumented. Panels mimicking the vibrational behavior of the real fuselage were equipped with accelerometers; the noise transmitted through the panels to an internal cavity was also measured. Modules supporting hot wires and microphones arrays were then placed in locations mirroring those of the panels. The three instrumented modules correspond to roof, windscreen and side panels. Wall-pressure measurements were performed using an array of MEMS microphones flush mounted onto a mask fitted to the geometry of the fuselage. Each array is composed of 40 digital microphones non-uniformly distributed on a cross whose main axis is aligned with the local flow direction. Photos of the set-up and microphone array are given in Fig. 9; further details will be found in [25, 30].

The three modules are placed in such positions that, respectively, a nearly zero pressure gradient, a very slight favorable gradient and a mild adverse gradient (on the side panel) were observed (see Fig. 10). Examples of pressure spectra measured at a velocity of 30 m s^{-1} are displayed in the external variables representation on Fig. 11. The spectra associated to ZPG and FPG positions have very similar shapes and

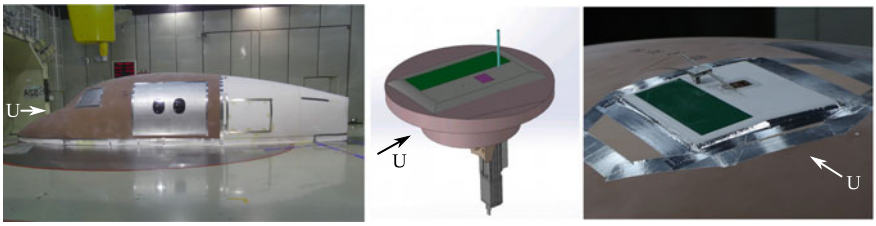

Fig. 9 In the left part of the figure, a photography of the business jet mock-up installed in S2A wind tunnel is shown. In the center and at right are displayed respectively a CAD view of the MEMS array and its implementation on the mock-up (in green: the microphone array; in red: surface hot films; a hot wire traverse is also apparent in the figure at right)

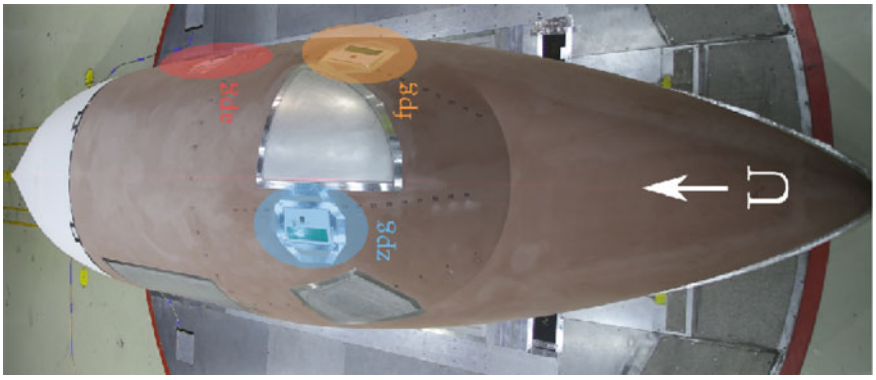

Fig. 10 On this top view of the mock-up, the three instrumented zones are shown, together with an indication of the corresponding type of local mean pressure gradient

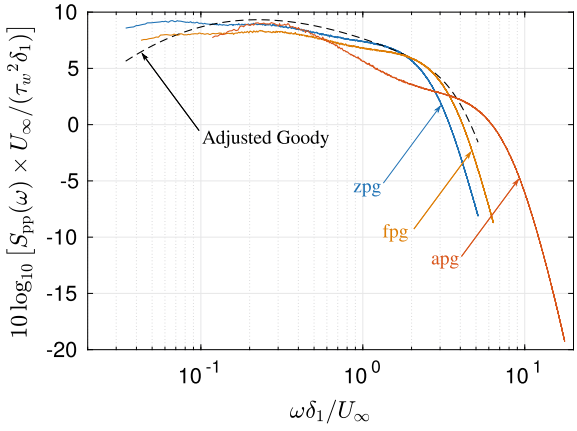

Fig. 11 Normalized wall pressure spectra measured during the CANOBLE experimental campaign and comparison with rms-adjusted Goody's spectrum for the zero pressure gradient position

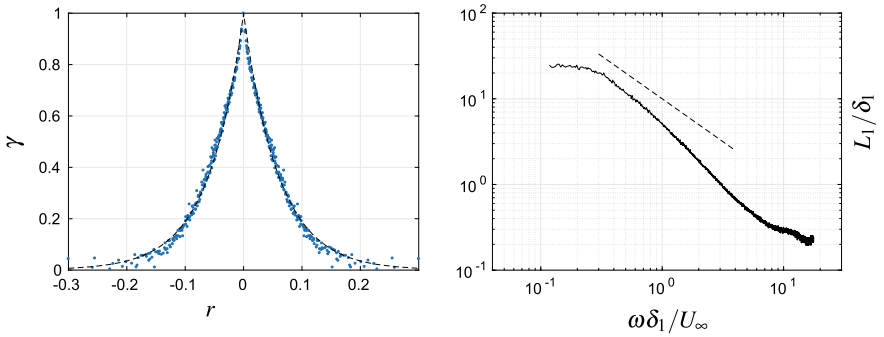

Fig. 12 Examples of the spatial coherence measured during the CANOBLE campaign. At left, spatial evolution of the stream-wise coherence measured for $f = 400\,\text{Hz}$ in APG conditions. At right, evolution with the reduced frequency of the longitudinal integral scale L_1 in APG conditions (δ_1 is the local TBL displacement thickness and U_c the convection velocity). The black dashed line corresponds to an exponential decay of the coherence length as suggested by the Corcos model

levels, which is not surprising as the boundary layers exhibit very similar profiles at these two positions. However the overall shape differs markedly from the predictions of the Goody model (the level was adjusted to match the rms value of measured pressure fluctuations); this may be attributed to the fact that the boundary layer development for these two positions is influenced by the presence of the model's nose and windshield and are not fully developed, but further studies are needed to clarify this point. Module 3, where APG measurements have been performed, is located on the lateral side of the model and the boundary layer is in a more classical state. As it was the case in the SONOBL set-up described above, the spectrum is characterized by two humps at both ends of the mid-frequency range and significant contributions in high frequencies. Beside point-spectra, longitudinal and transverse 2-point coherence functions were also measured, the derived coherence lengths serving as input to a numerical FEM code used to estimate panel vibration and internal radiated noise. An example of such functions is given in Fig. 12; the nearly exponential decrease of the coherence with the separation distance is reminiscent of the classical decay curves of the Corcos model.

Concerning panel vibration and noise radiated inside the internal cavity, the strategy used to compute levels and spectra and compare them to experiments is as follows. A CFD RANS code is used to obtain mean flow local characteristics along the fuselage (local external velocity, boundary layer thickness, friction velocity). For the time being, a simple Corcos model for the coherence functions and a Goody model for the spectra are then informed from the RANS data. A sampling approach in the space/frequency domain is used to compute the response of the structure subject to the load given by the cross-power spectral density matrix. The FEM vibroacoustic model is composed of the structural part and of an acoustic inner cavity; more details can be found in Leneveu et al. [17]. A comparison between computations and measurements is displayed in Fig. 13. For a first attempt, with relatively crude

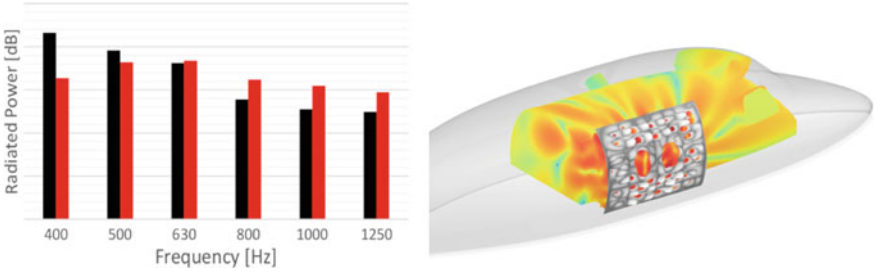

Fig. 13 One-third octave spectra of noise power radiated into the mock-up internal cavity: Comparison between experimental results in black and numerical simulations in red (1 dB per thin graduation). The spatial structure of noise computed inside the cavity at a frequency of 1 kHz is illustrated in the right part of the figure

models, the agreement can be considered as correct. Use of a more elaborate model constructed from the experimental data on the cross-spectra would probably permit to obtain a closer agreement.

2.3 Ducted Fan Noise Extraction from Array Measurements on the Inner Duct Wall

Modal analysis of the internal acoustic field is a common tool for the characterisation of the noise generated by ducted turbofan engines. Experimental campaigns are usually conducted using arrays of microphones flush-mounted on the duct inner walls. They however are sensitive to both the aerodynamic and acoustic pressure fluctuations and it is of interest to separate the two components. As the aerodynamic component is generally of much greater amplitude, extracting the acoustic component can be challenging. Denoising can be done by assuming that the aerodynamic contribution is concentrated along the diagonal of the cross-spectral matrix between the sensors of the array, but a less restrictive approach is based on the use of 1D wavenumber-frequency analysis of a large array of microphones. This approach can be very effective when the mean flow velocity is much lower than the speed of sound. This is illustrated in the following example.

A schematic view of the experimental set-up is given in Fig. 14. This low-Mach number ducted turbofan is equipped at inlet with a Turbulence Control Screen (TCS) and an anechoic termination downstream of fan stage. A digital MEMS array is flush-mounted inside the test-rig duct using a 2D-printed support. The 32 MEMS microphones are irregularly distributed, resulting in a co-array containing 488 elements. Further details can be found in Salze et al. [30]. In Fig. 15, photos of the rig show the exterior part of the set-up, with the TCS and the absorbing wedges of the anechoic environment (at left), and the board supporting the array of MEMS microphones (at right). Except at the blade passage frequency and its harmonics where

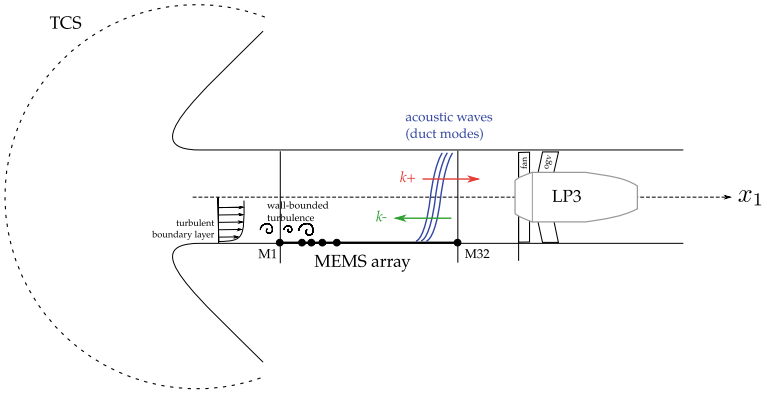

Fig. 14 Sketch of the fan noise rig at ECLyon (LP3 facility)

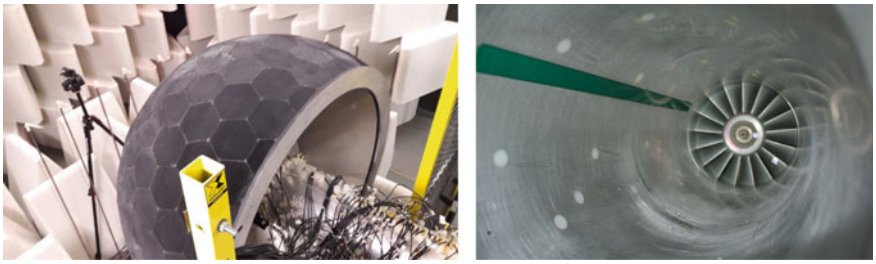

Fig. 15 Left: External view of the fan rig focusing on the Turbulence Control Screen and the absorbing wedges. Right: Internal view of the upstream portion of the duct; the MEMS array board and the rotor vanes of the fan are shown

strong acoustic tones are generated, point-spectra are nearly completely dominated by turbulent fluctuations. Only the use of array processing will be able to extract other noise components. A 1D $k-\omega$ wavenumber-frequency spectrum is displayed on Fig. 16 for a rotational speed of 10,000 rpm and a bulk velocity equal to 29.4 m/s. Except for the very low frequencies, two different regimes are evident. A first contribution is due to the turbulence wall-pressure fluctuations; it is concentrated around the convective wavenumber ω/U_c, $U_c \approx 80\%$ of the bulk velocity, with most of its energy in a frequency range limited to 2 kHz. The second contribution is of acoustic nature with wavenumbers situated in the triangle limited by the lines $\omega/(c+U_c)$ for downstream propagating waves and $-\omega/(c-U_c)$ for upstream propagating waves.

Figure 16 also displays the dispersion curves associated to the first 11 longitudinal duct modes, in dashed lines; these modes are progressively cut-on when the frequency increases. An excellent agreement between the theoretical curves and the experimental map is evident, in particular the appearance of a strong energetic spot at each cut-on frequency.

Another striking feature is that the acoustic energy is for the most part concentrated in negative values of the wavenumber, that is associated to upstream propagat-

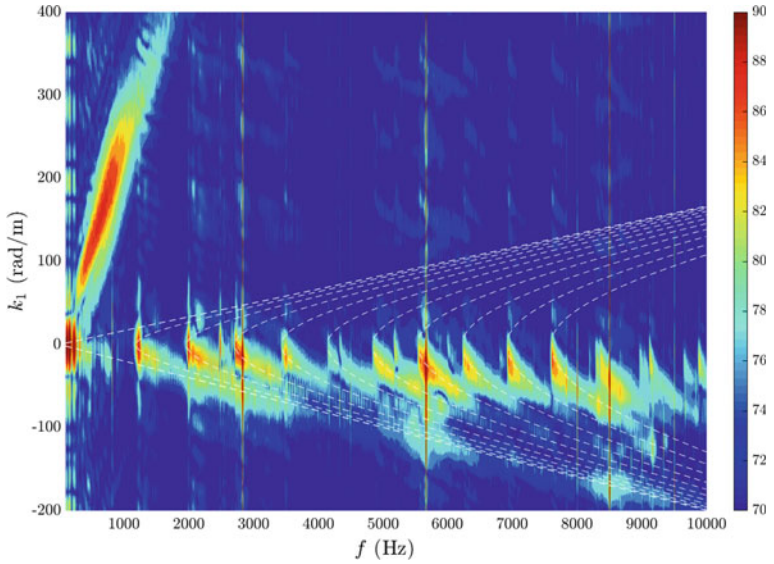

Fig. 16 1D wavenumber spectrum of wall-pressure fluctuations. Colormap of amplitudes (dB scale) is plotted as a function of frequency and axial wavenumber. The convective region and the acoustic one can clearly be distinguished; in dashed white lines, the limits of the acoustic zone and the dispersion curves of the 11 first axial acoustic modes are displayed

ing waves. The array thus essentially observes noise directly generated by the fan, upstream of which it is situated. Downstream propagating waves are generated by reflections at the inlet section, but in the frequency range of interest it is essentially non-reflecting; only a very small amount of upstream propagating waves are reflected back in the duct and recorded by the array.

The beauty of the wavenumber frequency approach is that it is nevertheless possible to estimate this small contribution by filtering this map and reconstructing the associated point-spectra. It consists of the integration at a given frequency over all the k_1 contributions in a well selected zone. This is illustrated in Fig. 17. The black line (1) corresponds to the basic-global- point spectrum: as said above, and except for three pure tones at BPFs, it is dominated by turbulent wall-pressure fluctuations. The green curve (2) shows the spectrum obtained by summing the contributions of wavenumbers between 0 and $-\omega/(c - U_c)$ for each frequency. This spectrum corresponds to the noise generated by the fan in the upstream direction. Smaller pure tones are now visible and, more importantly, the broadband noise component is now identified, some 10 to 20 dB below the turbulent wall-pressure contribution. The successive appearance of cut-on modes is also clearly apparent. Moreover, the contribution of downstream propagating acoustic waves reflected by the duct inlet, obtained by filtering between $k = 0$ and $k = \omega/(c + U_c)$, can also be extracted (see red line (3)). It exhibits a shape very similar to that of direct waves, but with a

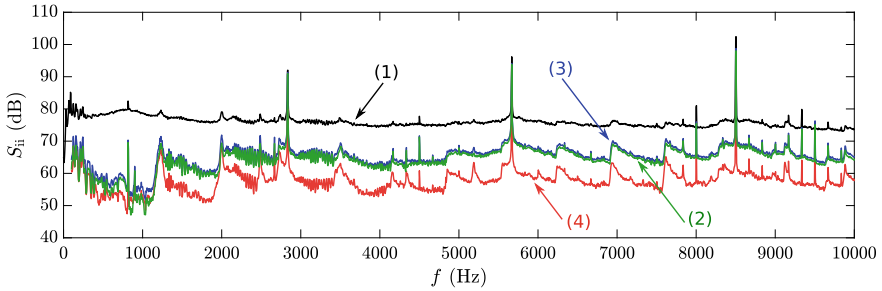

Fig. 17 Wall-pressure spectra measured or reconstructed from the filtering and k_1 integration of the 1D wavenumber spectrum. Curve (1): Direct measurement largely dominated by aerodynamic fluctuations; curve (2): Noise directly generated by the fan as extracted from the upstream array; curve (4): Estimation of the spectrum associated to acoustic waves reflected back in the duct from the inlet section; curve (3) corresponds to the total noise generated by the fan in upstream as well as in downstream directions

level reduced by nearly 10 dB, demonstrating the very good dynamic range of the wavenumber-frequency measurements in this configuration.

3 Conclusion

Measuring wall-pressure fluctuations beneath turbulent flows is still a challenge nearly sixty years after the publication of the first pioneering work by Willmarth, Corcos and others. Recent advances in the technology of microphones (i.e. MEMS microphones) pave the way for the use of arrays consisting of a very large number of sensors: several hundreds could become the norm in the near future. With such arrays the direct measurement of space-time cross-correlations and 2D wavevector-frequency spectra could be easily performed and used, for example, for filtering out the acoustic component from the aerodynamic one or vice versa. Development of deconvolution methods enhancing the wavenumber resolution of such arrays will also be of great help to obtain more precise results in the subconvective and acoustic regions. These experimental data, together with high-fidelity unsteady numerical simulations like those conducted by Cohen and Gloerfelt [7], will be of great utility for the calibration of existing models or the development of new ones which are crucial for industrial applications where the flow is far from being homogeneous.

Acknowledgements This work was performed within the framework of the Labex CeLyA of Université de Lyon, operated by the French National Research Agency (grant ANR-10-LABX-0060/ ANR-16-IDEX-0005). National and EU funding respectively through the SONOBL grant ANR-2011-BS09-065-02 and the CANOBLE CleanSky2 program (H2020-CS2-CFP02-2015-01, project id 717084) is also acknowledged.

References

1. B.M. Abraham, W.L. Keith, Direct measurements of turbulent boundary layer wall pressure wavenumber-frequency spectra. J. Fluids Eng. **120**, 29–39 (1998)
2. B. Arguillat, D. Ricot, C. Bailly, G. Robert, Measured wavenumber-frequency spectrum associated with acoustic and aerodynamic wall pressure fluctuations. J. Acoust. Soc. Am. **128**(4), 1647–1655 (2010)
3. P. Bremner, C. Todter, S. Clifton, Sideglass turbulence and noise sources measured with a high resolution surface pressure array. SAE 2015–01-2325 (2015)
4. T.M. Brooks, W.M. Humpfreys, A deconvolution approach for the mapping of acoustic sources (DAMAS) determined from phased microphone arrays. J. Sound Vib. **294**, 856–879 (2006)
5. D. Casalino, A.F.P. Ribero, E. Fares, S. Nölting, Latice Boltzmann aeroacoustic analysis of the LAGOON landing-gear configuration. AIAA J. **52**(6), 1232–1248 (2014)
6. D.M. Chase, The character of the turbulent wall pressure spectrum at subconvective wavenumbers and a suggested comprehensive model. J. Sound Vib. **112**, 125–147 (1987)
7. E. Cohen, X. Gloerfelt, Influence of pressure gradients on wall pressure beneath a turbulent boundary layer. J. Fluid Mech. **838**, 715–758 (2018)
8. G.M. Corcos, Resolution of pressure in turbulence. J. Acoust. Soc. Am. **35**(2), 192–199 (1963)
9. K. Ehrenfried, L. Koop, Experimental study of pressure fluctuations beneath a compressible turbulent boundary layer, in *AIAA Paper 2008–2800* (2008)
10. M. Goody, Empirical spectral model of surface pressure fluctuations. AIAA J. **42**(9), 1788–1794 (2004)
11. W.R. Graham, A comparison of models for the wavenumber-frequency spectrum of turbulent boundary layer pressures. J. Sound Vib. **206**(4), 541–565 (1997)
12. J.W. Gregory, H. Sakaue, T. Liu, J.P. Sullivan, Fast pressure-sensitive paint for flow and acoustic diagnostics. Annu. Rev. Fluid Mech. **43**, 303–330 (2014)
13. G. Grasso, P. Jaiswal, H. Wu, S. Moreau, M. Roger, Analytical models of wall-pressure spectrum under a turbulent boundary layer with adverse pressure gradient. J. Fluid Mech. **887**, 1007–1062 (2019)
14. S. Haxter, Improving the DAMAS2 results for wavenumber-space beamforming. BeBeC 2016–D8 (2016)
15. M.S. Howe, *Acoustics of Fluid-Structure Interactions* (Cambridge University Press, New-York, 1998)
16. D. Juvé, M. Berton, E. Salze, Spectral properties of wall-pressure fluctuations and their estimation from computational fluid dynamics, in *Flinovia-Flow Induced Noise and Vibration Issues and Aspects*, ed. by E. Ciappi, S. De Rosa, F. Franco, J.-L. Guyader, S.A. Hambric (Springer, Cham, 2015)
17. R. Leneveu, M. Rissmann, A. Alonso, E. Salze, Full-scale cabin noise from turbulent boundary layer excitation. Part 2: vibroacoustic modelling and transmission, in *ICSV26*, Montréal (2019)
18. C. Marchetto, L. Maxit, O. Robin, A. Berry, Experimental prediction of the vibration response of panels under a turbulent boundary layer excitation from sensitivity functions. J. Acoust. Soc. Am. **143**, 2954–2964 (2018)
19. L. Maxit, Simulation of the pressure field beneath a turbulent boundary layer using realizations of uncorrelated wall plane waves. J. Acoust. Soc. Am. **140**(2), 1268–1285 (2016)
20. R.H. Mellen, Wave-vector filter of turbulent flow. J. Acoust. Soc. Am. **95**(3), 1671–1673 (1994)
21. S. Oerlemans, M. Fisher, T. Maeder, K. Kögler, Reduction of wind turbine noise using optimized airfoils and trailing-edge serrations. AIAA J. **47**(6), 1470–1481 (2009)
22. J. Panda, N.H. Roozeboom, J.C. Ross, Wavenumber-frequency spectra on a launch vehicle model measured via unsteady pressure-sensitive paint. AIAA J. **57**(5), 1793–1800 (2019)
23. R. Panton, G. Robert, The wavenumber-phase velocity representation for the turbulent wall-pressure spectrum. J. Fluids Eng. **116**(3), 477–483 (1994)
24. L.J. Peltier, S.A. Hambric, Estimating turbulent boundary layer wall-pressure spectra from CFD RANS solutions. J. Fluids Struct. **23**, 920–937 (2007)

25. S.L. Prigent, E. Salze, E. Jondeau, C. Bailly, R. Leneveu, Full-scale cabin noise from turbulent boundary layer excitation. Part 1: wall-pressure measurements and analysis, in *ICSV26*, Montréal (2019)
26. S.L. Prigent, E. Salze, C. Bailly, Deconvolution of the wavenumber-frequency spectra of wall pressure fluctuations. AIAA J. **58**(1), 164–172 (2020). https://doi.org/10.2514/1.J058203
27. Y. Rozenberg, G. Robert, S. Moreau, pressure spectral model including the adverse pressure gradient effects. AIAA J. **50**(10), 2168–2179 (2012)
28. E. Salze, C. Bailly, O. Marsden, E. Jondeau, D. Juvé, An experimental characterization of wall pressure wavevector-frequency spectra in the presence of pressure gradients, in *AIAA Paper 2014–2909* (2014)
29. E. Salze, C. Bailly, E. Jondeau, D. Juvé, Experimental investigation of the influence of a mean pressure gradient on the turbulent wall pressure fluctuations, in *ICSV22*, Florence (2015)
30. E. Salze, E. Jondeau, A. Pereira, S.L. Prigent, C. Bailly, A new MEMS microphone array for the wavenumber analysis of wall-pressure fluctuations: application to the modal investigation of a ducted low-Mach number stage, in *AIAA Paper 2019–2574* (2019)
31. M. Slama, C. Leblond, P. Sagaut, A Kriging-based elliptic extended anisotropic model for the turbulent boundary layer wall pressure spectrum. J. Fluid Mech. **840**, 25–55 (2018)
32. A.V. Smol'yakov, V.M. Tkachenko, Measurement of turbulent fluctuations, in *The Measurement of Turbulent Fluctuations*, ed. by P. Bradshaw (Springer, Berlin, 1983)
33. J.R. Underbrink, Aeroacoustic phased arrays testing in low speed wind tunnels, in *Aeroacoustic Measurements*, ed. by T. Mueller (Springer, Berlin, 2002)
34. W.W. Willmarth, C.E. Wooldridge, Measurement of the fluctuating pressure at the wall beneath a thick boundary layer. J. Fluid Mech. **14**, 187–210 (1962)

Source Modeling

Chase Versus Corcos TBL Loading

Richard G. DeJong

Abstract The Corcos and Chase models for the wavenumber-frequency spectrum of fluctuating pressures in a turbulent boundary layer (TBL) fluid flow are compared. Some of the recent improvements to these basic models (in order to agree better with the measured data) are reviewed. In particular some suggested revisions to Chase's derivations to improve that model are presented. Also discussed are the coupling of the TBL pressures to structural vibrations, and areas were further research is needed.

1 Introduction

The need for an accurate wavenumber-frequency spectrum of the fluctuating pressure in turbulent fluid flow is illustrated by the example shown in Fig. 1 which compares the frequency spectra of the exterior turbulent pressure and resulting vibration measured on a side window of a vehicle in a wind tunnel. As the wind speed increases the turbulent pressure increases approximately with the fourth power of the speed. However, the window vibration increases at a higher rate. This is seen more clearly in Fig. 2 which compares the ratio of the vibration acceleration to the turbulent pressure for the two wind speeds. For comparison, the ratio obtained using an acoustic loudspeaker source is also shown. The reason this transfer function changes for different pressure source characteristics is because the coupling between fluids and structures depends on the spatial matching of the pressure and vibration fields (as represented by the wavenumber spectrum) and not just on the frequency matching [1].

The spatial matching for this case is illustrated in Fig. 3. For flow speeds, U_c, and bending wave speeds, c_b, less than the speed of sound, c_o, the dominant fluctuating TBL pressure wavelength is shorter than the acoustic pressure wavelength. (Typically for most frequencies of interest in transportation vehicles the structural bending vibration wavelength is in between the other two.) Represented in the wavenumber domain (the Fourier transform of the spatial domain), there is a spread in the wavenumber

R. G. DeJong (✉)
Engineering Department, Calvin University, 1712 Knollcrest Circle, Grand Rapids, MI 49546, USA
e-mail: dejong@calvin.edu

E. Ciappi et al. (eds.), *Flinovia—Flow Induced Noise and Vibration Issues and Aspects-III*, https://doi.org/10.1007/978-3-030-64807-7_2

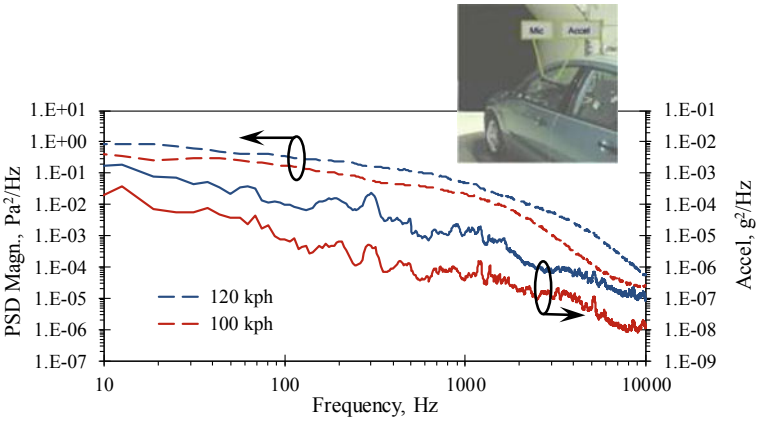

Fig. 1 Comparison of the measured frequency spectra for turbulent pressure (- - -) and window vibration (———) on a vehicle side window in a wind tunnel at flow speeds of 100 and 120 kph

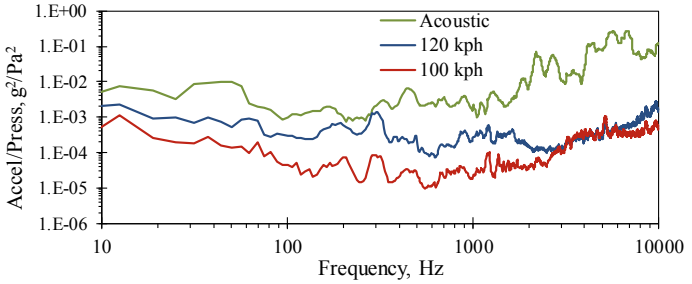

Fig. 2 Comparison of acceleration/pressure transfer function for turbulent and acoustic pressure excitations

content around the dominant wavenumber, $\boldsymbol{k}$, given by frequency, ω, divided by the free field wave speed. The coupling between a pressure and the vibration is given by the product of the two wavenumber spectra. The major contributions are indicated by the three shaded areas in Fig. 3.

Mathematically, the structural acceleration spectrum, $S_{aa}(\omega)$, at any frequency, ω, is given by the integral over the product of the wavenumber spectra [1]

$$(\rho_s h_s)^2 \eta_s S_{aa}(\omega) = \int \Phi_{oo}(k,\omega)|\Psi_s(k,\omega)|^2 dk + \int \Phi_{pp}(k,\omega)|\Psi_s(k,\omega)|^2 dk \tag{1}$$

where ρ_s, h_s, and η_s are the density, thickness and damping loss factor, respectively, of the structure. $\Phi_{oo}(\boldsymbol{k}, \omega)$ and $\Phi_{pp}(\boldsymbol{k}, \omega)$ are the wavenumber-frequency spectra of the acoustic and turbulent pressure fields, respectively, and $\Psi_s(\boldsymbol{k}, \omega)$ is the magnitude of the Fourier transform of the structural mode shape. For the acoustic pressure

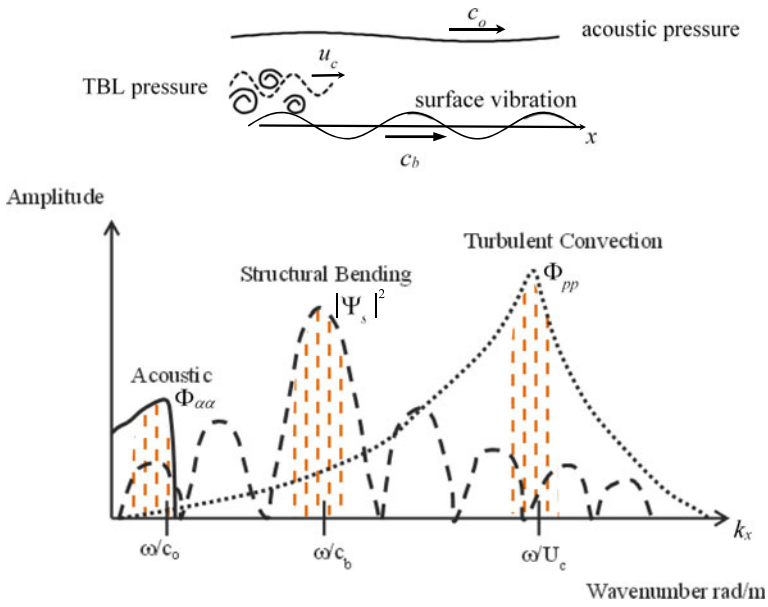

Fig. 3 Spatial matching of wave fields as represented by their wavelengths in the flow direction (x) and by the magnitudes of their wavenumber spectra along k_x for the case of $U_c < c_b < c_o$

excitation the major contribution to the integral is the acoustic spectrum peak times the low wavenumber side band level of the structural mode shape. For the turbulent pressure excitation there are two major contributions; 1. The turbulent spectrum peak (called the convective ridge) times the high wavenumber side band level of the structural mode shape, and 2. The structural mode shape peak times the low wavenumber level of the turbulent spectrum. The latter of these is the most challenging to compute because of the difficulty in determining the low wavenumber content of the turbulent spectrum. (If $c_b < U_c$, Eq. 1 still applies with their peaks reversed.)

Two of the more frequently used models for the wavenumber-frequency spectrum of the TBL pressure are by Corcos [2] and Chase [3]. Analytically both are based on the divergence of the Navier–Stokes equation for steady, incompressible flow, which in Cartesian indicial notation is

$$\frac{\partial^2 p}{\partial x_i^2} = -2\rho_o\left(\frac{\partial U_i}{\partial x_j}\right)\left(\frac{\partial u_j}{\partial x_i}\right) - \rho_o\frac{\partial^2\left(u_i u_j - \langle u_i u_j\rangle\right)}{\partial x_i \partial x_j} = -\mathrm{T}_M - \mathrm{T}_T \qquad (2)$$

where p is the fluctuating pressure, ρ_o is the ambient fluid density, U is the mean velocity, and u is the fluctuating velocity. The brackets $<\cdots>_t$ indicate the mean value over time, t. $\mathrm{T_M}$ and $\mathrm{T_T}$ represent the gradients of the Reynolds stresses ($\rho_o u^2$). The M term is called *mean-shear* (or fast or direct) because it represents the immediate interaction between the gradient of the mean flow (proportional to a shear

stress) and the fluctuating velocities. The M term is generally considered to be the dominant contribution to the surface pressure. The T term is called *pure-turbulent* (or slow or indirect) because it represents the secondary interaction between the various fluctuating velocity gradients.

Solving Eq. 2 is challenging because the velocity products make it a highly non-linear problem analytically and they are difficult to measure. Several assumptions are made to simplify Eq. 2 for steady flow over a rigid flat surface in the $\mathbf{X} = (x_1, x_3)$ plane at $x_2 = 0$:1. the boundary layer flow is two dimensional with the mean flow in the x_1 direction ($U_2 = 0 = U_3$ and the boundary layer thickness, δ, is constant over the area of interest), 2. $dp/dx_1 = 0 = dp/dx_3$, 3. $dp/dx_2|_{x2=0} = 0$. This allows the pressure response at the surface ($x_2 = 0$) to be evaluated by the integral of the Reynolds stress terms over the half space, $\mathbf{Y} = (y_1, y_2 > 0, y_3)$

$$p(\mathbf{X},\ t) = \frac{1}{2\pi} \iiint \frac{\mathrm{T}_M + \mathrm{T}_T}{|\mathbf{X} - \mathbf{Y}|} d^3\mathbf{Y} \tag{3}$$

The following sections review the Corcos and Chase models and some of the improvements made to them in order to agree better with measured data. Also discussed are the coupling of the TBL pressures to structural vibrations, and areas were further research is needed.

2 Corcos Model

Corcos used dimensional analysis of Eq. 3 and measurements [2, 4] of the spatial correlation function of the surface pressure, i.e. in the $(x_1, 0, x_3)$ plane,

$$R_{pp}(\xi, \eta, \tau) = < p(x_1, 0, x_3, t) p(x_1 + \xi, 0, x_3 + \eta, t + \tau) >_t \tag{4}$$

and its frequency transform the cross spectral density, $\Gamma_{pp}\ (\xi, \eta, \omega)$, to conclude there is a dominate similarity with the non-dimensional variables, $\omega\xi/U_c$ and $\omega\eta/U_c$., where U_c is the convection velocity. In particular, using correlation measurements in the stream-wise direction (x_1) (shown in Fig. 4) and in the cross-wise direction (x_3), Corcos determined a similarity relationship

$$\Gamma_{pp}(\xi,\ \eta,\ \omega) = S_{pp}(\omega)\ A\left(\frac{\omega\xi}{U_c}\right) B\left(\frac{\omega\eta}{U_c}\right) e^{i\omega\xi/U_c} \tag{5}$$

where $S_{pp}(\omega) = \Gamma_{pp}\ (0, 0, \omega)$ is the single point frequency spectrum of the surface pressure. This is an attractive formulation because it is separable in the space coordinates making it amenable to analytical representations of the coupling to structural vibration modes (at least for the separable modes of a simply supported, uniform cylinder or rectangular plate). Also, if A and B are given as decaying exponentials, $A = \exp(-\alpha\ \omega|\xi|/U_c)$, $B = \exp(-\beta\ \omega|\eta|/U_c)$, (which agree reasonably well with

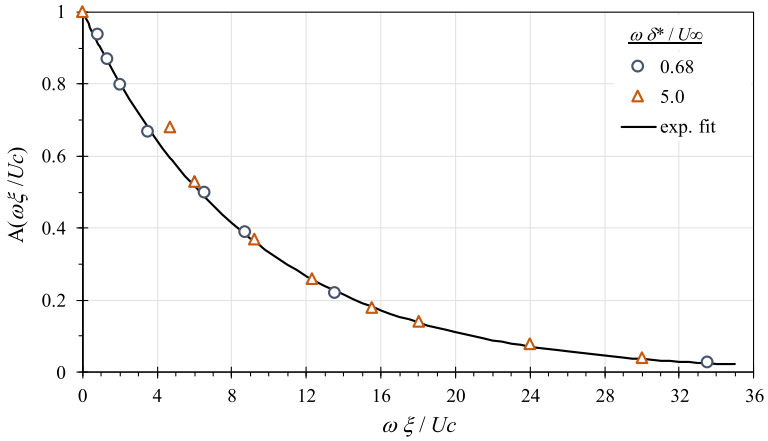

Fig. 4 Normalized stream-wise correlation function $A(\omega\xi/U_c)$, Ref. [2, 4]

measured data in the mid to high frequency range, $\omega > U_c/\delta$), the model represents a decaying wave propagating in the x_1 direction. Transforming to the wavenumber domain, $\mathbf{K} = (k_1, k_3)$, gives a wavenumber-frequency spectrum of the form

$$\Phi_{pp}(\mathbf{K},\ \omega) = S_{pp}(\omega)\frac{\alpha/\pi k_c}{\left[\alpha^2 + \left(1 - k_1/k_c\right)^2\right]}\frac{\beta/\pi k_c}{\left[\beta^2 + \left(k_3/k_c\right)^2\right]} \tag{6}$$

where $k_c = \omega/U_c$. $\alpha \sim 0.1$ and $\beta \sim 0.8$ are empirically determined constants.

Corcos acknowledged [5] that the similarity relationship in Eq. 5 only holds for Strouhal numbers $\omega\ \delta^*/U_o > 0.5$, where δ^* is the boundary layer displacement thickness (approximately $\delta/8$) and U_o is the free stream velocity (see, for example, Fig. 5). By definition the normalized correlation function goes to 1 as ξ goes to zero, but the data shows this is not true as ω goes to zero for a non-zero ξ. There appears to be a source of decorrelation (by dispersion or diffusion) in the turbulent pressures at low frequencies (long wavelengths) that is independent of frequency.

Another limitation of the basic Corcos model is that it over predicts the low wavenumber content of the wavenumber-frequency spectrum, Φ_{pp} ($\mathbf{K}$, ω), given by Eq. 6 as compared to measurements (shown in Fig. 6 for $k_3 = 0$). Several modifications to this model have been proposed to fix this problem. Ffowcs Williams [6] proposed applying the similarity formulation to the velocity source terms in Eq. 3. This gives a $k^2 = k_1^2 + k_3^2$ dependence to Φ_{pp} ($\mathbf{K}$, ω) at low wavenumbers which agrees with the (incompressible fluid) theoretical results of Phillips [8] and Kraichnan [9] that the wavenumber spectrum should go to zero as $k \rightarrow 0$. The modified Corcos model is then

$$\Phi_{pp}(\mathbf{K}, \omega) = S_{pp}(\omega)\left[a_o k^2/k_c^4\right]/[\alpha^2 + (k_1/k_c - 1)^2]\,[\beta^2 + (k_3/k_c)^2] \tag{7}$$

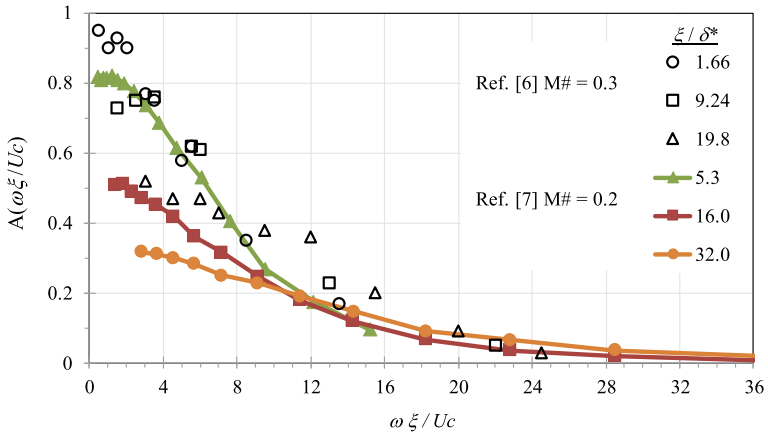

Fig. 5 Normalized stream-wise correlation function $A(\omega\xi/U_c)$ [6, 7]

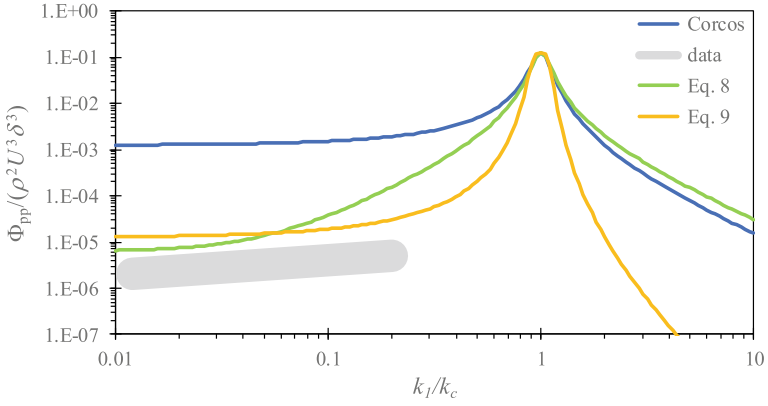

Fig. 6 Comparison of TBL surface pressure wavenumber-frequency spectra ($k_3 = 0$), data [10, 11]

with a_o an experimentally determined constant. Since the measured data does not go to zero as $k \rightarrow 0$, Ffowcs Williams suggested this was due to compressibility effects and included a correction term for low, but non-negligible, Mach number, $M_o = U_o/c_o$, where c_o is the speed of sound. A further correction to Eq. 7 is needed to roll off the high wavenumber content in order to agree with measured values of the frequency spectrum $S_{pp}(\omega)$ [12]. This modified Corcos model is then

$$\Phi_{pp}(\mathbf{K},\ \omega) = S_{pp}(\omega)\frac{\left[\left(a_o k^2/k_c^2 + a_1 M_o^2\right)\right]/\left(1 + k^2/k_c^2\right)k_c^2}{\left[\alpha^2 + \left(1 - k_1/k_c\right)^2\right]\left[\beta^2 + \left(k_3/k_c\right)^2\right]} \tag{8}$$

which is also shown in Fig. 6 (for $a_1 = 0.25$ and $M_o = 0.1$).

More recently Caiazzo et al. [13] has noted that the basic Corcos model is equivalent to a Butterworth filter of order 1. By generalizing that model to higher order filters the following result is obtained

$$\Phi_{pp}(\mathbf{K},\ \omega) = S_{pp}(\omega)\frac{A_n \big/ \pi k_c}{\left[\alpha^{2n} + \left(1 - k_1 \big/ k_c\right)^{2n}\right]}\frac{B_m \big/ \pi k_c}{\left[\beta^{2m} + \left(k_3 \big/ k_c\right)^{2m}\right]} \tag{9}$$

where n and m are the filter orders in the streamwise and spanwise directions, respectively, with derived constants A_n and B_m. This is also shown in Fig. 6 for $n = 2$ and $m = 1$. The filter orders can be modified to fit measured data.

Even with these modifications a more significant problem with the Corcos model can be seen in Fig. 7 where the contours of Φ_{pp} ($\mathbf{K}$, ω) values in the (k_1, k_3) plane are shown at a given frequency, compared to measured and CFD data. The separable

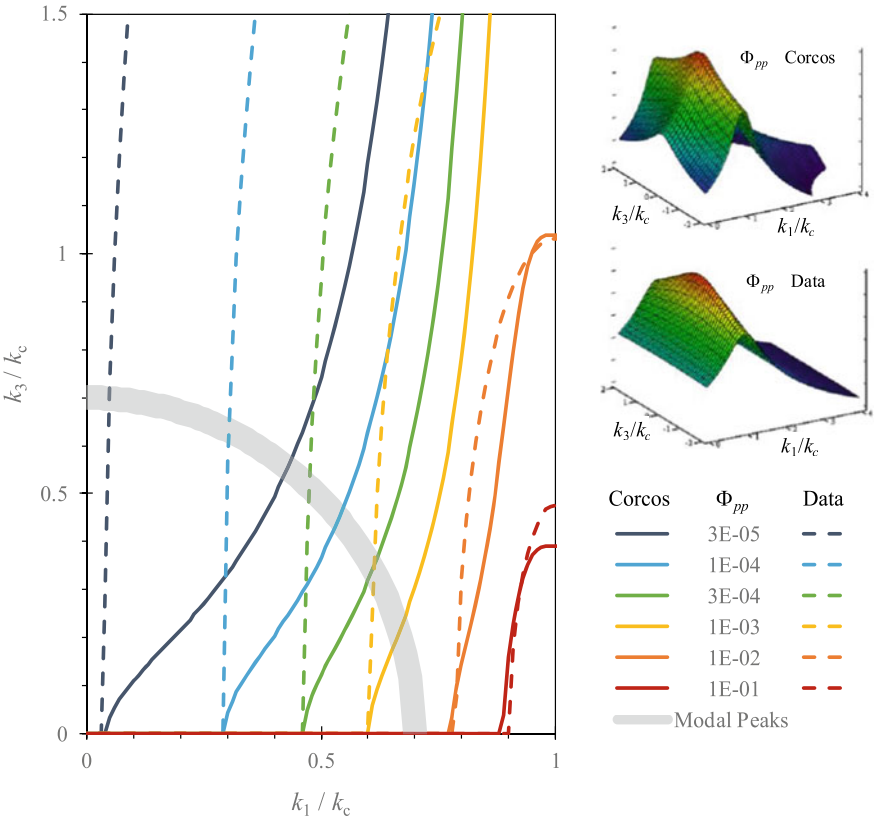

Fig. 7 Comparison of TBL surface pressure wavenumber-frequency spectra, Φ_{pp}, for modified Corcos model [13] and curve fit to data: CFD Ref. [14]; measurements Refs. [10, 15] using parameters for 40 m/s air flow excitation of a 1 mm thick steel plate at 500 Hz

product form of the Corcos model gives contours with a hyperbolic shape, whereas the measured data have an elliptical shape. Also shown are the loci of typical vibration modes of a flat plate at this frequency ($U_c < c_b$). Other than for the vibration modes with k_3 near zero, the peaks in the vibration modal responses are in a region where the Corcos model under estimates the measured pressure data. Therefore, using the Corcos model, with parameters adjusted to fit the streamwise and spanwise data values, it will underpredict the vibration levels of a coupled plate.

3 Chase Model

Chase developed his model by assuming a two-dimensional boundary layer over a rigid flat surface, in the $\mathbf{X} = (x_1, x_3)$ plane, with a constant thickness, δ, in the x_2 direction (normal to the surface). The wavenumber-frequency spectrum is then found by transforming the correlation functions of the velocity products in Eq. 3 to the planar wavenumber, $\mathbf{K} = (k_1, k_3)$, and frequency domains.

$$\Phi_{pp}(\mathbf{K},\ \omega) = \int_0^\infty dx_2 \int_0^\infty dx_2^{'} \left[\frac{e^{-k\left(x_2 + x_2^{'}\right)}}{k^2} \right] [\phi_{\mathrm{M}}(k_1,\ \zeta,\ k_3,\ \omega) + \phi_{\mathrm{T}}(k_1,\ \zeta,\ k_3,\ \omega)] \tag{10}$$

where

$$\phi_{\mathrm{M}}(k_1,\ \zeta,\ k_3,\ \omega) = \frac{1}{(2\pi)^3} \int \int_{-\infty}^{\infty} \int \left\langle \mathrm{T}_M \mathrm{T}_M^{'} \right\rangle_t e^{i(\mathbf{K}\cdot\mathbf{R} - \omega\tau)} d\mathbf{R}\, d\tau \tag{11a}$$

$$\phi_{\mathrm{T}}(k_1,\ \zeta,\ k_3,\ \omega) = \frac{1}{(2\pi)^3} \int \int_{-\infty}^{\infty} \int \left\langle \mathrm{T}_{\mathrm{T}} \mathrm{T}_{\mathrm{T}}^{'} \right\rangle_t e^{i(\mathbf{K}\cdot\mathbf{R} - \omega\tau)} d\mathbf{R}\, d\tau \tag{11b}$$

with $\zeta = (x_2\, x'_2)^{1/2}$, $\mathbf{R} = (x'_1 - x_1, x'_3 - x_3)$, $\tau = t' - t$, and the cross terms of the M and T velocity products are considered negligible.

Chase used measurements of the fluctuating velocity correlations to estimate the functional shapes of ϕ_{M} and ϕ_{T}. One set of data is from Morrison and Kronauer [16] who used hot wire anemometers to measure the correlation of the fluctuating velocity, u_1, in the axial direction of flow in a pipe. (The cylindrical coordinates, (x_1, $r_o - r$, $r\theta$), of the pipe are assumed to approximate the Cartesian coordinates, (x_1, x_2, x_3), of flow over a flat plate, where the pipe radius approximates the boundary layer thickness, δ.) These measurements indicate that the wavenumber transforms of the velocity correlation in the (x_1, x_3) plane at different distances, x_2, above the rigid surface can be represented by the similarity relation

$$k_1 k_3 \phi_{u1u1}(k_1, x_2, k_3) \;=\; F(kx_2)\phi_0(k_1, k_3) \tag{12}$$

with $k = (k_1^2 + k_3^2)^{1/2}$. Chase used the approximations

$$\mathrm{F}(kx_2) \;=\; \mathrm{c}_1(kx_2)^2\exp(-2kx_2) \tag{13a}$$

$$\phi_0(k_1, k_3) \;=\; \mathrm{c}_2 u_t^2/[1 \;+\; (\mathrm{c}_3\nu/u_\tau)^2((\gamma k_1)^2 \;+\; k_3^2)]^2 \tag{13b}$$

where $u_\tau = (\tau_w/\rho_o)^{1/2}$ is the friction velocity, τ_w is the wall shear stress, ν is the kinematic viscosity, and γ is a measure of the anisotropy of the wavenumber spectrum. Figure 8 compares Eqs. 13a and 13b with particular constants, c_1, c_2, c_3, to the measurements. A key feature of this similarity model is that it uses a functional form proportional to the wavenumber vector magnitude $k = ((\gamma\ k_1)^2 + k_3^2)^{1/2}$ (rather than products of separate functions of k_1 and k_3 as Corcos assumed).

Chase generalized and simplified the similarity relation of Eq. 12 to model ϕ_M and ϕ_T. Considering first the M term, $\mathrm{T_M} = 2\rho_o\ (\partial U_1/\partial x_2)\ (\partial u_2/\partial x_1)$, he used the log-layer formula for U_1 giving $\partial U_1/\partial x_2 = 2.5\ u_\tau/x_2$. For $\phi_{u2u2}(k_1, x_2, k_3, \omega)$ he assumed an isotropic ($\gamma = 1$) form $\rho_o^2\ u_\tau\ \zeta^{\ 3}\ \mathrm{e}^{-k\ (x2+x'2)}\ \mathrm{e}^{-(x2+x'2)/b\delta}$, where the last term is added to account for the roll off of u_2 beyond some fraction, $b \sim 0.5$, of the boundary layer thickness, δ, and the assumption is made that $\nu\ k/u_\tau << 1$ (since Chase focused on the low wavenumber region). Integrating over x_2, x_2', Eq. 10 gives (with a combined constant C for the overall amplitude)

$$\Phi_\mathrm{M}(\mathbf{K}, \omega) \;=\; \mathrm{C}\rho_o^2 u_\tau^3 k_1^2/k^2[k \;+\; 1/b\delta]^3 \simeq \mathrm{C}\rho_o^2 u_\tau^3 k_1^2/[k^2 \;+\; 1/(b\delta)^2]^{5/2} \tag{14}$$

where the second form is used to be consistent with the sum-of-squares form for the wavenumber vector.

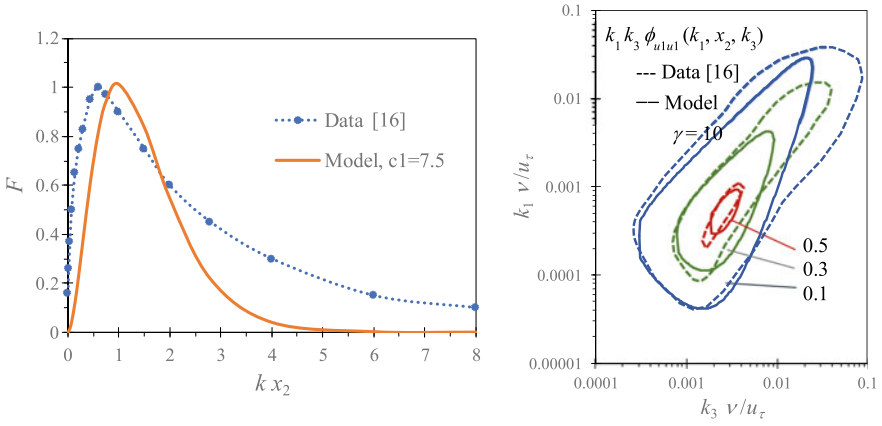

Fig. 8 Comparison of measured and modeled similarity functions for the axial velocity cross-spectra; c1 = 7.5, c2 = 0.001, c3 = 400

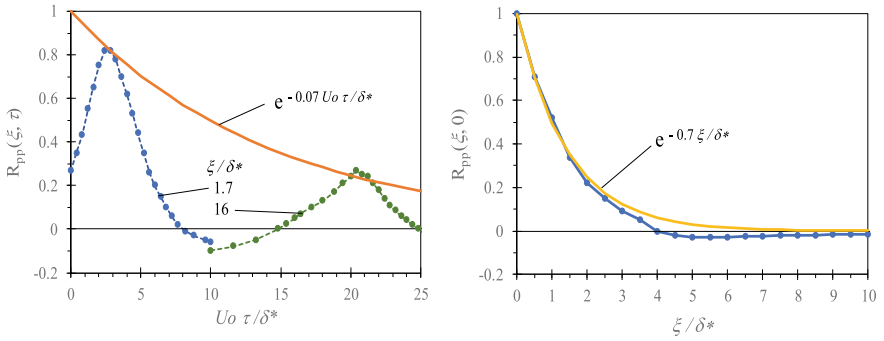

Fig. 9 Comparison of pressure correlation, R_{pp}, in convecting and fixed reference frames. $U_o = 30\ u_t$, data —•—, —•— from Ref. [6]

Equation 14 represents the reference frame of the fluid traveling at a convection velocity, U_c. To convert to the fixed reference frame of the surface two modifications are made. First, the Taylor hypothesis [17] assumes a frozen eddy structure of the convected fluctuating velocities and converts the frequency, ω, to $\omega - U_c\ k_1$ in the transforms of Eqs. 11a and 11b. Second, because the actual eddy structure decays slowly with time, a time delay, τ, in the convected frame is equivalent to a spatial separation, $h\ u_\tau\ \tau$, in the fixed frame, with h a constant (see Fig. 9). This corresponds to a fixed frame wavenumber shift of $\omega/h\ u_\tau$. Chase [3] assumes these two effects "add roughly in quadrature" (sum-of-squares) and models this in Eq. 14 by converting k^2 to $k^2 + (\omega - U_c\ k_1)^2/(h\ u_\tau)^2$ with $h \sim 3$.

The basic Chase model for the mean-shear component of the TBL pressure wavenumber-frequency spectrum is then

$$\Phi_{\mathrm{M}}(\mathbf{K},\ \omega) = C_{\mathrm{M}} \frac{\rho_o^2 u_\tau^3 k_1^2}{\left[k_1^2 + k_3^2 + \mu^{-2}(k_c - k_1)^2 + 1/(b\delta)^2\right]^{5/2}} \tag{15}$$

where $\mu = h\ u_\tau / U_c \sim 0.16$.

For the pure-turbulence component, $\mathrm{T_T} = \rho_o\ \partial^2[u_i\ u_j - <u_i\ u_j>_t]/\partial x_i \cdot \partial x_j$, Chase had much less data to work with. However, he assumed the same isotropic similarity relation held for all $u_i\ u_j$ terms so the velocity correlation spectra are given by $\phi_{uiuj}(k_1, x_2, k_3, \omega) = \rho_o^2\ u_\tau^3\ \zeta^3\ \mathrm{e}^{-k\,(x2+x'2)}\ \mathrm{e}^{-(x2+x'2)/b\delta}$, which gives the result

$$\Phi_{\mathrm{T}}(\mathbf{K},\ \omega) = C_{\mathrm{T}} \frac{\rho_o^2 u_\tau^3 \left(k_1^2 + k_3^2\right)}{\left[k_1^2 + k_3^2 + \mu^{-2}(k_c - k_1)^2 + 1/(b\delta)^2\right]^{5/2}} \tag{16}$$

The constants μ and b may be different in the M and T components, but Chase finds no evidence for substantial differences. Therefore, Eqs. 15 and 16 can be combined to give

$$\Phi_{pp}(\mathbf{K},\ \omega) = C\frac{\rho_o^2 u_\tau^3\left(k_1^2 + a\,k_3^2\right)}{\left[k_1^2 + k_3^2 + \mu^{-2}(k_c - k_1)^2 + 1\big/(b\delta)^2\right]^{5/2}} \tag{17}$$

where $C = C_M + C_T$ and $a = C_T/C$. (Chase uses $C \sim 0.15$, $a \sim 0.33$.)

Figure 10 compares the basic Chase model with measured data in the low wavenumber region for $k_3 = 0$. The Chase model under predicts the data.

Chase made several attempts to remedy this [18, 19] but recent measurements [10, 11] have shown the need for a revised model. This can be accomplished by reassessing the early assumption of a uniform boundary layer thickness. In reality the boundary layer grows approximately as $\delta = 0.16\, x_1/\mathrm{Re}_{x1}^{1/7}$ where the Reynolds number $\mathrm{Re}_{x1} = U_o\, x_1/\nu$ (see Fig. 11).

New kinetic energy enters the boundary layer at a rate proportional to the growth of the momentum thickness, $\theta \sim \delta/10$. An approximation for the added pressure is

$$p \sim \rho_o U_c^2 d\theta/dx_1 \sim \rho_o u_t^2 \mathrm{Re}_{x1}^{-1/7} \tag{18}$$

which has a very weak dependence on x_1. Approximating the wavenumber-frequency Fourier transform of p^2, for $k_1 < k_c$, gives

$$\Phi_{pp}(\mathbf{K}, \omega) \sim \rho_o^2 u_\tau^4/\omega k_c^2 \tag{19}$$

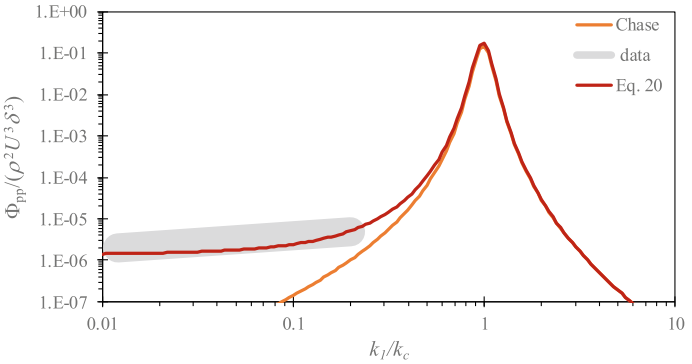

Fig. 10 Comparison of TBL surface pressure wavenumber-frequency spectra ($k_3 = 0$), data [10, 11]

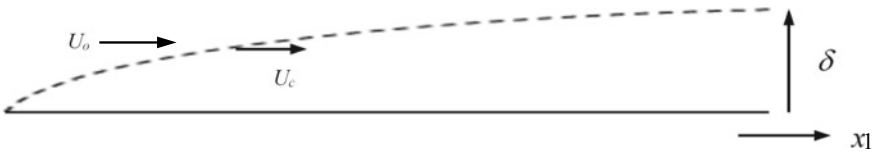

Fig. 11 Illustration of the growth of the boundary layer with the injection of kinetic energy

which can be included in Eq. 17 by adding a term to k_1^2 in the numerator proportional to k_c^2. A fit to the data in Ref. [20] gives a $1/\pi^{\,2}$ scaling for the k_c^2 term, thus

$$\Phi_{pp}(\mathbf{K},\ \omega) = C\frac{\rho_o^2 u_\tau^3\left(k_1^2 + a\,k_3^2 + k_c^2/\pi^2\right)}{\left[k_1^2 + k_3^2 + \mu^{-2}(k_c - k_1)^2 + 1/(b\delta)^2\right]^{5/2}} \tag{20}$$

Figure 12 compares measurements of the low wavenumber TBL pressure spectrum in both wind and water tunnels (using the vibration response of flat plates as a wavenumber filter [1, 20]) to the curve fit of Eq. 20.

Values from Eq. 20 are also included in Fig. 10 and show good agreement with the low wavenumber data.

The single point TBL pressure frequency spectrum, $S_{pp}(\omega)$, is obtained from Eq. 20 by integrating over k_1 and k_3. In the Chase model S_{pp} and Φ_{pp} are, therefore, interrelated (unlike the Corcos model where the wavenumber and frequency spectra are separate). The measurements shown in Figs. 1 and 2 clearly indicate that S_{pp} and Φ_{pp} are interrelated. The result of the integration is (for $\mu^{\,2} \ll 1$)

$$S_{pp}(\omega) = 2\pi C\frac{\rho_o^2 u_\tau^4}{\omega}\frac{1.1 + a\left[1 + \left(U_c/\omega b\delta\right)^2\right]}{\left[1 + \left(U_c/\omega b\delta\right)^2\right]^{3/2}} \tag{21}$$

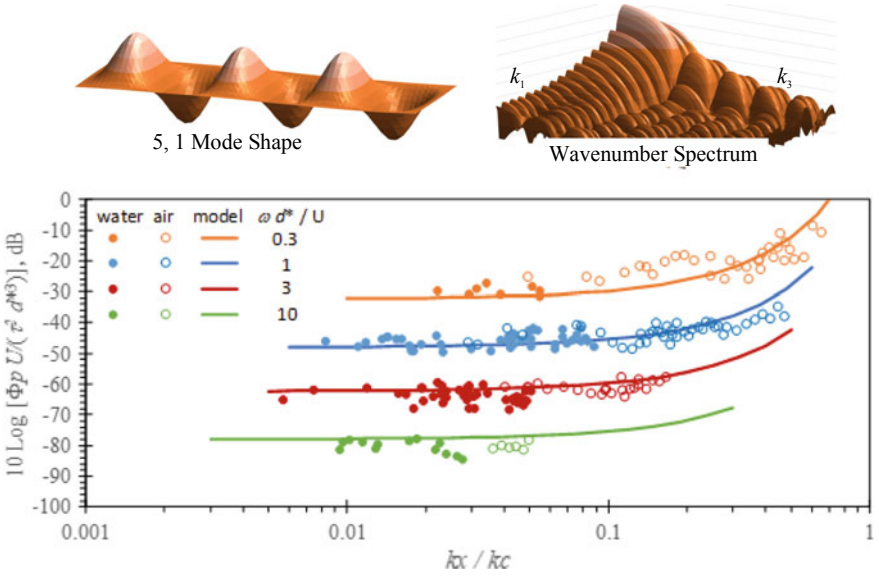

Fig. 12 Comparison of measured low wavenumber pressure spectra with model using Eq. 20

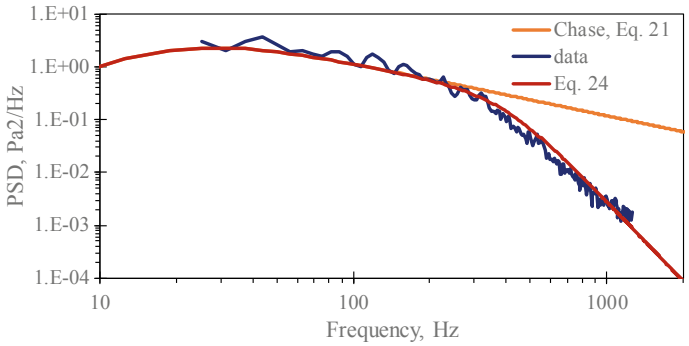

Fig. 13 Comparison of TBL single point frequency spectra (water tunnel, $U_c = 2.5$ m/s)

Figure 13 compares the frequency spectrum given by Eq. 21 (with $C = 0.15$, $a = 0.33$, $b = 0.5$) with measured data. It can be seen that the Chase model over predicts the measured levels at high frequency.

Chase acknowledged this [3] and suggested a means for correcting this: remove the assumption that $\nu\, k/u_\tau \ll 1$ in the form of $\phi_{u2u2}(k_1, x_2, k_3, \omega)$ used to derive Φ_M $(\mathbf{K}, \omega)$ in Eq. 14. Then

$$\phi_{u2u2}(k_1, x_2, k_3, \omega) \;=\; u_\tau \zeta^3 \mathrm{e}^{-k(x2+x'2)} \mathrm{e}^{-(x2+x'2)/b\delta} / [1 \;+\; (6k\nu/u_\tau)^2]^2 \qquad (22)$$

Since the additional term is independent of x_2, it is simply adjoined to the equations for Φ_{pp} $(\mathbf{K}, \omega)$

$$\Phi_{pp}(\mathbf{K},\ \omega) = C \frac{\rho_o^2 u_\tau^3 \left(k_1^2 + a\, k_3^2 + k_c^2 / \pi^2\right)}{\left[k_1^2 + k_3^2 + \mu^{-2}(k_c - k_1)^2 + 1/(b\delta)^2\right]^{5/2} \left[1 + \left(6k\nu / u_\tau\right)^2\right]^2} \qquad (23)$$

The integration over k_1 and k_3 is more complex, but to first order in $(6\, k\nu/u_\tau)^2$ the single point pressure spectrum is given by

$$S_{pp}(\omega) = 2\pi C \frac{\rho_o^2 u_\tau^4}{\omega} \frac{1.1 + a\left[1 + \left(U_c / \omega b\delta\right)^2\right]}{\left\{\left[1 + \left(U_c / \omega b\delta\right)^2\right]^{3/2} + \left(3\omega\nu / u_\tau^2\right)^4\right\}} \qquad (24)$$

This result is included in Fig. 13 (with $C = 0.15$, $a = 0.33$, $b = 0.5$) and shows good agreement with the data. It also agrees closely to the result obtained by Goody [21] as follows

$$S_{pp}(\omega) = \frac{3\rho_o^2 u_\tau^4 \left(\omega\delta/U_o\right)^3}{\omega\left\{\left[\left(\omega\delta/U_o\right)^{0.8} + 0.5\right]^{3.7} + \left[1.1\left(u_\tau^2\delta/U_o\nu\right)^{-0.57}\omega\delta/U_o\right]^7\right\}} \tag{25a}$$

$$S_{pp}(\omega) = 3\frac{\rho_o^2 u_\tau^4}{\omega}\frac{1}{\left\{\left[1 + 0.5\left(U_o/\omega\delta\right)^{0.8}\right]^{3.7} + \left(1.5\omega\nu/u_\tau^2\right)^4\right\}} \tag{25b}$$

with some small differences in the coefficients.

The spatial correlation functions for this model can be obtained from the inverse wavenumber transform of Eq. 23

$$\Gamma_{pp}(\xi,\ \eta,\ \omega) = S_{pp}(\omega)\left(1 + \frac{z}{1 + \pi^2 a\left[1 + \left(U_c/\omega b\delta\right)^2\right]}\right)e^{-z}\,e^{i\omega\xi/U_c} \tag{26}$$

where $z^2 = [1 + (U_c/\omega\, b\delta_j^2]\,[(\mu\ \xi_)^{\ 2} + \eta^{\ 2}]\ (\omega/U_c)^{\ 2}$ and $\mu \sim 0.16$. The correlation function has the sum-of-squares form for the separation variables which Chase [3] has shown to compare well with measured data [6, 16].

The normalized stream-wise correlation function is then given by

$$\frac{|\Gamma_{pp}(\xi,\ 0,\ \omega)|}{S_{pp}(\omega)} = A(\xi,\ \omega) = \left(1 + \frac{\sqrt{1 + \left(U_c/\omega b\delta\right)^2}\,\mu\omega\xi/U_c}{1 + \pi^2 a\left[1 + \left(U_c/\omega b\delta\right)^2\right]}\right)e^{-\sqrt{1+(U_c/\omega b\delta)^2}\,\mu\omega\xi/U_c} \tag{27}$$

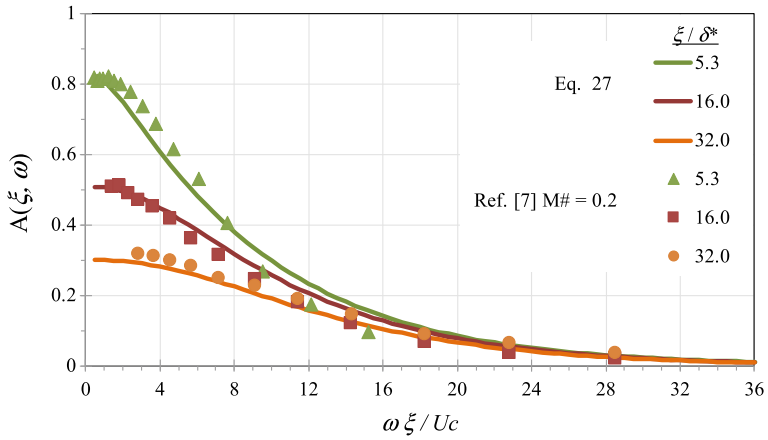

Fig. 14 Comparison of measured normalized stream-wise correlation function $A(\xi,\omega)$ with Eq. 27

This is plotted in Fig. 14 (with $\mu = 0.16$, $a = 0.33$, $b = 0.5$) compared to some of the data shown in Fig. 5.

The normalized cross-wise correlation function is given by

$$\frac{|\Gamma_{pp}(0,\ \eta,\ \omega)|}{S_{pp}(\omega)} = B(\xi,\ \omega) = \left(1 + \frac{\sqrt{1 + \left(U_c / \omega b\delta\right)^2}\,\omega\eta / U_c}{1 + \pi^2 a\left[1 + \left(U_c / \omega b\delta\right)^2\right]}\right) e^{-\sqrt{1+(U_c/\omega b\delta)^2}\,\omega\eta/U_c} \tag{28}$$

4 Structural Coupling

The wavenumber frequency spectrum of the TBL pressure plays an important role in understanding its excitation of structural vibration. Using the Corcos model, the separable formulation with products of k_1 and k_3 terms is often used to simplify the calculation of structural coupling. However, this only applies when the structural response functions are also separable, such as for a simply supported plate or cylinder. A more general approach uses a statistical (or mean value) coupling to the average mode shapes of an irregular structure [1, 22], assuming the structural mode shapes have a Gaussian spatial distribution rather than sinusoidal as in a simply supported rectangular plate (see Fig. 15).

Mathematically, the vibration response of a structure is found from the integral of the product of the excitation spectrum and the structural modal response spectrum in the wavenumber domain as given by Eq. 1. As illustrated in Figs. 3 and 16, there are three major contributions to the structural vibration (when $U_c < c_b < c_o$):

I. Convective TBL pressure coupled to the high wavenumber modal side bands. The high wavenumber response spectrum is given by $|\Psi_s(k_c,\omega)|^2 \sim \pi\ \omega\ (k_p^2/k_c^4)/(\pi\ \kappa\ c_L)$, where k_p is the wavenumber of the plate, κ is the bending radius of gyration and c_L is the longitudinal wave speed in the plate, ($k_p^2 = \omega/\kappa$

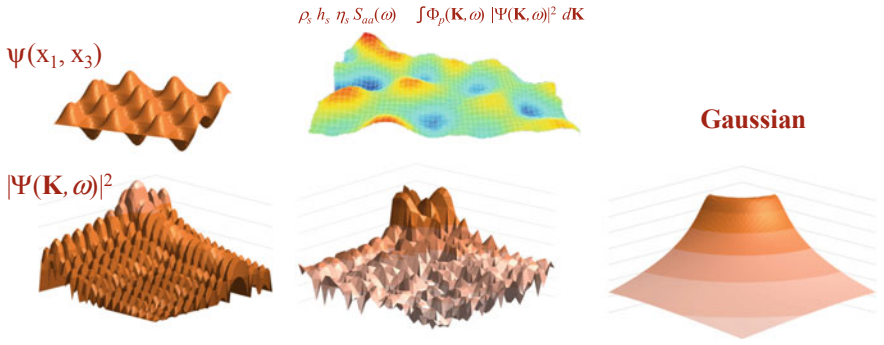

Fig. 15 Mode shapes and wavenumber spectra of simply supported, irregular, and Gaussian plates

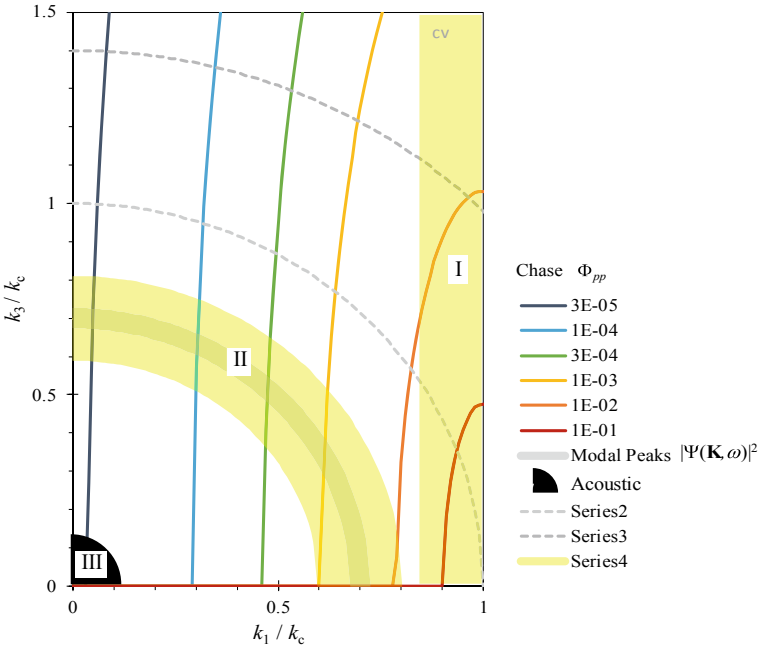

Fig. 16 Contour plot of wavenumber spectra for turbulent pressure, structural modal response, and acoustic pressure showing regions of dominant overlap

c_L). Then the power spectral density of the plate acceleration response is given by

$$S^{I}_{aa}(\omega) = S_{pp}(\omega)\left(k_p^4/k_c^4\right)/(\rho_s h_s)^2\eta_s \tag{29}$$

II. Low wavenumber TBL pressure coupled to the resonant modal peaks. The resonant acceleration response, a, of a single plate mode to a relatively smooth pressure spectrum is given by

$$a^2 = (2\pi)^2(\pi\omega/A_p)\Phi_{pp}(k_p,\omega)/(\rho_s h_s)^2\eta_s \tag{30}$$

where A_p is the area of the plate. Multiplying this by the modal density of the plate gives the power spectral density

$$S^{II}_{aa}(\omega) = a^2 A_p/(4\pi\kappa c_L) = \pi^2 k_p^2 \Phi_{pp}(k_p,\omega)/(\rho_s h_s)^2\eta_s \tag{31}$$

III. Acoustic pressure coupled to the low wavenumber modal side bands. The low wavenumber response spectrum is given by $|\Psi_s(k_c,\omega)|^2 \sim (\pi\ \omega/k_p^2)/(4\pi\ \kappa\ c_L)$. Then the power spectral density of the plate acceleration response is given by

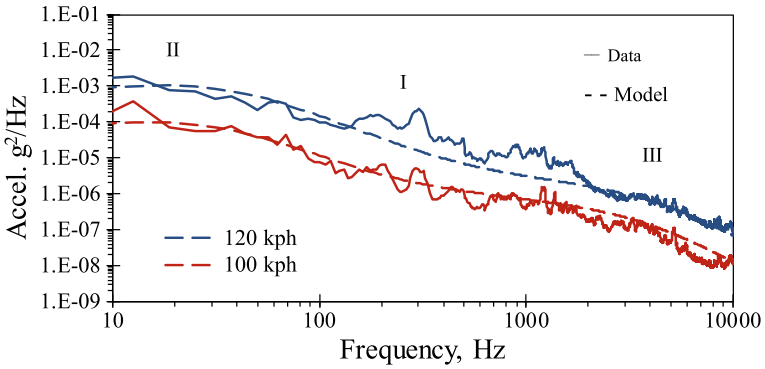

Fig. 17 Comparison of measured and calculated vibration response of vehicle window with TBL excitation

$$S_{aa}^{III}(\omega) = S_{oo}(\omega)\,/4(\rho_s h_s)^2 \eta_s \tag{32}$$

Adding these three contributions gives the total vibration response. Figure 17 shows the results for the example used in Figs. 1 and 2. Roman numerals are used to indicate the frequency ranges where each of the three contributions (Eqs. 29, 31, 32) dominates. Comparing the results for the two wind speeds, the window vibration increases more than the TBL pressure. This is because the spatial coupling factor is increasing with speed, as seen in the measurements in Fig. 2, and this is also predicted by the Chase model.

5 Conclusions

The Chase model for TBL pressure levels has been modified to improve the low wavenumber and high frequency correlation with measured data. One important feature of the Chase model is that it models the pressure spectrum with an elliptical shape which matches measured data much better than the Corcos model which gives a hyperbolic shape. Another important feature of the Chase model is that the frequency spectra and wavenumber spectra are coupled together analytically so that both change as the physical parameters of the TBL change.

In this work the dependence of the TBL pressure on the Reynolds number has not been developed explicitly. This dependence is implicit in that the parameters assumed here to be constant, such as h, m, a, b, C, etc., do in fact vary somewhat with the Reynolds number. One example of this is shown in Fig. 12 and Eq. 20 where the scaling of $1/\pi^{\,2}$ for the k_c^2 term works on average, but the data has a slightly wider spread than the model. Further work is needed to refine the model with more explicit Reynolds number dependence.

References

1. W.K. Blake, *Mechanics of Flow-Induced Sound and Vibration*, 2nd edn. (Academic Press, Cambridge, MA, 2017)
2. G.M. Corcos, The structure of the turbulent pressure field in boundary-layer flows. J. Fluid Mech. **18**(3), 353–375 (1964)
3. D.M. Chase, Modeling the wavevector-frequency spectrum of turbulent boundary layer wall pressure. J. Sound Vib. **70**, 29–67 (1980)
4. W.W. Willmarth, C.E. Wooldridge, Measurements of the fluctuating pressure at the wall beneath a thick turbulent boundary layer. J. Fluid Mech. **14**, 187–210 (1962)
5. G.M. Corcos, The resolution of turbulent pressures at the wall of a boundary layer. J. Sound Vib. **6**, 59–70 (1967)
6. M.K. Bull, Wall-pressure fluctuations associated with subsonic turbulent boundary layer flow. J. Fluid Mech. **28**(4), 719–754 (1967)
7. R.G. DeJong, I.J. Kuiper, Pressure gradient effects on turbulent pressure spectrum, in *Proceedings of Inter-Noise 2012*, New York, NY (2012)
8. O.M. Phillips, On the aerodynamic surface sound from a plane turbulent boundary layer. Proc. R. Soc. Lond. A **234**, 327–335 (1956)
9. R.H. Kraichnan, Pressure fluctuations in the turbulent flow over a flat plate. J. Acoust. Soc. Am. **28**, 378–390 (1956)
10. R.G. DeJong, P. Bootsma, K. DeVries, Low wavenumber pressure content of turbulent boundary layer flows, in *Proceedings of Inter-Noise 2018*, Chicago, IL (2018)
11. W. Bonness, D. Capone, S. Hambric, Low-wavenumber turbulent boundary layer wall-pressure measurements from vibration data on a cylinder in pipe flow. J. Sound Vib. **329**, 4166–4180 (2010)
12. R.G. DeJong, T.S. Bharj, J.L. Lee, Vehicle wind noise analysis using a SEA model with measured source levels. SAE Technical Paper 2001-01-1629 (2001). https://doi.org/10.4271/2001-01-1629
13. A. Caiazzo, R. D'Amico, W. Desmet, A generalized Corcos model for modelling turbulent boundary layer wall pressure fluctuations. J. Sound Vib. **372**, 192–210 (2016)
14. E. Cohen, X. Gloerfelt, Influence of pressure gradients on wall pressure beneath a turbulent boundary layer. J. Fluid Mech. **838**, 715–758 (2018)
15. E. Salze, C. Bailly, O. Marsden, D. Juve, Investigation of the wall pressure wavenumber-frequency spectrum beneath a turbulent boundary layer with pressure gradient, in *International Symposium on Turbulence and Shear Flow Phenomena*, Melbourne, Australia (2015)
16. W.R.B. Morrison, R.E. Kronauer, Structural similarity for fully developed turbulence in smooth tubes. J. Fluid Mech. **39**, 117–141 (1969)
17. G.I. Taylor, The spectrum of turbulence. Proc. R. Soc. Lond. A **164**, 476–490 (1938)
18. D.M. Chase, The character of the turbulent wall pressure spectrum at subconvective wavenumbers and a suggested comprehensive model. J. Sound Vib. **112**(1), 125–147 (1987)
19. D.M. Chase, Fluctuations in wall-shear stress and pressure at low streamwise wavenumbers in turbulent boundary-layer flow. J. Fluid Mech. **225**, 545–555 (1991)
20. R.G. DeJong, R.G. Tubergen, A comprehensive model for the turbulent boundary layer pressure spectrum, in *Proceedings of Inter-Noise 2019*, Madrid, Spain (2019)
21. M.C. Goody, Empirical spectral model of surface pressure fluctuations. AIAA J. **42**(9), 1788–1794 (2004)
22. R.H. Lyon, R.G. DeJong, *Theory and application of statistical energy analysis*, 2nd edn. (Butterworth-Heinemann, Boston, 1995)
23. J.E. Ffowcs Williams, Boundary-layer pressures and the Corcos model: a development to incorporate low-wavenumber constraints. J. Fluid Mech. **125**, 9–25 (1982)

Drone Propeller Noise Under Static and Steady Inflow Conditions

Con Doolan, Yendrew Yauwenas, and Danielle Moreau

Abstract Drone propeller noise under static and steady inflow conditions has been studied. A numerical model that couples a blade element momentum theory model with a frequency-domain acoustic model is presented. Experimental acoustic data for a 12-inch drone propeller under static and steady inflow are compared with the model. The model compares well against the experimental data for the fundamental tone and first 2–3 harmonics under steady inflow. Discrepancies at the higher harmonics are likely due to the point-loading assumption used to apply the aerodynamic loads in the acoustic model. Comparisons under static conditions are poor and this is thought to be caused by the limited nature of the aerodynamic model used. The results suggest that an accurate and versatile aerodynamics model is most important for accurate prediction of drone propeller noise over a wide range of operating conditions.

1 Introduction

Small unmanned aerial systems (sUAS), also known as *drones* are becoming increasingly useful for commercial, private and military activities. Despite their usefulness, drones create noise that is annoying to the public [1, 2] as well as reducing military stealth. Surprisingly, there are a lack of adequate safety and noise regulations for drones [3]. Given the need to reduce noise and develop appropriate standards, new research is required to understand the nature of drone noise production and develop novel methods of noise control.

Drone noise is dominated by the small propellers used as part of their propulsion systems. Thus, a good understanding of low-Mach number aeroacoustics and rotor flow is needed to appreciate drone noise production. Wright [4] provides an early framework to understand and predict noise from rotor blades. Here, tonal noise from steady aerodynamic forces, unsteady wake or vortex interaction are highlighted. Fur-

C. Doolan (✉) · Y. Yauwenas · D. Moreau
Flow Noise Group, School of Mechanical and Manufacturing Engineering,
UNSW Sydney, Sydney, NSW, Australia
e-mail: c.doolan@unsw.edu.au

E. Ciappi et al. (eds.), *Flinovia—Flow Induced Noise and Vibration Issues and Aspects-III*, https://doi.org/10.1007/978-3-030-64807-7_3

ther, broadband noise from the boundary layer is described as well as high-frequency noise from laminar/transitional boundary layers. The interaction of turbulence with the rotors was not considered by Wright, despite its importance as a broadband noise source.

The Ffowcs-William and Hawkings (FWH) equations [5] provide a near-universal framework to predict rotor noise. The FWH equations extend the formulations of Lighthill [6] and Curle [7] so that aerodynamically-generated sound can be calculated via three terms. The first is a loading term which for rotors takes into consideration the steady and unsteady forces present on the blades during operation. The second is a thickness-noise term that calculates the monopole contribution created by the unsteady volume displacement of the blades. The third is a quadrupole term that takes into account sound generated by the turbulent flow itself. As the flow about drones is almost exclusively low Mach number ($M_{\text{tip}} \ll 1$), this quadrupole term is normally ignored. Hence, the most important aerodynamic noise sources are the loading and thickness noise terms.

A useful extension of the FWH equations for propeller noise has been formulated by Hanson [8]. Here, the FWH equations are converted into a frequency-domain version for propellers. Hanson's technique can be used for steady loading and thickness noise and extended to unsteady and broadband sources [9]. Hanson's method was recently validated by Kotwicz-Herniczek et al. [10] for a range of propellers, albeit not drone propellers. Hanson used his theory to relate important design parameters to noise emission [11].

Leslie and Auld [12, 13] developed a noise and aerodynamic test apparatus for UAS propellers and studied the effect of boundary layer trips on the radiated spectrum. They showed that a trip removed laminar boundary layer separation and decreased broadband noise levels.

Gur and Rosen [14] used an FWH approach to successfully model UAV propeller noise. They combined the FWH solver with aerodynamic and structural models to perform a multi-dimensional design optimisation study. Reducing propeller tip speed is the most effective method for reducing noise. Further, increasing the number of blades reduces loading noise by lowering the aerodynamic forces on each section of each blade. In general, as design constraints become more strict (structural, power, etc.), the potential to reduce noise is reduced. Gur and Rosen's design was later tested [15] and shown to create lower levels of noise than a conventional design; however, vibration of the blades was considered an important noise source at higher thrust levels and should be taken into consideration during design optimisation.

Intaratep et al. [16] acoustically tested a DJI Phanton II quadcopter with various numbers of rotors. Like most drone propeller noise measurements, the spectrum was dominated by tones at the blade pass frequency (BPF) and its harmonics. They also measured significant levels of broadband noise which was affected by the number of rotors used with four rotors creating the highest amount of broadband noise. Interestingly, the overall A-weighted sound pressure level is nearly the same at the same thrust level regardless of the number of rotors.

A comprehensive experimental acoustic study of single and multiple drone propellers under static thrust conditions was performed by Tinney and Sirohi [17]. They

found that non-rotor noise (motor and speed controller) was equally important as the rotor noise. The number of rotors (at the same static thrust condition) affects noise emission. A database of thrust and noise was developed and the relative importance of thickness and loading noise was described. The importance of motor noise in future prediction methods was also found by Zawodny et al. [18] who have performed an experimental and numerical study of drone propeller noise at NASA Langley. McKay and Kingan [19] investigated motor noise and show that it occurs at harmonics of the BPF. They proposed that unsteady loading and thickness noise created by small variations in angular speed of the propeller are responsible for this noise.

Flight testing and acoustic beamforming was performed for a 2.1 kg quadcopter [3]. The sound pressure level was found to be a maximum approximately 45° from the horizontal during flight testing. Lab testing utilising the acoustic array confirmed the blades and motor systems were the dominant noise sources. Flyover acoustic measurements in a drone park [20, 21] illustrated the importance of both tonal and broadband noise sources as well as their directivity. Weather conditions significantly affected the noise levels and directivity. Flyover testing in a large anechoic chamber [22] eliminated the effects of weather and allowed the inclusion of manoevers such as hovering, yawing, take-off and descent. Flyover noise modelling [23] for large numbers of drones show that noise levels should be manageable if drones are kept above 60 m altitude.

Understanding the effects of steady inflow and inflow disturbances (such as turbulence and wakes) has not been comprehensively studied under controlled conditions. Early model-scale helicopter rotor experiments showed the importance of turbulence inflow on noise emission [24]. More recently, Yauwenas et al. [25] used a single rotor in an anechoic wind tunnel under uniform, grid-turbulence and wake-inflow test conditions. These results showed significant changes in noise level under steady flight conditions plus additional tones and broadband noise during wake interaction.

This paper presents an experimental and numerical study of drone propeller noise. A frequency-domain propeller noise prediction method is presented, which combines the method of Hanson [8] and an aerodynamic solver based on blade element momentum theory. Experimental results of a drone propeller placed in an anechoic wind tunnel are compared to gain an improved insight into drone propeller noise production and prediction during static and steady inflow conditions.

2 Predictive Model

The drone propeller predictive model combines an aerodynamic model based on blade element momentum theory with a frequency-domain acoustic model.

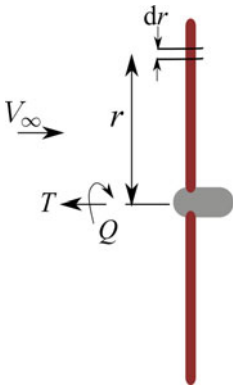

Fig. 1 Schematic of propeller operating in a steady inflow with freestream velocity V_∞. An elemental radial segment of width dr at radius r is shown along with thrust T and torque Q acting at the axis of rotation

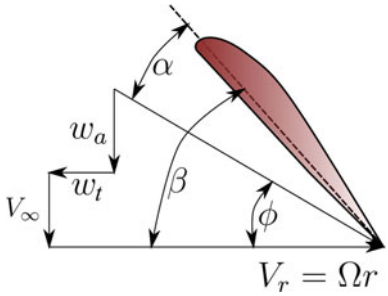

Fig. 2 Illustration of rotor section, showing induced velocities (w_a, w_t), pitch angle β, inflow angle ϕ and rotor rotational velocity $V_r = \Omega r$, where the angular velocity of the rotor is Ω

2.1 Blade Element Momentum Theory Model

The forces acting on the propeller blades are predicted using the blade element momentum theory (BEMT) approach [26]. Figure 1 shows a side view schematic of a drone propeller immersed in a uniform freestream air flow with velocity V_∞. BEMT requires that each blade be discretised into small segments of width dr at each radial location r. Summing the aerodynamic forces on each segment allows the computation of propeller thrust T and torque Q which is shown to act at the axis of rotation.

Figure 2 shows a section through a blade segment and illustrates the velocity vectors and relevant angles. Rotational motion creates velocity V_r that acts with freestream velocity V_∞ to generate aerodynamic loads. These loads, in turn, create axial induced velocity w_a and a tangential induced velocity w_t.

The velocity magnitude approaching the blade section (V_w) is therefore,

$$V_w = \sqrt{(V_\infty^2 + w_a)^2 + (V_r - w_t)^2} \tag{1}$$

where

$$V_r = \Omega r \tag{2}$$

where Ω is the rotational velocity of the rotor.

The inflow angle ϕ is,

$$\phi = \tan^{-1} \frac{V_\infty + w_a}{V_r - w_t} \tag{3}$$

The blade segment is set with pitch angle β, thus the angle of attack is,

$$\alpha = \beta - \phi \tag{4}$$

Lift per unit span (L') and Drag per unit span (D') are,

$$L'(r) = \frac{1}{2}\rho_\infty V_w(r)^2 c(r) C_l(r/R, Re, \alpha, M) \tag{5}$$

$$D'(r) = \frac{1}{2}\rho_\infty V_w(r)^2 c(r) C_d(r/R, Re, \alpha, M) \tag{6}$$

where ρ_∞ is the freestream density, $c(r)$ is the chord of the blade at radius r. The sectional lift and drag coefficients, C_l and C_d are functions of position (r/R, where R is the rotor outer radius), Reynolds number (Re, based on chord), angle of attack (α) and Mach number (M). As the tip Mach number is low, the Mach number dependence is ignored. The values of the lift and drag coefficients are set according to an empirical model, described in Sect. 2.2.

The thrust (T) and torque (Q) acting on each blade element are,

$$T = B\left[L'\cos\phi - D'\sin\phi\right]\mathrm{d}r \tag{7}$$

$$Q = B\left[L'\sin\phi + D'\cos\phi\right]r\mathrm{d}r \tag{8}$$

From a momentum balance, we also can show that thrust and torque are related to the induced velocities,

$$T = 4\pi\rho_\infty w_a[V_\infty + w_a]r\mathrm{d}r \tag{9}$$

$$Q = 4\pi\rho_\infty w_r r[V_\infty + w_a]r\mathrm{d}r \tag{10}$$

Equating the thrust Eqs. (7) and (9) we obtain a quadratic in w_a,

$$w_a^2 + V_\infty w_a - \frac{BcV_w^2[C_l\cos\phi - C_d\sin\phi]}{8\pi r} = 0 \tag{11}$$

where

$$C_l = \frac{L'}{\frac{1}{2}\rho_\infty V_w^2 c} \tag{12}$$

$$C_d = \frac{D'}{\frac{1}{2}\rho_\infty V_w^2 c} \tag{13}$$

The solution we use to this quadratic is,

$$w_a = \frac{1}{2}\left(\sqrt{V_\infty^2 + \frac{4BcV_w^2[C_l\cos\phi - C_d\sin\phi]}{8\pi r}} - V_\infty\right) \tag{14}$$

Equating the torque Eqs. (8) and (10) we obtain an update for w_t,

$$w_t = \frac{BcV_w^2}{4\pi r}\left[\frac{C_l\sin\phi + C_d\cos\phi}{v_\infty + w_a}\right] \tag{15}$$

The solution of the BEMT set of equations is iterative and this process is summarised in Fig. 3. The process begins by guessing values for the induced velocities w_a and w_t. Using BEMT and the aerodynamics solver, these values are updated and re-used until they do not change by more than a preset tolerance (nominally 10^{-4}). Practically, only a few iterations are required.

2.2 Empirical Aerodynamics Model

Lift and drag coefficients may be determined using an aerodynamics solver or empirical database. Here, aerodynamic data for a NACA 4412 airfoil at a chord-based Reynolds number of $Re = 100{,}000$ is used [27, 28]. These data are shown in Fig. 4. Note that the data extends beyond stall.

2.3 Acoustic Model

A frequency-domain tone noise prediction method has been implemented, based on the formulations presented by Hanson [8] and Glegg and Devenport [9]. The Ffowcs-Williams and Hawkings equation [5] can be recast into a form suitable for rotor tone noise [9] which are the steady loading and thickness noise components,

$$p'(\mathbf{x},t) = -\frac{\partial}{\partial x_i}\int_{S_0}\left[\frac{f_i}{4\pi r|1-M_r|}\right]\mathrm{d}S(\mathbf{z}) - \frac{\partial}{\partial t}\int_{S_0}\left[\frac{\rho_\infty \mathbf{V}\cdot\nabla h}{4\pi r|1-M_r|}\right]\mathrm{d}S(\mathbf{z}) \tag{16}$$

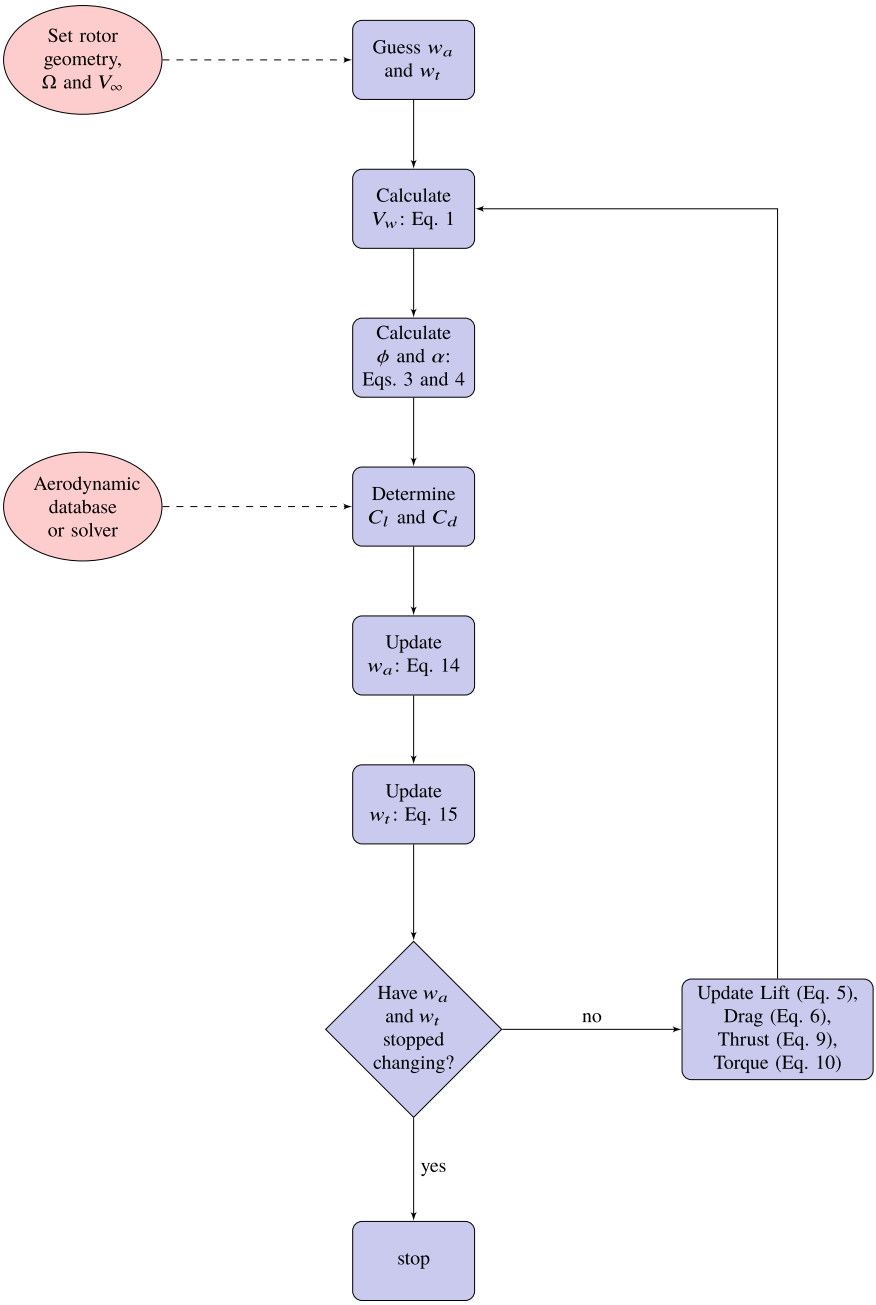

Fig. 3 Iterative solution methodology for blade element momentum theory

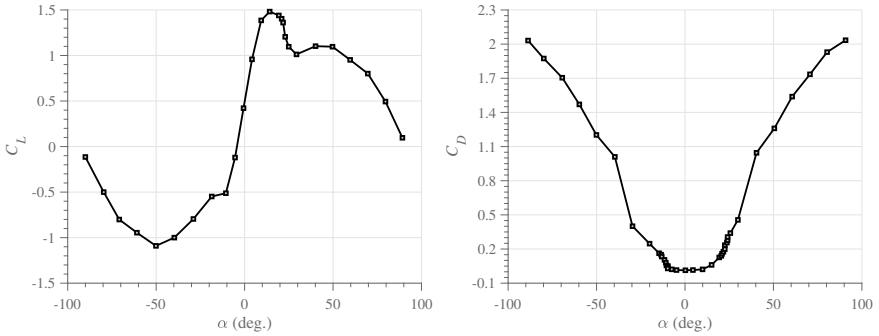

Fig. 4 NACA 4412 airfoil sectional **a** lift and **b** drag empirical aerodynamics model. Data obtained at $Re = 100{,}000$ [27, 28]

where $p'(\mathbf{x}, t)$ is the acoustic pressure at observer position $\mathbf{x}(x_1, x_2, x_3)$ and time t. The blade platform area is discretised into small radial segments of area $\mathrm{d}S(\mathbf{z})$ where vector $\mathbf{z}$ contains the coordinates of the source in the moving reference frame of the rotor blade. The planform area of the blades is S_0.

The forces per unit area acting on each rotor blade segment are f_i, noting that they are steady in the rotor frame and thus are responsible for the steady loading tones. The distance from the rotor segment to the observer is r (not to be confused with the same symbol used in Sect. 2.1) and the relative Mach number (between the rotor segment and observer) is M_r.

The thickness of each blade segment is h, which is used in the second term on the right hand side of Eq. 16 to estimate the thickness noise. The vector $\mathbf{V}$ is the velocity of the rotor segment in the fixed reference frame.

As each blade is assumed identical, we can assume the acoustic signal is periodic,

$$p'(\mathbf{x}, t) = \sum_{n=1}^{B} \mathcal{P}(\mathbf{x}, t + nT_p/B) \tag{17}$$

where B is the number of blades, $\mathcal{P}$ is the signature from one blade and T_p is the period of one revolution. The periodic nature of the signal allows the use of a Fourier series to represent the signature,

$$\mathcal{P}(\mathbf{x}, t) = \sum_{j=-\infty}^{\infty} c_j e^{-ij\Omega t} \tag{18}$$

where Ω is the rotational velocity of the rotor and c_j are the Fourier coefficients.

Using these, the acoustic pressure can be written [9],

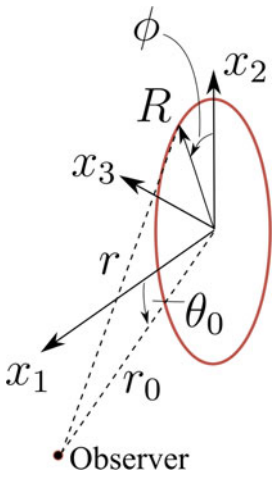

Fig. 5 Rotor acoustic coordinate system. The rotor segment of interest is at radius R and azimuthal angle ϕ. The observer position is described as (r_0, θ_0, ϕ_0), where the observer azimuthal angle, ϕ_0, is not shown but is measured from the x_2 axis, in an anti-clockwise sense

$$p'(\mathbf{x}, t) = B \sum_{m=-\infty}^{\infty} c_{mB} e^{-imB\Omega t} \tag{19}$$

The Fourier coefficients can be manipulated to yield [9],

$$c_n(\mathbf{x}) = \frac{in\Omega e^{in\Omega r_0/c_0}}{4\pi r_0 c_0} \sum_{m=-\infty}^{\infty} \int_{R_i}^{R_{\text{tip}}} Q_{m,n}(R, \mathbf{x}) J_m \left(\frac{n\Omega R \sin\theta_0}{c_0} \right) \mathrm{d}R \tag{20}$$

where R is the radial position of the blade segment from the rotor axis (see Fig. 5 for the rotor acoustic coordinate system), r_0 is the distance from the rotor centre and the observer, ϕ is azimuthal position and θ_0 is angle between the x_1 axis and the observer. The speed of sound is c_0, $J_m(\zeta)$ the Bessel function of the first kind of order m and $Q_{m,n}$ is a source term that will be defined below. The source contributions are integrated from the inner rotor radius, R_i, to the outer radius, R_{tip}.

The source term $Q_{m,n}$ is,

$$Q_{m,n}(R, \mathbf{x}) = \int_{\phi_{TE}}^{\phi_{LE}} \left\{ f_L(R, \phi_1) \cos\theta_0 \delta_{mn} + f_D(R, \phi_1) \sin\theta_0 \left(\frac{\delta_{n,m-1} - \delta_{n,m+1}}{2i} \right) + im\Omega\rho_\infty c_0 h(R, \phi_1) \delta_{mn} \right\} e^{-im(\phi_1 - \phi_0 + \pi/2)} R \, \mathrm{d}\phi_1$$

The source term is evaluated for each blade segment and is an integral over an arc formed between the trailing and leading edges of the rotor blade at radius R, where ϕ_1 is the azimuthal angle along this arc. The forces $f_L(R, \phi_1)$ and $f_D(R, \phi_1)$ are the thrust and drag per unit area acting on the blade surface and are taken from the BEMT aerodynamic model. Further, these forces are assumed to act at a point at the centre of the blade segment. Finally, δ_{mn} is the Kronecker delta function.

Both the BEMT and acoustic models are coded in Matlab and used to predict the tone noise sound pressure level.

3 Experiment

Drone propeller noise experiments were conducted in the UNSW Acoustic Wind Tunnel (UAT) [29]. A complete set of experiments that investigated static, clean inflow, ingested turbulence and wakes has been performed previously; full details of these, including the experimental setup, can be found in Yauwenas et al. [25]. In this paper, acoustic results for the static and uniform, steady inflow test cases are compared with the predictive model. A brief outline of the experimental setup is described below.

The UAT provides a uniform 0.455 m × 0.455 m test jet which exhausts into an anechoic room with dimensions 3 m × 3.2 m × 2.15 m. An Aerostar, APC-Style $12'' \times 6''$ drone propeller was used for this study. The drone propeller was powered by a 580 W brushless direct current electric motor, which was energised using a Lithium-Polymer battery and electronic speed-control system. The propeller and motor were positioned 280 mm downstream from the outlet plane of the test jet so that the propeller was in the approximate centre of the test jet. The motor and propeller were mounted in a 3D-printed housing assembly, details of which are illustrated in Yauwenas et al. [25].

Acoustic data were obtained on a 64-microphone array system; however, data from a single microphone located approximately perpendicular to the propeller axis at $r_0 = 1.33$ m and $\theta_0 = \phi_0 = 90°$ are used for comparison with the predictive model. GRAS 40-PH $\frac{1}{4}''$ microphones were used in the array. These were connected to a National Instruments PXI data acquisition system. Data were recorded for 32 s at a sampling rate of 65,536 Hz.

Data were obtained at static conditions for static ($V_\infty = 0$ m/s) and steady ($V_\infty = 20$ m/s) inflow conditions. Rotor angular speed varied between 4000 to 7000 RPM for the static cases. Under steady load, the advance ratios were set at $0.43 \leq J \leq 0.66$.

Definitions for advance ratio (J), thrust coefficient (C_T) and power coefficient (C_P) are,

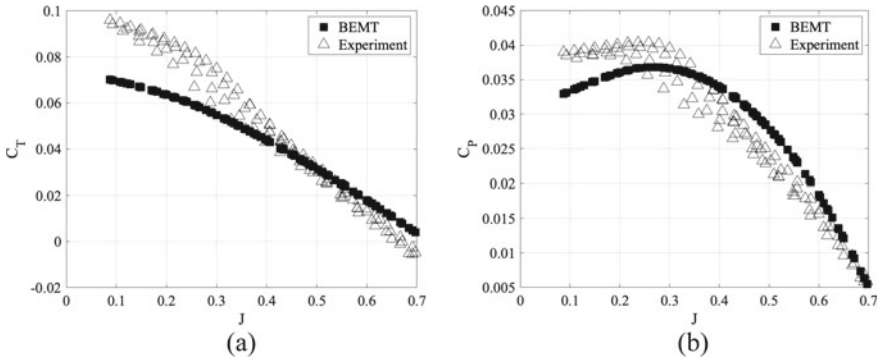

Fig. 6 Comparison of BEMT predictions with experimental measurements [30]; **a** thrust coefficient, **b** power coefficient

$$J = \frac{V_\infty}{N D} \tag{21}$$

$$C_T = \frac{T}{\rho_\infty N^2 D^4} \tag{22}$$

$$C_P = \frac{P}{\rho_\infty N^3 D^5} \tag{23}$$

where N is the rotational speed in revolutions per second and D is the rotor diameter.

4 Results

4.1 Aerodynamic Performance

The accuracy of the BEMT solver was assessed by comparing propeller thrust and power coefficient predictions against experimental data collected by the University of Illinois at Urbana-Champaign [30]. In this case, experimental data for the APC $10'' \times 5''$ 'thin-electric' propeller was used and the same propeller geometry used to construct the BEMT model. Blade aerodynamics was as presented in Sect. 2.2, despite the fact that the Reynolds numbers are different and the airfoil sections not identical.

In these experiments [30], $4005\,\text{RPM} \leq \Omega \leq 6710\,\text{RPM}$ and $0.085 \leq J \leq 0.7$ and, as both rotational speed and freestream velocity are varied independently, a variety of Reynolds numbers are experienced by the blade sections. The aerodynamic model does not account for changes in Reynolds number and was developed based on experimental data at $Re = 100{,}000$.

Figure 6 compares the thrust (C_T) and power (C_P) coefficients from the BEMT model and experiment. The model shows significant deviations from the experimental measurement points at lower values of J. There is, however, reasonable agreement of BEMT and experiment for the thrust coefficient over the advance coefficient range $0.41 \leq J \leq 0.55$. The power coefficient approaches the experimental values as advance ratio is increased.

While the level of agreement is acceptable in parts, the discrepancies can be attributed to the aerodynamic data used in the BEMT model. It appears that at low values of J, and at static conditions (not shown), the aerodynamic performance is poor. For some mid-range values of J, the agreement is better, and it is suspected that the angle of attack becomes low for most of the blade, thus the sectional aerodynamics approaches that described by thin-airfoil theory. Away from this range, non-linear viscous effects become important and affect the results.

4.2 Acoustics

A comparison of acoustic results are shown in Figs. 7 and 8. For these results, the prediction code used the APC $10'' \times 5''$ 'thin-electric' propeller geometry; however, all dimensions were scaled by a factor of 1.2 to accommodate the larger propeller diameter in the experiments. In this section, the acoustic predictions are labelled as 'BEMTN' (BEMT—Noise) in the figures.

Figure 7 compares acoustic measurements with prediction for three steady inflow cases. Note that these spectra are presented against multiples of the blade pass frequency (BPF) rather than Hertz. There is good comparison between measurement and prediction for the fundamental and first 2–3 harmonics. The agreement improves as the advance ratio reduces and it is suggested that this is because the aerodynamic predictions for thrust-level are more accurate for these values of J.

After the third or fourth BPF multiple, the experimental values are much higher than the associated harmonic level. It is surmised that this could be due to excessive vibration of the test rig or possibly the assumption of point force loading in the acoustic model. It has been suggested [9] that this can be a cause of poor agreement at higher harmonics.

Figure 8 compares acoustic data against the predictive model for four different values of rotational velocity for the static case (that is $V_\infty = 0$ m/s). The level of agreement is poor for the static case and this is attributed to the accuracy of the aerodynamic model for these operational conditions.

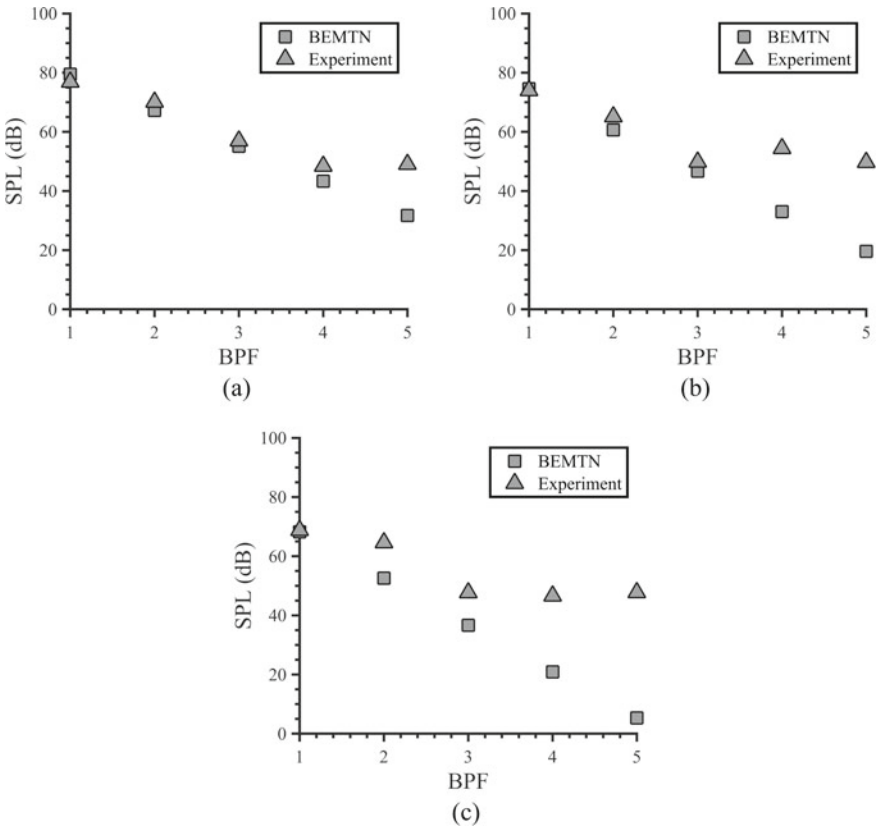

Fig. 7 Comparison of acoustic prediction (BEMTN) with experimental measurements for drone propeller in steady inflow; **a** $J = 0.437$, **b** $J = 0.492$, **c** $J = 0.562$

5 Conclusion

Drone noise will become an important and perhaps dominant component of environmental noise pollution in the future. This paper describes a coupled aerodynamic and frequency-domain acoustic solver for drone noise prediction studies. The model is compared against experimental data obtained at UNSW Sydney under static and steady inflow conditions.

The results show that the accuracy of the aerodynamic model is most important for achieving good quality acoustic predictions. The current implementation uses empirical data obtained at a fixed Reynolds number. In order to improve accuracy, a more sophisticated aerodynamic model is required that can take into account variable Reynolds numbers and geometry. Further, improvements in the accuracy of the levels at higher harmonics (BPF$\geq$ 4) might be achieved by removing the point-loading

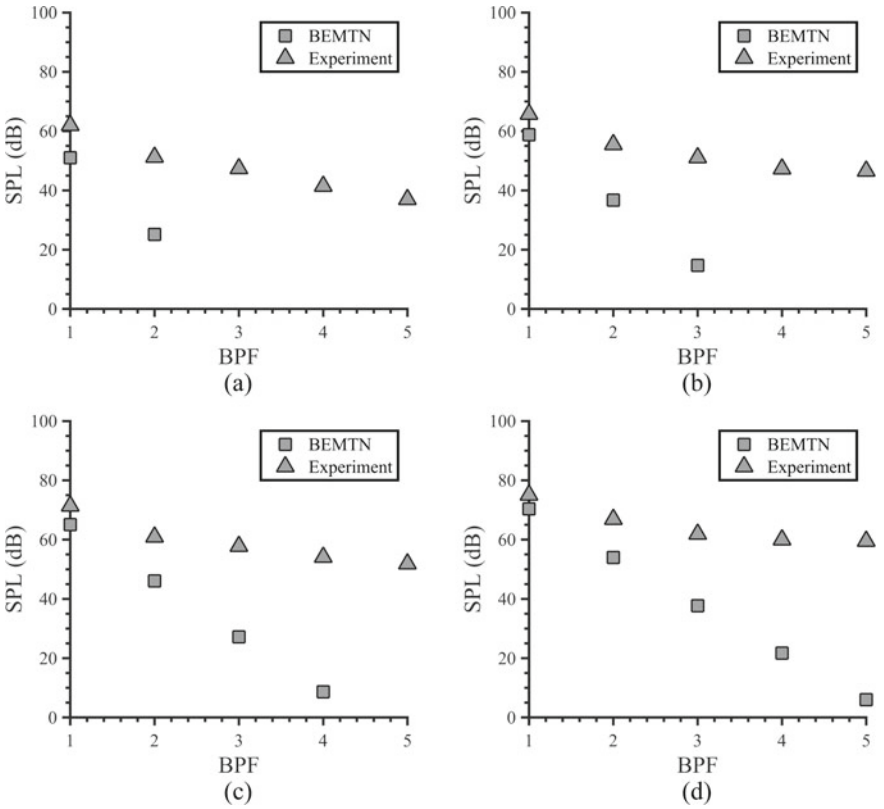

Fig. 8 Comparison of acoustic prediction (BEMTN) with experimental measurements for drone propeller for static case; **a** $\Omega = 4000$ RPM, **b** $\Omega = 5000$ RPM, **c** $\Omega = 6000$ RPM, **d** $\Omega = 7000$ RPM

assumption in the acoustic source term. Removing unwanted sources of vibration and vibroacoustic noise in the experiment may also help improve the comparison at the higher harmonics.

References

1. ABC News, *Whining drones bringing burritos and coffee are bitterly dividing Canberra residents* (2019), https://www.abc.net.au/news/2018-11-09/noise-from-drone-delivery-service-divides-canberra-residents/10484044. Accessed 11 Mar 2019
2. BBC News, Why your pizza may never be delivered by drone (2019), https://www.bbc.com/news/business-46483178. Accessed 11 Mar 2019
3. N. Kloet, S. Watkins, R. Clothier, Acoustic signature measurement of small multi-rotor unmanned aircraft systems. Int. J. Micro Air Veh. **9**(1), 3–14 (2017). February

4. S.E. Wright, The acoustic spectrum of axial flow machines. J. Sound Vib. **45**(2), 165–223 (1976)
5. J.E. Ffowcs Williams, D.L. Hawkings, Sound generation by turbulence and surfaces in arbitrary motion. Philos. Trans. R. Soc. Lond. Ser. A Math. Phys. Sci. **264**(1151), 321–342 (1969)
6. M.J. Lighthill, On sound generated aerodynamically I. General theory. Proc. R. Soc. Lond. Ser. A. Math. Phys. Sci. **211**(1107), 564–587 (1952)
7. N. Curle, The influence of solid boundaries upon aerodynamic sound. Proc. R. Soc. Lond. Ser. A. Math. Phys. Sci. **231**(1187), 505–514 (1955)
8. D. Hanson, Helicoidal surface theory for harmonic noise of propellers in the far field. AIAA J. **18**(10), 1213–1220 (1980)
9. S. Glegg, W. Devenport, *Aeroacoustics of Low Mach Number Flows* (2017)
10. M.T. Kotwicz Herniczek, D. Feszty, S. Meslioui, J. Park, F. Nitzsche, Evaluation of acoustic frequency methods for the prediction of propeller noise. AIAA J. **57**(6), 2465–2478 (2019)
11. D. Hanson, Influence of propeller design parameters on far-field harmonic noise in forward flight. AIAA J. **18**(11), 1313–1319 (1980)
12. A. Leslie, K.C. Wong, D. Auld, Broadband noise reduction on a mini-UAV propeller. In *14th AIAA/CEAS Aeroacoustics Conference (29th AIAA Aeroacoustics Conference)*, p. 3069 (2008)
13. A. Leslie, K.C. Wong, D. Auld, Experimental analysis of the radiated noise from a small propeller. In *Proceedings of 20th International Congress on Acoustics, ICA* (2010)
14. O. Gur, A. Rosen, Design of quiet propeller for an electric mini unmanned air vehicle. J. Propuls. Power **25**(3), 717–728 (2009)
15. G. Sinibaldi, L. Marino, Experimental analysis on the noise of propellers for small UAV. Appl. Acoust. **74**(1), 79–88 (2013)
16. N. Intaratep, W.N. Alexander, W.J. Devenport, S.M. Grace, A. Dropkin. Experimental study of quadcopter acoustics and performance at static thrust conditions. In *22nd AIAA/CEAS Aeroacoustics Conference*, June 2016 (2016)
17. C.E. Tinney, J. Sirohi, Multirotor drone noise at static thrust. AIAA J. **56**(7), 2816–2826 (2018). July
18. N.S. Zawodny, D. Douglas Boyd Jr., C.L. Burley, Acoustic characterization and prediction of representative, small-scale rotary-wing unmanned aircraft system components (2016)
19. R. McKay, M.J. Kingan, Multirotor unmanned aerial system propeller noise caused by unsteady blade motion. In *25th AIAA/CEAS Aeroacoustics Conference* (2019), p. 2499
20. W.N. Alexander, J. Whelchel, N. Intaratep, A. Trani, Predicting community noise of sUAS. In *25th AIAA/CEAS Aeroacoustics Conference* (2019), p. 2686
21. W.N. Alexander, J. Whelchel, Flyover noise of multi-rotor sUAS. In *2INTER-NOISE 2019* (2019)
22. T. Zhou, H. Jiang, Y. Sun, R.J. Fattah, X. Zhang, B. Huang, L. Cheng, Acoustic characteristics of a quad-copter under realistic flight conditions. In *25th AIAA/CEAS Aeroacoustics Conference* (2019), p. 2587
23. V. Bulusu, V. Polishchuk, L. Sedov, Noise estimation for future large-scale small UAS operations. In *INTER-NOISE and NOISE-CON Congress and Conference Proceedings*, vol. 254. Institute of Noise Control Engineering (2017), pp. 864–871
24. R.W. Paterson, R.K. Amiet, Noise of a model helicopter rotor due to ingestion of isotropic turbulence. J. Sound Vib. **85**(4), 551–577 (1982)
25. Y. Yauwenas, J.R. Fischer, D. Moreau, C.J. Doolan, The effect of inflow disturbance on drone propeller noise. In *25th AIAA/CEAS Aeroacoustics Conference* (2019), p. 2663
26. O. Gur, A. Rosen, Comparison between blade-element models of propellers. Aeronaut. J. **112**(1138), 689–704 (2008)
27. C. Ostowari, D. Naik, Post-stall wind tunnel data for NACA 44XX series airfoil sections. Technical report, Texas A and M University, College Station (USA). Department of Aerospace Engineering (1985)
28. M. McCrink, J.W. Gregory, Blade element momentum modeling of low-re small UAS electric propulsion systems. In *33rd AIAA Applied Aerodynamics Conference* (2015), p. 3296

29. C.J. Doolan, D. Moreau, M. Awasthi, C. Jiang, The UNSW anechoic wind tunnel. In *Proceedings of WESPAC 2018*, New Delhi, India (2018)
30. J.B. Brandt, R.W. Deters, G.K. Ananda, M.S. Selig, UIUC propeller database, University of Illinois at Urbana-Champaign (2019), http://m-selig.ae.illinois.edu/props/propDB.html Accessed 24 Oct 2019

Validation of a Simple Empirical Model for Calculating the Vibration of Flat Plates Excited by Incompressible Homogeneous Turbulent Boundary Layer Flow

Stephen Hambric and Peter Lysak

Abstract The vibration responses of three flat rectangular plates excited by turbulent boundary layer flow are calculated and compared to measured data. The measurements were made in three different facilities by Wilby at ISVR [1] (high speeds typical of aircraft), Han at Purdue University [2] (moderate speeds typical of automobiles), and Robin at University of Sherbrooke [3] (lowest speeds), spanning 50 years of time. The plates are different sizes, made from different materials, and have different boundary conditions. The boundary layers have different heights and flow speeds. The ratios of plate flexural and convective wavenumbers k_b/k_c over the three cases range from about 0.1 to 2. Plate vibrations are normalized by wall pressure fluctuation autospectra measured by the previous investigators. This wide range of structural and flow conditions and the use of plate vibration spectra normalized by wall pressure autospectra allows for an objective assessment of various TBL wall pressure fluctuation cross-spectral empirical models. Two cross-spectral models are considered: the widely used Corcos model [4] and the less well-known elliptical extension by Mellen [5]. Smolyakov's empirical models for convection velocity and streamwise and spanwise surface pressure length scales [6] supplement the Corcos and Mellen models. Calculations using the Corcos cross-spectral model overestimate the vibrations by about an order of magnitude at lower speed (and lower k_b/k_c) conditions. Including Smolyakov's convection velocity and length scale formulations improves accuracy at low frequencies. The Mellen cross-spectral pressure model, supplemented with Smolyakov's empirical models for convective wave speed and streamwise and spanwise surface pressure length scales, is therefore well suited for calculating plate vibrations due to TBL flows with flow speed/flexural wave speed ratios ranging from 0.1 to 2.

S. Hambric (✉) · P. Lysak
ARL/Penn State, PO Box 30, State College, PA 16804, USA
e-mail: sah19@arl.psu.edu

E. Ciappi et al. (eds.), *Flinovia—Flow Induced Noise and Vibration Issues and Aspects-III*, https://doi.org/10.1007/978-3-030-64807-7_4

1 Introduction

This study demonstrates a relatively simple and practical means of accurately estimating the vibration response of flat plates excited by spatially homogeneous turbulent boundary layer (TBL) flow over a wide range of panel and incompressible flow conditions. In spite of significant evidence to the contrary, the famous cross-spectral density model of TBL wall pressure fluctuations suggested by Corcos in 1963 [4] remains in popular use, and is often the first model considered by those beginning their studies or research in this field. However, Corcos developed this model to correct high frequency attenuation errors in circular and rectangular faced pressure sensor measurements, not to model TBL flow over large flexible surfaces. Many other cross-spectral models have been suggested [7] which make the simple (and appropriate) correction from a rhombic to an elliptical spatial coherence distribution. This article suggests one of the simpler models for general use, supplemented by improved estimates of the key variables of convection velocity and spatial decay coefficients of the wall pressures.

To evaluate the approaches robustly, more than one test case is required, preferably with a wide range of flow and structural conditions. Fortunately, many studies have been published. We chose three that include both structural vibration measurements as well as wall pressure autospectrum measurements. We therefore benchmark wall pressure cross-spectral models using plate vibration autospectra normalized by wall pressure autospectra; assuming that the pressure autospectra are homogeneous over the plate surface.

The plates have different sizes, materials and boundary conditions, and were measured in three different facilities in three different countries over three different decades at three different speed ranges: ISVR (high speed flow) in the 1960s [1], Purdue (medium speed) in the 1990s [2], and Sherbrooke (slow speed) in the 2010s [3]. This broad database provides a good opportunity to benchmark TBL models.

The approach used in this paper is based on the spatial cross-spectrum form of the TBL pressure models, rather than the wavenumber spectrum. Although some classical analytic problems are well suited to wavenumber analyses, most practical problems are not. For instance, inhomogeneous structural models (such as those with irregular material properties and/or stiffeners) do not have readily available simple wavenumber transforms.

2 Computational Methodology

2.1 Empirical Cross Spectral Density TBL Wall Pressure Models

TBL fluctuating wall pressure models are often split into the amplitude (autospectrum) and cross-coherence (cross spectrum) terms where the total forcing function

is:

$$G_{pp}(\xi_x, \xi_y, \omega) = \phi_{pp}(\omega)\Gamma_{pp}(\xi_x, \xi_y, \omega). \tag{1}$$

This equation assumes a spatially homogeneous TBL. For inhomogeneous pressure fields, the spatial dependence must also be included. For a review of autospectrum models, see Hwang et al. [8], and also two commonly used models compared in Appendix 1. Hwang et al. [7] and Graham [9] review many cross-spectrum models. This work focuses on two cross-spectral models—the famous Corcos model [4] and the modification proposed by Mellen [5].

The model suggested by Corcos is by far the most popular, because (1) it was one of the first, and addressed an important practical problem during the early years of TBL wall pressure testing—the spatial attenuation of the measurement; and (2) it is simple to use, since it is separable in the flow and cross flow directions. The pressure cross-spectral density is:

$$\Gamma_{pp}(\xi_x, \xi_y, \omega) = e^{-\alpha_x|\xi_x k_c|}e^{-\alpha_y|\xi_y k_c|}e^{i\xi_x k_c}. \tag{2}$$

There are two terms in the flow direction—a complex oscillating term convecting at wavespeed U_c (corresponding to the convective wavenumber $k_c = \omega/U_c$), and an exponential decay term with coefficient α_x. There is also an exponential decay in the cross-flow direction controlled by α_y. This functional form assumes homogeneity across the plate, such that the cross-spectrum depends only on the separation distances ξ_x and ξ_y. Note that the αk_c terms are actually the inverses of the integral length scales, so that the normalized Corcos cross-spectral model may also be written as:

$$\Gamma_{pp}(\xi_x, \xi_y, \omega) = e^{-|\xi_x/L_x|}e^{-|\xi_y/L_y|}e^{i\xi_x k_c} \tag{3}$$

where the decaying exponential arguments are just the ratios of separation distances and length scales.

While convenient analytically, the assumption of separability is not realistic. Mellen [5] (and others) recognized this and proposed a simple change to an elliptical representation:

$$\Gamma_{pp}(\xi_x, \xi_y, \omega) = e^{-\sqrt{(\alpha_x|\xi_x k_c|)^2+(\alpha_y|\xi_y k_c|)^2}}e^{i\xi_x k_c}. \tag{4}$$

Now, instead of a distribution of rhombic coherence zones, which makes little physical sense, the Mellen model simulates a distribution of elliptical coherence zones, with the shape of the ellipse controlled by the ratio α_x/α_y. While this model is more appropriate, it does not yet appear to be in wide use.

We examine the two models further, starting with sample spatial distributions at a specific wavenumber k_x shown in Fig. 1. The differences between the models are clear, with sharp discontinuities in the rhombic Corcos model, and a smoother spatial distribution for the elliptical Mellen model, which is physically more realistic and

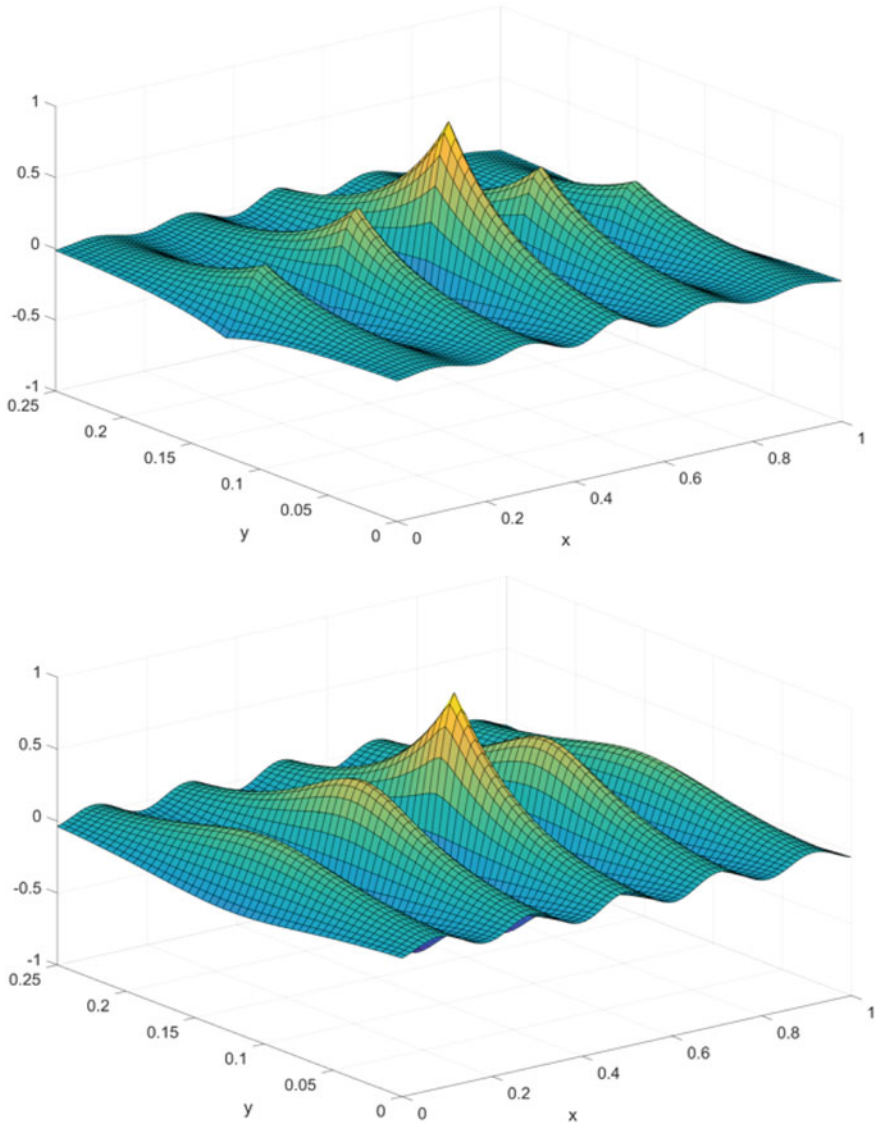

Fig. 1 Examples of Corcos (top) and Mellen (bottom) spatial cross spectral models normalized by peak value, reference at the plate center (point of positive peak amplitude)

better resembles measurements (Fig. 9 in Ref. [10]). It is more common to examine these models in wavenumber space. Fortunately, since the spatial functional forms are simple, the analytic wavenumber transforms are straight forward:

$$\text{Corcos}: \ \Gamma_{pp}(\bar{k}_x, \bar{k}_y) = \left\{ \frac{\alpha_x}{\pi\left[\alpha_x^2 + \left(1 - \bar{k}_x\right)^2\right]} \right\} \left\{ \frac{\alpha_y}{\pi\left[\alpha_y^2 + \left(\bar{k}_y\right)^2\right]} \right\} k_c^{-2} \tag{5a}$$

$$\text{Mellen}: \ \Gamma_{pp}(\bar{k}_x, \bar{k}_y) = \frac{1}{2\pi} \frac{\alpha_x^2 \alpha_y^2}{\left[\alpha_x^2 \alpha_y^2 + \alpha_y^2\left(1 - \bar{k}_x\right)^2 + \left(\alpha_x \bar{k}_y\right)^2\right]^{3/2}} k_c^{-2} \tag{5b}$$

where $\bar{k}_x = k_x/k_c$, and $\bar{k}_y = k_y/k_c$. As with the spatial forms of the models, these are normalized by the autospectrum amplitude, and therefore have dimensions of length squared (since they are two-dimensional wavenumber spectra). Figure 2 compares the distributions transformed into wavenumber space, and includes rectangles denoting the ranges of the peak modal wavenumbers typical of low flow speed excitation, such as that on automobiles. It is clear that the 'rhombic bias' in the Corcos model extends beyond $k_y = 0$, and will artificially amplify the response of any modes within the range shown.

It is most common to view the differences between these two models in k_x space with $k_y = 0$ as shown in Fig. 3. Both models have the usual strong convective 'ridge' at and around $k_x = k_c$, where the strongest pressure fluctuations propagate at an effective convection velocity, which is some fraction of the free stream velocity (more on this later). At low wavenumbers, we see a flat spectrum at constant level, referred to as the 'wavenumber white' region, which is a characteristic of any homogeneous TBL model that assumes a linear phase $e^{i\xi_x k_c}$ for the streamwise cross-spectrum. The reason for this is illustrated in Fig. 4, which shows the relationship between the cross-spectrum and the wavenumber spectrum. For a homogeneous field, the envelope of the cross-spectrum must be symmetric about $\xi_x = 0$. This gives a wavenumber spectrum that is also symmetric, but due to the phase $e^{i\xi_x k_c}$ the spectrum is shifted to the right and the symmetry is centered about k_c. Then, the value where the left-side tail crosses $k_x = 0$ appears as a wavenumber-white region when plotted on a logarithmic wavenumber axis. The model also gives values for negative wavenumbers, which have a questionable physical interpretation as they imply pressure disturbances propagating opposite to the flow (even though the flow model is incompressible, so there are no acoustic waves).

Theoretically, for a homogeneous incompressible flow over a plane surface, the conservation of mass requires that the value of the wavenumber spectrum at $k_x = k_y = 0$ be exactly zero [11]. Additional arguments based on the pressure Poisson equation suggest the spectrum should rise as k^2 at low wavenumbers, a feature incorporated in the Chase model [12] (Chase later considered the effect of acoustic contributions to the low wavenumbers, which modifies the result [13]). However, if the boundary layer thickness δ is large enough, the Chase model also predicts a wavenumber-white plateau in the intermediate low wavenumber range around $\delta^{-1} < k_x < 0.1k_c$ (see [14]). Experimental measurements [15, 16] have generally not observed the k^2 region and tend to support the notion of an approximately wavenumber-white low wavenumber region. Furthermore, in actual flows the

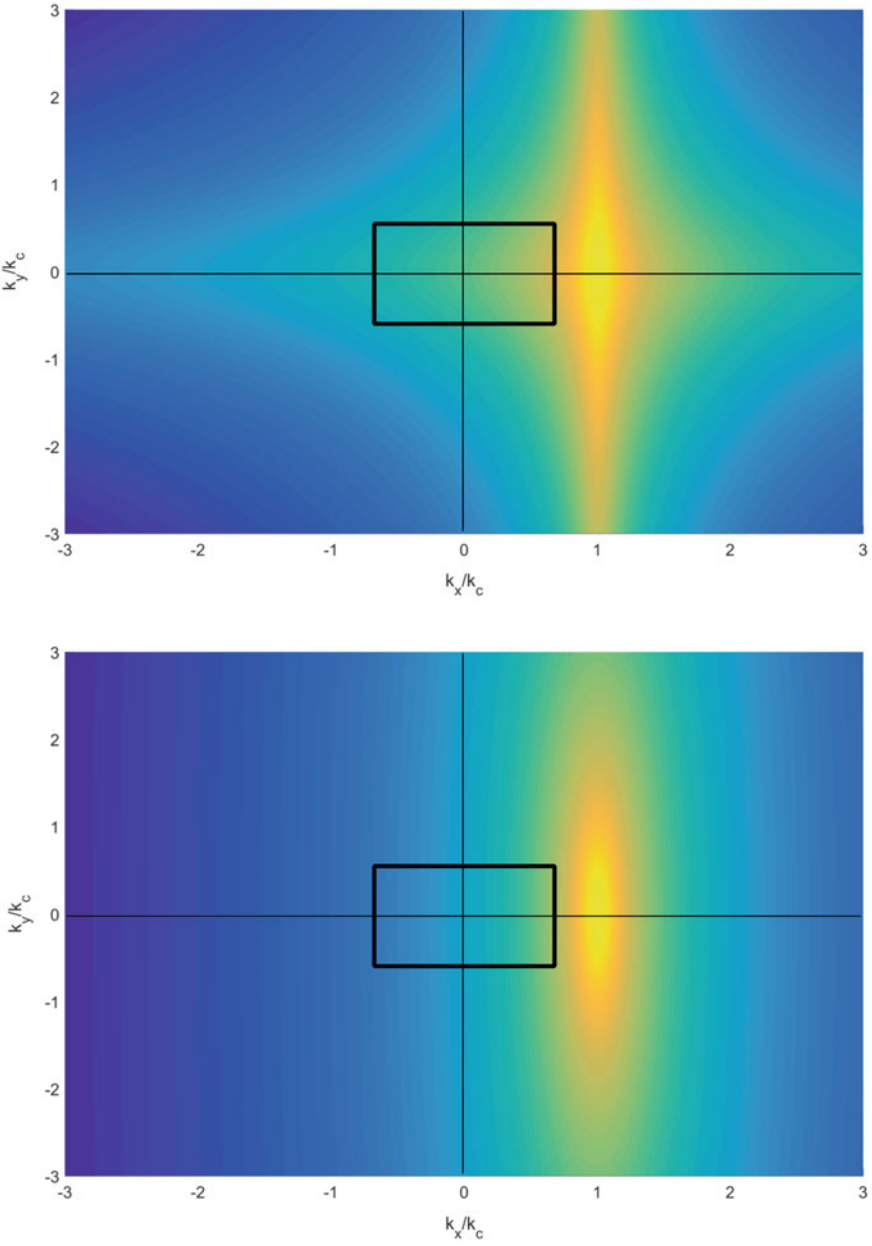

Fig. 2 Examples of Corcos (top) and Mellen (bottom) wavenumber distribution models with wavenumbers normalized by convective wavenumber. The convective 'ridge' is at k_x/k_c of 1. The rectangles represent typical regions of peak structural modal wavenumber response for low wavenumber excitation (where $k_b < k_c$)

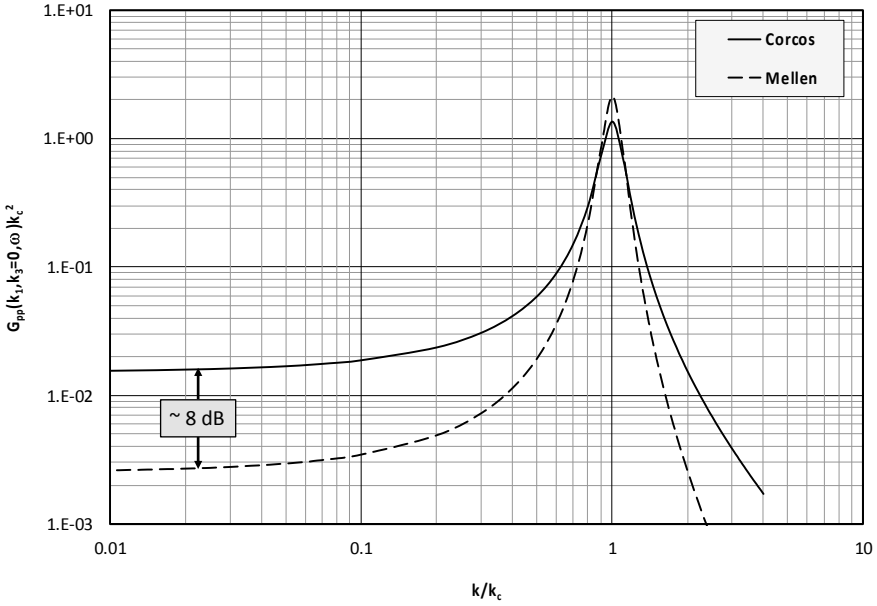

Fig. 3 Streamwise wavenumber content of TBL wall pressures for $k_y = 0$ and $\alpha_x = 0.11, \alpha_y = 0.7$

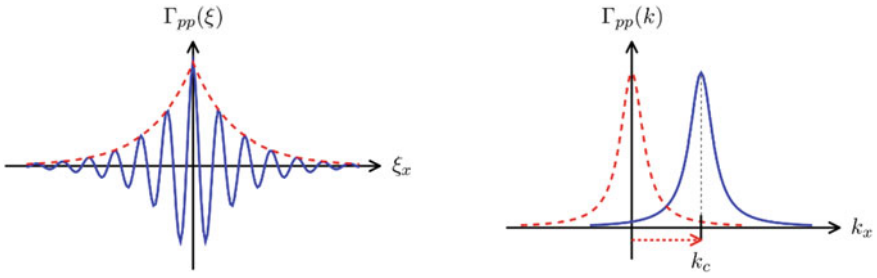

Fig. 4 Illustration of the relationship between the cross-spectrum (left) and wavenumber spectrum (right), showing how the rightward shift of the wavenumber spectrum for a linear phase cross-spectrum model gives a non-zero low wavenumber level

boundary layer grows along the plate, and thus the wall pressure field is not strictly homogeneous, so there may be other factors influencing the low wavenumber results.

Because our aim is to use a simple TBL model for plate excitation, we assume the linear phase and subsequent wavenumber-white approximation is reasonable. The plate vibration predictions shown later support this hypothesis, but it should be recognized that the theoretical justification for the model remains weak, and it is essentially just an engineering approximation rather than an exact description of the physics. Further consideration of low wavenumber modeling can be found in [14] and the accompanying chapter by DeJong [17] in this edition.

The obvious difference between the Corcos and Mellen models (at least where $k_y = 0$) is the reallocation of spectral energy to the convective peak in the Mellen model, and a corresponding reduction in the low wavenumber level, about 8 dB for the usual assumption of $\alpha_x = 0.11$ and $\alpha_y = 0.70$. The very low wavenumber limits of the two models for $k_y = 0$ depend on the two α coefficients and frequency:

$$\text{Corcos}: \ \Gamma_{pp}\left(k_x \to 0, k_y = 0, \omega\right) \approx \frac{\alpha_x}{\pi^2 k_c^2 \alpha_y}, \ \text{and} \tag{6a}$$

$$\text{Mellen}: \ \Gamma_{pp}\left(k_x \to 0, k_y = 0, \omega\right) \approx \frac{\alpha_x^2}{2\pi k_c^2 \alpha_y}. \tag{6b}$$

Since it is simple to adjust the α coefficients to set the low wavenumber level to an arbitrary value, there has been much abuse of the Corcos model over the years, with different α values chosen to best match measured data. In reality, the wavenumber energy distribution may indeed have been different for these cases (and likely more elliptical).

2.2 Convection Velocities and Decay Coefficients

All empirical TBL wall pressure cross-spectral models require some estimate of the effective convection velocities U_c of the propagating wall pressure field, and its spatial coherence, set by the α_x and α_y decay coefficients. Corcos [4] focused on the scale-independent region, where the only relevant length scale is U_c/ω. Physically, this corresponds to turbulent sources in the log-layer of the boundary layer, which exhibit a similar scale independence. While this is an appropriate assumption for correcting high frequency attenuation from sensor area-averaging (the intended application for Corcos's work), for plate excitation a wider frequency range often needs to be considered. Resulting from the popularity of the Corcos model, it is common, but overly simplistic, to assume constant convection velocities (typically between 65% and 75% of free stream velocity) and constant decay coefficients (usually 0.11 and 0.70) over all frequencies. This is usually only valid in the high frequency range that corresponds to the scale-independent assumption. Even early TBL wall pressure correlation measurements, such as the datasets by Wilby [1], Bull [10], and Abraham and Keith [18] show clear frequency dependencies at lower frequencies. The measurements also show that these parameters are limited by boundary layer height, particularly the decay coefficients.

Bull [10] suggested a simple model for convection velocity which remains in wide use:

$$\frac{U_c}{U_o} = 0.59 + 0.30e^{-0.89\omega\delta^*/U_o}. \tag{7}$$

The model depends on the nondimensional Strouhal number based on boundary layer displacement thickness δ^* and free stream velocity U_o. Smol'yakov [6] suggests a different model which exhibits a peak convective velocity near $\omega\delta^*/U_o$ of about 0.25, which is consistent with Abraham and Keith's measurements [18]:

$$\frac{U_c}{U_o} = 0.60 + \frac{1.6(\omega\delta^*/U_o)}{1 + 16(\omega\delta^*/U_o)^2}. \tag{8}$$

Both convection velocity models are compared in Fig. 5. The models converge to nearly the same high frequency values (0.59 and 0.60), but the Smolyakov model captures the low frequency convection velocity reduction associated with finite boundary layer heights, which is apparent in the Bull and Keith and Abraham measurements.

While the measurements of convection velocity provided in the literature exhibit only modest uncertainty (± 5-10% seems typical), measurements of spatial coherence lengths are much more uncertain. This is caused by difficulty in measuring coherence, and assuming an exponential decay, which may be inappropriate. Plots from Wilby are reproduced in Fig. 6. Along with the uncertainty, clear low frequency/separation distance plateaus are evident in the measured data. Wilby and Bull proposed limiting the effective length scale to 27 times the boundary layer displacement thickness. Smolyakov also suggests an adjustment based on boundary layer height, which make physical sense, and shows a 'hump' in length scale at low frequencies:

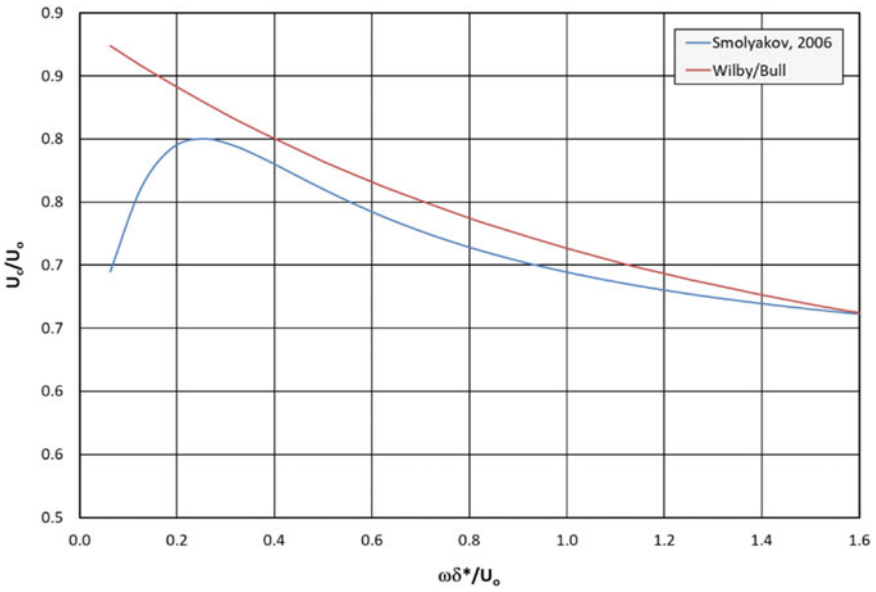

Fig. 5 Bull/Wilby and Smolyakov convective velocity models

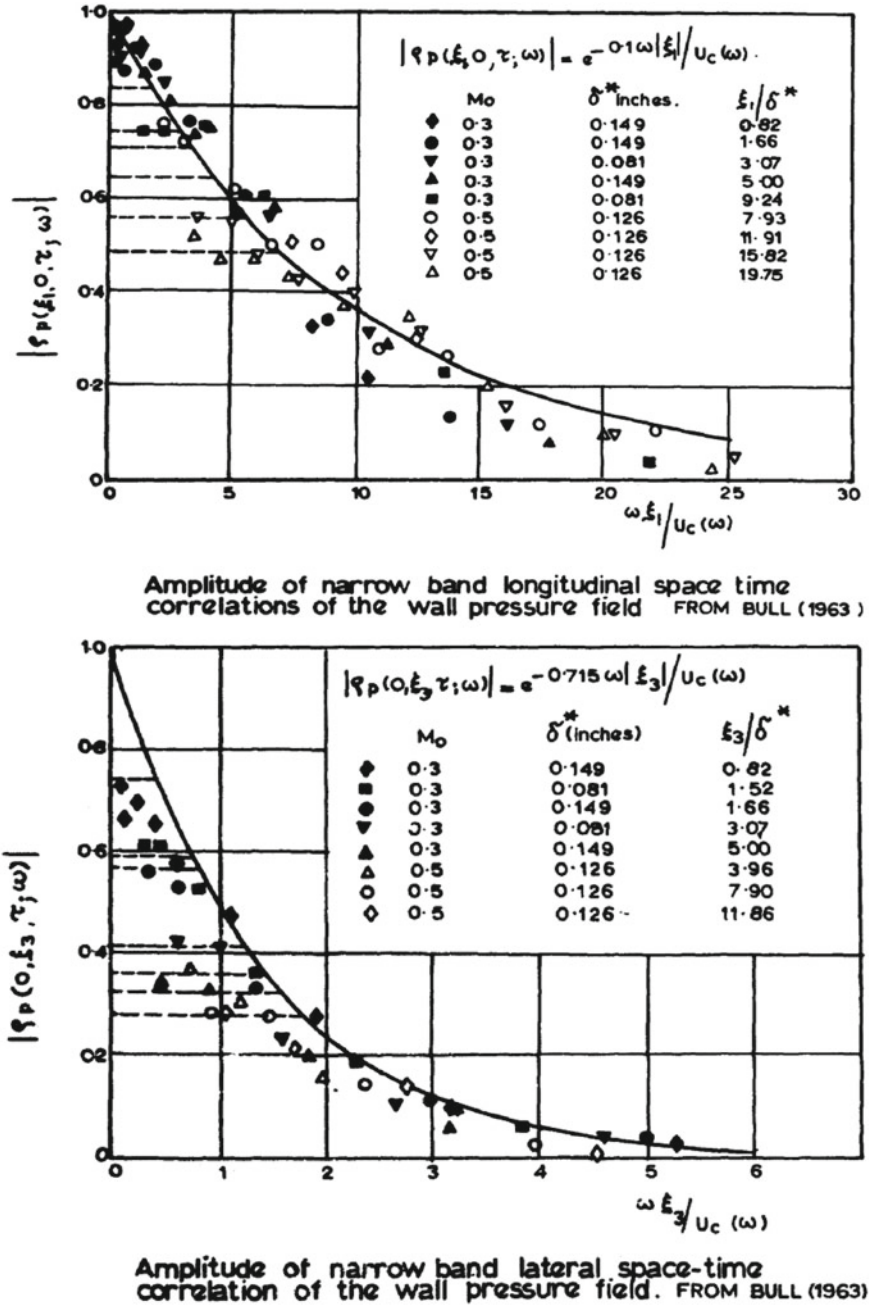

Fig. 6 Bull and Wilby measurements of streamwise (top) and cross-flow (bottom) spatial correlations. Reproduced from US Government Report [1]

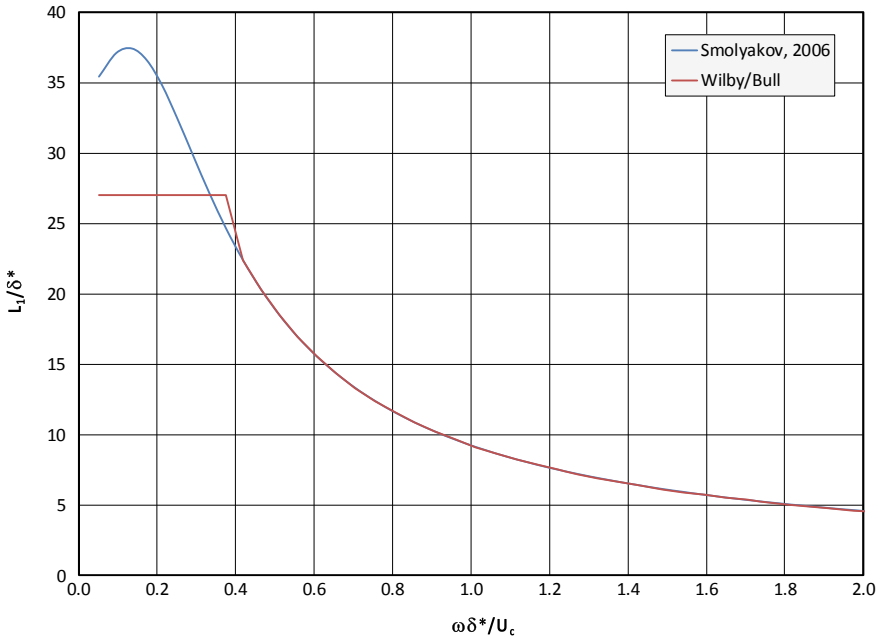

Fig. 7 Bull/Wilby and Smolyakov models of streamwise integral length scale where $L_1 = U_c/(\alpha_x \omega)$

$$\alpha_x = 0.124\sqrt{(1 - 0.25\left(\frac{U_c}{\omega\delta*}\right) + \left(0.25\frac{U_c}{\omega\delta*}\right)^2}. \tag{9}$$

Note that this equation requires computing the convective velocity U_c first. Also, Smolyakov assumes the usual ratio of α_y/α_x of 6.45.

The two models are compared in Fig. 7 in terms of streamwise length scale normalized by displacement thickness. In this study, we use the Smolyakov models for convection velocity and decay coefficients for both the Corcos and Mellen cross-spectrum model calculations.

2.3 Forced Response Calculations

The analytic forced response calculations are performed with the usual random response analysis approach, as described in [19–21]. Analytic resonance frequencies and mode shapes of the plates are calculated based on the dimensions, material properties, and boundary conditions. Since we are focusing on comparing the Corcos and Mellen cross-spectral forcing models, we equate the structural resonance frequencies and loss factors used in the calculations to those observed during the measurements.

This alignment allows us to more easily compare analytical and measured vibration spectra.

The response of the modes to the TBL pressure fields (sometimes termed the 'joint acceptance') is calculated over physical space, rather than wavenumber space. Many investigators prefer to calculate joint acceptance in wavenumber space to reduce computational times and memory requirements. However, since not all structures of interest are purely rectangular, and the TBL pressure autospectra are not always spatially homogeneous, the spatial approach is more appropriate for practical use.

Performing these calculations in the spatial domain, however, requires resolving the very high wavenumber content of the TBL wall pressure field, centered at the convective wavenumbers. Failing to resolve these high wavenumber forcing oscillations biases the calculated vibration response significantly higher. For low speed flows the convective wavenumber can be 10 times higher (or more) than the structural modal peak wavenumber response. This requires many more spatial points than is necessary to resolve the mode shapes. Convergence studies show that at least four divisions per convective wavelength are required for both models. For the Corcos model, four divisions/wavelength are also required in the cross-flow direction. For the Mellen model, 16 divisions/wavelength in the cross-flow direction are necessary. Fortunately, since high wavenumber forcing does not couple well with lower wavenumber structural modes, asymptotic approaches like those described in [21], which effectively filter the high wavenumber excitation from the forcing distribution, may be used to compute structural response more efficiently.

3 Measurements

Table 1 summarizes the three measurements and Fig. 8 compares the panel and boundary layer sizes. The Wilby panels are small to ensure the TBL field is homogeneous over the panel surface and to set the resonance frequencies above 300 Hz. The ISVR facility had known low frequency background noise problems below that frequency. This problem is common to all facilities, with the Purdue and Sherbrooke background noise significant for frequencies below about 100 Hz. These acoustic background noise signals can excite the test panels more efficiently than TBL flow, biasing the measurements (see Appendix 2 for a discussion of this topic).

The Purdue and Sherbrooke panels are larger than Wilby's, and in fact the TBL fields may not have been truly homogeneous in those facilities. The boundary layers in the ISVR facility were larger (about 35% of the panel length) than those in the Purdue and Sherbrooke facilities (5% of the panel lengths). The three tests have different combinations of plate materials and edge boundary conditions. ISVR and Purdue used clamped boundaries (or as close as they could realize such boundaries, which are difficult to emulate in practice). In general, clamped boundaries are preferred as they weaken the high wavenumber responsiveness of the panel modes near the convective peak of the forcing field (see the examples in [19]). However, simple supports (used in the Sherbrooke facility) are easier to model analytically. Data for

Table 1 Summary of three measurements. Results for **bold** flow speeds shown here

	ISVR (Wilby [1])	Purdue (Han [2])	Sherbrooke (Robin et al. [3])
Facility	Wind tunnel with open ends Pressurized injected flow	Wind tunnel with open ends Fan drive	Nozzle discharge into anechoic room
Plate area (cm^2)	71.4	1739	2016–3150
Plate thickness (mm)	0.38	1.59	3.17
h/L	0.0037	0.0034	0.0051
Plate boundary conditions	Clamped	Clamped	Simply supported
Plate materials	Steel	Steel	Aluminum
δ/L	~0.35	~0.05	~0.05
Flow speeds	**103 m/s** 172 m/s	35.8 m/s **44.7 m/s**	20 m/s **28 m/s**
Notes	Small panels avoid inhomogeneous flow Panels very thin to increase vibration	Clamped boundaries reduce convective and acoustic wavenumber panel excitation	Panel A2 Simply supported boundaries simplify comparisons to analytic calculations

two flow speeds are available for each test, with results for the **bold faced** speeds shown here.

Figure 9 compares the plate modal wavenumbers to the TBL wavenumber frequency spectrum (with $k_y = 0$) and the convective wavenumbers. Figure 9a plots each panel modal wavenumber normalized by the convective wavenumber at the corresponding modal resonance frequencies. The k/k_c ratios decrease with increasing frequency as the panel flexural wavespeeds increase. The three test cases overlap to cover the range $0.09 < k/k_c < 1.6$. The k/k_c ranges for each panel are denoted on the wavenumber-frequency spectra plot in Fig. 9b. The differences between the Corcos and Mellen low wavenumber frequency spectra should manifest in the panel vibration results.

4 Results and Comparisons

Figures 10, 11, and 12 compare simulated and measured normalized acceleration PSDs (G_{aa}/G_{pp}) for the Wilby, Purdue, and Sherbrooke panels. Vibration measurements are only available for a single point on the Wilby panel. The spectra for the Purdue and Sherbrooke data are averaged over several locations. The figures show the

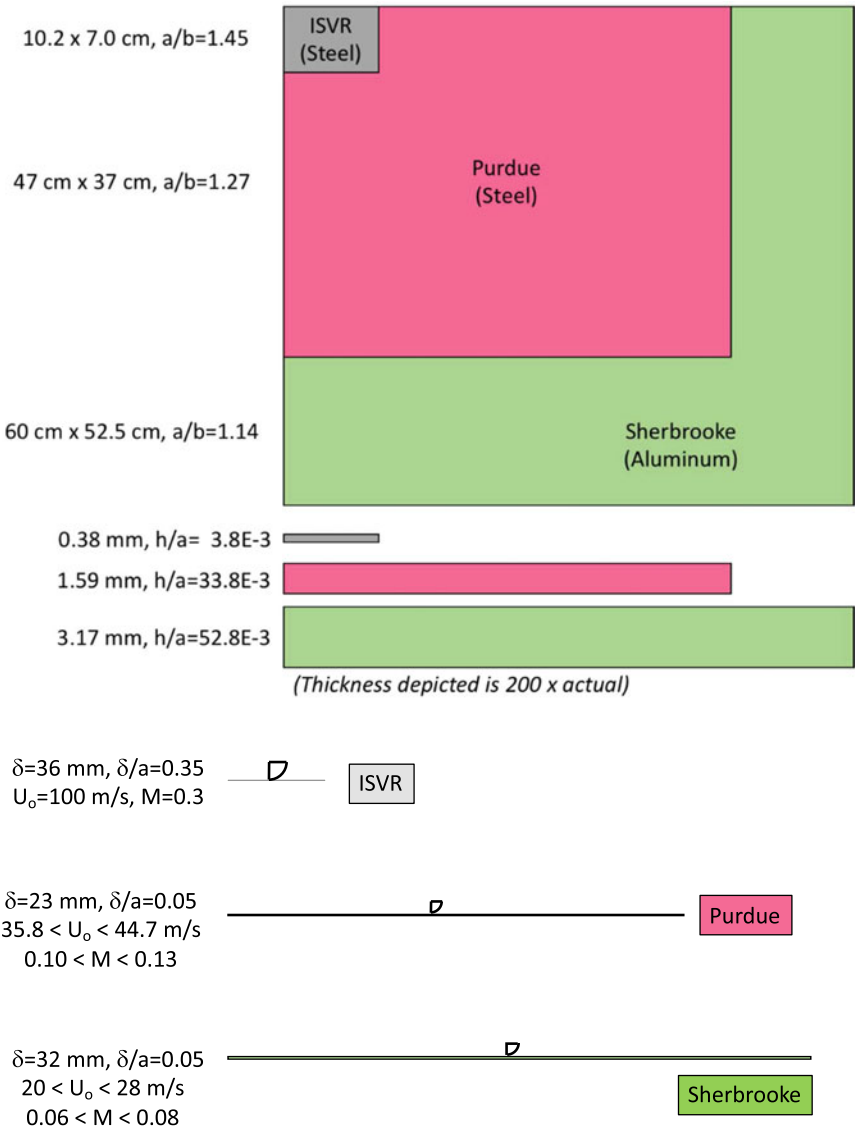

Fig. 8 Plate comparison. Top—dimensions, Bottom—flow parameters

measurement point locations, assumed structural loss factors, and convection velocities and streamwise length scale coefficients computed using Smolyakov's methods. The spectral plots are shown versus frequency, and also against wavenumber ratio k_b/k_c (see the top horizontal axes). As mentioned earlier, the ranges of the three k_b/k_c ranges overlap nicely, spanning a complete range of $0.09 < k_b/k_c < 1.6$. The structural loss factors were inferred from the measured peak responses using the

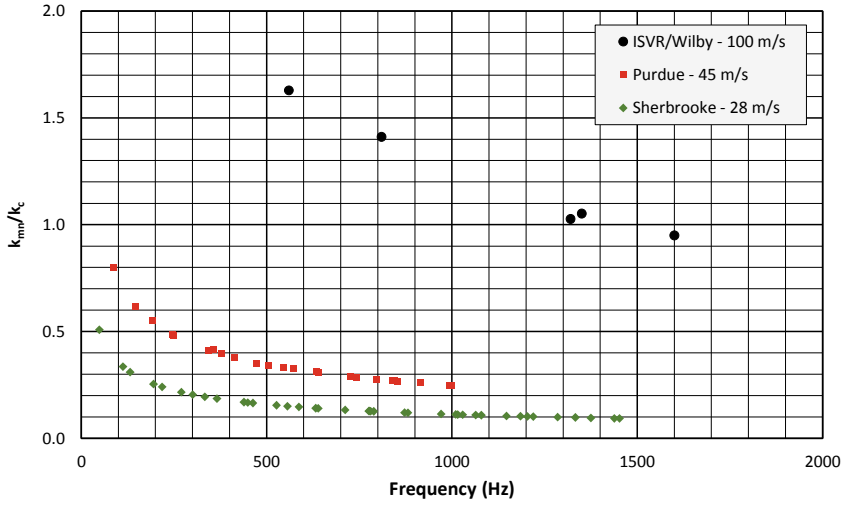

(a)

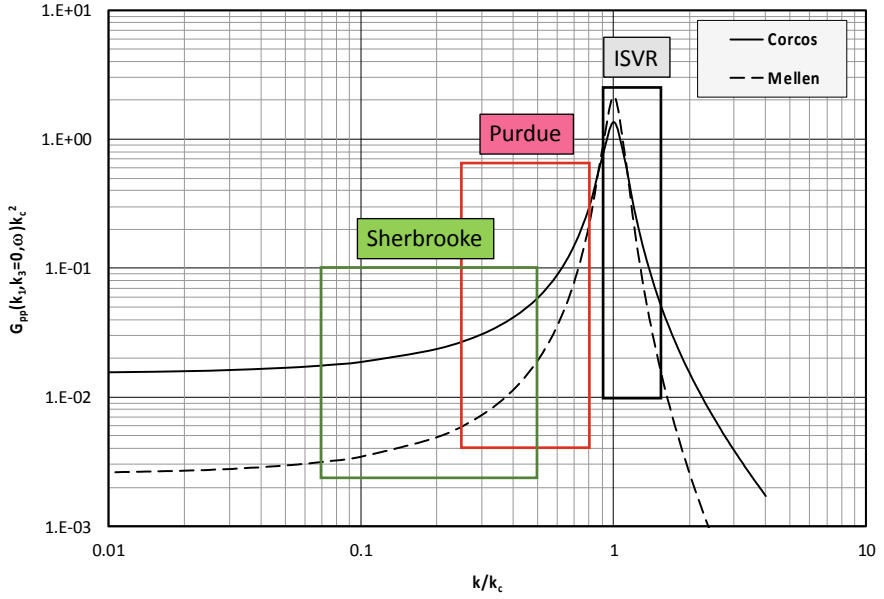

(b)

Fig. 9 **a** Ratios of panel modal wavenumbers and convective wavenumbers. **b** Streamwise wavenumber content of TBL wall pressures for $\alpha_x = 0.11$, $\alpha_y = 0.7$ with ranges of panel modal wavenumbers

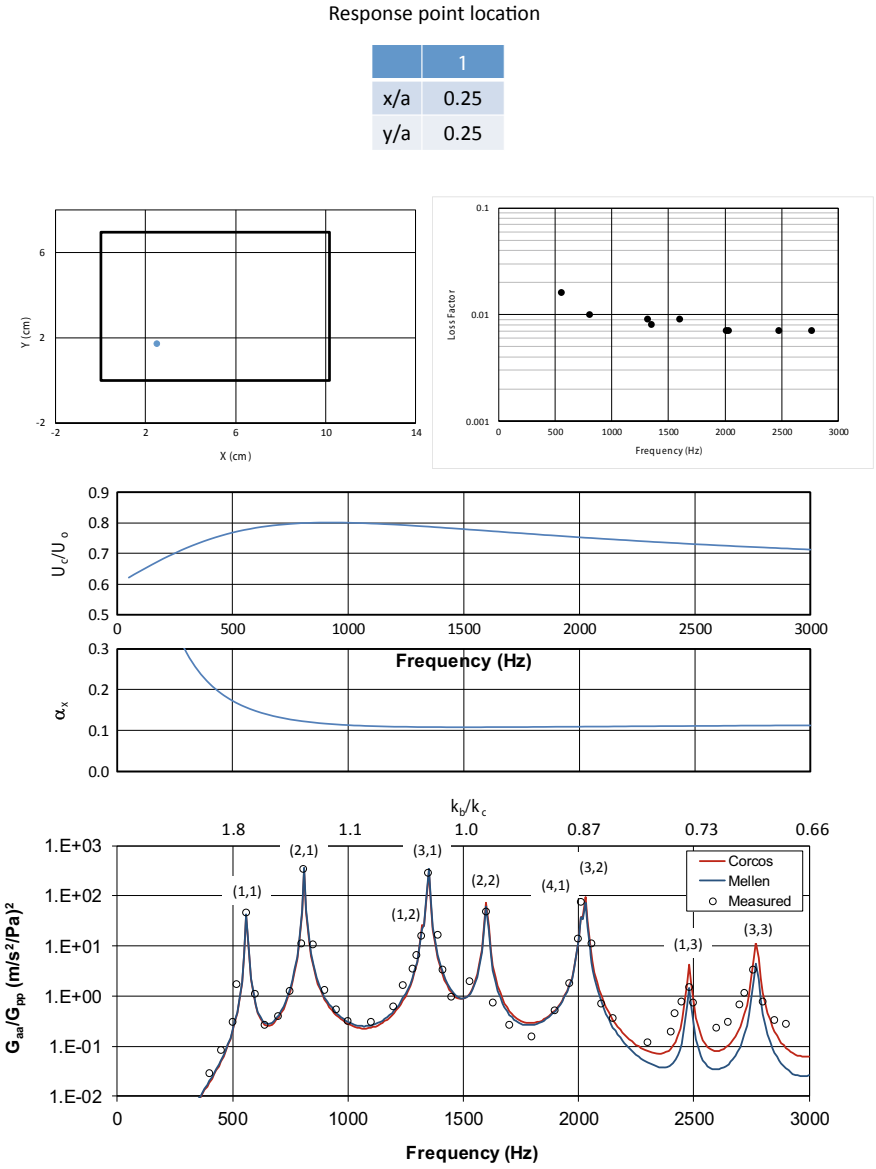

Fig. 10 Wilby/ISVR panel, 103 m/s

Response point locations

	1	2	3	4	5	6	7	8	9	10	11	12
x/a	.13	.19	.26	.32	.45	.51	.57	.64	.70	.77	.83	.89
y/b	.49	.32	.81	.32	.24	.57	.89	.49	.24	.81	.49	.89

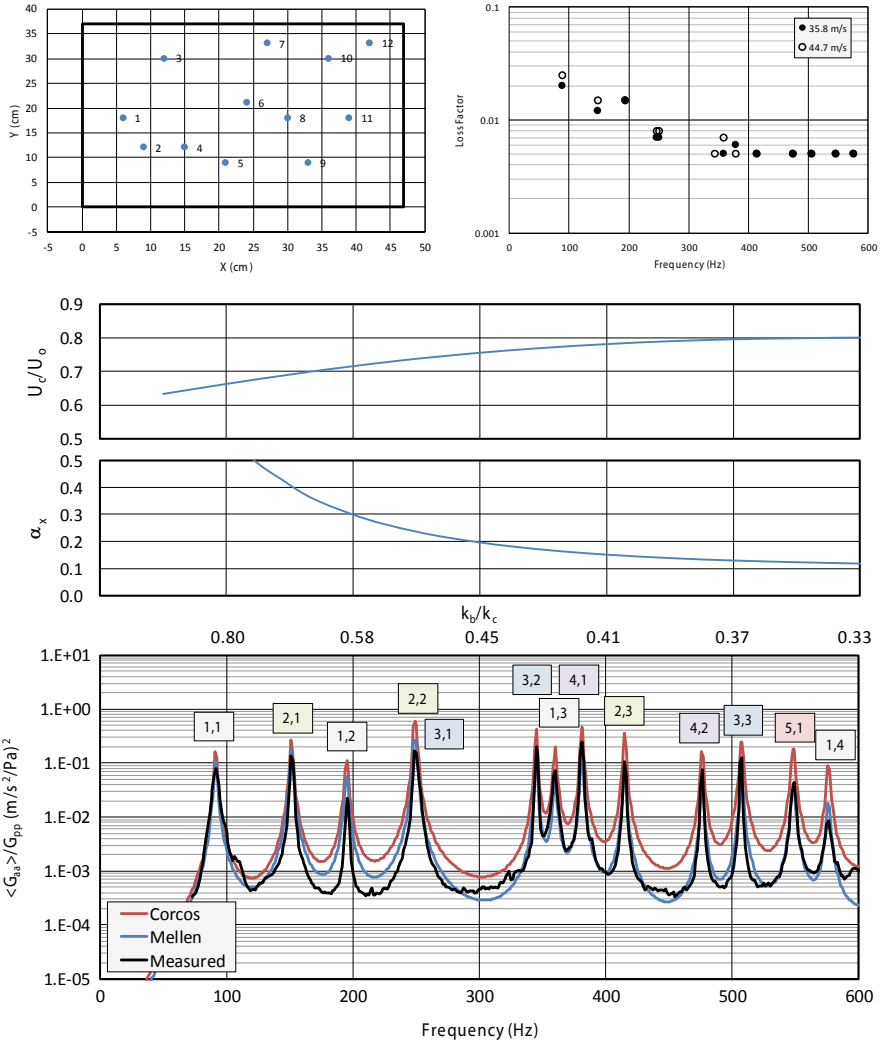

Fig. 11 Han/Purdue plate Data, 45 m/s

Response point locations

	1	2	3	4	5	6	7
x/a	0.50	0.63	0.50	0.33	0.88	0.71	0.56
y/b	0.50	0.37	0.78	0.33	0.29	0.83	0.50

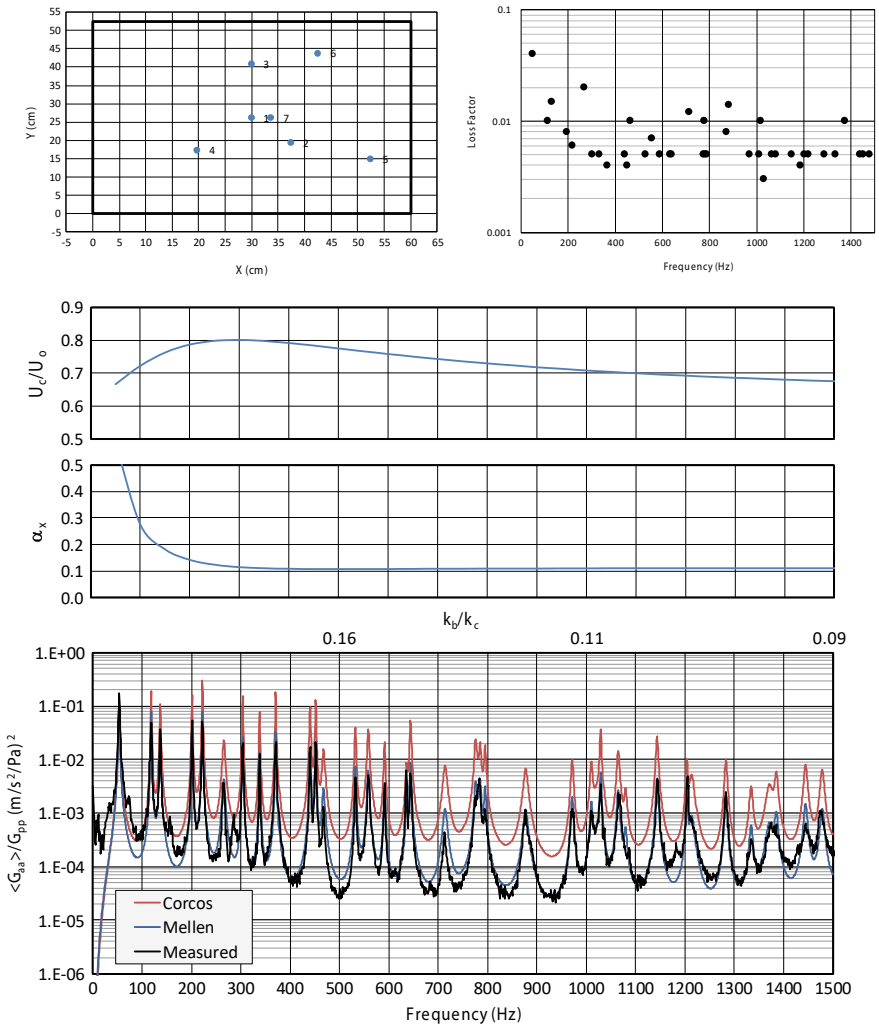

Fig. 12 Sherbrooke panel A2, 28 m/s

traditional half power bandwidth method for the Wilby and Purdue data. Acceleration cross-spectral densities are available for the Sherbrooke data, and were input to an Operational Modal Analysis (OMA) algorithm to estimate damping more accurately. Loss factors which could not be accurately assessed were set to 0.005 for the Han and Sherbrooke plates.

The streamwise length scale coefficient α_x increases with decreasing frequency, limiting the spatial correlation length scale to a multiple of the boundary layer height (as shown in Fig. 7). *Using a constant* α_x *(which some investigators have done, including the authors in past papers) will inappropriately bias the low frequency loading higher, leading to higher simulated vibrations.* The effective convection velocity decreases with decreasing frequency, shifting the loading wavenumbers higher, and generally further away from the plate vibration wavenumbers. *Again, assuming a constant convection velocity over all frequencies will not capture this effect, biasing simulations high.* Figure 13 compares the Purdue panel calculations made with the Mellen cross-spectral model and (a) Bull's convection velocity and correlation coefficients and (b) convection velocity and correlation coefficients computed using Smolyakov's equations. Using Smolyakov's estimates clearly improves the low frequency simulations.

The three sets of results show a clear trend: either the rhombic Corcos or elliptical Mellen models may be used for conditions where $k_b \approx k_c$ (the high speed ISVR/Wilby case). However, for lower k_b/k_c ratios the rhombic Corcos model leads to vibration overestimates. The overestimates worsen with decreasing k_b/k_c. Also, vibrations simulated with the Mellen model supplemented with Smolyakov convection velocities and length scales agree well with all three sets of measurements, showing good robustness for a wide range of structural and flow conditions. This robustness is

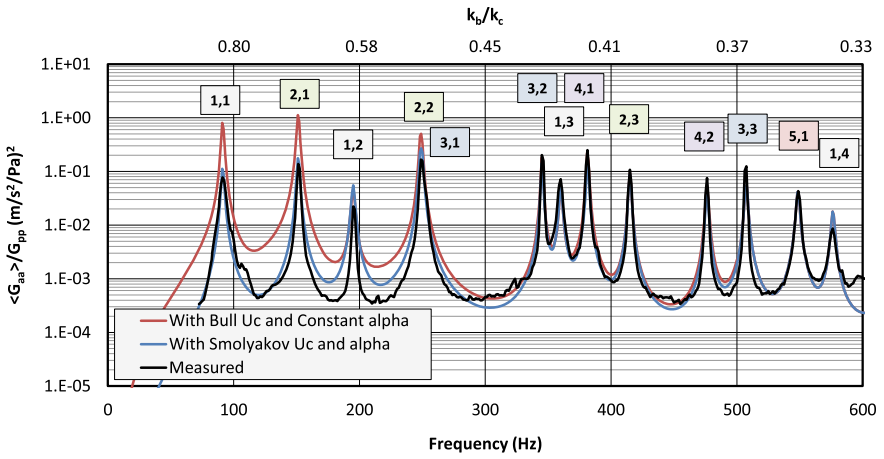

Fig. 13 Purdue panel vibration computed with Mellen model with different convection velocities and spatial coherences

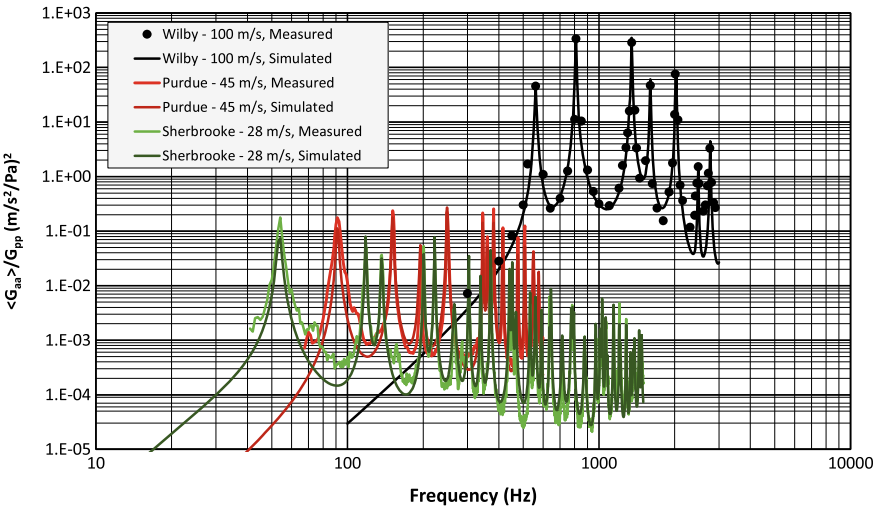

Fig. 14 ISVR, Purdue, and Sherbooke simulated and measured normalized vibration spectra

shown clearly in Fig. 14, which combines measurements and simulations for all three cases.

5 Summary and Conclusions

We demonstrate conclusively, based on benchmarking with three widely differing measurements, that the simple elliptical model of the TBL wall pressure cross-coherence proposed by Mellen is more appropriate for TBL-excited panel vibration simulations than the more widely used rhombic Corcos model for $k/k_c < 1$. Recent work by Karimi et al. [22] also shows that the Mellen model is more appropriate for general use. Supplementing the Mellen model with Smolyakov's empirical formulae for convection velocity and spatial coherence factors (which accounts for the effects of finite boundary layer height) improves low-frequency accuracy.

Although this study shows that the Mellen/Smolyakov approach works well for a wide range of conditions, we must acknowledge there remain uncertainties in the test data which will likely remain unresolved, and could affect the conclusions here. For example, it is common for test cases like those of Purdue and Sherbrooke (low wavenumber TBL excitation of mode shapes) to be biased by the presence of acoustic sources in the test facilities. Recall Fig. 3 which shows how weak the low-wavenumber excitation is. Acoustic waves, either those which are fairly deterministic and propagate in fairly constant directions, or random collections of waves which behave like a diffuse field, often excite structural modes far more efficiently than TBL wall pressures. These sources are seldom fully quantified in wind or water tunnel facilities. See Appendix 2 for a discussion of these effects.

Also, except for Wilby's small plates, it is highly likely that the actual TBL wall pressure fields acting on the Purdue and Sherbrooke plates are nonhomogeneous, with the boundary layer continually growing as it propagates downstream. This leads to larger integral length scales on the downstream portion of the plate, and reduced spatial cancellation of convective wavenumber energy. The effects of this reduced cancellation remain unknown, but it will certainly increase the panel modal acceptance functions and overall vibration. It is therefore possible that other low-wavenumber cross-spectrum models, such as those of Chase [12, 13] and De Jong [16, 17], with even lower low wavenumber amplitudes than those in the Mellen model may actually be more accurate.

Also, as mentioned earlier, practitioners commonly adjust the α coefficients in their model of choice to simply amplify or attenuate the low-wavenumber forcing function region to obtain better agreement in their benchmarking. This is usually inappropriate except in cases with rough surfaces where the decay coefficients can be higher, reducing the extents of the spatially coherent regions.

These uncertainties and the continued elusiveness of pure, unbiased low-wavenumber TBL wall pressure measurements, along with remaining theoretical questions about the nature of the low-wavenumber spectrum, make clear the need for further experimental studies in this area. However, there is little doubt that using a separable rhombic Corcos model for TBL-induced vibration and noise analysis is inappropriate when subconvective wavenumbers are important in panel excitation. Past measurements [10] and high resolution CFD simulations [23] conclusively show that the spatially coherent wall pressure zones resemble ellipses, not rhombuses. The proper representation of decay coefficients and convection velocities, however, is certainly a valid subject for future debate but only using elliptical or similar models as a basis.

Appendix 1: Autospectra Comparisons

Although this study focuses on the cross-spectral behavior of TBL wall pressure fluctuations, autospectra were measured in the three facilities also. The ISVR pressure spectra are not available in digital form, but the empirical model of Goody [24] was derived in part on these data. The wall pressure spectra at multiple speeds in the Purdue and Sherbrooke facilities scale well with each other, and single speed data from each are compared here. There are many empirical wall pressure spectrum models [8], but we compare the measurements to only two: the model of Goody, and a modified form of a model suggested by Howe [25].

The single-sided cyclic frequency Goody model is:

$$\phi_{pp}(f) = 2\pi\left(\frac{\rho^2 U_\tau^4 \delta}{U_e}\right)\frac{a\left(\frac{2\pi f\delta}{U_e}\right)^b}{\left[\left(\frac{2\pi f\delta}{U_e}\right)^e + d\right]^e + \left\{f\left[\left(\frac{U_\tau}{U_e}\right)\left(\frac{U_\tau\delta}{\nu}\right)\right]^g\left(\frac{2\pi f\delta}{U_e}\right)\right\}^h} \tag{10}$$

where ρ is the fluid density, U_τ is the friction velocity, δ is the boundary layer thickness, U_e is the boundary layer edge velocity (free-stream velocity for a flat plate), ν is the kinematic viscosity, and the empirical constants are $a = 3.0, b = 2, c = 0.75, d = 0.5, e = 3.7, f = 1.1, g = -0.57, h = 7$. Goody performed a thorough analysis of a large number of datasets to arrive at the empirical constants, but it should be noted that there is considerable spread in the reported data, which limits the precision of any empirical model.

The Howe model [25] is based on a simplification of the autospectrum developed by Chase [12], and several authors (following the lead of Goody) have referred to it as the Chase-Howe model. The single sided cyclic frequency Chase-Howe model can be written in the form

$$\phi_{pp}(f) = 2\rho^2 U_\tau^4 \left[\frac{f^2}{\left(f_\delta^2 + f^2\right)^{3/2}} \right] \tag{11}$$

where $f_\delta = 0.12 U_e/(2\pi\delta^*)$ and δ^* is the displacement thickness. As Goody and others have noted, the model does not include the steep roll-off at high frequencies associated with viscous dissipation, and therefore cannot be integrated to get the mean-square pressure.

Lysak [26] developed a model in terms of integration of the turbulence—mean shear interaction sources in the boundary layer, based on the solution of the pressure Poisson equation. This model can be evaluated numerically for a given boundary layer mean velocity profile and assumed turbulence characteristics. The mid-to-high frequency range of the solution depends entirely on the log and viscous regions of the boundary layer, so it can be normalized using inner variable scaling (ρ, U_τ, ν). Due to the characteristics of the log region, the mid-frequency range asymptotically approaches an f^{-1} slope as the Reynolds number tends to infinity, so it can be matched to the Chase-Howe model. At high frequencies, an exponential decay factor was found to closely match the computed viscous region. This leads to following modification to the Chase-Howe model:

$$\phi_{pp}(f) = 3\rho^2 U_\tau^4 \left[\frac{f^2}{\left(f_\delta^2 + f^2\right)^{3/2}} \right] exp\left(-14 \frac{f\nu}{U_\tau^2} \right) \tag{12}$$

where the constant has been changed from 2 to 3 to match the computed f^{-1} region, and the exponential decay factor has been included to model the viscous region. The form of the low frequency peak has not been changed from the Chase-Howe model. We refer to Eq. 12 as the 'Chase–Howe–Lysak' TBL autospectrum model.

The Purdue and Sherbrooke wall pressure measurements are corrected for sensor spatial resolution bias errors, scaled on outer variables and compared to the Goody and Chase–Howe–Lysak empirical models in Fig. 15. The agreement is mixed, with both empirical models matching well over different frequency ranges and datasets. The Sherbrooke low frequency pressures are known to be affected by the non-TBL

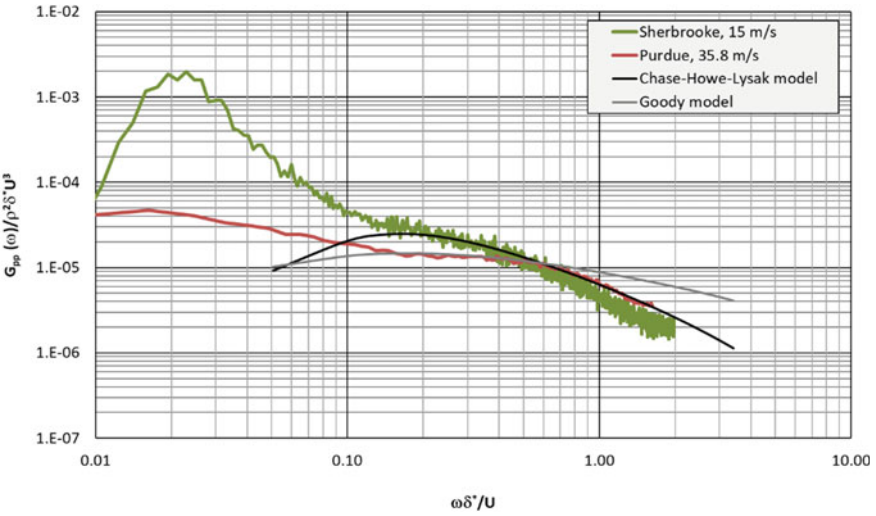

Fig. 15 Nondimensionalized single-sided wall pressure autospectra measured in Purdue and Sherbrooke facilities compared to Goody and Chase–Howe–Lysak empirical models

flow-induced noise source in their facility. This comparison is typical of the results found when comparing pressure spectra reported in the literature, and illustrates the difficulty in choosing appropriate wall pressure autospectra models for general use. The low frequency corruption shown here is, unfortunately, quite typical of most wind and water tunnel facilities. These low frequency sources will induce structural vibration of unknown strength (since their spatial correlations are not readily known).

Appendix 2: Diffuse Acoustic Field Effects

All test facilities have background vibration and sound levels caused by various sources. Acoustic background noise in wind and water tunnels can be caused by the turbulent flow itself (usually quite low at small Mach Numbers), and more importantly from sound generated by the turbulence convecting over surfaces, exiting ducts, and impinging on bodies in the flow path. Sound within tunnels can be particularly strong at low frequencies, where 'humps' in the spectra caused by turbulent flow are often centered. Also, acoustic waves can be one dimensional at very low frequencies in tunnels, and therefore of comparable amplitude throughout the facility. These effects are visible in all three facilities considered in this study.

However, at higher frequencies the modal density in a tunnel acoustic volume increases significantly such that the acoustic sound field becomes statistically diffuse. The effects of Diffuse Acoustic Fields (DAF) on panel vibration can be significant, particularly for stiff panels where flexural and acoustic wavenumbers are comparable.

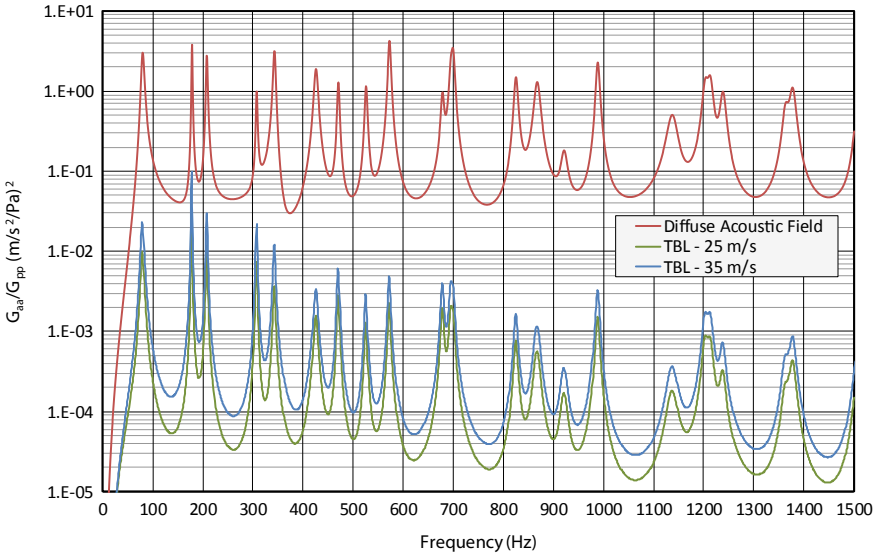

Fig. 16 Simulated Sherbrooke panel response to TBL flow at two speeds and Diffuse Acoustic Field loading

The DAF acoustic loading must therefore always be considered when measuring TBL-excited structural response. The relative response of the Sherbrooke panel to slow TBL flow and DAF loading is shown in Fig. 16. Once again, we compare the normalized G_{aa}/G_{pp} functions. The DAF spatial pressure distribution is modeled with the usual $\sin(k_o r)/k_o r$ empirical model, where r is the separation distance between points on the panel.

The plot shows that the panel is much more responsive to the DAF, by one to two orders of magnitude at low frequencies, and three orders of magnitude at higher frequencies. *This implies that any diffuse acoustic background noise that is three orders of magnitude lower than the TBL wall pressure autospectrum will cause plate vibration comparable to that of the TBL pressures.* In most cases, three orders of magnitude of signal to noise is acceptable. This is not the case with TBL-excited plate measurements, however. It is therefore quite common to see 'tail-ups' at higher frequencies in TBL-excited plate vibration measurements. This is a sign that acoustic background noise has corrupted the data.

References

1. J.F. Wilby, The response of simple panels to turbulent boundary layer excitation, October 1967. Technical Report AFFDL-TR-67-70 (1967)
2. F. Han, Prediction of flow-induced sound and vibration using the energy flow analysis method. Ph.D. thesis, Purdue University (1999)

3. O. Robin et al., *Exact Geometric Similitude Laws for Flat Plate Vibrations Induced by a Turbulent Boundary Layer* (Springer, Flinovia II, 2019)
4. G.M. Corcos, Resolution of pressure in turbulence. JASA **35** (1963)
5. R.H. Mellen, On modeling convective turbulence. JASA **88**(6) (1990)
6. A.V. Smol'yakov, A new model for the cross spectrum and wavenumber-frequency spectrum of turbulent pressure fluctuations in a boundary layer. Acoust. Phys. **52**(3), 331–337 (2006)
7. Y.F. Hwang, W.K. Bonness, S.A. Hambric, On modeling structural excitations by low speed turbulent boundary layer flows. ARL/Penn State Technical Report 03-008, DTIC Accession Number ADA465806 (2003)
8. Y.F. Hwang, W.K. Bonness, S.A. Hambric, Comparison of semi-empirical models for turbulent boundary layer wall pressure spectra. J. Sound Vib. **319**, 199–217 (2009)
9. W.R. Graham, A comparison of models for the wavenumber-frequency spectrum of turbulent boundary layer pressures. J. Sound Vib. **206**(4), 541–565 (1997)
10. M.K. Bull, Wall pressure fluctuations associated with subsonic turbulent boundary layer flow. J. Fluid Mech. **28**, 719–754 (1967)
11. M.K. Bull, Wall-pressure fluctuations beneath turbulent boundary layers: Some reflections on forty years of research. J. Sound Vib. **190**(3), 299–315 (1996)
12. D.M. Chase, Modeling the wavevector-frequency spectrum of turbulent boundary layer wall pressure. J. Sound Vib. **70**(1), 29–67 (1980)
13. D.M. Chase, The character of the turbulent wall pressure spectrum at subconvective wavenumbers and a suggested comprehensive model. J. Sound Vib. **112**(1), 125–147 (1987)
14. P.D. Lysak, W.K. Bonness, J.B. Fahnline, *Low Wavenumber Models for Turbulent Boundary Layer Excitation of Structures, Flinovia II* (Springer, 2019)
15. W.K. Bonness, D.E. Capone, S.A. Hambric, Low-wavenumber turbulent boundary layer wall-pressure measurements from vibration data on a cylinder in pipe flow. J. Sound Vib. **329**, 4166–4180 (2010)
16. R. DeJong, R. Tubergen, A comprehensive model for the turbulent boundary layer pressure spectrum, in *Proceedings of Inter-Noise 2019*, 16–19 June 2019, Madrid, Spain (2019)
17. R. DeJong, *Chase vs. Corcos TBL Loading, Flinovia III* (Springer, 2021)
18. B.M. Abraham, W.L. Keith, Direct measurements of turbulent boundary layer wall pressure wavenumber-frequency spectra. ASME J. Fluids Eng. **120**, 29–39 (1998)
19. S.A. Hambric, Y.F. Hwang, W.K. Bonness, Vibrations of plates with clamped and free edges excited by low-speed turbulent boundary layer flow. J. Fluids Struct. **19**, 93–110 (2004)
20. S.A. Hambric, D.A. Boger, J.B. Fahnline, R.L. Campbell, Structure- and fluid-borne acoustic power sources induced by turbulent flow in 90 degree piping elbows. J. Fluids Struct. **26**, 121–147 (2010)
21. W.K. Bonness, J.B. Fahnline, P.D. Lysak, M.R. Shepherd, Modal forcing functions for structural vibration from turbulent boundary layer flow. J. Sound Vib. **395**, 224–239 (2017)
22. M. Karimi, P. Croaker, L. Maxit, O. Robin, A. Skvortsov, S. Marburg, N. Kessissoglou, A hybrid numerical approach to predict the vibrational responses of panels excited by a turbulent boundary layer. J. Fluids Struct. **92** (2020)
23. E. Cohen, X. Gloerfelt, Influence of pressure gradients on wall pressure beneath a turbulent boundary layer. J. Fluid Mech. **838**, 715–758 (2018)
24. M. Goody, Empirical spectral model of surface pressure fluctuations. AIAA J. **42**, 1788–1794 (2004)
25. M.S. Howe, *Acoustics of Fluid-Structure Interactions* (Cambridge University Press, Cambridge, 1998), pp. 207–209
26. P.D. Lysak, Modeling the wall pressure spectrum in turbulent pipe flows. J. Fluids Eng. **128**(2), 216–222 (2006)

Vibroacoustic Testing of Panels Under a Turbulent Boundary Layer Excitation Using a Space-Time Spectral Synthesis Approach

Olivier Robin, Marc Pachebat, Nicolas Totaro, and Alain Berry

Abstract The experimental study of a structure's response to a turbulent boundary layer (TBL) excitation using wind-tunnel or in-vehicle testing generally requires considerable efforts, including the measurement of both turbulent wall-pressure fluctuations and the structure's vibration response. As an alternative method to highly demanding testing procedures and numerical simulations, this paper proposes a computationally efficient method to predict vibroacoustic responses of a panel under a TBL excitation. Space-time realizations of a TBL wall pressure field obtained using a spectral synthesis approach are coupled to a deterministic model so as to predict mean quadratic velocity, and radiated sound pressure and power from a panel under a TBL excitation. Each realization of the wall pressure field and obtained vibroacoustic results can be considered as a virtual experiment. The radiated sound pressure as a function of time can be also obtained, and possibly later used for listening and psychoacoustics studies objectives. A summary of existing experimental and numerical methods for obtaining the vibroacoustic response of panels to a TBL excitation is first presented. The proposed method is then detailed. Results obtained using this method are finally compared to results obtained using controlled laboratory experiments and analytical calculations for a low subsonic flow speed.

O. Robin (✉) · A. Berry
Groupe d'Acoustique de l'Université de Sherbrooke, 2500,
boulevard de l'université, Sherbrooke J1K2R1, Canada
e-mail: olivier.robin@usherbrooke.ca

A. Berry
e-mail: alain.berry@usherbrooke.ca

M. Pachebat
LMA - UMR 7031 AMU - CNRS - Centrale Marseille,
13453 Marseille Cedex 13, France
e-mail: pachebat@lma.cnrs-mrs.fr

N. Totaro
Univ Lyon, INSA Lyon, LVA, EA677, 69621 Villeurbanne, France
e-mail: nicolas.totaro@insa-lyon.fr

E. Ciappi et al. (eds.), *Flinovia—Flow Induced Noise and Vibration Issues and Aspects-III*, https://doi.org/10.1007/978-3-030-64807-7_5

1 Introduction

1.1 General Problem Statement

Vibration of and radiated noise from structures under a turbulent boundary layer (TBL) excitation have been studied for decades with various applications and scales ranging from cars to aircrafts as well as vessels and submarines [1, 2]. It remains a critical research topic that is still looking for accurate and cost-effective simulation and measurement techniques, a major objective being the control of flow-induced noise in a vehicle.

The first documented experimental works concerning TBL-excited panels were conducted in the 1960s [3–6]. Wind-tunnel investigations were mostly conducted on flat plates of various materials, dimensions and thicknesses, with flow conditions ranging from low-subsonic to high-subsonic flow speeds. The corresponding literature essentially reports wall pressure fluctuations spectra and space-time correlations and vibration spectra of panels and sound power spectra radiated by panels, that correspond to the excitation and the response parts of this vibroacoustic problem, respectively. The measurement of the wall pressure fluctuations (the excitation part) also began in the 1960s [7, 8], this research being still regarded as highly complex in terms of implementation and associated post-processing [9, 10].

Since these pioneering studies, the literature has recorded very few experimental results especially concerning radiated sound power [11–14]. A great majority of publications report results of numerical calculations that are consequently seldom experimentally validated. Surprisingly, the results of vibroacoustic measurements or calculations are mostly provided in terms of amplitude/frequency representations and using energetic quantities (mean squared velocity, sound power or ratios like sound transmission loss). These quantities are sometimes averaged as a function of frequency (practically, in octave bands or fractional octave bands such as a third or a twelfth of an octave), or even expressed in terms of a single overall level. This provides compact data representations that are certainly useful but nevertheless opposite to a detailed analysis including human perception. As pointed out by Oettle and Sims-Williams [15],

> The human brain is not only sensitive towards the level of steady broadband noise, but distinctive features such as tonality or modulation draw the attention of the vehicle occupant and impact negatively on perception. (…) A key to achieving future vehicle refinement is bringing together an understanding of unsteady onset flow conditions, their impact on cabin sound pressure level and modulation and, in turn, the impact of noise level and modulation on psychoacoustic perception.

Among the keypoints that are currently missing towards a better understanding and comprehension of TBL-induced problems, two can be highlighted:

- The measurement of both wall-pressure fluctuations and structure's response using wind-tunnel or in-vehicle testing generally require considerable efforts, with associated data that nevertheless show large scatter. A reduced number of experiments

is thus conducted and then available for validating the results of numerical computations. Alternative methods to highly demanding testing or simulation procedures are thus needed.
- The perception of the radiated sound from TBL-excited structures as a function of time is hardly considered even if it should be a primary goal. This is especially true for transportation applications for which flow conditions are usually slightly unsteady and lead to fluctuations of level and frequency content as a function of time.

1.2 Alternative Experimental Methods to Conventional Wind-Tunnel Testing

Several strategies have been proposed to reduce technical constraints and increase the precision of measurements related to TBL-induced problems. The standardized method using coupled rooms for testing the transmission loss of panels under a diffuse acoustic field (DAF) excitation has been occasionally used as an alternative measurement, but is known to be not representative of a TBL excitation.

Compared with the generation of a DAF that only involves acoustic components, the specific case of a TBL means reproducing acoustic and convective components, the latter having smaller spatial scales than the acoustic scale for subsonic flows. The wall-pressure fluctuations induced by a TBL surface pressure are indeed a superposition of hydrodynamic and acoustic pressures whose levels differ by several orders of magnitude [16]. In addition to level difference, a keypoint in TBL-related vibroacoustics problems lies in the introduction of other dimensions than the classical acoustic wavelength λ_0 and the structural wavelength λ_s, that is the convective wavelength λ_c. Let's consider a low speed flow (for example, a Mach number of 0.1). The convective velocity U_c is a fraction of the free flow velocity U_∞ (usually taken as $U_c \approx 0.6 - 0.7U_\infty$). The ratio between acoustic and convective scales thus reaches a value of approximately ten and for a speed of sound of 340 m/s and at a frequency 1000 Hz, the acoustic wavelength equals 34 cm, while the convective wavelength will be approximately 2.4 cm ($=340 \times 0.1 \times 0.7/1000$). Due to the large range of scales and levels, the simultaneous measurement and/or generation of both acoustic and convective components is an experimental challenge.

Several approaches relying on sound synthesis has been considered so as to recreate an actual TBL excitation using loudspeaker arrays. Kirkeby and Nelson [17] were the first to propose the generation of plane sound waves. Several researchers extended this approach to the reproduction of random pressure fields such as Bravo and Maury [18–21] who obtained theoretical and experimental results concerning the reproduction of a DAF- and a TBL-induced wall pressure field using a near-field array of loudspeakers and a least squares method to define the complex signal to be fed to each reproduction source. Nevertheless, in the case of the TBL, the reproduction of its statistics was only feasible at low frequency due to the rapid decay

of the TBL streamwise and especially spanwise correlation lengths with frequency. Bravo and Maury suggested that the synthesis of the TBL-induced panel vibroacoustic response could be a more viable strategy, since focusing on the panel response helps to significantly reduce the number of reproduction sources required.

Another approach based on the concept of uncorrelated plane waves, a least squares approach and a synthetic source array was proposed by Aucejo et al. [22]. The synthetic array principle allows simulating the effect of an array of acoustic sources from sequential measurements using a single source. This allows a higher flexibility of the experimental set-up regarding the total number of monopoles required to suitably reconstruct wall pressure statistics, compared with the work of Bravo and Maury [20, 21]. The results obtained on an academic structure, a clamped panel, showed that the structural velocity autospectral density function of the panel subjected to TBL excitation could be effectively reproduced.

Robin et al. [23] used three different approaches to define the reproduction sources complex amplitudes (a least squares based approach, a Wave Field Synthesis based approach and a Planar Nearfield Acoustic Holography based approach), that were then coupled to the synthetic source array concept introduced by Aucejo et al. [22]. Experimental results were obtained for a simply supported panel, that confirmed that even with a synthetic source array approach, the technical constraints for the reproduction of a TBL excitation were still dictated by the acoustic wavelength and the convective wavelength (the smallest wavelength to be reproduced for a subsonic excitation). It was also confirmed that the exact reproduction of the TBL wall pressure fluctuations was not fundamental for the reproduction of the TBL-induced panel response, as suggested by Bravo and Maury [20, 21]. Recently, Merlo et al. [24] investigated the control of loudspeaker arrays via their acoustic radiation modes (ARM) to replace complex and costly flight and wind-tunnel measurements, but no example of TBL reproduction was yet provided in this work. Pasqual [25] suggested on his side using the ARM of a spherical array to reproduce complex sound fields. In summary, the proposed methods are generally not able to accurately and directly reproduce the most energetic components of a subsonic TBL that are located outside the acoustic wavenumber domain.

Marchetto et al. [26] suggested another approach to experimentally predict the vibration response of panels under a TBL excitation, by explicitly separating the forcing wall-pressure fluctuations from the vibration behavior of the panel. In this work, the idea of an ex situ characterization of a panel's response under TBL excitation is suggested and validated: once the excitation is characterized, the response of a panel under the considered excitation can be deduced, making the experimental facility no longer needed.

A last possibility to alleviate some constraints linked to wind-tunnel testing relies in the similitude concept, a main application field of this concept being surely aerodynamics with tests on a scale-model aircraft to define the aerodynamic characteristics of a full-scale aircraft [27]. The similitude concept has been also widely applied in structural engineering, see a review in [28]. Recent works related to vibroacoustics have especially aimed at defining scaling laws for predicting the vibration response of a structure using a scaled model in a wind tunnel. In this case, structural param-

eters as well as flow parameters must be properly scaled. Vibration measurements on a simplified cylindrical structure in wind-tunnel were put in similitude between a scaled model and a full-scale model [29]. In [30], both vibration auto-spectral and cross-spectral density functions, previously measured in a wind-tunnel facility on a set of three plates, were successfully scaled which opens the possibly of scaling the radiated sound pressure under a TBL excitation.

1.3 Numerical Methods for the Prediction of the Vibroacoustic Response of Panels

Two main strategies are generally considered for predicting the vibro-acoustic response of structures excited by surface pressure fluctuations. The first one relies on computational fluid dynamics (CFD) and computational aeroacoustics (CAA) to solve external flow problems. Incompressible large eddy or detached eddy simulations are used to compute the surface pressure fluctuations for vehicles or simplified structures, that are then coupled to finite element method or statistical energy analysis approaches for interior noise simulation [31]. CFD or CAA simulations are nevertheless highly demanding, and usually require intense parallel computing. So as to relax computational constraints that are important for such simulations, reduced-order modeling methods like the dynamic mode decomposition and the proper orthogonal decomposition are usually employed to better describe the wall pressure excitation on a structure [15]. As an example, Druault et al. [32] proposed an application of the proper orthogonal decomposition to characterize and separate of both acoustic and turbulent components of the wall pressure excitation, that was tested from wall pressure fields synthesized from theoretical averaged models or obtained from lattice Boltzmann method simulations. Hu et al. tested the use of synthetic turbulence generated by the fast random particle-mesh method to simulate flat plate turbulent boundary layers under zero pressure gradient [33], and wall-pressure fluctuations on an Airbus-A320 fuselage in flight conditions [9].

The other approach that is used in many numerical approaches in order to predict vibrational responses of structures excited by turbulent flow couples the cross-spectral density function describing the wall pressure fluctuations to a deterministic vibroacoustic model (generally defined through the use of finite element modeling). Since a very large number of distributed points on the surface of the structure needs to be considered according to theory, usual requirements in terms of ideal mesh size are deemed unrealistic in many practical cases and many works aim at reducing the computational cost of such approaches. Modeling techniques considered as hybrid approaches which combine statistical and deterministic methods were investigated in [34] so as to relax meshing constraints. In order to implement a numerical synthesis of aeroacoustic wall-pressure field, Hekmati et al. [35] proposed a method based on the Cholesky decomposition of analytical expressions of the cross power spectral density of a DAF and a TBL (defined using the Corcos's model, [7]). Recently,

Karimi et al. [36, 37] combined the uncorrelated wall plane wave (UWPW) technique [38] with a finite element method. The cross spectrum density function of the wall pressure field was defined either by empirical models from literature or from experimental data. The response of a structure subject to a TBL excitation was then obtained from an ensemble average of the different realizations of the UWPW and the technique was shown to be computationally efficient as it rapidly converged using a small number of realizations. Predicted velocity spectra compared well with measured velocity spectra in two different anechoic wind tunnels and on two different panels.

In [39], it was proposed to couple a space-time synthesis approach (i.e. several consecutive realizations of a wall pressure field) to a deterministic model so as to predict sound transmission loss of and radiated sound pressure from panels under a DAF excitation. Both quantities were efficiently predicted and good agreement was obtained with measurements and finite element method predictions. The formalism is similar to the UWPW technique [38], but the applied probability density functions (PDF) can be varied (i.e. can be defined as Gaussian, or not). This can not be achieved with the UWPW technique, for which the normalized sum of plane waves that is used will tend toward a Gaussian distribution according to the central limit theorem.

This space-time, 2D+t, synthesis approach is here extended to the case of TBL-excited panels. Besides an additional flexibility gained compared with the UWPW technique in terms of PDF definition, the proposed 2D+t method has several advantages, that can provide adequate solutions to the keypoints previously expressed in Sect. 1.1: (1) Each realization of the wall pressure field and obtained vibroacoustic results can be considered as a virtual experiment, or a series of them can mimic an experiment of variable length, and (2) The radiated sound pressure as a function of time and under a random excitation (DAF-TBL) can be obtained and used for listening purposes.

This chapter first describes the suggested calculation process. Measurements made on a rectangular aluminum panel with controlled simply-supported boundary conditions and tested in a low-speed anechoic wind-tunnel at a flow speed of 40 m/s [40] are used as a test case for extending the approach to the case of a TBL excitation.

2 Spectral Synthesis of the Wall Pressure Field Induced by a TBL

In the proposed method, each particular realization of a turbulent pressure (random draw) corresponds to an induced flexural response as well as a radiated pressure field. Among the difficulties encountered, the three physical scales of the problem

(convective, structural and acoustic) cover very different intervals. As indicated in the introduction part, the experimental methods that intend to mimic vibroacoustic tests in wind tunnel have difficulty to describe wave numbers associated with subsonic convective phenomena [20, 22], while inversely numerical methods in fluid mechanics require huge efforts for correctly simulating the acoustic waves generated by the flow [41].

In this context, a representation of the turbulent pressure by the realization of a random process allows on the one hand, to integrate in the synthesis process the relevant physical information for all scales, and on the other hand, to solve a direct formulation of the vibroacoustic problem giving access in a simple way to the time radiated pressure.

In the hypothesis of a homogeneous and stationary flow, the synthesis by Cholesky decomposition of the cross-correlation matrix [35, 42] is replaced by a spectral synthesis [43, 44] which largely reduces the computational effort. This is achieved by inverse fast Fourier transform (FFT) of a physical model in the wavenumber-frequency domain. Thanks to the FFT algorithm efficiency, the generation of turbulent wall pressure field in the physical domain (x, y, t) is very fast compared to other approaches.

2.1 Space Time Spectral Synthesis (2D+t)

In this work, a low speed subsonic Mach number flow ($M_\infty = 0.12$) is considered to generate a homogeneous and stationary turbulent boundary layer with no pressure gradient over a smooth rigid wall (see Tables 1 and 2). The flow is assumed to be

Table 1 Physical characteristics of the considered turbulent boundary layer

Fluid density	ρ (kg m^{-3})	1.20
Sound velocity	c_0 (m s^{-1})	343
Kinematic viscosity	ν (m^2 s^{-1})	$15.1 \cdot 10^{-6}$
Free stream velocity	U_∞ (m s^{-1})	40
Convection velocity	$U_c = 0.6\, U_\infty$ (m s^{-1})	24

Table 2 Physical characteristics of the panel

Streamwise length	L_{px} (m)	0.600
Spanwise width	L_{py} (m)	0.525
Young modulus	E_p (Pa)	$70 \cdot 10^9$
Density	ρ_p (kg m^{-3})	2700
Poisson ratio	ν_p	0.3
Thickness	h_p (mm)	2.4

both homogeneous (in space) and stationary (in time). As a consequence, a sample of a pressure field over the spatio-temporal domain $L_x \times L_y \times T$ can be generated as a draw of a stochastic process using a spectral synthesis method, as explained in the following.

Let $p(x, y, t)$ denote the fluctuating boundary pressure over a rigid wall in the (Oxy) plane: we propose to simulate $p(x, y, t)$ as a random Gaussian field with zero-mean even though observations of $p(x, y, t)$ beneath a TBL exhibit slightly non Gaussian statistics, see e.g. Schewe [45]. The main interest is that the prescription of its correlation function, or equivalently its Fourier spectrum, completely specifies a Gaussian process. Then the space-time correlation function $R =< p(x, y, t)p(x + \xi_x, y + \xi_y, t + \tau) >$ (<> denotes an ensemble average, and $\xi_{x,y}$ are the separations between two points in x and y directions, respectively) of an homogeneous and stationary process $p(x, y, t)$ reduces to $R(\xi_x, \xi_y, \tau)$. It can equivalently be described by its 2D+t Fourier transform $P(k_x, k_y, \omega)$ called the wavenumber-frequency power spectrum.

In this case, the simulation of a wall pressure field according to a spectral model sums up to a simple and fast spectral synthesis algorithm which permits to generate draws of a stationary Gaussian process. The principle of this method is to filter a Gaussian white noise using the targeted spectrum. In practice, one first draws a discrete set of $N_x \times N_y \times N_t$ independently and identically distributed Gaussian real random variables g_{lmn} with zero mean, thanks to a pseudo-random number generator. The discrete indices (l, m, n) correspond to continuous variables (x, y, t). Then the 3D Discrete Fourier Transform of g_{lmn} denoted by $G_{l'm'n'}$ is a set of $N_x \times N_y \times N_t$ identically distributed Gaussian complex random variables [44]. By construction $G_{l'm'n'}$ obeys the Hermitian symmetry of the Fourier transform of real signals (where discrete indices (l', m', n') correspond to continuous variables (k_x, k_y, ω)).

In a discrete representation, the relationship between the space-time correlation R_{lmn} and the wavenumber-frequency power spectrum $P_{l'm'n'}$ is given by the following 3D discrete Fourier transform:

$$P_{l'm'n'} = \sum_{l=0}^{N_x-1} \sum_{m=0}^{N_y-1} \sum_{n=0}^{N_t-1} R_{lmn}.e^{2\mathrm{j}\pi\left(\frac{n.n'}{N_t} - \frac{l.l'}{N_x} - \frac{m.m'}{N_y}\right)}, \tag{1}$$

where $N_x \times N_y \times N_t$ is the numerical size of the domain in space and time.

The physical domain is defined by (L_x, L_y, T) where T is the duration of the simulation. The dimensions $L_x \times L_y$ of the simulated wall pressure are chosen to be slightly greater than the size of the panel: $L_x/L_{px} = 1.2$ and $L_y/L_{py} = 1.2$.

The physical domain is sampled by $N_x \times N_y \times N_t$ points (see Table 3):

$$\begin{cases} N_x = k_x^{max} L_x/\pi & = 2\pi(\Delta x \Delta k_x)^{-1}, \\ N_y = k_x^{max} L_y/\pi & = 2\pi(\Delta y \Delta k_y)^{-1}, \\ N_t = 2 f^{max} T & = (\Delta t \Delta f)^{-1}. \end{cases} \tag{2}$$

Table 3 ($N_x \times N_y \times N_z$): numerical size of the simulated wall pressure; (Δx, Δy, Δt): corresponding time and space resolution; (Δk_x, Δk_y, Δf): wavenumber and frequency steps; (L_x, L_y, T) and ($\pm k_x^{max}$, $\pm k_y^{max}$, $\pm f^{max}$): intervals covered by the simulated wall pressure in physical and Fourier domain respectively

$N_x \times N_y \times N_t =$		$256 \times 256 \times 2048$	
Δx	0.0028 m	k_x^{max}	1108.3 rad m^{-1}
Δy	0.0025 m	k_y^{max}	1266.7 rad m^{-1}
Δt	$4.883 \cdot 10^{-4}$ s	f^{max}	1023 Hz
L_x	0.72 m	Δk_x	8.727 rad m^{-1}
L_y	0.63 m	Δk_y	9.973 rad m^{-1}
T	1 s	Δf	1 Hz

Following the 1D algorithm from Davies and Harte [43] and formally applying it to space-time (2D+t) case, the pressure field p_{lmn} is given by the inverse discrete Fourier transform of the product $\sqrt{P}.G$ where P is a given discrete wavenumber-frequency power spectrum $P_{l'm'n'}$ (the targeted physical model), and G is a draw of $N_x \times N_y \times N_t$ identically distributed Gaussian complex random variables with Hermitian (transconjugate) symmetry:

$$p_{lmn} = \sum_{l'=0}^{N_x-1} \sum_{m'=0}^{N_y-1} \sum_{n'=0}^{N_t-1} \frac{\sqrt{P_{l'm'n'}}\, G_{l'm'n'}}{N_x N_y N_t} e^{-2\mathrm{j}\pi\left(\frac{n.n'}{N_t} - \frac{l.l'}{N_x} - \frac{m.m'}{N_y}\right)}. \tag{3}$$

In practice, G is obtained from the 3D Fourier transform of ($N_x \times N_y \times N_t$) pseudo-random real values drawn from the Gaussian distribution, to ensure the Hermitian symmetry of G.

The resulting 2D+t discrete pressure field p_{lmn} is a sample of a real valued spatio-temporal process; it is Gaussian, and has zero mean as soon as $P_{000} = 0$. The wavenumber-frequency power spectrum of p_{lmn} is imposed by $P_{l'm'n'}$.

In order to avoid aliasing artifacts, the size of the synthesis ($N_x \times N_y \times N_t$) is adapted to cover the domain where the energy in $P_{l'm'n'}$ is present. This depends upon the flow parameters and physical model used.

On Fig. 1, the simulated pressure obtained from the spectral synthesis is shown for three neighbouring instants. As in a turbulent field, it exhibits a superposition of a large number of spatial scales that are convected along the streamwise axis Ox. The spectral synthesis and the statistical properties of the pressure field shown on Fig. 1 are detailed in the next section.

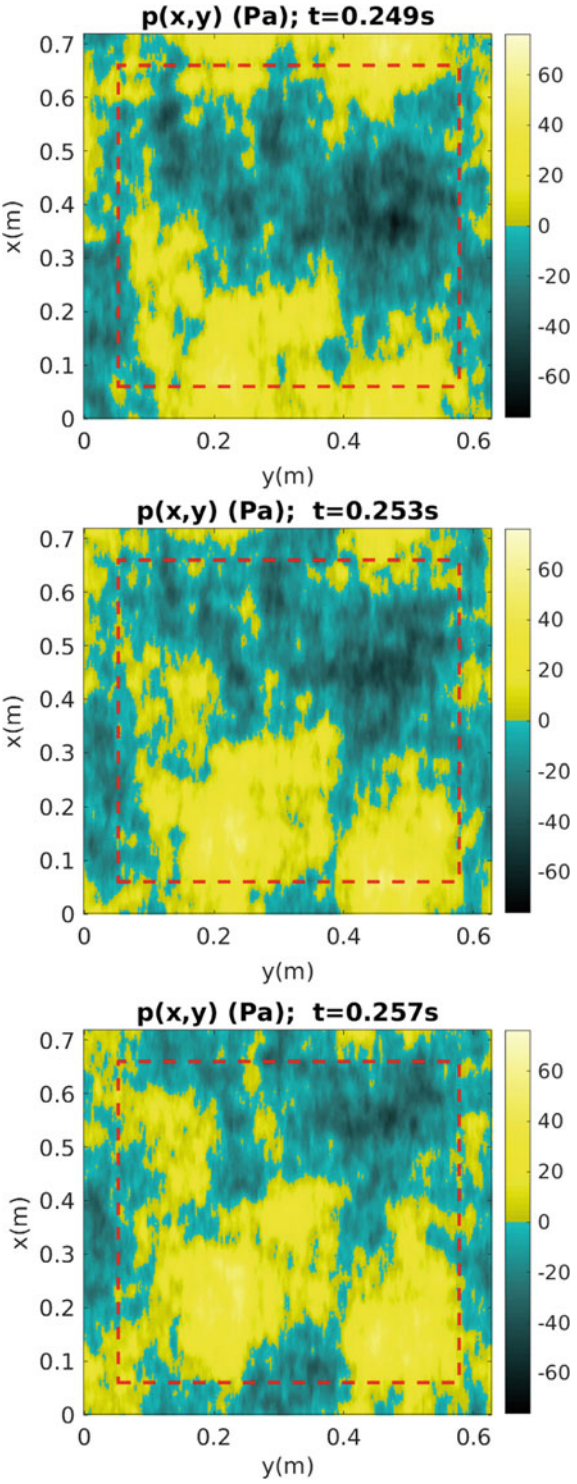

Fig. 1 Three snapshots separated by $\Delta t = 4.10^{-3}$ s, of the time pressure simulated over the flat surface. The time step is chosen to highlight the streamwise convection of the fluctuations, along the vertical axis and oriented as Ox. The red dash line indicates the physical size of the considered panel. The instantaneous pressure amplitude in Pascals is given by the color bar

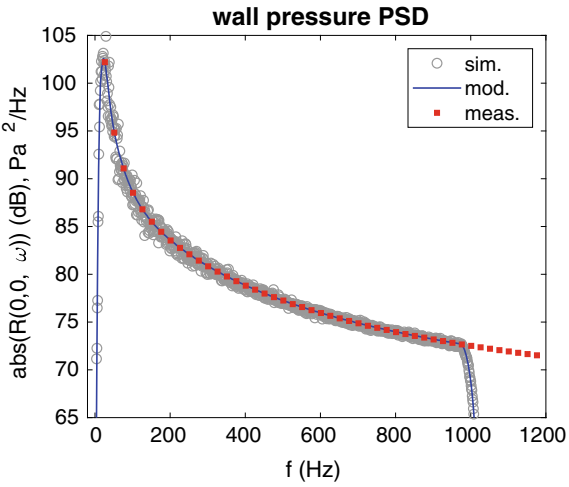

Fig. 2 Power Spectrum Density (PSD) of the wall (point) pressure: measured (red square see Sect. 4), interpolated from measurements (blue line), estimated (grey circles) from the simulated wall pressure and averaged over the panel area

2.2 *Validation of the Synthesized Wall Pressure Statistics*

The statistical properties of the wall pressure are chosen here according to the Mellen model [46]:

$$P(k_x, k_y, \omega) = S_{pp}(\omega) \frac{2\pi(\alpha\beta k_c^2)^2}{[(\alpha\beta k_c^2)^2 + (\beta k_c k_y)^2 + (\beta k_c)^2.(k_c - k_x)^2)]^{3/2}}, \quad (4)$$

where the streamwise and spanwise decay wave numbers are fixed to $\alpha = 0.12$ and $\beta = 0.7$. The convective wavenumber is $k_c = \omega / U_c$ (rad m^{-1}) where the value of the convection velocity $U_c = 0.6\, U_\infty$ is fixed for each frequency.

In Eq. (4), the spectrum of the pressure $S_{pp}(\omega)$ [Pa^2] must be specified before the spectral synthesis. To that aim, the measured autospectral density (in red on Fig. 2) is filtered at high frequency, extended towards low frequencies, and interpolated according to the frequency resolution of the desired simulation (see Table 3). The result is shown in blue solid line on Fig. 2 and is used to specify the spectrum of the pressure $S_{pp}(\omega)$ in Eq. (4).

The wavenumber-frequency spectrum, Eq. (4), is then introduced into Eq. (3) to obtain one draw of p_{lmn} that represents one realization of the simulated wall pressure field $p(x, y, t)$.

In order to check the statistical properties of the simulated wall pressure from the spectral synthesis (Eq. (3)), the wavenumber-frequency spectrum can be estimated, and defined as:

$$\hat{P}(k_x, k_y, \omega) = \frac{1}{N} \sum_{1}^{N} \left[\lim_{L_x, L_y, T \to \infty} \frac{1}{L_x L_y T} \frac{\hat{p}(k_x, k_y, \omega) \hat{p}^*(k_x, k_y, \omega)}{\Delta k_x \Delta k_y \Delta f} \right], \quad (5)$$

where $\hat{p}(k_x, k_y, \omega)$ is the Fourier transform of $p(x, y, t)$, $\hat{p}^*$ is its complex conjugate, and N the number of averaging used for the estimation. Using the inverse Fourier transform of $\hat{P}(k_x, k_x, \omega)$ over (k_x, k_y) and then ω, we can obtain respectively the frequency cross-correlation $R(\xi_x, \xi_y, \omega)$, and the broad-band space cross-correlation $r(\xi_x, \xi_y, \tau)$ where ξ_x, ξ_y and τ denote separations along Ox, Oy and time axis.

In practice, since we are using here a single discrete realization of p_{lmn}, the estimator used to compare $\hat{P}(k_x, k_x, \omega)$ of Eq. (5) and $P(k_x, k_y, \omega)$ of Eq. (4) is reduced to:

$$\hat{P}_{l'm'n'} = \frac{1}{L_x L_y T} \frac{\hat{p}_{l'm'n'} \hat{p}^*_{l'm'n'}}{\Delta k_x \Delta k_y \Delta f} , \tag{6}$$

where $\hat{p}_{l'm'n'}$ is the 3D discrete Fourier transform of p_{lmn}.

The frequency cross-correlation $R(\xi_x, \xi_y, \omega)$ of the simulated field is obtained after a 2D inverse Fourier transform of $\hat{P}_{l'm'n'}$ (Eq. (6)). The result noted $R_{l'm'n'}$ is represented in PSD units for zero-space separation $R(0, 0, \omega)$ on Fig. 2 (grey circles). It corresponds to the point pressure spectrum averaged over the $(N_x \times N_y)$ spatial points and exhibits a good statistical convergence towards the PSD interpolated from the measurements (blue line).

Figure 2 shows that the simulated space-time pressure field p_{lmn} exhibits a point spectrum that statistically converges towards $S_{pp}(\omega)$ chosen in Eq. (4).

In order to check the simulated space-time pressure field p_{lmn} in the wavenumber domain, the wavenumber-frequency spectrum $\hat{P}_{l'm'n'}$ from Eq. (6) is plotted on Fig. 3 (symbols) and compared to the Mellen model of Eq. (4) (solid lines). Three particular frequencies are chosen for the streamwise (top) and spanwise (bottom) plots. Since Eq. (6) is estimated on a single realization (no ensemble averaging), the resulting standard deviation is high. But exactly like experimenters do, one can verify that an averaging over N realizations of the simulated pressure using Eq. (5), reduces the standard deviations and shows a statistical convergence of $\hat{P}_{l'm'n'}$ towards the Mellen model of Eq. (4), as shown on Fig. 4 whith $N = 10$.

The space-time wall pressure obtained with the spectral synthesis of Eq.(3) is now checked to be statistically compliant with the targeted properties, and can be used in the following as an excitation term for a flat baffle panel.

3 Coupling Wall Pressure Statistics to a Model of a Structure

The acoustic radiation of the plate excited by the synthesized wall pressure field is computed in a two-step process: the acoustic field is obtained from the velocity field of the plate computed in a preliminary step. It is thus assumed that:

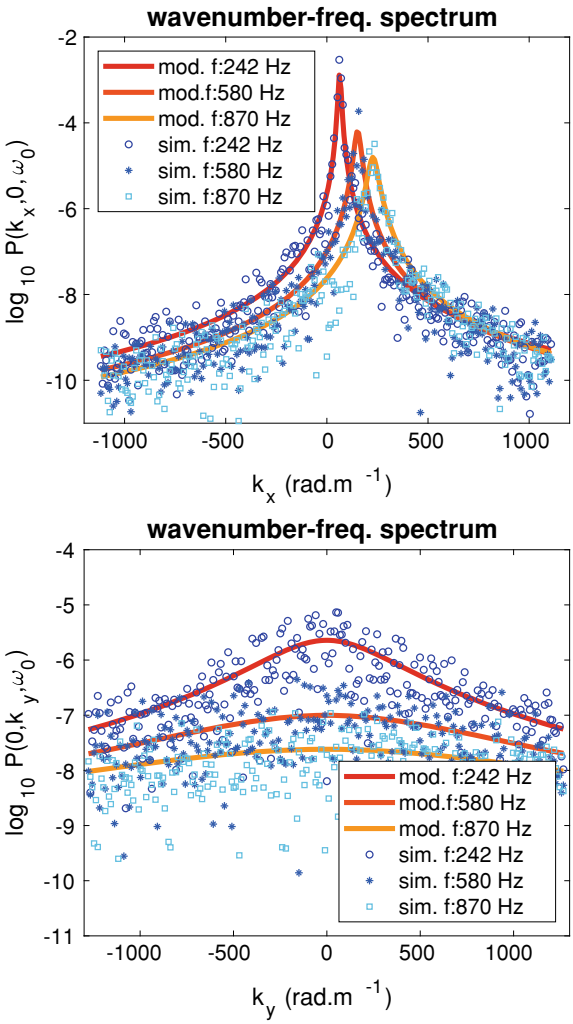

Fig. 3 Wavenumber-frequency spectrum $P(k_x, k_y, \omega)$ at three chosen frequencies. Bottom: spanwise $P(0, k_y, \omega_0)$. Top: streanwise $P(k_x, 0, \omega_0)$: the peak corresponding to the convective ridge appears at $k_x = 2\pi f / U_c$ rad m^{-1}. Solid curves: Mellen model (Eq. (4)). Symbols: estimation from one draw of the simulated wall pressure (Eq. (6))

- the fluid is light enough to be neglected when computing the velocity response of the plate.
- the vibration of the plate does not affect the wall pressure field.

3.1 Vibration Response of the Panel

The panel under study is a simply supported rectangular thin plate of dimensions $L_{Px} \times L_{Py}$ and of thickness h_P. It is made of a homogeneous isotropic material

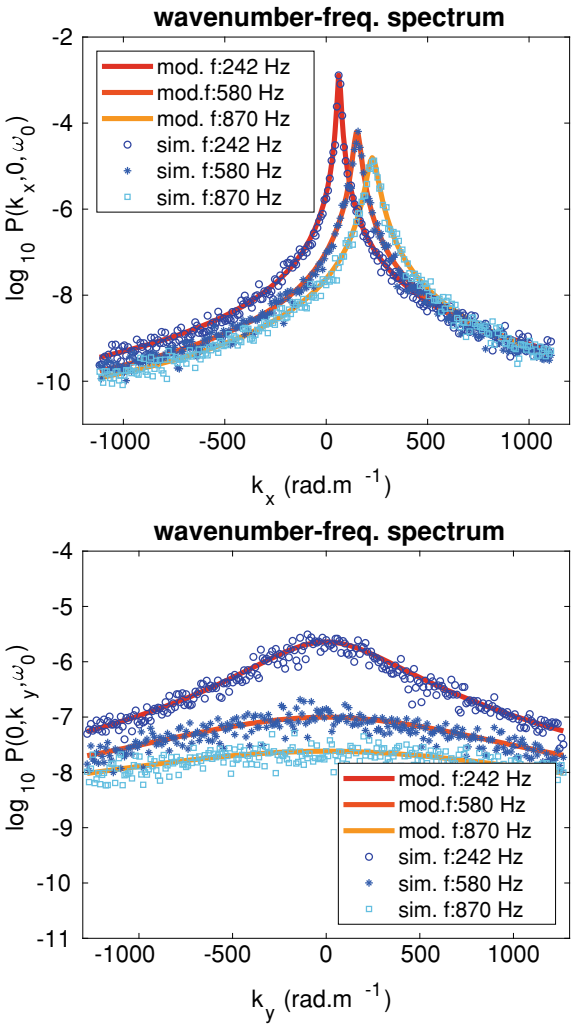

Fig. 4 Wavenumber-frequency spectrum $P(k_x, k_y, \omega)$ at three chosen frequencies. Bottom: spanwise $P(0, k_y, \omega_0)$. Top: streanwise $P(k_x, 0, \omega_0)$: the peak corresponding to the convective ridge appears at $k_x = 2\pi f/U_c$ rad m^{-1}. Solid curves: Mellen model (Eq. (4)). Symbols: estimation from 10 realizations of the simulated wall pressure (Eq. (5) with $N = 10$)

having a Young's modulus E_P, a density ρ_P and a Poisson's ratio ν_P. In this configuration, natural angular frequencies ω_{rs} and mode shapes $\phi_{rs}(x, y)$ of the panel are respectively given by Eqs. (7) and (8):

$$\omega_{rs} = \sqrt{\frac{D}{M}} \left(\left(\frac{r\pi}{L_{Px}} \right)^2 + \left(\frac{s\pi}{L_{Py}} \right)^2 \right), \tag{7}$$

$$\phi_{pq}(x, y) = \sin\left(\frac{r\pi}{L_{Px}} x \right) \sin\left(\frac{s\pi}{L_{Py}} y \right). \tag{8}$$

The vibrational velocity of the panel can be expressed as a sum of contributions of mode shapes as

$$V(x, y, \omega) = \sum_{r=1}^{\infty} \sum_{s=1}^{\infty} \frac{\mathrm{j}\omega F_{rs}(\omega)\phi_{rs}(x, y)}{M_{rs}\left(\omega_{rs}^2 - \omega^2 + \mathrm{j}\eta\omega\omega_{rs}\right)}, \tag{9}$$

where $M_{pq} = \rho_P h_P \frac{L_{Px} L_{Py}}{4}$ is the modal mass, ω is the excitation angular frequency and η is the damping loss factor (considered constant as a function of frequency). The modal force $F_{rs}(\omega)$ is defined as:

$$F_{rs}(\omega) = \int_0^{L_{Px}} \int_0^{L_{Py}} \tilde{p}_{lmn}(x, y, \omega)\phi_{rs}(x, y)\, \mathrm{d}x\, \mathrm{d}y, \tag{10}$$

where $\tilde{p}_{lmn}(x, y, \omega)$ is the Fourier transform of $p_{lmn}(x, y, t)$. All the information coming from the pressure field is condensed in only one complex value per mode at each frequency. To not lose any information, Eq. (10) is discretized using the grid mesh of the pressure field as listed in Table 3. Finally, the spatially averaged mean square velocity $\left\langle V^2 \right\rangle$ of the plate is calculated as:

$$\left\langle V^2(M, \omega) \right\rangle_{S_P} = \frac{1}{S_P} \int_{S_P} V(M, \omega) V^*(M, \omega)\, \mathrm{d}S_P. \tag{11}$$

3.2 Acoustic Response of the Panel

In case of a flat baffled panel, the radiated pressure can be computed using the Rayleigh's integral:

$$P(M_0, \omega) = \int_{S_P} \mathrm{j}\omega\rho_0 V(M, \omega) G(M_0, M, \omega)\, \mathrm{d}S_P, \tag{12}$$

where M is a point of coordinates $(x, y, 0)$ on the surface of the plate and M_0 is a listening point of coordinates (x_0, y_0, z_0). The Green's function $G(M_0, M, \omega)$ is

$$G(M_0, M, \omega) = \frac{1}{2\pi} \frac{e^{-\mathrm{j}kR}}{R}, \tag{13}$$

with $R = \sqrt{(x - x_0)^2 + (y - y_0)^2 + z_0^2}$. The radiated sound power from the plate can be expressed as a function of plate velocity $V(M, \omega)$ and of pressure radiated on the surface of the plate $P(M_0, \omega)$

$$\Pi^{\text{rad}}(\omega) = \frac{1}{2}\int_{S_P} \Re\left(P(M,\omega)V^*(M,\omega)\right)\,\mathrm{d}S_P \tag{14}$$

where $\Re(\bullet)$ and $\bullet^*$ stand respectively for the real part and the complex conjugate of $\bullet$.

4 Experimental Methods

4.1 Description and Setup of the Structure Under Test

The considered TBL excitation in this study was obtained in a low-speed anechoic wind tunnel at Université de Sherbrooke, and is considered to be a zero-pressure-gradient TBL developing over a flat plate with a free-flow velocity of 40 m/s. The panel under study had controlled simply-supported boundary conditions along its four edges obtained using a dedicated procedure and setup [47]. The geometrical and mechanical properties of the panel are reported in Table 2. A value of 0.95% for the average structural loss factor was determined following the −3dB method on the ten first vibration modes.

A $1.22 \times 2.44\,\text{m}^2$ rigid panel made of medium density fiberboard (0.019 m thickness) was mounted in the anechoic wind tunnel at the end of the convergent (see Fig. 5a, b). In order to help the TBL excitation develop, a sandpaper strip was glued at the intersection of the convergent and of the panel so as to prevent any discontinuity between the convergent and the baffle. The panel was installed into the baffle and was positioned on its own supporting stand (see Fig. 5c), and thus no mechanical link exists between the panel and the baffle.

The measurement space below the panel under test was acoustically treated using rigid ceiling tiles and backed by panels of compressed 1-in thick glass wool. Sound absorbing material was placed on the panel's stand so as to limit sound reflections, and even if the floor of the measurement space opens towards the anechoic room, it was covered will compressed glass wool panels.

4.2 Wall Pressure Fluctuations Characteristics

In [26], a precise characterization of the flow was conducted in the same wind tunnel with a strictly similar setup (i.e. identical position from the wind-tunnel convergent, same flow speed and environmental conditions). The wall-pressure fluctuations of the turbulent flow generated over the baffle were measured with a flush-mounted microphone array [48]. The decay rates and the convection velocity were extracted as a function of frequency from these measurements (the Mellen model [46] was fitted to the measured WPF using the least square method). At the exception of the convection

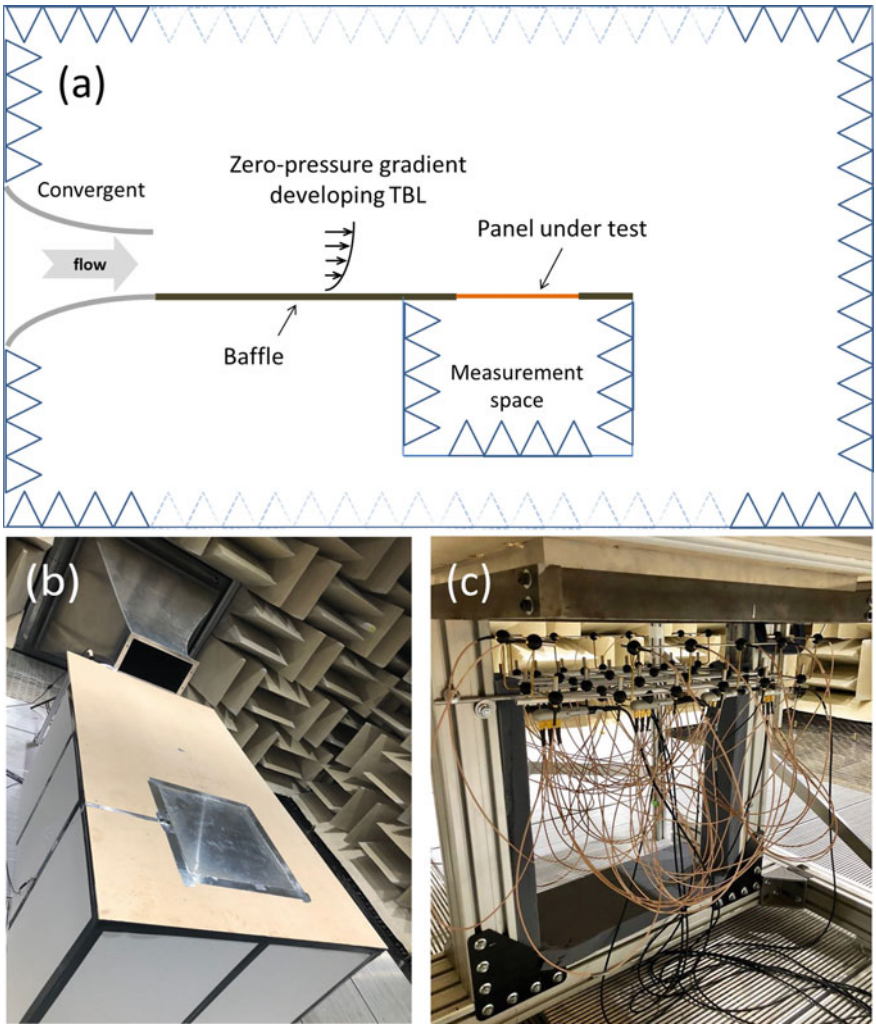

Fig. 5 **(a)** Schematic description of the experimental setup—**(b)** Picture of the panel installed in the anechoic wind-tunnel—**(c)** Picture of the panel on its own stand, including the microphone array

velocity that was considered constant as a function of frequency, the frequency-dependent results of this identification (decay rates, autospectral density), were used for all the calculations made using the proposed spectral synthesis approach.

4.3 Measurement of Vibration of and Radiated Sound Pressure and Sound Power from the Panel

Vibration measurements were made using a set of five mono-axis low weight accelerometers so as to limit the added mass (approximately 15 g total added mass per measurement, including cables). Four sets of five measurements points were used and the average quadratic velocity was finally calculated using 20 discrete measurement points.

The radiated sound power was estimated using a 48-microphone array placed along a parallelepipedic measurement surface following ISO3744 standard [49], see Fig. 5c. The calculation of sound pressure level averaged over the measurement surface and sound power level were made according to ISO3744 standard. Concerning sound pressure comparison with results obtained using the proposed approach, a single microphone from the array was considered.

5 Results

5.1 Mean Quadratic Velocity

In the upper part of Fig. 6 is presented a comparison between analytical calculations (Eq. (11)) and experimental results for the mean quadratic velocity. It can be seen that numerical results are in excellent agreement with analytical results.

The middle part of Fig. 6 shows five different results, that were obtained using the proposed procedure and five different realizations of the simulated WPF using Eq. (3). These can be considered as five different virtual experiments results (tests under different realizations of the same excitation), and are superimposed to previous analytical and experimental results. The agreement between these virtual experiments and analytical and experimental results is overall very satisfactory.

The lower part of Fig. 6 shows the same results on a reduced frequency range (100–300 Hz), illustrating the results of the different draws of the WPF. Each virtual experiment lead to a result that is distributed around the smooth analytical result. The mean quadratic velocity value at peaks varies with the considered draw, showing that the procedure leads to variations in terms of coupling between the wall-pressure field and the panel.

5.2 Radiated Sound Power

In the upper part of Fig. 7 is presented a comparison between analytical calculations (Eq. (14)) and experimental results for the radiated sound power. As for the mean

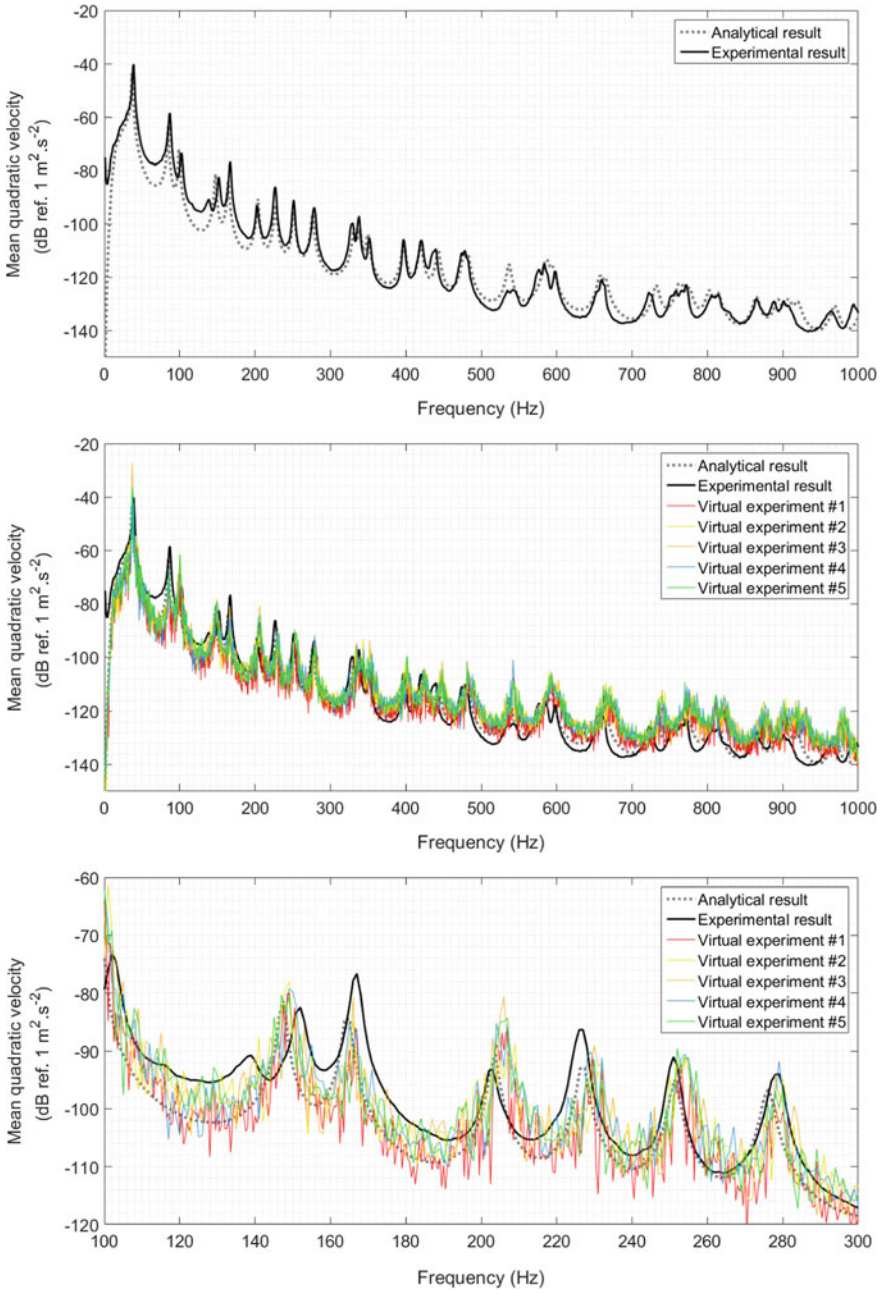

Fig. 6 (Upper part) Analytical calculations (Eq. (11)) and experimental results for the mean quadratic velocity; (Middle part) Results of the proposed procedure for five different draws of the wall-pressure field on the 0–1000 Hz frequency range; (Lower part) Results of the proposed procedure for five different draws of the wall-pressure field on the 100-300 Hz frequency range

quadratic velocity, the agreement between analytical and measured mean quadratic velocity is very satisfactory.

The middle part of Fig. 7 shows five different results, that were obtained using the proposed procedure and three different realizations of the simulated WPF using Eq. (5). As for the mean quadratic velocity, the agreement between these virtual experiments and analytical and experimental results is overall very satisfactory, despite a level difference that rises with increasing frequency.

The lower part of Fig. 7 shows the same results on a reduced frequency range (now from 20 to 200 Hz). It appears that the sound power level, especially at peaks, is a function of the considered draw (with a mean that will tend to the analytical result) showing that the approach can mimic a series of short-time experiments.

5.3 Radiated Sound Pressure

Successive draws can be also used to construct a short-time Fourier transform representation of the radiated sound pressure (spectrum as a function of time), and then an inverse short-time Fourier transform can be used to recover a signal of varying length (provided that the constant overlap-add constraint is followed [50, 51]).

The synthesized sound pressure was in this case obtained using the inverse Fourier transform of four successive draws (leading to a signal of 4 s with a sampling frequency 2048 Hz). The measured and calculated sound pressure as a function of time are shown in Fig. 8 on a zoomed time scale (over a second). The amplitude of the measured signal as well as its variations as a function of time are well captured. Note that no phase alignment was performed in this case. In other words, the starting point for each signal is arbitrary.

6 Conclusion

A method based on spectral synthesis was proposed for generating space-time wall pressure fields for random excitations like DAF or TBL. In this work, this approach was coupled to an analytical model of a simply-supported panel and was used to predict its vibracoustic behavior under a low-speed TBL excitation. It was shown that it could be used to perform virtual experiments on plane structures, these virtual experiments corresponding to consecutive realizations of the wall-pressure field.

Based on this first proof-of-concept, a first perspective consists in coupling the synthesis approach with FEM models in order to apply it to complex structures like stiffened panels, and directly obtain the radiated sound pressure as a function of time.

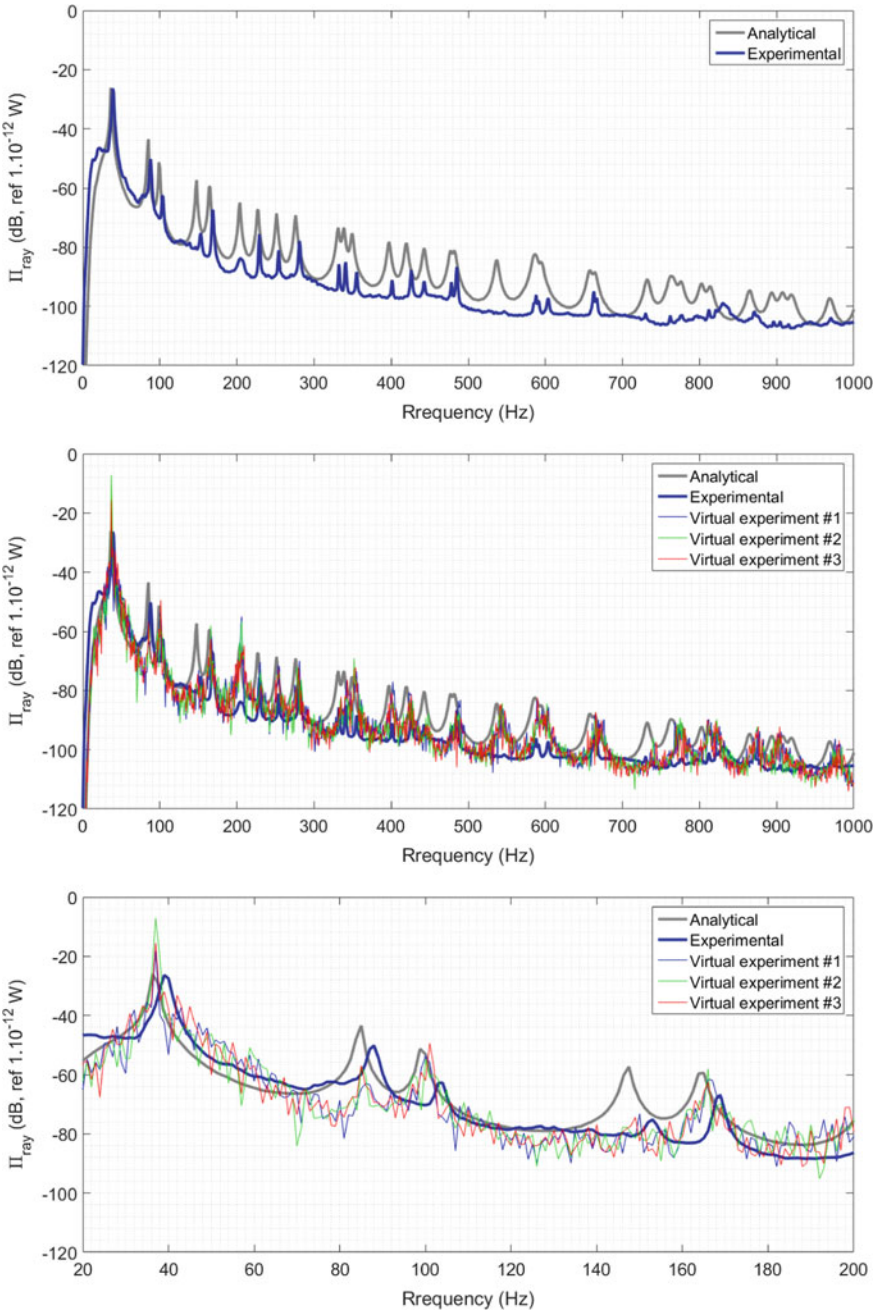

Fig. 7 (Upper part) Analytical calculations (Eq. (14)) and experimental results for the radiated sound power; (Middle part) Results of the proposed procedure for three different draws of the wall-pressure field on the 0−1000 Hz frequency range; (Lower part) Results of the proposed procedure for three different draws of the wall-pressure field on the 20−200 Hz frequency range

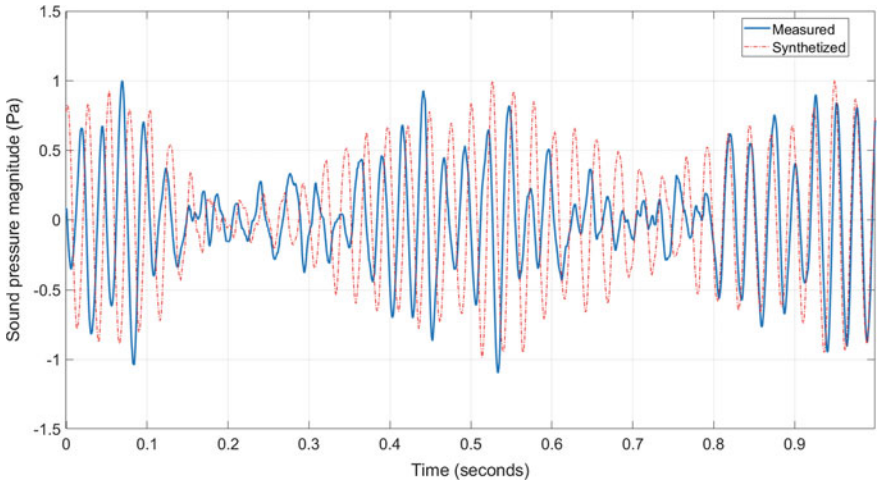

Fig. 8 Comparison of the measured sound pressure level at the considered microphone position (continuous line) and the synthesized sound pressure level at the same position (dashed line)

Another perspective lies in the use of these virtual experiments realizations to study dispersion in actual laboratory measurements under random excitations, and to identify main sources of data scattering as in coupled rooms [52] and wind-tunnel measurements.

Acknowledgements This work was performed within the framework of the Labex CeLyA of "Université de Lyon" (ANR-10-LABX-0060/ANR-11-IDEX-0007) and of the VIRTECH project (ANR-17-CE10-0012), operated by the French National Research Agency. The support of "International Research Project—Centre Acoustique Jacques Cartier" (supported by the French National Research Agency) is also acknowledged. Finally, the authors thank Pierre Chainais for his fruitful suggestions that rooted this work.

References

1. E. Ciappi, S. De Rosa, F. Franco, J.-L. Guyader, S.A. Hambric (eds.), *Flinovia - Flow Induced Noise and Vibration Issues and Aspects - A Focus on Measurement, Modeling, Simulation and Reproduction of the Flow Excitation and Flow Induced Response* (Springer, 2015), 358pp
2. E. Ciappi, S. De Rosa, F. Franco, J.-L. Guyader, S.A. Hambric, R.C.K. Leung, A.D. Hanford (eds.), *Flinovia - Flow Induced Noise and Vibration Issues and Aspects II - A Focus on Measurement, Modeling, Simulation and Reproduction of the Flow Excitation and Flow Induced Response* (Springer, 2017), 372pp
3. G.R. Ludwig, An experimental investigation of the sound generated by thin steel panels excited by turbulent flow (boundary layer noise). UTIA report NO. 87 (1962)
4. L. Maestrello, Measurement of noise radiated by boundary layer excited panels. J. Sound Vib. **2**(2), 100–115 (1965)
5. D.A. Bies, A review of flight and wind tunnel measurements of boundary layer pressure fluctuations and induced structural response. NASA CR626 (1966), 96pp

6. H.G. Davies, Sound from turbulent-boundary-layer-excited panels. J. Acoust. Soc. Am. **49**(3B), 878–889 (1969)
7. G.M. Corcos, Resolution of pressure in turbulence. J. Acoust. Soc. Am. **35**, 192–199 (1963)
8. M. Bull, Wall-pressure fluctuations associated with subsonic turbulent boundary layer flow. J. Fluid Mech. **28**(4), 719–754 (1967)
9. N. Hu, C. Appel, S. Haxter, S. Callsen, A. Klabes, Simulation of wall pressure fluctuations on Airbus-A320 fuselage in cruise flight condition, in *25th AIAA/CEAS Aeroacoustics Conference*, Delft, The Netherlands, 20–23 May 2019 (2019)
10. S.L. Prigent, É. Salze, C. Bailly, Deconvolution of wave-number-frequency spectra of wall pressure fluctuations. AIAA J. **58**(1), 164–173 (2020)
11. Y.M. Chang, P. Leehey, Vibration of and acoustic radiation from a panel excited by adverse pressure gradient flow. MIT report No. 70208-12 (1976), pp. 1–33
12. M. Smith, E. Latorre Iglesias, Vibration and noise radiation from a panel excited by a turbulent flow, in *Proceedings of Acoustics, Société Française d'Acoustique*. Nantes, France (2012), pp. 1845–1850
13. B. Liu, H. Zhang, Z. Qian, D. Chang, Q. Yan, W. Huang, Influence of stiffeners on plate vibration and radiated noise excited by turbulent boundary layers. Appl. Acoust. **80**, 28–35 (2014)
14. J. Osterziel, F.J. Zenger, S. Becker, Sound radiation of aerodynamically excited flat plates into cavities. Appl. Sci. **7**, 1062 (2017)
15. N. Oettle, D. Sims-Williams, Automotive aeroacoustics: an overview. Proc. Inst. Mech. Eng. Part D: J. Automob. Eng. **231**(9), 1177–1189 (2017)
16. M.K. Bull, Wall-pressure fluctuations beneath turbulent boundary layers: some reflections on forty years of research. J. Sound Vib. **190**(3), 299–315 (1996)
17. O. Kirkeby, P.A. Nelson, Reproduction of plane wave sound fields. J. Acoust. Soc. Am. **94**(5), 2992–3000 (1993)
18. T. Bravo, C. Maury, The experimental synthesis of random pressure fields: methodology. J. Acoust. Soc. Am. **120**, 2702 (2006)
19. N.B. Roozen, Q. Leclère, D. Urbán, L. Kritly, C. Glorieux, Assessment of the sound reduction index of building elements by near field excitation through an array of loudspeakers and structural response measurements by laser Doppler vibrometry. Appl. Acoust. **140**, 225–235 (2018)
20. T. Bravo, C. Maury, A synthesis approach for reproducing the response of aircraft panels to a turbulent boundary layer excitation. J. Acoust. Soc. Am. **129**(1), 143–153 (2011)
21. C. Maury, T. Bravo, Laboratory synthesis of the response of aircraft panels to a turbulent boundary layer excitation. J. Sound Vib. **330**, 4970–4971 (2011). Invited contribution in Aeroacoustics research in Europe: The CEAS-ASC report on 2010 highlights
22. M. Aucejo, L. Maxit, J.-L. Guyader, Experimental simulation of turbulent boundary layer induced vibrations by using a synthetic array. J. Sound Vib. **331**(16), 3824–3843 (2012)
23. O. Robin, A. Berry, S. Moreau, Experimental vibroacoustic testing of plane panels using synthesized random pressure fields. J. Acoust. Soc. Am. **135**, 3434 (2014)
24. C.A. Merlo, A.M. Pasqual, E.B. Medeiros, Sound field synthesis on flat panels using a planar source array controlled by its active and reactive radiation modes. Acta Acust. United Acust. **105**, 139–151 (2019)
25. A.M. Pasqual, Analysis of the complex sound power in the near field of spherical loudspeaker arrays. J. Sound Vib. **456**, 331–352 (2019)
26. C. Marchetto, L. Maxit, O. Robin, A. Berry, Experimental prediction of the vibration response of panels under a turbulent boundary layer excitation from sensitivity functions. J. Acoust. Soc. Am. **143**(5), 2954–2964 (2018)
27. C.S. Wolowicz, J.S. Bowman, W.P. Gilbert, Similitude requirements and scaling relationships as applied to model testing. NASA Technical paper 1435 (1979)
28. A. Casaburo, G. Petrone, F. Franco, S. De Rosa. A review of similitude methods for structural engineering. ASME Appl. Mech. Rev. **71**(3), 030802 (2019)

29. X. Zhao, B. Ai, Predicting the structural response induced by turbulent boundary layer in wind tunnel. AIAA J. **55**(4), 1221–1229 (2017)
30. F. Franco, O. Robin, E. Ciappi, S. De Rosa, A. Berry, G. Petrone, Similitude laws for the structural response of flat plates under a turbulent boundary layer excitation. Mech. Syst. Signal Process. **129**, 590–613 (2019)
31. H. Yao, L. Davidson, Vibro-acoustics response of a simplified glass window excited by the turbulent wake of a quarter-spherocylinder body. J. Acoust. Soc. Am. **145**(5), 3163–3176 (2019)
32. P. Druault, A. Hekmati, D. Ricot, Discrimination of acoustic and turbulent components from aeroacoustic wall pressure field. J. Sound Vib. **32**(26), 7257–7278 (2013)
33. N. Hu, N. Reiche, R. Ewert, Simulation of turbulent boundary layer wall pressure fluctuations via Poisson equation and synthetic turbulence. J. Fluid Mech. **826**, 421–454 (2017)
34. C. Hong, K.-K. Shin, Modeling of wall pressure fluctuations for finite element structural analysis. J. Sound Vib. **329**(10) (2010)
35. A. Hekmati, D. Ricot, P. Druault, Numerical synthesis of aeroacoustic wall pressure fields over a flat plate: Generation, transmission and radiation analyses. J. Sound Vib. **332**(13), 3163–3176 (2013). https://doi.org/10.1016/j.jsv.2013.01.019
36. M. Karimi, P. Croaker, H. Peters, S. Marburg, A. Skvortsov, N. Kessissoglou, Vibro-acoustic response of a flat plate under turbulent boundary layer excitation, in *Proceedings of NOVEM 2018 - Noise and Vibration Emerging Methods*, Ibiza, Spain (2018)
37. M. Karimi, P. Croaker, L. Maxit, O. Robin, A. Skvortsov, S. Marburg, N. Kessissoglou, A hybrid numerical approach to predict the vibrational responses of panels excited by a turbulent boundary layer. J. Fluids Struct. **92**, 102814 (2020)
38. L. Maxit, Simulation of the pressure field beneath a turbulent boundary layer using realizations of uncorrelated wall plane waves. J. Acoust. Soc. Am. **140**, 1268 (2016)
39. O. Robin, M. Pachebat, N. Totaro, A. Berry, Évaluation d'une méthode de synthèse spectrale 2D+T pour la transparence de parois sous champ acoustique diffus. CFA, VISHNO, Le Mans, France, April 2016 (2016)
40. M. Jenzri, O. Robin, N. Atalla, Vibration of and radiated acoustic power from a simply-supported panel excited by a turbulent boundary layer excitation at low Mach number. Noise Control. Eng. J. **67**(4), 241–251 (2019)
41. X. Gloerfelt, J. Berland, Direct computation of turbulent boundary layer noise, in *Proceedings of the 15th AIAA/CEAS Aeroacoustics Conference (30th AIAA Aeroacoustics Conference)*, May 2009. American Institute of Aeronautics and Astronautics (2009)
42. L.E. Wittig, A.K. Sinha, Simulation of multicorrelated random processes using the FFT algorithm. J. Acoust. Soc. Am. **58**, 630–634 (1975)
43. R.B. Davies, D.S. Harte, Tests for Hurst effect. Biometrika **74**(1), 95–101 (1987)
44. A. Papoulis, U. Pillai, *Probability, Random Variables and Stochastic Processes*. McGraw-Hill Higher Education (2002), pp. 515–519
45. G. Schewe, On the structure and resolution of wall-pressure fluctuations associated with turbulent boundary-layer flow. J. Fluid Mech. **134**, 311–328 (1983)
46. R.H. Mellen, Wave-vector filter analysis of turbulent flow. J. Acoust. Soc. Am. **95**, 1671–1673 (1994)
47. O. Robin, J.-D. Chazot, R. Boulandet, M. Michau, A. Berry, N. Atalla, A plane and thin panel with representative simply supported boundary conditions for laboratory vibroacoustic tests. Acta Acust. United Acust. **102**(1), 170–182 (2016)
48. O. Robin, S. Moreau, T. Padois, A. Berry. Measurement of the wavenumber-frequency spectrum of wall pressure fluctuations: spiral-shaped rotative arrays with pinhole-mounted quarter inch microphones, in *Proceedings of the 19th AIAA/CEAS Aeroacoustics Conference*, Berlin, Germany (2013)
49. ISO 3744:2015, Acoustics – determination of sound power levels and sound energy levels of noise sources using sound pressure – engineering methods for an essentially free field over a reflecting plane. International Organization for Standardization, Geneva, Switzerland
50. R.E. Crochiere, A weighted overlap-add method of short-time Fourier analysis/synthesis. IEEE Trans. Acoust. Speech Signal Process. **28**(1) 99–102 (1980)

51. J.O. Smith. *Spectral Audio Signal Processing*, online book, 2011 edn. (2019), https://ccrma.stanford.edu/~jos/sasp/. Accessed Dec 2019
52. A. Dijckmans, G. Vermeir, Numerical investigation of the repeatability and reproducibility of laboratory sound insulation measurements. Acta Acust. united with Acust. **99**(3), 421–432 (2013)

Experimental Techniques (or Experimental Characterization)

Underwater Flow Noise from a Turbulent Boundary Layer over a Wavy Surface

Jan Abshagen and Volkmar Nejedl

Abstract Results from an underwater experiment on turbulent boundary layer flows over a plate with a spanwise wavy pattern are presented. The experiments were performed with a towed body measurement system at depths between −90 and −150 m in Sognefjord, Norway. Flow-induced noise on the reverse side of the wavy plate as well as wall pressure fluctuations beneath the turbulent boundary layer were studied for outer flow velocities U_∞ between 2.2 and 5.5 ms^{-1}, which corresponds to towing speeds between 4 kn and 10 kn, respectively. For the lowest flow velocity within this range a substantial reduction in turbulent wall pressure fluctuations is found in comparison to a flat plate configuration. This reduction is, however, accompanied with an increase of flow-induced noise in the interior. Both effects are even enhanced at a larger pitch angle of the towed body. For higher flow velocities the differences between wavy and flat plate configuration are substantially less pronounced or even absent in some frequency ranges.

1 Introduction

Flow-induced interior noise [1, 2] plays a crucial role in underwater acoustics, since it acts as an interference noise source that limits the performance of a hydroacoustic antenna [3–5]. Flow-induced noise provides, in general, the dominant contribution to the so-called *self-noise* level of a sonar system, either towed or platform mounted, at high speeds [6]. Hydroacoustic noise [7] in the fluid-filled (quiescent) interior of an antenna origins from the excitation of an elastic (hull) structure [8–10] by outer wall pressure fluctuations beneath a surrounding turbulent boundary layer flow [11, 12].

Reduction measures concerning flow-induced noise in the interior of a mechanical structure have in principle two starting points, the elastic wall structure or the

J. Abshagen (✉) · V. Nejedl
Bundeswehr Technical Center for Ships and Naval Weapons, Maritime Technology and Research (WTD 71), 24340 Eckernförde, Germany
e-mail: JanAbshagen@bundeswehr.org

E. Ciappi et al. (eds.), *Flinovia—Flow Induced Noise and Vibration Issues and Aspects-III*, https://doi.org/10.1007/978-3-030-64807-7_6

turbulent boundary layer [13]. Elastic hull materials of hydroacoustic antennas are typically designed to reduce flow-induced noise on the one hand, but require, on the other hand, also preferable hydroacoustical properties. A hydroacoustic antenna is designed to detect signals in the sea, so noise reduction is evaluated in the light of the signal-to-noise ratio, instead of the (interfering) noise level alone.

In this work the possibility of a reduction of turbulent wall pressure fluctuations as well as of interior flow-induced noise by a spanwise wavy pattern is investigated in an underwater experiment. The reduction of turbulent fluctuations in wall-bounded flows is highly desirable not only with respect to interference noise in underwater or other interior noise problems, such as cabin noise in aircrafts [14] or cars [15], but also in many other applications. In fact, by far most of the work in this field is aimed towards reducing drag [16]. Drag reduction aims to the reduction of wall shear stress (or skin friction) and has been approached, e.g., by additives [17, 18], by gas injection [19], by ripplet surface structures [20], and by superhydrophobic surfaces [21]. More recently, water-repellent surfaces have also been investigated with respect to the reduction of flow-induced noise for sonar applications [22, 23]. Those approaches are often inspired from biological surfaces [24, 25].

The wavy pattern studied in this work follows a different approach, since the amplitude and (half-)wavelength of the pattern are in the order of the boundary layer thickness of a comparable flat plate configuration. The behavior of the flat plate configuration with respect to wall pressure fluctuations and interior noise has been investigated in previous studies [26, 27]. Though different in surface shape, both configurations follow the same sandwich design principles and have the same mass density (per unit area) in order to achieve a most similar vibroacoustic response behavior. The effect of the (spanwise) wavy pattern on turbulent wall pressure fluctuations and on interior flow-induced noise is presented in this work for different (outer) flow velocities.

2 Underwater Experiment

The underwater experiments with the flat and the wavy plate configuration were both conducted during a research cruise with RV Elisabeth Mann Borgese (IOW, Germany) in Sognefjord, Norway, in 2014. The two plate configurations as well as the towed body measurement system and the towing experiments are described below. Further information, for instance, on sensor calibration under sea conditions [27] are given in Refs. [5, 26].

2.1 Towing System

The towing experiments were performed with the so-called FLAME towed body (Flow Noise Analysis and Measurement Equipment), a measurement system

Fig. 1 FLAME towed body with (spanwise) wavy surface after a towing experiment in Sognefjord, Norway (**a**). Detailed view on the wavy surface with hydroacoustic window (white) and flush-mounted hydrophones (black points) in the mid wave trough downstream of the acoustic window (**b**)

advanced for the experiments by ATLAS Elektronik (Bremen, Germany) in collaboration with WTD 71. The system is designed for investigations of interior flow-noise generation from turbulent boundary layers under sea conditions. The towed body has a length, width, and height of 5.26 m, 1.353 m (0.935 m without fins), and 1.715 m, respectively. The total mass in water and the net buoyancy are about 3500 kg and 3000 N, respectively. In air the system weights about 2800 kg.

A pictures of the towed body with the laterally attached wavy plate is depicted in Fig. 1a. It was taken directly after a towing experiment. The wavy plate (brown) with the acoustics window (white rectangle) of 575 mm × 300 mm in length and width, respectively, and the flush-mounted hydrophones (black points) is shown in more detail in Fig. 1b. It should be noted, that the foremost hydrophone was not operative during the experiments. The plate has a size of 2000 mm × 770 mm in length and width, respectively, and is built in a sandwich design. At the outside it is made from

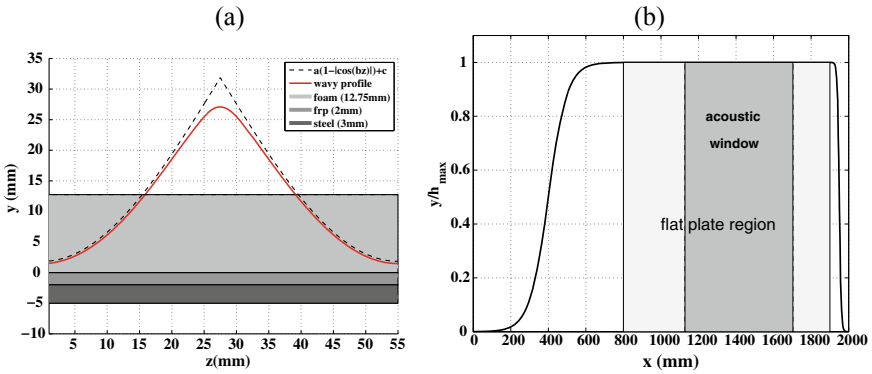

Fig. 2 Spanwise wavy pattern (single wavelength) (**a**) and (normalized) streamwise profile with in- and outflow region (**b**). The size of the outer layer of the flat plate configuration (12.75 mm) is given in **a** for comparison. Wavy and flat plate have the same mass per (spanwise) wavelength within the flat plate region depicted in **b**

a hard foam except for the acoustic window region, which is acoustically almost transparent (see Sect. 2.3 for details).

Flow noise measurements were performed well below to local thermocline in Sognefjord at towing depths between −90 m and −150 m. In order to achieve a sufficient reduction of interfering noise from the towing vessel, a minimum towing cable length of 400 m was chosen. A length of 600 m was found to be sufficient for the higher towing speeds. Measurements of the wavy plate configuration were conducted at towing speeds between 4 and 10 kn, which correspond to outer flow velocities U_∞ between 2.2 and 5.5 ms^{-1} (see Ref. [26] for calculation method). For each towing speed a measurement was started after transient dynamics was relaxed and stopped $T \approx 300$ s after the start. In the transient phase the tail fins were controlled remotely from the research vessel in order to adjust pitch and roll angle (the front fins are fixed). During the measurement the towed body went on a straight track without any motion of the fins.

2.2 *Wavy Surface Pattern*

A schematic view on the wavy plate configuration in streamwise (a) and spanwise direction (b) is depicted in Fig. 2. A single wavelength of the spanwise wavy pattern (a) and the streamwise profile (b) of the plate are depicted schematically in Fig. 2.

The wavy and a corresponding flat plate were designed to have the same mass per spanwise wavelength within the flat plate region. Both configurations differ only in the shape of the outer layer, which is build in both cases either from a hard foam or an acoustically (almost) transparent material in the acoustic window region. The shape of the outer layer of wavy (red curve) and flat plate (light grey rectangle) can

be seen Fig. 2a. In spanwise direction the surface pattern of both configurations are given by:

$$h_z(z) = \begin{cases} h_p & \text{(flat plate)} \\ h_0 \left(1 - \sqrt{\epsilon + \cos^2(\pi z/\lambda_z)}\right) + d & \text{(wavy plate)} \end{cases}$$

The height of the outer layer of the flat plate $h_p = 12.75\,\text{mm}$ is constant. The parameters for the wavy plate are $\lambda_z = 55\,\text{mm}$ (wavelength), d = 1.85 mm (offset), $h_0 = 30\,\text{mm}$ (maximum height of theoretical profile without offset), and $\epsilon = 0.025$. The parameter ϵ was introduced in order to smooth the periodic function $|\cos(kx)|$. The maximum height of the wavy plate is (theoretically) given by $h_{\max} = 27.1\,\text{mm}$. Below the outer layer each plate consists of a thin layer of 2 mm thickness which is made from fiber-reinforced plastic (frp). This layer is glued onto a steel plate of 3 mm thickness which has a recess in the acoustic window region. The three layers of the sandwich design can be seen in Fig. 2a. The steel plate is supported from below by an additional damping layer of about 10 mm thickness (not shown in Fig. 2a).

The upper edge of the frp-layer is mounted flush to the surface of the towed body and the surface pattern $h(x, y)$ is compose from the product of a spanwise $h_z(z)$ and a streamwise pattern $h_x(x)$

$$h(x, y) = h_x(x) \cdot h_z(z) \tag{1}$$

The streamwise pattern $h_x(x)$ consists of a smooth flow entrance ($0\,\text{mm} \leq x < 800\,\text{mm}$) and outflow region ($1900\,\text{mm} \leq x < 2000\,\text{mm}$) in order to avoid separation at a forward-facing and backward-facing step, respectively. The smooth profile is achieved by

$$h_x(x) = \frac{1}{2}\left(1 \pm \tanh\left(\frac{x - \bar{x}_{i,o}}{\delta x_{i,o}}\right)\right) \quad \text{with} \begin{cases} + & \text{inflow}(x_i) \\ - & \text{outflow}(x_o) \end{cases}$$

The parameters of the profile are $\bar{x}_i = 400\,\text{mm}$ and $\delta x_i = 100\,\text{mm}$ for the inflow and $\bar{x}_o = 50\,\text{mm}$ and $\delta x_o = 10\,\text{mm}$ for the outflow region. In between the in- and outflow region $h_x(x)$ equals one.

2.3 Measurement Setup

Flow-induced noise in the interior of the towed body as well as wall pressure fluctuations on the outer surface were measured simultaneously during each measurement run. The principle measurement setup is depicted in Fig. 3. The flush-mounted hydrophones of type Reson TC4050 were located downstream of the measurement area on the (spanwise) centerline of the plate. For the wavy plate this position is in the mid wave trough of the wavy pattern, as can be seen in Fig. 1b. Streamwise

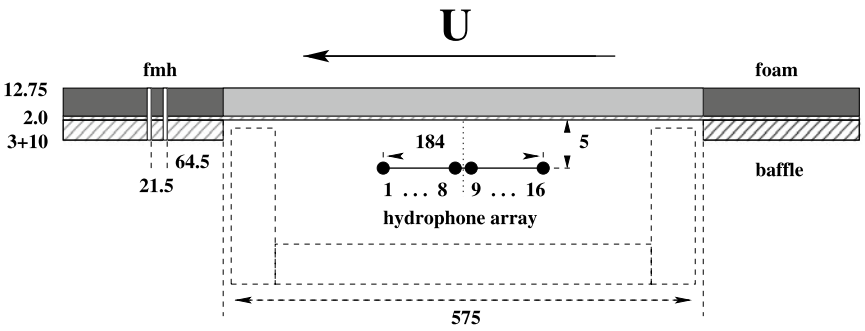

Fig. 3 Principle measurement setup with two flush-mounted hydrophones (fmh) and a hydrophone array located downstream of and beneath the hydroacoustic window, respectively. For reasons of clarity the flat plate configuration is shown here. Positions of hydrophones are the same for the wavy plate configuration

coherence is determined between the two rear hydrophone positions shown in Fig. 1b having a spacing of 21.5 mm (see Fig. 3). With an equidistant line array of 16 Reson TC4013 hydrophones with spacing $d_s = 11.5$ mm flow-induced noise is measured in the interior of the towed body. The array is aligned along the centerline and mounted inside a cavity at a distance of 5 mm beneath the plate. The cavity shields the array from (interior) structure-borne sound and ambient noise emitted from the reverse side of the towed body.

The sampling frequency for all measurements was $f_s = 31{,}250$ Hz and the measurement time for each run was T ≈ 300 s, as described in Sect. 2.1. Power spectral densities are calculated from an average of 300 non-overlapping short-time spectra (with $T_s = 1.0485$ s) with a bandwidth of $\Delta f = 1/T = 0.9537$ Hz. The effective noise bandwidth amounts $\Delta f_e = 1.36\ \Delta f$ since Hamming windowing is applied to each (short) time series.

3 Wall Pressure Fluctuations

In Fig. 4 a comparison between (Corcos-corrected [28, 29]) power spectral densities of turbulent wall pressure fluctuations for the wavy and the flat plate configuration are depicted for flow velocities between $U_\infty = 2.2$ and 5.6 ms^{-1}. These flow velocities correspond to towing speeds between 4 and 10 kn. The flow velocities of the wavy plate configuration differ only slightly from the respective velocities of the flat plate configuration. Measurements were performed in general at two different pitch angles for the wavy plate configuration except for a towing speed of 10 kn. At this speed towing experiments with a pitch angle larger than 2° were not feasible. It should be noted, that within a range of ±2° no substantial differences in spectral level were found for the flat plate configuration. All measurements with this configuration were adjusted to a pitch angle of 2°.

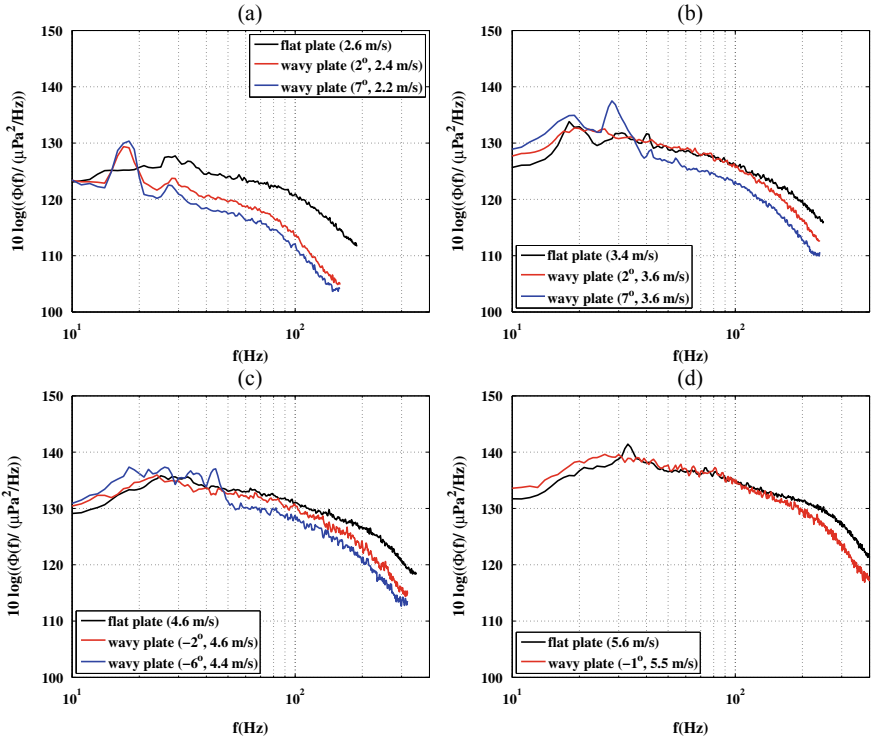

Fig. 4 Power spectral density $\Phi(f)$ of turbulent wall pressure fluctuations measured for the wavy and the flat plate configuration at four different flow velocities U_∞ (flat plate): 2.6 ms^{-1} (**a**), 3.4 ms^{-1} (**b**), 4.6 ms^{-1} (**c**), and 5.6 ms^{-1} (**d**). Measurements of the wavy plate configuration were performed at comparable speeds and two different pitch angles (except for **d**). All power spectral densities are Corcos-corrected [28, 29]

The difference in spectral level between flat and wavy plate configuration is most striking for the lowest towing speed (4 kn). The reduction in spectral level is up to 6 dB for the small and up to 10 dB for the larger pitch angle. It should be noted, that a frequency peak at 18 Hz is visible in the spectrum, which is absent for the flat plate configuration at comparable speed. The available data, however, do not allow a definite clarification of its physical origin.

For higher flow velocities U_∞ and small pitch angles the difference in spectral level is much less pronounced and occurs only in the high frequency regime. Below 100 Hz the spectral levels are almost identical for wavy and flat plate configuration. For larger pitch angles the difference remains significant, but is substantially reduced. At very low frequencies the spectral levels for the wavy plate configuration are slightly larger compared to those of the flat plate configuration. The appearance of pronounced spectral peaks can also be observed for the wavy plate configuration.

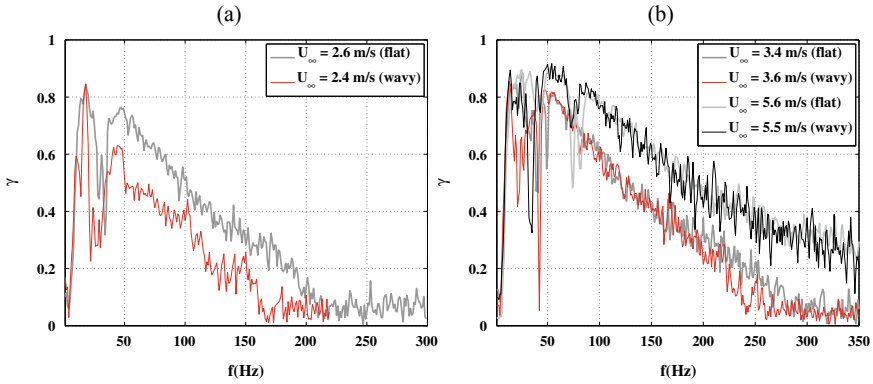

Fig. 5 Streamwise coherence γ for the wavy and the flat plate configuration is depicted in **a** for the lowest towing speeds (flat: $2.6\,\mathrm{ms}^{-1}$; wavy: $2.4\,\mathrm{ms}^{-1}$) and in **b** for higher towing speeds. The separation distance of the hydrophones was 21.5 mm

The spatial coherence γ for a separation distance of 21.5 mm is depicted in Fig. 5a for the lowest and in (b) for highest towing speeds. The reduction in spectral level of the turbulent wall pressure fluctuations at low speeds, shown in Fig. 4a, is found to be accompanied with a significant reduction in streamwise coherence. At higher flow velocities the spatial coherence is (almost) equal for both configurations at comparable towing speeds. This can be seen from Fig. 5b.

4 Flow-Induced Interior Noise

For a hydroacoustic antenna a reduction in turbulent wall pressure fluctuations is primarily of relevance only to that extend, as it is accompanied with a reduction in flow-induced interior noise.

A wavenumber-frequency spectrum of interior noise measured with the hydrophone array on the reverse side of the wavy plate is shown in Fig. 6a. It is qualitatively similar to that of the flat plate configuration [27]. Since the hydrophone spacing is small compared to the hydroacoustic wavelength in this frequency regime, underwater sound waves contribute only to the central bin of the spectrum located around $\mathrm{k} = 0\,\mathrm{m}^{-1}$. Spectral contributions with different physical origin can, however, be identified due their dispersion relation. In particular bending waves, that have a larger wavenumber than underwater sound waves in this frequency regime, can be separated from sound waves. The dispersion relation of bending waves for the flat plate (not wavy plate) configuration is depicted in Fig. 6a. The comparison reveals a similar spectral behavior of the flat and wavy plate configuration (see Ref. [27] for kf-spectrum of flat plate configuration).

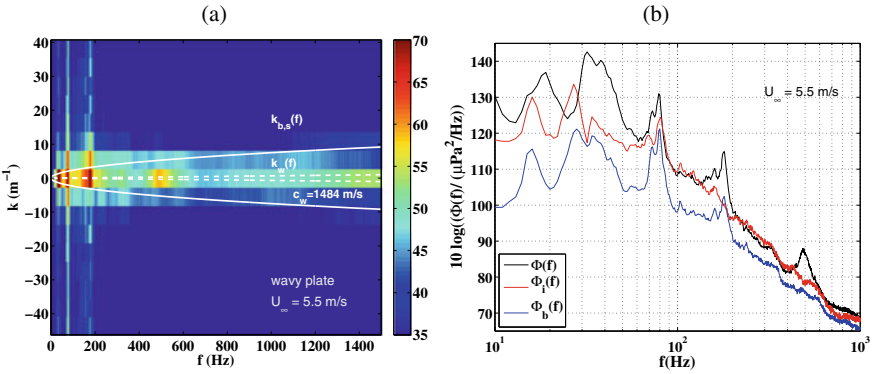

Fig. 6 Wavenumber-frequency spectrum of flow-induced interior noise measured beneath the wavy plate at $U_\infty = 5.6\,\mathrm{ms}^{-1}$ (**a**). Corresponding power spectral density Φ and filtered spectral densities Φ_i and Φ_b at $U_\infty = 5.6\,\mathrm{ms}^{-1}$ in **b**. The acoustic regime $k_\mathrm{w}(f)$ and the bending wave regime $k_\mathrm{b,s}$ of the corresponding flat plate are shown in **a** for comparison [27]

The mean spectral level within the bending wave regime provides a measure for the structural response to excitation from turbulent wall pressure fluctuations. This level is determined for each frequency by filtering out the acoustic contributions and the non-acoustic contributions having wavenumbers larger than the bending waves. The filtered power spectral density Φ_b is depicted in Fig. 6b. An additional measure is the power spectral density Φ_i of the spatially incoherent part of hydroacoustic noise. This measure is also shown in Fig. 6b. It incorporates in principle spectral contributions from both the acoustic and the (large wavenumber) non-acoustic regime, but removes spatially coherent noise. This filter is aimed to remove (low-frequency) noise that origins from external hydroacoustic noise sources, such as the towing vessel. Both filter techniques are described in Ref. [27].

The differences in spectral level between wall pressure fluctuations at the outside and (incoherent) noise in the interior of the towed body are depicted in Fig. 7 for different towing speeds. A difference in spectral level can be considered as a reduction measure which reflects the response of the plate to boundary layer excitations. The reduction index increases significantly with frequency and is much larger than a reduction of an acoustics wave damped by Berger's mass law. The solid and dashed curves in Fig. 7 originate from the analysis of the flat plate configuration [26, 27] and are plotted for comparison. This comparison reveals that the reduction index of the wavy plate displays a very similar behaviour than that of the flat plate, except for the low speed case (4 kn). Here, the reduction index is significantly below the other curves.

Filtered power spectral densities of (incoherent) flow-induced interior noise are depicted in Fig. 8a for the flat and the wavy plate configuration at small pitch angles. The differences in spectral level are shown in (b). It can be seen that for the lowest towing speed (4 kn) the spectral level of interior noise on the reverse side of the wavy plate is significantly larger than the corresponding level beneath the flat plate.

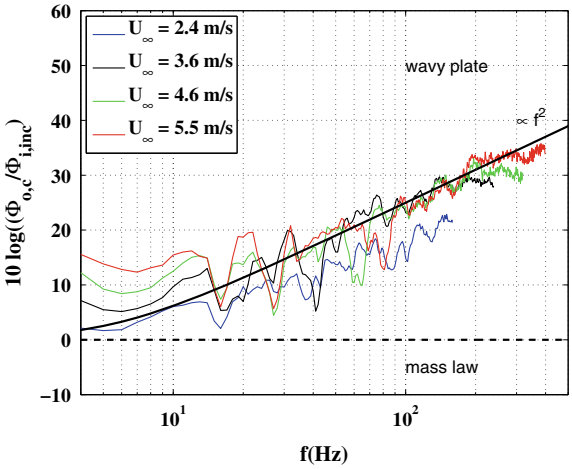

Fig. 7 Differences between (Corcos corrected) power spectral density $\Phi_{o,c}$ of turbulent wall pressure fluctuations and (incoherent) flow-induced interior noise $\Phi_{i,inc}$ at the out- and the inside of the wavy plate, respectively

This behavior is opposite to that of the (outer) wall pressure fluctuations measured simultaneously. Here, the spectral level is lower for the wavy plate configuration (see Fig. 4a). While this result seems unexpected, it should be stressed that only limited information on the flow and and vibration field are available in this experiment. For larger flow velocities the differences in spectral level of interior noise are much less pronounced.

In Fig. 8c, d the differences in spectral level of the bending wave regime are depicted for small and large pitch angle, respectively. A behavior qualitatively similar to that found for the level differences in Φ_i (b) can be seen also in the level differences in Φ_b at small pitch angle. For the large pitch angle the level differences in Φ_b even increase.

5 Conclusion

Results from an underwater experiment on turbulent boundary layer flows over a (spanwise) wavy surface are presented. The measurements were performed under sea conditions with a towed body measurement system in Sognefjord, Norway. The wavy surface pattern was designed in a way that (spanwise) wavelength and amplitude are in the order of the boundary layer thickness of a comparable flat plate configuration. Spectral level and spatial coherence of turbulent wall pressure fluctuations are found to be substantially reduced for the wavy plate configuration in comparison to the flat plate configuration for an outer flow velocity of about 2 ms^{-1}. For this velocity the spectral level of flow-induced interior noise is found, on the other hand, to be

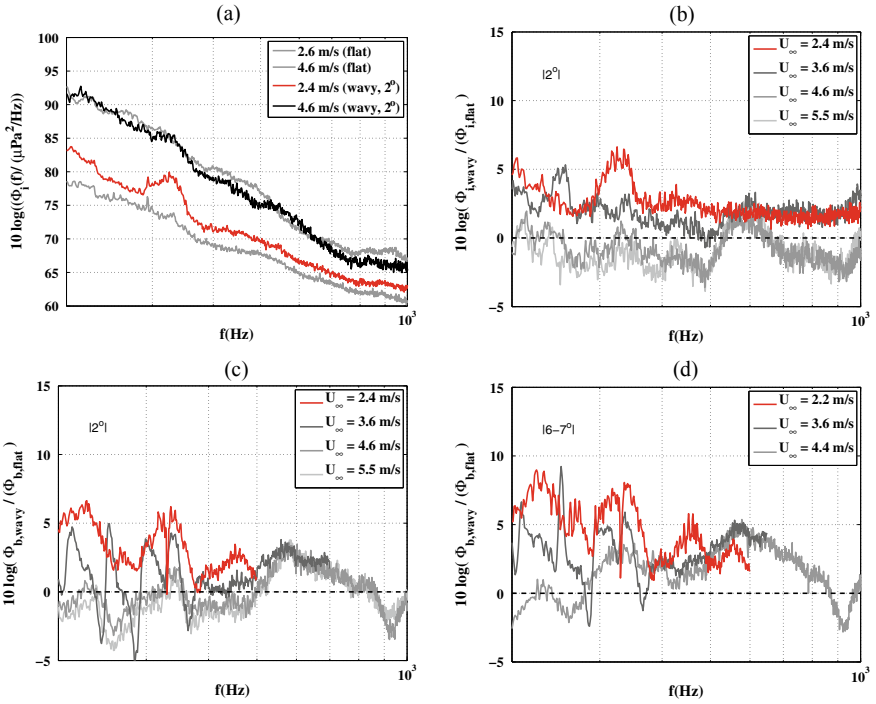

Fig. 8 Comparison of filtered power spectral densities Φ_i beneath the flat and the wavy plate for towing speeds of (about) 4 and 8 kn (**a**) and difference in Φ_i for all towing speeds (**b**). Difference in (mean) spectral level of bending wave regime for the wavy ($\Phi_{b,wavy}$) and the flat ($\Phi_{b,flat}$) plate configuration at small (**c**) and large (**d**) pitch angle

substantially increased despite of a reduction in wall pressure fluctuations. For higher velocities the differences between the two configurations are much less pronounced or even absent.

Wall pressure fluctuations are of importance in many applications, including underwater acoustics, and this work has revealed the principle potential of spanwise waviness as an effective method for a (at least local) reduction. In a future work a systematic parameter study might shed more light on the hydrodynamic and the vibroacoustic mechanisms involved in the reduction of pressure fluctuations and in flow-noise generation at this inhomogeneous surface. This might also contribute to an optimization of the wavy pattern for underwater applications.

Acknowledgements The excellent support from the engineering branch of WTD 71, from ATLAS Elektronik, and from Captain and Crew of RV Elisabeth Mann Borgese (IOW, Germany) is gratefully acknowledged.

References

1. E. Ciappi, S. De Rosa, F. Franco, J.L. Guyader, S.A. Hambric (eds.), *Flinovia - Flow Induced Noise and Vibration Issues and Aspects* (Springer, Cham, 2015)
2. E. Ciappi, S. De Rosa, F. Franco, J.L. Guyader, S.A. Hambric, R. Chi Kin Leung, A.D. Hanford (eds.), *Flinovia - Flow Induced Noise and Vibration Issues and Aspects II* (Springer, Cham, 2019)
3. A.P. Dowling, Underwater flow noise. Theor. Comput. Fluid Dyn. **10**, 135–153 (1998)
4. W.L. Keith, K.M. Cipolla, D. Furey, Turbulent wall pressure fluctuation measurements on a towed model at high Reynolds numbers. Exp. Fluids **46**, 181–189 (2009)
5. J. Abshagen, V. Nejedl, Towed body measurements of flow noise from a turbulent boundary layer under sea conditions. J. Acoust. Soc. Am. **135**(2), 637–645 (2014)
6. R. Urick, *Principles of Underwater Sound*, 2nd edn. (McGraw-Hill, New York, 1975)
7. J. Abshagen, I. Schäfer, Ch. Will, G. Pfister, Coherent flow noise beneath a flat plate in a water tunnel experiment. J. Sound Vib. **340**, 211–220 (2015)
8. S.A. Hambric, Y.F. Hwang, W.K. Bonness, Vibration of plates with clamped and free edges excited by low-speed turbulent boundary layer. J. Fluids Struct. **19**, 93–110 (2004)
9. S. De Rosa, F. Franco, Exact and numerical response of a plate under turbulent boundary layer excitation. J. Fluids Struct. **24**, 212–230 (2008)
10. E. Ciappi, F. Magionesi, S. De Rosa, F. Franco, Analysis of the scaling laws for the turbulence driven panel responses. J. Fluids Struct. **32**, 90–103 (2013)
11. H. Schlichting, *Grenzschicht-Theorie (Engl.: Boundary Layer Theory)* (G. Braun, Karlsruhe, 1965)
12. T.M. Farabee, M.J. Casarella, Spectral features of wall pressure fluctuations beneath turbulent boundary layers. Phys. Fluids A **10**, 2410–2420 (1991)
13. W.K. Blake: *Mechanics of Flow-Induced Sound and Vibration*, vol. 1, 2 (Academic Press, New York, 1986)
14. N. Hu, H. Buchholz, M. Herr, C. Spehr, S. Haxter, Contribution of different aeroacoustic sources to aircraft cabin noise, in *19th AIAA/CEAS Conference* (2013). https://doi.org/10.2514/6.2013-2030
15. S. Müller, S. Becker, Ch. Gabriel, R. Lerch, F. Ulrich, Flow-induced input of sound to the interior of a simplified car model depending on various setup parameters, in *19th AIAA/CEAS Conference* (2013). https://doi.org/10.2514/6.2013-2019
16. Kwing-So Choi, European drag-reduction research - recent developments and current status. Fluid Dyn. Res. **26**, 325–335 (2000)
17. J.L. Lumley, Drag reduction by additives. Annu. Rev. Fluid Mech. **1**, 367–384 (1969)
18. I. Procaccia, V.S. L'vov, Theory of drag reduction by polymers in wall-bounded turbulence. Rev. Mod. Phys. **80**, 225–247 (2008)
19. S.L. Ceccio, Friction drag reduction of external flows with bubble and gas injection. Annu. Rev. Fluid Mech. **42**, 183–203 (2010)
20. R. García-Mayoral, J. Jimenéz, Drag reduction by riblets. Philos. Trans. R. Soc. A **369**, 1412–1427 (2011)
21. J.P. Rothstein, Slip on superhydrophobic surfaces. Annu. Rev. Fluid Mech. **42**, 89–109 (2010)
22. T. Elboth, B.A. Reif, Ø. Andreassen, M.B. Martell, Flow noise reduction from superhydrophobic surfaces. Geophysics **77**, P1–P10 (2012)
23. F. Veronesi, M. Raimondo, G. Boveri, E. Ciappi, C. Nicolai, F. La Gala, A. Conforti, F. Sajeva, Attenuation of turbulent boundary layer induced vibration using water-repellent coatings, in *INTER-NOISE and NOISE-CON Congress and Conference Proceedings NOVEM 2018*, vol. 10 (2018), pp. 562–571
24. D.M. Bushnell, K.J. Moore, Drag reduction in nature. Annu. Rev. Fluid Mech. **21**, 65–79 (2010)
25. D.W. Bechert, M. Bruse, W. Hage, R. Meyer, Fluid mechanics of biological surfaces and their technological application. Naturwissenschaften **87**, 157–171 (2000)
26. J. Abshagen, D. Küter, V. Nejedl, Flow-induced interior noise from a turbulent boundary layer of a towed body. Adv. Aircr. Spacecr. Sci. **3**(3), 259–269 (2016)

27. J. Abshagen, D. Küter, V. Nejedl, Turbulent flow noise generation under sea conditions, in *Flinovia - Flow Induced Noise and Vibration Issues and Aspects II*, ed. by E. Ciappi, S. De Rosa, F. Franco, J.L. Guyader, S.A. Hambric, R. Chi Kin Leung, A.D. Hanford (Springer, Cham, 2019)
28. G.M. Corcos, Resolution of pressure in turbulence. J. Acoust. Soc. Am. **35**, 192–199 (1963)
29. R.M. Lueptow, Transducer resolution and the turbulent wall pressure spectrum. J. Acoust. Soc. Am. **97**, 370–378 (1995)

Some Aspects of Experimental Investigations of Fluid Induced Vibration in a Hydrodynamic Tunnel for Naval Applications

Jacques-André Astolfi

Abstract Experiments providing high fidelity experimental data are strongly required for physical analysis and numerical validation regarding of modelling and computation of Fluid Induced Vibration for hydrodynamics applications. This requires the development of advanced experiments and methods in very well controlled configurations as in hydrodynamic tunnels to analyse both the structure response and the flow dynamics. The paper presents original Fluid Induced Vibration experiments performed in the hydrodynamic cavitation tunnel of the French Naval Academy along the past few years. The experiments are generally conducted at a relative high Reynolds numbers typically ranging from about one hundred thousand to more than one million. The experiments are conducted on relatively small scale elastic or rigid lifting surfaces or elastic flat plates undergoing various flow conditions as turbulent boundary layer, Laminar Separation Bubble inducing transition, vortex shedding and cavitation. The structural response is analysed through local strains and stresses and vibration measurements for modal analysis. The deformed shape of the structure is obtained from a specific distance laser measurement device. Local stresses are obtained from strain gauges embedded in the structure. The vibration modal response is analysed by means of mono-point and scanning non contact laser Doppler vibrometers. The flow dynamics is examined through instantaneous wall-pressure field measurements using arrays of pressure transducers and through instantaneous velocity field measurement based on Time Resolved-Particle Image Velocimetry measurements and data-driven modal decompositions as Proper Orthogonal Decomposition. High speed cameras and image processing can be also used to analyse both the structure and flow dynamics particularly in cavitating flow. The paper presents the general experimental set-up and methods. Selected results are reported and briefly discussed.

J.-A. Astolfi (✉)
Naval Academy Research Institute, Naval Academy - Arts et Metiers Institute of Technology, BCRM Brest Ecole Navale, IRENAV, 29240 Brest, France
e-mail: jacques-andre.astolfi@ecole-navale.fr

E. Ciappi et al. (eds.), *Flinovia—Flow Induced Noise and Vibration Issues and Aspects-III*, https://doi.org/10.1007/978-3-030-64807-7_7

1 Introduction

Flow Induced Vibration is a relevant topic for naval applications particularly for structural resistance, acoustic stealth or passenger comfort. Due to the large density of water, large viscosity and very small Mach numbers compared to air, Fluid Structure Interactions is much different for naval applications than for aerodynamic ones. Moreover the flow conditions can induce low pressures beneath the water vapor pressure leading to cavitation known to induce vibration and noise. The proximity of the free surface can also induce ventilation with complex FIV problems in two-phase flow [1]. This is particularly true for the development of very fast sailing yachts and innovative high-speed ships using surface-piercing hydrofoils that have placed the flow induced vibrations, cavitation or ventilation issues as a major concern during the design process. Composite compliant lifting structures have started to be used for the control of performances for a wide range of ship control systems as hydrofoils, rudders, stabilizers or propeller blades [2]. The flexibility is aim to control passively or actively the structure shape in order to control the performances. For instance using active or passive compliant structures to control hydrodynamic forces and cavitation inception remains a very challenging task for naval applications [3]. Moreover as a non negligible advantage the weight is generally reduced due to the low average density of the compliant structure compared to the equivalent metallic one. Using such materials bring also fundamental questions about Fluid Induced Vibration on lightweight structures immersed in a fluid of high density. The questions refer to mass effect, damping, stiffness, hydro-elastic instabilities for various flow conditions including complex cavitating flow, [4–9].

In the latter case, various cavitation patterns can be observed on the suction side of a lifting structure depending on the pressure distribution. This includes convected vapor bubbles, attached partial cavities,cloud cavitation, cavitating vortex, or super-cavitation [10]. The cavitation patterns can coexist on a same structure and are closely related to the wall-pressure distribution in the non cavitating flow. On lifting structures operating at moderate angles of incidence, an attached cavity can take place at the leading edge resulting on the strong low pressure peak and the strong positive pressure gradient close to the leading edge [10, 11]. This cavity is intrinsically unsteady even in the early stage of development. As the cavity grows (at about 30 per cent of the chord length) it becomes strongly unstable leading to a growing and collapsing cycle with cavity break-up and low frequency periodical shedding of large bubble clusters. The latter generates high level of pressure fluctuations or shock-wave of high intensity when collapsing inducing vibration and noise [12]. A large number of studies deals with the analysis of cavitation on rigid bodies but only recently studies refer to cavitation developing on flexible structures [13, 14]. Over the past two decades significant advances have been done regarding modelling and computation of FIV problems for many applications. It is based on advanced coupled CSD/CFD solvers with various levels of complexity depending on the flow and structure models and the coupling methods. Numerical simulation have been developed to analyze both the fluid and the structure dynamics for marine propellers [15–20] or for more

simple elastic lifting surfaces with a certain degree of flexibility [21–25]. Theses studies deal with 3D elastic lifting surfaces or 2 DOF rigid hydrofoils in heaving and pitching motion including cavitation. They pointed out that complex interactions can occur as frequency lock-in between the flow, the cavity dynamics and the structure modes for specific conditions. References [13, 14] performed both experimental and numerical studies of the hydroelastic response of homogeneous elastic hydrofoils based on coupling FD/CSD solvers. The numerical approach is based on the coupling of a URANSE model for the flow coupled with a Finite Element Model for the structure. It was shown that the flow-structure dynamics could be well reproduced qualitatively and that a fairly quantitative agreement was obtained with experimental data provided specific model constants were correctly tuned. Even if large advances were performed for FIV simulations, it appears that FIV experiments are still highly needed to provide a high fidelity experimental data bank for numerical validation and physical analysis.

The present paper deals with the presentation of an original experimental program that was conducted in the recent past years in a hydrodynamic tunnel in order to analyze the hydro-elastic response of structures in various flow conditions. The experimental procedure was based on the study of the hydro-elastic response of elastic hydrofoils or elastic flat plate undergoing various flow conditions as fully-wetted turbulent flow, transition flow, separated flow inducing vortex shedding or cavitating flow.

The originality of the experimental procedure comes from the measurements of both structure and flow characteristics. The structure response was analyzed through the measurements of the static deformation, the instantaneous local strain and stresses and the vibration. The stains and the stresses were obtained from an integrated gauge embedded in the structure. The vibration was analyzed through non contact laser vibrometers allowing us to perform modal analysis. The flow analysis was performed through wall-pressure measurements using a specific array of pressure transducers and through the velocity field measurement using 2D Time Resolved-Particle Image Velocimetry coupled to Proper Orthogonal Decomposition. The cavitating flow dynamics was analyses through a high frequency camera and specific image processing. Hydrodynamics forces could be also measured using multi-component hydrodynamic balances.

2 FIV Experimental Set-Up

The experiments were carried out in the cavitation tunnel of Naval Academy Research Institute (IRENav) fitted with a 192 mm square test section of 1 m long, (Fig. 1). The flow velocity ranges between 0.5 and 15 m/s and the pressure inside the tunnel test section can be controlled between 0.1 and 3 bars. The velocity-pressure couple is controlled through an automate. The inlet turbulence intensity measured about two chords upstream from the hydrofoil leading edge by Laser Doppler Velocimetry is close to 2%. The general experimental set-up for FSI analysis of lifting surfaces in

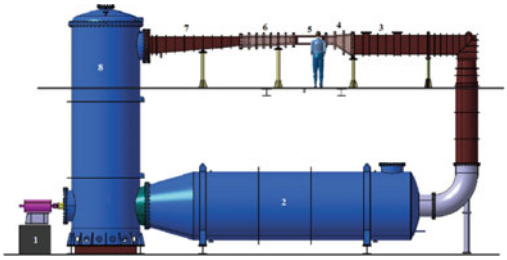

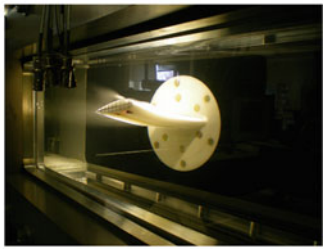

Fig. 1 Overview of the cavitation tunnel at Naval Academy. Flexible hydrofoil in the test section

Table 1 Mechanical characteristics of the material

	Steel	POM
Young mod. (E, GPa)	203	2.9
Poisson coef. (ν)	0.30	0.35
Density (ρ, kg m^{-3})	8010	1420

the cavitation tunnel is depicted at a glance on Fig. 2. It depicts clearly the different experimental devices that are necessary for both structure and flow analysis. It includes deformed shape measurement, local strain and stress and vibration measurements for the structure and flow analysis through Particle Image Velocity technics for flow measurements, wall-pressure and forces measurements as well as image processing of high speed cameras specially for cavitation analysis.

Hydrofoils are fabricated in stainless steel for non deformable structures or with a POlyoxyMethylene plastic (POM) in the flexible case. The material characteristics are given on Table 1. Depending on the application the foils have a 2D NACA015 section or a NACA66 section. The stainless steel hydrofoil is one-piece design composed of a cylindrical beam at the root of a rectangular lifting surface (Fig. 2). The center of rotation is at 1/4 chord length. The cylindric base is clamped on a 5 axes-hydrodynamic balance for forces and moment measurements. The flexible hydrofoil was constituted of a one-piece design composed of a large disk base to get a fully clamped condition all along the foil root (Fig. 2). In that case, the rotation axis of foil is at mid chord. It can be pointed out that the quality of the experimental boundary conditions are of primary importance particularly for numerical comparisons.

The hydrofoil chord lengths are generally ranging between 100 and 150 mm. For rectangular plane form hydrofoils the span is 191 mm close to the test section width leading to 1 mm clearance between the foil tip and the vertical tunnel wall. This results in a secondary flow at the foil tip that can not be totally neglected. Moreover It must be also pointed out that blockage effect (characterized by the ratio between the frontal area of the structure and the test section area) can not be neglected specially at large angles of incidence. This can be of primary importance for comparison to results in other tunnels or to numerical results.

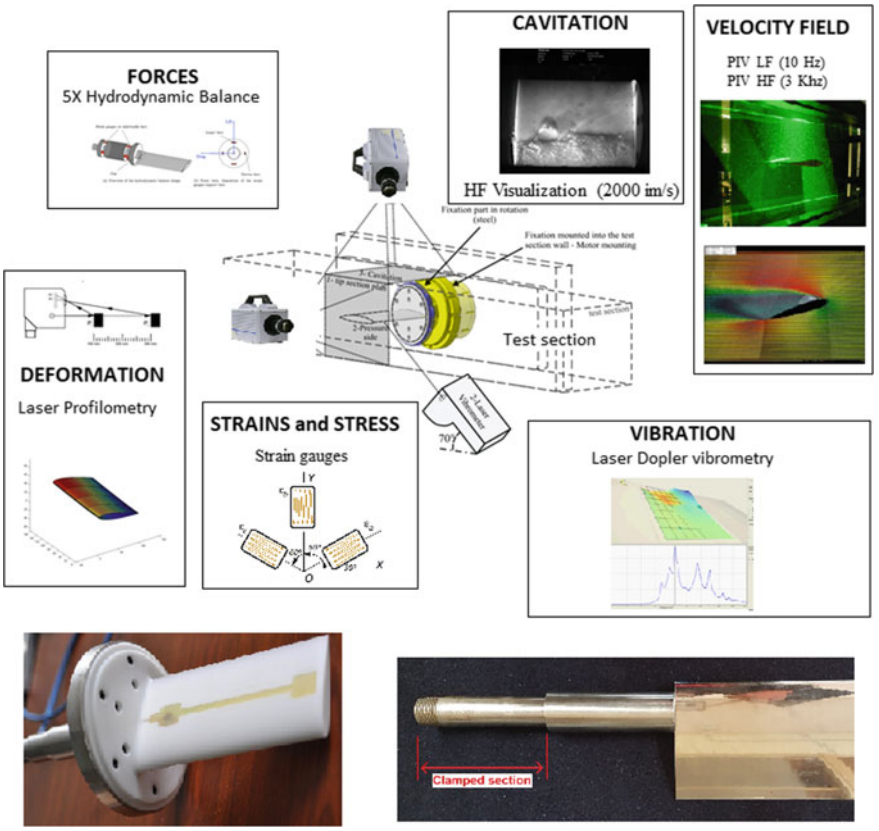

Fig. 2 Overview of the experimental set-up for FIV analyses of lifting surfaces in cavitation tunnel and typical flexible and rigid NACA series hydrofoils made of POM or stainless steel

FIV Experiments could be also conducted on a flat plate specifically build for turbulent boundary layer-induced vibration in the hydrodynamic tunnel as depicted on Fig. 3. It is a rigid stainless structure with a rectangular vibrating thin aluminium plate of 1mm thickness typically. The thin plate is clamped on the support on its upstream side and free on the three other sides. Note that the plate can be changed as it is modular. The model is also equipped of wall pressure transducers downstream the thin plate and an hydrophone in the cavity beneath the vibrating part of the plate. This allows us to analyse the wall-pressure, the plate vibration as well as the radiated noise in the cavity as shown in Fig. 3. The non-dimensional wall-pressure Power Spectral Density was found to scale rather well using the external variables obtained from the boundary layer analysis using Laser Doppler Velocimetry and was in good agreement with the model of Chase. It is particularly true on the medium and high frequency range. In the low frequency region, more discrepancies are found due to low-frequency noise of the tunnel. The vibration response of the thin rectangular flat

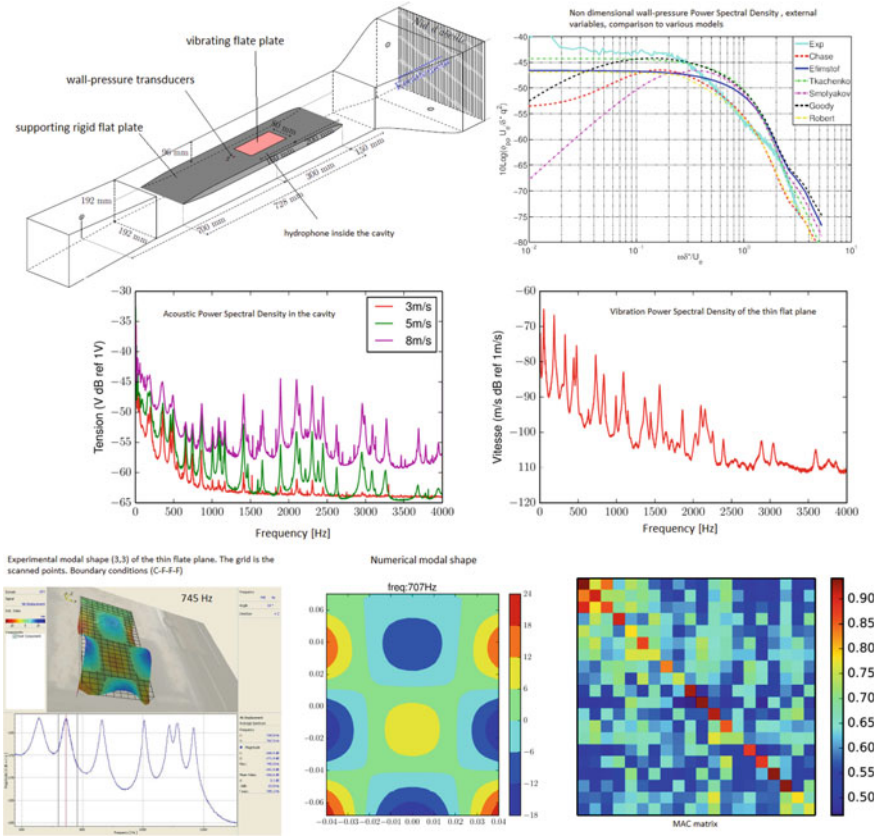

Fig. 3 Rigid flat plate (in grey) located in the middle of the tunnel test section for analysis of turbulent boundary layer wall-pressure fluctuations inducing vibration. The red rectangular part is the modular vibrating thin plate. Non dimensional wall-pressure spectrum, thin plate vibration spectrum (C-F-F-F), acoustic pressure spectrum recorded by an hydrophone located in the cavity beneath the vibrating flat plate, example of modal shape extracted from the scanning Laser Doppler Vibrometer and Modal Assurance Criterion [26, 27]

plate exhibited a large number of very well-defined peaks originating from the modal response of the structure up 2500 Hz depending on the flow velocity. The modal response was cleanly identified and the MAC matrix shows the good agreement between the theoretical ad experimental modes. The acoustic response in the cavity shows peaks clearly related to the modal response of the structure with an increase of the spectra level within the high frequency range as the flow velocity increases.

2.1 Structure Analysis

2.1.1 Static Deformation Measurements

The static deformation was measured using a laser distance measurement system mounted on a 2D translation system on the upper side of the test section. The system allowed us to measure the position of the hydrofoil suction side along various sections selected along the span. The deformation was obtained by subtracting the position of the surface in still water and the position obtained at a given flow velocity as shown on Fig. 4. From a signal processing program, it was then possible to extract the bending and twisting of the hydrofoil for a given angle of incidence and flow velocity. It can be pointed that the laser distance measurement needs to be calibrated in order to take into account the beam laser path crossing the Plexiglas and the water layers. The calibration consisted to measure the position of a well-known geometrical system in air to be compared to the measurement through the water and Plexiglas layers. A correction factor was then determined and applied to the measurements.

It was observed that the hydrofoil experiences bending principally and very small twisting. The bending ranges from about 1 mm to 5 mm at the foil tip and was found to be very close to the theoretical bending of uniformly loaded cantilevered beams. The clamped condition at the root section was found to be very well satisfied. On the other hand the angle of twist was found to be very small (lower than 0.5°) and rather difficult to measure with high accuracy.

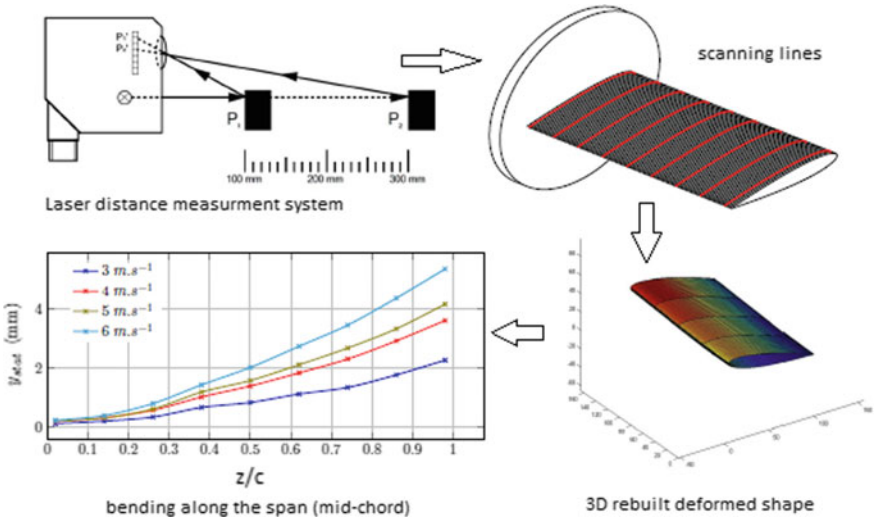

Fig. 4 Experimental analysis of the deformed flexible hydrofoil. Distance laser measurement device, Scanned lines on the foil surface. Resulting foil bending for various flow velocity at $\alpha = 6°$ and reconstructed deformed shape for $\alpha = 8°$ and $U = 5$ m/s

2.1.2 Strain Measurements

To determine the plane strain components, the hydrofoil is equipped with three identical strain gauges build in a rosette way. They are glued in a hole close to the root of the foil. The cavity is filled with a resin whose mechanical characteristics are close to the foil's material. The cavity is then polished manually with sand paper to obtain a smooth continuous surface.

The strain gauges are L2A_13-125WW-120 from Vishay Micro Measurements. They are made in constant an and have a K-factor equal to 2.11. Their accuracy is ±6%. The strain gauges are assembled in a Quarter Bridge. The strain gauges measure the strains $\varepsilon_{1,2,3}$ in the direction of their own axis. The gauges' axes are separated by a 45° angle. ε_1 is in the span direction, ε_3 is in the chord direction. The data are first amplified (Quantum mx16, HBM) and then recorded by the acquisition software CATMAN (HBM). The values of ε_i are recorded during 10 s and the mean value is computed together with the rms value. In order to study the strains resulting from the flow only, the values in still water are removed. As the hydrofoil section is symmetrical, the strains are null for $\alpha = 0°$. This allows us to adjust precisely the value of the incidence α_0 at the beginning of the experiments. The results are generally presented in terms of the Von Mises stress given by the set of the following equations.

The principal strains $\varepsilon_{I,II}$ are given by:

$$\varepsilon_{I,II} = \frac{\varepsilon_1 + \varepsilon_3}{2} \pm \frac{1}{2}\sqrt{(\varepsilon_3 - \varepsilon_1)^2 + 4 * \left(\varepsilon_2 - \frac{1}{2}(\varepsilon_1 + \varepsilon_3)\right)^2} \tag{1}$$

The principal stresses $\sigma_{I,II}$ are given by:

$$\sigma_{I,II} = \lambda(\varepsilon_I + \varepsilon_{II}) + 2\mu\varepsilon_{I,II} \tag{2}$$

where $\lambda = \frac{E\nu}{(1+\nu)(1-2\nu)}$ and $\mu = \frac{E}{2(1+\nu)}$ are the Lame parameters. The Von Mises stress is finally computed by:

$$\sigma_{VM} = \sqrt{\sigma_I^2 + \sigma_{II}^2 - \sigma_I\sigma_{II}} \tag{3}$$

Concerning the strain gauge measurements, the experiments were performed from −10° to 10° with a step $\Delta\alpha = 0.5°$. Figure 5 shows the strains in the rosette directions, the principal stresses and the Von Mises stress for 5 m/s. As shown, the general trend is quasi-linear. The Von Mises stress is symmetrical when passing from negative to positive angles that is interesting to check the zero lift angle of incidence for a symmetrical hydrofoil. It is linear up to 5°. Beyond 5° it starts to deviate progressively from the initial linear evolution with a slope change. This is a consequence of the lift force that was found to follow the same trend. It is the consequence of the boundary layer transition due to a short Laminar Separation Bubble on the rear part of the hydrofoil suction side observed at moderate Reynolds numbers and small angles of

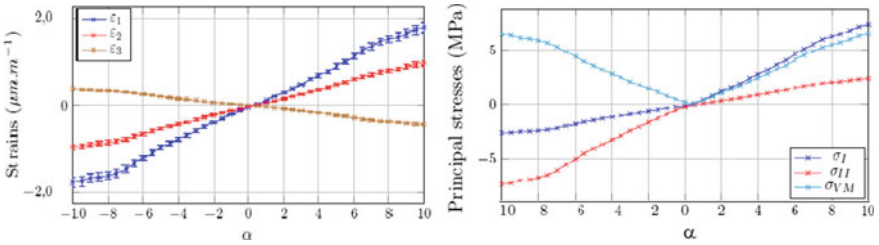

Fig. 5 Left: strains. Right: principal stresses and Von-Mises Stress versus the angle of incidence, flexible POM NACA0015 hydrofoil, $U = 5\,\text{m/s}$

incidence as shown by [28]. It was observed that triggering the boundary layer by roughening the leading edge suppress this peculiar behaviour.

2.1.3 Vibration Measurements

The vibration measurements were performed using two Polytec laser vibrometers. The first one is a one-point measurement laser and is taken as a reference measurement point whereas the second one is a PSV-400 scanning vibrometer that allows to scan the surface structure on a predefined grid. The technology is based on the Doppler effect, sensing the frequency shift of back-scattered light from a moving surface. It is equipped with a HeNe laser ($\lambda = 633\,\text{nm}$) and two analog velocity decoders VD-04 and VD-06. It can measure velocity up to 10 m/s. The scanner is a high precision scan unit, with an angular resolution lower than 0.002°. Because of laser light diffusion in the POM material, reflecting tapes were glued over the foil surface to enhance the signal to noise ratio. The spatial resolution of the reflected laser beam was less than 1 mm, which is very small compared to the hydrofoil size. The scanning laser allows us to measure the vibration level on a user-defined grid over the structure surface. The cross-spectrum between the one-point reference laser and a scanned point is computed to preserve the phase at a given frequency. This allowed us to get by interpolation the vibration shape of the structure at a given frequency. This was particularly useful to identify the modal shape associated to a modal frequency as for the bending and twisting modes. However, it can be pointed out that according to the grid size, the time sample and the number of spectrum average on each point of the grid, a scan can take some hours to be completed.

The natural response of the foil and the damping were first measured in air and in still water. It was obtained by FFT analysis obtained from series of shocks using an electrodynamic shaker. The damping was estimated by the $-3\,\text{dB}$ bandwidth. It must be pointed out that this analysis was performed as the foil was mounted on its own mechanical support in the tunnel to take into account of the real structural boundary conditions in the tunnel. Then the vibration analysis could be performed under various flow conditions. The frequency resolution of the measurements was $\Delta f = 0.625\,\text{Hz}$. The repeatability of the experiment was tested and the accuracy

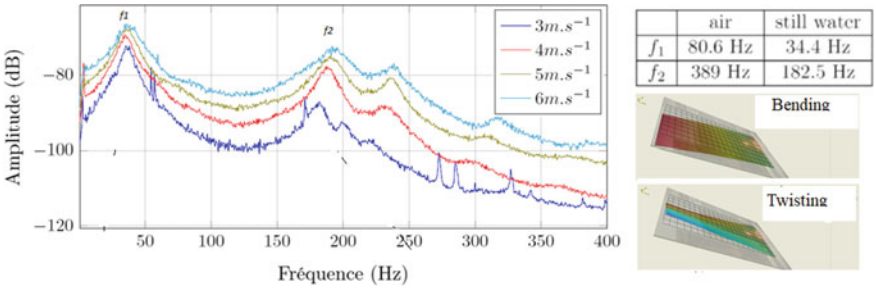

Fig. 6 Vibration spectra (FFT), mode shapes and natural frequency. POM hydrofoil, $\alpha = 8°$, U = 3 to 6 m/s at atmospheric pressure (non-cavitating flow)

was then lower than 2%. The vibration were measured in air then in still water. The values of the benfing and twisting mode frequencies were determined for the flexible hydrofoil and are reported on Fig. 6. As shown the frequencies decrease strongly in water due to the added-mass effect. The bending and twisting modal shapes obtained from scanning the surface are given respectively on Fig. 6 too. It can be pointed out that no significant effect were observed on the modal shapes in water compared to the experiments in air. Moreover it was observed that the modal shapes compare very favourably to the modes of the clamped-free beam theory indicating that the cantilevered hydrofoil has a quasi-beam-like behaviour for the two first modes of vibration at least.

Vibration measurements were then carried out for various velocities and various angles of incidence at a constant pressure close to the atmospheric pressure on the flexible hydrofoil. They were performed for angles of incidence from 0° to 8° with a step $\Delta\alpha = 2°$, the flow velocity was 3, 4, 5 and 6 m/s, corresponding to Reynolds numbers based on the chord length ranging from 3.10^5 to 6.10^5. The vibration spectra for $\alpha = 8°$ are given on Fig. 6.

It is observed on Fig. 6 that (1) the bending frequency does not change with the flow velocity whereas (2) the twisting and third mode frequencies tend to increase. This is also true for higher modes appearing progressively as the flow velocity increases. It can be mentioned that for small incidences (0 to 4°) and low flow velocity (3 m/s), a pure peak was clearly observed close to the twisting mode's frequency. It was observed that the peak could lead to a strong fluid structure interaction when it coincided with the twisting mode frequency. It was observed that this peak frequency increases as the velocity increases and disappears suddenly for a given velocity (beyond about 3 m/s or $R_e = 3.10^5$) or by increasing the angle of incidence (generally beyond 5°). It was also observed that the peak disappeared when the boundary layer was triggered by adding roughness bands at the leading edge. It is believed that the vibration peak can be related to a complex interaction between an unsteady Laminar Separation Bubble (LSB) inducing transition and vortex shedding at low angles of attack and moderate flow velocities as mentioned previously [23, 28, 29].

2.2 Flow Analysis

2.2.1 Hydrodynamics Force Measurements

The hydrodynamic forces were measured using an immersed specific balance delivering signals corresponding to the lift, the drag and the moment. Tests were carried out generally from −15° to 15° with a step of 0.5°. The experimental uncertainties of the balance obtained from calibrations was ±5 N for the lift, ±1.6 N for the drag and ±1 Nm for the moment. The weight of the hydrofoil and the buoyancy force were first removed by measuring the response balance in still water for each angle of incidence that will be selected. Then the tunnel velocity was set at a selected value and measurements were performed for various angles of incidence during ten seconds at a sample frequency 1000 Hz. The signals were converted in forces by means of a calibration matrix in the coordinate frame of the balance rotating with the hydrofoil. Finally, the values are projected in the test section coordinate frame to obtain the hydrodynamic coefficients C_l, C_d and C_m. Measurements were performed in non cavitating flow. The measurements in cavitating flow are not possible (excepted at the early stage of development) because of the decrease of the static pressure in the test section to promote the cavitation that can cause the detachment of the strain gauges that are glued at atmospheric pressure on the sensitive part of the balance.

2.2.2 Wall-Pressure Measurements

Pressure measurements were carried out using piezoresistive transducers Keller AG 2 MI PAA100-075-010 of 10 bars maximum pressure to support strong unsteady cavitating. The wall-pressure set-up is given on Fig. 7. As shown, an array of ten transducers was aligned along the chord on the suction side from x/c = 0.05 up to the trailing x/c = 0.90 with a step of 0.10 from x/c = 0.10. Two sets of three transducers were arranged parallel to this line in order to analyse three-dimensional effects. One transducer was also mounted on the suction side. The pressure transducers were mounted into small cavities with a 0.5 mm diameter pinhole at the foil surface to increase spatial resolution and to avoid any flow perturbations as shown on Fig. 7b.

The Helmoltz natural frequency of the cavity is 85 kHz in water. Before mounting the hydrofoil in the test section, the transducer cavities were filled with water using a syringe through the pinhole. An in-situ calibration was then performed to take transducer assembly into account. The transducers were calibrated simultaneously by decreasing the static pressure in the test section from 1.5 to 0.05 bars with a step of 0.05 bars at zero flow velocity. The transducers responses were found to be linear and the static coefficients of the linear regression were used to convert Volts in Pascals even for dynamics measurements. To control deviation during the experiments, the calibration procedure was performed systematically before and after each series of measurements particularly in cavitating flow. The instantaneous wall-pressure field provides many informations about the characteristics of the flow that

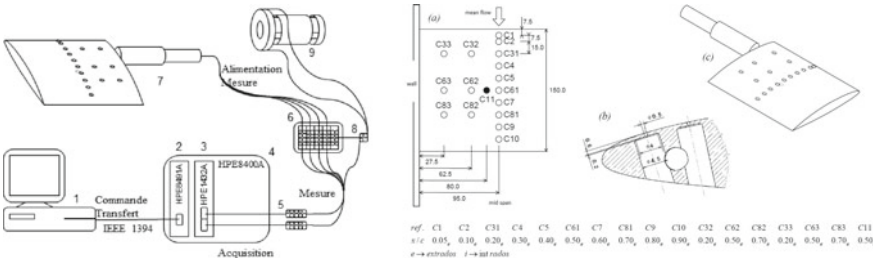

Fig. 7 Wall-pressure measurement set-up and transducer mounting

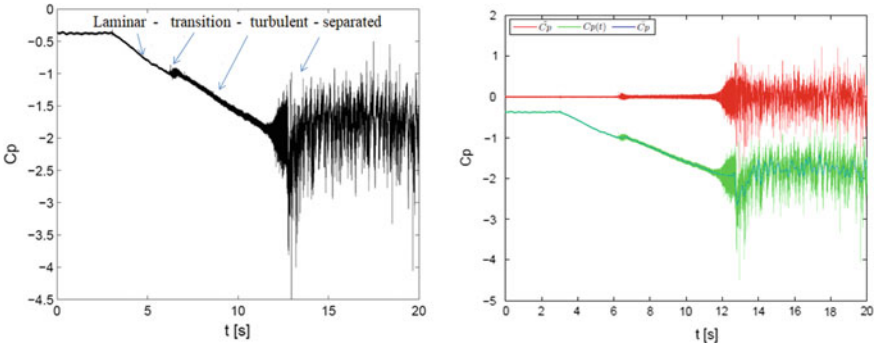

Fig. 8 Transient wall-pressure coefficient close to the leading edge of a quasi-static pitching hydrofoil and modal decomposition by Empirical Modal Decomposition method [30]

interacts with the adjacent structure. As an example, Fig. 8 shows a wall pressure time series measured close to the leading edge (x/c = 0.2) on the suction side of an hydrofoil experiencing a quasi-static pitching motion from 0° to 15° at a very low angular velocity (0.6 deg/s). It can be seen that the pressure decreases globally and exhibit various fluctuation features that are related to boundary layer regimes passing over the wall-pressure transducer. At a first stage, the pressure decreases with no significant fluctuations that can be related to a laminar boundary layer. Then sudden strong spots of wall-pressure fluctuations occur whereas the wall-pressure coefficient exhibits a plateau behaviour revealing boundary layer transition. Then the pressure coefficient decreases again with an increase of the pressure fluctuations due to turbulent boundary layer. Finally low frequency wall-pressure fluctuations occur as the results of boundary layer detachment and vortex shedding before stall. The multi-scale of wall-pressure fluctuations is clearly depicted on Fig. 8 showing the modal reconstruction for the low and high frequency modes obtained from the Empirical Modal Decomposition method. This clearly shows that a structure can be submitted to a large variety of multi-scale flow loadings with different spectral contents in both time and space depending on the boundary layer regimes.

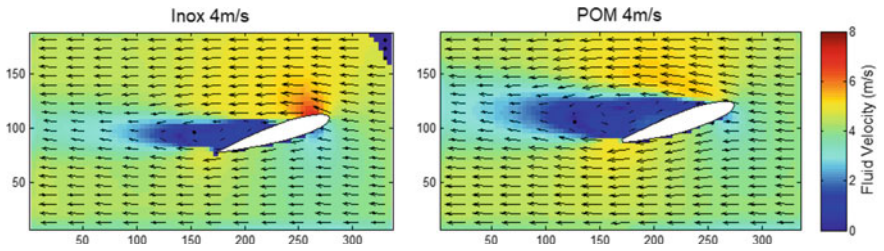

Fig. 9 Mean PIV velocity fields, for rigid stainless steel and flexible POM hydrofoils $\alpha = 17°$, $U = 4\,m/s$

2.2.3 TR-PIV Measurements

2D Time Resolved -Particle Image Velocimetry (PIV) technology was used for the measurement and the space-time characterization of the flow around the structures and in the wake. The PIV measurement plane is located at mid-span generally (see on Fig. 2). The PIV device consists of two pulsed YAG laser used to lighten the flow, a high precision CCD camera with a high resolution and a maximum sampling frequency equal to 3KHz. The Proper Orthogonal Decomposition was used on he PIV measurements [31]. This allows us to perform statistical analysis and to analyse accurately the vortex shedding in the wake. This was done for various angles of incidence and various flow velocities for the flexible and rigid hydrofoils. Figure 9 shows the mean flow field for 4m/s. As shown, the flexibility promotes the flow detachment passing from the mid-chord on the rigid hydrofoil to the vicinity of the leading edge. It is observed that the boundary layer detachment results into a periodical vortex shedding in the wake.

Figures 10 and 11 show the results of the POD decomposition of the velocity field an a reconstruction of the flow dynamics based on the two main modes. The two first modes show clearly the coherent vortex shedding structure. Its dynamics can be analysed through the time series of the mode coefficients. It can be observed that the vortex shedding amplitude is strongly reinforced on the flexible structure compared to the steel hydrofoil enlightening the Fluid Structure Interaction. Spectral analysis of the mode coefficients allows us to get the frequency contents and particularity the vortex shedding frequency f_0. This allows us to clearly identify this frequency in the structural vibration spectral response (Fig. 12). It is observed that f_0 increases as the velocity increases corresponding to a Strouhal number—based on the flow velocity and the front projection of the chord length (ie: c sin(α))—very close to 0.2. In the same time it is observed that the modal bending frequency f_1 decreases as the velocity increases (Fig. 12). This is particularly true beyond 4 m/s. The frequencies versus the flow velocity are reported on the right part of (Fig. 12). As shown by assuming a linear evolution of both frequencies versus the flow velocity, a coincidence velocity can be extrapolated. This velocity corresponds to the condition for which the vortex shedding frequency is equal to the bending frequency. It was found to be $U = 13.7\,m/s$ for $f_0 = f_1 = 97\,Hz$. It can be pointed out that the coincidence velocity is much lower

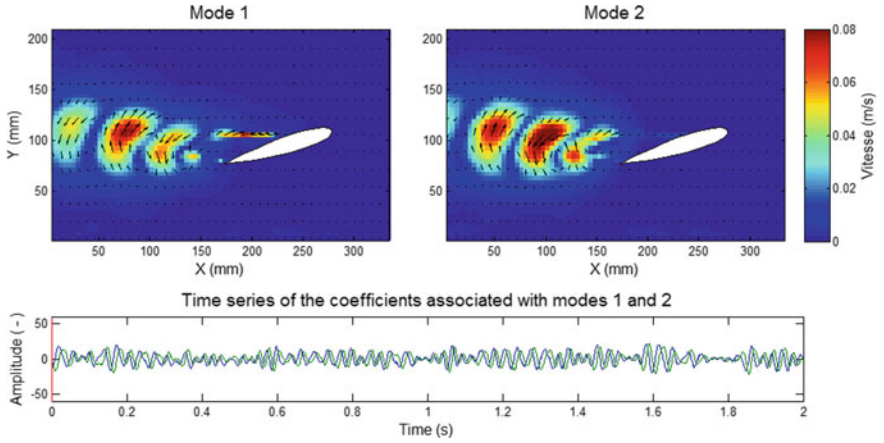

Fig. 10 POD analysis, Inox hydrofoil, $\alpha = 17°$, U = 4 m/s

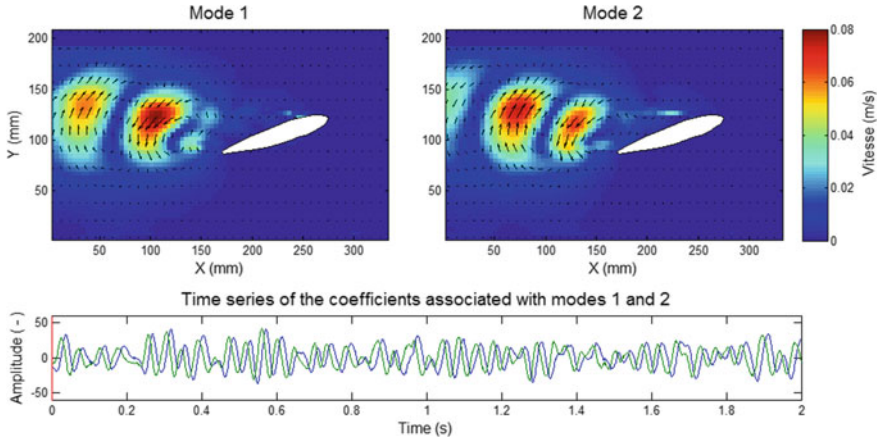

Fig. 11 POD analysis, POM hydrofoil, $\alpha = 17°$, U = 4 m/s

from the one that would have been extrapolated assuming a constant (or not coupled) bending frequency versus the flow velocity. This result can be of primary importance for hydrofoil designs.

2.2.4 Cavity Dynamics Measurements

The cavitation number is defined by

$$\sigma = \frac{(P_0 - P_v)}{0.5\rho U^2} \tag{4}$$

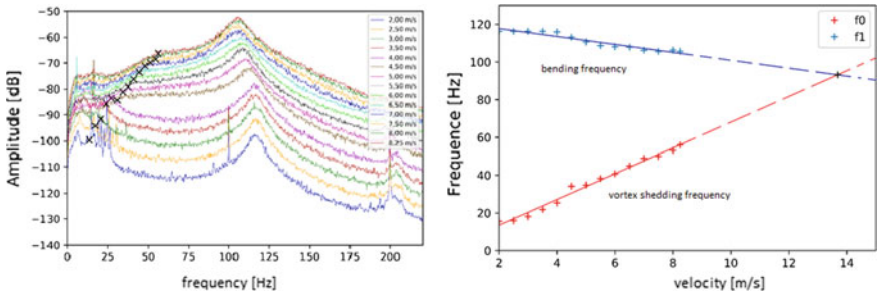

Fig. 12 Left: Velocity vibration spectrum (dB ref 1 m/s) versus flow velocity, the cross symbols are the shedding vortex frequency and the main peak is the bending frequency. Right: vortex shedding frequency and bending frequency versus the flow velocity, dashed line is a not explored zone due to cavitation inception. Stainless steel, $U = 2$ m/s to 8.25 m/s, $\alpha = 17°$

where P_0 is the prescribed pressure at the middle of the test section, P_v the vapor pressure at the water temperature, U is the flow velocity and ρ is the water density. The cavitation was then controlled by decreasing the pressure P_0 at a fixed flow velocity. It can be pointed out that the static pressure variation can have an influence on the structural response particularly for compliant structures and that it is important to record the static pressure at which the experiments are performed. The cavitation appeared as a vapour cavity attached to the leading edge and extending over the suction side as shown on the left of Fig. 13. A high speed camera was fixed over the test section for vapour cavity analysis on the suction side.

The model used is a Fastcam SA3 120 K from Photron. It is equipped with a CMOS image sensor, which sensor size is 17.4 mm * 17.4 mm. The frame rate is spread from 60 to 2000 fps for the full sensor resolution (1024 * 1024 pixels), when the pixel size is 17 μm. A specific image processing program was developed to study the cavity dynamics as depicted on Fig. 13. The method is based on extracting a band of an image at mid-span and to analyse the time evolution of the spatial average of the grey level intensity in the band. This allows us to extract a signal directly related to the cavity length dynamics and to measure particularly the spectral content. It was very reliable to measure the oscillating frequency of the oscillating vapour cavity.

2.3 Uncertainties on Flow Conditions

Because of the numerous technics developed for FSI analysis there are a lot of sources of uncertainties in the experiment presented herein. Even if it can be appear obvious we have to pointed out that the main characteristics that are need to be primary measured with accuracy is the inflow velocity as well as the angle of incidence. The flow rate was obtained using two high-precision Paroscientific Series 1000 transmitters to measure the static pressure difference between the test section and a upstream larger

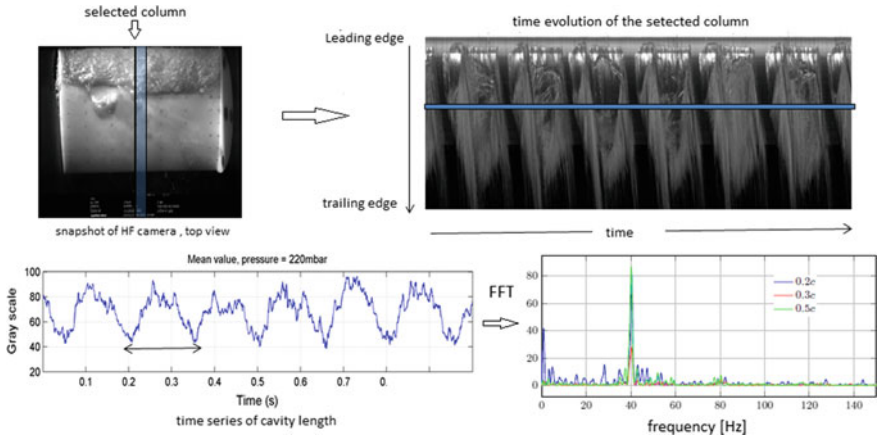

Fig. 13 Set-up of cavity image processing from image acquisition up to FFT analysis

section. The static pressure differences were then related to the flow rate by using the classical Bernoulli formulation for pipe flows. The transmitters have an accuracy of 0.01% for up to 40 psi (2.75 bars). The mean inflow velocity was measured also for comparison using the PIV system or using a 2D Laser Doppler Velocimetry (LDV) at the inlet of the test section. The latter technics allow us to measure the velocity field upstream of the hydrofoil or the studied structure. The uncertainty of the flow velocity is then found to be ± 0.02 m/s. The incidence of the foil in the tunnel is controlled by a Baldor drive system that allows us to control with high accuracy the angle step $\Delta\alpha$, the acceleration and the rotational speed. Considering the mechanical mounting system and several trials, the uncertainties of the angle of attack was found to be lower than $0.1°$. The zero angle of incidence is set using a specific gauge as well as the horizontal free surface in the test section during the tunnel filling. It can be pointed out that several controls of the incidence were performed during the experiments particularity at the beginning and the end of the experiments. This was done by taking lateral pictures that can be compared during the experiments. Moreover, the hydrodynamic force measurements as strain gauge measurements when available are also very good and complementary means to measure the hydrodynamic zero angle that can be taken as a reference value.

For cavitating flow, the measurements are performed at a given angle of incidence and flow velocity and the pressure is regulated at a given prescribed values. Taking into account of the monitoring system of the tunnel regulation, it was established that the cavitation number uncertainties is about ± 0.02.

It must be pointed out that the uncertainties on flow conditions increase when the cavitation unsteadiness increase in the test section.

3 Selected Results

The following part presents some selected results of experiments performed in the hydrodynamic tunnel for FIV analysis in various flow conditions and particularly for cavitating flow.

3.1 Wall-Pressure in Cavitating Flow

Figure 14 shows the mean pressure coefficient distribution in cavitating flow and the root mean square value of the fluctuations together with the spectral analysis. It is shown that the mean pressure coefficient is rather constant beneath the cavity and very close to the opposite of the cavitation number meaning that the pressure in the cavity is close to the vapour pressure. At the cavity closure, the pressure coefficient experiences an adverse pressure gradient, and recovers the non-cavitating value downstream. The vertical bars on Fig. 14 represent the wall-pressure fluctuation intensity. It is observed that the compression is accompanied by a local increase of the intensity of pressure fluctuations. The relative intensity of pressure fluctuations is more clearly depicted on Fig. 14 for various cavity lengths. As shown, a pressure peak is located at the cavity closure. The peak level increases within 10–19% of the dynamic pressure as the cavitation number decreases (i.e. the cavity increases). Within the cavity ($x/c < l/c$), the intensity of the pressure fluctuations is fairly constant and lower than the non-cavitating flow. A net increase in the pressure fluctuations is recorded in the cavity wake. The spectral analysis shown also on Fig. 14 reveals that the increase of the pressure fluctuations intensity at the cavity closure is associated with a low frequency 19 Hz in the present case. As shown, this frequency still exists at $x/c = 0.5$ but it spreads at $x/c = 0.6$ in the cavity wake and is no longer detected at $x/c = 0.7$. On the other hand, a secondary frequency 40 Hz about twice the dominant frequency is detected in the cavity wake. The main frequency in the closure region was also observed for others cavity lengths. The peak frequency decreased as the cavity length increased. It 23 Hz for $l/c = 0.3$ 14 Hz for $l/c = 0.5$. It was shown that the cavity frequency exhibits a Strouhal number law close to 0.2 taking the maximum cavity length and the free stream velocity as scaling parameters. When l/c was closed to 0.5, the cavity frequency drops down suddenly at a lowe frequency about 5 Hz in the present case together with the higher frequency of 40 Hz. At this stage a slight decrease in the cavitation number leads to an unstable cavity characterized by a cavity inception/growth/destabilization cycle. The frequency of the cycle was much smaller than the previous ones and increased linearly with the velocity leading to a Strouhal number $fc/U = 0.11$.

The spatial-time evolution of the wall-pressure during the cavity growth/destabilization is complex and more clearly depicted on Fig. 15 showing the instantaneous wall pressure fluctuations carried out from the array of the wall pressure transducers. The figure depicts the instantaneous pressure signals during two cycles

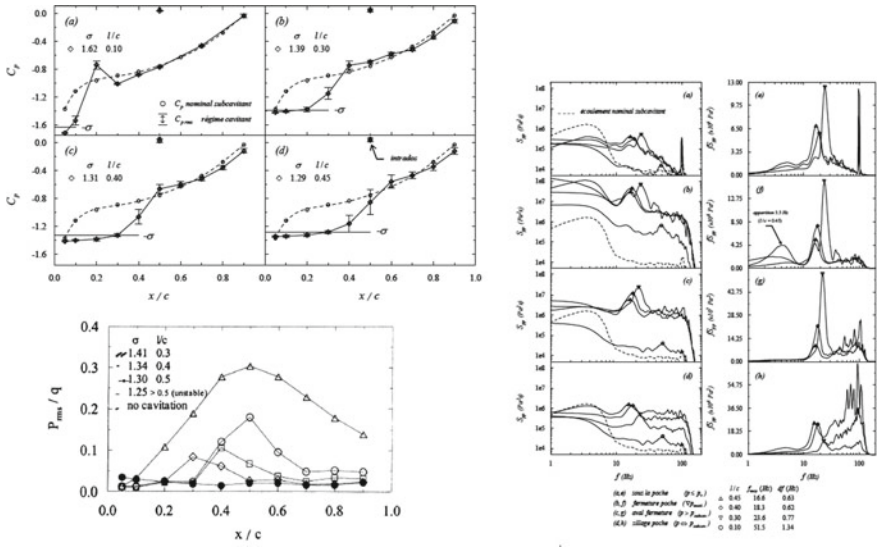

Fig. 14 Mean wall-pressure coefficient in cavitating flow, (open symbols are for the non cavitating flow), RMS wall pressure fluctuations and spectral analysis [12]

of cavity growth/destabilization on the suction side together with the pressure on the pressure (last signal, C11). It allows us to follow step by the step the wall-pressure field. As shown, on the suction side the transducers (between x/c = 0.1 and x/c = 0.7 − 0.8) pass alternately from the vapour pressure to the non cavitating flow pressure. Between [0.13 s, 0.17 s] (resp. [0.41 s, 0.46 s]) the pressure increases over the whole suction side (see dashed vertical lines on Fig. 15 for C31 to C81): the cavity is destabilized and disappears. For [0.17 s, 0.41 s] (resp. [0.46 s, 0.64 s]) the cavity length increases. As the cavity grows, the transducers experience, one after the other, an increase of the pressure fluctuations before falling to the vapour pressure (see arrows for C4, C5, C61 and C7): this corresponds to the cavity closure passing over the transducers. It is observed that when the cavity length is half the foil chord, the decrease in pressure to the vapour pressure is slowed down and more fluctuating (see C61). At that time, pressure fluctuations are convected in the cavity wake. This corresponds to the shedding of a vapour cloud. Inohers words it means that when the cavity length is half of the foil chord, the cavity growth is slowed down and counterbalances by a vapour cloud shedding. The frequency of the cloud shedding was estimated at 40 Hz and the convection velocity was 3.2 m/s about half the velocity at x/c = 0.8. As the cavity length increased more (l/c > 0.5), the intensity of the pressure fluctuations associated to cloud shedding increased. When the cavity length was maximum (l/c = 0.7 – 0.8), a major pressure perturbation was observed at approximately the middle of the cavity and destabilized the cavity. It can be pointed out that, as far as this experiment is concerned, the pressure transducers did not detected a clear sign of a re-entrant jet prior to the cloud shedding and the cavity destabilization.

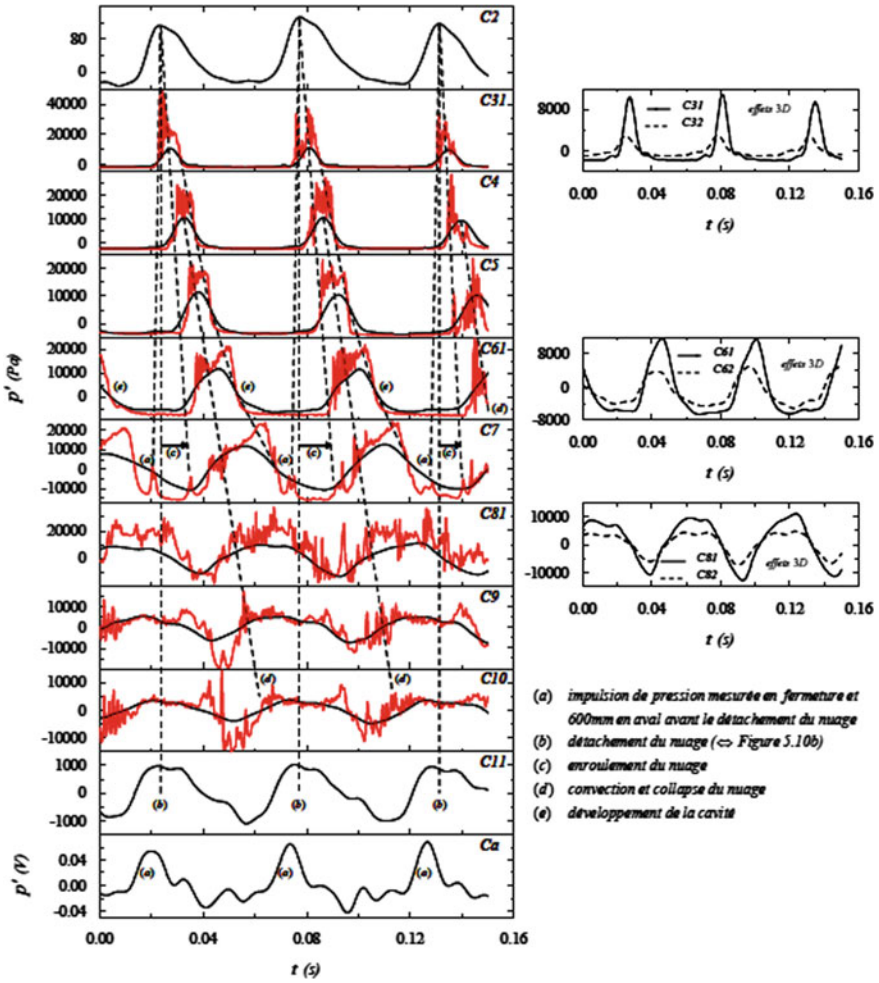

Fig. 15 Instantaneous wall-pressure during cavity growing and collapsing, [12]

Finally, it is interesting to observe the pressure measured on the pressure side during cavity destabilization (see Fig. 15, C11). It is shown that the decreases just before cavity destabilization. This can be considered to be equivalent to a decrease of the angle of incidence that can induce a recompression on the suction side. It was shown numerically that the stagnation point moved significantly towards the leading edge as the cavitation develops comparable to a virtual change of the angle of incidence.

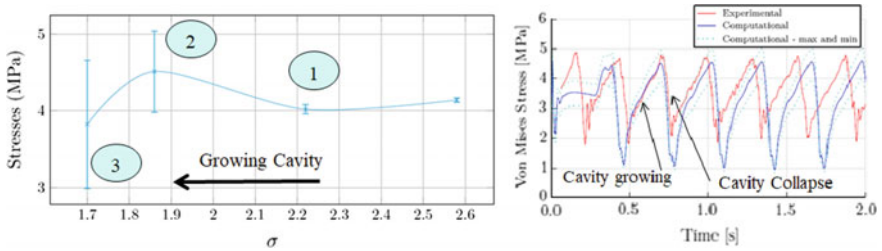

Fig. 16 Left: Mean values of Von Mises stress versus cavitation number, vertical bars are the RMS value. Right: experimental instantaneous time series of the Von Mises stress during cavity instability. Comparison with a CFD/CSD computation [14]

3.2 Structural Stress

The average value of the Von Mises stress as function of the cavitation number is shown on the left part of Fig. 16. The vertical bars stand for the root mean square values. It is observed (1) that the Von-Mises stress starts to increase slowly as σ decreases. It reaches a maximum value (2) and decreases sharply (3) as the cavitation number decreases again. It can be observed that the fluctuation intensity (vertical bars) increase strongly at the same time.

This originates from the periodic growth and collapse of the vapour cavity clearly depicted on the right part of Fig. 16 showing about six oscillations of a sawtooth signal resulting of the very short time scale of the cavity collapse compared to the cavity growing time scale. It was shown that the lift coefficient response shows exactly the same trend [12]. The close relationship between the structural stress and the lift force points out that a simple and cheap strain gauge embedded in a structure could a powerful mean to get instantaneous information about hydrodynamics forces acting on the structure. This could be very useful for control in real situations.

3.3 Flow Induced Vibration

3.3.1 Cavitation Induced Vibration

Experiments were performed by decreasing progressively the cavitation number. The structural response was performed through laser vibrometry and cavity dynamics through high speed video at 2000 frames per second. For a high degree of cavitation development a strong increase of the vibration level is observed all over the frequency range as shown on Fig. 17 for the flexible hydrofoil. In that case, a strong coupling between the cavity mode frequency and the bending mode frequency is observed. This can be considered as a pumping effect on the bending mode coming from the cavity oscillation. The evolution of the cavity frequency f_c and the bending frequency

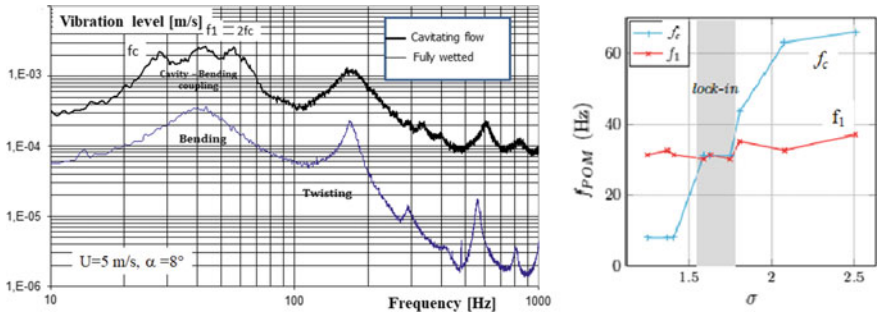

Fig. 17 Flexible hydrofoil vibration spectra (FFT) in highly unsteady cavitating flow compared to the fully wetted flow, POM NACA66, 150 mm chord length $\alpha = 8°$, U = 5 m/s, f_c and f_1 are the cavity frequency oscillation and the bending frequency respectively

f_1 is clearly depicted on the right part of the Fig. 17. As shown the cavity frequency decreases clearly as the cavitation number decreases (i.e. the cavity increases). A close examination indicated that the bending mode's frequency tended to decrease slightly as the cavitation increases as the consequence probably of an increase of added damping in a highly cavitating flow. As shown, a lock-in appears in a narrow band of the cavitation number correspond=ding to a high level of fluid structure coupling.

Vibration spectra (up 100 Hz) and the corresponding cavity snapshots are shown for various cavitation number on Fig. 18 for the flexible hydrofoil. It is observed that at cavitation inception ($\sigma = 2.42$), intermittent cavitating spots appear on the foil with no significant effect on the vibration level. As the pressure decrease ($\sigma = 2.08$), a sheet cavitation was clearly attached at the leading edge and oscillated periodically between about 30 and 40% of the chord length. This lead to an increase of the vibration level from the bending mode frequency f_1 up to the cavity frequency f_c close to 60 Hz As the cavitation number decreases again ($\sigma = 1.81$) the bending mode frequency disappears and the vibration is mainly driven by the cavity oscillation (at about $f_c = 35$ Hz) and the first harmonic. By decreasing again the cavitation number ($\sigma = 1.63$) the cavity frequency merges with the bending frequency and a strong coupling is observed for a narrow range of cavitation number (lock-in) resulting in a very high level peak of vibration at the bending frequency. As the cavitation number decreases again (lower than $\sigma = 1.41$), the cavity frequency decreases suddenly at a very low frequency (8 Hz). In that case the vapour cavity oscillates from fully wetted condition to 100% of the chord length. It can be observed strong harmonics and the fourth is strongly coupled with the bending mode.

3.3.2 Vortex Shedding Induced Vibration

Finally we would like to mention original results of a recent work focusing on the experimental characterization of the vortex shedding and on the induced vibrations

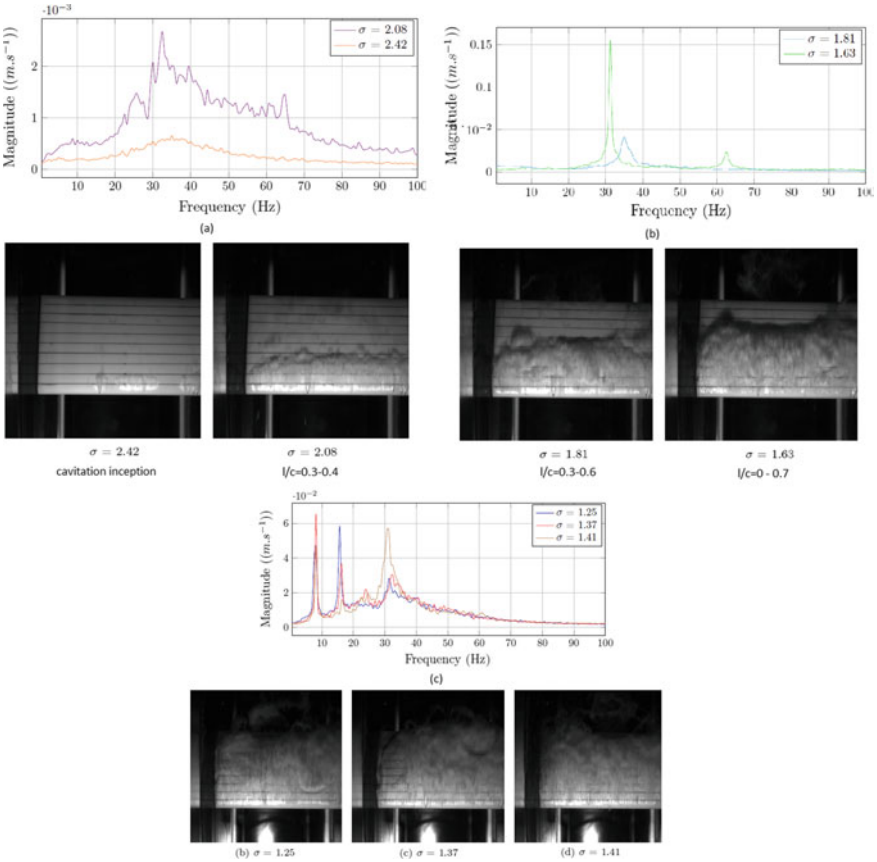

Fig. 18 Vibration spectra in cavitating flow and corresponding cavity snapshots, $\alpha = 8°$, U = 6 m/s

of an elongated cantilevered blunt rectangular aluminium plate of 100 mm length and 6 mm thickness immersed in a uniform flow in the hydrodynamic tunnel of the Naval Academy. The topic is related to the understanding and the control of the trailing edge sound emission of marine propellers. Experiences were conducted by varying very progressively the Reynolds numbers Re (based on chord length) from about one hundred thousand to one million at a zero degree of incidence. Special attention was paid to the interaction of the structural response and the flow dynamics at the twisting mode frequency close 200 Hz. For this purpose, wake structures have been analysed by Time Resolved Particle Image Velocimetry (TR-PIV) and the structural response of the plate has been examined by Laser Doppler Vibrometry. The Von Karman vortex street was characterized by Proper Orthogonal Decomposition of PIV velocity fields (Fig. 19). This allows to obtain the pseudo-spectrogram depicted on Fig. 20 showing the evolution of the vibration response versus the Reynolds number. It is

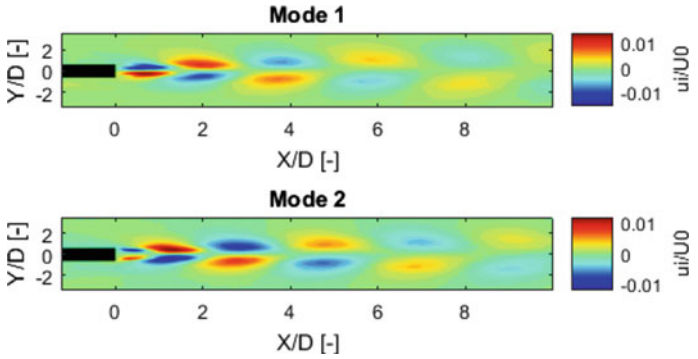

Fig. 19 Proper orthogonal decomposition of the longitudinal fluid velocity fluctuations u'. Downstream a blunt rectangular flat plate Re = 300.000

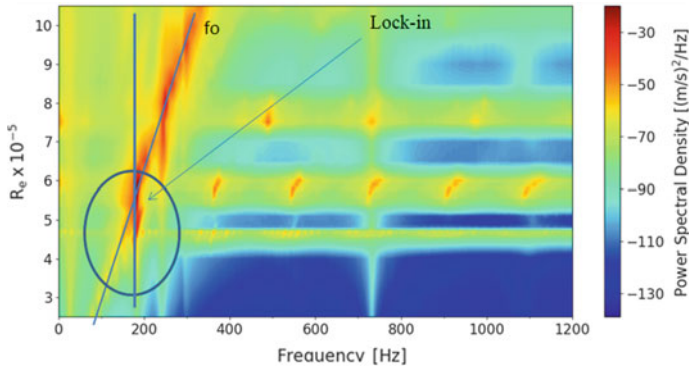

Fig. 20 Vibration power spectral density of a blunt rectangular flat plate versus Reynolds number

clearly observed a mechanical resonance characterized by high amplitude structural velocities and high amplitude harmonics resulting of a lock-in between the vortex shedding and the twisting mode for a narrow band of Reynolds number ranging between 510.000 and 600.000. This results in a high level of vibration together with the strengthening of the vortex shedding and noise radiation. The understanding then the control of such mechanisms is of primary importance for naval and civilian applications.

4 Discussion

Several observations and recommendations can be pointed out from the experimental procedure presented herein to analyse Fluid Structure Interaction on cantilevered lifting structures in a hydrodynamic tunnel through multiple sensor analysis. The

procedure is based on a step by step analysis. The structure response to external calibrated impacts has to be analysed in air with strictly the same mounting device than for the operating conditions in the tunnel. It was shown recently that the use of piezoelectric patches embedded in the structure can be a very reliable mean to excite the structure and to get the transfer function. The scanning laser vibrometry allows us to clearly identified the natural frequencies together with the associated modal shapes. This is particularly reliable to identify the first bending and the twisting modes and higher modes in some cases. In the case of cantilevered hydrofoils it is shown that the bending and twisting modes are fairly similar to the theoretical bending and twisting modes of a clamped-free beam with an equivalent cross-section quadratic moment. This can be very reliable for theoretical and numerical development on cantilevered structures It must be pointed out that a major attention must be paid to the quality of the experimental structural boundary conditions particularly for theoretical or numerical comparison purpose. A quantification of the modal damping based on the -3dB bandwidth or the logarithmic decrement (not shown in the present paper) can be also performed. Then the tunnel section can be filled out and the structural response is analysed in still water through laser vibrometry. The added-mass effect due to the water density can be then clearly quantified by the large decrease of the modal frequencies. Due to homogenous water loading in calm water the modal shapes are not changed compared to air. Due to modal added-mass it is observed that modal shifting or crossing can appear in water compared to air. The effect of water on the modal added-damping can be measured in the same way as in air. Then the structural analysis can be performed for different flow conditions or angle of incidences. In that case the structural response can be also analysed through a strain gauge rosette response located at the hydrofoil root providing a more precise evaluation of strain close to the surface. This allows us to measure the principal planar strains and the principal stresses as well as the local Von-Mises stress. Because the Von-Mises stress contains intrinsically the structure response and the flow loading it is found to be a very reliable characteristic for comparison and validation of CFD/CSD computation. It can be pointed out that this needs a reliable evaluation of the material characteristics (as the tensile strength modulus). This is performed through tip bending measurements under calibrated loadings. It can be pointed out that the stain gauge rosette is also a reliable mean to accurately determine the zero lift angle of incidence. Indeed the strains pass through zero for the lift passing from positive to negative value. Moreover, because of the relative high sensitivity the strain gauges was found to be a reliable mean for dynamic structural analysis. It was also interesting to observe that the strain gauges response are linear versus the lift forces measured by a hydrodynamic balance. This shows that a simple strain gauge rosette correctly embedded in the structure can be a cheap and reliable mean to get information about the fluid loading as well as on the structure dynamics. This can be particularly interesting for fluid structure control. The wall-pressure field analysis through an array of transducers specifically mounted with care in small cavities is a powerful mean for local flow analysis. It highlights complex features with various time-spatial scales depending on the boundary layer regime or the cavitating flow characteristics. Concerning flow characteristics data-driven decompositions of

Particle Image Velocimetry measurements are widely used for a variety of purposes as the characterisation of coherent features (e.g., vortical structures), filtering operations (e.g., outlier removal or random noise mitigation), data reduction and compression. In the present program the temporal and time-mean characteristics of the flow are investigated using Time-Resolved Particle Image Velocimetry (TR-PIV) system and the analysis technique of Proper Orthogonal Decomposition particularly for vortex shedding analysis. This bring new information on FIV when they are coupled with the modal analysis of the structure.

Several observations can be reported from these experiments. From the vibration analysis in fully wetted flow it is observed that the bending mode's frequency remains rather constant as the flow velocity increases for moderate angle of incidence (lower than 8 degrees) whereas the twisting mode frequency (as well as the third mode and higher modes) tends to increase resulting from the flow coupling. A peculiar vibration phenomenon was observed at very low angles of incidences and low velocity inducing a peak at a given frequency close to the twisting frequency. This is believed to be related to the organized wake vortex shedding and a Laminar Separation Bubble inducing transition observed on the rear part of the lifting structure by laser velocimetry and wall-pressure measurements. It can be pointed out that the pure tone disappeared as the leading edge was roughened. In cavitating flow, several observations can be also reported. The wall-pressure fluctuations revealed the complexity of the flow particularly when a strong unsteady cavity develops (typically larger than about 0.3 chord length). Concerning the structural response the strains and stresses as well as the Von-Mises Stress tend to increase slightly in the early stage of cavitation towards a maximum. At this stage as the cavity increases again the averaged strains and stresses decrease sharply with a strong increase of fluctuations. This is related to the periodical growth and collapse of the cavity with vapour cloud shedding at a given frequency.

Vibration measurements reveals that the cavity frequency is clearly detectable on the vibration spectrum. On the compliant hydrofoil for instance, it is observed that the cavity frequency progressively decreases as the cavity length increases until it merges with the bending frequency. Then a frequency lock-in occurs between the cavity oscillation mode and the bending mode for a narrow range of cavitation number. The scanning laser vibrometry reveals a relative complex coupled mode of vibration resulting of the bending mode and the cavity oscillation mode. By lowering the cavitation number again, the cavity frequency decreases suddenly to a very low value (a few Hertz) and a coupling occurs between harmonics of the cavity frequency and the bending frequency. On the rigid (stainless steel) hydrofoil the cavity oscillation frequency is clearly observed too in the vibration response. However it is well separate from the bending frequency. As a matter of fact, conversely to the flexible case, the bending frequency tend to increase progressively as the vapour cavity length increases probably as the result of added-mass decreasing in cavitating flow. In that case the two frequencies tend to separate and no frequency lock-in is observed. It was also observed that the twisting mode's frequency tends to increase as the cavity length increases that can be related to a decrease of the added mass in cavitating flow.

Flow induced vibration measurements were also performed for a large angle of incidence (e.g., 17°) inducing boundary layer separation and vortex shedding on the suction side. The vibration measurements were performed at various velocities together with Time Resolved-PIV measurements. The Proper Order Decomposition allows us to detect the vortex shedding frequency mode very accurately. The vortex shedding frequency is clearly observed in the structural response. It is found to increase with the flow velocity and corresponds to a Strouhal number very close to 0.2. It is observed that the bending frequency tends to decreases towards the shedding frequency as the velocity increases. It induces a coincidence flow velocity for which the shedding frequency is equal to the bending frequency that is much lower than the one predicted from a constant bending frequency. This is also true for higher vibration modes. Finally it is observed that the vortex shedding intensity is strongly reinforced on the compliant hydrofoil by the bending mode enlightening a strong Fluid Structure Interaction phenomenon.

It is believed that the experimental program for FIV analyses presented here have brought new information and quantitative reliable data related to hydro-elasticity applications. Many questions are still open mainly for FIV in cavitating flow but the collected data can be very useful for validation of complex CSD/CFD computation. It is showed clearly that in many cases strong coupled CSD/CFD simulations are necessary to take into account of the FSI phenomenon observed during the experiments particularly when strong unsteady features occur in the flow. Finally from a technological point of view, it can be pointed out also that using means for FIV survey—as for instance strain gauges, optical fibres or piezo-electric patches embedded in the structure coupled to an expert system—could a very interesting way to get real-time information about hydrodynamics loadings in real conditions to support control systems for smart naval structure applications.

Acknowledgements The support of French naval academy is gratefully acknowledged. The constant support of the technical staff of the Naval Academy is warmly appreciated. Special thanks to Ing. Alain Boulch and Ing. Pierre Guiffand for several technical developments and assistance. The assistance of associate professor Patrick Bot for PIV measurements and discussions is warmly appreciated. Dr. Antoine Ducoin, Dr. Alexandra Lelong, Dr. Fabien Gaugain, Dr. Pierre-Luc Delafin and PhD student Yann Wattine are also gratefully acknowledged for their nice works during their Ph.D. preparation at the Naval Academy.

References

1. Y.L. Young, S. Brizzolara, Numerical and physical investigation on a surface-piercing hydrofoil (2013)
2. Y.L. Young, M.R. Motley, R. Barber, E.J. Chae, N. Garg, Adaptive composite marine propulsors and turbines: progress and challenges. Appl. Mech. Rev. **68**(6), 10 (2016)
3. F. Mohamed-Arab, B. Augier, F. Deniset, P. Casari, J.A. Astolfi, Morphing hydrofoil model driven by compliant composite structure and internal pressure. J. Mar. Sci. Eng. **7**(12), 423 (2019). https://doi.org/10.3390/jmse7120423

4. D.T. Akcabay, E.J. Chae, Y.L. Young, A. Ducoin, J.A. Astolfi, Cavity induced vibration of flexible hydrofoils. J. Fluids Struct. **49**, 463–484 (2014)
5. G.A. Zarruk, P.A. Brandner, B.W. Pearce, A.W. Phillips, Experimental study of the steady fluid structure interaction of flexible hydrofoils. J. Fluids Struct. **51**, 326–343 (2014)
6. S.R. Hutchison, Numerical modelling of hydrofoil fluid structure interaction. Ph.D. thesis, Australian Maritime College (2012)
7. M. Benaouicha, J.A. Astolfi, A. Ducoin, S. Frikha, O. Coutier-Delgosha, A numerical study of cavitation induced vibration, in *ASME 2010 Pressure Vessels and Piping Division/K-PVP Conference*, July 2010, vol. 4 (2010), pp. 35–42
8. M. Benaouicha, J.-A. Astolfi, Analysis of added mass in cavitating flow. J. Fluids Struct. **31**, 30–48 (2012)
9. P. Ausoni, M. Farhat, X. Escaler, E. Egusquiza, F. Avellan, Cavitation influence on von Karman vortex shedding and induced hydrofoil vibrations. J. Fluids Eng. **129**, 966 (2007)
10. C.E. Brennen, *Cavitation and Bubble Dynamics* (Oxford University Press, 1995)
11. R.E.A. Arndt, Some remarks on hydrofoil cavitation. J. Hydrodyn. Ser. B **24**, 305–314 (2012)
12. J.-B. Leroux, O. Coutier-Delgosha, J.-A. Astolfi, A joint experimental and numerical study of mechanisms associated to instability of partial cavitation on two-dimensional hydrofoil. Phys. Fluids (1994-Present) **17**, 052101 (2005)
13. A. Ducoin, J.-A. Astolfi, F. Deniset, J.-F. Sigrist, An experimental and numerical study of the hydroelastic behavior of an hydrofoil in transient pitching motion, in *First International Symposium on Marine Propulsors* (2009)
14. F. Gaugain, Analyse experimentale et simulation numerique de l'interaction fluide-structure d'un hydrofoil elastique en ecoulement subcavitant et cavitant. PhD thesis, Ecole Navale, Ecole Nationale Superieure des Arts et Metiers (2013)
15. T. Sontvedt, Propeller blade stresses, application of finite element methods. Comput. Struct. **4**, 193–204 (1974)
16. H.J. Lin, J.J. Lin, T.J. Chuang, Strength evaluation of a composite marine propeller blade. J. Reinf. Plast. Compos. **24**, 1791–1807 (2005)
17. Y.L. Young, Hydroelastic beahavior of flexible composite propellers in wake inflow, in *16th International Conference of Composite Materials* (2007)
18. Y.L. Young, Fluid structure interaction analysis of flexible composite marine propellers. J. Fluids Struct. **24**, 799–818 (2008)
19. N.L. Mulcahy, B.G. Prusty, C.P. Gardiner, Flexible composite hydrofoils and propeller blades, in *International Maritime Conference 2010: Maritime Industry Challenges, Opportunities and Imperatives* (2010), pp. 438–448
20. M.R. Motley, Y.L. Young, Performance-based design and analysis of flexible composite propulsors. J. Fluids Struct. **27**, 1310–1325 (2011)
21. A. Ducoin, J.-A. Astolfi, F. Deniset, J.-F. Sigrist, Fluid structure interaction analysis on a transient pitching hydrofoil, in *ASME 2009 Pressure Vessels and Piping Conference*, vol. 4 (2009), pp. 665–671
22. M.C. Reese, Vibration and damping of hydrofoils in uniform flow. Ph.D. thesis, Pennsylvania State University (2010)
23. A. Ducoin, J.-A. Astolfi, J.-F. Sigrist, An experimental analysis of fluid structure interaction on a flexible hydrofoil in various flow regimes including cavitating flow. Eur. J. Mech. B. Fluids **36**, 63–74 (2012)
24. F. Gaugain, F. Deniset, J.A. Astolfi, J.-F. Sigrist, Numerical and experimental study of hydroelastic behaviour of a hydrofoil, in *10th International Conference on Flow-Induced Vibrations* (2012), pp. 67–74
25. D.T. Akcabay, Y.L. Young, Influence of cavitation on the hydroelastic stability of hydrofoils. J. Fluids Struct. **49**, 170–185 (2014)
26. M.-L. Gobert, Etude de l'interaction entre un ecoulement de couche limite instable et une structure d'formable. Application la prediction du bruit propre hydrodynamique d'une antenne Sonar. Ph.D. thesis, Ecole navale, Ecole Centrale de Nantes (2009)

27. A. Clement, Etude hydroacoustique de la reponse dâune structure a une excitation de couche limite turbulente. Ph.D. thesis, Ecole navale, Ecole Nationale Superieure des Arts et Metiers (2015)
28. P.L. Delafin, F. Deniset, J.A. Astolfi, Effect of the laminar separation bubble induced transition on the hydrodynamic performance of a hydrofoil. Eur. J. Mech. B. Fluids **46**, 190–200 (2014)
29. P.-L. Delafin, Analyse de l'ecoulement transitionnel sur un hydrofoil. Application aux hydroliennes a axe transverse avec controle actif de l'angle de calage. Ph.D. thesis, Ecole navale, Universite de Bretagne Occidentale (2014)
30. S. Benramdane, J.-C. Cexus, A.-O. Boudraa, J. Astolfi, Transient turbulent pressure signal processing using empirical mode decomposition, in *Physics in Signal and Image Processing (PSIP)*, 02 (2007)
31. J.M. Moubogha, U. Ehrenstein, J.-A. Astolfi, Forces on a pitching plate: an experimental and numerical study. Appl. Ocean Res. **69**, 27–37 (2017)

Wavenumber Characterization of Surface Pressure Fluctuations on the Fuselage During Cruise Flight

Stefan Haxter and Carsten Spehr

Abstract When trying to predict the acoustic experience in aircraft cabins during flight, it is of importance to characterize the possible excitation mechanisms. In the following, we will focus on the fuselage surface pressure fluctuations on the outside of the aircraft hull and to determine its characteristics. The primary focus of this chapter is set on measurement and data processing rather than a deep interpretation of the results found. Flight test measurements using a pressure transducer array installed in window banks at two longitudinal positions on the fuselage are examined. The main focus is set on distinguishing between acoustic and hydrodynamic pressure fluctuations by means of phase propagation velocity. Differentiation between propagation velocities is achieved per-frequency by means of a wavenumber representation of the surface pressure fluctuations: at constant frequency, different propagation velocities will result pressure fluctuations to appear at different locations in the domain. A wavenumber filter can then be easily applied to separate pressure fluctuations with different characteristics. Prior to filtering, a deconvolution scheme is applied to the wavenumber maps in order to attempt to remove the array pattern from the resulting images, thus increasing resolution. The analysis results in two separated frequency spectra for acoustic and hydrodynamic pressure.

1 Introduction

In subsonic flows, there are acoustic and hydrodynamic propagation mechanisms which differ in their velocity. Information about this characteristic is useful for surface excitation prediction as the response of a surface may be different with different types of excitation. In the past, several researchers have been concerned with determining these propagation characteristics. Tests were mostly performed in wind tunnels, but some studies were conducted in flight-test-like environments.

S. Haxter (✉) · C. Spehr
German Aerospace Center (DLR), 37073 Göttingen, Germany
e-mail: stefan.haxter@dlr.de

C. Spehr
e-mail: carsten.spehr@dlr.de

E. Ciappi et al. (eds.), *Flinovia—Flow Induced Noise and Vibration Issues and Aspects-III*, https://doi.org/10.1007/978-3-030-64807-7_8

1.1 Characterization in Wind Tunnel Environments

In 1962, Willmarth and Wooldridge [1] performed measurements in the wind tunnel using several longitudinal transducer spacings ranging from $\Delta x = 7.6$ mm up to $\Delta x = 390$ mm. The sensitive surface of the transducers had a diameter of 4.1 mm (0.163in) with the boundary layer having a thickness of 128 mm (0.42 ft) at a velocity of $u_\infty = 62\,\mathrm{m\,s^{-1}}$ (204 ft/s). In normal environments, this corresponds to Mach numbers of approximately $M < 0.2$. In their analysis, the authors performed a space-time correlation and are able to identify both, the speeds and the relative magnitude of hydrodynamic and acoustic pressure fluctuations. The data set provided by the authors was used by Corcos [2] to set up the microphone size correction.

Bull [3] performed measurements with the emphasis set on studying the detailed structure of the pressure field by means of characterizing the frequency- and wavenumber contents. Bull pointed out the importance of having a small transducer size relative to the boundary layer thickness which—if not accounted for—would result in signal attenuation of the desired surface pressure fluctuations. Measurements were conducted at $M = 0.3$ and $M = 0.5$ using small-size pressure transducers with a diameter of 0.74 mm (0.029 in.). In order to characterize the two-dimensional characteristic of the surface pressure field, correlation measurements were performed with various transducer separations aligned at various angles relative to the flow direction.

Blake and Chase [4] used a flush-mounted four-microphone array with the sign of the signals being switched alternately. With this arrangement and the attenuation of high wavenumber surface pressure fluctuations by means of averaging over the sensitive surface, they were able to selectively filter out low-wavenumber features of the pressure fluctuations and selectively amplify features at other wavenumbers.

Abraham and Keith [5] used a linear array of 48 flush mounted hydrophones to distinguish between acoustic and hydrodynamic pressure fluctuations underneath a turbulent boundary layer. With their one-dimensional array, they were able to generate a frequency-dependent wavenumber-frequency plot from which they deduced the convective velocity by means of determining the position of the convective ridge.

Arguillat et al. [6, 7] performed direct measurements of the two-dimensional wavenumber spectrum using a rotary array of 63 pressure taps of various sizes. The pressure fluctuations were measured using 0.5 mm pinhole taps which were connected to 1/4" microphones via a tubing system of 140 mm to 150 mm each. The microphone was placed perpendicular to the tubing and the tube was chocked with a final vinyl tube of approximately 2 mm diameter and 2 m length in order to avoid reflections. The smallest tubes had a diameter of 0.7 mm and a minimum distance of 2 mm. The intermediate tubes had a diameter of 2 mm and the largest tubes had a diameter of 5 mm. The number of pinholes at the surface was increased with the size of the underlying tubing. Using various rotational positions of the rotary array, many cross-spectral features of the boundary layer flow were determined and a wavenumber analysis was performed. In the wavenumber spectrum, a first attempt was made to isolate the acoustic pressure fluctuations from the entire set of surface pressure fluctuations.

A wavenumber analysis and separation of both, acoustic and hydrodynamic power spectra was also performed by Ehrenfried and Koop [8] at high subsonic Mach number of $M = 0.85$. The transducers in this investigation were pinhole-mounted to reduce the sensitive surface of the transducers to a diameter of 0.5 mm. A sparse array of 48 sensors with transducer separations ranging from $\Delta x = 6$ mm to $\Delta x = 400$ mm was used to characterize the flow field underneath a boundary layer with a thickness of approximately 25 mm. The authors provided a method to process the cross-spectra of all the transducer separations and to find a wavenumber representation of the data. In the wavenumber domain, the phase velocity and the magnitude of the hydrodynamic and acoustic pressure were determined. Besides providing a method, the authors showed that—like in most wind tunnels—the acoustic noise in the transonic wind tunnel used in the investigation was particularly dominant in the lower frequencies. They surpassed the hydrodynamic pressure fluctuations in amplitude which hindered a characterization of the flow in this region.

Using a similar setup in the same wind tunnel, this limitation was addressed by Haxter et al. [9] who tried to remove the dominant acoustic pressure fluctuations at low frequency by applying a modified greedy-type data processing algorithm. They were able to significantly lower the threshold of acoustic dominance and were able to characterize the phase velocity of hydrodynamic pressure fluctuations as a function of frequency.

1.2 Characterization in Flight-Test-like Environments

Concerning flight tests and flight-test-like environments, Bhat [10] used a microphone array mounted on a Boeing 737 in a cruise flight scenario to determine the spatial correlation and propagation velocity. The array consisted of five 1/2-inch microphones that were flush mounted in a dummy window which was placed in a window bank located in the front section and—in a separate test—in the aft section. The results were stated to be comparable to laboratory measurements. However, the unknown local angle of attack of the flow relative to the array orientation was estimated to have a significant effect on decay rates of the turbulent boundary layer pressure fluctuations. No attempt was made in this test to estimate the separate levels of hydrodynamic pressure fluctuations. This was rather described in another publication by Bhat [11]. Here, the separate levels were estimated by using array-microphone measurements from a forward and an aft location in flight, as well as an aft measurement on the ground. The forward measurement was used to extrapolate the correlation characteristics from the front section to the aft section. The ground measurement was used to estimate the correlation of sole engine noise over the array. The aft measurement from the flight was used as a reference for the total power of the pressure fluctuations.

Palumbo [12] addressed the topic of boundary layer fluctuations characteristics. A spatially highly resolved array of surface pressure transducers was used to investigate the pressure fluctuations underneath the boundary layer in the front section of a

Gulfstream G550 aircraft. The array was mounted in the front window and shaped as a cross with the two axes being oriented in the predominant flow and cross flow direction. It consisted of 43 transducers of which the separation spanned from 3 mm to 477 mm in flow direction and from 3 mm to 81 mm in cross-flow direction. Much care was taken when aligning the local flow direction with the array orientation during flight in order to avoid attenuation effects as had been observed by Bhat [10]. The transducers were pinhole-mounted with an opening diameter of 0.5 mm.

Haxter and Spehr [13] performed measurements in the front section of an Airbus A320 aircraft. The array consisted of 30 pinhole mounted transducers which were mounted in three adjacent window banks in the front of the aircraft. The transducers positions were distributed in a two dimensional fashion over the three windows. This allowed for a determination of the local flow direction in post-processing rather than during flight. The array had a width of approximately 1.2 m in aircraft length axis and approximately 0.4 m in circumferential direction with pinhole diameters of 0.3 mm.

Both investigations by Palumbo [12] and by Haxter and Spehr [13] mentioned above were focused on the hydrodynamic pressure fluctuations—especially on the size of the pressure footprints of turbulent structures on the surface. Both findings pointed towards that considering the local flow direction is crucial to finding the correct values for the size of these patches.

1.3 Objective of This Contribution

While in the past, focus of recent research in flight test measurements has been set on the characteristics of hydrodynamic pressure fluctuations, it has not yet been achieved to frequency-wise separate acoustic from hydrodynamic pressure fluctuations in a flight test. The objective of this paper is to apply an evaluation technique similar to the one by Ehrenfried and Koop [8] to flight test data similar to the one recorded by Haxter and Spehr [13]. The wavenumber representation of the surface pressure fluctuations will be generated in which the acoustic and hydrodynamic sources will show up at different locations. By means of applying a wavenumber filter, the separation of spectra into a hydrodynamic and an acoustic part is possible.

Therefore, the flight test experiment and data set used for evaluation will be given a brief overview in Sect. 2, “Experimental Setup”. Following this, the data evaluation methods will be described in Sect. 3, “Signal Processing”. Finally, the results will be shown in Sect. 4 followed by a discussion in Sect. 5. A similar preliminary analysis has been given by Haxter and Spehr in [14].

2 Experimental Setup

The experiments were conducted on the DLR’s ‘ATRA’ flight test carrier (Fig. 1). In two separate flights, a set of three adjacent regular windows were replaced with aluminum dummy windows which enclosed a pressure transducer array of 30 pressure

Fig. 1 Test carrier D-ATRA (Advanced Technology Research Aircraft). *Source* DLR CC-BY 3.0

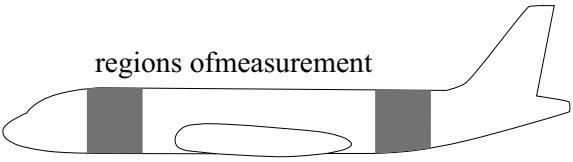

Fig. 2 Sketch of the installation region of the in-flight array in the front and in the aft of the fuselage

transducers. These pressure transducers were of type Kulite *XCL-093* and were pinhole mounted in order to further decrease the size of the sensitive surface to 0.3 mm. The pinhole mounting resulted in a Helmholtz resonator frequency of approximately 3.75 kHz at flight conditions. The total array width and length were approximately 1.2 m in aircraft length direction and approximately 0.3 m across. The minimum transducer spacing in both, lengthwise and cross direction was 10 mm. The signals from the pressure transducers were preamplified in the vicinity of the window banks where they had been installed and then collectively routed to the data recorder of type Dewetron DEWE-51-PCI-128. Data were sampled at a rate of 50 kHz at a word length of 24 bits. Periods of 60 s were recorded for each measurement.

In between the two separate flights that were conducted in the experiment, the location of the three-window pressure transducer array was moved from a front location to an aft location. It was presumed that at the front location there would be little to no acoustic influence from the jet or fan, while at the aft location, there would be a lot of acoustic pressure power on the surface, originating from the jet. A sketch of the two regions of measurement is given in Fig. 2.

2.1 Array Specifics

Within the three dummy windows installed, the 30 pressure transducers were distributed as an array. The sensor positions are shown in Fig. 3. A clustering of the transducer positions into three separate groups is visible, due to the three windows used to set up the array.

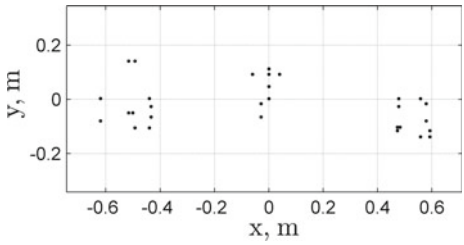

Fig. 3 Sketch of the microphone positions in the array installed on the test carrier

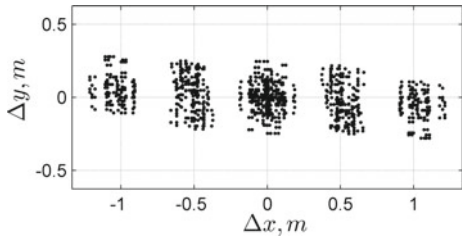

Fig. 4 Sketch of the array spacings (coarray)

In homogenous ergodic conditions relative positions of the transducers can be used for evaluation rather than absolute positions. This will lead to the coarray which contains all the spacings of transducer combinations mn between all the transducers m and n in the array. The transducer spacings for the coarray are calculated by

$$\begin{aligned} \Delta x_{mn} &= x_m - x_n \\ \Delta y_{mn} &= y_m - y_n \,. \end{aligned} \tag{1}$$

and are shown in Fig. 4. When looking at the transducer spacings, the three clusters visible in the display of the sole transducer positions in Fig. 3 have now turned into five clusters as shown in Fig. 4. This pattern will resurface when looking at the array's point spread function which will be done in Sect. 3.3 "DAMAS2.1 Deconvolution" on page 8.

2.2 *Flight Conditions*

Data concerning the flight conditions were recorded on the Basic Flight Test Instrumentation Unit (FTI) which taps into the values provided and used by the aircraft's avionic system, mostly at a rate of 10 Hz. The flight condition chosen for this particular experiment were at a high subsonic Mach number and a typical cruise altitude. Absolute values cannot be provided due to non-disclosure. In order to check for consistency, four parameters from the aft measurement were related to parameters from the front measurement. The barometric altitude was matched within 0.02 %, the Mach number was matched within 0.16 %, the outside static temperature within

1.6 %, and the velocity within 1 %. The mean pressure ratio at the engines during the cruise flight in the front measurement was $EPR = 1.267$ and in the aft measurement it was $EPR = 1.278$.

3 Signal Processing

In the following, the signal processing will be described. The processing is as follows, with references to further literature given:

1. Time domain data is transformed into the frequency domain by means of a windowed Fourier Transform [15].
2. Narrow-band wavenumber beamforming is applied to the data [8].
3. A deconvolution scheme is applied to the wavenumber output [16].
4. The acoustic and hydrodynamic regions in the deconvolution output is integrated to obtain the narrow-band separated spectra [8].

Each of the points stated above will be explicated in a short paragraph in the following.

3.1 Windowed Fourier Transform

The first step in data processing is to transform the time-domain pressure data X into the frequency domain. The overlapping averaged scheme introduced by Welch [15] was used in order to reduce the variance of the output. The window length was chosen to $L = 4096$ and a Hanning weighting function w was used to reduce sidelobes in the frequency domain. The windowing resulted in the signal being divided into K windows with index k. An overlap factor of $r = 0.5$ was used. From the windowed Fourier Transforms

$$\underline{\phi}\,(f)_m^k = \frac{1}{L}\int_{-\infty}^{+\infty} w(t)\cdot X(t)_m^k \cdot e^{-2\pi i f t}\mathrm{d}t\,, \tag{2}$$

the cross- and autospectra were calculated for every transducer combination of m and n. The entire set of cross- and autospectra constituted the cross-spectral matrix $\mathbf{R}$ with

$$\mathbf{R}\,(f)_{mn} = \frac{1}{K}\sum_{k=1}^{K}\left(\underline{\phi}\,(f)_m^k\right)\cdot\left(\underline{\phi}\,(f)_n^k\right)^*. \tag{3}$$

A measurement time of 60 s at the sample rate of $f_s = 50$ kHz will result in a number of $K = 1463$ averages when using the window size of $L = 4096$ samples. Using these parameters, the frequency resolution results in $\Delta f = 12.2$ Hz. Choosing a window size in this setup is a balance between frequency resolution, number of averages, and

ensuring that turbulent structures will propagate over the entire array in the amount of time given by the window length. A reasonable estimated convection velocity of a turbulent structure passing lengthwise over the array of $150\,\mathrm{m\,s^{-1}}$ will result in a delay of 400 samples which corresponds to a delay time $t_D = 400/f_s$. This is considered to be reasonably small when compared to the window length L with window delay time $t_L = L/f_s$. The remaining coherence γ in this worst case scenario can be estimated (see also Ref. [17]) to be

$$\gamma\,(t_D, t_L) = 1 - \frac{t_D}{t_L} \approx 0.903\,. \tag{4}$$

3.2 Wavenumber Beamforming

The beamforming algorithm is applied to the cross-spectral matrix $\mathbf{R}$

$$b(k_x, k_y, f) = \frac{\underline{e}(k_x, k_y)^H \cdot \mathbf{R}(f) \cdot \underline{e}(k_x, k_y)}{N^2}\,. \tag{5}$$

In Eq. (5), H denotes the Hermitian. This type of beamforming uses planar waves to generate the steering vectors $e(k_x, k_y)$. N is the number of transducers in the analysis. The steering vector $\underline{e}$ is composed from the arbitrarily chosen focus grid coordinates (k_x, k_y) and the vectors of transducer positions in x- and y-direction $(\underline{x}, \underline{y})$

$$\underline{e}(k_x, k_y) = exp\left(-i \cdot 2\pi \left(k_x \underline{x} + k_y \underline{y}\right)\right)\,. \tag{6}$$

The diagonal elements of $\mathbf{R}$ represent the autospectra of each sensor signal. They sometimes are removed from the analysis in order to enhance the results. As a deconvolution scheme is applied to the results in this investigation, the diagonal elements are left unchanged and are included in the analysis.

As mentioned before, the focus grid can be chosen arbitrarily. Its values can be normalized by the acoustic wavenumber $k_0(f) = f/c_0$, which results in a frequency-dependent scaling of the map. c_0 is the speed of sound. This is especially convenient as the features in the source maps resulting from the analysis scale with frequency as well. The steering grid size is chosen in the present investigation using normalized values of $-10 \leq k_{x,0} \leq 10$ and $-10 \leq k_{y,0} \leq 10$ with a resolution of 255 samples. Each map therefore consists of 65025 grid points $(k_x, k_y)_f$ that are set up at each frequency f via scaling with $k_0(f)$

$$(k_x, k_y)_f = k_0(f) \cdot (k_{x,0}, k_{y,0})\,. \tag{7}$$

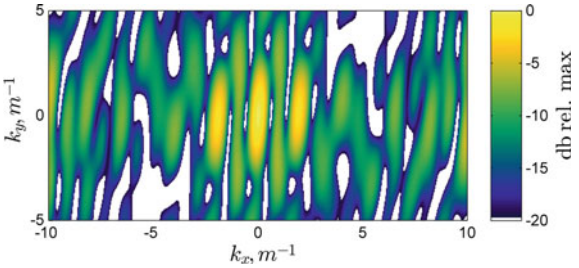

Fig. 5 Point-spread function of the in-flight array in wavenumber space. The dynamic of the image is set to 20 dB below which the values are displayed in white. The three-window-array configuration results in two additional dominant sidelobes in the point spread function

3.3 DAMAS2.1 Deconvolution

When applying the beamforming algorithm to the data, the characteristics of the array positions are still contained in the resulting beamforming map. If a single planar wave were to pass over the array it's representation ideally would be a single point. However, when using a sparse array for sampling, the result would not be a single point but rather a distribution of sources as shown in Fig. 5 (here, the source was located at $k_{x,0} = k_{y,0} = 0$). This special distribution is called the point spread function and the arrangement of lobe features in it is a direct consequence of the transducer placement in the array. In Three major lobes are visible in the center of the point spread function. Two additional minor lobes can be adumbrated to the left and right of the dominant three-lobe arrangement in the center. These five lobes are a direct representation of the five clusters in the coarray mentioned in Sect. 2.1.

The point spread function is obtained by assuming a single source at known position (in this case: $k_{x,0} = k_{y,0} = 0$) and—using wave propagation—to project from this single source the effects to all the sensor locations. This way, a synthetic cross-spectral matrix can be constructed which is then evaluated in the same way as the actual data in order to obtain the point spread function. The point spread function is independent of frequency and a function of k_x and k_y only.

The algorithm chosen for this task is DAMAS2.1 [16] which is an extension of the DAMAS2 algorithm [18]. This algorithm works well in the wavenumber domain, as it assumes a shift-invariant point spread function which is provided by the planar wave approach for the steering vector. The implicit expression

$$b = p * q \tag{8}$$

with the beamforming output b and the point spread function p is solved iteratively for the source map q. The difference between DAMAAS2.1 and DAMAS2 is that DAMAS2.1 implements a zero-padded domain for the iterative solving of Eq. 8 which prevents the wrapping of sources at the edges of the domain. If b is chosen as an $Mx1$ vector with M being the number of points in the focus grid, Eq. (8) can be

written as

$$\underline{b} = P \cdot \underline{q}\,, \tag{9}$$

with P being the MxM-Matrix of point spread functions specific for each location in the steering grid. This is the problem solved by DAMAS. In DAMAS2 and DAMAS2.1, due to the assumption of shift-invariance, it is possible to utilize the convolution theorem to iteratively solve Eq. (8) for the unknown source map q. In the present investigation, a total number of $N = 10^5$ iterations were used.

3.4 Separated Spectra

In order to quantify the relative amplitudes of the acoustic and hydrodynamic spectra, a separation is performed. The separation is carried out via a filtering in the wavenumber domain.

The filtering is performed by integrating over different regions of the source map in the wavenumber domain

$$\tilde{\phi(f)}_A = \iint_A q(f)\mathrm{dk}\,, \tag{10}$$

where A is the region of integration which will be shown below. This area is determined by utilizing the fact that sources with different phase velocities will appear at different locations in the wavenumber domain. The boundary between acoustic and hydrodynamic pressure fluctuations in the wavenumber domain can be estimated. A location in wavenumber space is linked to the phase velocity on the surface via the relation

$$u(f) = \frac{f}{k}\,, \tag{11}$$

where $u(f)$ is the phase velocity, f is the frequency of the map under evaluation, and k is the wavenumber magnitude of the chosen position in the map. $u(f)$ reportedly is frequency-dependent [9, 10, 19]. Acoustic pressure fluctuations will have a propagation speed of c—the speed of sound and thus

$$k_0(f) = \frac{f}{c}\,, \tag{12}$$

where $k_0(f)$ is the acoustic wavenumber. In subsonic flows, this acoustic wavenumber confines the region where the propagation is of acoustic nature. In the presence of a flow, this region can be distorted. The distortion in k_x and k_y-direction due to the flow in terms of Mach number is described by Ref. [20] as

$$\frac{k_x}{k_0} = \frac{\cos\theta}{1 + M\cos\theta} \quad \text{and} \quad \frac{k_y}{k_0} = \frac{\sin\theta}{1 + M\cos\theta}\,. \tag{13}$$

Equation (13) yields pairs of k_x, k_y (or k_x/k_0, k_y/k_0 when normalized) which enframe the distorted acoustic domain depending on the direction from the origin, θ, with $0 \leq \theta < 2\pi$. Thus, the integration region A in Eq. (10) equals all points on and confined by the boundary for acoustic pressure fluctuations and outside the boundary for hydrodynamic pressure fluctuations. Note that the wavenumber with unit [m^{-1}] is used in this publication rather than the circular wavenumber with unit [$\mathrm{rad\,m}^{-1}$]. The resulting values of $\tilde{\phi}(f)_{acoustic}$ and $\tilde{\phi}(f)_{hydrodynamic}$ are summed over third-octaves to form a separate spectral representation of both, acoustic and hydrodynamic pressure fluctuations.

4 Results

In the following result section, first the deconvolved, third-octave averaged wavenumber spectra at selected frequencies at front and aft position will be shown. At each frequency, the elliptical shape of the acoustic domain is displayed. Sources contained inside this region are characterized by a propagation speed at or larger than the speed of sound. All wavenumber spectra are normalized by the peak level found in the map.

Subseeding the wavenumber spectra are the separated spectra of acoustic and hydrodynamic surface pressure. They will be shown separately for the front measurement and for the aft measurement.

4.1 Wavenumber Maps

The wavenumber spectra at a third-octave center frequency of $f_c = 160\,\mathrm{Hz}$ are shown in Figs. 6 (front section) and 7 (aft section). The dominant feature in both spectra is the convective ridge in the right side of each figure. The k_x-position of the convective ridge in the front section measurement is located slightly further away from the

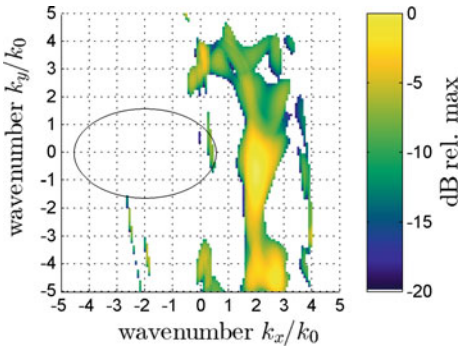

Fig. 6 Third-octave averaged wavenumber spectrum at front position at $f = 160\,\mathrm{Hz}$

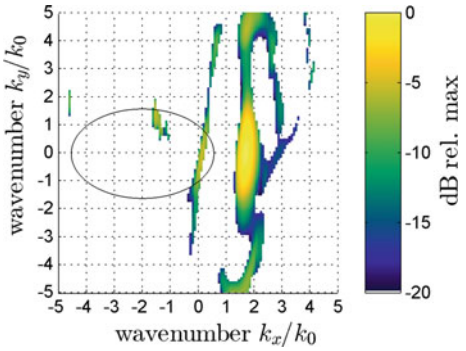

Fig. 7 Third-octave averaged wavenumber spectrum at front position at $f = 160\,\text{Hz}$

origin of the plot, with the center being located at approximately $k_x/k_0 \approx 2$. In the aft section, the convective ridge is located between $k_x/k_0 \approx 1.5$ and $k_x/k_0 \approx 2$. This indicates that—at this particular frequency—the hydrodynamic pressure fluctuations in the aft sections propagate faster over the array than in the front section. The shape of the convective ridge appears more defined and ellipse-shaped in the aft section at this frequency. In the front, the slightly distorted appearance might be caused by two things. First, by the limited spatial resolution of the array, which limits the coherent signals obtained from the rather short hydrodynamic coherence lengths. (Hydrodynamic coherence lengths scale roughly with boundary layer thickness, please refer to Efimtsov [21] or Haxter [22]). Second, the thinner boundary layer in the front is likely to cause small-scale pressure fluctuations at higher frequency. Thus the signal a center frequency of $f_c = 160\,\text{Hz}$ is reduced leading to a distortion of the convective ridge.

Concerning the acoustic domain, there are some signal processing artifacts visible on the right hand side of the acoustic domain of the front-section measurement (at approximately $(k_x, k_y) = (0.5, 0)$). The structure visible there is considered an artifact as it has a very elongated shape and its orientation resembling the orientation of the convective ridge. For the aft measurement, there are two sources visible, of which the elongated one at $(k_{x,0}, k_{y,0}) \approx (0, 0)$ is considered an artifact, due to its elongated shape and its close resemblance of the convective ridge. The other acoustic source at $(k_{x,0}, k_{y,0}) \approx (-1.5, 1.3)$ is considered to possibly be a valid acoustic source due to its compact size with no connection or resemblance of other structures. At this frequency of $f_c = 160\,\text{Hz}$, its amplitude is approximately 6 dB below the amplitude of the convective ridge. Its position within the acoustic region and relative to the origin indicates that of the origin of the acoustic pressure fluctuations is located below and downstream relative to the array. As the source is located not on the border of the acoustic domain but rather slightly to the inside, the acoustic pressure fluctuations do not strike the array in parallel but rather at an incident angle. No estimation of the distance of the acoustic source can be given here. However, it is likely that these acoustic pressure fluctuations originate from the fan located downstream from the array position.

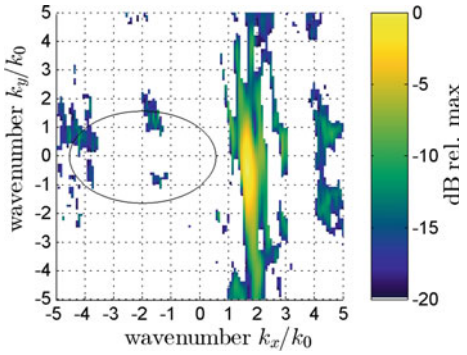

Fig. 8 Third-octave averaged wavenumber spectrum at front position at $f = 500\,\text{Hz}$

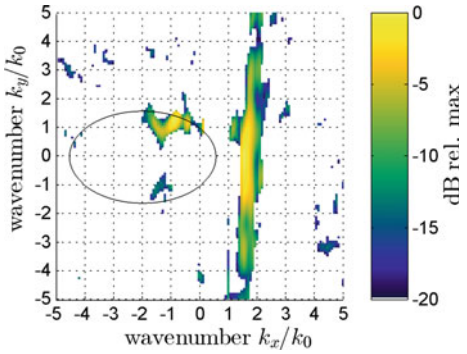

Fig. 9 Third-octave averaged wavenumber spectrum at front position at $f = 500\,\text{Hz}$

In Figs. 8 and 9, with a center frequency of $f_c = 500\,\text{Hz}$, the dominant feature in the wavenumber spectra is still the convective ridge which has decreased slightly in size. Additionally, a slight tilt in the convective ridge is visible for both cases. For the front case in Fig. 8 the convective ridge is tilted slightly in counter-clockwise direction which indicates that the flow over the array deviates slightly upwards from the aircraft length direction. In the aft section in Fig. 9, the convective ridge is tilted slightly in clockwise direction, which indicates the flow being directed slightly downwards from the aircraft length axis. Such slight variations in local flow direction may be caused by the downwash influence of the wing. In both, the front and the aft case, the convective ridge is shaped asymmetrically with the point of highest magnitude not lying in the center of the convective ridge but rather leaning towards the origin of the spectrum. This is an indicator of the measured flow speed increasing with increased distance in the coarray in flight direction. (see also Keith [28] and see also Haxter et al. [9]). The overall position of the convective ridge has not changed in comparison to the case at $f_c = 160\,\text{Hz}$.

Concerning the acoustic region of the front section measurement, there is one source and two artifacts visible. The source is located close to the upper edge and just inside the acoustic domain. It's amplitude is approximately 12 dB below the maximum of the convective ridge. The source's location indicates that the origin of

the acoustic pressure fluctuations is located below and downstream of the array at a slightly inclined angle. As this wavenumber spectrum is a third-octave average it could just be that one of the harmonics of the fan rotational frequency is visible here. Concerning the two artifacts: one is located on the far left side of the acoustic region. The reason why it is considered an artifact is that it has a rather rugged shape and no confinement to either the outside or the inside of the acoustic region. The other artifact is located below we source. The reason why it is considered an artifact is due to its rugged shape.

In the aft measurement, the number of acoustic sources increases and overall and their portion of the entire spectrum increases. The source formerly located at $(k_{x,0}, k_{y,0}) \approx (-1.5, 1.3)$ has moved downwards to $k_{y,0} = 1.0$. A new dominant source has appeared at $(k_{x,0}, k_{y,0}) \approx (-1.0, 1.2)$ with an amplitude just short of the amplitude of the convective ridge. Two small sources appear on the same $k_{y,0}$-position, but further towards $k_{x,0} = 0$. The overall position of the acoustic sources suggests again that the jet noise is responsible for the peaks appearing at these positions in the wavenumber spectra. With the acoustic sources moving towards $k_{x,0} = 0$, it appears as if the origin of the dominant acoustic sources is shifted from downstream of the array towards a position facing the array. Apparently, the jet exhaust has a radiation pattern in which the dominant sources have a different location depending on frequency.

At a slightly higher frequency of $f_c = 800\,\text{Hz}$, shown in Figs. 10 (front) and 11 (aft), the convective characteristics remain unchanged. The convective ridge size has slightly decreased which indicates longer hydrodynamic coherence lengths. The tilt at both locations remains the same as at previous frequencies. In the front measurement some noise and no acoustic source is visible. In the aft measurement, the acoustic sources on the upper right side of the acoustic domain have become more dominant. Overall, the acoustic sources form a continuous line from negative to positive wavenumber on the edge of the acoustic domain. This indicates that the origin of these acoustic pressure fluctuations are located below the array spanning from upstream to downstream. The maximum acoustic level is found at a positive wavenumber, which means that the origin of this particular dominant acoustic pressure fluctuation lies upstream of the array.

At $f = 1000\,\text{Hz}$, shown in Fig. 12 (front position), the convective ridge is still the dominant feature in the wavenumber spectrum. No acoustic sources are visible within the dynamic range plotted. The convective ridge again shows a similar small counter-clockwise tilt as it had before. In the aft section, shown in Fig. 13, the acoustic pressure fluctuations are now the dominant feature in the wavenumber map. Again, the acoustic sources are located on the upper right hand side which is an indicator of their origins being located on a line from upstream to downstream below the array position. At this current frequency however, the rightmost acoustic source is very prominent. Its amplitude lies approximately 8 dB above the peak of the convective ridge. The convective ridge is well visible and again displays the same slight clockwise tilt as it had at the other frequencies.

The highest and last frequency for which exemplary wavenumber maps are shown is $f_c = 2500\,\text{Hz}$. The maps are shown in Figs. 14 (front) and 15 (aft). In the front

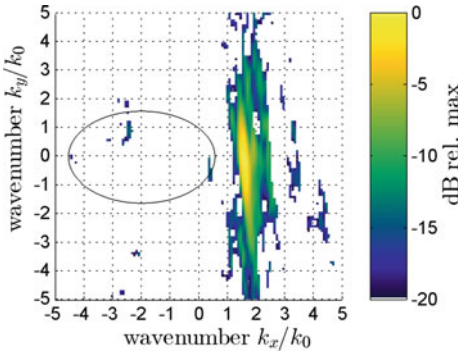

Fig. 10 Third-octave averaged wavenumber spectrum at front position at $f = 800\,\text{Hz}$

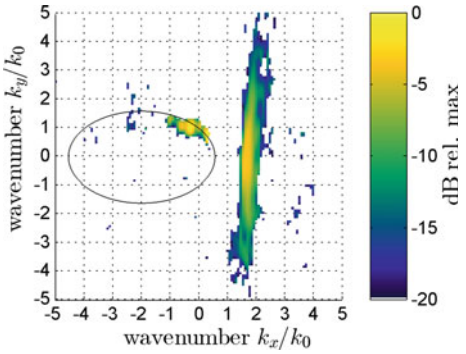

Fig. 11 Third-octave averaged wavenumber spectrum at front position at $f = 800\,\text{Hz}$

section, the convective ridge is very dominant. Yet, at this frequency, its size starts to grow bigger which indicates a decrease in hydrodynamic coherence length over the array. The increasingly rugged appearance of the convective ridge is likely caused by the transducer distances in the coarray starting to reach the threshold where their resolution is capable of resolving the hydrodynamic surface pressure fluctuations. On the left hand side of the acoustic domain, a small region of possible distributed

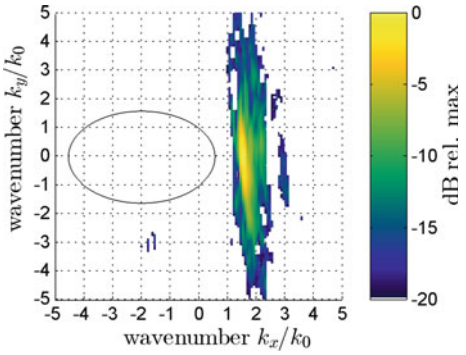

Fig. 12 Wavenumber spectrum at front position at $f = 1000\,\text{Hz}$

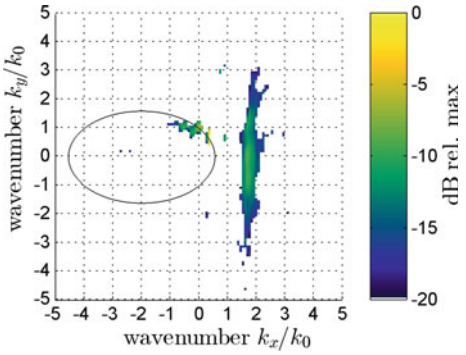

Fig. 13 Third-octave averaged wavenumber spectrum at front position at $f = 1000\,\text{Hz}$

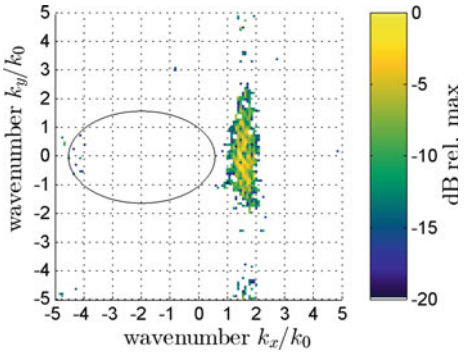

Fig. 14 Third-octave averaged wavenumber spectrum at front position at $f = 2500\,\text{Hz}$

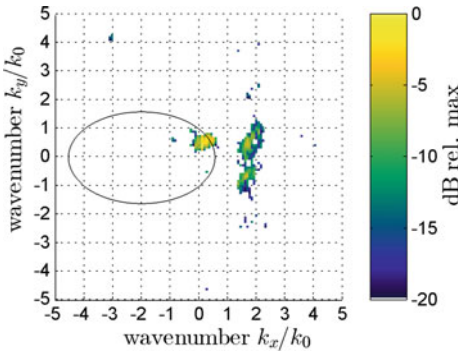

Fig. 15 Third-octave averaged wavenumber spectrum at front position at $f = 2500\,\text{Hz}$

minor sources is visible. Their maximum is located on the border of the domain at $k_y = 0$. The origin of these sources is however unknown.

In the aft section, again the acoustic sources are the dominant feature at $(k_{x,0}, k_{y,0}) \approx (0.25, 0.5)$. This source position indicates again a source origin located below and upstream of the array at inclined position. Acoustic sources to the left of the origin are not visible. The convective ridge is observed at the usual position, however its peak level is 7 dB below the acoustic peak.

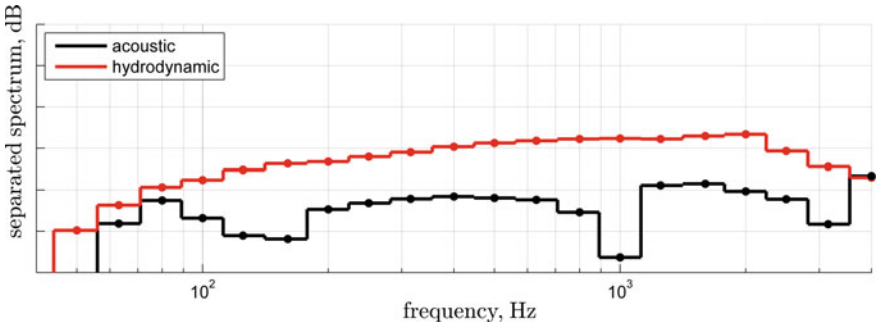

Fig. 16 Separated third-octave spectra from the **front** region measurement. The grid spacing is 5 dB

4.2 Separated Spectra

When integrating the sources in the wavenumber spectra over the area of the acoustic domain, a separated representation the acoustic power spectrum can be obtained (see Sect. 3.4). Integrating over the remaining part of the wavenumber spectrum (which contains the convective ridge) will yield a representation of the separated hydrodynamic spectrum.

For the front position, both, acoustic and hydrodynamic spectra are shown in Fig. 16. The hydrodynamic spectrum exhibits an overall broadband level increase of 10 dB from $f_c = 50$ Hz to the peak at $f_c = 1800$ Hz. At higher frequency, the hydrodynamic level starts to drop again. The power levels of the acoustic spectrum at low frequency are slightly below the hydrodynamic power levels. This energy in the acoustic domain is likely caused by signal processing artifacts caused by an incomplete or improper deconvolution of the map. At higher frequencies, two broadband humps are obseverd, one reaching from 180 Hz $\leq f_c \leq$ 1 kHz and the second one reaching from 1.2 kHz $\leq f_c \leq$ 3 kHz. Looking at the wavenumber spectra, it appears that these seemingly acoustic sources are caused by bleeding of signal artifacts of the hydrodynamic sources into the acoustic domain.

For the aft position, the acoustic and hydrodynamic power spectra are located closer together. The hydrodynamic spectrum shows a steep level increase of 5 dB from $f_c = 50$ Hz to $f_c = 90$ Hz. From $f_c = 90$ Hz on, the level continues to increase but at a much more moderate slope to reach a maximum at approximately $f_c = 400$ Hz. From here on, the hydrodynamic level moderately decreases again with increasingly steep slope.

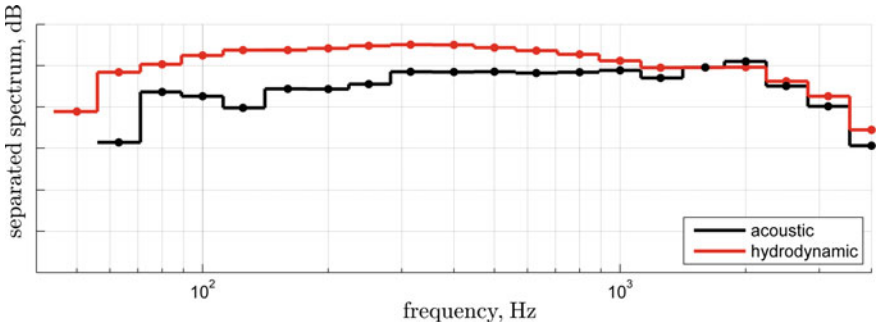

Fig. 17 Separated third-octave spectra from the **aft** region measurement. The grid spacing is 5 dB

The acoustic spectrum starts out at approximately 8 dB below the hydrodynamic level at low frequency of 60 Hz. The level very slightly increases and eventually slightly exceeds the hydrodynamic power level at a frequency of $f_c = 2$ kHz. From here on, the slope starts to decrease at the same rate as the hydrodynamic spectrum with the acoustic level again being slightly below the hydrodynamic spectrum (Fig. 17).

5 Discussion

In both, the front section measurement and in the aft section measurement, hydrodynamic pressure fluctuations are very dominant at many frequencies. This especially applies to the front section measurement where there seem to be almost no acoustic or potentially acoustic sources present.

Tilted Convective Ridge

Concerning the convective ridge, a dominant feature is the tilting of it due to the flow not being aligned with the length axis of the aircraft. In the front section measurement, the flow appears to be tilted slightly upwards and in the aft section measurement, the flow appears to be tilted slightly downwards. This can be seen as an indicator of the wing's downwash effect to provide the momentum to keep the aircraft flying. Haxter and Spehr [23] had observed a tilted and shifted influence of the wing's pressure field on the convective ridge. However, that measurement was performed in closer proximity of the wing. In the present measurement, only a tilt of the convective ridge about the origin of the wavenumber spectrum is observed.

Hydrodynamic Spectrum

The drop in frequency from front to aft measurements of the location of the maximum of the separated convective spectrum is in accordance with the findings of Farabee and Casarella [19]. In low-speed wind tunnel tests, they found the spectral maximum positions at various flow speeds to collapse when scaled with the time scale δ/u_τ (with δ being the boundary layer thickness and u_τ being the wall shear velocity). Unfortunately, no measurements of the wall shear stress and the boundary layer thickness were performed in the present investigation to confirm the maximum location at $2\pi f\delta/u_\tau \approx 50$. An indication that the extrapolation of these findings at low speed to the high speeds of a flight test measurements is possible is given by Mull [24] who state in their conclusions that "The wall-pressure fluctuations measured on the forward-fuselage section of the aircraft agree well with an extrapolation of boundary-layer data obtained in the laboratory when the relative size of the microphone as compared with the boundary -layer thickness is the same."

Similar findings of good collapse are reported by Bull [3, p.728 and Fig. 5] although the flow velocity u_∞ is used to collapse the spectral amplitude data rather than the wall shear velocity. Bull's measurement were performed at various positions in a wind tunnel at two Mach numbers of $M = 0.5$ and $M = 0.5$.

As mentioned in the introduction, an attempt to estimate the separated hydrodynamic and acoustic power spectral densities was done by Bhat [11, Fig. 5]. Contrary to the present measurements, Bhat found that the separated spectra are on roughly the same level below a frequency of 800 Hz and "substantially higher" at frequencies between 1 kHz and 2 kHz. At higher frequencies, the acoustic and hyrdodynamic levels appear to approximate each other again. However, it is likely that the small scale turbulent boundary layer pressure fluctuations were not picked up by the rather large transducers due to the averaging effect of the sensitive surface. The results at higher frequency of Bhat [11] are therefore to be interpreted with caution.

Position of Acoustic Sources and Directivity

The finding of dominant acoustic sources moving from a downstream position upwards to the nozzle exit as the frequency increases has been observed by Papamoschou [25]. Contrary to the present investigation, Papamoschou used a setup which allowed for the movement of the microphone array aperture to allow for measuring the directivity of noise sources. As the directivity of jet noise sources of different nature had already been indicated in studies previous, this allowed them to determine the position of certain source mechanisms by means of comparing the results taken at different radiation angles.

In the present investigation, the amplitude of the separated acoustic spectrum increases with frequency which is contrary to the findings of Papamoschou. However, the jet observation angle of the array installed in the airplane in the present investigation was different from the one suggested to result in increased low-frequency amplitudes by Papamoschou. This might explain the difference in results.

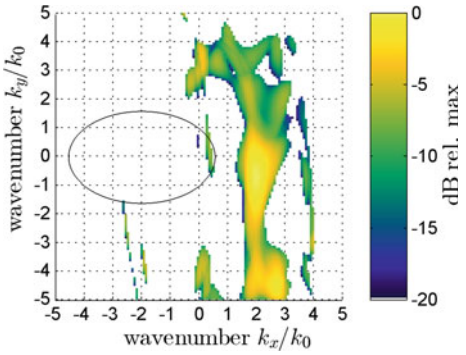

Fig. 18 Third-octave averaged wavenumber spectrum at front position at $f = 160\,\text{Hz}$ with $N = 10^5$ DAMAS2.1 iterations

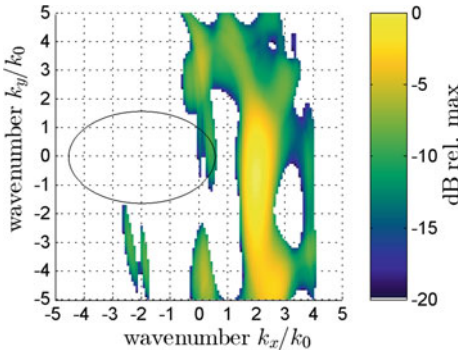

Fig. 19 Third-octave averaged wavenumber spectrum at front position at $f = 160\,\text{Hz}$ with $N = 10^4$ DAMAS2.1 iterations

Number of Iterations for Deconvolution

When looking at the results, the possible effects of deconvolution need to be kept in mind. Some acoustic sources might be mistaken for signal processing artifacts and vice versa. Signal processing artifacts mostly consist of remains from the point spread function not entirely being removed from the dirty map by the DAMAS2.1 deconvolution algorithm. They might also be caused by the point spread function not being suitable for the cause due to flow deviations over the array. For the present array used, the convergence of the deconvolution algorithm is reduced due to the fact that the point spread function exhibits two dominant sidelobes as seen in Fig. 5. These sidelobes are causing very dominant copies of actual features in the wavenumber domain which will only be removed after an extensive number of iterations. The effect of choosing different numbers of iteration for the deconvolution is shown in Figs. 18 and 19. In the upper figure, the wavenumber spectrum from a front section measurement is shown with $N = 10^5$ iterations, which was used for all other maps as well. On the lower figure, a map from the same measurement is shown with an intermediate iteration number of $N = 10^4$ iterations. The features of both maps are similar, but their broadness is reduced with the higher iteration count. Especially the sources in the acoustic domain have been greatly reduced in dominance.

Array limitations

Just like with regular acoustic beamforming methods, there are some limitations imposed on the analysis originating from the array shape and dimensions. These have not necessarily been compensated for in the current investigation but are provided to the reader nevertheless to give an overview of what should further be paid attention to when performing a similar analysis.

- Aperture size
  The aperture size in relation to the wavelength of pressure fluctuations over the array is of concern mainly for acoustic propagation mechanism at low frequency. A large wavelength compared to the aperture size will result in a poor source resolution. The large propagation velocity of acoustic waves results in large wavelengths which—especially at low frequencies and propagation in flow direction—decreases the ability to discern between two adjacent sources (Sparrow's limit [26]) and to determine the position in the acoustic domain. In theory, this should be compensated by the deconvolution scheme. If no scheme were applied, an estimate of the lower frequency limitation would be the wavelength of pressure fluctuations to be of similar size as the aperture. With the flow speed and ambient temperature taken into account, this would lead to a frequency limit in flow direction of approx 440 Hz. This is however the worst case with the acoustic wavelength being spread out by the convection of sound waves in the flow (distortion of the acoustic domain). In adverse flow direction, this frequency limit drops to far below 100 Hz. Concerning the hydrodynamic pressure fluctuations, there is usually only one convective source present in the spectra (the convective ridge). The size of the coherent pressure patch left by a convective source on a surface is limited by the coherence length which itself is limited by the boundary layer thickness, maximum values reported by Willmarth[1] (Λ/δ) ≈ 6), by Farabee and Casarella [19] (Λ/δ) ≤ 5), and by Haxter and Spehr [13] ($l_x/\delta \approx 7$). As opposed to the acoustic pressure fluctuations, the spread of the convective ridge in the wavenumber domain is an inherent characteristic of the coherence properties of the turbulent pressure fluctuations.

- Smallest transducer separation
  Contrary to the aperture size constituting an array limit at low frequencies, the smallest transducer separation is a measure for the array limitation at high frequencies. Following the Nyquist-Shannon theorem, the smallest transducer separation is a measure for the shortest wavenumber to be captured by the aperture. However, with typical values of separation being on the scale of mm, the frequency at which an acoustic wavenumber reaches the Nyquist limit is in the order of a few tens of kHz, depending on speed of sound an propagation velocity (see Eq. (12)). For measurements with flow speeds in the low subsonic range, the convective phase propagation is likely to be affected by the Nyquist limit. However, since the coherence length gets shorter with increasing frequency, the actual limitation comes from the coherent pressure patch to bee too small to yield a coherent hydrodynamic signal on several sensors. In the present investigation, at the highest

frequency under consideration, the shortest coherence length in the front section case is approximately $l_x \approx 50$ mm [13] which is five times the smallest transducer separation.

- Sensor size
  With low propagation velocities and large sensor sizes comes an attenuation of pressure fluctuations due to the integration effect of the sensor's sensitive surface. This is commonly known as the Corcos attenuation [2]. If the wavelength of the pressure fluctuation smaller than the size of the transducer, the pressure fluctuation will be averaged across the surface. The effect is described in detail for various shapes of the sensitive surface by Ko [27]. With small MEMS sensors or pinhole mounting, the effect of sensor size is negligible.

- Transducer density
  Generally, the transducer density of a coarray decreases with increasing transducer separation. An example is the three-window design of the array in the present investigation. The center cluster of the coarry in Fig. 4 incorporates transducer separations from all three windows. The off-center cluster incorporate less transducer separations due to there only being two window combinations with a two-window-spacing. This introduces a small weighting effect on propagation characteristics that are intensified at small distances. For acoustic waves, there is little to no such effect. For hydrodynamic pressure fluctuations however, the rate of phase change is not constant with the distance to the coarray center. The rate of phase change increases slightly with increased transducer separation (see Haxter et al. [9], Farabee and Casarella [19], Keith and Abraham [28], and Bhat [10]). This is due to turbulent structures from different depth of the boundary layer (and thus different propagation velocities) dominate the rate of phase change for different transducer separations.

6 Summary

Flight test measurements of surface pressure fluctuations were performed on an Airbus model A320 aircraft. An array spanning three consecutive window banks and incorporating 30 pressure transducers was used to determine the pressure fluctuations at two positions on the aircraft. Using a wavenumber analysis technique, a wavenumber representation of the surface pressure fluctuations was created at various frequencies. This analysis technique included the application of a deconvolution algorithm to remove array-specific broadening effects of sources in the resulting maps. In the wavenumber maps, the hydrodynamic pressure fluctuations were identified by means of their convective ridge. Acoustic pressure fluctuations were identified by their position inside the acoustic domain. By means of discussing the source appearance and shape, signal processing artifacts were identified. In the front region measurement, barely any acoustic sources were visible. In the aft section measurement, several acoustic sources are found, the level of which increases with frequency. At high

frequency, the acoustic level is found to dominate the wavenumber maps. In the aft, the position of the acoustic sources was found to move with increasing frequency: while the sources of acoustic pressure fluctuations at low frequencies were located behind the array, their location moved to a forward position relative to the array at higher frequencies.

By means of integrating the wavenumber maps separately over both, the acoustic domain and over the hydrodynamic domain, separated spectra of the hydrodynamic and the acoustic surface pressure fluctuations were generated. In accordance with the wavenumber spectra, the separated spectra from the front displayed dominant hydrodynamic pressure fluctuations over the entire bandwidth of frequencies under consideration. For the aft section measurements, the hydrodynamic pressure fluctuations were found to dominate the spectrum at low frequencies. However, with increasing frequency, the acoustic influence was found to grow stronger and at higher frequency, the acoustic level was the dominant part of the spectrum.

The separated spectra still included the signal processing artifacts mentioned earlier. Nevertheless, the separation of spectra for a flight test measurement was achieved and the spectra can be used for prediction of surface excitation.

Acknowledgements The authors would like to thank the following institutions for their support:
• The federal ministry of Economics (BMWi) for the financial support of the research as part of the Luftfahrtforschungsprogramm IV (LuFo-IV).
• Airbus S.A.S. for the help provided in conducting the flight test and the modifications on the aircraft.

References

1. W.W. Willmarth, C.E. Wooldridge, J. Fluid Mech. **14**(02), 187 (1962). https://doi.org/10.1017/s0022112062001160
2. G. Corcos, J. Acoust. Soc. Am. **35**(2), 192 (1963)
3. M.K. Bull, J. Fluid Mech. **28**(04), 719 (1967). https://doi.org/10.1017/s0022112067002411
4. W.K. Blake, D.M. Chase, J. Acoust. Soc. Am. **49**(3B), 862 (1971). https://doi.org/10.1121/1.1912427
5. B.M. Abraham, W.L. Keith, J. Fluids Eng. **120**(1), 29 (1998). https://doi.org/10.1115/1.2819657
6. B. Arguillat, D. Ricot, G. Robert, C. Bailly, in *11th AIAA/CEAS Aeroacoustics Conference Proceedings Paper 2005–2855* (2005). https://doi.org/10.2514/6.2005-2855
7. B. Arguillat, D. Ricot, C. Bailly, G. Robert, J. Acoust. Soc. Am. **128**(4), 1647 (2010). https://doi.org/10.1121/1.3478780
8. K. Ehrenfried, L. Koop, in *14th AIAA/CEAS AeroAcoustics Conference Proceedings Paper 2008–2800* (2008)
9. S. Haxter, J. Brouwer, J. Sesterhenn, C. Spehr, J. Sound Vib. **402**, 85 (2017). https://doi.org/10.1016/j.jsv.2017.05.011
10. W. Bhat, J. Sound Vib. **14**(4), 439 (1971). https://doi.org/10.1016/0022-460x(71)90574-8
11. W. Bhat, J. Sound Vib. **17**(3), 349 (1971). https://doi.org/10.1016/0022-460x(71)90647-x
12. D. Palumbo, J. Sound Vib. **331**(16), 3721 (2012). https://doi.org/10.1016/j.jsv.2012.03.015
13. S. Haxter, C. Spehr, J. Sound Vib. **390**, 86 (2017). https://doi.org/10.1016/j.jsv.2016.10.038
14. S. Haxter, C. Spehr, in *2018 AIAA/CEAS Aeroacoustics Conference Proceedings Paper 2018–3275* (2018)

15. P. Welch, IEEE Trans. Audio Electroacoust. **15**(2), 70 (1967). https://doi.org/10.1109/tau.1967.1161901
16. S. Haxter, in *6th Berlin Beamforming Conference* (2016)
17. A. Seybert, J. Hamilton, J. Sound Vib. **60**(1), 1 (1978). https://doi.org/10.1016/0022-460x(78)90396-6
18. R.P. Dougherty, in *14th AIAA/CEAS Aeroacoustics Conference (29th AIAA Aeroacoustics Conference) Proceedings Paper 2005–2961* (2005)
19. T.M. Farabee, M.J. Casarella, Phys. Fluids A: Fluid Dyn. **3**(10), 2410 (1991)
20. L. Koop, K. Ehrenfried, in *14th AIAA/CEAS Aeroacoustics Conference (29th AIAA Aeroacoustics Conference) Proceedings Paper 2008–2907* (2008). https://doi.org/10.2514/6.2008-2907
21. B. Efimtsov, Sov. Phys. Acoust.-USSR **28**(4), 289 (1982)
22. S. Haxter, C. Spehr, in *20th AIAA/CEAS Aeroacoustics Conference Proceedings Paper 2014–3064* (2014)
23. S. Haxter, C. Spehr, in *23rd AIAA/CEAS Aeroacoustics Conference Proceedings Paper 2017–3205* (2017)
24. H.R. Mull, J.S. Algranti, Flight measurement of wall-pressure fluctuations and boundary-layer turbulence. Technical report, NASA-TN-D-280, NASA Lewis Research Center (1960)
25. D. Papamoschou, A. Dadvar, in *12th AIAA/CEAS Aeroacoustics Conference Proceedings Paper 2006–2644* (2006)
26. C.M. Sparrow, Astrophys. J. **44**, 76 (1916)
27. S.H. Ko, J. Acoust. Soc. Am. **93**(3), 1293 (1993). https://doi.org/10.1121/1.405414
28. W.L. Keith, B.M. Abraham, The influence of convection velocity on the turbulent wall pressure wavenumber-frequency spectrum. Technical report, Naval Undersea Warfare Center Division, Newport, RI (1995)

A Comparison Between Different Wall Pressure Measurement Devices for the Separation and Analysis of TBL and Acoustic Contributions

Quentin Leclère, Alice Dinsenmeyer, Edouard Salze, and Jérôme Antoni

Abstract The wall pressure measured by an array of flush mounted microphones subject to a flow results from two components. The first one is due to the pressure fluctuations generated by vortices convected by the flow in the turbulent boundary layer developed on the wall, and the second one results from acoustic waves that are emitted by some acoustic sources. Different type of sensor arrays can be used to characterize the first or second components, or even both. In all cases, a major difficulty is to separate as well as possible their contributions to the measurements. Different techniques are reviewed in this chapter to achieve this goal, based on either the measurement device itself or the post processing method. All approaches are implemented in a unique experimental setup, conducted in the frame of the ADAPT Clean Sky 2 project, allowing to objectively highlight their advantages and drawbacks.

1 Introduction

Microphone array measurements are commonly used for the characterization of aeroacoustic sources in wind tunnels. The object of interest (or a mockup of it) is installed in the tunnel and a flow is established so as to generate aeroacoustic sources. The difficulty, in these conditions, is that the pressure fluctuations observed at one given point in the tunnel result from the acoustic pressure, radiated by the aeroacoustic source of interest, but also from fluctuations caused by the flow itself. For practical reasons, microphones are often installed on a wall of the tunnel. The acoustic pressure radiated by the source of interest is then disturbed by the pressure due to the turbulent boundary layer developed on the wall, with often strongly negative signal to noise ratios (SNRs). The post-processing of such data, for acoustic imaging

Q. Leclère (✉) · A. Dinsenmeyer · J. Antoni
Univ Lyon, INSA Lyon, LVA, EA677, 69621 Villeurbanne, France
e-mail: quentin.leclere@insa-lyon.fr

E. Salze
Univ Lyon, Ecole Centrale de Lyon, Laboratoire de Mecanique des Fluides et d'Acoustique, 69134 Ecully, France

E. Ciappi et al. (eds.), *Flinovia—Flow Induced Noise and Vibration Issues and Aspects-III*, https://doi.org/10.1007/978-3-030-64807-7_9

purpose, requires the separation of these two contributions (acoustic and TBL). This separation relies on statistical and/or physical properties of these two components. Statistically, correlation lengths of the TBL are very short, the resulting coherence between different sensors of the array being very low. The contribution of the TBL to averaged cross-spectral quantities is thus limited (except for auto-spectra). Many acoustic imaging techniques are based on the post-processing of averaged cross-spectral quantities, either excluding [1] or reconstructing [2] auto-spectra. These approaches require averaged cross-spectra, which in turn requires quite long time records. Moreover, transient acoustic events cannot be analyzed using such averaged spectral quantities.

Other separation techniques rely on the different physical properties of the TBL and acoustic fields, more specifically their properties in the wavenumber domain. The acoustic part is by definition limited to the low wavenumber domain (lower or equal to the acoustic wavenumber). The support of the TBL is much wider, with a maximum around the convective wavenumber in the direction of the flow. A separation of acoustic and TBL contributions can thus be processed by a filtering operation in the wavenumber domain. This filtering can be operated either by post-processing wall pressure fields sampled using high density microphone arrays, or alternatively using a low-pass physical filtering operating before data acquisition. Post-processing filtering requires high density microphone arrays to avoid aliasing problems at the stage of spatial sampling, the high number of required microphones is often reached using multi-pass measurements [3]. Physical filtering is achieved by various ways, using surface or remote microphones, the filtering being realized by an averaging of the pressure over a surface determined by the sensor area or by the section of the tube connected to remote sensors [3, 4]. Another possibility is to use filtering properties of thin structures: a thin plate submitted to a wall pressure field will act as a low pass filter, with a cut-off frequency equal to its natural wavenumber. The vibration of the plate can be used to recover the low wavenumber part of the incident pressure field using inverse methods [5, 6].

The aim of the present contribution is to compare different experimental approaches to separate TBL and acoustic contributions in the frame of a unique academic experiment. The experimental setup has been realized in the frame of the ADAPT Cleansky EU project, in a small wind tunnel at Ecole Centrale de Lyon. The first section of this work is dedicated to the experimental setup, including a detailed description of the three different sensor arrays that have been tested. The beamforming processing that is used to analyze the measured pressure fields is presented in a second section, with an original way of formulating the quadratic problem using vectorization, offering interesting options to easily process partial CSMs (Cross Spectral Matrices). The third section finally enumerates different separation techniques based on physical assumptions, statistical properties, or spatial filtering approaches with their basic principle and hypothesis, together with some illustrations based on the different datasets.

In order to ease the reading of the work, a list of main acronyms used in the text is provided hereafter.

- ADAPT: ADvanced Aeroacoustic Processing Techniques (EU project)
- CSM: Cross Spectral Matrix
- CS(s): Cross Spectrum (Spectra)
- MEMS: Micro Eletro-Mechanical System
- PCB: Printed Circuit Board
- PDF: Probability Density Function
- PFA: Probabilistic Factor Analysis
- SNR: Signal to Noise Ratio
- TBL: Turbulent Boundary Layer.

2 Experimental Setup

The experimental campaign described in this section has been conducted in the frame of the ADAPT Cleansky EU project. The experiment was conducted in the main subsonic wind tunnel at Ecole Centrale de Lyon, LMFA, Centre Acoustique. The flow was generated using a 850 kW Houden centrifugal blower. Air passes through settling chambers including honeycombs and several wire meshes designed to reduce freestream turbulence. For the project, a closed-section wind tunnel was used (see Fig. 1). The first section of the wind tunnel is a 2-meter long zero-gradient tunnel, designed to measure wall-pressure fluctuations beneath a turbulent boundary layer. The second section is a divergent tunnel, designed to lower the exhaust flow speed. The side walls and roof of these two sections are equipped with porous liners, so as to limit acoustic reflections. The third section is an exponential horn, also with an acoustic treatment, designed to suppress the acoustical reflections on the exhaust of the tunnel.

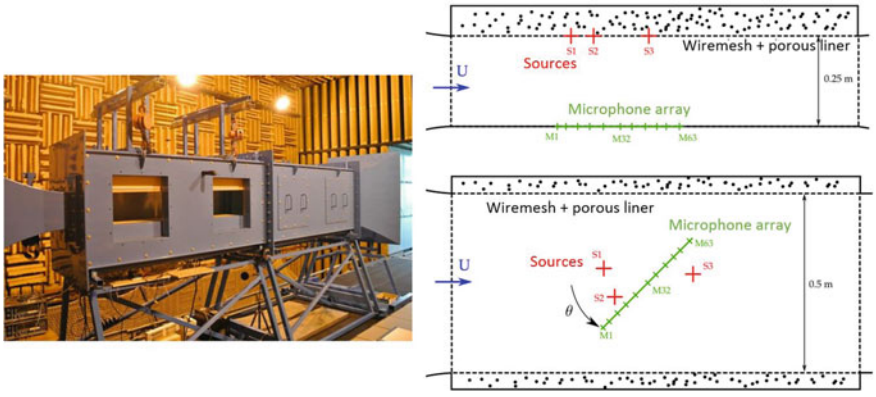

Fig. 1 Left: Picture of the wind tunnel. Right: sketch of the test section, side view (top) and top view (bottom)

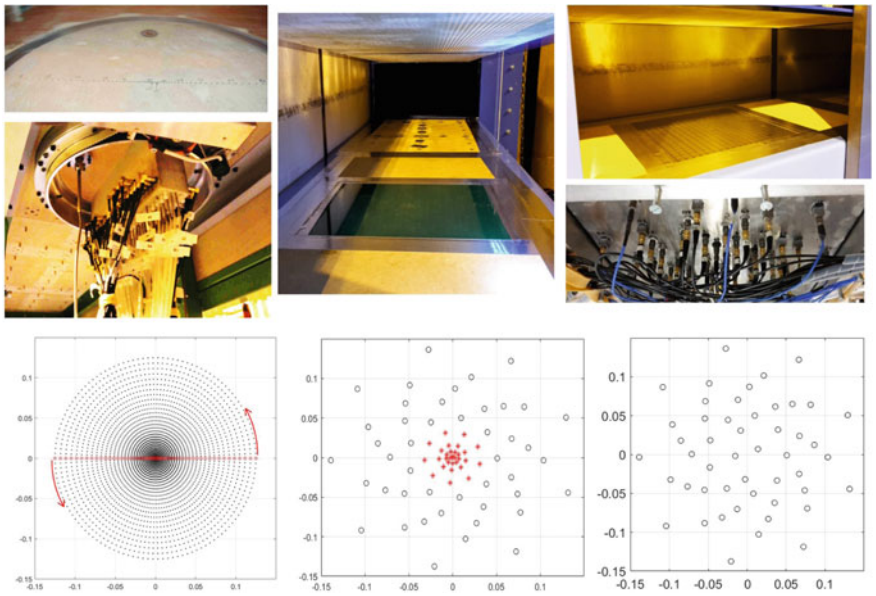

Fig. 2 Top, from left to right: the rotating linear array, the MEMS array, the accelerometer array. Bottom: corresponding sensor layouts

Three acoustic sources are mounted in the roof of the tunnel. Two of them are placed very close to one another, and wired in opposite phase, so as to generate a dipole type source. The third source is placed at about $20cm$ from the two former, and is driven by an independent generator so as to obtain incoherent sources.

Three different wall pressure field measurement devices are successively mounted in the floor of the test section (see Fig. 2):

- ***The rotating linear array***. 63 remote microphone probes are mounted on a rotating disk, following a linear non uniform distribution (see Fig. 2). The smallest distance between two neighbour microphones is 1 mm, and the largest distance is 250 mm. A number of 63 angular positions has been retained for this study, from 0 to 180 degrees. For each measurement configuration, and each angular position of the array, the 63 signals are recorded simultaneously during 60s (sampling frequency 51.2kHz), which makes a total of 3907 measurement positions. However, the full cross spectral matrix is not measured : a cross spectral matrix is computed for each array position, cross spectra are thus measured only between measurement positions belonging to the same acquisition (same array position). It means that considering the whole CSM between the 3907 measured positions, only about 250×10^3 cross spectra are measured, over the $3907^2 \approx 15 \times 10^6$ elements of the full CSM (which means that about 1.5% of the full CSM is actually measured). However, it represents a quite heavy amount of data, that necessitates also a long

measurement time ($60s \times 63$ positions, only considering acquisition duration) for each measurement configuration.

- ***The MEMS array***. 76 digital MEMS microphones are distributed on the backside of a PCB (Printed Circuit Board), with pinholes in front of each sensor. The microphone arrangement has a spiral-like distribution of 9 arms for 45 sensors, classically used for acoustic imaging purposes (see Fig. 2, black o markers). The last 41 microphones (red star markers) are distributed in the central part of the PCB using a denser polar-like distribution, so as to obtain more information about high wavenumbers. Four additional channels are used for 2 accelerometers glued on the backside of the PCB and 2 microphones placed in a small cavity facing the backside of the PCB (the frontside being exposed to the flow). These additional channels are expected to be much less affected by the flow than wall pressure sensors, because of the filtering effect the PCB plate—intending to use them as references to apply referenced-based denoising techniques. All channels are acquired simultaneously, at a sampling frequency of 51.2 kHz, a full 80×80 CSM is measured for each configuration.
- ***The accelerometer array***. 49 accelerometers (weight 5mg each, bandwidth $[0.1 - 10]$kHz) are fixed on a thin aluminium plate (thickness 1mm), with a layout similar to the MEMS array, at least for the 45 spiral subset. Four additional sensors are fixed in the central part (instead of 31 for the MEMS microphone array). The wavenumber filtering effect of the plate implies that high wavenumbers will not excite the plate, it is thus not necessary to have a high density distribution. The excitation pressure field has to be recovered from the plate vibration measured by the 49 accelerometers. The inverse method that is necessary to achieve this goal is described in Sect. 4.4. The 49 accelerations are acquired simultaneously, during 30s (sampling frequency 64kHz), so as to fill-in the whole 49×49 CSM for each measurement configuration. Note that the mass of accelerometers, as well as the cables, have a significant effect on the dynamic behaviour of the plate. This aspect is discussed in Sect. 4.4.

For the three measurement devices, CSMs are estimated using the Welch's method, with a frequency resolution 12 Hz (snapshot length of about 83ms, Hanning window, overlap 66%).

Different measurement configurations are considered, with or without acoustic sources, with or without flow, for different flow speeds. Results presented in this work focus on the 3 following configurations :

- **Configuration A**: no flow, acoustic sources switched on.
- **Configuration T30**: flow speed at 30m/s, acoustic sources switched off.
- **Configuration AT30**: flow speed at 30m/s, acoustic sources switched on.

As a preliminary result, the average autospectra obtained for each array and each configuration are displayed in Fig. 3. Averaged pressure autospectra obtained by the two microphone arrays are very similar. The contribution of the TBL is much stronger on the whole frequency range, the acoustic to TBL ratio lying between -25 dB at low frequencies and -5 dB at high frequencies. The averaged accelerometer

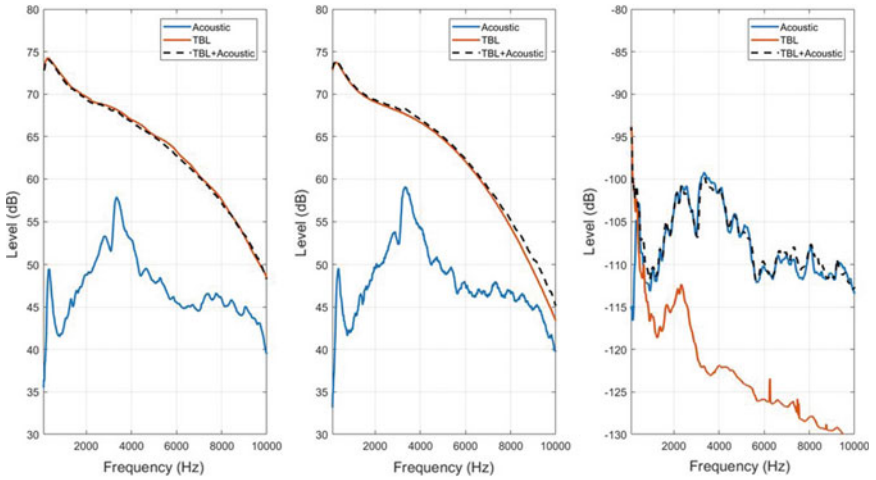

Fig. 3 Averaged autospectra measured by the different arrays for configuration A (solid blue), T30 (solid red) and AT30 (dashed black). From left to right: averaged pressure autospectra of the rotating array, averaged pressure autospectra of the MEMS array, averaged acceleration autospectra of the accelerometer array

autospectrum is, as expected, different from pressure autospectra (measured accelerations resulting from the response of the plate to the pressure field). However, it is interesting to note that for the accelerometer array, the acoustic to TBL ratio is much favourable than for the two former, lying between 0 dB at low frequency and +15 to +20 dB at high frequency. This preliminary result illustrates well the interest of using accelerometers instead of microphones if one is interested in the acoustic part: the gain in terms of SNR can be estimated roughly to 25 dB in this case.

3 Beamforming Processing

Beamforming is a well known processing method for microphone array measurements. Let $\mathbf{p}$ be the complex pressure field measured at a given frequency on the microphone array, and $\mathbf{w_i}$ the theoretical complex contribution of a given wave (plane or spherical), indexed i, at microphone positions. The beamforming output associated to this particular wave is noted $|q_i|^2$, where the complex coefficient q_i minimizes the quantity $\|\mathbf{p} - q_i \mathbf{w_i}\|$. It is the solution of a classical linear regression problem, corresponding to the projection of $\mathbf{p}$ on $\mathbf{w}$; it is equal to

$$q_i = \frac{{\mathbf{w_i}}^H \mathbf{p}}{\|\mathbf{w}\|^2}, \tag{1}$$

where subscript ^{H} stands for the hermitian transpose. $|q_i|^2$ is then represented as a function of wave parameters, either wavenumber (plane wave beamforming) or source position (spherical wave beamforming). In aeroacoustics, considering the random nature of source phenomena, the acoustic pressure field is generally available under the form of an averaged CSM, representing experimental estimations of expected values of auto and cross spectra of microphone signals. That is why Eq. (1) is commonly written in a quadratic form:

$$|q_i|^2 = \frac{\mathbf{w_i}^H \mathbf{S_{pp}} \mathbf{w_i}}{\|\mathbf{w_i}\|^4} \tag{2}$$

Still considering aeroacoustic applications, it is generally recommended to set to zero the diagonal of the CSM to remove the contribution of incoherent noise. The right part of Eq. (2) is in this case not always positive anymore, the resulting squared source amplitude can be set to zero when found negative. In the literature, Eq. (2) is sometimes formulated in a vectorized form,

$$S_{ii} = \frac{\text{Vec}\left(\mathbf{w_i}\mathbf{w_i}^H\right)^H \text{Vec}\left(\mathbf{S_{pp}}\right)}{\|\text{Vec}\left(\mathbf{w_i}\mathbf{w_i}^H\right)\|^2}, \tag{3}$$

where S_{ii} is an estimation of the expected value of $|q_i|^2$ and where Vec $(\mathbf{A})$ stands for a vector resulting from the vertical concatenation of columns of matrix $\mathbf{A}$. Equation (3) is strictly equivalent to (2), however it is interesting to note also the similarity with Eq. (1), where it appears explicitely that S_{ii} is the coefficient of the linear regression operated on quadratic values (minimization of $\|\text{Vec}\left(\mathbf{S_{pp}}\right) - S_{ii}\,\text{Vec}\left(\mathbf{w_i}\mathbf{w_i}^H\right)\|$).

An interesting option considering the vectorized form is that it is possible to skip some terms in the vectorization operation of both $\mathbf{S_{pp}}$ and $\mathbf{w_i}\mathbf{w_i}^H$, for instance autospectra. This leads to a result similar to the diagonal removal operation, yet with a slightly different normalisation term. It is also advised, in order to optimize the computational cost, to skip the whole upper or lower part of vectorized matrices, which are hermitian (the information being redundant). By doing so, only the real part of the resulting value of S_{ii} should be considered. In some situation, the whole CSM $\mathbf{S_{pp}}$ is not available (typically if the measured data result from several array positions recorded successively). In such a case the vectorized form is easily considered only for cross spectral quantities that are actually measured. More generally, it is possible to process only a subset of measured cross spectra, following additional criteria based on geometrical of statistical consideration (this possibility is illustrated in Sect. 4.1).

Some beamforming maps, calculated from measurements described in Sect. 2, are drawn in Fig. 4 for a frequency equal 2100 Hz. Wave functions $\mathbf{w_i}$ are here plane waves determined by their x and y wavenumbers k_{xi} and k_{yi}:

$$\mathbf{w_i} = \exp\left(\imath k_{xi} x\right) \exp\left(\imath k_{yi} y\right). \tag{4}$$

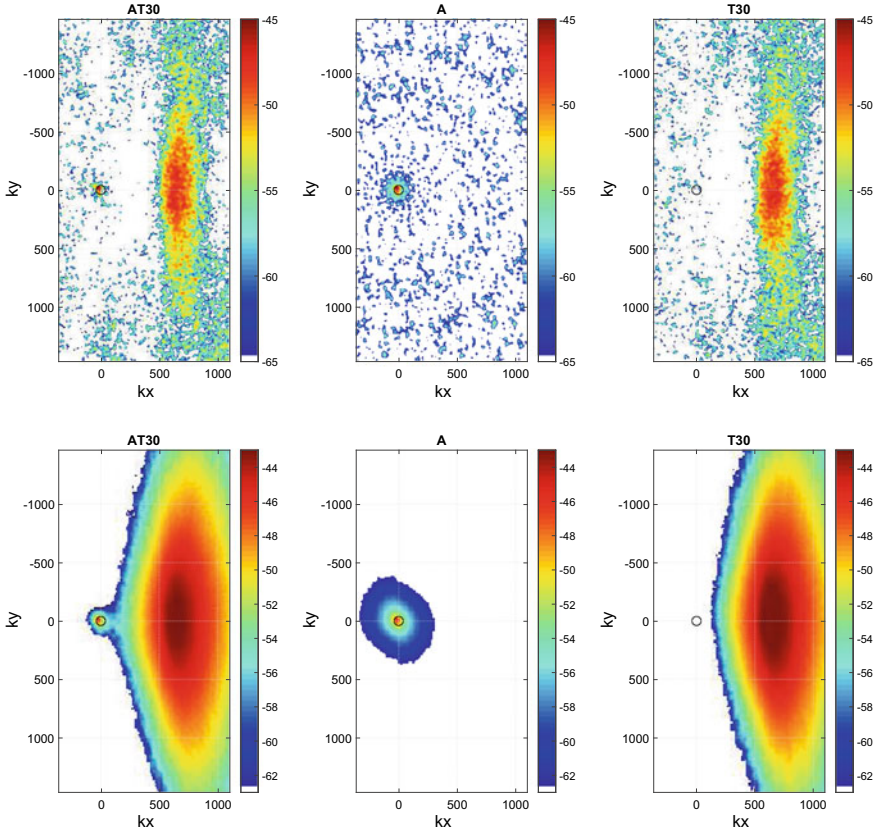

Fig. 4 Plane wave beamforming maps obtained for measurement configurations AT30, A, T30 (left to right) using the MEMS array (top) and the rotating array (bottom) 2100 Hz

Beamforming is calculated using Eq. (3) from averaged CSMs (see Sect. 2 for details), skipping autospectrum entries in the vectorization operation. Results are presented as a function of k_{xi} and k_{yi}, for two different microphone arrays (the MEMS array and the rotating array), and for three measurement configurations with acoustic sources and TBL at $30m/s$ (AT30), with acoustic sources only (A), and with TBL only (T30). Note that for the rotating array, a large proportion of the full CSM is not available because the cross spectra are measured only between measurement points that are acquired simultaneously. Missing entries are however easily skipped using the vectorized form of quadratic beamforming.

Beamforming maps allow the qualitative assessment of the wavenumber content of the measurements. For configuration A, the energy is mainly concentrated inside the acoustic circle ($k_x^2 + k_y^2 < k_a^2$, where $k_a = \omega/c_0$ is the acoustic wavenumber, ratio between the angular frequency and the sound speed). With the TBL (configuration T30), the convective ridge clearly appears around $k_x = k_c$ (where $k_c = \omega/U_c$ is the

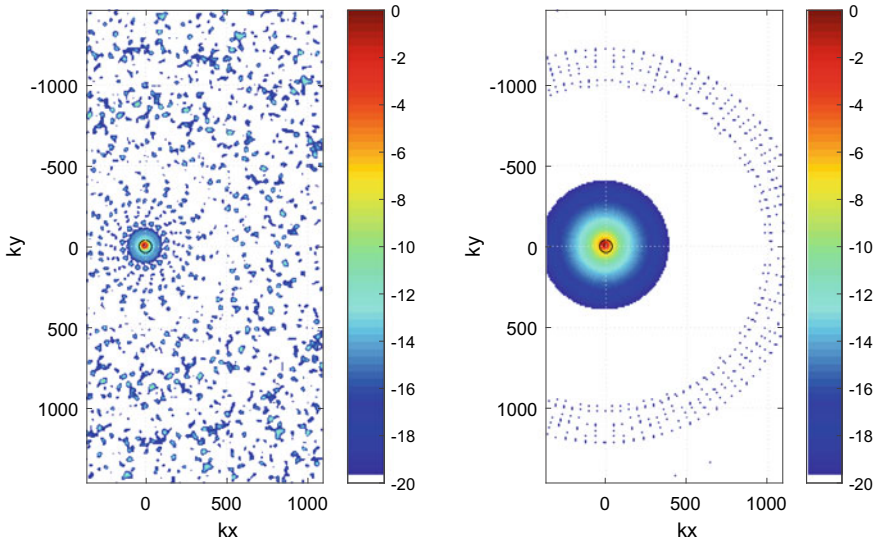

Fig. 5 Point Spread Functions of the rotating (left) and MEMS (right) arrays (2100Hz), for a plane wave with normal incidence ($k_x = k_y = 0$)

convection wavenumber, ratio between the angular frequency and the convective velocity of the flow), and both contributions are observed on the map obtained from configuration AT30. An important point, when comparing results obtained with the two arrays, is that beamforming results strongly depend on the microphone array used for the measurements. Even if main features and levels are similar for the two arrays, it appears for instance that maps obtained from the rotating array are much smoother than maps obtained with the MEMS array. An explanation is simply that the rotating array is much denser, with many more measurement points. Even if a large part of its CSM is not measured, the number of effectively measured cross spectra ($63 \times 62 \times 63/2 = 123 \times 10^6$) for the rotating array is much larger than the number of cross spectra measured with the MEMS array ($76 \times 75/2 = 2850$).

Point Spread functions (PSF) of both arrays are drawn at the same frequency (2100 Hz) in Fig. 5, for a plane wave of normal incidence. Clearly, the PSF of the MEMS array is polluted by a lot of grating lobes caused by the lack of information. It is also seen that the main lobe is larger for the rotating array than for the MEMS array because of the strong heterogeneity of the rotating array microphone density that is much higher at the center of the array.

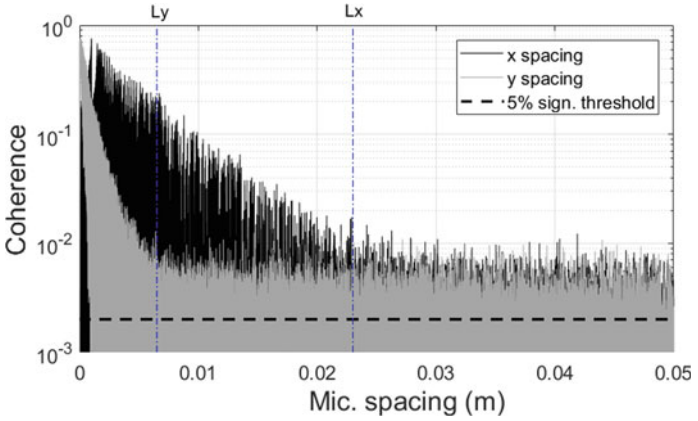

Fig. 6 Coherence between the microphone pairs of the rotating array as a function of the microphone spacing along the x and y direction

4 Separation Approaches

4.1 Space Domain Cross-Spectra Selection

A first separation can be simply operated by splitting cross-spectral data into two subsets based upon geometrical considerations. It is indeed known that the turbulence can have relatively short correlation lengths, and may contribute strongly only to cross spectra of close microphone pairs. This is clearly the case for TBL analytical models like Corcos [8], that predicts an exponential decrease of the coherence as a function of the microphone pair distance. On the other hand, the contribution of an acoustic field is modulated in amplitude only by the source-microphone distance, that may not vary so much as a function of the microphone positions. The coherence of an acoustic field is thus be not too affected by the microphone distance. In order do illustrate these considerations, the coherence between microphone pairs are drawn in Fig. 6 as a function of the x and y spacings, for the configuration AT30 (acoustics and TBL at $30m/s$) for the rotating array. When the distance is close to zero, the exponential decrease predicted by the TBL analytical model is well observed, with a stronger decay rate in the y direction (perpendicular to the flow). Above a given critical length, different on x and y, the coherence reaches a floor level being not dependent on the distance anymore. It can be assumed that above these critical distances noted L_x and L_y, the acoustic field is stronger than the TBL, and inversely below. Thus, considering the vectorized quadratic formulation of beamforming, it is possible to split cross-spectral data into two subsets, a first one satisfying $(\Delta x/L_x)^2 + (\Delta y/L_y)^2 < 1$ (resp. > 1) for which the TBL (resp. acoustics) is the major contribution. Note that this criterion assumes an elliptic form of the contour of the 2D coherence function [9, 10]. Resulting plane wave beamforming maps 2100 Hz are displayed in Fig. 7

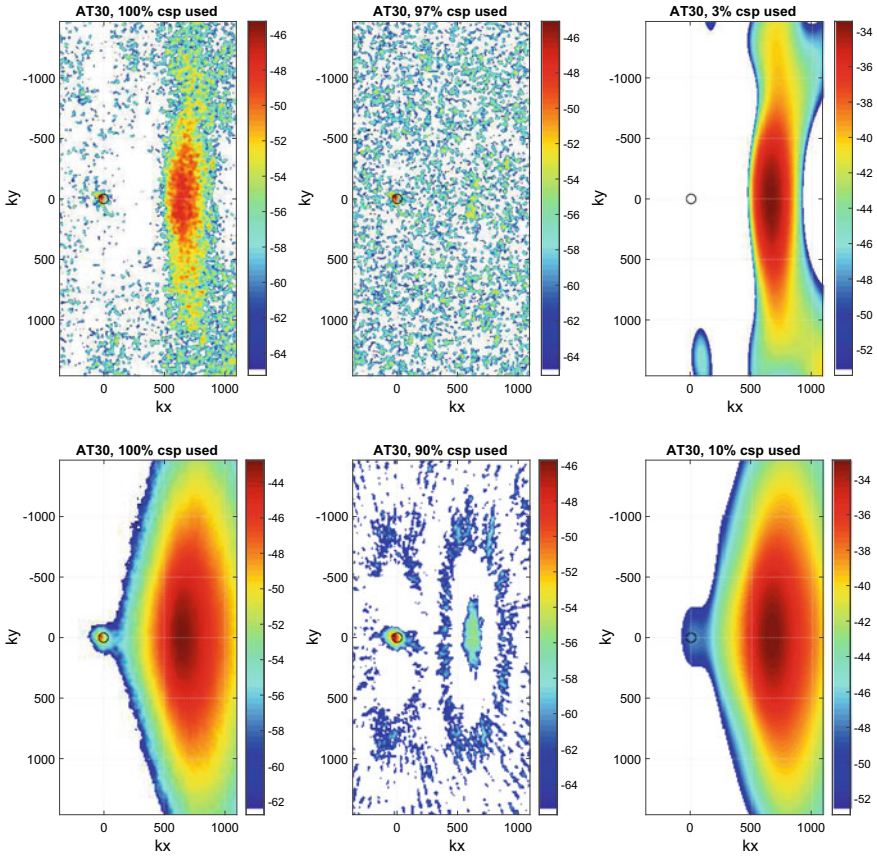

Fig. 7 Plane Wave beamforming maps obtained for the measurement configuration AT30 using the MEMS array (top) and the rotating array (bottom) 2100 Hz. From left to right : using all CSs, using CSs satisfying $(\Delta x/L_x)^2 + (\Delta y/L_y)^2 > 1$, using CSs satisfying $(\Delta x/L_x)^2 + (\Delta y/L_y)^2 < 1$

for the rotating and MEMS arrays. They illustrate well that the information relative to the TBL is mainly carried by cross spectra of close microphones, and that distant microphones are essentially carrying acoustics. However, it is seen that the separation is not perfect: some energy of the convective ridge is still visible on beamforming maps from CSs (Cross Spectra) of distant microphones, and a bit of acoustics is still noticeable on the maps from CSs of close microphones (at least for the rotating array). Another difficulty related to the splitting approach is that it affects the PSFs (Point Spread Functions): maps from CS of close microphones are clearly over-smoothed, while the ones from distant microphones are more strongly polluted by secondary lobes due to the severe undersampling.

4.2 CSM Denoising

An alternative to cross-spectra selection is to process each term of the CSM to extract the contribution of acoustics and TBL parts. In this section the physical structure of the acoustic field is not exploited, this possibility will be inspected in Sect. 4.3 dedicated to wavenumber filtering.

A first possibility illustrated in this section is to separate the two contributions using some reference signals, a priori known to result from one component only and in a sufficient number to represent completely this component. A second possibility is to try to proceed blindly (without any reference), but using a statistical model of the two contributions. The two approaches presented in this section are using full measured CSMs of microphones, they are thus illustrated only with the MEMS array data.

4.2.1 Reference Based Denoising

Considering the problem of separating acoustics and TBL contributions, the reference signals cannot be used to capture the TBL, because of the statistical complexity of the field that would require an infinite number of references. On the other hand, the acoustical field is known to result from the contribution of few components, it is thus possible to represent it with few reference sensors only. The difficulty is to choose these references so as to minimize the contribution of the TBL on it. In the present application, 2 accelerometers are placed on the back side of the PCB supporting the MEMS microphones, and 2 additional microphones are positioned in the acoustic volume below the PCB. These 4 sensors are expected to benefit from the filtering effect of the PCB: in the frequency range of interest, the PCB behaves like a thin plate, filtering out high wavenumbers related to the TBL structures (this phenomenon is discussed more deeply in Sect. 4.4). Let us denote $\mathbf{S_{pp}}$ and $\mathbf{S_{rr}}$ the CSMs of the microphones and the references, respectively, and $\mathbf{S_{pr}}$ the matrix of cross-spectra between microphones and references. The reference microphone CSM is finally calculated by using the following equation

$$\begin{aligned} \mathbf{S_{pp}}^{ref} &= \mathbf{S_{pr}} \left(\mathbf{S_{rr}}\right)^{-1} \mathbf{S_{pr}}^{H}, \\ \mathbf{S_{pp}}^{res} &= \mathbf{S_{pp}} - \mathbf{S_{pp}}^{ref}, \end{aligned} \tag{5}$$

where $\mathbf{S_{pp}}^{ref}$ is the referenced CSM, representing the part of the CSM that is coherent with the references, and where $\mathbf{S_{pp}}^{res}$ is the residual CSM. Note that this approach can simply be interpreted as a generalization of the Coherent Spectrum to the multiple reference case (cf. [7]).

The efficiency of the method is illustrated on plane wave beamforming maps 2100 Hz, for the configuration AT30, in Fig. 8. Qualitatively, results correspond quite nicely to maps obtained from measurements T30 and A (see Fig. 4). Contrary

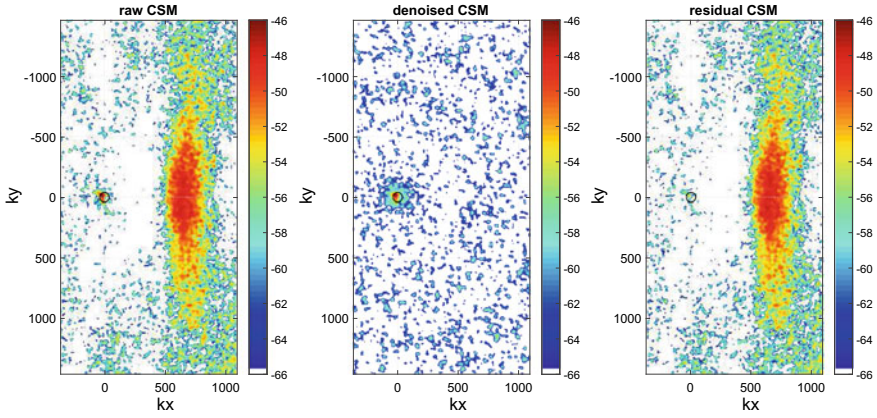

Fig. 8 Plane Wave beamforming maps obtained for the measurement configuration AT30 using the MEMS array 2100 Hz. From Left to right : measured CSM ($\mathbf{S_{pp}}$), reference based denoised CSM ($\mathbf{S_{pp}}^{ref}$), residual CSM ($\mathbf{S_{pp}}^{res}$)

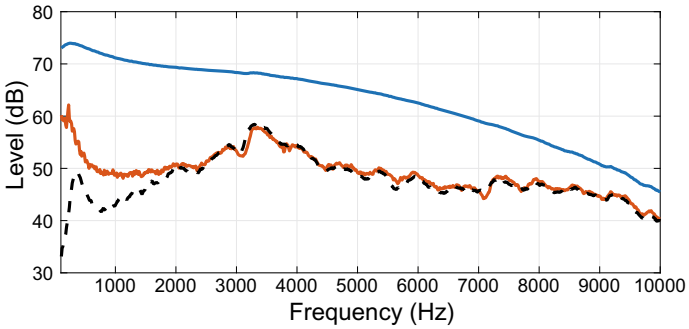

Fig. 9 MEMS array averaged Autospectra. Measurement configurations AT30 (solid blue), A (dashed black) and referenced based denoised AT30 (solid red)

to the results of the previous section using the basic cross-spectra selection approach, the PSF is here not affected by the separation method.

The effect of the referenced denoising approach can be also illustrated on averaged autospectra (see Fig. 9). Denoised autospectra of configuration AT30 are compared to autospectra measured with acoustics only (configuation A). Note that the contribution of acoustic sources is affected by the presence of the convection, so that perfectly denoised data measured with flow should not fit exactly measurements without flow. However, considering the relatively low convection velocity and short distance between microphones and sources, the effect of the presence of the flow is expected to be limited. As a matter of fact, the averaged denoised autospectrum (config. AT30) is very close to the averaged autospectrum without flow (config. A) above 2kHz. Below 2 kHz, the referenced denoising approach performs less well,

a possible reason being the very low SNR that goes below −20 dB. Better results may have been achieved using longer measurements to get a better convergence of statistical estimates.

4.2.2 Blind Extraction of the Acoustical Contribution by the Use of Stochastic Modeling

The Probabilistic Factor Analysis (PFA) is used in many fields to capture the underlying correlation structures in a dataset. Using the fact that the acoustical and TBL pressure fields have different correlation structures, PFA can be used to separate them. Let us assume that the measured CSM results from the sum of three major contributions, at each frequency:

1. The acoustical field produced by a small number of sources (compared to the number of sensors), with a correlation length higher than the average sensor interspacing. As explained in the previous sections, the acoustical measured spectrum can thus be statistically described by a few latent variables, at the jth snapshot:

$$\mathbf{a}_j = \mathbf{L}\mathbf{c}_j, \qquad j = 1, \ldots, N_s, \tag{6}$$

   where $\mathbf{L}$ is a $M \times K$ complex matrix that mixes the $K \leq M$ latent factor vectors $\mathbf{c}_j$. This leads to a low-rank acoustical CSM, averaged over the snapshots:

$$\mathbf{S_{aa}} = \mathbf{L}\mathbf{S_{cc}}\mathbf{L}^H. \tag{7}$$

2. The TBL noise, which has a known correlation structure given by a Corcos-like model [8], that can also be expressed using latent variables:

$$\mathbf{n}_j = \mathbf{P}\boldsymbol{\nu}_j, \qquad j = 1, \ldots, N_s, \tag{8}$$

   where $\mathbf{P} = \lceil \mathbf{p} \rfloor$ is a diagonal matrix containing the complex spectrum amplitudes $\mathbf{p} \in \mathbb{C}^M$. The variance of the latent variables $\nu_j \in \mathbb{C}^M$ is supposed to have a Corcos-like correlation shape. The noise cross-spectra between the k^{th} and l^{th} microphones with coordinates (x_k, y_k) and (x_l, y_l) are :

$$\mathbb{E}\{n_k n_l^*\} = p_k p_l^* \mathrm{e}^{-\frac{2\pi f}{U_c}\left(\frac{|x_k - x_l|}{\alpha_x} + \frac{|y_k - y_l|}{\alpha_y} - \imath(x_k - x_l)\right)}, \qquad k, l = 1, \ldots, M, \tag{9}$$

   where α_x and α_y are the longitudinal and transverse coherence-loss and U_c is the vortex convection velocity. This model is not totally in accordance with the Corcos' one since these parameters are allowed to change with frequencies as well as the power of the autospectra.
3. All the other random contributions, not carried by the previous terms, which are supposed to be uncorrelated over the microphones (e.g. ambient or electronic noise), tend to have a diagonal matrix :

$$\mathbf{S}_\epsilon = \lceil \epsilon^2 \rfloor. \tag{10}$$

The proposed denoising is finally an inference problem that aims at fitting the measured CSM with the sum of these contributions :

$$\mathbf{S_{pp}} \approx \mathbf{S_{aa}} + \mathbf{S_{nn}} + \mathbf{S}_\epsilon \tag{11}$$

$$= \mathbf{L}\mathbf{S_{cc}}\mathbf{L}^H + \mathbf{P}\mathbf{S}_{\nu\nu}\mathbf{P}^H + \lceil \epsilon^2 \rfloor. \tag{12}$$

A Bayesian approach is adopted in order to estimate all the unknowns in Eq. (12) that best fit the data, by maximizing the posterior density function (PDF) :

$$\mathbf{L}^\star, \mathbf{S_{cc}}^\star, \mathbf{p}^\star, \mathbf{S}_{\nu\nu}{}^\star, \boldsymbol{\epsilon}^{2\star} = \text{argmax}\left[\mathbf{L}, \mathbf{S_{cc}}, \mathbf{p}, \mathbf{S}_{\nu\nu}, \boldsymbol{\epsilon}^2 \mid \mathbf{S_{pp}}\right] \tag{13}$$

where $[x \mid y]$ stands for the conditional PDF of x given y. As the PDF in Eq. (13) has no closed-form, the optimization problem is solved numerically using the Gibbs sampler, a commonly used Monte Carlo Markov Chain algorithm [11]. The pseudo-code for this procedure is given in Algorithm 1. After a thousand iterations, the returned estimates are the mean of the last 500 draws of the Gibbs sampler.

Algorithm 1 PFA solved with the Gibbs sampler

Initialization $\mathbf{L}_0$, $\mathbf{S}_{cc_0}$, $\mathbf{p}_0, \mathbf{S}_{\nu\nu_0}, \boldsymbol{\epsilon}_0^2$ and hyperparameters
Require: $\mathbf{S}_{pp}, U_c, \alpha_x, \alpha_y$
  for $j = 1, \ldots, N_{\text{run}}$ **do**
    for $\theta = \mathbf{L}, \mathbf{S}_{cc}, \mathbf{p}, \mathbf{S}_{\nu\nu}, \boldsymbol{\epsilon}^2$ and hyperparameters **do**
      sample θ following $\left[\theta \mid \infty_{-\theta}\right]$
    end for
  end for
  return $\mathbf{L}^\star, \mathbf{S}^\star_{cc}, \mathbf{p}^\star, \mathbf{S}^\star_{\nu\nu}, \boldsymbol{\epsilon}^{2\star}$

In the Bayesian approaches, all the unknowns are assigned a prior PDF, as well as the parameters (called hyperparameters) of these priors. A complex Gaussian prior is used for all the parameters, the variance of which follows itself a flat inverse gamma law. These priors and hyperpriors are gathered in Tab. 1. The parameter ν, which describes the correlation structure of the TBL noise over the antenna is also Gaussian, with a Corcos-like variance, as given by $\mathbb{E}\{\nu\nu^H\}$ in Eq. (9). This variance is expressed as a function of three TBL parameters (U_c, α_x, α_y). They could be inferred along with all the other unknowns of the model, but a simpler approach is to estimate them directly from the measured CSM, before applying the PFA denoising. This can be done by a non-linear least mean square procedure, as previously done in Ref. [3].

Previous applications of PFA for denoising have shown promising results in the medium frequency range [12, 13, 24], with a lack of performance in the low frequency domain, where the TBL noise is highly correlated over the microphone. This problem is here overcome by taking into account a TBL noise contribution in the inference problem. The choice of the TBL model (Corcos here) is of course important, it has

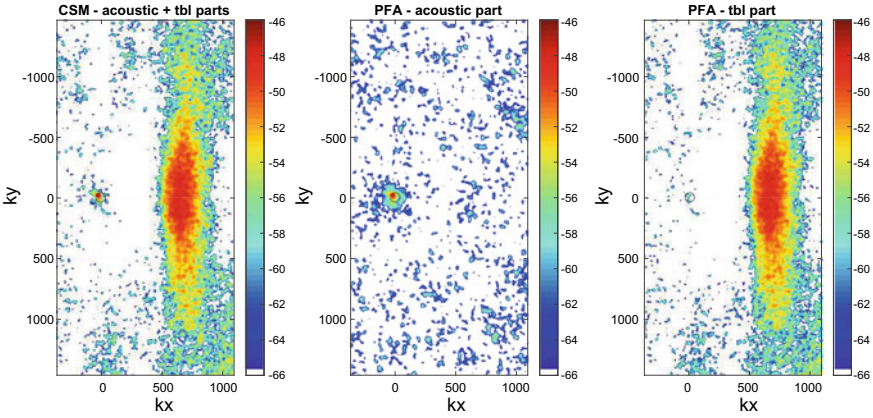

Fig. 10 Plane Wave beamforming maps obtained for the measurement configuration AT30 using the MEMS array 2100 Hz. Blind extration of acoustic and TBL parts using PFA. From left to right: Acoustics + TBL, Acoustics only, TBL only

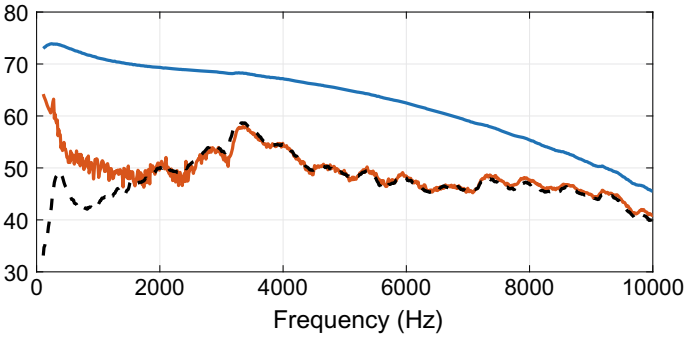

Fig. 11 MEMS array averaged Autospectra. Measurement configurations AT30 (solid blue), A (dashed black) and PFA based denoising AT30 (solid red)

to be pertinent in regard of the application case. However, the CSM associated to the TBL contribution is infered from the data, which gives a certain flexibility in order to update the model so as to make it fit to measurements. The analysis of this infered CSM is also a way to validate a posteriori the chosen model [25].

Plane wave beamforming and averaged autospectra are plotted in Figs. 10 and 11. PFA provides the same amount of denoising than the reference-based approach, but without requiring any extra noise-free measurements.

Table 1 Prior PDF assigned to each parameter and hyperparameter of the PFA model. $\mathcal{N}_{\mathbb{C}}$ stands for the multivariate complex normal distribution and $\mathcal{IG}$ is the inverse-gamma distribution. The input parameters U_c, α_x and α_y are given by a least mean squares procedure

Priors	Hyper-priors	Inputs
$[\mathbf{L}] = \mathcal{N}_{\mathbb{C}}(\mathbf{0}, \mathbf{I}_{MK}/K)$		
$[\mathbf{c}] = \mathcal{N}_{\mathbb{C}}(\mathbf{0}, \lceil {\boldsymbol{\sigma_c}}^2 \rfloor)$	$[{\boldsymbol{\sigma_c}}^2] = \mathcal{IG}(\mathbf{a}_c, \mathbf{b}_c)$	$\mathbf{a}_c, \mathbf{b}_c = 10^{-3}$
$[\mathbf{p}] = \mathcal{N}_{\mathbb{C}}(\boldsymbol{\mu_p}, \lceil {\boldsymbol{\sigma_p}}^2 \rfloor)$	$[{\boldsymbol{\sigma_p}}^2] = \mathcal{IG}(\mathbf{a}_p, \mathbf{b}_p)$	$\boldsymbol{\mu_p} = \text{Trace}(\mathbf{S_{yy}})/M$ and $\mathbf{a}_p, \mathbf{b}_p = 10^{-3}$
$[\epsilon^2] = \mathcal{IG}(\mathbf{a}_\epsilon, \mathbf{b}_\epsilon)$		$\mathbf{a}_\epsilon, \mathbf{b}_\epsilon = 10^{-3}$
$[\nu] = \mathcal{N}_{\mathbb{C}}\left(\mathbf{0}, {\boldsymbol{\sigma_\nu}}^2(U_c, \alpha_x, \alpha_y)\right)$		U_c, α_x, α_y

4.3 Wavenumber Filtering

Wavenumber filtering is applied in this work only for the case of the rotating linear array, that offers the best spatial resolution. In a first section, basic principles are given for a 1D processing, and the extension to 2D is exposed in a second section.

4.3.1 One-Dimensionnal Approach

For a given angular position of the line array, the one-dimensionnal streamwise wavenumber-frequency spectrum can be directly computed by discretizing the following Fourier integral:

$$\Phi_{pp}(k_1, \omega) = \frac{1}{(2\pi)} \int S_{ij}(\xi_1, \omega) e^{-ik_1\xi_1} d\xi_1$$

where k_1 is the streamwise wavenumber. Note that the wall-pressure field is assumed to exhibit homogeneous properties over the microphone array, the cross spectrum $S_{ij}(\xi_1, \omega)$ is assumed to depend spatially only on the microphone spacing ξ_1. In practice, the number of elements of the CSM ($63 \times 63 = 3969$) can be reduced down to approximately 500 by considering the symmetry properties of the cross-spectral matrix, and the symmetry of the line array (see Fig. 12).

The one-dimensionnal wavenumber spectrum, obtained beneath a turbulent boundary layer for increasing flow speed, with additionnal sound sources, are plotted in Fig. 13. Each plot is obtained using the same level of acoustic sound source, only the flow speed is varied from 0 to 50 m/s. At a given frequency f_0, the wavenumber spectrum is characterized by two contributions [16, 18–20]: an acoustic contribution around k_a, and an hydrodynamic contribution due to the convection of wall-bounded turbulence, located around k_c. These two contributions are clearly visible in the spec-

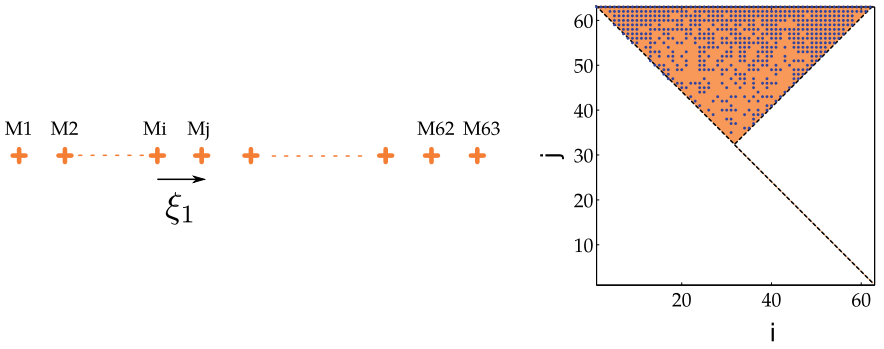

Fig. 12 One-dimensionnal case: extraction of the cross-spectral matrix with a line array of 63 microphones

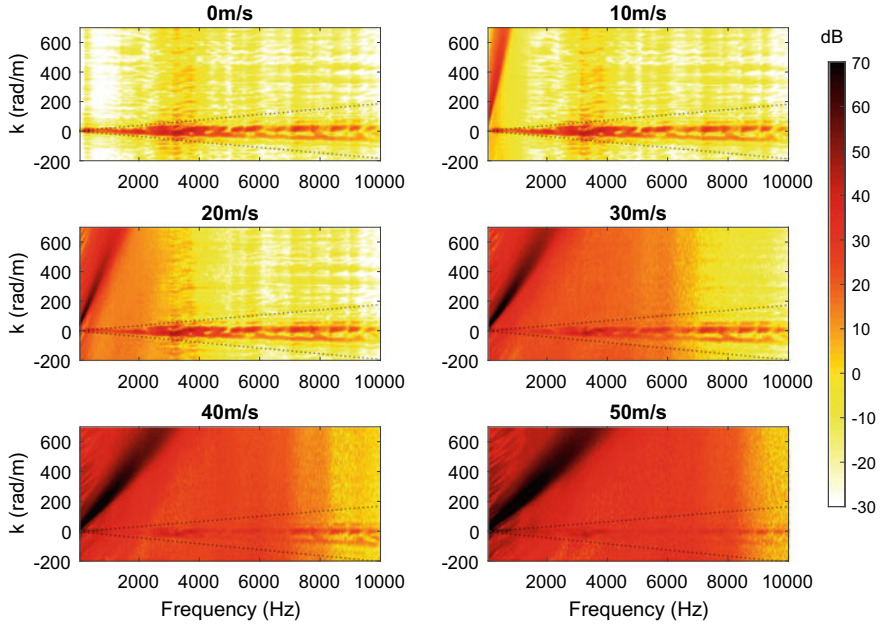

Fig. 13 One-dimensionnal wavenumber spectra beneath a turbulent boundary layer for increasing flow speed from 0 to 50 m/s, with additional sound sources

tra from Fig. 13. Furthermore, the hydrodynamic contribution can be observed by the change in its slope as the flow speed is increased.

If the frequency is higher 500 Hz approximately, the wavenumber representation allows for an explicit separation between those two components. This filtering is possible by integrating all wavenumber components from the acoustic region as

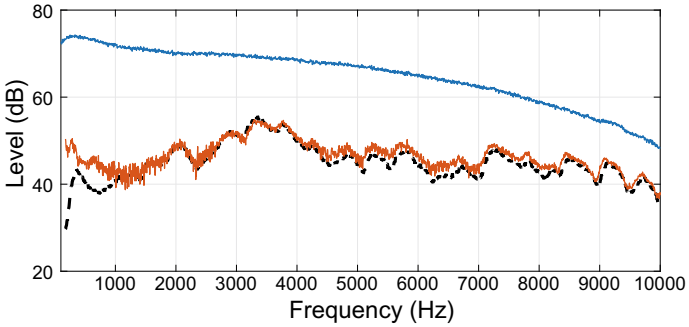

Fig. 14 Rotating linear array Autospectra (streamwise direction) for measurement configuration AT30 with (solid red) and without (solid blue) wavenumber filtering, and for configuration A (dashed black)

$$S_{\mathrm{ii}}^{\mathrm{ac}}(\omega) = \int_{-(k0+\Delta k/2)}^{k0+\Delta k/2} \Phi_{pp}(k_1, \omega)\mathrm{d}k_1. \tag{14}$$

In this example, the spatial filtering enables the direct extraction of the acoustic spectrum apart from the hydrodynamic pressure, without any assumption on the pressure field. Note that at lower frequencies (500 Hz), the separation is not possible due to overlapping of the two contributions in the wavenumber domain. The spectral broadening, due to the limited spatial extent of the windows, is accounted for by adding the wavenumber resolution Δk in the integration limits of Eq. (14). This approach has also been validated in the context of turbomachinery noise using a line array of MEMS microphones [22].

The resulting acoustic spectrum is plotted in red in Fig. 14 for a flow speed of 30m/s, the acoustic spectrum obtained without flow is recalled (in dashed black). The acoustic spectrum is recovered with an agreement within ± 1 dB above 1kHz.

4.3.2 Two-Dimensionnal Approach

The same procedure as described in Sect. 4.3.1 can be applied on a two-dimensionnal basis using multiple angular positions of the array [3, 21]. In that case, only cross-spectral densities of the same angular positions are computed. All spatial separations $\mathbf{x}_i$ can then be achieved by combining all the angular positions of the array (see Fig. 15).

The wavevector—frequency spectrum is then directly computed by discretizing the following Fourier integral,

$$\Phi_{pp}(\mathbf{k}, \omega) = \frac{1}{(2\pi)^2} \iint R_{pp}(\mathbf{r}, \omega) e^{-i\mathbf{k}\cdot\mathbf{r}} d\mathbf{r}.$$

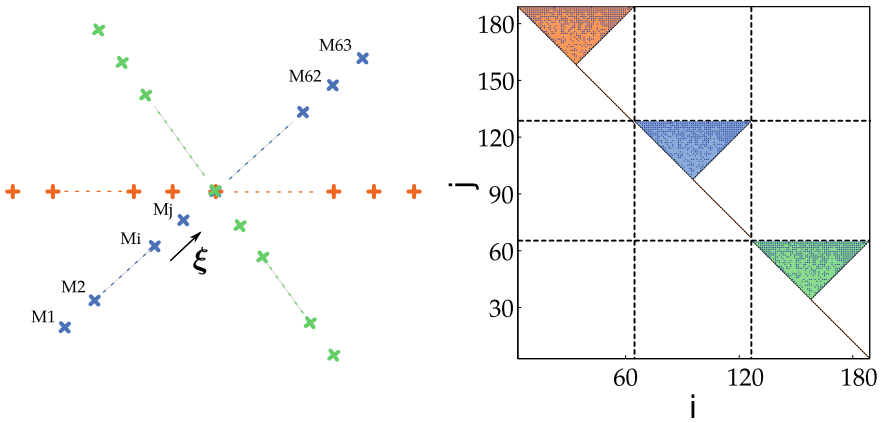

Fig. 15 Two-dimensionnal case : extraction of the cross-spectral matrix with a line array of 63 microphones and 3 angular positions, for example

The transducer locations are denoted by $\mathbf{r}_{nm} = (d_n, \theta_m)$ in polar coordinates. For a given angle of the linear antenna, all the cross-spectra between the different microphones are available since the pressure signals are simultaneously recorded over the $n_p = 63$ probes. The irregular radial distribution of the microphones is presented in the next section. A regular polar distribution $\theta_m = m\Delta\theta$ has been chosen with $\Delta\theta = \pi/m_\theta$ and $m_\theta = 63$. In a straightforward approach, the wavenumber-frequency spectrum can be computed as

$$\Phi_{pp}(\mathbf{k}, \omega) = \frac{1}{(2\pi)^2} \sum_{m=0}^{m_\theta - 1} \sum_{n=0}^{n_r} R_{pp}(\mathbf{r}_{nm}, \omega) e^{-i(k_1 d_n \cos\theta_m + k_2 d_n \sin\theta_m)} ds_n$$

over a given grid $\mathbf{k} = (k_1, k_2)$. In this particular and simple case, the central microphone corresponds to $d_0 = 0$, the location of a half of the linear antenna is defined by the radial distance d_n with $1 \leq n \leq 31$ and $n_r = (n_p + 1)/2$. The corresponding elementary area can be expressed as

$$ds_n = \pi(l_{n+1}^2 - l_n^2) \times \frac{\Delta\theta}{2\pi}, \qquad l_n = \frac{d_n + d_{n+1}}{2}.$$

The two-dimensionnal wavenumber spectra, obtained at $30\,\mathrm{ms}^{-1}$, with additional sound sources, are plotted in Fig. 16 at 1, 2 and 10 kHz, for the same flow speed and the same level of acoustic sound source. These two contributions are clearly visible in the spectra from Fig. 16.

The acoustic spectrum is then obtained through the two-dimensionnal integration of the wavenumber components within the acoustic domain. The resulting spectrum is plotted in Fig. 17 and compared to the one-point spectra obtained with or without flow, using the same acoustic source.

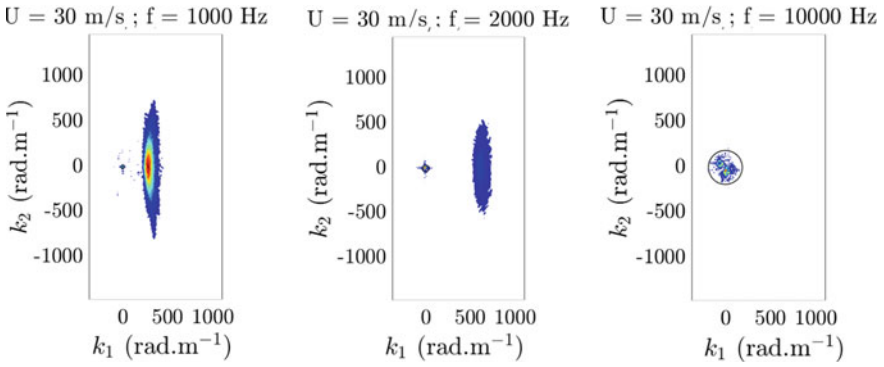

Fig. 16 Two-dimensionnal wavevector spectra beneath a turbulent boundary layer at 30 m/s, with additionnal sound sources, at 1 kHz (left), 2 kHz (center) and 10 kHz (right). Solid black line: acoustic region limit defined as $|\mathbf{k}| < k_0$

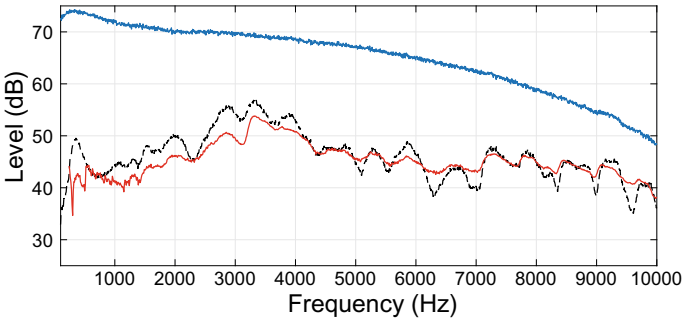

Fig. 17 Frequency spectra obtained by integrating the wavenumber components from the two-dimensionnal wavenumber spectra (Fig. 16). Integration on the whole wavenumber plane (blue), in the acoustic region (red), and the spectrum without flow (black)

4.4 Physical Filtering with the Accelerometer Array

The interest of using accelerometer measurements is that the thin structure on which sensors are fixed will be more efficiently excited by acoustic waves than by the turbulent structures of the flow, due to the characteristic lengths of phenomena. A pressure field will excite efficiently the plate-like structure if its wavenumber content is lower than the natural flexural wavenumber of the structure. The convective ridge of a TBL excitation, at relatively low flow speeds, goes rapidly above the flexural wavenumber when increasing the frequency, while the acoustic wavenumber stays below up to the critical frequency. In the present work, a thin aluminium plate of 1mm thickness is used, its critical frequency is about 12 kHz. This means that the whole wavenumber content lying in the acoustic circle is efficiently transmitted to the plate up to 12 kHz.

The idea to use accelerometers to access to the acoustic part of an excitation field is not new, it has been investigated in several previous studies [5, 6]. In these works, an analytical model of the structure is used, together with a local method to identify the pressure field. This method suffers however from two drawbacks, firstly the added mass and rotation inertia of the sensors is not taken into account in the method, which can be a limitation when using a lot of sensors and a light structure, as it is the case in this work. A second drawback is that the method requires the use of a regular sampling mesh respecting the Shannon's rule (two sensors at least by natural wavelength of the structure). This would require too much sensors to cover the frequency range of interest in this work (up to 10kHz). Another option is investigated in the present work: the structure, equipped with accelerometers, is characterized experimentally so as to avoid model and sampling issues. A regular excitation mesh is drawn on the frontside of the plate (the side exposed to the pressure excitation). Transfer functions between forces at excitation points and accelerations are measured using an impact hammer. The use of a spatial sampling of 15mm guarantees to respect the Shannon's limit for an acoustic wave up to 10kHz. The dimension of the plate being 30 cm$\times$ 30 cm, a total of 400 excitation points have to be considered, which requires a significant measurement effort. This preliminary experimental stage can be seen as a calibration of a 2D sensor constituted by the plate with its boundary conditions, and embedding the accelerometers. Note that a numerical model of the structure with sensors and cables could have been an option, with limitation related to the difficulty to correctly take into account boundary conditions and cables effects in a frequency range up to 10 kHz. The experimental option has been chosen so as to limit as much as possible bias effects that would inevitably be introduced by the use of a numerical model.

The identification of the load distribution requires to inverse a linear system with 400 unknowns (excitation dofs) and 49 equations (number of accelerometers). This inversion is underdetermined, and requires additional a priori information so as to define a unique solution. This additional information is in this work that the pressure field should be expressed in the specific basis of spherical waves generated by point sources situated at a specific distance of the array (25cm in this work, corresponding to the height of the wind tunnel in which source are located). Finally, the whole processing can be written as follows

$$\mathbf{S_{pp}} = (\Delta S)^{-2}\mathbf{G_2}\,(\mathbf{HG_1})^{+}\,\mathbf{S_{aa}}\,(\mathbf{HG_1})^{+H}\,\mathbf{G_2}^{H}$$

where $\mathbf{G_1}$ stands for the spherical propagator through the flow from the source plane to excitation points on the plate (analytical), $\mathbf{S_{aa}}$ is the CSM of acceleration acquired during the measurement configurations, $\mathbf{H}$ is the preliminarily measured transfer matrix between excitation points and accelerometers, and ΔS the square of the discretization step of the excitation grid. $\mathbf{G_2}$ is a second analytical acoustic transfer matrix from sources to the plate, to be defined as a function of the points where one wants to generate the pressure field. In this work, the pressure field is assessed at points corresponding to the microphone layout of the MEMS array, so as to compare results in the wavenumber domain with the same PSFs. $\mathbf{A}^{+}$ denotes the regularized pseudo-inverse of $\mathbf{A}$, which is obtained using bayesian approaches (see [23]

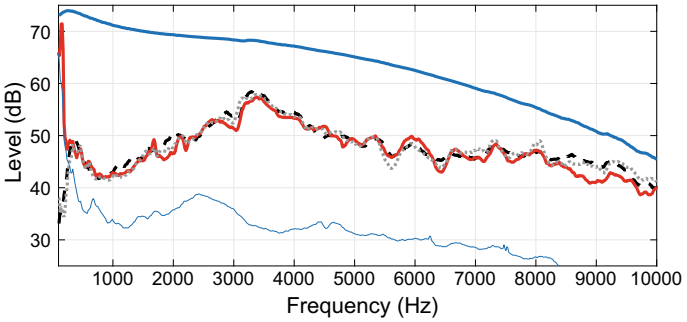

Fig. 18 Identified average spectrum from the accelerometer array at the microphone positions of the MEMS array for measurement configuration AT30 (solid red), A (dotted gray), and T30(solid thin blue). The average pressure spectrum measured with the MEMS array is recalled for comparison for the same configurations AT30 (solid blue) and A (dashed black)

for details). The averaged pressure autospectrum identified with the accelerometer array is shown in Fig. 18, for configuration A and AT30, together with the one directly measured with the MEMS microphone array. A first observation is that the inverse procedure recovering pressures from accelerations seems to perform quite well from a quantitative point of view. The difference between the recovered pressures (configurations A or AT30) and the directly measured ones (configuration A) lays between $\pm$ 1dB 500, 5000 Hz (even 100 Hz for the configuration without flow), and does not exceed ± 2 to 3dB up to 10kHz. Clearly, the pressure recovered from the accelerometer array is not much sensitive to the presence of the flow: 200 Hz autospectra obtained from configuration with or without the flow are very similar. The pressure autospectrum recovered for the configuration T30 (without acoustics) is also drawn in Fig. 18 so as to estimate the denoising dynamic. For the whole frequency range 200 Hz, the reduction as compared to the TBL pressure level measured by microphones is between 30 and 40 dB, which illustrates well the denoising potential of this approach—at least for the studied flow speed.

Beamforming maps are displayed in Fig. 19 at a frequency 2100 Hz for the pressure field identified with the accelerometer, configurations AT30, A and T30. These results can be directly compared to the ones in Fig. 4 (top figures corresponding to the MEMS array). It is verified qualitatively that the wavenumber content of the identified pressure field is not affected by the presence of the flow: the convective peak is thus efficiently filtered out by the structure for the configurations AT30 (center) and T30 (right). Note that color scales are intentionally left the same for the three maps, so as to highlight the very low level of energy in the map obtained from configuration T30 (without acoustics).

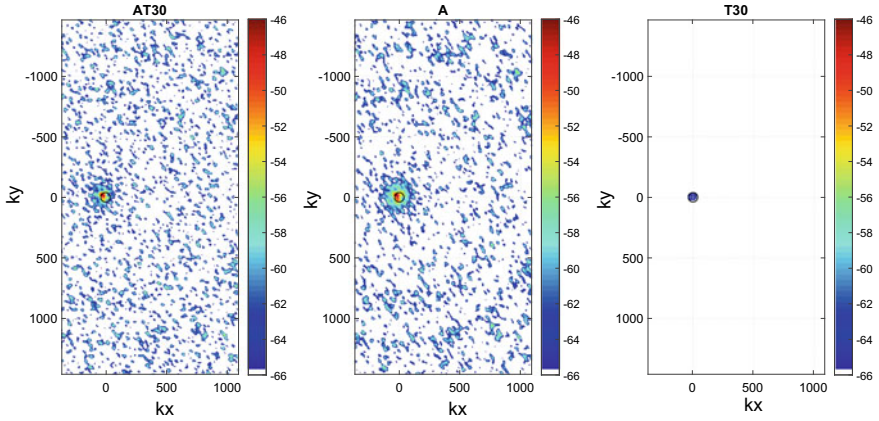

Fig. 19 Plane Wave beamforming maps for the pressure field obtained with the accelerometer array at the MEMS microphone positions, 2100Hz. From left to right : Acoustics + TBL, Acoustics only, TBL only

5 Conclusion

In this chapter, different experimental measurement devices and associated post processing techniques have been presented, aiming at separating acoustic and flow contributions in a pressure field. All approaches have been applied to the same measurement configuration, so as to highlight objectively advantages and drawbacks of each. From a general point of view, the methods can be classified into two categories, depending on the hypothesis formulated on either the statistical or geometrical properties of the signals. The former can be implemented with or without reference signals, the latter results from a space domain filtering approach, either based on a high spatial sampling or using structural filtering. Of course, it could be possible to combine the different methods to eventually achieve an optimal separation, this option is left for future work. Another perspective of this work is to find indicators so as to assess objectively the quality of the separation.

Acknowledgements This work was performed within the framework of the Labex CeLyA of Université de Lyon, operated by the French National Research Agency (ANR-10-LABX-0060/ANR-16-IDEX-0005), and of the Clean Sky 2 Joint Undertaking, European Union (EU), Horizon 2020, CS2-RIA, ADAPT project, Grant agreement no 754881.

References

1. Robert P. Dougherty. *Beamforming In Acoustic Testing*, pages 62–97. Springer Berlin Heidelberg, Berlin, Heidelberg, 2002
2. Alice Dinsenmeyer, Jérôme Antoni, Quentin Leclère, and Antonio Pereira. On The Denoising Of Cross-spectral Matrices For (Aero)Acoustic Applications. In *BeBec 7th Berlin Beamforming Conference*, Berlin, Germany, 2018
3. Blandine Arguillat, Denis Ricot, Christophe Bailly, Gilles Robert, Measured wavenumber Frequency spectrum associated with acoustic and aerodynamic wall pressure fluctuations. The Journal of the Acoustical Society of America **128**(4), 1647–1655 (2010)
4. Michel Roger. Microphone Measurements in Aeroacoustic Installations. In *AVT-287 STO AVT-VKI Lecture Series held at the von Karman Institute*, Rhode St. Genese, Belgium, 2017
5. D. Lecoq, C. Pézerat, J.-H. Thomas, W.P. Bi, Extraction of the acoustic component of a turbulent flow exciting a plate by inverting the vibration problem. Journal of Sound and Vibration **333**(12), 2505–2519 (2014)
6. Q. Leclère, E. Chéron, A. Pereira, C. Picard, and P. Souchotte. Design and experimental validation of an array of accelerometers for in-flow acoustic beamforming applications. In *Proceedings of the 22nd AIAA/CEAS Aeroacoustics Conference*, Lyon, France, 2016
7. Q. Leclère, J. Antoni, E. Julliard, A. Pintado-Peno, *Consideration of estimation error in multiple coherence approaches: application to the inside/outside coherence analysis of aircraft flight tests In Proceedings of ISMA 2018* (Belgium, Leuven, 2018)
8. G.M. Corcos, Resolution of pressure in turbulence. The Journal of the Acoustical Society of America **35**(2), 192–199 (1963)
9. Robert H. Mellen, On modeling convective turbulence. Journal of the Acoustical Society of America **88**(6), 2891–2893 (1990)
10. Bart A. Singer. Turbulent wall-pressure fluctuations: New model for off-axis cross-spectral density. Technical Report CR 198297, NASA, 1996
11. Andrew Gelman, *John B Carlin, Hal S Stern, David B Dunson, Aki Vehtari, and Donald B Rubin* (Chapman and Hall/CRC, Bayesian data analysis, 2013)
12. Alice Dinsenmeyer, Quentin Leclère, Jérôme Antoni, and Emmanuel Julliard. Comparison of microphone array denoising techniques and application to flight test measurements. In *25th AIAA/CEAS Aeroacoustics Conference*, page 2744, 2019
13. Pieter Sijtsma, Alice Dinsenmeyer, Jérôme Antoni, and Quentin Leclère. Beamforming and other methods for denoising microphone array data. In *25th AIAA/CEAS Aeroacoustics Conference*, page 2653, 2019
14. Howard H Schloemer. Effects of pressure gradients on turbulent boundary-layer wall-pressure fluctuations. *The Journal of the Acoustical Society of America*, 40(5): 1254, 1966
15. Theodore M Farabee and Mario J Casarella. Spectral features of wall pressure fluctuations beneath turbulent boundary layers. *Physics of Fluids A: Fluid Dynamics*, 3(10): 2410–2420, 1991
16. B.M. Abraham, W.L. Keith, Direct measurements of turbulent boundary layer wall pressure wavenumber-frequency spectra. J. Fluid Eng. **120**, 29–39 (1998)
17. J.S. Bendat, A.G. Piersol, *Random data, analysis and measurement procedures, New York* (John Wiley & Sons, New York, 1986)
18. Blake, W. K., 1986, Essentials of turbulent wall-pressure fluctuations, in Mechanics of flow-induced sound and vibration, Vol. II Complex flow-structure interactions, *Academic Press Inc.*, Orlando, Florida
19. M.K. Bull, Wall-pressure fluctuations beneath turbulent boundary layers: some reflections on forty years of research. J. Sound Vib. **190**(3), 299–315 (1996)
20. G.M. Corcos, The structure of the turbulent pressure field in boundary-layer flows. J. Fluid Mech. **18**(3), 353–378 (1964)
21. E. Salze, C. Bailly, O. Marsden, E. Jondeau, D. Juvé, An experimental characterization of wall pressure wavenumber-frequency spectra in the presence of pressure gradients, 20th AIAA/CEAS Aeroacoustics Conference. AIAA Paper 2014–2909 (2014)

22. Salze, E., Jondeau, E., Pereira, A., S.L. Prigent and Bailly, C., 2019, A new MEMS microphone array for the wavenumber analysis of wall-pressure fluctuations: application to the modal investigation of a ducted low-Mach number stage, 25th AIAA/CEAS Aeroacoustics Conference, AIAA Paper 2019–2574
23. Antonio Pereira, Jérôme Antoni, Quentin Leclère, Empirical Bayesian regularization of the inverse acoustic problem. Applied Acoustics **97**, 11–19 (2015)
24. Alice Dinsenmeyer, Jérôme Antoni, Quentin Leclère, Antonio Pereira, A probabilistic approach for cross-spectral matrix denoising: Benchmarking with some recent methods (accepted for publication). The Journal of the Acoustical Society of America (2020)
25. Alice Dinsenmeyer, Quentin Leclère, Jérôme Antoni, and Emmanuel Julliard. Separation of the acoustic and aerodynamic wall pressure fluctuations. In *Proceedings of Forum Acusticum 2020*, Lyon, France, 2020

Analytical Developments for Vibration and Noise

Flow Generated Noise Produced by a Blunt Edged Plate in a Water Tunnel

Paul Croaker, James Venning, Mahmoud Karimi, Paul A. Brandner, Con Doolan, and Nicole Kessissoglou

Abstract A numerical and experimental investigation into the flow and noise produced by a blunt-edged flat plate with a Reynolds number based on chord of 6.8 million and a Mach number of 0.0053 is presented. The flat plate had a 4:1 aspect ratio elliptic leading edge and a square trailing edge with a thickness-to-chord ratio of 0.0054. Experimental measurements were performed in a reverberant water tunnel. Pressure sensors were flush mounted on the top, bottom and rear faces of the blunt edge at the mid-span plane. Further, a hydrophone was mounted in a flooded cavity in the tunnel wall beneath a polyurethane diaphragm. An analytical model for trailing edge scattering was extended to account for near-field effects and to consider reflection of pressure waves by the tunnel walls. A large eddy simulation was also conducted, with hydrodynamic pressures on the surface of the plate extracted and combined with the analytical scattering model to predict the pressure fluctuations on the wall of the water tunnel. Numerical predictions are found to agree well with the experimental measurements.

P. Croaker (✉)
Maritime Division, Defence Science and Technology Group, Melbourne, VIC, Australia
e-mail: paul.croaker@dst.defence.gov.au

J. Venning · P. A. Brandner
Cavitation Research Laboratory, University of Tasmania, Launceston, TAS, Australia
e-mail: james.venning@utas.edu.au

P. A. Brandner
e-mail: p.brandner@utas.edu.au

M. Karimi
Centre for Audio, Acoustics and Vibration, University of Technology Sydney, Sydney, NSW, Australia
e-mail: Mahmoud.Karimi@uts.edu.au

C. Doolan · N. Kessissoglou
School of Mechanical and Manufacturing Engineering, University of New South Wales, Sydney, NSW, Australia
e-mail: c.doolan@unsw.edu.au

N. Kessissoglou
e-mail: n.kessissoglou@unsw.edu.au

E. Ciappi et al. (eds.), *Flinovia—Flow Induced Noise and Vibration Issues and Aspects-III*, https://doi.org/10.1007/978-3-030-64807-7_10

1 Introduction

The aim of the present work is to numerically predict flow generated noise for hydroacoustic applications, with a particular focus on the generation and propagation of flow generated pressure waves for confined flows, such as axial and centrifugal pumps. One of the mechanisms by which these devices produce sound is the scattering of boundary layer pressures from trailing edges. This work focuses on the development of a numerical technique to estimate the near-field radiation of flow generated pressures from trailing edges in water, with experimental measurements also obtained to validate the numerical technique.

Development and application of flow generated noise prediction techniques have focused almost exclusively on aerodynamically produced sound, see for example [1–4]. The vast majority of analytical methods derived to estimate flow generated noise focus on the far-field acoustic response in air [5–8]. Further, a large number of high quality aeroacoustic flow and noise measurements have been conducted [9–12]. These studies provide a valuable source of benchmark data for development of predictive numerical models. Applying aeroacoustic prediction techniques to study the generation and propagation of flow generated noise in water is not always straightforward. The characteristic Reynolds number for marine applications is typically very high. This is accompanied by a very low Mach number which further widens the separation of hydrodynamic and acoustic scales that are present in aeroacoustic problems. Recent work of Ianniello [13–16] and Cianferra et al. [17] has suggested that non-linear flow noise sources, traditionally neglected in low Mach number aeroacoustics, may make a significant contribution to the flow generated noise produced by objects moving in water. Ianniello et al. [13–15] combined the Ffowcs-Williams and Hawkings (FW-H) analogy with hydrodynamic data from incompressible computational fluid dynamics (CFD) analyses to demonstrate that the non-linear flow noise sources make a significant contribution to the far-field noise produced by marine propellers. Cianferra et al. [17] extended this work to consider non-rotating bodies moving in water and concluded that non-linear flow noise sources may also make a significant contribution to the far-field sound produced by non-rotating bodies. However, hydroacoustic scattering from sharp geometrical features is not captured when the Ffowcs-Williams and Hawking analogy is combined with hydrodynamic data from incompressible CFD simulations. This is because the incompressible CFD simulation does not capture the propagation and interaction of flow generated pressures with the trailing edge geometry [18]. As such, the technique developed by Ianniello et al. cannot be applied to predict the noise produced by trailing edge scattering and an alternate strategy is pursued here.

In the present work, experiments on the flow and noise produced by a blunt edged flat plate are conducted in a cavitation tunnel. A computational fluid dynamics (CFD) analysis of the flow is also conducted using large eddy simulation (LES). The surface pressure on the plate is extracted and combined with an analytical trailing edge scattering model originally proposed by Amiet [6] and modified by Roger

and Moreau to account for leading edge back-scatter [8, 19]. The analytical model is modified here to account for the near-field effects and reflection of pressure waves off the tunnel walls. Numerical results and measured data are compared and discussed.

2 Experimental Setup

All experiments were carried out in the closed recirculating variable-pressure water tunnel of the Cavitation Research Laboratory at the Australian Maritime College (AMC). A schematic diagram of the tunnel circuit is shown in Fig. 1. The tunnel test section is 0.6 m square by 2.6 m long and the tunnel volume is 365 m^3 with demineralised water as the working fluid. The nominal operating velocity and absolute-pressure ranges are 2 to 13 m/s and 4 to 400 kPa, respectively. The circuit has low background noise and vibration levels due to low velocities and isolation from the surrounding building and all noise-generating machinery. The cavitation tunnel design and specification is described in detail in [20].

A stainless steel rectangular plate with elliptical leading edge of 4:1 aspect ratio was mounted vertically at the mid-span of the tunnel test section as shown in Fig. 2. The thickness H is 46 mm and chord 2b is 850 mm, giving a test section blockage of 7.7%. The freestream velocity was maintained at 7.93 m/s such that the chord-based Reynolds number was 6.8×10^6 and the Mach number was 5.3×10^{-3}. The freestream absolute pressure was maintained at 105 kPa and no cavitation was observed.

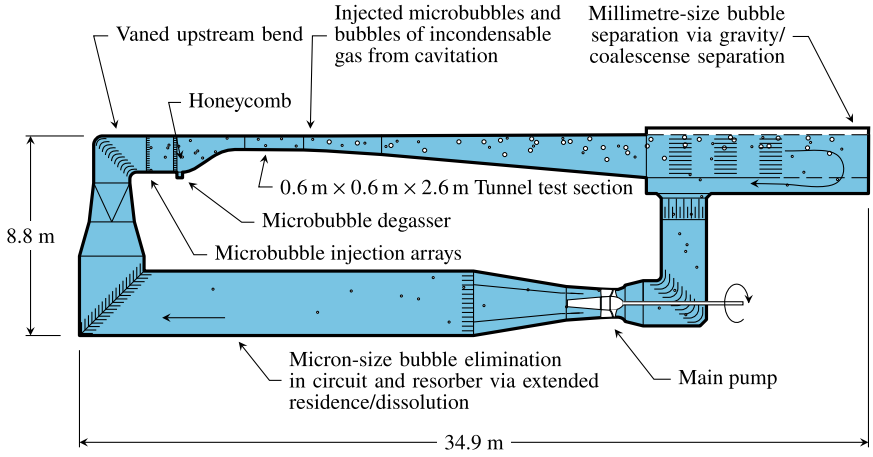

Fig. 1 Schematic diagram of the AMC variable-pressure water tunnel. Circuit architecture for continuous removal of microbubbles or large volumes of injected incondensable gas as well as ancillaries for microbubble seeding and for degassing of water are shown. Microbubbles may be either injected for modelling cavitation nucleation or generated by the cavitation itself

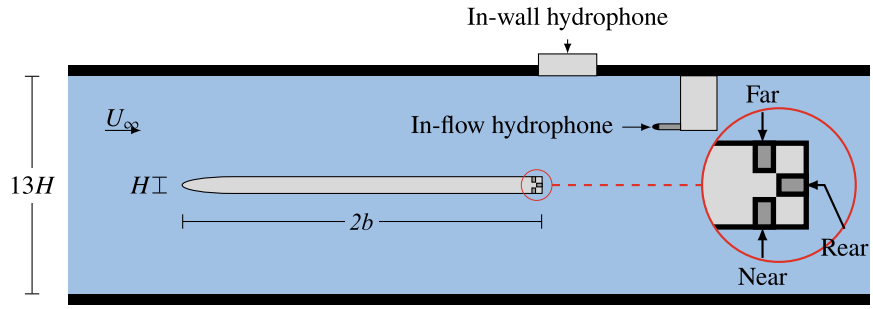

Fig. 2 Top view of the bluff plate in the AMC tunnel test section

The hydrodynamic noise was measured with two hydrophones and three pressure sensors. The hydrophones were Brüel & Kjær type 8103 models with a frequency range up to 180 kHz. One hydrophone was mounted in the tunnel wall 70 mm downstream of the trailing edge of the plate. The wall-mounted hydrophone was installed in a flooded cavity behind a 149 mm diameter, 10 mm thick polyurethane diaphragm as described in [21]. The acoustic impedance of polyurethane is similar to water, thus providing a near reflection-free acoustic interface. The large sensing area of the diaphragm provides attenuation of the turbulent boundary layer noise. The in-flow hydrophone was positioned 150 mm away from the tunnel wall and 280 mm downstream of the plate trailing edge. Both these hydrophone signals were conditioned with a Brüel & Kjær type 2692 charge amplifier with a 0.1 Hz high-pass filter and a 100 kHz low-pass filter. Signals were recorded for 81 s with an acquisition rate of 204.8 kHz. Only results for the wall-mounted hydrophone are presented here as the measured flow generated noise relative to background noise is greatest for this hydrophone.

The three pressure sensors were quartz-type PCB 105C02 sensors with 2.5 mm diameter sensing surfaces and a resonant frequency of over 250 kHz. Two pressure sensors were mounted in the two sides of the plate, 23 mm upstream of the trailing edge. These are labelled ‘near’ and ‘far’ and are situated 311.5 and 288.5 mm from the tunnel ceiling, respectively. The third pressure sensor is located in the rear surface of the plate and 300 mm from the ceiling. These signals were conditioned with a Kistler 5080A amplifier.

3 Numerical Flow-Induced Noise Prediction

3.1 Hydrodynamic Data and Acoustic Sources

An LES of the unsteady flow field around the plate was performed by filtering the incompressible Navier-Stokes equations to separate the hydrodynamic fluctuations

Table 1 CFD mesh resolutions used for current study

Mesh	x^+	y^+	z^+	Cells
1	100	24	120	22×10^6
2	100	24	60	44×10^6
3	50	24	60	88×10^6
4	50	12	60	120×10^6

into resolved and sub-grid scale components. The filtered incompressible Navier-Stokes equations are given by

$$\rho_0 \frac{\partial \hat{u}_i}{\partial t} + \rho_0 \frac{\partial}{\partial y_i}\left(\hat{u}_i \hat{u}_j\right) = -\frac{\partial \hat{p}}{\partial y_j} + 2\left(\mu_0 + \mu_{\mathrm{SGS}}\right) \frac{\partial}{\partial y_j} \hat{S}_{ij} \tag{1}$$

$$\frac{\partial \hat{u}_j}{\partial y_j} = 0 \tag{2}$$

where $\hat{p}$ is the filtered pressure and $\hat{u}_i$ represents components of the resolved velocity vector. μ_0 and ρ_0 are the viscosity and density of the fluid at rest. $\hat{S}_{ij}$ is the strain rate tensor of the resolved scales. The wall-adapting local eddy-viscosity model in [22] was used to define the eddy viscosity, μ_{SGS}, which accounts for the influence of the sub-grid scales on the filtered motion. Due to the high Reynolds number, it is computationally impractical to resolve the velocities into the plate viscous sublayer. Instead, the wall model of Spalding [23] is used to model the effect of the near wall stresses on the flow. Equations (1) and (2) were solved using OpenFOAM [24].

A hybrid mesh comprising a fully structured core mesh around the plate and in the wake region was constructed. An unstructured mesh was also created away from the plate to reduce cell count. Further, only a 0.07 m spanwise section of the model has been considered with periodic boundary conditions applied to further reduce the total number of CFD mesh cells. A baseline mesh was created with near wall cell sizes of $x^+ \approx 100$, $y^+ \approx 24$ and $z^+ \approx 120$, resulting in a total of 22×10^6 hexahedral cells. A systematic grid refinement procedure was then followed to investigate the influence of mesh resolution on the accuracy of the LES results. For each subsequent mesh, the grid size in one of the principal directions was halved, with the mesh first refined in the spanwise, then streamwise and finally wall normal directions. Table 1 presents a summary of the different LES meshes. Similar to the experimental setup, the plate is mounted in a water tunnel with cross-section of 0.6 m $\times$ 0.6 m. The CFD model extends 1.5 m upstream of the leading edge and 3.65 m downstream of the trailing edge. Figure 3 shows the CFD model and associated mesh.

The pressure implicit with splitting of operator algorithm was used to deal with the pressure-velocity coupling during solution of the LES equations. A second-order backward implicit scheme was used for the temporal discretisation. A blended spatial

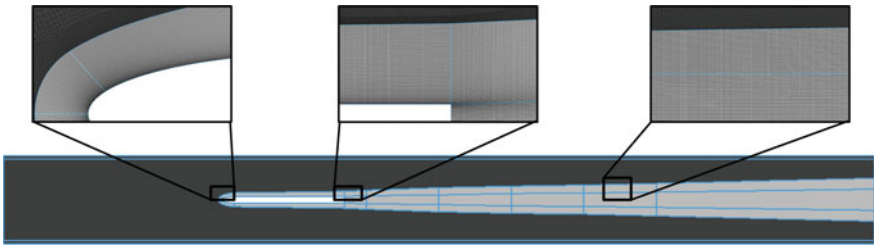

Fig. 3 CFD mesh model for the blunt edge flat plate. Inserts show the CFD mesh near the leading and trailing edges and the far wake

differencing scheme was used with 80% second order central differencing and 20% second order upwind differencing for the non-linear terms in the momentum equations. A standard second order central differencing scheme was used for all other spatial discretisations.

The transient simulation was executed with a time step size of 2.5×10^{-6} s and was allowed to progress until the flow field achieved quasi-periodicity. Recording of the surface pressures on the plate then commenced with the pressure stored at intervals of 5×10^{-4} s. Time histories of the surface pressures were divided into equal segments with a length of 458 time steps with 50% overlap. A Hanning window function was applied to each segment of the surface pressure time histories before converting them to frequency spectra.

4 Propagation of Flow-Induced Pressure Waves

4.1 Analytical Scattering and Propagation

A simple modification to the analytical scattering technique originally developed by Amiet [6] and later extended by Roger and Moreau [8] is proposed to investigate scattering and propagation of the flow-induced pressure waves that are generated in the tunnel. Figure 4 shows the idealised geometry and coordinate system used for prediction of the flow-induced pressure wave propagation.

For a surface pressure distribution of wavenumber $\mathbf{K} = (K_1, K_2)$, with K_1 and K_2 respectively denoting the streamwise and spanwise wavenumbers, Roger and Moreau [8, 19] derived the following expression for the far-field pressure produced by trailing edge scattering and radiation from the trailing edge of a flat plate

$$p_K(\mathbf{x}, \omega) = \frac{-\mathrm{i}\, k_a x_3}{4\pi S_0^2} \int_{-2b}^{0} \int_{-L/2}^{L/2} \Delta P(K_1, K_2)\, \mathrm{e}^{\mathrm{i} k_a R_t}\, \mathrm{d}\, y_1\, \mathrm{d}\, y_2 \tag{3}$$

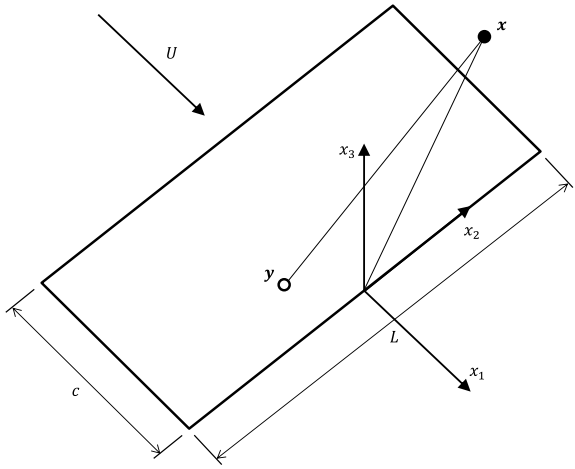

Fig. 4 Schematic diagram showing geometry and coordinate system used for trailing edge scattering

p_K is the far-field pressure produced by a surface pressure distribution denoted by $\Delta P\,(K_1, K_2)$ associated with wavenumbers K_1 and K_2. ω is the angular frequency, $k_a = \omega/c_0$ is the acoustic wavenumber with c_0 representing the speed of sound in the fluid at rest and $i = \sqrt{-1}$. R_t represents the distance between source point **y** and field point **x**. In the original work of Roger and Moreau [8], the effect of background convection on acoustic waves was included. However, for applications in water with very low Mach number, the effect of background convection on the propagation of pressure waves becomes negligible. The distance between source and field points can be expressed by

$$R_t = S_0 \left(1 - \frac{x_1 y_1 + x_2 y_2}{S_0^2}\right) \tag{4}$$

where $S_0^2 = x_1^2 + x_2^2 + x_3^2$ is the distance from the coordinate system origin at the trailing edge to the far-field location **x**. This representation of distance is convenient for use with analytical scattering methods as the contributions from individual components of the source vector **y** are decoupled. However, it must be noted that Eq. (4) is a simplification of the distance and only approaches the true distance between source and field points when $|\mathbf{x}| >> |\mathbf{y}|$.

Amiet [6] and Roger and Moreau [8] have shown that the autospectral density of the acoustic pressure at a far-field receiver location is given by

$$S_{pp,\mathrm{ff}}\,(\mathbf{x}, \omega) = \left(\frac{\omega x_3 L b}{2\pi c_0 S_0^2}\right)^2 \frac{1}{b} \int_{-\infty}^{\infty} \Pi_0 \left(\frac{\omega}{U_c}, K_2\right) \mathrm{sinc}^2 \left(\frac{L}{2b}\left(\bar{K}_2 - \bar{k}_a \frac{x_2}{S_0}\right)\right) \times \left|I\left(\bar{K}_c, \bar{K}_2\right)\right|^2 \mathrm{d}\,\bar{K}_2 \tag{5}$$

where x_i represents the ith component of the far-field receiver position vector. L is the span of the plate and b is the half chord. The convection velocity of the surface pressure is denoted by U_c. K_2 is the spanwise wavenumber of the surface pressure and $K_c = \frac{\omega}{U_c}$ is the convective wavenumber. Function $\text{sinc}\, y = \frac{\sin y}{y}$ and $\Pi_0\left(\bar{K}_c, \bar{K}_2\right)$ represents the energy of the fluctuating wall pressure at wavenumber K_2 and frequency ω. The form of Π_0 is discussed later. $I\left(\bar{K}_c, \bar{K}_2\right)$ is the radiation integral which accounts for how the fluctuating wall pressure at wavenumber K_2 and frequency ω radiates to the far field as sound. Wavenumbers with an overbar indicate that the wavenumber has been normalised by the half-chord length b, for example $\bar{K}_c = K_c\, b$. The radiation integral derived by Roger and Moreau [8] and including the effect of leading edge back-scatter is used in the present work.

4.2 Near-Field Radiation

The radiation of sound to the far field is obtained by considering a distribution of dipoles on the surface of the plate, with each dipole's force obtained from the disturbance pressure on the plate due to trailing edge scattering [6, 8]. As Amiet [6] and Roger and Moreau [8] were primarily concerned with far-field sound, the near-field component of the dipole's radiation kernel was not included. To investigate the impact of the near-field term of the dipole radiation kernel, we consider the sound pressure radiated by a point force F oriented in the wall normal direction x_3, which corresponds to

$$p_a\left(\mathbf{x}, \omega\right) = F\left(\mathbf{y}, \omega\right) \frac{\partial G_h\left(\mathbf{x}, \mathbf{y}, \omega\right)}{\partial x_3} \tag{6}$$

$G_h\left(\mathbf{x}, \mathbf{y}, \omega\right)$ is the harmonic free-field Green's function between the source point $\mathbf{y}$ and receiver point $\mathbf{x}$. In the context of the analytical scattering models of Amiet [6] and Roger and Moreau [8], the harmonic free-field Green's function is given by

$$G_h\left(\mathbf{x}, \mathbf{y}, \omega\right) = \frac{e^{\mathrm{i}k_a R_t}}{4\pi S_0} \tag{7}$$

The derivative of Eq. (7) with respect to x_3 yields

$$\begin{aligned} \frac{\partial G_h\left(\mathbf{x}, \mathbf{y}, \omega\right)}{\partial x_3} &= \frac{e^{\mathrm{i}k_a R_t}}{4\pi S_0^2}\left(\mathrm{i}k_a S_0 - 1\right)\frac{x_3}{S_0} \\ &= \frac{\mathrm{i}k_a x_3 e^{\mathrm{i}k_a R_t}}{4\pi S_0^2} - \frac{x_3 e^{\mathrm{i}k_a R_t}}{4\pi S_0^3} \end{aligned} \tag{8}$$

Here, $\frac{\partial R_t}{\partial x_3} \approx \frac{x_3}{S_0}$ has been used to simplify the derivation of Eq. (8) and retain the form of the radiation kernel used in Refs. [6, 8]. The first term on the right hand side of

Eq. (8) represents the far-field component of the dipole radiated from a point force, with the second term representing the near-field component. To include the effects of the near-field component on trailing edge noise, Eq. (3) is modified as follows

$$p_K(\mathbf{x}, \omega) = \left(\frac{\mathrm{i}\, k_a x_3}{4\pi S_0^2} - \frac{x_3}{4\pi S_0^3}\right) \int_{-2b}^{0} \int_{-L/2}^{L/2} \Delta P(K_1, K_2)\, \mathrm{e}^{\mathrm{i}\, k_a R_t}\, \mathrm{d}\, y_1\, \mathrm{d}\, y_2 \tag{9}$$

An expression for the autospectral density of the sound pressure including near-field effects becomes

$$S_{pp,\mathrm{nf}}(\mathbf{x}, \omega) = \left(\frac{\mathrm{i}\, k_a x_3}{4\pi S_0^2} - \frac{x_3}{4\pi S_0^3}\right)^2 4L^2 b \int_{-\infty}^{\infty} \Pi_0\left(\frac{\omega}{U_c}, K_2\right) \mathrm{sinc}^2\left(\frac{L}{2b}\left(\bar{K}_2 - \bar{k}\frac{x_2}{S_0}\right)\right) \times \left|I\left(\bar{K}_c, \bar{K}_2\right)\right|^2 \mathrm{d}\, \bar{K}_2 \tag{10}$$

It should be noted that Eqs. (9) and (10) represent a significant simplification as variation in distance between source and receiver points has not been considered when calculating the derivative of the Green's function.

Figure 5 compares the autospectral density of the acoustic pressure in the far-field and near-field respectively given by Eqs. (5) and (10), for a receiver located directly above the trailing edge, with $\Pi_0\left(\bar{K}_c, \bar{K}_2\right) = 1,\ \forall\ \bar{K}_c, \bar{K}_2$. For spanwise wavenumbers $k_2/(\beta\mu) \leq 1$, where $\beta = \sqrt{1 - M^2}$ and $\mu = k_a b/\beta^2$, the intersection of the gust with the trailing edge travels faster than the speed of sound. These are called supercritical gusts and have the greatest contribution to the far-field sound produced by large span airfoils. For spanwise wavenumbers $k_2/(\beta\mu) \geq 1$, the intersection of the gust with the trailing edge travels slower than the speed of sound. These are called subcritical gusts and typically do not contribute significantly to the far-field sound. Figure 5 shows that as the distance between source and field points decrease, the relative contribution of subcritical wavenumbers increases, with subcritical wavenumbers dominating the radiated pressure field for small separation distances. Figure 5 also shows a significant increase in the radiated pressure when the near-field contribution from the dipole radiation kernel is included in the transfer function for small separation distances.

4.3 Reflections from Tunnel Walls

The tunnel walls are assumed to be perfectly rigid and the method of images is used to approximate the reflection of radiated pressure by the tunnel walls. Figure 6 shows a schematic diagram of the method of images technique used to account for tunnel reflections. Virtual receivers are placed where mirror images of the actual receiver would be positioned beyond the tunnel walls. Pressures recorded at the actual receiver and each virtual receiver are combined together to predict the total response. In the

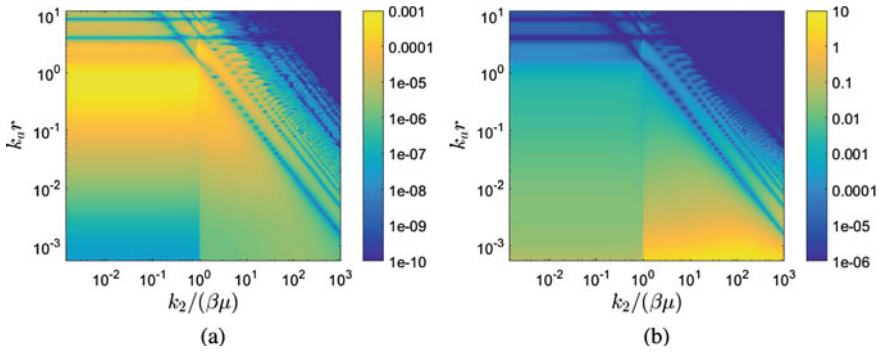

Fig. 5 Autospectral density of the radiated pressure for a unit gust input for **(a)** the far-field scattering model given by Eq. (5), and **(b)** the near-field scattering model given by Eq. (10). The vertical axis represents the distance between source and receiver points, normalised by the acoustic wavenumber k_a. The horizontal axis represents the spanwise wavenumber normalised by Graham's parameter which marks the cut-off between supercritical and subcritical wavenumbers

present work, a total of 10 virtual receivers positioned beyond each wall of the tunnel was sufficient to obtain a converged solution.

Figure 6 also shows that the spanwise extent of the plate was discretised into a finite number of spanwise strips. This is because the in-wall hydrophone is in close proximity to the plate and the distance from the plate to the hydrophone varies considerably based on spanwise position along the plate. By discretising the plate into a number of spanwise strips and calculating the hydroacoustic response of each strip individually, the influence of this spanwise variation in distance is captured in the results.

The coordinate system origin identified in Fig. 4 must be placed in the centre of each spanwise segment at the trailing edge. Hence, the source and receiver points vary considerably for each spanwise segment. Recognising that the phase information must be preserved when combining actual and virtual receiver pressures, and further, the autospectral density of the pressure predicted for each spanwise segment can simply be added together, the total autospectral density of the near-field pressure is given by:

$$S_{pp,\mathrm{nf}}(\mathbf{x},\omega) = \sum_{d=1}^{D} 4L_d^2 b \int_{-\infty}^{\infty} \Pi_0\left(\frac{\omega}{U_c}, K_2\right) \left(\sum_{n=1}^{N} \left[\left(\frac{\mathrm{i}\, k_a x_{3,dn}}{4\pi S_{0,dn}^2} - \frac{x_{3,dn}}{4\pi S_{0,dn}^3}\right) \mathrm{sinc}\left(\frac{L_d}{2b}\left(\bar{K}_2 - \bar{k}_a \frac{x_{2,dn}}{S_{0,dn}}\right)\right) \times \left|I\left(\bar{K}_c, \bar{K}_2\right)\right|\right]\right)^2 \mathrm{d}\,\bar{K}_2 \tag{11}$$

where L_d is the span of spanwise segment d and D is the total number of segments. n is the receiver number, where $n = 1$ corresponding to the actual in-wall hydrophone location and N is the total number of receivers. $x_{2,dn}$ and $x_{3,dn}$ correspond to the 2nd

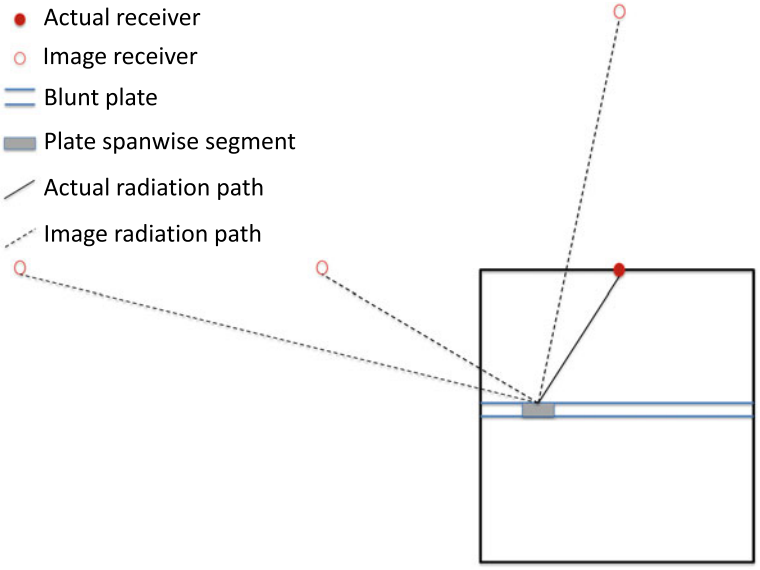

Fig. 6 Schematic diagram illustrating the method of images used to approximate the effect of tunnel reflections on the radiated pressure. Orientation is from downstream of the plate, looking upstream with the in-wall hydrophone positioned above the plate. Flow is out of the page

and 3rd components of the position vector for the nth receiver location relative to the dth spanwise segment, with $S_{0,dn}$ the associated distance.

4.4 Estimating the Pressure Field from LES

The final step in the analytical treatment of near-field pressure radiation from trailing edge scattering is to approximate the energy of the fluctuating wall pressure, $\Pi_0\left(\frac{\omega}{U_c}, K_2\right)$. In the present work, the following relationship is used [8]

$$\Pi_0\left(\frac{\omega}{U_c}, K_2\right) = \frac{1}{\pi}\Phi_{pp}(\omega)\, l_y(K_2, \omega) \tag{12}$$

where $\Phi_{pp}(\omega)$ is the autospectral density of the pressure near the blunt edge, and $l_y(K_2, \omega)$ is the spanwise correlation length of the pressure fluctuations.

Two alternate spanwise correlation length models are herein investigated. The model derived by Corcos [25] is widely used to estimate the cross-correlation of surface pressures under a turbulent boundary layer. The Corcos model is known to over-predict the low wavenumber response of the cross-correlation function, however it is easy to implement which adds to its popularity. The other model considered

here is the model of Smol'yakov [26] which aims to address the deficiencies in the Corcos model. Details of these two models for the cross spectrum can be found in Refs. [25, 26].

Combining Eqs. (11) and (12) gives the final form of the analytical expression for near-field scattering as

$$S_{pp,\mathrm{nf}}(\mathbf{x},\omega) = \sum_{d=1}^{D} 4L_d^2 b \Phi_{pp}(\omega) \int_{-\infty}^{\infty} l_y(K_2,\omega) \left(\sum_{n=1}^{N} \left[\left(\frac{\mathrm{i}\, k_a x_{3,dn}}{4\pi S_{0,dn}^2} - \frac{x_{3,dn}}{4\pi S_{0,dn}^3} \right) \right.\right.$$
$$\left.\left. \mathrm{sinc}\left(\frac{L_d}{2b} \left(\bar{K}_2 - \bar{k}_a \frac{x_{2,dn}}{S_{0,dn}} \right) \right) \times \left| I\left(\bar{K}_c, \bar{K}_2\right) \right| \right] \right)^2 \mathrm{d}\,\bar{K}_2 \tag{13}$$

5 Results and Discussion

5.1 Hydrodynamic Flow Field

Figure 7 presents isosurfaces of the Q-criterion coloured by the magnitude of the vorticity vector and shows the flow structures in the flow past the plate. Slightly downstream of the elliptical leading edge, the flow undergoes laminar to turbulence transition with the turbulent boundary layer developing along the length of the plate. At the blunt trailing edge the flow separates, forming two shear layers which roll up into vortices that are shed into the wake forming a von Karman vortex street. Figure 7 shows that the vortices contain flow features with a wide range of scales. Hence the pressure waves produced at the vortex shedding frequency and its harmonics are likely to contain significant broadening of the tonal peaks. Also, the smaller scale turbulent structures in the boundary layer that convect past the blunt trailing edge are expected to produce broadband noise at higher frequencies. The results shown in Fig. 7 were prepared using the finest grid corresponding to Mesh 4 in Table 1, with near wall grid resolutions of $x^+ \approx 50$, $y^+ \approx 12$ and $z^+ \approx 60$.

5.2 Surface Pressure Results

Figure 8 compares measured and predicted surface pressure at the 'near' pressure sensor location shown in Fig. 2. Figure 8a shows the prediction obtained using the finest mesh resolution, corresponding to Mesh 4 in Table 1. The broadened tonal peaks correspond to the vortex shedding frequency and its harmonics. The LES simulation predicts that the vortex shedding frequency occurs at $St_h = 0.252$, which is within 7% of the measured value of 0.236. Within the frequency range 10–400 Hz, the autospectral density of the trailing edge pressure predicted with the LES follows the same general shape observed in the measured data, with the vortex shedding

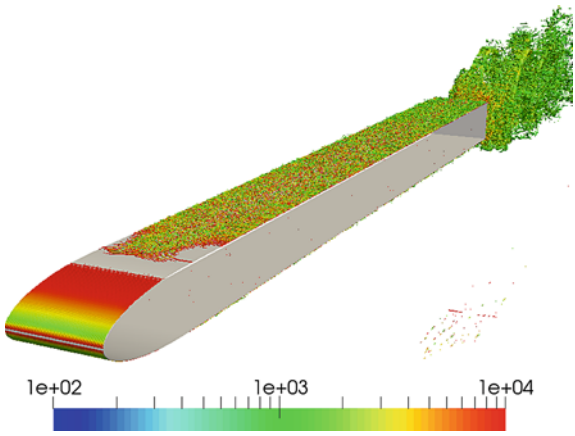

Fig. 7 Isosurfaces of Q-criteria showing flow structures, coloured by magnitude of vorticity

frequency and its second and third harmonics well captured. However, the magnitude of the autospectral density of the trailing edge pressure predicted by the LES within this frequency range is between 3 to 6 dB higher than the measured value. In this low frequency region, all of the LES meshes considered produced similar results. It is important to note that the same frequency bandwidth was used for both numerical and experimental data processing to ensure that the tonal peaks from both data sets encounter the same averaging. Overprediction at these low frequencies is attributed to the reduced span of the model with the periodic boundary conditions, which enforces greater coherence of the larger scale turbulence flow structures.

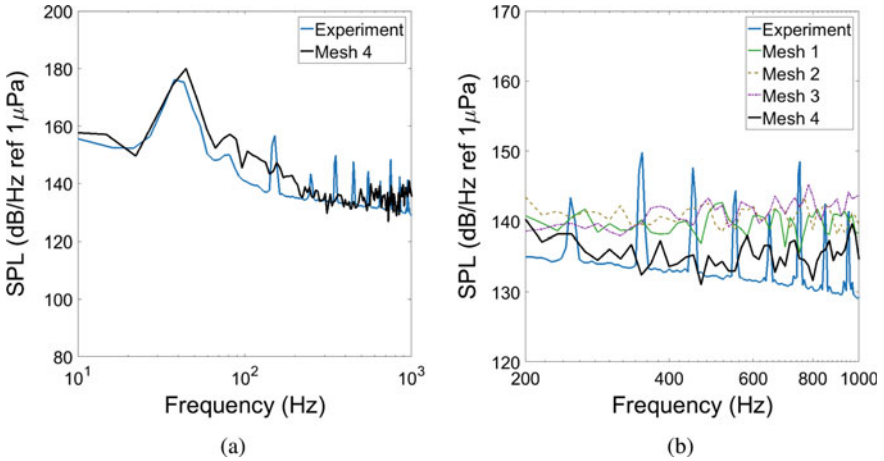

Fig. 8 **(a)** Autospectral density of the surface pressure at the trailing edge of the plate predicted using Mesh 4. **(b)** Influence of mesh resolution on the spectral content of the autospectral density of the trailing edge pressure

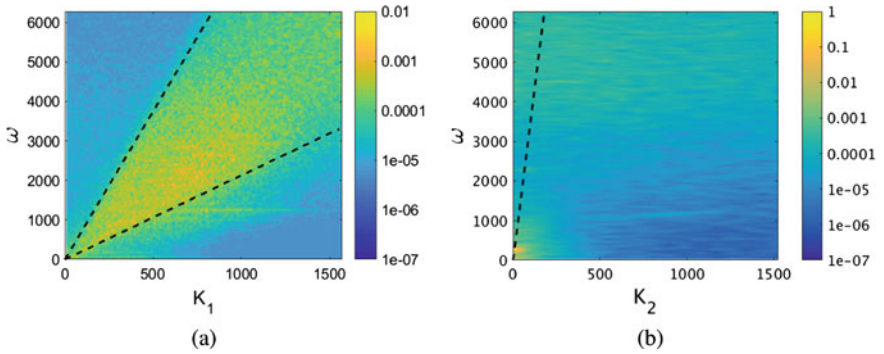

Fig. 9 Wavenumber-frequency content of the surface pressures for **(a)** the streamwise wavenumbers, and **(b)** the spanwise wavenumbers, showing the energy contained at each wavenumber of the surface pressure for a given frequency

Figure 8b shows the influence of mesh resolution on the higher frequency surface pressure predictions obtained using LES. Significant deviation is observed between the high frequency surface pressure predicted by the LES for Mesh 1, 2 and 3. The agreement between measured and predicted surface pressure improves substantially when Mesh 4 is used for the LES, with good agreement over most of the frequency range. However, even for Mesh 4 the predicted surface pressure begins to deviate as the frequency increases, indicating that additional grid refinement may be necessary to more accurately resolve the high frequency turbulence.

Figure 9 presents the wavenumber-frequency decomposition of the surface pressures on the top surface of the plate. Figure 9a shows the streamwise wavenumber distribution of the surface pressures as a function of angular frequency, ω. The majority of the surface pressure transport occurs between the two dashed black lines, representing convection velocities of 2.1 and 7.5 m/s. This wide spread of convection velocities is due to the vortex shedding phenomenon, whereby the boundary layer is alternatively accelerated and decelerated by the roll-up and shedding of the trailing edge vortices. Figure 9b presents the spanwise wavenumber distribution of the surface pressure as a function of angular frequency. The dominant concentration of spanwise wavenumbers to the surface pressure occurs at the vortex shedding frequency with the peak comprised of relatively low wavenumbers. This indicates that the large spanwise structures in the vortices makes the most significant contribution to the surface pressures on the plate. The dashed line in Fig. 9b represents a wavenumber 100 times larger than the cut-on wavenumber between subcritical and supercritical gusts. In Fig. 5, this corresponds to a vertical line at $k_2/(\beta\mu) = 100$ with energy to the left of this line having the greatest contribution to the radiated pressure. Hence, a large proportion of the energy represented in Fig. 9b, corresponding to the energy to the right of the dashed line, does not make a significant contribution to the radiated pressure.

5.3 Wall Mounted Hydrophone Results

The autospectral density of the surface pressure near the blunt edge of the plate predicted using LES is combined with spanwise correlation length estimates of Corcos, $L_{y,C}$ and Smol'yakov $L_{y,S}$ and the near-field analytical scattering model given by Eq. (13). Including ten image receivers to account for reflections off the tunnel walls and discretising the span into eight spanwise segments, the pressure at the in-wall hydrophone location is estimated. Figure 10a shows that there is excellent agreement between the sound pressure level (SPL) predicted from the LES/analytical scattering approach and the measured pressure at the wall mounted hydrophone when Smol'yakov's correlation length is used. The broadened tonal peak at the vortex shedding frequency is well predicted as is the broadband pressure at higher frequencies. The low frequency pressures were over-predicted when the spanwise correlation length of Corcos was applied. Figure 10a also shows the background noise level measured for 8 m/s flow in the tunnel with no plate present. There is sufficient difference between background noise levels and the pressure levels measured at the wall mounted hydrophone when the plate is present to allow for meaningful comparison between numerical and measured data.

It is interesting to note that, although the surface pressure autospectral density at the trailing edge is over-predicted by the LES at low frequencies (see Fig. 8a), the estimated radiated pressure received at the in-wall hydrophone is in excellent agreement with the experimental measurements. The over-prediction in the surface pressure autospectral density at the trailing edge is caused by the reduced span of the model and the periodic boundary conditions enforcing greater coherence of the larger

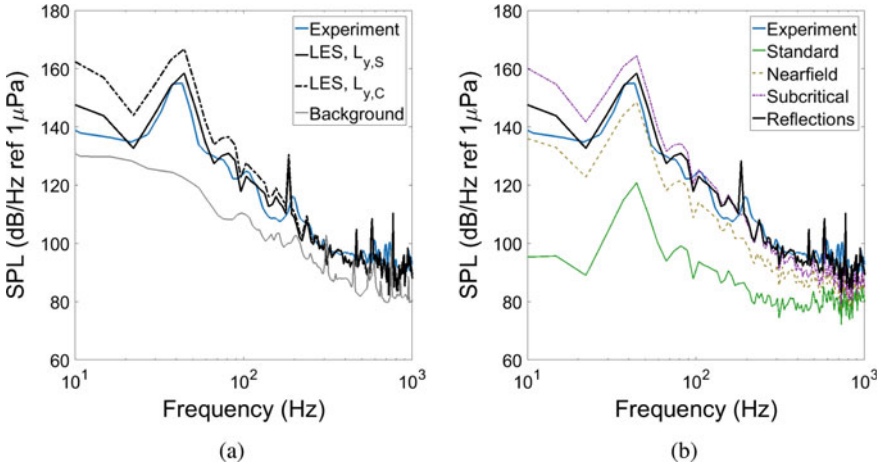

Fig. 10 **(a)** Comparison of SPL predicted using the spanwise correlation length proposed by Smol'yakov, $L_{y,S}$ and Corcos, $L_{y,C}$. **(b)** Changes in predicted pressure with incremental enhancement of the analytical scattering model, using the correlation length of Smol'yakov

scale flow structures. Figure 9b shows that only a small component of the total energy of the surface pressure fluctuations make a significant contribution to the radiated pressure. Hence, it seems likely that the boundary-condition-induced increase in surface pressure autospectral density is predominantly generated by wavenumber components that do not radiate efficiently from the trailing edge. This will be further investigated in future work.

Figure 10b presents changes in predicted pressure from incremental modifications to the scattering model. The 'standard' curve represents the result obtained using the analytical scattering model of Roger and Moreau [8], including leading edge back-scattering but considering only supercritical wavenumbers. The 'near-field' curve shows the incremental change when the influence of near-field effects are included in the analytical model. The 'subcritical' curve presents the additional effect arising from inclusion of subcritical wavenumbers. The 'reflections' curve further considers the reflection of the pressure from the rigid duct walls. All results presented in Fig. 10b have been calculated using the Smol'yakov length scale model. Figure 10b shows that both near-field effects and subcritical wavenumbers contribute significantly to the predicted pressure for this case study. Subcritical wavenumbers produce evanescent pressure waves which decay rapidly away from the source region and typically do not radiate to the far field as sound. However, in the current study, the receiver hydrophone is well within the near-field of the source region. Hence subcritical wavenumbers, near-field propagation effects and duct wall reflections must be included to give an accurate estimate of the pressure.

6 Conclusions

Experimental measurements and numerical predictions of the flow and noise produced by a blunt edged flat plate in a reverberant water tunnel has been presented. The experimental data indicates that the flow-induced noise levels measured at a wall mounted hydrophone are significantly above the background noise levels of the tunnel and hence are suitable for validation of numerical predictions of the flow and noise. An analytical scattering model originally developed to predict far-field sound radiated from turbulent flow over the trailing edge of an airfoil in free stream conditions has been extended here to account for near-field effects and reflections from the side walls of the water tunnel. The LES of the flat plate, and subsequent prediction of the pressure fluctuations at the wall mounted hydrophone location using the near-field analytical scattering model agree well with the measured data. The results indicate that subcritical wavenumbers and near-field propagation effects must be included to give an accurate estimate of the pressure for the case considered here.

References

1. J. Seo, Y. Moon, Aerodynamic noise prediction for long-span bodies. J. Sound Vib. **306**, 564–579 (2007)
2. M. Wang, S. Moreau, G. Iaccarino, M. Roger, LES prediction of wall-pressure fluctuations and noise of a low-speed airfoil. Int. J. Aeroacoust. **8**, 177–198 (2009)
3. W.R. Wolf, S.K. Lele, Acoustic analogy formulations accelerated by fast multipole method for two-dimensional aeroacoustic problems. AIAA J. **48**, 2274–2285 (2010)
4. M. Karimi, P. Croaker, N. Peake, N. Kessissoglou, Acoustic scattering for rotational and translational symmetric structures in nonuniform potential flow. AIAA J. **55**(10), 3318–3327 (2017)
5. R.K. Amiet, Acoustic radiation from an airfoil in a turbulent stream. J. Sound Vib. **41**, 407–420 (1975)
6. R.K. Amiet, Noise due to turbulent flow past a trailing edge. J. Sound Vib. **47**, 387–393 (1976)
7. M.S. Howe, Edge-source acoustic Green's function for an airfoil of arbitrary chord, with application to trailing-edge noise. Q. J. Mech. Appl. Mech. **54**, 139–155 (2001)
8. M. Roger, S. Moreau, Back-scattering correction and further extension of Amiet's trailing-edge noise solution. Part 1: theory. J. Sound Vib. **286**, 477–506 (2005)
9. M.C. Jacob, D. Boudet, D. Casalino, M. Michard, A rod-airfoil experiment as a benchmark for broadband noise modelling. Theor. Comput. Fluid Dyn. **19**, 171–196 (2005)
10. W.J. Devenport, J.K. Staubs, S.A.L. Glegg, Sound radiation from real airfoils in turbulence. J. Sound Vib. **329**, 3470–3483 (2010)
11. D. Moreau, L. Brooks, C. Doolan, The effect of boundary layer type on trailing edge noise from sharp-edged flat plates at low-to-moderate Reynolds number. J. Sound Vib. **331**, 3976–3988 (2012)
12. D.J. Moreau, C.J. Doolan, W.N. Alexander, T.W. Meyers, W.J. Devenport, Wall-mounted finite airfoil-noise production and prediction. AIAA J. **54**(5), 1637–1651 (2016)
13. S. Ianniello, R. Muscari, A. Di Mascio, Ship underwater noise assessment by the acoustic analogy part I: nonlinear analysis of a marine propeller in a uniform flow. J. Mar. Sci. Technol. **19**(4), 547–570 (2013)
14. S. Ianniello, R. Muscari, A. Di Mascio, Ship underwater noise assessment by the acoustic analogy part II: hydroacoustic analysis of a ship scaled model. J. Mar. Sci. Technol. **19**(1), 52–74 (2014)
15. S. Ianniello, R. Muscari, A. Di Mascio, Ship underwater noise assessment by the acoustic analogy part III: measurements versus numerical predictions on a full-scale ship. J. Mar. Sci. Technol. **19**(2), 125–142 (2014)
16. S. Ianniello, The Ffowcs Williams-Hawkings equation for hydroacoustic analysis of rotating blades. Part 1. The rotpole. J. Fluid Mech. **797**, 345–388 (2016)
17. M. Cianferra, V. Armenio, S. Ianniello, Hydroacoustic noise from different geometries. Int. J. Heat Fluid Flow **70**, 348–362 (2018)
18. S. Glegg, W. Devenport, The Ffowcs Williams and Hawkings equation (Chap. 5), in *Aeroacoustics of Low Mach Number Flows*, ed. by S. Glegg, W. Devenport (Academic Press, 2017), pp. 95–114
19. M. Roger, S. Moreau, Addendum to the back-scattering correction of Amiet's trailing-edge noise model. J. Sound Vib. **331**, 5383–5385 (2012)
20. P.A. Brandner, Y. Lecoffre, G.J. Walker, Design considerations in the development of a modern cavitation tunnel, in *Proceedings of the 16th Australasian Fluid Mechanics Conference*, Crown Plaza, Gold Coast, Australia (2007), pp. 3–7
21. C. Doolan, P. Brandner, D. Butler, B. Pearce, D. Moreau, L. Brooks, Hydroacoustic characterisation of the AMC cavitation tunnel, in *Acoustics 2013 - Victor Harbor*, Victor Harbor, Australia (2013)
22. F. Nicoud, F. Ducros, Subgrid-scale stress modelling based on the square of the velocity gradient tensor. Flow Turbul. Combust. **62**(3), 183–200 (1999)
23. D.B. Spalding, A single formula for the "law of the wall". J. Appl. Mech. **28**, 455–458 (1961)

24. H.G. Weller, G. Tabor, H. Jasak, C. Fureby, A tensorial approach to computational continuum mechanics using object-oriented techniques. Comput. Phys. **12**, 620–631 (1998)
25. G.M. Corcos, The structure of the turbulent pressure field in boundary-layer flows. J. Fluid Mech. **18**, 353–378 (1964)
26. A.V. Smol'yakov, A new model for the cross spectrum and wavenumber-frequency spectrum of turbulent pressure fluctuations in a boundary layer. Acoust. Phys. **52**, 331–337 (2006)

Absorption and Transmission of Boundary Layer Noise through Micro-Perforated Structures: Measurements and Modellings

Cédric Maury, Teresa Bravo, and Daniel Mazzoni

Abstract Mitigating flow-induced noise is currently a major goal in the acoustic design of automotive and aircraft cabins. In order to avoid the introduction of active or massive components, structures made up of backed or unbacked micro-perforated panels (MPP) are potential lightweight solutions that could enhance the absorption and decrease the transmission of flow-induced noise. The present work describes experimental and modelling studies that examine the effect of MPPs, either flush-mounted or in a recessed configuration, on the wall-pressure fluctuations induced by a low-speed turbulent boundary layer (TBL) of air. The first part of this paper focuses on the vibro-acoustic properties of flush-mounted MPP-Cavity-Panel partitions forced by an aero-acoustic excitation. Parametric studies are carried out that show the influence of the MPP and of the excitation parameters on the absorption and transmission loss of the partition. In a second part, experimental studies and Lattice-Boltzmann simulations are presented that examine the effect of a recessed MPP, located at the floor of a shallow cavity, on the attenuation of the tunnel-cavity resonances and of the broadband noise components under a low-speed TBL.

C. Maury (✉)
Laboratory of Mechanics and Acoustics (LMA), Aix Marseille University, CNRS Centrale Marseille, 38 rue Frédéric Joliot-Curie, 13013 Marseille, France
e-mail: cedric.maury@centrale-marseille.fr

T. Bravo
Instituto de Tecnologías Físicas y de la Información (ITEFI), Consejo Superior de Investigaciones Científicas (CSIC), Serrano 144, 28006 Madrid, Spain
e-mail: teresa.bravo@csic.es

D. Mazzoni
Aix Marseille University, CNRS Centrale Marseille, Institut de Recherche sur les Phénomènes Hors Equilibres (IRPHE UMR 7342), 38 rue Frédéric Joliot-Curie, 13013 Marseille, France
e-mail: daniel.mazzoni@centrale-marseille.fr

E. Ciappi et al. (eds.), *Flinovia—Flow Induced Noise and Vibration Issues and Aspects-III*, https://doi.org/10.1007/978-3-030-64807-7_11

Nomenclature

.	
$\tilde{\mathbf{a}}$	vector of the cavity modal amplitudes
A	magnitude of the acoustic component in the aero-acoustic excitation
$A_{\mathrm{MPP,P}}$	MPP and panel surface
b_h	holes separation distance
c_0	sound speed in air
$\tilde{d}$	blocked pressures on the front panel
$\tilde{\mathbf{d}}$	vector of blocked pressures on the front panel
d_h	holes diameter
d_{R}	reattachment distance of the flow in the cavity
D	cavity depth
$\mathbf{D}$	modal damping matrix of the partition
f	frequency
f_{AC}	aerodynamic coincidence frequency
f_{FW}	Ffowcs-Williams critical frequency
f_{H}	Helmholtz resonance frequency
f_{MAM}	mass-air-mass resonance frequency
$f_{n_z,\mathrm{TC}}$	TC transverse resonance frequency of order n_z
$f_{n_z,\mathrm{T}}$	T transverse resonance frequency of order n_z
F_M	flow-correction reactance factor for the MPP transfer impedance
$\hat{F}_{w_P}$	spatial Fourier transform of the back panel displacement
$\mathbf{G}$	dynamic stiffness matrix of the partition
H	height of the tunnel test section
$\mathbf{H}$	cavity-hole-cavity modal coupling matrix
H_C	cross-coupling coefficient of the cavity modes through the MPP holes
$H_0^{(1)}$	Hankel function of the first kind of order 0
J_n	Bessel function of the first kind of order n
k_c	convective wavenumber
k_f	flexural wavenumber
k_h	perforate constant
k_0	acoustic wavenumber
k_y	streamwise wavenumber
L	MPP panel length
$\mathbf{L}$	panel-cavity modal coupling matrix
$L_{(\mathrm{MPP,P})}$	modal coupling coefficient between the cavity and the MPP or the panel
$L_{x,y}$	TBL correlation lengths along the spanwise and streamwise directions
M	Mach number
$\mathbf{M}$	diagonal mass matrix of the partition
M_{C}	number of cavity modes accounted for
$M_{\mathrm{C},m}$	generalized mass of the m-th cavity mode
$M_{(\mathrm{MPP,\ P}),n}$	generalized mass of the n-th MPP or panel mode
n_z	transverse order of the tunnel mode

$N_{\text{MPP, P}}$	number of MPP or panel modes accounted for
$\tilde{p}$	acoustic pressure in the cavity
$\tilde{p}_d$	external wall-pressure
$\tilde{p}_{\text{rad}}$	pressure back-radiated by the front panel
$\tilde{\mathbf{q}}_{\text{MPP,P}}$	vector of MPP or panel modal amplitudes
$\mathbf{Q}$	generalized modal excitation vector
$\hat{Q}_{p_d}$	spatial Fourier transform of the pressures over the front panel
$\hat{Q}_{v_d}$	spatial Fourier transform of the normal velocities over the front panel
r, r_x, r_y	moduli of the vector position over the front panel and its spanwise and streamwise components
$\mathbf{r}$	vector position in the cavity partition.
R_e	external holes resistance
$\mathbf{R}_{\text{rad}}$	radiation resistance matrix
$\mathbf{S}$	diagonal stiffness matrix of partition
S_{MPP}	MPP surface area
$S_{dd}, \mathbf{S_{dd}}$	CSD function and matrix between the blocked wall-pressure fluctuations
$\bar{S}_{\mathbf{dd}}$	Spatially-averaged PSDs of the blocked pressures over the MPP
$\bar{S}_{\mathbf{d(d-p)}}$	Spatially-averaged PSDs of the product between the blocked pressures and the pressure jumps across the MPP
$S_{p_d v_d}$	CSD function between the pressures and normal particle velocities over the MPP
$S_{p_P v_P}, \mathbf{S_{p_P v_P}}$	CSD function and matrix between the back panel pressures and velocities
$\mathbf{S_{q_P q_P}}$	CSD matrix between the back panel modal amplitudes
$\mathbf{S_{QQ}}$	CSD matrix between the generalized modal excitations
$\mathbf{S_{QX}}$	CSD matrix between the partition modal amplitudes and the generalised modal excitations
St_h	hole-based Strouhal number
St_d	Strouhal number based on the boundary layer displacement thickness
$\langle \bar{S}_{\mathbf{v_{MPP} v_{MPP}}} \rangle$	Frequency- and spatially-averaged PSDs of the normal velocity distribution over the MPP
$S_{w_P w_P}$	ASD of the back panel normal displacement
$\mathbf{S_{XX}}$	CSD matrix between the partition modal amplitudes
$\hat{S}_{xy}$	wavenumber Fourier transform of the CSD function S_{xy}
S_0	point-power spectrum of the excitation
t	time
U_c	flow convection velocity
U_G	one-sided grazing flow velocity
U_∞	flow free-stream velocity
$\lvert\tilde{v}\rvert$	magnitude of the flow velocity fluctuations
$\tilde{v}_{\text{MPP,P}}$	normal velocity of the MPP and back panel
V_C	cavity volume
$\tilde{w}_\text{P}$	normal displacement of the back panel

W	MPP panel width
$\mathrm{W}_{\mathrm{flow}}$	power injected in the partition
$\langle \mathrm{W}_{\mathrm{flow}} \rangle$	frequency-averaged power injected in the partition
$\mathrm{W}_{\mathrm{inc}}$	incident power
$\mathrm{W}_{\mathrm{trans}}$	transmitted power
$\mathbf{x}$	vector position on the MPP and on the back panel
$\tilde{\mathbf{X}}$	vector of MPP cavity and panel modal amplitudes
Z_{MPP}	holes transfer impedance
Z_0	air characteristic impedance

Greek Symbols

α	absorption coefficient
$\alpha_{x,y}$	empirical coefficients for the Corcos TBL model along the spanwise and streamwise directions
δ	TBL thickness
δ_v	viscous boundary layer thickness
δ^*	TBL displacement thickness
η	air dynamic viscosity
η_{MPP}	MPP damping loss factor
λ	acoustic wavelength
μ_{MPP}	MPP surface mass density
$\xi_{\mathrm{C},m}$	modal damping ratio of the m-th cavity mode
$\xi_{(\mathrm{MPP,\ P}),n}$	modal damping ratio of the n-th MPP or panel mode
ρ_0	air density
σ	perforation ratio
σ_{2D}	2D MPP perforation ratio
ϕ_m	cavity m-th acoustic mode
$\mathbf{\Phi}$	vector of cavity acoustic modes
$\psi_{(\mathrm{MPP,\ P}),n}$	MPP or back panel n-th structural mode
$\mathbf{\Psi}_{\mathrm{MPP,\ P}}$	vector of MPP or back panel structural modes
ω	angular frequency
$\omega_{\mathrm{C},m}$	natural angular frequency of the m-th cavity mode
$\omega_{(\mathrm{MPP,\ P}),n}$	natural angular frequency of the n-th MPP-panel mode
Ω	third-octave band central frequency
$\mathbf{\Omega}$	flow vorticity vector
Ω_y, $\tilde{\Omega}_y$	y-component of the flow instantaneous vorticity and its fluctuating part
$\Delta s_{\mathrm{MPP,P}}$	elemental area over the discretized MPP or panel surface
$\Delta\phi$	phase difference between wall-pressures
Δx, Δz	spatial resolution along the x- and z- directions for the 2D LBM
Δt	temporal resolution for the 2D LBM

Acronyms

APS	Auto-Power Spectrum
CSD	Cross-Spectral Density

LBM	Lattice Boltzmann Method
MPP	Micro-Perforated Panel
MPPCP	MPP-Cavity-Panel
PCP	Panel-Cavity-Panel
PL	Pressure Levels
PSD	Power Spectral Density
T	Tunnel
TBL	Turbulent Boundary Layer
TC	Tunnel-Cavity
TC-P	Tunnel-Cavity-Panel
TL	Transmission Loss
WT	Wind-Tunnel

1 Introduction

Mitigating flow-induced noise is currently a major goal in the acoustic design of automotive and aircraft cabins. The problem of reducing the airframe noise under a low-speed flow is complex as it should comply with low drag and mass-saving constraints. Moreover, the current use of lighter and stiffer structures with a low critical frequency enables a more efficient transmission of the mid-frequency noise components towards the cabin, such as those induced by a turbulent boundary layer (TBL) of air. In order to avoid the introduction of massive components such as active systems [1, 2], porous materials [3] or damping treatments [4], structures made up of micro-perforated panels (MPP) are potential lightweight solutions that could be used to enhance the absorption and decrease the transmission of flow-induced noise.

MPP resonance absorbers have been initially introduced [5] in the frame of building acoustics. They are composed of sub-millimetric holes backed by an air cavity. They are known to be efficient in the mid-frequency range, typically over one or two octaves around the Helmholtz resonance, under plane wave and diffuse field excitations [6]. Visco-thermal dissipation of the acoustic energy occurs within and at the inlet/outlet of the MPP apertures, but acoustically-induced vorticity has also been observed when the MPP is exposed to high sound pressure levels [7]. Moreover, MPPs are tunable control devices. Their optimal performance can be targeted by a suitable selection of their constitutive parameters, such as the panel thickness, the size and shape of the perforations, the perforation ratio and the cavity depth. For instance, their input impedance has been optimized to maximize the axial decay rate of the least attenuated mode propagating in a duct, thereby leading to a compact locally-reacting silencer with partitioned cavity [8]. Unbacked MPPs are also able to provide damping due to their sole acoustic flow resistance [9].

The great bulk of studies on MPPs consider pure acoustic excitations. However, there is a great number of applications dealing with flow-excited MPPs. They include dissipative mufflers and external liners but also, when unbacked, deployable

high-drag perforated spoilers mounted on aircraft wings [10], perforated cladding panels wrapped around buildings to control light level exposure, but prone to wind-induced noise [11] and double-glazed ventilation window systems [12]. The interaction between a TBL and a perforated facesheet has been assessed theoretically [13, 14] and experimentally [15, 16]. These studies showed that additional broadband and tonal sound is generated for values of the hole-based Strouhal number, $\mathrm{St_h} = f d_h / U_\infty$, greater than 0.1, with f the frequency, d_h the holes diameter and U_∞ the flow free-stream velocity. Considering MPPs of locally- or extended-reaction types, the influence of a low-speed grazing flow on their acoustical impedance has been characterized from flow duct measurements [17].

In practice, both aerodynamic and acoustic wall-pressures excite the MPP structure. Moreover, the use of lightweight micro-perforated facesheet with sub-millimetric thickness requires to account for the effect of elasticity on the MPP acoustical performance. The objective of the present work is to provide modelling and experimental methodologies to assess the ability of elastic MPPs to enhance the absorption and/or to reduce the transmission of aero-acoustic wall-pressures induced by low speed flows through partitions, without the drawback of generating additional noise. Wind-tunnel aero-vibroacoustic experiments as well as simulations have been conducted on two configurations shown in Fig. 1 and assuming a low-speed subsonic TBL:

1. A flush-mounted elastic MPP backed by a single layer cavity and excited by a fully-developed TBL.
2. A recessed unbacked MPP constituting the flexible floor of a shallow cavity in transitional flow regime.

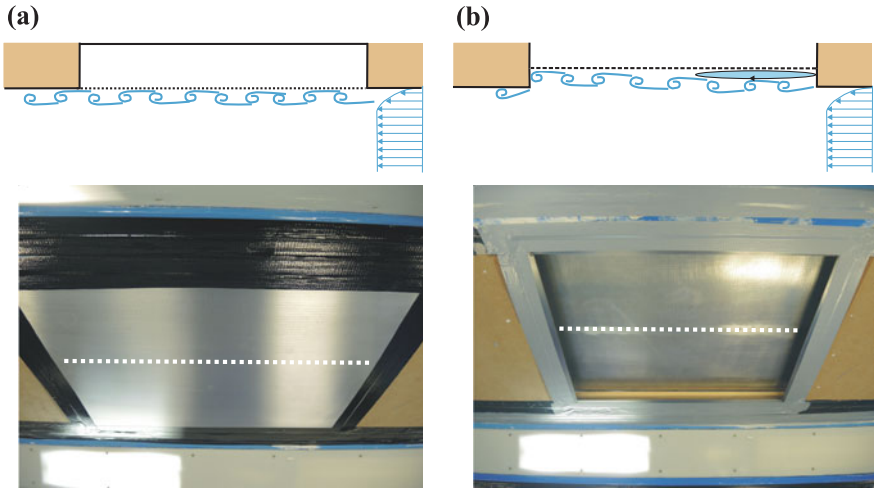

Fig. 1 Drawings and photos of a MPP mounted-flush (**a**) and in a recessed position (**b**) at the top wall of a low-speed wind-tunnel, respectively in backed (**a**) and unbacked (**b**) configurations; the white points on the MPP (**a**) and on the cavity floor (**b**) are the wall-pressure measurement positions

The paper is organized as follows. Section 2 addresses the absorption and transmission of boundary layer noise through flush-mounted MPP partitions. Predictions from analytical methods are assessed against measurements of the powers injected and transmitted through the structure. The sensitivity of the system acoustical performance is evaluated with respect to both the excitation and the MPP constitutive parameters. Section 3 focuses on the wall-pressures distributed over an unbacked MPP located at a recessed position, thus forming the base wall of a shallow cavity exposed to an incoming TBL. Lattice-Boltzmann simulations have been performed to interpret the attenuation results observed in the wall-pressure measurements. Section 4 summarizes the main results of the paper.

2 Absorption and Transmission of Boundary Layer Noise through Flush-Mounted MPP Partitions

The goals of this section are (i) to provide cost-efficient models able to predict the absorption and transmission of boundary layer noise through flush-mounted elastic MPP partitions and (ii) to propose an experimental methodology in order to determine part of the incident power injected or transmitted through these partitions. Although multiple-layer MPP partitions have been studied, they do not substantially modify the methods that will be presented here on a single-layer MPP partition, as the one shown in Fig. 2.

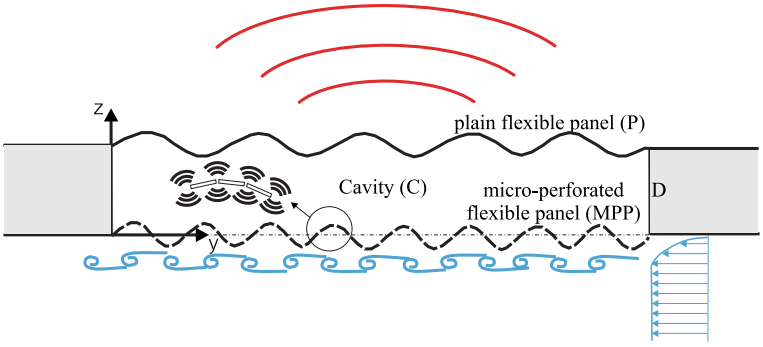

Fig. 2 Sketch of a single-layer MPP partition flush-mounted in a rigid wall and with a front face excited by a TBL

2.1 Modelling Study

Formulations are presented that predict the vibro-acoustic response of a MPP partition to an aeroacoustic random excitation in the modal and wavenumber domains, assuming respectively finite- and infinite-sized partitions.

2.1.1 MPP Impedance Model

One assumes that the MPP is made up of circular holes uniformly distributed and separated by a distance b_h, that is much lower than the acoustic wavelength ($b_h < \lambda/4$) to deduce effective properties, but greater than the holes diameter d_h ($b_h > 5d_h$) to neglect the aperture interaction effects. The acoustical effects of the MPP subject to a grazing flow of Mach number M are described by an overall transfer impedance, Z_{MPP}/σ, given by

$$\frac{Z_{\mathrm{MPP}}}{\sigma} = \frac{\mathrm{j}\omega\rho_0 t_h}{\sigma}\left[1 - \frac{2}{k_h\sqrt{-\mathrm{j}}}\frac{J_1\left(k_h\sqrt{-\mathrm{j}}\right)}{J_0\left(k_h\sqrt{-\mathrm{j}}\right)}\right]^{-1} + \frac{\mathrm{j}\omega\rho_0}{\sigma}\frac{8d_h}{3\pi}F_M + \frac{4R_e}{\sigma} + \frac{K|M|}{\sigma}Z_0, \tag{1}$$

where σ is the perforation ratio, J_0 and J_1 are Bessel functions of the first kind and of respective orders 0 and 1, $k_h = \left(d_h/2\right)/\delta_v$, is the perforate constant, e.g. the ratio of the holes radius to the viscous boundary layer thickness, $\delta_v = \sqrt{\eta/\rho_0\omega}$, with η the dynamic viscosity of the air and ρ_0 the air density. The first term in Eq. (1) represents inner viscous dissipation and inertial effects while the second and third terms account for added mass and frictional loss end-corrections that occur at the inlet/outlet of the MPP holes [6]. The latter correction involves the external resistance, $R_e = \sqrt{\eta\rho_0\omega/2}$, for holes with rounded edges, which is the case when dealing with drilled perforations. Flow induced corrections [18] appear in the second and fourth terms of Eq. (1). They increase the MPP resistance by $K|M|Z_0/\sigma$, with $Z_0 = \rho_0 c_0$ the air characteristic impedance and c_0 the sound speed in air. A value of $K = 0.15$ has been obtained from flow duct measurements for $|M| < 0.15$. The flow also decreases the transfer reactance by a factor $F_M = \left[1 + (12.6\,|M|)^3\right]^{-1}$, but this is second-order effect with respect to the increased resistance. Note that Eq. (1) is valid for $1 \leq k_h \leq 10$.

2.1.2 Modal Formulation

A fully-coupled modal formulation is established for a single-layer flexible MPP partition set in an infinite rigid baffle and undergoing boundary layer noise random

excitation, as shown in Fig. 2. In frequency domain ($e^{j\omega t}$), stochastic variables such as the velocities $\tilde{v}_{\mathrm{MPP,P}}$ at a location $\mathbf{x}$ on the MPP and on the back panel, as well as the acoustic pressure $\tilde{p}$ at a location $\mathbf{r}$ within the cavity, are respectively expanded as truncated series of the panels structural modes and of the acoustic modes of the rigid-walled cavity as follows

$$\tilde{v}_{\mathrm{MPP,P}}(\mathbf{x};\omega) = \mathrm{j}\omega\, \boldsymbol{\psi}_{\mathrm{MPP,P}}^{\mathrm{T}}\, \tilde{\mathbf{q}}_{\mathrm{MPP,P}}, \tag{2}$$

$$\tilde{p}(\mathbf{r};\omega) = -\mathrm{j}\omega\, \rho_0 \boldsymbol{\Phi}^{\mathrm{T}} \tilde{\mathbf{a}}, \tag{3}$$

with $\boldsymbol{\psi}_{\mathrm{MPP,P}}^{\mathrm{T}} = \left\{ \psi_{(\mathrm{MPP,P}),n}(\mathbf{x}) \right\}_{n=1,\ldots,N_{\mathrm{MPP,P}}}$ and $\boldsymbol{\Phi}^{\mathrm{T}} = \{\phi_m(\mathbf{r})\}_{m=0,\ldots,M_{\mathrm{C}}-1}$ the vectors of the panels structural modes and cavity acoustic modes. $\tilde{\mathbf{q}}_{\mathrm{MPP,P}}$ and $\tilde{\mathbf{a}}$ are the vectors of the unknown modal amplitudes gathered in $\tilde{\mathbf{X}} = \{\tilde{\mathbf{q}}_{\mathrm{MPP}}, \tilde{\mathbf{a}}, \tilde{\mathbf{q}}_{\mathrm{P}}\}^{\mathrm{T}}$, the vector of stochastic modal variables, with $^{\mathrm{T}}$ the transpose operator. Continuity of the air particle velocity on the panel surfaces may be written as

$$\frac{1}{\mathrm{j}\omega\rho_0} \frac{\partial \tilde{p}}{\partial z}\bigg|_{z=0} = (1-\sigma)\, \tilde{v}_{\mathrm{MPP}} + \frac{\sigma}{Z_{\mathrm{MPP}}} (\tilde{p}_d - \tilde{p}), \tag{4}$$

over the front MPP [19] and,

$$\frac{\partial \tilde{p}}{\partial z}\bigg|_{z=D} = \mathrm{j}\omega\rho_0 \tilde{v}_{\mathrm{P}}, \tag{5}$$

on the back panel. In Eq. (4), $\tilde{p}_d - \tilde{p}$ is the pressure jump across the MPP holes, $\tilde{p}_d$ is the external wall-pressure and $\sigma \big/ Z_{\mathrm{MPP}}$ is the overall acoustic admittance of the MPP obtained from Eq. (1). Equation (4) is valid provided that the MPP holes pitch is much smaller than the acoustic wavelength. It shows that the average air particle velocity over the MPP is the sum of the panel normal velocity $\tilde{v}_{\mathrm{MPP}}$ and of the air particle velocity flowing through each hole $(\tilde{p}_d - \tilde{p}) \big/ Z_{\mathrm{MPP}}$, weighted by their respective filling fraction $1-\sigma$ and σ.

Substituting the boundary conditions (4) and (5) into Green's integral representation for the acoustic pressure in the cavity (see Eq. (6) in [20]) and using the orthogonality property between the cavity modes ϕ_m, one obtains the following set of M_{C} coupled algebraic equations for the cavity pressure modal amplitudes $\tilde{\mathbf{a}}$:

$$V_{\mathrm{C}} M_{\mathrm{C},m} \left(\omega_{\mathrm{C},m}^2 + 2\mathrm{j}\omega\xi_{\mathrm{C},m}\omega_{\mathrm{C},m} - \omega^2\right) \tilde{a}_m - \mathrm{j}\,\omega\, c_0^2 \left(\sum_{n=1}^{N_{\mathrm{MPP}}} \tilde{q}_{\mathrm{MPP},n} L_{\mathrm{MPP},mn} + \sum_{n=1}^{N_{\mathrm{P}}} \tilde{q}_{\mathrm{P},n} L_{\mathrm{P},mn} - \frac{\sigma\, \rho_0}{Z_{\mathrm{MPP}}} \sum_{m'=0}^{M_{\mathrm{C}}-1} \tilde{a}_{m'} H_{\mathrm{C},mm'} \right) = -\frac{\sigma\, c_0^2}{Z_{\mathrm{MPP}}} \tilde{p}_{d,m}, \tag{6}$$

where V_C is the cavity volume and $M_{C,m}$ the cavity acoustic generalized mass such that $\iiint_{V_C} \phi_m \phi_{m'} \mathrm{d}V = V_C M_{C,m} \delta_m^{m'}$. $\omega_{C,m}$ is the natural frequency corresponding to the m-th cavity normal mode and $\xi_{C,m}$ the associated acoustic modal damping ratio. $L_{(\mathrm{MPP,P}),mn}$ are the modal coupling coefficients between the m-th acoustic mode of the cavity and the n-th structural mode of either the MPP or the back panel. They are given by $L_{(\mathrm{MPP,P}),mn} = \iint_{A_{(\mathrm{MPP,P})}} \phi_m \psi_n \, \mathrm{d}A$ with $A_{\mathrm{MPP,P}}$ the MPP and back panel surfaces. Cross-coupling of the cavity modes by the MPP apertures involves the factor $H_{C,mm'}$ that reads $H_{C,mm'} = \iint_{A_{\mathrm{MPP}}} \phi_m \phi_{m'} \mathrm{d}A$. The right-hand side of Eq. (6) is associated to the overall generalized force exerted on the m-th cavity mode by the external wall-pressures through the MPP holes. It involves the term $\tilde{p}_{d,m} = \iint_{A_{\mathrm{MPP}}} \tilde{p}_d \, \phi_m \mathrm{d}A$ where $\tilde{p}_d = \tilde{d} + \tilde{p}_{\mathrm{rad}}$ is the sum of the blocked pressure $\tilde{d}$, as if the MPP was rigid, plus the pressure back-radiated by both the panel and the micro-perforations, $\tilde{p}_{\mathrm{rad}}$.

The structural modal equations are obtained after inserting the expansions (2) into the panels Kirchhoff equations [19] governing the MPP and back panel vibrations and projecting these equations onto the structural modal basis functions $\psi_{(\mathrm{MPP,P}),n}$. Orthogonality of the structural modes leads to a set of $N_{(\mathrm{MPP,P})}$ coupled algebraic equations given by

$$M_{(\mathrm{MPP,P}),n}\left(\omega^2_{(\mathrm{MPP,P}),n} + 2\mathrm{j}\omega\xi_{(\mathrm{MPP,P}),n}\omega_{(\mathrm{MPP,P}),n} - \omega^2\right)\tilde{q}_{(\mathrm{MPP,P}),n} + \mathrm{j}\omega\rho_0 \sum_{m=0}^{M_C-1} \tilde{a}_m L_{(\mathrm{MPP,P}),mn} = -\tilde{F}_{(\mathrm{MPP,P}),n} \,, \tag{7}$$

with $\tilde{F}_{\mathrm{P},n} = 0$ and $\tilde{F}_{\mathrm{MPP},n} = \iint_{A_{\mathrm{MPP}}} \tilde{p}_d \, \psi_{\mathrm{MPP},n} \mathrm{d}A$, the generalized force due to the external wall-pressures $\tilde{p}_d$ exerted on the MPP n-th structural mode. In Eq. (7), $M_{(\mathrm{MPP,P}),n}$ are the structural generalized masses of the panels, $\omega_{(\mathrm{MPP,P})n}$ their natural frequencies and $\xi_{(\mathrm{MPP,P}),n}$ the corresponding structural modal damping ratio.

Equations (6) and (7) constitute a set of $N_{\mathrm{MPP}} + M_C + N_P$ coupled algebraic equations for the MPP-Cavity-Panel (MPPCP) system. It is given by $\mathbf{G}\tilde{\mathbf{X}} = \tilde{\mathbf{Q}}$ where $\mathbf{G} = -\omega^2\mathbf{M} + \mathrm{j}\omega\,(\mathbf{D} + \mathbf{L} + \mathbf{H}) + \mathbf{S}$ is the modal dynamic stiffness matrix of the MPPCP partition with $\mathbf{M}$, $\mathbf{D}$ and $\mathbf{S}$ the diagonal mass, damping and stiffness matrices. $\mathbf{L}$ and $\mathbf{H}$ are sparse matrices related respectively to panel-cavity and cavity-hole-cavity modal coupling. All these matrices are defined in the above.

Numerical simulations showed that the power back-radiated by the MPP was negligible with respect to the power injected by the blocked pressures due to $\tilde{p}_{\mathrm{rad}} << \tilde{d}$. The generalized modal excitation vector $\tilde{\mathbf{Q}}$ thus reduces to $\left\{-\boldsymbol{\psi}_{\mathrm{MPP}}\tilde{\mathbf{d}}; -\sigma\, c_0^2 \boldsymbol{\Phi}\, \tilde{\mathbf{d}} \Big/ Z_{\mathrm{MPP}}; \mathbf{0}; \mathbf{0}\right\}^{\mathrm{T}}$ with $\tilde{\mathbf{d}}$ the vector of the blocked pressures on the partition front wall. The associated Cross-Spectral Density (CSD) matrix is defined as $\mathbf{S_{QQ}} = \mathrm{E}\left[\tilde{\mathbf{Q}}\tilde{\mathbf{Q}}^{\mathrm{H}}\right]$ with $\mathrm{E}[\tilde{x}\,\tilde{y}]$ the expectation operator between the

stochastic variables $\tilde{x}$ and $\tilde{y}$, and $^{\mathrm{H}}$ the transpose conjugate operator. $\mathbf{S_{QQ}}$ may be written as

$$\mathbf{S_{QQ}} = \begin{bmatrix} \boldsymbol{\psi}_{\mathrm{MPP}}\mathbf{S_{dd}}\boldsymbol{\psi}_{\mathrm{MPP}}^{\mathrm{T}} & c_0^2\frac{\sigma}{Z_{\mathrm{MPP}}^*}\boldsymbol{\psi}_{\mathrm{MPP}}\mathbf{S_{dd}}\boldsymbol{\Phi}^{\mathrm{T}} & \mathbf{0}\ \mathbf{0} \\ c_0^2\frac{\sigma}{Z_{\mathrm{MPP}}}\boldsymbol{\Phi}\mathbf{S_{dd}}\boldsymbol{\psi}_{\mathrm{MPP}}^{\mathrm{T}} & c_0^4\frac{\sigma^2}{|Z_{\mathrm{MPP}}|^2}\boldsymbol{\Phi}\mathbf{S_{dd}}\boldsymbol{\Phi}^{\mathrm{T}} & \mathbf{0}\ \mathbf{0} \\ \mathbf{0} & \mathbf{0} & \mathbf{0}\ \mathbf{0} \\ \mathbf{0} & \mathbf{0} & \mathbf{0}\ \mathbf{0} \end{bmatrix}, \tag{8}$$

in terms of $\mathbf{S_{dd}} = \mathrm{E}\left[\tilde{\mathbf{d}}\tilde{\mathbf{d}}^{\mathrm{H}}\right]$, the CSD matrix between the blocked wall-pressure fluctuations. $\mathbf{S_{QQ}}$ is composed of four non-zero blocks: the (1, 1) block represents the cross-coupling between the MPP modes and the external blocked pressures; the (2, 2) block describes how the cavity modes are cross-coupled by the excitation through the MPP holes; the (1, 2) and (2, 1) blocks determine how the MPP and the cavity modes are cross-coupled by the random forcing. One thus obtains the CSD between the modal amplitudes as $\mathbf{S_{XX}} = \mathrm{E}\left[\tilde{\mathbf{X}}\tilde{\mathbf{X}}^{\mathrm{H}}\right] = \mathbf{G}^{-1}\mathbf{S_{QQ}}\left(\mathbf{G}^{-1}\right)^{\mathrm{H}} = \mathbf{G}^{-1}\mathbf{S_{QX}}$.

From the components of $\mathbf{S_{XX}}$, one can then calculate the transmission loss (TL) of the partition as $\mathrm{TL} = 10\log_{10}\left(\mathrm{W_{inc}}/\mathrm{W_{trans}}\right)$ with

$$\mathrm{W_{inc}} = \frac{\Delta s_{\mathrm{MPP}}}{\gamma_{\mathrm{E}}\rho_0 c_0}\mathrm{Tr}\left[\mathbf{S_{dd}}\right], \tag{9}$$

the equivalent incident power [4] due to an acoustic diffuse field ($\gamma_{\mathrm{E}} = 4$) or to a pure TBL excitation ($\gamma_{\mathrm{E}} = 8$) and Δs_{MPP} the elemental area over the discretized MPP surface, and

$$\mathrm{W_{trans}} = \frac{\rho_0\omega^2}{2}\Delta s_P\,\mathrm{Tr}\left[\boldsymbol{\psi}_{\mathrm{P}}^{\mathrm{T}}\mathbf{S_{q_P q_P}}\boldsymbol{\psi}_{\mathrm{P}}\mathbf{R}_{\mathrm{rad}}\right], \tag{10}$$

the sound power radiated by the transmitting baffled panel. It depends on Δs_{P} the elemental area over the discretized back panel surface and $\mathbf{R}_{\mathrm{rad}}$ the radiation resistance matrix [21]. In Eqs. (9) and (10), Tr[**A**] denotes the trace of the matrix **A**, e.g. the sum of its diagonal elements.

The absorption coefficient of the partition corresponds to the part of incident power flowing through the structure. It is defined as $\alpha = \mathrm{W_{flow}}/\mathrm{W_{inc}}$ with

$$\mathrm{W_{flow}} = \frac{\Delta s_{\mathrm{MPP}}}{2}\mathrm{Re}\left\{\mathrm{Tr}\left[\mathrm{E}\left(\tilde{\mathbf{d}}\tilde{\mathbf{v}}_{\mathbf{d}}^{\mathrm{H}}\right)\right]\right\}, \tag{11}$$

and Re the real part operator. Inserting the modal decompositions for the MPP velocity and the cavity pressures, respectively given by Eqs. (2) and (3), into Eqs. (4) and (11) provides the following expression for the power $\mathrm{W_{flow}}$ injected by the blocked pressures into the MPPCP

$$\mathrm{W}_{\mathrm{flow}} = \frac{1}{2}\mathrm{Re}\Big\{ -\mathrm{j}\omega(1-\sigma)\mathrm{Tr}\Big[\mathbf{S}_{\mathbf{QX}}^{[1,1]}\Big] + \frac{\sigma}{Z_{\mathrm{MPP}}^{*}}\Big(\Delta s_{\mathrm{MPP}}\mathrm{Tr}[\mathbf{S}_{\mathbf{dd}}] - \frac{\mathrm{j}\omega\rho_0 Z_{\mathrm{MPP}}}{\sigma\, c_0^2}\mathrm{Tr}\Big[\mathbf{S}_{\mathbf{QX}}^{[2,2]}\Big]\Big)\Big\}, \tag{12}$$

in terms of the sub-blocks (1, 1) and (2, 2) of $\mathbf{S_{QX}} = \mathbf{G}\mathbf{S_{XX}} = \mathbf{S_{QQ}}\big(\mathbf{G}^{-1}\big)^{\mathrm{H}}$ the expressions of which are detailed in [22]. The absorption and the transmission loss still require knowledge of the CSD matrix for the random excitations modelled in Sect. 2.1.4.

2.1.3 Wavenumber Formulation

A simplified 2D model is formulated in the wavenumber domain to predict the absorption and TL of a single layer MPP partition of infinite extent, undergoing an aeroacoustic excitation along the streamwise direction. From Parseval's theorem applied to the definition of $\mathrm{W}_{\mathrm{trans}}$ in the space-frequency domain, one gets:

$$\mathrm{W}_{\mathrm{trans}} = \frac{1}{2}\mathrm{Re}\left\{\int_{-\infty}^{\infty} S_{p_{\mathrm{P}}v_{\mathrm{P}}}(y;\omega)\,\mathrm{d}y\right\} = \frac{1}{2}\mathrm{Re}\left\{\int_{-\infty}^{\infty} \hat{S}_{p_{\mathrm{P}}v_{\mathrm{P}}}\big(k_y;\omega\big)\,\mathrm{d}k_y\right\}, \tag{13}$$

with $\hat{S}$ the wavenumber Fourier transform of S. Helmholtz integral representation of the transmitted pressure leads to

$$S_{p_{\mathrm{P}}v_{\mathrm{P}}}(y;\omega) = \frac{\rho_0 c_0 k_0\,\omega^2}{2}\int_{-\infty}^{\infty} H_0^{(1)}\big(k_0\big|y-y'\big|\big)\, S_{w_{\mathrm{P}}w_{\mathrm{P}}}\big(y';\omega\big)\,\mathrm{d}y', \tag{14}$$

with $H_0^{(1)}$ the Hankel function of the first kind of order zero, $k_0 = \omega/c_0$ the acoustic wavenumber and $S_{w_{\mathrm{P}}w_{\mathrm{P}}}$ the auto spectral density of the back panel normal displacement $\tilde{w}_{\mathrm{P}}$. Applying the convolution theorem to Eq. (14) provides the following representation of $S_{p_{\mathrm{P}}v_{\mathrm{P}}}$in the wavenumber-frequency domain:

$$\hat{S}_{p_{\mathrm{P}}v_{\mathrm{P}}}\big(k_y;\omega\big) = \frac{\rho_0 c_0 k_0\,\omega^2}{2k_z}\,\hat{S}_{w_{\mathrm{P}}w_{\mathrm{P}}}\big(k_y;\omega\big), \tag{15}$$

with $k_z = \sqrt{k_0^2 - k_y^2}$ when dealing with supersonic trace wavenumbers ($\big|k_y\big| \le k_0$) and $k_z = -\mathrm{j}\sqrt{k_y^2 - k_0^2}$ when dealing with subsonic trace wavenumbers ($\big|k_y\big| > k_0$). Because the infinite back panel is a space- and time-invariant system, its wavenumber-frequency response $\hat{S}_{w_{\mathrm{P}}w_{\mathrm{P}}}$ to a random excitation is related to the excitation wavenumber-frequency spectrum $\hat{S}_{dd}$ as follows [23]

$$\hat{S}_{w_P w_P}(k_y;\,\omega) = \left|\hat{F}_{w_P}(k_y)\right|^2 \hat{S}_{dd}(k_y;\,\omega), \tag{16}$$

with $\hat{F}_{w_P}(k_y)$ the spatial Fourier transform of the back panel normal displacement when the front MPP is excited by a wave of trace wavenumber k_y. The sound power transmitted by the partition can then be obtained from Eqs. (13), (15) and (16):

$$\mathrm{W}_{\mathrm{trans}} = \frac{\rho_0 c_0 k_0\,\omega^2}{2} \int_{-k_0}^{k_0} \frac{\left|\hat{F}_{w_P}(k_y)\right|^2}{\sqrt{k_0^2 - k_y^2}} \hat{S}_{dd}(k_y;\,\omega)\,\mathrm{d}k_y, \tag{17}$$

which involves a finite integration over the supersonic trace wavenumbers.

A similar derivation can be achieved for the sound power injected by the aeroacoustic excitation into the partition. One first applies Parseval's theorem to its definition in the space-frequency domain:

$$\mathrm{W}_{\mathrm{flow}} = \frac{1}{2}\mathrm{Re}\left\{\int_{-\infty}^{\infty} S_{p_d v_d}(y;\,\omega)\,\mathrm{d}y\right\} = \frac{1}{2}\mathrm{Re}\left\{\int_{-\infty}^{\infty} \hat{S}_{p_d v_d}(k_y;\,\omega)\,\mathrm{d}k_y\right\}. \tag{18}$$

It can shown [23] that

$$\hat{S}_{p_d v_d}(k_y;\,\omega) = \frac{k_z}{\rho_0 c_0 k_0}\,\hat{Q}_{p_d}(k_y)\,\hat{Q}^*_{v_d}(k_y)\,\hat{S}_{dd}(k_y;\,\omega), \tag{19}$$

where $\hat{Q}_{p_d}(k_y)$ and $\hat{Q}_{v_d}(k_y)$ are respectively the spatial Fourier transform of the pressures and normal particle velocities over the MPP excited by a wave with either supersonic or subsonic trace wavenumber. Hence, one obtains

$$\mathrm{W}_{\mathrm{flow}} = \frac{1}{2\rho_0 c_0 k_0} \int_{-\infty}^{\infty} \mathrm{Re}\left[\hat{Q}_{p_d}(k_y)\;\hat{Q}^*_{v_d}(k_y)\,k_z\right] \hat{S}_{dd}(k_y;\,\omega)\,\mathrm{d}k_y. \tag{20}$$

The indefinite integral in Eq. (20) is evaluated by a Gauss-Legendre quadrature over an interval that will be discussed in Sect. 2.1.4.

2.1.4 Random Excitation Models

Wall-pressure measurements in an anechoic wind-tunnel showed that both the acoustic and the turbulent components coexist in the aeroacoustic excitation of a smooth panel by a fully-developed TBL [24]. Their spatial correlation properties may be described by assuming an additive aeroacoustic excitation whose CSD is given by

$$S_{dd}(r_x, r_y;\, \omega) = \frac{S_0(\omega)}{1+A}\left[\mathrm{e}^{-|r_x|/L_x}\mathrm{e}^{-|r_y|/L_y}\mathrm{e}^{-\mathrm{j}\,\omega\, r_y/U_c} + A\,\mathrm{sinc}\,(k_0 r)\right], \tag{21}$$

with $S_0(\omega) = S_{dd}(0;\omega)$ the excitation point-power spectrum, k_0 the acoustic wavenumber and A the magnitude of the acoustic component. Measurements in [24] at $U_\infty = 55\ \mathrm{m\,s^{-1}}$ provided an acoustic contribution of $A = 5\%$ above 1kHz, with a magnitude that may significantly increase at low frequencies due to the wind-tunnel resonances. The first term in (21) is a Corcos-type model [25] that accounts for pure aerodynamic excitation in which U_c is the convection velocity, $L_{x,y} = \alpha_{x,y}\, U_c / \omega$ are the correlation lengths, respectively along the spanwise x- and streamwise y-directions, and $\alpha_{x,y}$ are empirical coefficients estimated from wall-pressure measurements.

The convection velocity was estimated from $U_c \approx -\omega\, r_y / \Delta\phi$ where $\Delta\phi$ is the phase difference between the wall-pressure signals of two microprobes separated by a distance r_y along the streamwise direction. It followed Chen's law [26], $U_c = U_\infty\left(0.6 + 0.4\,\mathrm{e}^{-2.2\ \mathrm{St_d}}\right)$, for Strouhal numbers, $\mathrm{St_d} = \omega\delta^* / U_\infty$, greater than 0.2, with $\delta^*$the boundary layer displacement thickness. This provides a steady decay of the convection velocity down to $U_c = 0.6\, U_\infty$ when the frequency increases.

Moreover, the values of α_x and α_y have been made frequency-dependent in order to obtain a good correlation between the measured and predicted cross-correlation functions of the TBL wall-pressures along the spanwise and streamwise directions, as those presented in Fig. 5 of Sect. 2.2. The values of α_x and α_y were found to be lower than those initially provided by Corcos for a high-speed subsonic TBL [25]. They provided amplitudes of the TBL sub-convective components that complied, in the wavenumber domain, with those predicted by the Smol'yakov-Tkatchenko model [27]. More details are given in Sect. 2.2. on the correlation lengths frequency dependence.

The second term in Eq. (21) is related to an acoustic diffuse field excitation [28]. By taking the spatial Fourier transform of Eq. (21) along the streamwise direction, one obtains a 2D model for $\hat{S}_{dd}$ the CSD of the excitation in the wavenumber domain, as follows

$$\hat{S}_{dd}(k_y;\, \omega) = \frac{S_0(\omega)}{1+A}\left\{\frac{\alpha_y k_c}{\pi\left[k_c^2 + \alpha_y^2\left(k_c - k_y\right)^2\right]} + \frac{\pi\, A}{k_0}\right\}, \tag{22}$$

with $k_c = \omega / U_c$ the convective wavenumber. It accounts for both supersonic and subsonic trace wavenumbers, respectively associated to the acoustic and turbulent components. The incident sound power is then readily obtained as $\mathrm{W_{inc}} = \pi\, \hat{S}_{dd}(k_y = 0;\, \omega) / (4\rho_0 c_0)$. Given $\mathrm{W_{inc}}$ and substituting Eq. (22) into Eqs. (17) and (20), the transmission loss and the absorption coefficient of the MPPCP partition under an aeroacoustic excitation can be calculated from the 2D wavenumber model. Note that a suitable interval of integration for Eq. (20) is *a priori* given by $\left[-k_y^{\max}, k_y^{\max}\right]$ with $k_y^{\max} = 4\max(k_c, k_f)$, k_f being the flexural wavenumber of

the MPP. For low-speed flow applications and for frequencies well-above the aerodynamic coincidence frequency ($k_c >> k_f$), this criterion reads $k_y^{\max} = 4k_c$. In practice, it can further be reduced to $k_y^{\max} = 4k_f$ due to the weak contribution of the convective peak with respect to the structural filtering effect [26], as shown in [29] for an infinite stiffened panel under a TBL excitation.

2.1.5 Finite- Versus Infinite-Sized Models Predictions

Figure 3 shows the TL and absorption coefficient of a MPPCP partition made up of two steel simply-supported panels of dimensions 0.22 m × 0.35 m with a modal damping ratio of 0.01. The 1 mm thick front MPP has circular holes of diameter 0.5 mm and a perforation ratio 0.52%. The back panel is 0.7 mm thick. They are separated by an air cavity depth $D = 0.15$ m so that the Helmholtz resonance theoretically occurs at 216 Hz [6].

The TL and absorption curves present variations consistently predicted by both modal and wavenumber formulations under a pure TBL or an acoustic diffuse field

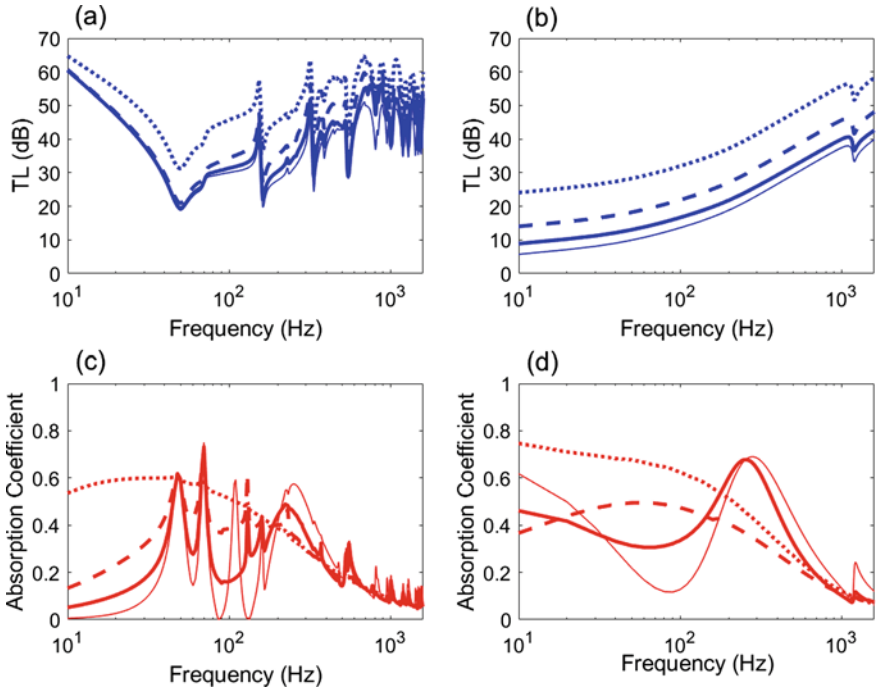

Fig. 3 Predictions of the TL and absorption coefficient of a MPPCP partition using modal [(**a**), (**c**)] and wavenumber [(**b**), (**d**)] formulations for a pure TBL (TL: blue; absorption coefficient: red) with increasing values of the flow free-stream velocity ($U_\infty = 10$ m s^{-1}: dots; 100 m s^{-1}: dashed; 300 m s^{-1}: thick solid) and for an acoustic diffuse field (thin solid)

with, as expected, an underestimate of the TL below the first MPPCP mode resonance frequency at 52 Hz. For increasing values of the flow free-stream velocity, e.g. for $U_\infty = 10\ \mathrm{m\,s^{-1}}$, $100\ \mathrm{m\,s^{-1}}$ and $300\ \mathrm{m\,s^{-1}}$, the MPP is efficiently excited over an aerodynamic coincidence frequency range of increasing extent, namely up to 6 Hz, 648 Hz and 5800 Hz respectively. Moreover, the TBL correlation area increases accordingly and couples more and more efficiently with the MPP modes up to $k_c = k_f$. As a consequence, both formulations lead to a gradual decrease of the TL by about 16 dB, as seen in Fig 3a, b, due to an increase of $\mathrm{W_{trans}}$ with U_∞.

The absorption coefficient shown in Fig. 3c, d also presents variations consistently predicted by both formulations. When U_∞ increases from $10\ \mathrm{m\,s^{-1}}$ to $300\ \mathrm{m\,s^{-1}}$, a maximum of absorption due to the Helmholtz-type resonance of the MPPCP partition progressively emerges at 230 Hz, due to the half-bandwidth supersonic components of the TBL that growingly fall into of the acoustic domain. It is preceded by absorption peaks that correspond to the MPP volumetric resonances that efficiently couple with the supersonic forcing field components. When $U_\infty = 10\ \mathrm{m\,s^{-1}}$, the absorption coefficient stays above 0.5 below 200 Hz due to weak back-scattering and significant transmission of the hydrodynamic pressures by the MPP holes. It complies with Ffowcs-Williams theory [13] that predicts a dipole-type behavior of the circular orifices beneath a fully-developed TBL as long as the hole-based Strouhal number, $\mathrm{St_h} = f d_h / U_\infty$, stays lower than 0.1. It provides, in the low-speed regime, a critical frequency, $f_{\mathrm{FW}} = 2\sigma\, c_0 / \left(\pi^2 d_h\right)$, here at 716 Hz, above which the turbulence is efficiently back-scattered into sound by the MPP apertures that behave like monopoles above f_{FW}. It explains the low values of absorption and transmission observed in Fig. 3c, d above 716 Hz.

One should bear in mind that the above results do not consider aeroelastic coupling effects between the MPP structural response and the turbulent boundary layer of air. These effects are negligible for a low speed TBL, but, as the flow Mach number increases and approaches 1, they lead to a downshift of the panel natural frequencies and an increase in the level of aeroelastic damping, e.g. an increase of the transmission loss [30]. So, this effect may counterbalance for high subsonic flow speeds, the monotonic decrease of TL observed in Fig. 3a, b. However, the beneficial effect of aeroelastic damping on the transmitted sound power is overwhelmed by the TBL point-power spectrum that increases, at a faster rate, with the square of the mean flow speed [31].

2.2 *Comparisons Against Wind-Tunnel Measurements*

The absorption and TL results predicted using the modal formulation have been assessed against measurements performed in a closed-loop wind tunnel (WT) of the IRPHE Fluid Dynamics Laboratory ("Institut de Recherche sur les Phénomènes Hors Equilibre", Marseille, France). A sketch and photos of the experimental facility is shown in Fig. 4.

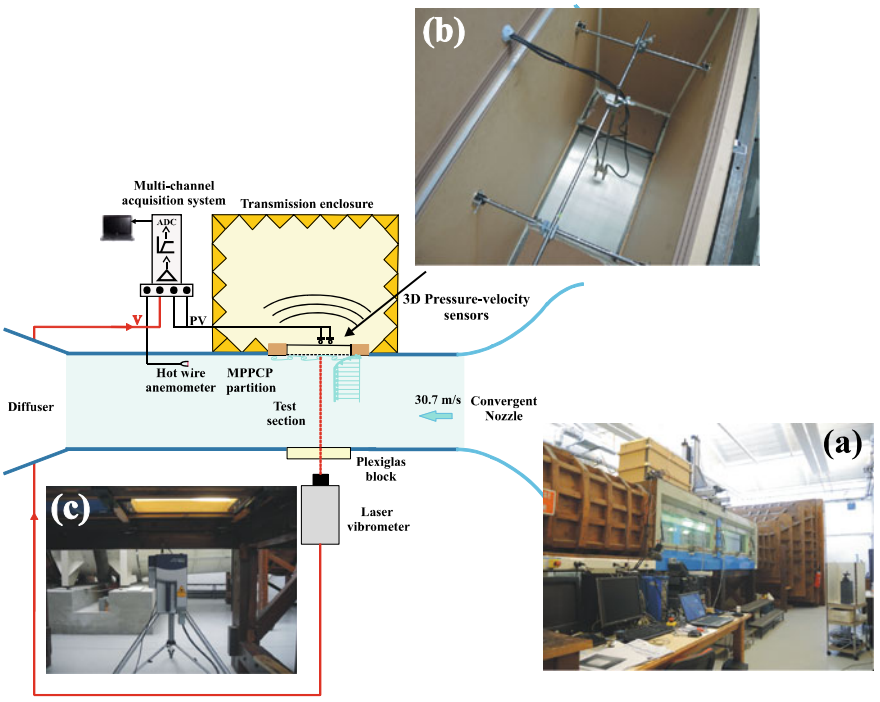

Fig. 4 Sketch and overall view (**a**) of the experimental facility used to estimate the TL and the absorption of a MPP partition flush-mounted onto the top wall of a low-speed WT test section and excited by a fully-developed TBL; The transmitted sound power is estimated from two collocated pressure-velocity sensors (**b**) and the front panel vibrations are obtained from laser vibrometer measurements (**c**)

The MPPCP test partition is made up of two aluminium panels, 1 mm thick, of dimensions 0.38 m × 0.47 m, clamped along their edges and separated by an air gap $D = 0.03$ m. The MPP apertures are circular holes, 0.5 mm diameter and with a perforation ratio of 0.59%. The measurement plan was as follows:

- Flow characterization has been achieved from hot-wire probe measurements performed at several distances from the top wall where the partition was flush-mounted. They showed that a fully-developed TBL is established in the test section with a free-stream velocity $U_\infty = 30.7\ \mathrm{m\,s^{-1}}$. The TBL mean flow velocity follows a seventh power law of the wall distance normalized by the boundary layer thickness, $\delta = 0.115$ m. The boundary layer shape factor is nearly equal to 1.28 so that it precludes the effect of an axial pressure gradient.
- Wall-pressure measurements have been carried out using two pinhole micro-probes, one of them being sequentially displaced over the flush-mounted MPP surface, and then over a plain panel ahead of the MPP. The spatially-averaged auto-power spectra (APS) collapse between both experiments [23], showing spatial homogeneity of the TBL wall-pressures. Moreover, the APS well correlate with

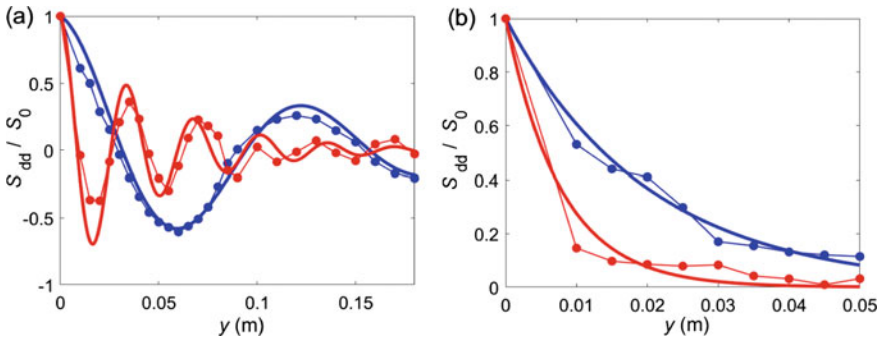

Fig. 5 Comparison between wall-pressure measurements (dots) performed over the flush-mounted MPP and updated Corcos-type model (solid) of the correlation functions of the TBL pressure fluctuations estimated at 200 Hz (blue) and at 600 Hz (red) along the streamwise [real part, (**a**)] and spanwise (**b**) directions

Goody's model [32] above 100 Hz. When spatially-averaged over the front panel partition, they provide a measure of the incident sound power W_{inc}. As shown in Fig. 5, the CSDs of the wall-pressures estimated along the streamwise and spanwise directions are in reasonable agreement with those calculated by a Corcos-type model provided that the empirical coefficients $\alpha_{x,y}$ are made-frequency-dependent as well as the convection velocity U_c. This implies that the correlation lengths $L_{x,y}$ are upper bounded by δ at low frequencies with a steady decay of their values as the frequency increases, following a $\omega^{-(1+\varepsilon)}$-dependency above 500 Hz with $\varepsilon \approx 0$ along the spanwise direction and $\varepsilon \approx 0.3$ along the streamwise direction. For instance, L_x (resp. L_y) decreased from 0.020 m (resp. 0.114 m) at 200 Hz down to 0.008 m (resp. 0.048 m) at 600 Hz. Above 500 Hz, α_x and α_y asymptote towards values (1.1 and 7.6) somewhat lower than the classical ones (1.4 and 8.6) which were found to overestimate the true correlation lengths.

- The TL measurements require an estimate of the active sound power radiated by the partition transmitting panel, that scales on $\mathrm{Tr}\left[\mathbf{S}_{\mathbf{p}_P\mathbf{v}_P}\right]$. This has been achieved using two collocated near-field pressure-velocity sensors sequentially positioned over a plane surface at a distance 0.01 m apart from the transmitting panel that radiates into an enclosure of 0.56 m^3 plugged onto the WT top wall, as shown in Fig. 4a, b. Figure 6 shows a good agreement between the predicted and measured TLs assuming a TBL excitation, with a higher transmission performance (by up to 20 dB) with respect to that due to a pure acoustic excitation, as already observed in Sect. 2.1.5. The acoustic forcing was experimentally achieved using a loudspeaker in the test section, thus leading to a multimodal excitation of the partition. It was accounted for in the model through an acoustic diffuse field, thereby leading to a greater variability in the correlation with the experiment, when compared to the TBL.
- The absorption coefficient requires an estimate of part of the incident power flowing into the MPP. When frequency-averaged, it reads

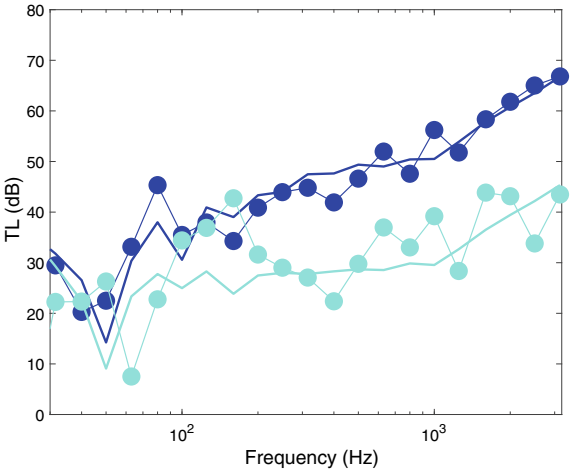

Fig. 6 Comparison between measurements (dots) and predictions (solid) of the third-octave averaged TL of a MPPCP partition undergoing TBL wall-pressure fluctuations (blue) and acoustic multimodal propagation condition (cyan)

$$\langle \mathrm{W}_{\mathrm{flow}} \rangle \approx \Omega\, \eta_{\mathrm{MPP}}\, \mu_{\mathrm{MPP}}\, S_{\mathrm{MPP}} \langle \bar{S}_{\mathbf{v_{MPP}} \mathbf{v_{MPP}}} \rangle + S_{\mathrm{MPP}} \mathrm{Re} \left\{ \langle \sigma\, Z_{\mathrm{MPP}}^{*-1}\, \bar{S}_{\mathbf{d(d-p)}} \rangle \right\}, \tag{23}$$

where Ω is the central frequency and the overbar denotes spatial averaging of the PSDs over the MPP surface area S_{MPP}. The first term in Eq. (23) accounts for the power structurally dissipated by the MPP with η_{MPP} its damping loss factor taken to be 0.002 and μ_{MPP} its surface mass density. $\langle \bar{S}_{\mathbf{v_{MPP}} \mathbf{v_{MPP}}} \rangle$ is readily evaluated from laser vibrometer measurements performed by transparency through a thick rigid block of Plexiglas flush-mounted in the bottom wall of the test section, as shown in Fig. 4c. The second term represents the power injected through the holes and either dissipated through or radiated by the apertures. It depends on $Z_{\mathrm{MPP}} / \sigma$ defined in Eq. (1) and on $\bar{S}_{\mathbf{d(d-p)}}$, the CSD between the wall-pressures and the pressure jump across the MPP. This term requires collocated measurement of the pressures on the external and cavity sides of the MPP. This could not be achieved in the experiment, so this term was approximated in Eq. (23) by $\bar{S}_{\mathbf{dd}}$ obtained by microprobe measurements over the MPP external side. The model showed that neglecting the wall back-pressures in the cavity overestimates the absorption coefficient below 200 Hz, which is confirmed by the trends observed in Fig. 7. In accordance with the predictions discussed in Sect. 2.1.5, Fig. 7 shows that most of the power injected by the aerodynamic pressures into the MPPCP partition are transmitted at low frequencies through the apertures that exhibit inefficient back-scattering properties below $f_{\mathrm{FW}} \approx 716$ Hz. In the case of a Panel-Cavity-Panel (PCP) with a plain front panel, $\mathrm{W}_{\mathrm{flow}}$ is only dissipated through the first volumetric panel modes highly excited by the TBL correlation function below the aerodynamic coincidence frequency of 64 Hz.

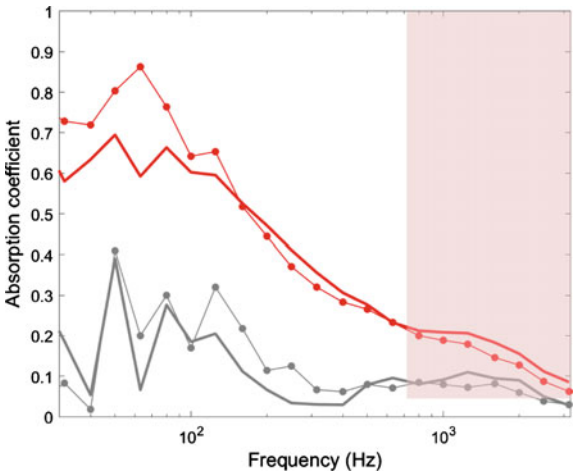

Fig. 7 Comparison between measurements (dots) and predictions (solid) of the third-octave averaged absorption coefficient of a flush-mounted single layer partition undergoing TBL wall-pressure fluctuations: MPPCP (red) and PCP (grey); the pink shaded area corresponds to the frequency range over which efficient back-scattering of the TBL wall-pressures into sound by the MPP apertures is predicted [13]

2.3 Influence of the Excitation and of the MPP Parameters

Cost-efficient parametric studies have been performed using the wavenumber formulation presented in Sect. 2.1.3 to assess the effect of the acoustic component and of the MPP constitutive parameters on the TL and on the absorption coefficient of a MPPCP partition. The nominal layout is made up of two aluminium panels, 1 mm thick, separated by an air gap $D = 0.03$ m. The front panel is a MPP with circular holes, 1 mm diameter and with a perforation ratio of 0.2%, undergoing an aeroacoustic TBL excitation with free-stream velocity $U_\infty = 30\ \mathrm{m\,s^{-1}}$ and an acoustic component $A = 5\%$.

- It can be seen from Fig. 8a that, as soon as the acoustic magnitude exceeds the TBL component by at least 20%, an absorption peak due to the Helmholtz-type resonance starts to appear and increases up to 0.4 for equal magnitudes of the acoustic and aerodynamic components ($A = 100\%$). When $A > 20\%$, absorption peaks occur at both the aerodynamic coincidence frequency f_{AC} and at the Helmholtz resonance frequency f_{H} of the partition. Otherwise, large absorption only occurs up to f_{AC}. Moreover, Fig. 8b shows that a small increase, say 5%, of the acoustic component already lowers the TL by 5 dB with a systematic TL dip and change of slope at f_{H}.
- Figure 9a shows that increasing the MPP perforation ratio as from 1 % significantly widens the absorption bandwidth around f_{AC} since f_{FW} linearly increases with σ. This is accompanied by an efficient damping of the mass-air-mass resonance

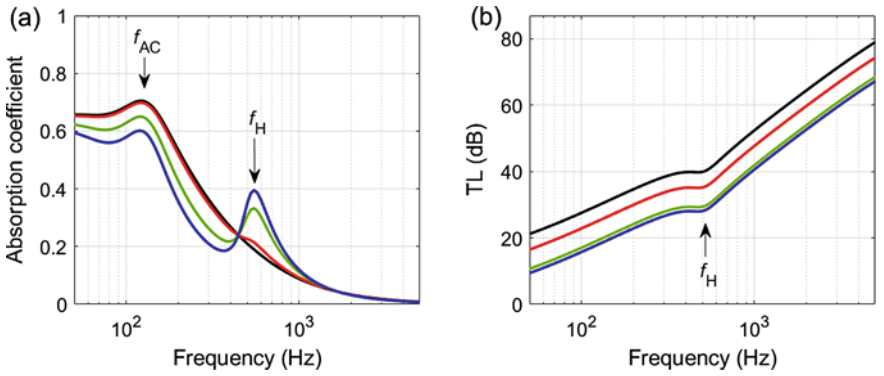

Fig. 8 Influence of the acoustic component A (%) on the absorption coefficient (**a**) and TL (**b**) of a MPPCP partition undergoing an aeroacoustic excitation [modelled by Eq. (13)] and assuming a free-stream velocity of 30 m s^{-1}: $A = 0\%$ (black), 5% (red), 50% (green) and 100% (blue); the frequencies at which aerodynamic coincidence (f_{AC}) and Helmholtz-type resonance (f_H) occur are also shown

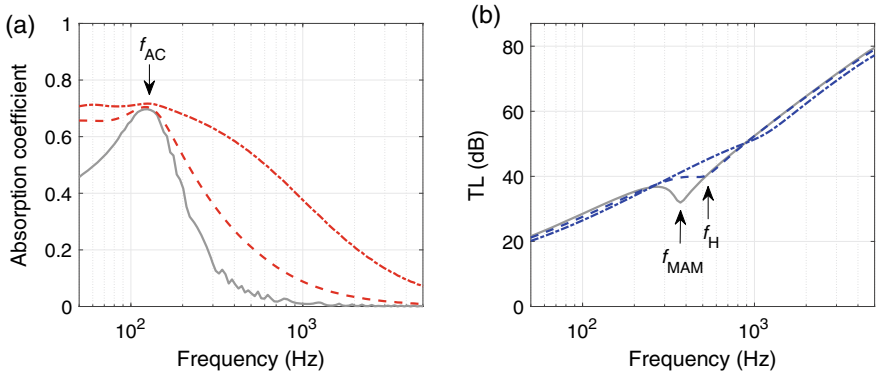

Fig. 9 Influence of the perforation ratio σ (%) on the absorption coefficient (**a**) and TL (**b**) of a partition undergoing an aeroacoustic excitation assuming $U_\infty = 30$ m s^{-1} and A = 5 %: $\sigma = 2$ % (MPPCP, dash-dotted), $\sigma = 0.2$ % (MPPCP, dashed), $\sigma = 0$ % (PCP, grey solid); the frequencies at which aerodynamic coincidence (f_{AC}), mass-air-mass resonance (f_{MAM}) and Helmholtz-type resonance (f_H) occur are also shown

that occurs as a drop of TL at $f_{MAM} = 365$ Hz, as it can be seen from Fig. 9b for the PCP partition ($\sigma = 0$ %).

- Figure 10a shows that increasing the holes diameter from 0.1 to 1 mm downshifts f_H from 580 Hz down to 360 Hz while reducing the absorption bandwidth when $d_h \leq 0.5$ mm. This is due respectively to an increase the magnitude of the MPP reactance and to a decrease of the MPP resistance. These combined effects reduce the absorption around f_H but hardly affect the absorption values around f_{AC}. Note

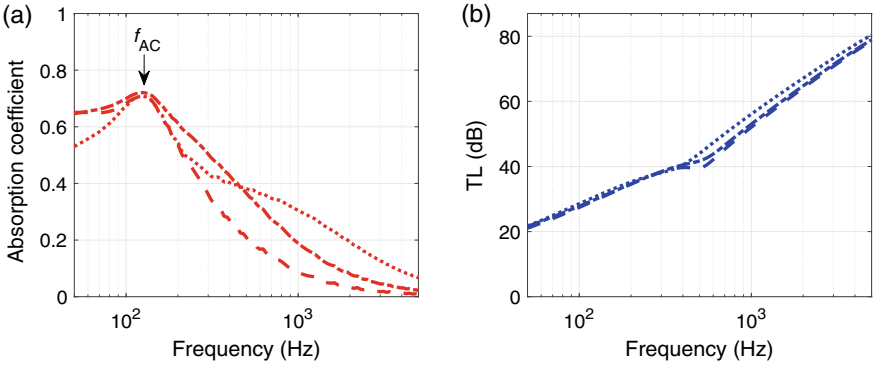

Fig. 10 Influence of the holes diameter d (mm) on the absorption coefficient (**a**) and TL (**b**) of a MPPCP partition undergoing an aeroacoustic excitation assuming $U_\infty = 30$ m s^{-1} and A = 5 %: $d = 0.1$ mm (dotted), $d = 0.5$ mm (dash-dotted), $d = 1$ mm (dashed); the frequency at which aerodynamic coincidence (f_{AC}) occurs is also shown in **a**

that enlarging the holes diameter lowers the TL above f_H by up to 6 dB, as observed in Fig. 10b.

3 Absorption of Flow Cavity Noise by an Unbacked MPP

An alternative configuration is studied experimentally and numerically in this section, examining the effect of a recessed MPP, as shown in Fig. 1b and (11), to reduce the cavity noise induced by a low-speed flow. One considers an unbacked panel, either plain or microperforated, of dimensions $L \times W = 0.53\,\text{m} \times 0.41\,\text{m}$, of thickness 1 mm and clamped along its edges. It constitutes the floor of a cavity of depth $D = 0.05$ m. The MPP has circular holes of diameter 0.5 mm and a perforation ratio 0.8%. It is exposed to a flow boundary layer of free-stream velocity $U_\infty = 30.7$ m s^{-1}. Given a length-to-depth ratio $L/D = 10.6$, the cavity is in transitional flow regime, e.g. flow reattachment may occur at the cavity floor due to the shear layer that only extends over part of the cavity length, as confirmed by the simulations shown in Fig. 16.

3.1 Experimental Study

As seen in Fig. 11, wall-pressure measurements have been performed in the low-speed WT test section on top of which was plugged the shallow cavity. They were performed using a pinhole micro-probe with tip diameter 1.25 mm, flush-mounted over the flow side of the cavity floor, as shown in Fig. 11a. The micro-probe was sequentially displaced over 19 positions evenly distributed along a streamwise line on the cavity base that was either plain or microperforated. The positions, separated by a distance

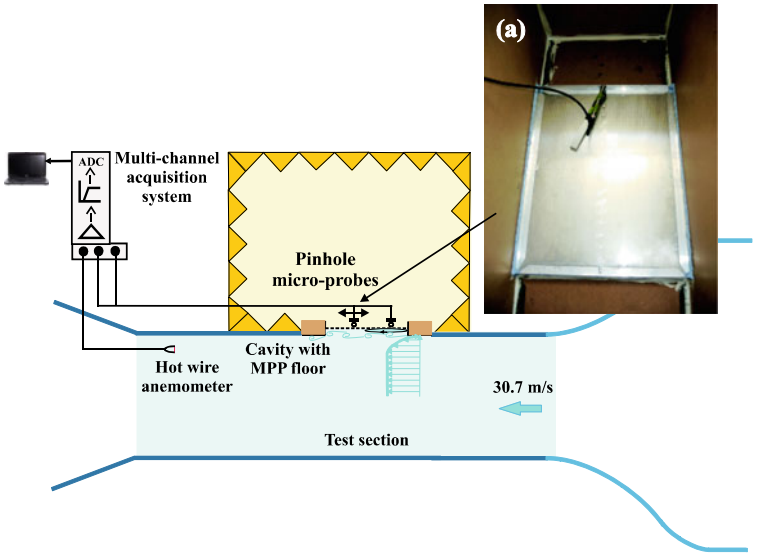

Fig. 11 Drawing and photos of the experimental set-up used to measure wall-pressures on the MPP floor of a flow cavity with a view in **a** of the micro-probe pressure sensor used to measure the wall-pressure fluctuations on the cavity floor from the MPP no-flow side

of 0.028 m, are represented by white dots in Fig. 1b and their numbering is shown in Fig. 12. Because one is interested in the reduction of the impinging aerodynamic wall-pressures by the sole MPP apertures, the cavity floor was unbacked during the measurements, thus transmitting flow-induced noise within an enclosure, the same than that used in Sect. 2.2.

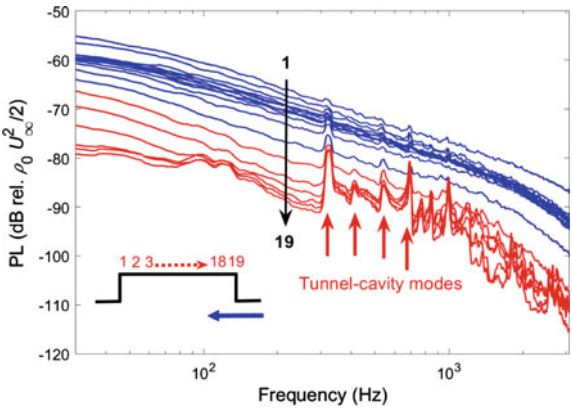

Fig. 12 Spatial distribution of the wall-pressure levels (PL) measured at 19 observation points evenly distributed along the mid-line of a plain cavity floor in transitional flow regime ($L/D = 10.6$, $U_\infty = 30.7$ m s^{-1}); the broadband spectra are in blue and those involving tonal components are in red

3.1.1 Characterization of the Cavity Flow-Induced Noise

Variations of the wall-pressure PSDs along the 19 base wall positions are shown in Fig. 12 for a plain cavity floor. It can be seen that the flow broadband components (blue curves) are more intense towards the downstream edge of the cavity, e.g. at about 3.64 D from the leading edge, whereas tonal components emerge towards the cavity leading edge (red curves).

As the observation point gets closer to the upstream edge, one observes in Fig. 12 an overall decay of the wall PLs with a clear emergence of tonal peaks above the broadband components. These dominant peaks are related to the resonance frequencies of the Tunnel-Cavity (TC) and Tunnel (T) transverse modes of the non-symmetric cavity test section. The TC modes have a cut-on frequency lower than that of the corresponding T modes, so they emerge in a frequency range bounded by the cut-on frequencies of a TC mode and of the corresponding T mode. This has already been observed by Alvarez and Kerschen [33] that showed the existence of confined transverse modes with high amplitude in the TC section of a low-speed WT and with small radiation leakage due to the non-symmetric cavity configuration. Moreover, the transverse TC resonances, experimentally detected above the background noise levels up to $n_z = 6$, systematically occur below the expected range of frequencies, respectively left- and right-bounded by $f_{n_z,\mathrm{TC}} = n_z c_0 \big/ (H + D)$ and $f_{n_z,\mathrm{T}} = n_z c_0 \big/ H$, the TC and T transverse resonance frequencies, with H the height of the tunnel test section and n_z the transverse modal order. This could be interpreted by elasto-acoustic coupling with the volumetric panel flexural modes of the thin cavity floor that well couple with the TC transverse modes and that are resonant at the same frequency, thereby causing a significant downshift of the TC resonance [34]. Hence, the observed resonances are related to TC-Panel modes nearly-trapped by the cavity-test section configuration.

3.1.2 Effects of Micro-Perforating the Cavity Floor

The plain panel has been replaced in the experiment by a MPP. Figure 13 shows that microperforating the cavity floor reduces by up to 8 dB the amplitudes of the first TC-P resonances between 300 Hz and 2 kHz. A priori, such reduction may be due to a large airframe relative normal velocity within the micro-holes that damps the TC-P transverse modes by thermo-viscous dissipation. However, numerical simulations presented in Sect. 3.2 will show that other mechanisms such as acoustically-induced vorticity play an important role. This is plausible since the perforate constant k_h [see Eq. (1)] takes values between 3 and 5 between 324 and 990 Hz, respectively the first and last peaks detected, so that the viscous boundary layer thickness is respectively only 1/3 and 1/5 of the holes radius at these frequencies.

Figure 13a also shows that the MPP is less efficient in reducing the small peaks that emerge above the broadband flow noise components, preponderant towards the cavity downstream edge, with only a 3 dB reduction on the first peak. Moreover, it can be seen that interaction between the flow and the MPP generates excess broadband

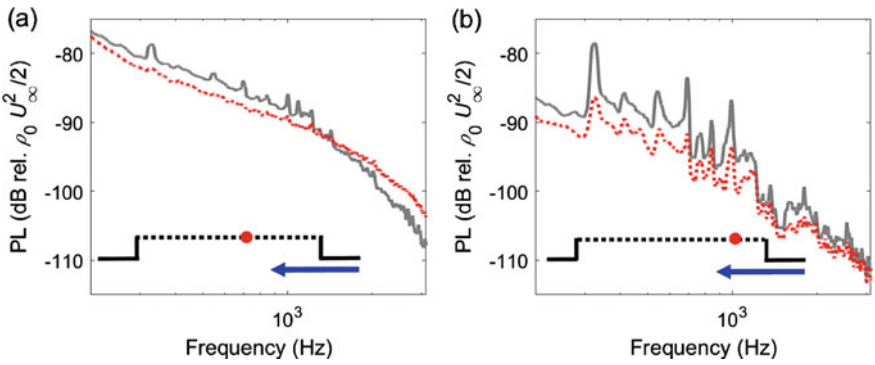

Fig. 13 Effect of a microperforated base wall on the spectra of the pressure levels measured at 16.8 cm (**a**) and at 8.4 cm (**b**) after the upstream edge of a cavity in transitional flow regime; the grey and red curves correspond respectively to plain and microperforated floors

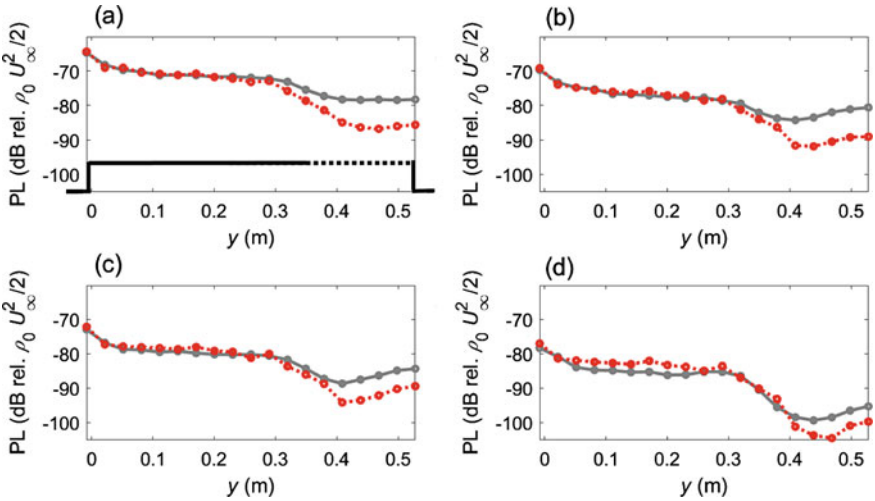

Fig. 14 Effect of microperforations on the spatial distribution of the pressure levels measured along 19 observation points along the streamwise direction over the base wall of a transitional cavity at 324 Hz (**a**), 690 Hz (**b**), 990 Hz (**c**) and 1800 Hz (**d**); the grey and red curves correspond respectively to plain and microperforated floors; also shown in **a** a semi-microperforated cavity

wall-pressures above 1.2 kHz. This complies with the potential of circular microperforations, in contact with a uniform one-sided flow of grazing velocity U_G, to efficiently back-scatter aerodynamic wall-pressures into sound for a hole-based Strouhal number $f d_h / U_G \geq 0.6$, as found in [14]. Assuming a value of $U_G = 2\ \mathrm{m\,s^{-1}}$, as suggested from the numerical simulations of Sect. 3.2, back-scattering occurs above 2.4 kHz, as confirmed by the measurements.

Figure 14 shows that one consistently observes an attenuation zone that occupies about one third of the cavity length towards the upstream edge. The MPP is inefficient to attenuate the wall-pressure fluctuations out of this zone. It even generates extra noise, up to 5 dB at 1800 Hz, as seen in Fig. 14d, due to back-scattering of the aerodynamic wall-pressures as frequency increases.

Thus, a strategy for reducing the flow-induced wall-pressure levels would be to microperforate only part of the cavity floor towards the upstream edge, as sketched in Fig. 14a, in order to achieve attenuation of the TC-P resonances without enhancing the aerodynamic wall-pressures further downstream.

3.2 *Lattice Boltzmann Numerical Study*

The Lattice Boltzmann Method (LBM) has been used to numerically assess the potential of microperforations to reduce the amplitude of the TC-P resonances excited by the flow-induced noise above the cavity. The LBM is well-suited for simulating the dynamics of complex gas flows. Instead of discretizing the macroscopic Navier-Stokes equations, it tracks the evolution of discretized particle velocity distribution functions defined at mesoscopic scales. They satisfy the Boltzmann kinetic equation with a suitable collision operator [35] and with restricted advection and collision rules. It is shown in [36] that the LBM equation with a third-order expansion of the Bhatnagar-Gross-Krook collision operator [35] in terms of the fluid velocity, reproduces exactly the Navier–Stokes equations for a weakly-compressible flow for Mach numbers less than 0.4. The LBM has been used to analyse the non-linear behaviour of MPP holes [37], the sound absorption by a circular orifice termination in a turbulent pipe flow [38] and the aeroacoustic resonances of partially-covered cavities [39].

As shown in Fig. 15, the 2D LBM is here implemented on a square lattice structure with nine neighboring lattice nodes, also termed the D2Q9 lattice Boltzmann scheme.

A laminar boundary layer flows with a free-stream velocity of 30.7 m s^{-1} in a tunnel of height $H = 0.24$ m towards a cavity of depth $D = 0.05$ m and length $L = 0.53$ m. The tunnel height has been reduced with respect to the experiment to

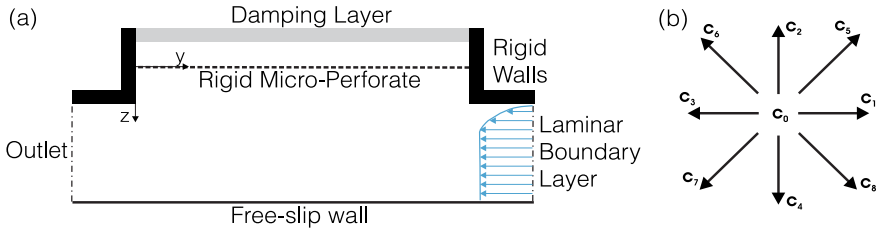

Fig. 15 **a** 2D geometry and boundary conditions of the computational domain used in the LBM simulations of the flow cavity noise; **b** D2Q9 lattice Boltzmann scheme defining at each node of the computational domain restricted advection and collision rules along 8 directions

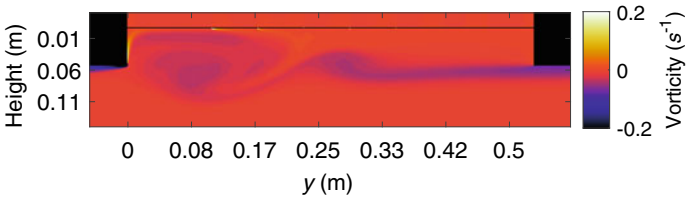

Fig. 16 Snapshot of the vorticity calculated by LBM over and within a cavity in transitional flow regime undergoing a laminar boundary layer flowing from the right to the left

lower the computational cost. The cavity floor, 1 mm thick, is rigid as well as the cavity side walls and the leading and trailing edges. The cavity floor is either plain or micro-perforated with sharp-edged apertures of width $d_h = 0.5$ mm. In order to keep the same perforation ratio, $\sigma_{2D} = d_h / b_h = 0.8\,\%$, than in the experiment, $\sigma_{\text{exp.}} = \pi d_h^2 / \left(4 b_h^2\right) = 0.8\,\%$, the apertures in the LBM model have a larger separation distance $b_h = 6.25$ cm. The temporal and spatial resolution in the whole domain with a plain cavity floor was set to $\Delta t = 6.33\ 10^{-6}$ s and $\Delta x = \Delta z = 50\ \mu$m, which provided a numerical error on c_0 lower than 1% in the 8 directions of the D2Q9 scheme. When the cavity floor is micro-perforated, a minimum number of 80 cells per aperture length is required for the wall-pressure levels to converge up to 3 kHz.

Figure 16 shows a snapshot of the component Ω_y of the flow instantaneous vorticity, $\mathbf{\Omega} = \nabla \wedge \mathbf{v}$, over the whole cavity domain. The vortical flow structure is characterized by a roll-up of the shear layer that extends up to half of the cavity length from the leading edge. The shed vortices, no more than 3 over a cycle of oscillations, have dimensions of nearly the cavity depth, and reattach at a distance $d_R / D \approx 6.2$ from the leading edge, in accordance with Direct Numerical Simulation results [40].

Figure 17 shows the effect of microperforating the cavity floor on the levels of the pressure fluctuations, calculated respectively over the base wall and at the mouth of the cavity. Transverse TC modes are well predicted by the 2D LBM. They occur in a frequency range limited by the cut-on frequencies of the TC and T modes. For instance, the first dominant peak is predicted at 703 Hz which is in-between $f_{1,TC} = c_0 / 2(H + D) = 694$ Hz and $f_{1,T} = c_0 / (2H) = 708$ Hz.

The model well captures the attenuation effect induced by the microperforations on the transverse modes, not only at the floor, but also at the mouth of the cavity. The pressure levels are attenuated at the cavity floor by 10 dB at 703 Hz and 16 dB at 1391 Hz and 2083 Hz, and at the cavity mouth by 9 dB at 703 Hz, 13 dB at 1391 Hz and 7 dB at 2083 Hz. They clearly overestimate the measured attenuations that were not exceeding 8 dB on the second transverse mode at the cavity floor, but 3D flow effects as well as extraneous sources of leakage/dissipation are likely to occur in the WT test section. Moreover, the 2D MPP radiation conditions may not be fully representative of the 3D ones.

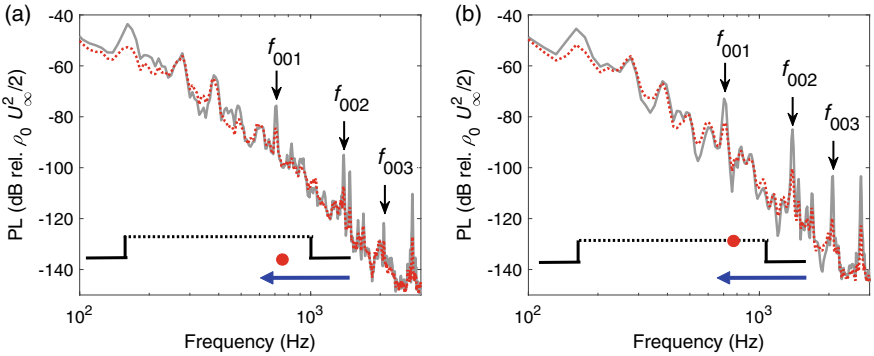

Fig. 17 Effect of microperforations on the pressure levels calculated by LBM at a horizontal distance 8.4 cm from the upstream edge of a cavity in transitional flow regime: **a** over the cavity floor and **b** at the cavity mouth; grey solid (resp. red dotted) curves correspond to a plain (resp. microperforated) floor

The interaction between the cavity flow and the MPP apertures has been further examined through the LBM simulation results shown in Fig. 18. The vorticity fluctuations $\tilde{\Omega}_y$ shown in Fig. 18a scale on $10\mathrm{sgn}\left(\tilde{\Omega}_y\right)\log_{10}\left(\left|\tilde{\Omega}_y\right|/\Omega_0\right)$ with $\Omega_0 = 10^{-2}\Omega_{\max}$ in order to correctly visualize the variations of fluctuations across the apertures over a 20 dB dynamic range. The velocity fluctuations $\tilde{v}$ scale on $10\log_{10}\left(|\tilde{v}|/v_0\right)$ with $v_0 = 10^{-3}v_{\max}$ in order to correctly visualize the variations of velocity over a 30 dB dynamic range. Note that the apertures pitch has been reset to 5 mm, as in the experiment, but this does not drastically modify the vorticity and velocity dynamics.

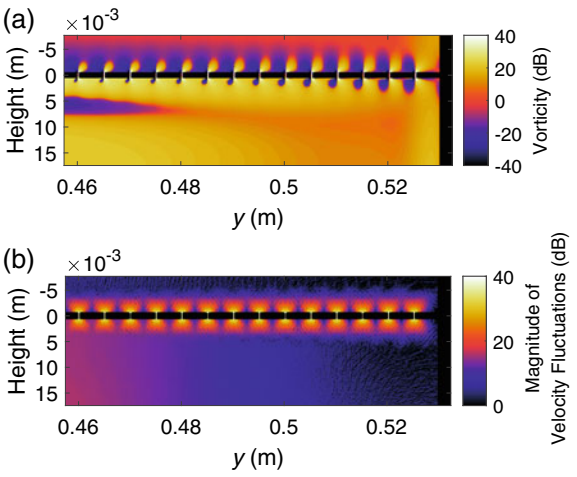

Fig. 18 Snapshots of instantaneous vorticity (**a**) and magnitude of the velocity fluctuations (**b**) calculated by the LBM across a microperforated floor and towards the upstream edge of a transitional cavity under a laminar boundary layer

Figure 18a shows outflow conditions that occur across the apertures from the cavity side ($z > 0$) towards the back of the MPP ($z < 0$). These conditions generate clockwise (resp. counterclockwise) vortex shedding at the inlet and outlet of the apertures right (resp. left) side. On the MPP cavity side, the holes inlet vortices located away from the upstream edge tend to be swept by the near-wall vorticity. On the MPP no-flow side, vortex shedding from the holes is not prone to convection effects and occurs parallel to the orifices axis.

It can be seen from Fig. 18b that the regions of maximum velocity fluctuations occur within and at the inlet-outlet of the MPP apertures, the most intense being induced by well-established outflow conditions, in relation to Fig. 18a. The dissipation of energy takes place in these regions and, given a boundary layer viscous thickness lower than one third of the apertures half-width above 350 Hz (as in the experiment), it is likely that vortex shedding plays a more important role than the viscosity in the dissipation mechanisms at the origin of the attenuation of the TC resonances.

4 Conclusions

Experimental methodologies have been presented for evaluating, in a low-speed wind-tunnel, the potential of flush-mounted or recessed microperforated partitions to absorb the wall-pressures induced by a TBL, but also by the transverse acoustic modes of the test section. The latter modes were found to be nearly-trapped by the non-symmetric cavity configuration, in which case they are tunnel-cavity modes, whereas they are propagating when cut-on in the symmetric flush-mounted configuration, in which case they are pure tunnel modes. When micro-perforating the flush-mounted flow side of the partition, broadband absorption and large transmission of the boundary layer noise have been observed around the MPP aerodynamic coincidence frequency, as long as the hole-based Strouhal number stays lower than 0.1. At higher frequencies, low absorption and high TL values occur due to significant back-scattering of the TBL pressure fluctuations into sound. Micro-perforating a single recessed MPP, thereby constituting the floor of a shallow cavity, attenuates by up to 8 dB the first tonal peaks caused by the flow-excited tunnel-cavity resonances, that efficiently couple with the MPP volumetric modes. These peaks only emerge on one third of the cavity floor towards the leading edge whereas they are drowned in the broadband flow noise further downstream. A strategy would thus be to micro-perforate only one third of the cavity floor to reduce the tonal peaks without enhancing the broadband flow components.

The measured acoustical performance have been confirmed by wavenumber and fully-coupled modal formulations in case of a flush-mounted MPP partition under an aeroacoustic TBL excitation and by 2D LBM numerical simulations in case of a microperforated cavity floor under a laminar boundary layer. In the latter case, the simplified geometry used in the LBM simulations captured, but overestimated the amount of attenuation of the tonal peaks. It however pointed out the key role played

by acoustically-induced vorticity in the attenuation mechanisms of the transverse test section resonances. These validated models could serve to optimize the MPP parameters (shape, diameter, perforation ratio…) in order to enhance the absorption, the TL or the attenuation of the flow-induced noise over the partition.

Acknowledgements This study and its dissemination have been funded by The Ministerio de Economía y Competitividad in Spain, project TRA2017-87978-R, AEI/FEDER, UE, "Programa Estatal de Investigación, Desarrollo e Innovación Orientada a los Retos de la Sociedad". It was supported in France by the Labex Mechanics and Complexity AAP2 managed by the Excellence Initiative Programme of Aix-Marseille University (A*MIDEX) and by the French National Research Agency (VIRTECH project, ANR-17-CE10-0012).

References

1. G.P. Gibbs, R.H. Cabell, J. Juang, Controller complexity for active control of TBL-induced sound radiation from aircraft style panels, in *Proceedings of the 6th AIAA/CEAS Aeroacoustics Conference and Exhibit*, Lahaina, Hawaii, USA, AIAA-2000-2043 (2000)
2. A. Caiazzo, N. Alujević, B. Pluymers, W. Desmet, Active control of turbulent boundary layer sound transmission into a vehicle interior, in *Proceedings of the 13th International Conference on Motion and Vibration Control (MOVIC2016) and the 12th International Conference on Recent Advances in Structural Dynamics* (RASD2016). Published in J. Phys.: Conf. Ser. **744**, 012026 (2016). IOP Publishing
3. J. Zhou, A. Bhaskar, X. Zhang, Sound transmission through double cylindrical shells lined with porous material under turbulent boundary layer excitation. J. Sound Vib. **357**, 253–268 (2015)
4. O. Collery, J.-L. Guyader, P. Neple, Add-on damping patch efficiency on sound transmission of a thin plate under aerodynamic or acoustic excitation. Noise Control. Eng. J. **3**, 302–309 (2010)
5. D.-Y. Maa, Microperforated-panel wideband absorbers. Noise Control. Eng. J. **29**, 77–84 (1987)
6. D.-Y. Maa, Potential of microperforated panel absorbers. J. Acoust. Soc. Am. **104**, 2861–2866 (1998)
7. M.A. Temiz, J. Tournadre, I.L. Arteaga, A. Hirschberg, Non-linear acoustic transfer impedance of micro-perforated plates with circular orifices. J. Sound Vib. **366**, 418–428 (2016)
8. R. Kabral, L. Du, M. Åbom, Optimum sound attenuation in flow ducts based on the "exact" cremer impedance. Acta Acoust. United Acoust. **102**, 851–860 (2016)
9. B. Fenech, G. Keith, F. Jacobsen, The use of microperforated plates to attenuate cavity resonances. J. Acoust. Soc. Am. **120**, 1851–1858 (2006)
10. K.D. Sakaliyski, J.I. Hileman, Z.S. Spakovsky, Aero-acoustics of perforated drag plates for quiet transport aircraft, in *Proceedings of the 45th AIAA Aerospace Science Meeting and Exhibit*, Reno, Nevada, U.S.A., AIAA 2007-1032 (2007)
11. K. Tanner, N. Mackenzie, R. Jones, Y.-K. Lee, Aeroacoustic assessment of facades, in *Proceedings of Acoustics 2016, the 2nd Australasian Acoustical Societies Conference*, Brisbane, Australia, Paper 149 (2016)
12. X. Yu, L. Cheng, J.-L. Guyader, Modeling vibroacoustic systems involving cascade open cavities and micro-perforated panels. J. Acoust. Soc. Am. **136**, 659–670 (2014)
13. J. E. Ffowcs Williams, The acoustics of turbulence near sound-absorbent liners, J. Fluid Mech. **54**, 737–749 (1972).
14. M.S. Howe, Sound generated by turbulence and discrete vortices interacting with a perforated elastic plate in low-Mach-number flow. Q. J. Mech. Appl. Math. **50**, 279–301 (1997)

15. C.Y. Tsui, G.A. Flandro, Self-induced sound generation by flow over perforated duct liners. J. Sound Vib. **50**, 315–331 (1977)
16. P.A. Nelson, Noise generated by flow over perforated surfaces. J. Sound Vib. **83**, 11–26 (1982)
17. S. Allam, M. Åbom, Experimental Characterization of Acoustic Liners with Extended Reaction, in *14th AIAA/CEAS Aeroacoustics Conference*, Vancouver, Canada, AIAA paper 2008-3074 (2008)
18. S. Allam, M. Åbom, A new type of muffler based on microperforated tubes. J. Vib. Acoust. **133**, 1–8 (2011)
19. T. Bravo, C. Maury, C. Pinhède, Sound absorption and transmission through flexible micro-perforated panels backed by an air layer and a thin plate. J. Acoust. Soc. Am. **131**, 3853–3863 (2012)
20. E.H. Dowell, G.F. Gorman III, D.A. Smith, Acoustoelasticity: general theory, acoustic natural modes and forced response to sinusoidal excitation, including comparisons with experiments. J. Sound Vib. **52**, 519–542 (1977)
21. S.J. Elliott, M.E. Johnson, Radiation modes and the active control of sound power. J. Acoust. Soc. Am. **9**, 2194–2204 (1993)
22. T. Bravo, C. Maury, C. Pinhède, Absorption and transmission of boundary layer noise through flexible multi-layer micro-perforated structures. J. Sound Vib. **395**, 201–223 (2017)
23. C. Maury, P. Gardonio, S.J. Elliott, A wavenumber approach to modelling the response of a randomly excited panel, Part II: Application to aircraft panels excited by a turbulent boundary layer. J. Sound Vib. **252**, 115–139 (2002)
24. B. Arguillat, D. Ricot, C. Bailly, G. Robert, Measured wavenumber-frequency spectrum associated with acoustic and aerodynamic wall pressure fluctuations. J. Acoust. Soc. Am. **128**, 1647–1655 (2010)
25. G.M. Corcos, The resolution of pressures in turbulence. J. Acoust. Soc. Am. **35**, 192–199 (1963)
26. W.K. Blake, *Mechanics of Low-Induced Sound and Vibration,* vol. I. General Concept and Elementary Sources, vol. II. Complex Flow-Structure Interaction, Orlando, Florida (Academic Press, Inc., 1986)
27. A.V. Smol'yakov, V.M. Tkachenko, Model of a field of pseudosonic turbulent wall pressures and experimental data. Sov. Phys.-Acoust. **37**, 627–631 (1991)
28. F. Jacobsen, The sound field in a reverberation room, Technical University of Denmark, Department of Electrical Engineering, Acoustic Technology, Report no 31261 (2011)
29. L. Maxit, V. Denis, Prediction of flow induced sound and vibration of periodically stiffened plates. J. Acoust. Soc. Am. **133**, 146–160 (2013)
30. K.H. Lyle, E.H. Dowell, Acoustic radiation damping of flat rectangular plates subjected to subsonic flows. Parts I and II. J. Fluids Struct. **8**, 711–746 (1994)
31. R.L. Clark, K.D. Frampton, Aeroelastic structural acoustic coupling: implications on the control of turbulent boundary-layer noise transmission. J. Acoust. Soc. Am. **102**, 1639–1647 (1997)
32. M. Goody, Empirical spectral model of surface pressure fluctuations. AIAA J. **42**, 1788–1794 (2004)
33. J.O. Alvarez, E.J. Kerschen, Influence of wind tunnel walls on cavity acoustic resonances, in *Proceedings of the 11th AIAA/CEAS Aeroacoustics Conference*, Monterey, California, U.S.A., AIAA 2005-2804 (2005)
34. C. Maury, T. Bravo, D. Mazzoni, The use of micro-perforations to attenuate the cavity pressure fluctuations induced by a low-speed flow. J. Sound Vib. **439**, 1–16 (2019)
35. P.L. Bhatnagar, E.P. Gross, M.A. Krook, A model for collision processes in gases. I. Small amplitude processes in charged and neutral one-component systems. Phys. Rev. **94**, 511–525 (1954)
36. S. Chapman, T.G. Cowling, *The Mathematical Theory of Non-uniform Gases*, Third. edn. (Cambridge Mathematical Library, 1991)
37. F. Chevillotte, P. Marchner, M. Martinez, R. Roncen, F. Simon, Analysis of the non-linear behavior of micro-perforated plates using Lattice-Boltzmann method, in: *Proceedings of SAPEM 2017 (Symposium on the Acoustics of Poro-Elastic Materials)*, Le Mans, France (2017). Presentation downloaded the 21/04/20 from http://sapem2017.matelys.com/proceedings/Flow/000041.pdf

38. K. Habibi, L. Mongeau, Prediction of sound absorption by a circular orifice termination in a turbulent pipe flow using the Lattice-Boltzmann method. Appl. Acoust. **87**, 153–161 (2015)
39. A.T. de Jong, H. Bijl, A. Hazir, J. Wiedemann, Aeroacoustic simulation of slender partially covered cavities using a Lattice Boltzmann method. J. Sound Vib. **332**, 1687–1703 (2013)
40. H. Le, P. Moin, J. Kim, Direct numerical simulation of turbulent flow over a backward-facing step. J. Fluid Mech. **330**, 349–374 (1997)

Noise Radiated from Fluid Loaded Stiffened Cylindrical Shells Subject to a Turbulent Boundary Layer

Valentin Meyer, Laurent Maxit, Oriol Guasch, and Mahmoud Karimi

Abstract Cylindrical shells are often employed as simplified models to represent the physics of underwater vehicles. When a vehicle is moving underwater, the flow is likely to create a turbulent boundary layer (TBL) over the shell surface. The TBL induces vibrations on the shell, which results in the radiation of noise. Semi-analytical formulations are nowadays widely used to predict the vibro-acoustics of structures and re-design them to mitigate the flow-induced noise. However, most of the methods available in literature tackle the case of flat plates and only few results can be found for cylindrical shells. In this chapter, we give an overview of a method for calculating both the response of a fluid loaded cylindrical shell and the outward emitted noise, with different degrees of complexity. The considered test cases involve various phenomena and underlying physics. Aspects such as the role of propagative Bloch-Floquet waves in noise radiation by periodically stiffened structures, or the influence of mechanical coupling between the shell and non-axisymmetric inner structures are addressed. An explanation is also given for the very different behavior of the radiated acoustic pressure in the near and far fields.

V. Meyer (✉)
Naval Group Research, 199 Av. Pierre-Gilles de Gennes, 83190 Ollioules, France
e-mail: valentin.meyer@naval-group.fr

L. Maxit
Univ Lyon, INSA Lyon, LVA, EA677, 69621 Villeurbanne, France
e-mail: laurent.maxit@insa-lyon.fr

O. Guasch
GTM – Grup de Recerca En Tecnologies Mèdia, La Salle, Universitat Ramon Llull, C/Quatre Camins 30, 08022 Barcelona, Catalonia, Spain
e-mail: oriol.guasch@salle.url.edu

M. Karimi
Centre for Audio, Acoustics and Vibration, University of Technology Sydney, Sydney, NSW 2019, Australia
e-mail: mahmoud.karimi@uts.edu.au

E. Ciappi et al. (eds.), *Flinovia—Flow Induced Noise and Vibration Issues and Aspects-III*, https://doi.org/10.1007/978-3-030-64807-7_12

1 Introduction

Cylindrical shells are often used to model industrial systems. At early design stages, numerical models give insight on the physical behavior of the system. This chapter focuses on the response of a cylindrical shell excited by a turbulent boundary layer. This problem can be typically encountered for an airplane fuselage or for a submarine hull. For underwater applications, Chevalier and Audoly [1] highlighted the importance of the TBL excitation for warfare strategy. In a scenario where two submarines are chasing each other, they must be as quiet as possible, while being the most efficient in detecting the opponent. Radiated noise and self-noise (i.e. the noise polluting the sonar array) need to be as low as possible. Predicting the vibrations and radiated pressure of a cylindrical shell is therefore an important practical issue. As experimental procedures are long, costly and cannot be used at the early stage of a submarine design, numerical methods are required to solve this problem. However, several factors make that difficult, namely,

- the dimensions of the structures are large and the frequency range of interest is wide (for naval applications, the radiated and self-noise noise must be controlled from a few Hz to several kHz);
- the cylindrical shell may have stiffeners and other internal structures;
- in the case of underwater applications, the strong coupling between the cylindrical shell and the surrounding fluid must be accounted for.

The approach adopted here is based on the wavenumber formulation of the structure excited by random wall-pressure fields. Several assumptions are made:

- the Turbulent Boundary Layer (TBL) is assumed to be fully developed, stationary and homogeneous over the surface of the cylindrical shell;
- the vibrations of and the radiated pressure from the cylindrical shell do not interact with the TBL wall-pressure field. The wall-pressure is thus taken as an input to the vibro-acoustic problem.

The method relies on the reciprocity principle and setting the response of the fluid-loaded structure in the wavenumber domain. On the one hand, the TBL is a partially space-correlated random pressure field that can be characterized by means of the wall pressure cross-spectral density (CSD). As in typical practical applications the radius of the cylindrical shell is large in comparison with the TBL thickness, classical models for planar TBLs can be used with minor adaptations. On the other hand, one can define the sensitivity function at a point on the shell surface as its vibroacoustic response when excited by a cylindrical acoustic plane wave. This allows one to compute the auto-spectral density (ASD) of the radiated noise by integrating the product of the TBL wall pressure CSD with the sensitivity functions, over the wavenumber domain. Besides, Lyamshev's reciprocity principle shows that such sensitivity functions are totally equivalent to the radial velocity response of the shell when excited by an acoustic unit monopole in the wavenumber domain (i.e. using a

Fourier transform along the axial coordinates and a Fourier series along the circumferential coordinates). Resorting to the reciprocity principle has the advantage of considerably reducing the number of load cases which shall be considered to obtain the sensitivity functions.

In this work, the above technique is applied to predict the acoustic pressure radiated by different submerged cylindrical shells under TBL excitation. For infinite shells, an analytical formulation is described to calculate the sensitivity functions. That also includes the case of an infinite shell with regularly spaced stiffeners. For finite shells with arbitrary internal structures, a dedicated sub-structuring approach is employed. This sub-structuring approach, known as condensed transfer functions (CTF) method, permits coupling the analytical model of a submerged cylindrical shell with a finite element model (FEM) of its internal structures. The CTF method allows for a significant geometric versatility at a very reasonable computational cost, which makes it very appealing for industrial applications up to several kHz.

2 Vibro-Acoustic Response of a Cylindrical Shell Under a TBL

2.1 Presentation of the Problem

Let us consider a cylindrical shell as depicted on Fig. 1. It is excited by a TBL on its external surface Σ_p. The TBL acts on the whole circumference of the cylindrical shell but can be of finite extent in the axial direction (as in Fig. 1) or of infinite extent. The thickness of the shell h is supposed to be small compared to the radius of the cylinder R, allowing us to use thin shell theory for describing its vibratory motions. Cylindrical coordinates are used as shown in Fig. 1.

The shell is made of isotropic homogeneous material of density ρ, Young's modulus E, Poisson's coefficient ν and structural damping η. The complex Young's modulus accounting for the structural damping is defined as $E^* = E(1 + j\eta)$.

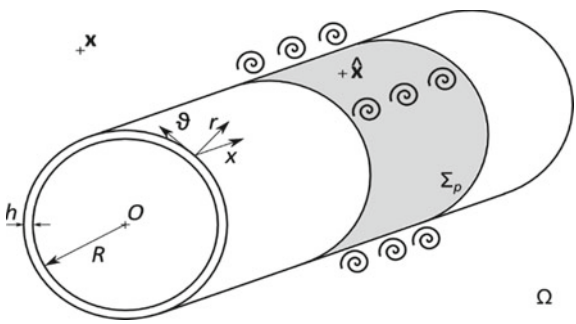

Fig. 1 Cylindrical shell excited by a turbulent boundary layer on Σ_p

2.2 Mathematical Formulation

Strawderman presented an extensive review of wavenumber and frequency analysis techniques in vibro-acoustics [2]. In particular, the wavenumber domain can be used to describe the response of a linear system under random pressure fields. Maury et al. [3] developed the formalism to link the statistics of the random forcing field to the structural response. They showed that the response can be written either in the physical domain or in the spectral domain for space and time. In this study, the approach using spectral descriptions in space and time is chosen. Considering a point $\boldsymbol{x}$ of cylindrical coordinates (x, r, θ), the auto-spectral density (ASD) of the pressure radiated by the cylindrical shell excited by the TBL can be expressed as follows [4],

$$S_{pp}(\boldsymbol{x}, \omega) = 2\pi \sum_{n=-\infty}^{+\infty} \int_{-\infty}^{+\infty} \left|\widetilde{H}_p(x, \theta, r, k_x, n, \omega)\right|^2 \widetilde{\phi}_{pp}^{tbl}(k_x, n, \omega) dk_x, \tag{1}$$

where ω is the angular frequency. $\widetilde{H}_p$ is called the sensitivity function and describes the dynamic behavior of the structure. It expresses the radiated pressure at $\boldsymbol{x}$ when the system is excited by a unit wall-pressure field $p(x, \theta) = e^{-j(k_x x + n\theta)}$ with $x \in \mathbb{R}$ and $\theta \in [-\pi; \pi]$. $\widetilde{\phi}_{pp}^{tbl}$ is the cross-spectrum density of the wall-pressure in the (k_x, n) space and characterizes the wall pressure induced by the TBL on the shell. k_x and n are respectively the Fourier transform variables of x and θ.

There are several ways to solve the problem described here [5]. Equation (1) requires the sensitivity function of the structure to be calculated for a large number of wall-pressure excitation fields to describe the wavenumber domain defined by k_x and n. The next section explains how the reciprocity principle can be used to make the calculation process more efficient.

2.3 The Reciprocity Principle

The reciprocity principle in acoustics was formally established by Lyamshev in 1959 and later by Fahy [6]. It states that the transfer function remains identical when the source and receiver positions are exchanged. Fahy extended the reciprocity principle to vibroacoustics problems. He showed the that the transfer function of the pressure p at location $\boldsymbol{x}$ in the fluid when the structure is excited by a point force F at $\widehat{\boldsymbol{x}}$, equals the transfer function of the velocity v at $\widehat{\boldsymbol{x}}$ when excited by a monopole of volume velocity Q placed at $\boldsymbol{x}$. This sentence can be summarized in the following equation,

$$\frac{p(\boldsymbol{x})}{F(\widehat{\boldsymbol{x}})} = \frac{v(\widehat{\boldsymbol{x}})}{Q(\boldsymbol{x})}. \tag{2}$$

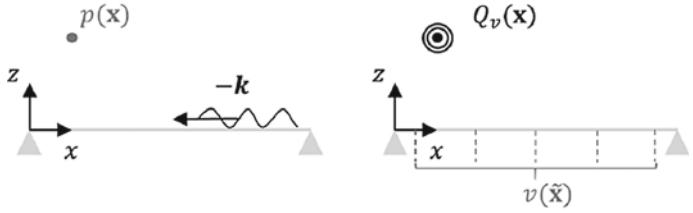

Fig. 2 Illustration of the reciprocity principle for the calculation of sensitivity functions, from Marchetto et al. [6]

The reciprocity principle remains valid in the wavenumber domain, as demonstrated by Marchetto et al. [7], who used sensitivity functions to derive it. As illustrated in Fig. 2, the pressure radiated by the structure excited by a unitary wall-pressure field of wavenumber vector $\boldsymbol{k}$ equals the spectral velocity of the structure, when excited by a monopole of unitary volume velocity. If the sensitivity function with the direct approach is written as,

$$\widetilde{H}_p(x,\theta,r,k_x,n,\omega) = \frac{R}{2\pi}\int_{-\infty}^{+\infty}\int_{0}^{2\pi} H_{p/F}\left(x,\theta,r,\widetilde{x},\widetilde{\theta},R,\omega\right)e^{-j\left(k_x\widetilde{x}+n\widetilde{\theta}\right)}d\widetilde{\theta}d\widetilde{x}, \quad (3)$$

with $H_{p/F}$ being the transfer function of pressure over force, then the sensitivity function using the reciprocal approach (i.e. using Eq. (2)) becomes

$$\widetilde{H}_p(x,\theta,r,k_x,n,\omega) = \frac{R}{2\pi}\int_{-\infty}^{+\infty}\int_{0}^{2\pi} H_{v/Q}\left(\widetilde{x},\widetilde{\theta},R,x,\theta,r,\omega\right)e^{-j\left(k_x\widetilde{x}+n\widetilde{\theta}\right)}d\widetilde{\theta}d\widetilde{x}, \quad (4)$$

where $H_{v/Q}$ is the transfer function of velocity over volume velocity. This approach has been experimentally validated for a panel excited by an acoustic diffuse field [7], as well as by a pressure field beneath a TBL [8].

Using the reciprocity principle for calculating the sensitivity functions is more efficient because in most cases it is easier to calculate the velocity in all points of the structure due to a single excitation, rather than the radiated pressure in one point, but for a large number of excitations. Analytical and numerical methods to calculate sensitivity functions are presented in Sect. 3 for fluid-loaded cylindrical shells. Next section describes the excitation term used in Eq. (1) due to the TBL.

2.4 Wall-Pressure Fluctuations on a Cylindrical Shell

Most models in literature for characterizing the wall-pressure fluctuations of a TBL were developed using experimental data acquired on planar surfaces. These

models usually take TBL parameters as inputs, such as the convection flow speed, the boundary layer thickness and the friction velocity. The TBL parameters can be measured experimentally or calculated through computational fluid dynamics. The readers are referred to the first issue of Flinovia for an extensive literature review of TBL models for flat plates [9]. For naval applications, the radius of the cylindrical shell is large compared to the TBL thickness and the curvature occurs in the cross-wise direction of the flow. In this situation, classical models of wall-pressure fields for planar surfaces can be used [10], but need to be adapted to the present mathematical formulation. Assuming the cross-spectral density of the wall-pressure for a planar surface $S_{pp}^{tbl}(x, y, \omega)$ to be known in the spatial domain, Maxit et al. adapted the formulation for cylindrical coordinates [4]. If the cross-spectral density of the wall-pressure for a planar surface in the wavenumber domain is given by

$$\widetilde{S}_{pp}^{tbl}\left(k_x, k_y, \omega\right) = \int_{-\infty}^{+\infty}\int_{-\infty}^{+\infty} S_{pp}^{tbl}(x, y, \omega) e^{-j\left(k_x x + k_y y\right)} dx dy, \tag{5}$$

then one can establish the following relation (see [4]),

$$\widetilde{\phi}_{pp}^{tbl}(k_x, n, \omega) = \frac{1}{2\pi R}\widetilde{S}_{pp}^{tbl}\left(k_x, \frac{n}{R}, \omega\right) \tag{6}$$

2.5 Numerical Aspects

The calculation of the radiated pressure ASD in Eq. (1) involves a summation of an infinite number of terms and an integral over an infinite domain. To compute it, first a discretization of the axial wavenumber is done to calculate the functions in the integrand for a finite number of k_x values. A constant and small discretization step δk_x is chosen to properly describe the peaks of the responses in the axial wavenumber domain. Then, the integration domains must be truncated and the integrand needs to be discretized along k_x. Williams et al. showed that in the wavenumber domain, the structure filters the vibro-acoustic response for frequencies beyond the hydrodynamic coincidence frequency [11]. Above the flexural wavenumber, the amplitude of the spectral displacement drastically decreases with increasing wavenumber. Therefore, the flexural wavenumber serves as a criterion to truncate the integration domain and Eq. (1) can be approximated as

$$S_{pp}(\boldsymbol{x}, \omega) = 2\pi \sum_{n=-\overline{N}}^{+\overline{N}} \sum_{-\overline{k}_x}^{+\overline{k}_x} \left|\widetilde{H}_p(x, \theta, r, k_x, n, \omega)\right|^2 \widetilde{\phi}_{pp}^{tbl}(k_x, n, \omega)\delta k_x, \tag{7}$$

with,

$$\begin{bmatrix} N \\ k_x \end{bmatrix} = \begin{bmatrix} \kappa_N R \\ \kappa_x \end{bmatrix} \max(k_f, k_0). \tag{8}$$

k_f in Eq. (8) is the flexural wavenumber of a plate of thickness h and k_0 stands for the acoustic wavenumber. κ_N and κ_x are safety coefficient to truncate the domains at wavenumbers bigger than the flexural wavenumber k_f. Typically, κ_N and κ_x are taken between 1.5 and 2.

3 Sensitivity Function Calculations

3.1 Analytical Method for an Infinite Cylindrical Shell

As explained in the previous section, the reciprocity principle is used to calculate the sensitivity functions in Eq. (1) to obtain the ASD of the acoustic pressure at $\boldsymbol{x}$, radiated by a cylindrical shell under TBL excitation. We will first consider the case of an infinite cylindrical shell. To get the sensitivity functions, the spectral velocities on the surface of the cylindrical shell in response to a monopole excitation of unit volume velocity must be calculated. The Flügge shell operator for thin shells is chosen to write the dynamic equations of the fluid-loaded cylindrical shell because of its ease of implementation and its good agreement with other theories [12]. The Flügge equations are given along with further shell theories in Leissa's book on shell vibrations [13]. A very clear expression was written by Fuller and used to analyze the dispersion curves of a cylindrical shell [14]. Besides, Maxit and Ginoux employed Fourier transforms along the axial coordinate and Fourier series along the circumferential coordinates to express the Flügge equations in the wavenumber domain [15],

$$\left[\widetilde{\mathcal{L}}(k_x, n)\right] \begin{bmatrix} \widetilde{U}(k_x, n) \\ \widetilde{V}(k_x, n) \\ \widetilde{W}(k_x, n) \end{bmatrix} = -\gamma \begin{bmatrix} 0 \\ 0 \\ \widetilde{p}(k_x, n) + \widetilde{F}_e(k_x, n) \end{bmatrix} \tag{9}$$

where $\widetilde{\mathcal{L}}$ denotes the spectral Flügge operator, $\widetilde{U}$, $\widetilde{V}$, $\widetilde{W}$ are respectively the axial, tangential and radial spectral displacement, $\gamma = \left(1 - \nu^2\right) R^2 / E^* h$, $\widetilde{p}$ is the spectral reacting pressure from the external fluid loading and $\widetilde{F}_e$ the spectral excitation force applied on the cylindrical shell. Considering a monopole source at $\boldsymbol{x}$, the blocked pressure generated on the shell is (see [16]),

$$\widetilde{F}_e(k_x, n) = \frac{j\omega\rho_0}{2\pi k_r R} \frac{H_n^{(2)}(k_r r)}{H_n^{(2)\prime}(k_r R)} e^{-j(k_x x + n\theta)} \tag{10}$$

where ρ_0 is the fluid density, $k_r = \left(k_0^2 - k_x^2\right)^{1/2}$ and $H_n^{(2)}$ and $H_n^{(2)\prime}$ respectively stand for the Hankel function of the second kind and its derivative. The spectral reacting pressure can be linked to the radial displacements through [17],

$$\widetilde{p}(k_x, n) = \frac{\rho_0 \omega^2}{k_r} \frac{H_n^{(2)}(k_r R)}{H_n^{(2)\prime}(k_r R)} \widetilde{W}(k_x, n). \tag{11}$$

The solution to Eq. (9) has been derived in [18] and reads,

$$\widetilde{W}(k_x, n) = \frac{i\omega\rho_0\gamma e^{-j(k_x x + n\theta)}}{2\pi k_r R} \frac{H_n^{(2)}(k_r r)}{H_n^{(2)\prime}(k_r R)} \widetilde{\Lambda}(k_x, n) \tag{12}$$

The term $\widetilde{\Lambda}$ depends on the shell characteristics and represents the response of the fluid-loaded shell to a unitary point force (see Eq. (17) in [15] and Eq. (20) in [18], for details). The sensitivity function is the response in terms of spectral velocities so it can be deduced from Eq. (12) as,

$$\widetilde{H}_p(x, \theta, r, k_x, n, \omega) = j\omega R \widetilde{W}(k_x, n) \tag{13}$$

3.2 *Analytical Method for an Infinite Stiffened Cylindrical Shell*

In industrial applications, stiffeners are usually added to the cylindrical shell to increase the resistance of the structure while limiting the additional weight. These stiffeners have an influence on the dynamic behavior of the system and need to be accounted for in the mathematical model. In our model, the contacts between the stiffeners and the cylindrical shell are assumed perfect and along a circumferential line at discrete positions in the axial direction. Considering a regular stiffener spacing d, Eq. (9) becomes,

$$\left[\widetilde{\mathcal{L}}(k_x, n)\right] \begin{bmatrix} \widetilde{U}(k_x, n) \\ \widetilde{V}(k_x, n) \\ \widetilde{W}(k_x, n) \end{bmatrix} = -\gamma \begin{bmatrix} 0 \\ 0 \\ \widetilde{p}(k_x, n) + \widetilde{F}_e(k_x, n) \end{bmatrix} + \gamma \sum_{m=-\infty}^{+\infty} \begin{bmatrix} \bar{L}_m(n) \\ \bar{T}_m(n) \\ \bar{F}_m(n) - jk_x \bar{M}_m(n) \end{bmatrix} e^{-jk_x md}, \tag{14}$$

where $\overline{L}_m, \overline{T}_m, \overline{F}_m$ and $\overline{M}_m$ designate the axial force, tangential force, radial force and tangential moment applied by the m-th stiffener to the cylindrical shell, respectively. These forces are unknown and expressed in the circumferential order space. The stiffeners are characterized by their circumferential admittance matrix $\overline{\boldsymbol{Y}}$, which links the forces $\overline{\boldsymbol{F}}_m^r$ along the 4 degrees of freedom (DoF) at the junction of the stiffeners with the displacements $\overline{\boldsymbol{W}}_m^r$ along the 4 same DoF,

$$\overline{\boldsymbol{F}}_m^r(n) = -\overline{\boldsymbol{Y}}^{-1}(n)\overline{\boldsymbol{W}}_m^r(n). \tag{15}$$

The circumferential admittance matrix $\overline{\boldsymbol{Y}}$ is a 4×4 matrix for each circumferential order n and pulsation ω. It can be obtained from a standard FEM simulation. Unlike beam models, FEM modelling allows to account for all stiffener's deformations. Writing the displacement and rotation continuity at the junctions between the stiffeners and the cylindrical shell, and imposing force equilibrium, yields [4],

$$\widetilde{W}(k_x, n) = \overline{\boldsymbol{I}}(k_x, n)\left[\overline{\boldsymbol{F}}_{\boldsymbol{e}}(k_x, n) - \frac{1}{d}\left[\overline{\boldsymbol{Y}}(n) + \overline{\boldsymbol{S}}_0(k_x, n)\right]^{-1}\overline{\boldsymbol{T}}_0(k_x, n)\right]. \tag{16}$$

In Eq. (16), $\overline{\boldsymbol{I}}$ is the spectral admittance of the fluid loaded shell. $\overline{\boldsymbol{S}}_0$ and $\overline{\boldsymbol{T}}_0$ are terms that depend on $\overline{\boldsymbol{I}}$ and $\overline{\boldsymbol{F}}_{\boldsymbol{e}}$. The developments are detailed in [4]. As for the unstiffened case, the sensitivity function can be deduced through Eq. (13).

3.3 Numerical Method for Finite Shells with Various Internal Structures

Analytical formulations are not well-adapted to deal with more complex systems, such as a stiffened cylindrical shell coupled with internal structures, like floors or engine foundations. For this purpose, a specific numerical method, the condensed transfer function (CTF) approach was developed in [19]. It consists of a substructuring technique based on the concept of mechanical admittance. The method was first developed for a non-regularly stiffened shell having invariant geometry along the circumferential coordinate [15], and then extended to non-axisymmetric cases. The system under analysis is divided into several subsystems, as illustrated in Fig. 3. These are,

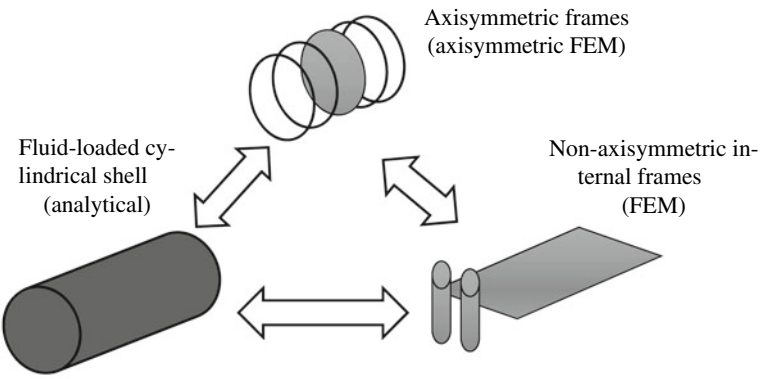

Fig. 3 Illustration of the substruturing approach

- The infinite fluid loaded cylindrical shell;
- The axisymmetric internal structures (stiffeners, bulkheads);
- The non-axisymmetric internal frames.

A set of condensation functions is defined at the interfaces between the subsystems to serve as a basis to physical quantities needed for the coupling. The coupling between subsystems is considered by means of the mechanical admittances at the junctions of each uncoupled subsystem, and taking into account the displacement continuity and force equilibrium between subsystems at the junctions [20]. One of the main advantages of this approach is that the admittances of each subsystem can be calculated separately by any method. For the case of a stiffened cylindrical shell, the chosen approach is to describe it with Flügge's equations. These are solved in the wavenumber domain, in a similar manner as described in Sect. 3.1, to yield the mechanical admittances at the junctions with the stiffeners. Conversely, the stiffener admittances are calculated with axisymmetric FEM models. The non-axisymmetric internal frames are also characterized with 3D FEM models. More details on the principle of CTF and its practical implementation for modelling stiffened shells with non-axisymmetric internal frames can be found in [19, 20].

In our case, the monopole excitation is applied to the cylindrical shell when it is uncoupled with the other subsystems, yielding what is called the free displacements of the shell. These are used as the right-hand term to calculate the coupling forces between the subsystems (see [19], Eq. (7)).

As the method uses Flügge's analytical formulation for the cylindrical shell, the system is of infinite extent. However, the finite extension of the shell can be approached using two simple tricks. First, clamped boundary conditions are defined at the end of the cylindrical shell by setting virtual stiffeners of null admittance (infinite rigidity). By comparison to the FEM model of a cylindrical shell, it has been shown that the boundary conditions only play a role at very low frequencies and that the analytical approach is able to model the radiation of a finite cylindrical shell [21]. Then, in accordance with the reciprocity principle, the sensitivity functions of a finite section of the shell is deduced from the Fourier transforms of the displacement field of the infinite shell excited by the monopole windowed to the finite section. This is equivalent to saying that these sensitivity functions are equal to the convolution in the axial wavenumber domain of the sensitivity functions of the infinite shell, with a sinus cardinal.

4 Applications and Discussion

4.1 Test Case Definitions

Three configurations are considered to illustrate the previously presented method, which correspond to the three approaches to calculate the sensitivity functions shown

in Sect. 3. All structures are made of steel having the following properties: $\rho = 7800$ kg m^{-3}, $E = 2.1 \times 10^{11}$ Pa, $\nu = 0.3$ and $\eta = 0.02$. Their geometries are defined as follows, showing an increasing complexity,

A. Infinite fluid-loaded cylindrical shell with $R = 5$ m, $h = 0.03$ m.
B. Cylindrical shell A + regularly spaced stiffeners. The stiffeners spacing is $d = 1.35$ m and they are all identical, having a T-shaped cross-section of dimensions $200 \times 15/200 \times 15$ mm (see Fig. 4d).
C. Cylindrical shell B, but of finite length of 42.3 m and including a non-axisymmetric internal frame. The internal frame is an 8.1 m long floor depicted in Fig. 4e.

Our goal is to predict the radiated acoustic pressure at a point located at distance D_{obs} from the shell's surface. In the case of the finite shell, the observation point is at a distance $x = 22.05$ m from the end of the shell. In the case of the raft, the latter is connected to the shell at the distances $x = 18.9$ and $x = 27$ m, as shown in Fig. 4c.

The TBL excitation is characterized by a convection flow speed of $U_c = 3.2$ m/s, a friction velocity $v_f = 0.16$ m/s and a thickness $\delta_{tbl} = 0.11$ m. For the numerical applications, the Chase model [22] adapted for the cylindrical problem through Eq. (6) is used,

$$\widetilde{\phi}_{pp}^{tbl}(k_x, n, \omega) = \frac{(2\pi)^2 \rho_0^2 v_f^3}{R\left[K_+^2 + (b\delta_{tbl})^{-2}\right]^{\frac{5}{2}}} \left(C_M k_x^2 + C_T K^2 \left[\frac{K_+^2 + (b\delta_{tbl})^{-2}}{K^2 + (b\delta_{tbl})^{-2}} \right] \right) \quad (17)$$

with $K_+^2 = (\omega - U_c k_x)^2 / \left(3 v_f\right)^2 + K^2$, $K^2 = k_x^2 + n^2/R^2$ and recommended parameters $b = 0.75$, $C_M = 0.1553$ and $C_T = 0.0047$.

The calculations are performed between 100 and 1000 Hz with 400 values with logarithmic separation.

4.2 Results for the Infinite Cylindrical Shell

Let us first plot in Fig. 5 the wall-pressure spectrum defined by Eq. (17) in the wavenumber domain, for two frequencies, 100 and 1000 Hz. For our case of interest, the coincidence frequency between the flexural and acoustic waves is around 7.6 kHz. Likewise, the coincidence frequency between the flexural and convective waves (i.e. hydrodynamic coincidence frequency) is around 0.03 Hz. This means that the frequency domain of interest is in the subconvective subsonic region [23]. There, the spectrum decreases with frequency for a fixed wavenumber, as can be seen by comparing the colors in Fig. 5a, b. For a given frequency, the wavenumber-frequency spectrum increases with wavenumber

Examples of sensitivity functions for the infinite cylindrical shell (test case A) are given in Fig. 6 for two frequencies and two observation distances, $D_{obs} = 0.1$ m and 10 m. The white dashed line represents the flexural wavenumber for the equivalent

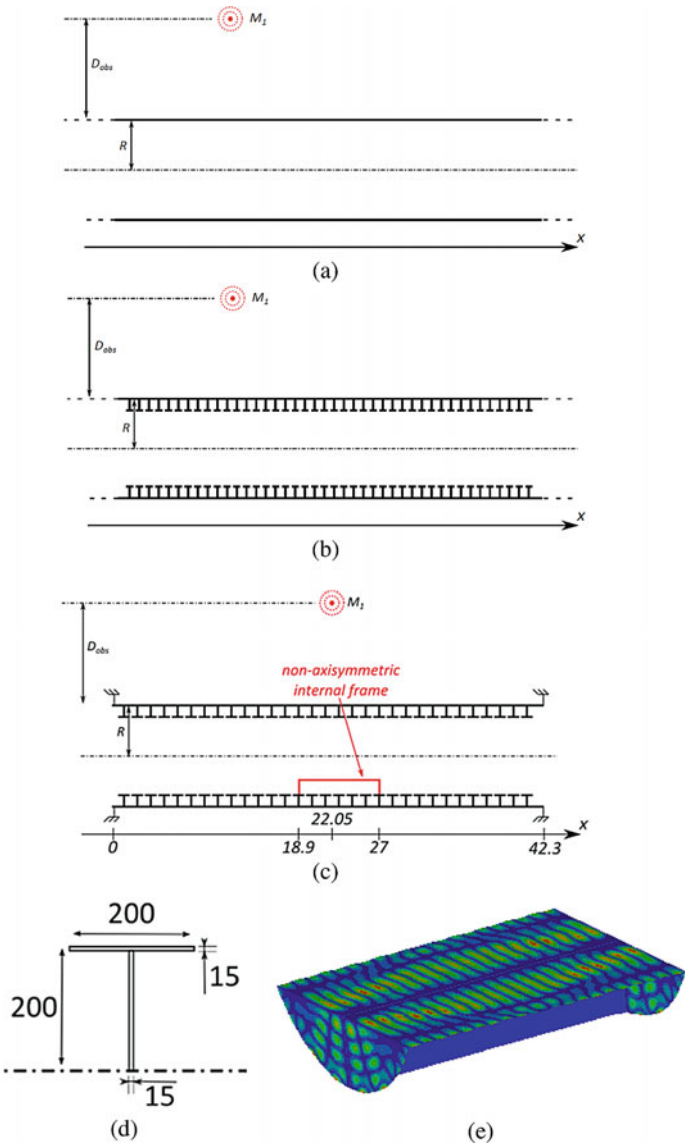

Fig. 4 Sketches of **a** test case A, **b** test case B, **c** test case C (dimensions in m), **d** the cross-section of the stiffeners used in test cases B and C (dimensions in mm), **e** example of a mode of vibration of the non-axisymmetric internal frame used in test case C

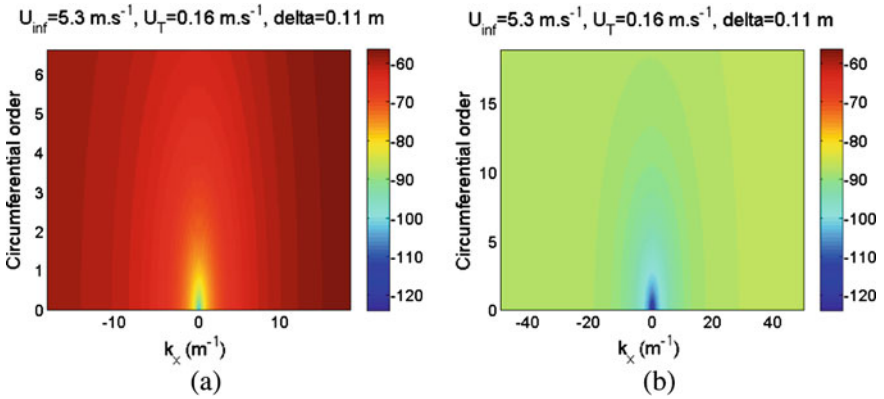

Fig. 5 Wall-pressure spectrum as a function of the axial wavenumber and the circumferential order for **a** 100 Hz and **b** 1000 Hz

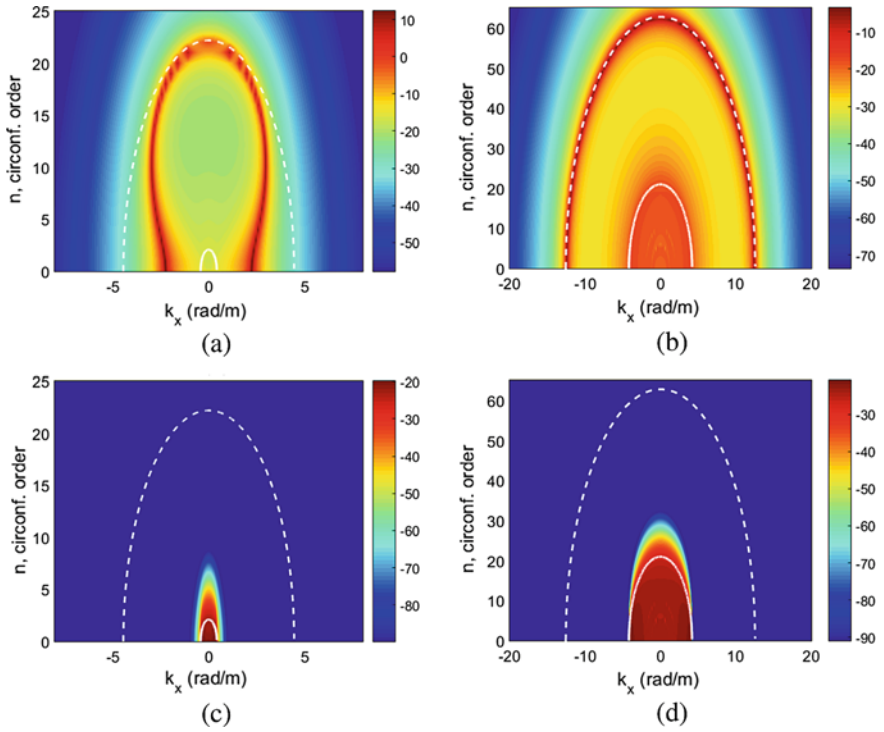

Fig. 6 Sensitivity functions of the infinite cylindrical shell (test case A) at **a** 100 Hz and $D_{obs} = 0.1$ m, **b** 1000 Hz and $D_{obs} = 0.1$ m, **c** 100 Hz and $D_{obs} = 10$ m and **d** 1000 Hz and $D_{obs} = 10$ m

fluid-loaded plate, while the white solid line represents the acoustic hemi-ellipse. In Fig. 6a, at 100 Hz and $D_{obs} = 0.1$ m, the maxima of spectral velocities form a horse-shoe shape, fitting the flexural wavenumbers of the equivalent plate for k_x close to 0. This shape is typical of cylindrical shells for frequencies below the ring frequency, which in this case is 173 Hz. Above this frequency, the flexural waves on the fluid loaded cylindrical shell resemble those in a plate of equal thickness, and taking into account the fluid loading [24], as seen in Fig. 6b. As observed for the sensitivity functions at $D_{obs} = 0.1$ m, the cylindrical shell responds to all wavenumbers up to the flexural wavenumber. Above the flexural wavenumber, the amplitude of the spectral velocity decreases, validating the truncation discussed in Sect. 2.5.

When the pressure is collected far away the shell, at $D_{obs} = 10$ m, the sensitivity functions shown in Fig. 6c, d become quite different. In this case, only the wavenumbers inside the acoustic domain contribute to radiation [11].

The pressure ASD at 100 Hz, for instance, is calculated from Eq. (1) by multiplying the wall-pressure spectrum in Fig. 5a by the sensitivity functions in Fig. 6a or c and integrating over the wavenumber domain. Doing this for each frequency yields the frequency response represented in Fig. 7. The ASD is obviously higher at $D_{obs} = 0.1$ m than at $D_{obs} = 10$ m. But this is not only due to geometric losses (i.e. divergence of cylindrical waves), but also to the fact that more components of the sensitivity functions play a role at short distances than at long distances, as shown in Fig. 6. It can also be observed that oscillations occur close to the shell in the low frequency range, which disappear when the frequency increases. These oscillations are due to the cut-on frequencies of the circumferential order contributions to the near-field radiation. The oscillations do not appear at large distances from the shell because of the acoustic filtering effect mentioned earlier. In this case, the higher order modes play a less important role than the lower order modes whose cut-on frequencies are below the lowest frequency of interest [18].

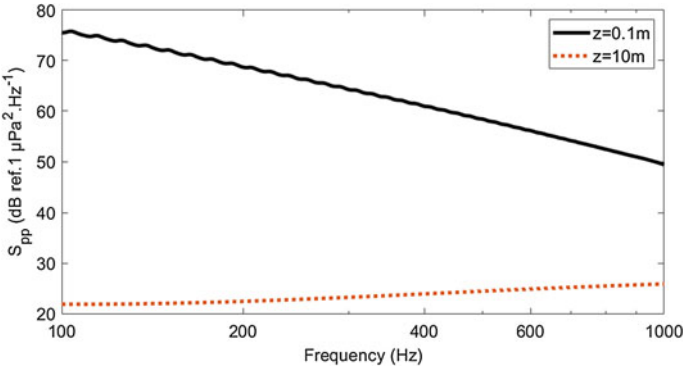

Fig. 7 ASD function of the radiated pressure for the infinite cylindrical shell for two observation distances

4.3 *Influence of Stiffeners*

The response of test case B is calculated using the analytical model presented in Sect. 3.2. The frequency response of the radiated pressure at $D_{obs} = 10$ m is plotted in Fig. 8 and compared to the non-stiffened case presented in the previous section. A noticeable increase in the ASD is observed over several regions of the frequency domain.

To understand the reason for that behavior, the sensitivity functions are examined in Fig. 9 for two frequencies, namely 310 Hz where there is only a small pressure level increment and 495 Hz where a huge rise is appreciated. If we first compare Fig. 9a, b, we can observe that the sensitivity functions of the unstiffened and stiffened cylindrical shells are similar, the only difference being the size of the acoustic domain for low wavenumbers. The stiffener effects on the sensitivity functions is clear when comparing e.g., Figure 9a, c. The stiffeners create periodic copies of the acoustic domain along the axial wavenumbers with a period of $2\pi/d$. This phenomenon is also observed for the sensitivity function in Fig. 9d. There is however a difference between Fig. 9c, d. For stiffened plates, it has been highlighted that Bloch-Floquet waves can be propagative for some frequency bands called pass-bands and evanescent for other frequency bands, called stop-bands [25, 26]. Recently, similar behaviors have been observed for stiffened cylindrical shells [4]. If a Bloch-Floquet wave has a wavenumber within the acoustic domain, or one of its periodic copies, it will contribute to the far-field radiated pressure. In Fig. 9d, this coincidence occurs around $|k_x| = 10$ m^{-1}, where spots with significant amplitudes (10 dB higher than the ones in the acoustic semi-ellipse) are localized in the second copy of the acoustic semi-ellipse. The locations of these spots can be related to the wavenumbers associated to propagative Bloch-Floquet waves as shown in [4] through the analysis of dispersion curves. It can be concluded that the bumps observed in the radiated noise spectrum

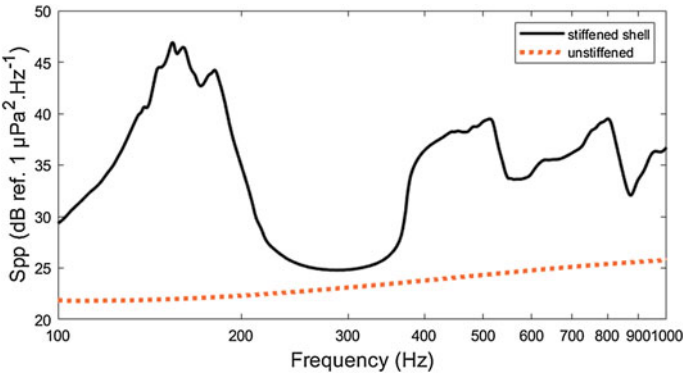

Fig. 8 ASD function of the radiated pressure for the infinite cylindrical shell with and without stiffeners

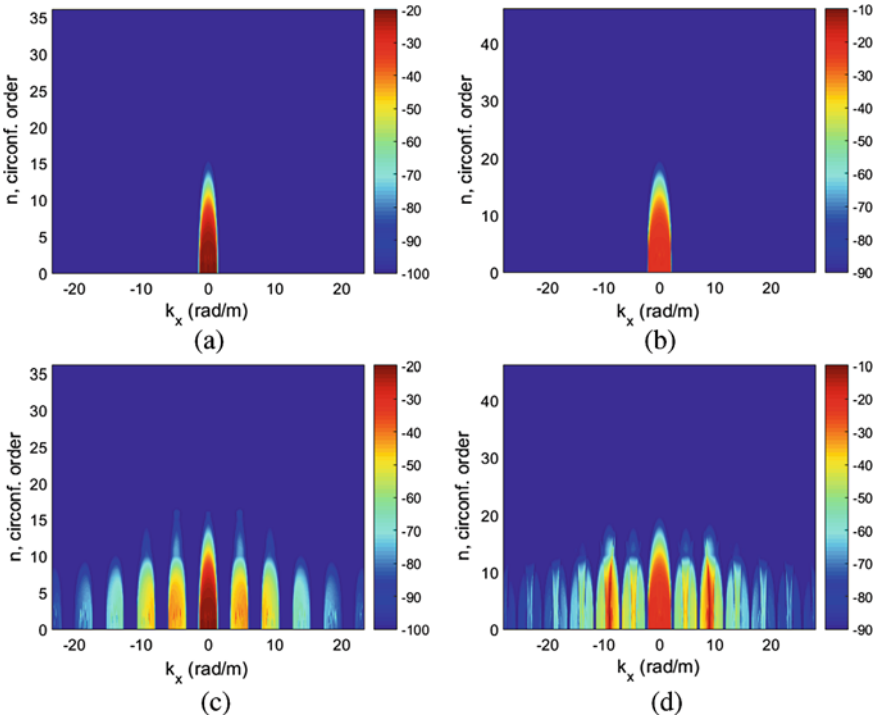

Fig. 9 Sensitivity functions of the infinite cylindrical shell at $D_{obs} = 10$ m **a** without stiffeners at 310 Hz **b** without sitffeners at 495 Hz, **c** with stiffeners at 310 Hz and **d** with stiffeners at 495 Hz

of Fig. 8 can be attributed to propagative Bloch-Floquet waves, which barely suffer from acoustic filtering and thus radiate to the far field (see [4] for details).

4.4 Influence of the Finite Length

Before addressing test case C, let us study the influence of the finite length of the cylindrical stiffened shell without considering the non-axisymmetric internal frame. The results are compared to those of test case B in Fig. 10. The sensitivity functions for the finite shell have been calculated using the numerical approach presented in Sect. 3.3. The ASD for the finite and infinite shells in Fig. 10 are close one to the other, meaning that the finite shell also exhibits the propagative Bloch-Floquet phenomena. An additional peak is observed at low frequencies for the finite shell due to its resonances (i.e. axial standing waves).

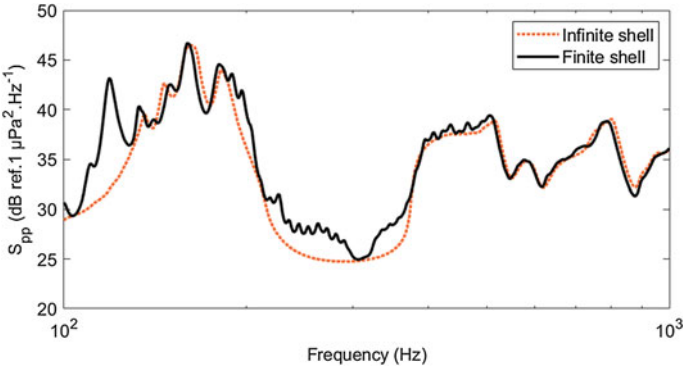

Fig. 10 ASD function of the radiated pressure for the infinite and finite stiffned cylindrical shell

4.5 Influence of the Non-axisymmetric Internal Frame

The influence of a non-axisymmetric internal frame is next examined by comparing the ASD function of the radiated pressure at $D_{obs} = 10$ m for the finite stiffened shell with and without the raft. The results, in Fig. 11 show a level increase due to the non-axisymmetric frame. The underlying physics can be grasped again from the sensitivity functions. These are represented in Fig. 12 for two frequencies (310 and 495 Hz, as in the previous section), with and without the non-axisymmetric internal frame (compare Fig. 12a with c and Fig. 12b with d). Let us remember from the exposition of the reciprocal approach in Sect. 2.3, that a monopole placed far away from the axisymmetric shell only excites the circumferential orders within the acoustic semi-ellipse. When the non-axisymmetric internal frame is added to the system, it tends to transfer energy from the low to the higher circumferential

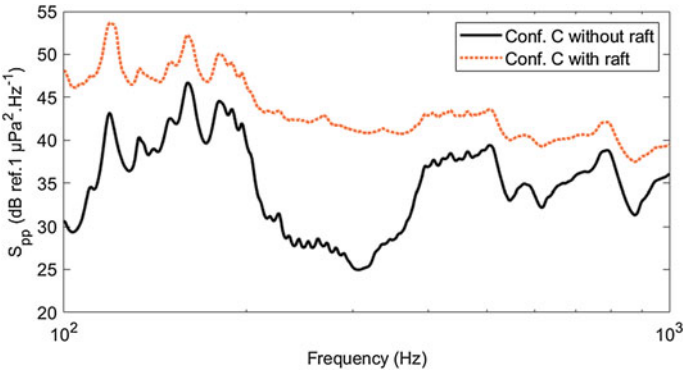

Fig. 11 ASD function of the radiated pressure with and without the raft for the finite stiffened cylindrical shell

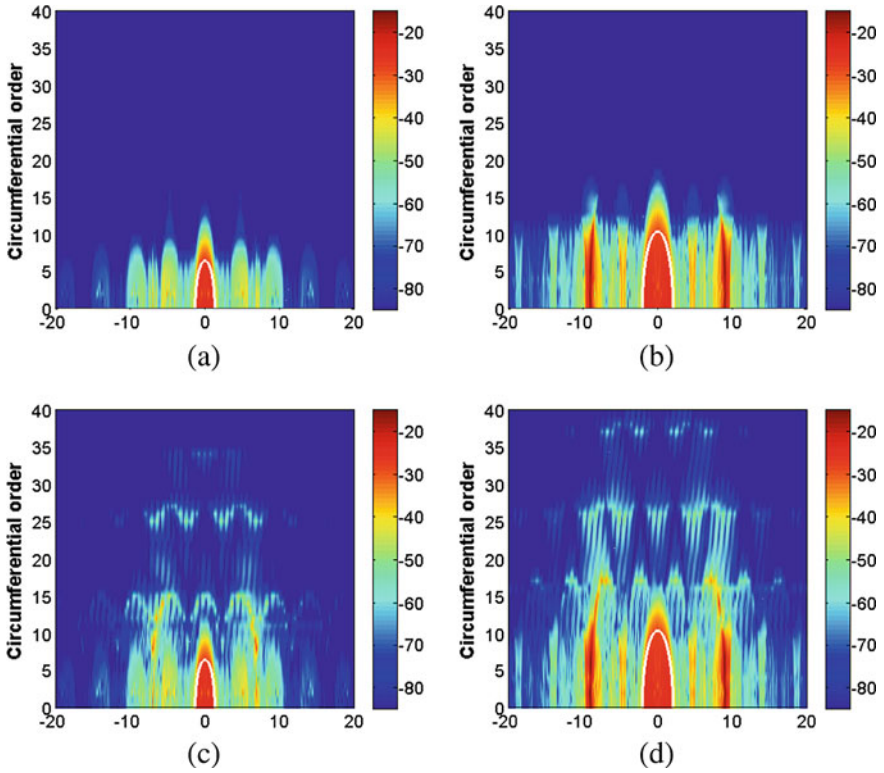

Fig. 12 Sensitivity functions of the finite stiffened cylindrical shell at $D_{obs} = 10$ m **a** without raft at 310 Hz **b** without raft at 495 Hz, **c** with raft at 310 Hz and **d** with raft at 495 Hz

orders, as seen in the sensitivity functions of Fig. 12c, d. Actually, the effect of non-axisymmetric geometries on the circumferential orders coupling has been highlighted before in the literature [19, 24, 27]. Moreover, Fig. 5 showed that the wall-pressure spectrum level increases with the circumferential order. Inserting these quantities in Eq. (1) explains the strong influence of the non-axisymmetric internal frame on the ASD of the radiated pressure.

5 Conclusions

A general approach based on wavenumber formulations and on the reciprocity principle has been presented to calculate the radiated pressure from various submerged cylindrical shells under a TBL excitation. The proposed method is based on analytical formulations for relatively simple shells and on hybrid approaches for more complex ones, covering various configurations which include axisymmetric and non-axisymmetric internal frames. One of the main advantages of the method is that the

response to different TBL excitations can be calculated at a low numerical cost if the sensitivity functions are stored in a database. This makes it a very powerful tool for parametric studies. Physical phenomena have been analyzed, showing that the acoustic radiated pressure noticeably increases with complexity (i.e., when including stiffeners, assuming finite length shells or considering non-axisymmetric internal frames).

References

1. F. Chevalier, C. Audoly, Turbulent flow-induced self noise and radiated noise in naval systems – an industry point of view, in *Flinovia – Flow Induced Noise and Vibrations Issues and Aspects: A Focus on measurement, modeling, simulation and reproduction of the flow excitation and flow induced response* (Springer International Publishing Switzerland, 2015), pp. 211–226
2. W.A. Strawderman, *Wavevector-frequency analysis with applications to acoustics* (Technical report, DTIC, 1994)
3. C. Maury, P. Gardonio, S.J. Elliott, A wavenumber approach to modelling the response of a randomly excited panel. Part I: general theory, J. Sound Vib. 252:83–113, 2002
4. L. Maxit, O. Guasch, V. Meyer, M. Karimi, Noise radiated from a periodically stiffened cylindrical shell excited by a turbulent boundary layer. J. Sound Vib. **466**, 115016 (2020)
5. L. Maxit, M. Berton, C. Audoly, D. Juvé, Discussion about different methods for introducing the turbulent boundary layer excitation in vibroacoustic models, in *Flinovia – Flow Induced Noise and Vibrations Issues and Aspects: A Focus on Measurement, Modeling, Simulation and Reproduction of the Flow Excitation and Flow Induced Response* (Springer International Publishing Switzerland, 2015), pp. 249–278
6. F.J. Fahy, Some applications of the reciprocity principle in experimental vibroacoustics. Acoust. Phys. **49**(2), 217–229 (2003)
7. C. Marchetto, L. Maxit, O. Robin, A. Berry, Vibroacoustic response of panels under diffuse acoustic field excitation from sensitivity functions and reciprocity principles. J. Acoust. Soc. Am. **141**, 4508–4521 (2017)
8. C. Marchetto, L. Maxit, O. Robin, A. Berry, Experimental prediction of the vibration response of panels under a turbulent boundary layer excitation from sensitivity functions. J. Acoust. Soc. Am. **143**, 2954–2964 (2018)
9. Flinovia – Flow induced noise and vibrations issues and aspects: A focus on measurement, modeling, simulation and reproduction of the flow excitation and flow induced response (Springer International Publishing Switzerland, 2015)
10. R.M. Lueptow, Turbulent boundary layer on a cylinder in axial flow, September 1988. NUSC Technical report 8389, Naval Underwarter Systems Center, USA, New London (1988)
11. E.G. Williams, B.H. Houston, J.A. Bucaro, Experimental investigation of the wave propagation on a point-driven, submerged capped cylinder using K-space analysis. J. Acoust. Soc. Am. **87**(2), 513–522 (1990)
12. R. Ruotolo, A comparison of some thin shell theories used for the dynamic analysis of stiffened cylinders. J. Sound Vib. **243**(5), 847–860 (2001)
13. A.W. Leissa, *Vibration of Shells*, vol. 288. Scientific and Technical Information Office, National Aeronautics and Space Administration Washington, DC, USA (1973)
14. C.R. Fuller, The effects of wall discontinuities on the propagation of flexural waves in cylindrical shells. J. Sound Vib. **75**(2), 207–228 (1981)
15. L. Maxit, J.-M. Ginoux, Prediction of the vibro-acoustic behavior of a submerged shell non periodically stiffened by internal frames. J. Acoust. Soc. Am. **128**(1), 137–151 (2010)
16. E.A. Skelton, J.H. James, Acoustics of an anisotropic layered cylinder. J. Sound Vib. **161**(2), 251–264 (1993)

17. M.C. Junger, D. Feit, *Sound, structures, and their interaction*, vol. 240 (MIT press, Cambridge, MA, 1972)
18. L. Maxit, M. Karimi, V. Meyer, N. Kessissoglou, Vibroacoustic responses of a heavy fluid loaded cylindrical shell excited by a turbulent boundary layer. J. Fluids and Structures. **92**, 102758 (2020)
19. V. Meyer, L. Maxit, J.-L. Guyader, T. Leissing, Prediction of the vibroacoustic behavior of a submerged shell with non-axisymmetric internal substructures by a condensed transfer function method. J. Sound Vib. **360**, 260–276 (2016)
20. V. Meyer, L. Maxit, J.-L. Guyader, T. Leissing, C. Audoly, A condensed transfer function method as a tool for solving vibroacoustic problems. Proc IMechE Part C: J Mech. Eng. Sci. **230**(6), 928–938 (2016)
21. V. Meyer, C. Audoly, D. Liu, N. Kessissoglou, L. Maxit, Bridging the frequency gap for vibro-acoustic prediction of a submerged shell, in *Proceedings of WESPAC*, New Delhi (2018)
22. D.M. Chase, The character of the turbulent wall pressure spectrum at subconvective wavenumbers and a suggested comprehensive model. J. Sound Vib. **112**, 125–147 (1987)
23. R. Camussi, A. Di Marco, Wall pressure fluctuations induced by supersonic turbulent boundary layer, in *Flinovia – Flow Induced Noise and Vibrations Issues and Aspects: A Focus on Measurement, Modeling, Simulation and Reproduction of the Flow Excitation and Flow Induced Response* (Springer International Publishing Switzerland, 2015), pp. 67–90
24. V. Meyer, L. Maxit, Y. Renou, C. Audoly, Experimental investigation of the influence of internal frames on the vibroacoustic behavior of a stiffened cylindrical shell using wavenumber analysis. Mech. Syst. Sign. Process. **93**, 104–117 (2017)
25. B. Mace, Periodically stiffened fluid-loaded plates, I: response to convected harmonic pressure and free wave propagation. J. Sound Vib. **73**, 473–486 (1980)
26. L. Maxit, V. Denis, Prediction of flow induced sound and vibration of periodically stiffened plate. J. Acoust. Soc. Am. **133**, 146–160 (2013)
27. D.M. Photiadis, B.H. Houston, E.G. Williams, J.A. Bucaro, Resonant response of complex shell structures. J. Acoust. Soc. Am. **108**(3), 1027–1035 (2000)

A Viscoelastic Model of Rough-Wall Boundary-Layer Noise

Ian MacGillivray, Alex Skvortsov, and Paul Dylejko

Abstract We present an analytical framework that can be used for quantitatively estimating the effect of wall roughness on turbulent boundary-layer noise. For this purpose we extend the viscous-elastic analogy for boundary-layer noise (the well-known analogy between the motion of a viscoelastic medium and a viscous fluid) that was proposed in our previous work. The refined model accounts for the elastic (impedance) properties of the underlying surface with some fine-scale morphological features (natural roughness or special engineering coating). Our analysis is restricted to significantly-subsonic flows. The speed of the flow is also assumed to be much less that the speed of elastic waves (both longitudinal and shear) in the material of the underlying surface.

Keywords Flow noise · Turbulent boundary layer · Vibroelastic materials · Roughness

Nomenculture

$\langle\cdot\rangle$	Ensemble average
$\lvert\cdot\rvert$	Magnitude of a complex quantity
$\lVert\cdot\rVert$	Magnitude of a vector quantity
B_0	Smooth surface log-law constant of Eq. (3)
B_1	Constant of Eq. (9)
c_f	Local friction coefficient, in Eq. (4)
c_l	Longitudinal (sound) wave speed (m/s)

I. MacGillivray (✉) · A. Skvortsov · P. Dylejko
Defence Science and Technology, Fishermans Bend, VIC 3207, Australia
e-mail: Ian.MacGillivray@dst.defence.gov.au

A. Skvortsov
e-mail: Alex.Skvortsov@dst.defence.gov.au

P. Dylejko
e-mail: Paul.Dylejko@dst.defence.gov.au

E. Ciappi et al. (eds.), *Flinovia—Flow Induced Noise and Vibration Issues and Aspects-III*, https://doi.org/10.1007/978-3-030-64807-7_13

c_s	Shear (transverse) wave speed, actual or effective (m/s), Eq. (19)
C_1	TBL thickness scale constant in Eq. (8)
C_2	Normalisation constant for E in Eq. (15)
C_f	Total (average) friction coefficient, Eq. (10)
E	von Karman energy spectrum (m^3/s^2), Eq. (15)
f	Roughness shift term for the log law of Eq. (3)
$F_{\mathbf{v}}(\mathbf{k}, \omega)$	Fourier transform (in $\mathbf{x}$ and t) of $\mathbf{v}$ (m^4), Eq. (20)
$G(\mathbf{k}, \omega)$	Reflected velocity squared energy spectrum (m^5/s), Eq. (22)
h	Equivalent sand-grain roughness or scale (m), Eq. (5)
k	General wavenumber, $k = \|\mathbf{k}\| = \|(k_1, k_2, k_3)\|$
$\mathbf{k}_s$	Shear wavevector, with magnitude $k_s = \omega/c_s$
$\mathbf{k}_n, \mathbf{k}$	General wavevector, $\mathbf{k} = (k_1, k_2, k_3)$
k_i, k_j	Wavevector components (1/m)
K	Turbulent kinetic energy (m^2/s^2), Eq. (15)
L	Downstream dimension (m)
M	Mach number U/c_l
$Q_{ij}(\mathbf{r}, t)$	Fluctuation velocity correlation function (m^2/s^2), Eq. (16)
$Q_{ij}(\mathbf{k}, \omega)$	Fourier transform (in $\mathbf{r}$ and t) of $Q_{ij}(\mathbf{r}, t)$ (m^5/s), Eq. (17)
$\mathbf{r}$	Space vector (m)
$R(\tau, k)$	Time correlation function (dimensionless)
$R(\omega, k)$	Fourier transform (in time τ) of $R(\tau, k)$ (s), Eq. (18)
Re_x, Re_L	Reynolds numbers Ux/ν, UL/ν
SNGR	Stochastic noise generation and radiation methods
t, τ	Time (s)
TBL	Turbulent boundary layer
$T(\theta, \omega)$	Shear-to-sound energy coefficient (dimensionless), Eq. (25)
$u(z)$	Mean velocity profile at distance z from the wall (m/s)
U	Fluid free-stream flow velocity (m/s)
$\mathbf{v}$	Fluid velocity fluctuation, $\mathbf{v} = (v_1, v_2, v_3)$ (m/s)
v_i, v_j	Velocity fluctuation vector components (m/s)
v_τ	Frictional velocity (m/s), Eq. (4)
$\widehat{\mathbf{v}}_n$	Velocity amplitude of mode n (m/s), Eq. (1)
$V, V(\mathbf{k}, \omega)$	Shear-to-sound $\mathbf{v}$ (amplitude) reflection coefficient, Eqs. (2), (21)
V_*	V for a rigid surface
w	Radiated acoustic power per unit surface area (kg/s^3), Eq. (24)
$\mathbf{x}$	Space vector (m)
x	Downstream distance (m)
z	Distance from the wall surface (m)
κ_e	Wavenumber of energy-containing eddies, Eq. (15)
$\mu = \mu_r + i\mu_i$	Effective shear modulus of the fluid, following Eq. (19)
ν	Kinematic viscosity of the fluid (m^2/s), Eq. (3)
ν_e	Effective fluid viscosity caused by roughness h (m^2/s), Eq. (6)
ρ	Mass density of the fluid (kg/m^3), Eq. (2)

$\rho^{(1)}$	Mass density of an elastic half-space (kg/m^3), Eq. (2)
τ_0	Correlation time (s), Eq. (18)
φ_n	Phase of mode n, Eq. (1)
ω, ω_n	Angular frequency, angular frequency of mode n (rad/s), Eq. (1)

1 Introduction

Generation of acoustic waves by turbulent flow near elastic boundaries has been traditionally the focus of many studies on aeroacoustics (flow noise), geophysics (mechanisms of ambient noise of atmosphere and ocean) and industrial applications (exhaust noise, new sensor design, soundproofing). There is a vast amount of literature devoted to this subject (see [1, 2] and references therein).

For many realistic geometries and operational conditions, the direct computer simulation of aeroacoustic sources of turbulent flow using DNS and LES is still a challenging task, imposing severe limitations on achievable frequencies and Reynolds numbers for any credible prediction. When coupled with FE models of the elastic (impedance) boundary this computational framework often becomes unusable in an operational context or for prototyping studies. This necessitates development of different techniques based on underlying physical principles that can promptly provide approximate solutions and indicate the main trends of the phenomena. Future numerical refinement can be implemented at a later stage.

One of the promising approaches often applied in this context employs so-called synthetic turbulence reconstruction methods. The basis of the method goes back to by Kraichnan [3] and different revisions of this model have been presented since then [4–9]. Early attempts relied on expressing the turbulent velocity field as a finite sum of Fourier modes

$$\mathbf{v} = 2\sum_n \widehat{\mathbf{v}}_n \cos(\mathbf{k}_n \cdot \mathbf{x} - \omega_n t + \varphi_n), \tag{1}$$

where mode amplitudes $\widehat{\mathbf{v}}_n$, wavevectors $\mathbf{k}_n$, frequencies $\omega_n(\mathbf{k}_n)$ and random phases φ_n are chosen in such a way to match the properties of the turbulent flow (usually the modified Von-Karman spectrum for isotropic turbulence, see below). This approach is used to model aeroacoustic sources and is often referred to as Stochastic Noise Generation and Radiation methods (SNGR) [4–6].

In application to the problem of flow noise generated by a turbulent boundary layer (TBL) over an elastic (impedance) surface, the framework of the SNGR method has been presented in our earlier work (see Fig. 1) [10]. More specifically, if the boundary layer turbulence is modelled as an ensemble (sum) of random shear waves trapped near the boundary then transformation into longitudinal waves (sound) at the boundary (elastic interface) can be evaluated by applying the well-known analogy between the motion of a viscoelastic medium and a viscous fluid. For a single harmonic (Fourier mode) TBL 'reflecting' at a simple interface between a fluid and a soft

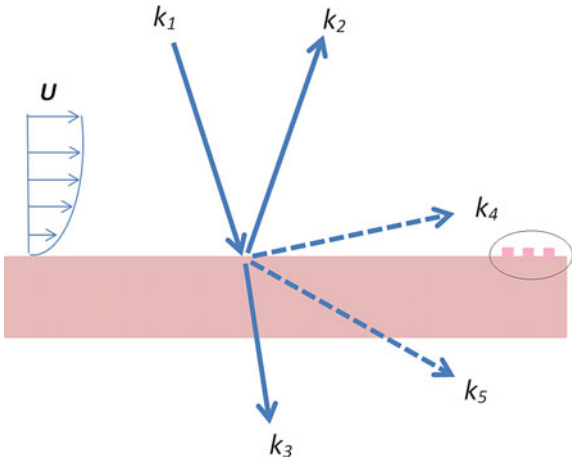

Fig. 1 Transformation of vorticity perturbations (shear waves, solid) in a turbulent boundary-layer into sound waves (longitudinal waves, dashed) at the elastic wall: $\mathbf{k}_1$ is the wavevector of the incident shear (vorticity) wave, $\mathbf{k}_2$ is the wavevector of the reflected shear wave, $\mathbf{k}_3$ is the wavevector of the transmitted shear wave; and $\mathbf{k}_4$, $\mathbf{k}_5$ are wavevectors of generated sound waves

medium (such as a rubber) the effectiveness of this transformation was calculated explicitly in [10]. Analysis of this effectiveness can provide insightful criteria for material selection for TBL noise reduction that would be very difficult to deduce by other means. For instance, for a TBL over a viscoelastic half-space, as with a water–rubber boundary, the expression of effectiveness of vortex-sound transformation can be simplified to [10]

$$V/V_* \simeq \rho^{(1)}/\rho - 1\,, \tag{2}$$

where $\rho^{(1)}$ is the density of the material in the elastic half-space, ρ is the density of the fluid medium, V is the shear-to-sound amplitude reflection coefficient (including phase), and V_* is V for a rigid surface. This equation therefore provides an estimation of the *relative* change of TBL noise caused by the change of the material properties of the underlying surface (for the range of validity of this expression see [10]).

Equation (2) implies that the intensity of TBL noise can be significantly decreased if the material underlying the TBL has fluid-like properties (such as with rubber) and its density is close to the density of the fluid. More complex multi-layer-material calculations, which avoid this assumption, can be made using the theory of Lévesque and Piché [11] and are presented in [10].

If the elastic surface underlying the TBL has some fine-scale morphological features (natural roughness or special engineering coating) then the problem becomes even more challenging since these features affect the parameters of the turbulent flow (e.g. drag) and the fluctuating forces acting on the surface. Both effects will change the level of TBL generated sound. This problem has recently attracted significant attention and extensive experimental efforts (see [12–18] and references therein). Such research motivates development of a simplified physics-based model, similar to SNGR, that can be applied in this context to provide prompt trend analysis and reasonable estimations before more advanced modelling tools can be applied.

The purpose of the paper is twofold. First we generalise our previous work to be able to provide an *absolute* prediction of flow noise generated by a TBL over an elastic surface. This is implemented by integrating the contribution from all vorticity modes of the TBL, assuming the von Karman model of its turbulence spectrum [19]. Second, we demonstrate how a simple model of interface roughness can be integrated into the viscous-elastic analogy leading to quantitative estimation of the effect of roughness on TBL noise. We emphasise that there are many well-known models of roughness noise generated by turbulent flows over a rigid surface [1, 17]. The aim of the reported study is a consistent integration of the effect of surface elasticity in the SNGR-based models of roughness noise.

2 Turbulent Boundary Layer over a Rough Surface

Following our previous work [10] we assume that the elastic surface does not affect the flow in the TBL. This assumption imposes some limitation on the velocity of turbulent flow for which the proposed framework can be applied. More specifically, it is required that the flow speed should be significantly less than the velocity of any elastic (longitudinal, shear and surface) waves in the material of the underlying surface. This allows the decoupling of fluctuations in the TBL from the acoustic response of the underlying surface.

The topic of a TBL over a rough surface is one of the traditional subjects of engineering hydrodynamics [20–22] and geophysical fluid dynamics [23, 24]. It is still an area of active research and there is a vast body of work on this subject (for review see [1, 17, 25–30] and references therein). It is well recognised [1, 17, 22, 26, 28, 29] that the effect of roughness concentrates in a thin layer adjacent to the underlying surface and can be accounted for by a downward shift f (called the roughness function) in the conventional log law

$$\frac{u(z)}{v_\tau} = \frac{1}{\kappa} \ln\left(\frac{v_\tau z}{\nu}\right) + B_0 - f, \tag{3}$$

where u is the mean velocity parallel to the surface, z is the distance from the surface, $\kappa = 0.41$, $B_0 = 5.5$, ν is kinematic viscosity of the fluid,

$$v_\tau = U\sqrt{\frac{c_f}{2}} \tag{4}$$

is the frictional velocity, U is the free stream velocity, and c_f is the surface friction coefficient (in general modified by roughness). The limit $f = 0$ corresponds to the TBL over a smooth surface.

There are numerous models for the roughness function f (sometimes referred as the Hama roughness function [21]) that have been extensively validated numerically and experimentally. These models provides different trade-off between feasibility

and complexity and can be tailored to a modelling scenario [1, 17, 20, 22, 25, 26, 28]. To illustrate the capabilities of the proposed framework we use the traditional Colebrook model [31, 32] that leads to a simple analytical treatment and provides reasonable agreement with experimental data over a broad range of roughness parameters. More complex models of the roughness function can be integrated into the proposed framework in a similar manner.

In the Colebrook model (also see [28]) the roughness function is given by the expression

$$f = \frac{1}{\kappa} \ln\left(1 + 0.3\frac{v_\tau h}{\nu}\right), \tag{5}$$

where h is the scale of the so-called equivalent sand-grain roughness (a unified measure that can be derived for an arbitrary rough surface, see [18, 20, 33]). Condition $h = 0$ (smooth surface) corresponds to $f = 0$ in Eq. (3).

In order to make a connection with our earlier work on shear–sound transformation at the fluid-solid interface [10], we introduce an effective (turbulence) viscosity ν_e that accounts for the effect of roughness. More specifically, we define a scaling parameter q according to

$$\nu_e = q\nu, \tag{6}$$

and derive q by substituting this expression into Eq. (3). This results in $q = \exp(\kappa f)$ or

$$q = 1 + 0.3v_\tau h/\nu. \tag{7}$$

For $h = 0$ (no roughness) we have $q = 1$ and $\nu_e = \nu$, as expected.

The next step is to deduce an equation for c_f. As shown in [34, 35] it can be derived from the condition $u(\delta) = U$, where δ is the TBL thickness as a function of downstream distance x. The estimation for $\delta(x)$ follows from kinematic relation

$$\frac{d\delta}{dx} \simeq \frac{\delta}{x} = C_1 \frac{v_\tau}{U}, \tag{8}$$

where $C_1 = 0.3$ [34]. Combining Eqs. (3)–(8) we arrive at the closed equation for c_f:

$$\frac{1}{\sqrt{c_f}} = \frac{1}{\kappa\sqrt{2}} \ln\left(\frac{c_f \mathrm{Re}_x}{q}\right) + B_1, \tag{9}$$

where $B_1 = [B_0 - \ln(C_1/2)/\kappa]/\sqrt{2}$ and $\mathrm{Re}_x = Ux/\nu$ is the Reynolds number at the downstream location x. Note that q here is also a function of c_f through Eqs. (4) and (7). The solution of Eq. (9) provides c_f as function of Reynolds number and roughness scale h. When used in Eqs. (3), (4), and (8) this solution describes the effect of roughness on boundary layer parameters and $u(z)$, v_τ and δ.

In many practical applications the total friction coefficient C_f is measured. For a plate of length L this coefficient is related to the 'local' friction coefficient $c_f(x)$ by a formula

$$C_f(L) = \frac{1}{L}\int_0^L c_f(x)\,dx. \tag{10}$$

As we will see below, $c_f(x)$ is a weak function of downstream distance x, so up to a numerical factor $C_f(L) \approx c_f(L)$. To translate all the above equations to C_f we can therefore use this approximation with $\mathrm{Re}_x \approx \mathrm{Re}_L = UL/\nu$, where Re_L is the Reynolds number defined for full length of the plate surface.

In general, Eq. (9) can be readily solved numerically, but to get insights into its analytical solution we employ the method recently proposed in [36]. The method uses the definition of the Lambert-W function $W(\zeta)$, defined as [36, 37]

$$W(\zeta) + \ln W(\zeta) = \ln \zeta, \tag{11}$$

and then Eq. (9) is reduced to this form, assuming $C_f = c_f(L)$. The straightforward transformation (for details see [36]) leads to the following limit solutions,

$$C_f = \frac{\kappa^2}{2\,W^2(\zeta)}, \quad \zeta = (\kappa/\sqrt{2})\exp(\kappa B_1/\sqrt{2})\sqrt{Re_L} \approx 0.35\sqrt{Re_L}, \tag{12}$$

for a hydrodynamically smooth plate ($v_\tau h/\nu \ll 1$), and

$$C_f = \frac{2\kappa^2}{W^2(\zeta)}, \quad \zeta = (2/0.3)\kappa\exp(B_1\kappa\sqrt{2})(L/h) \approx 3.9L/h, \tag{13}$$

for the completely rough case ($v_\tau h/\nu \gg 1$) .

The properties of the Lambert-W function are well documented [37]; its leading term is approximately logarithmic, $W(\zeta) \approx \ln\zeta$, and this allows us to write the limiting solutions, Eqs. (12) and (13), in terms of elementary functions with $C_f \propto 1/\ln^2\zeta$. Although Eq. (9) is easily solved numerically, the following simple approximation for C_f is presented, which preserves the functional form of Eqs. (12) and (13) and smoothly interpolates these two limits. With additional data fitting constants (similar to the Colebrook equation [20]) the approximation is

$$C_f = \frac{1}{[1.350 - 1.43\ln(0.82h/L + 57.7/\mathrm{Re}_L)]^2}. \tag{14}$$

There are many more complex formulas relating C_f with roughness parameters such as the effective roughness height and morphology [18, 20, 33]) that could be integrated to improve the predictions of the model.

As discussed further in Sect. 3, we use the effective viscosity ν_e, given by Eqs. (4), (6), (7), and (14), to generate the effective shear modulus $\mu = \mu_r + i\mu_i$ for the water as an effective 'soft' medium, with $\mu_r \simeq \rho U^2$, $\mu_i \simeq 2\rho\omega\nu_e$. We then apply the theoretical framework proposed for a smooth surface [10] to estimate dependency of TBL noise on the roughness parameter h/L and elastic properties of the underlying surface.

In modelling of statistical properties of turbulent flow we follow the approach of [19, 38, 39]. The energy content of turbulent fluctuations in a TBL is given by a von Karman spectrum

$$E(k) = C_2(K/\kappa_e)(k/\kappa_e)^4[1 + (k/\kappa_e)^2]^{-17/6}, \tag{15}$$

where parameter κ_e represents the wavenumber associated with the energy-containing eddies, K is the kinetic energy of the turbulent flow, and $C_2 = 0.97$ [19]. In general, parameters K and κ_e should be derived from RANS calculations, but for the purpose of the current study we can use the scaling relations with the 'global' parameters of the TBL flow and assume $\kappa_e = 2\pi/0.55\delta$ and $K = 4.5v_\tau^2$ [40].

The fully defined energy spectrum $E(k)$ of Eq. (15) leads to parametrisation of the velocity correlation function

$$Q_{ij}(\mathbf{r}, \tau) = \langle v_i(\mathbf{x}, t)v_j(\mathbf{x} + \mathbf{r}, t + \tau)\rangle, \tag{16}$$

transformed to the wavenumber-frequency domain [38, 39]

$$Q_{ij}(\mathbf{k}, \omega) = \frac{E(k)}{4\pi k^2} R(\omega, k)[\delta_{ij} - k_i k_j/k^2], \tag{17}$$

where $R(\omega, k)$ is the Fourier transform of the dimensionless time correlation function $R(\tau, k)$. Function $R(\omega, k)$ is assumed to be a universal function of one dimensionless variable $\xi = \omega\tau_0$ [38, 39], where $\tau_0 = \tau_0(k)$ is the wavenumber-dependent correlation time of fluctuations in the turbulent flow. For the current study we use the stretched-exponential form

$$R(\omega, k) = \frac{1}{2\pi} \int_{-\infty}^{+\infty} \exp\left(-|\tau/\tau_0|^\varsigma - i\omega\tau\right)\, d\tau, \tag{18}$$

where $\varsigma = 2/3$ in agreement with the Kolmogorov scaling [34]. This integral can be evaluated in terms of conventional Levy distribution, but for the current study it was evaluated numerically. Two models for τ_0 were incorporated in Eq. (17), viz. $1/\tau_0 = K^{1/2}k$ and $1/\tau_0 = K^{1/2}(\kappa_e k^2)^{1/3}$ which corresponds to Eulerian and Lagrangian correlation time, respectively [38, 39]. A selection of a particular expression for τ_0 will slightly change the high frequency tail of the spectral density of TBL noise.

3 Viscous-Elastic Analogy

Our analysis is restricted to that of a slightly compressible fluid, i.e. flows for which Mach number $M = U/c_l$ is much less than unity, where c_l is the speed of sound and U is the velocity of unperturbed flow far from the the underlying surface. The surface

is assumed elastic with the speed of elastic waves in its material much greater than U.

The main step in the viscous-elastic analogy is to assume that the ensemble of random shear (vortex) waves, Eq. (1), propagates in a soft (rubber-like) medium (see Fig. 1). By considering the decoupled equation describing the vorticity perturbations in a fluid with constant flow velocity U, then linearizing, using harmonic solutions, and matching the wavenumber real and imaginary terms, it can be shown (see [10, 41, 42]) that the properties of this soft medium can be consistently mapped to the parameters of the turbulent flow in the TBL with the condition

$$\omega/k_s = c_s = U - i\nu k_s. \tag{19}$$

Here c_s is the phase velocity of the shear waves, k_s is their wavenumber, and ν is is the kinematic viscosity of the fluid. The effective longitudinal sound speed c_l for the fluid in flow is unaltered, with $c_l = c$. Equation 19 can also be expressed in terms of the effective shear modulus of the medium, $\mu = \mu_r + i\mu_i$, with $c_s = \sqrt{\mu/\rho}$ where ρ is the fluid density. Therefore $\mu_r \simeq \rho U^2$ and $\mu_i \simeq 2\rho\omega\nu$. In line with the assumptions of SNGR [4–6] the condition $c_s \approx U$ implies that the shear waves are 'convected' with the mean flow velocity. Note that Eq. (19) follows from the mathematics as described in [10], that $c_s \approx U$ is not an assumption, and that the imaginary term of c_s is included in this work for the shear–longitudinal conversion.

Next, conventional methods of elastic wave transformation can be applied to study the process of flow noise generation near the elastic boundary by considering the transformation of vorticity perturbations (shear waves) into sound waves (longitudinal waves) at the boundary. In this work, such transformation is expressed using potential or energy-based reflection coefficients for multilayered materials. Such coefficients quantitatively give the vortex–sound conversion efficiency at the underlying surface that takes into account elastic properties of both the fluid and the boundary (for more details see [10]). These coefficients can be used for absolute estimation of flow noise from a TBL over an elastic interface.

The starting point for this estimate is the full space-time correlation function $Q_{ij}(\mathbf{r}, \tau)$ of Eq. (16) for velocity within the flow near the surface, which has full spatial-temporal Fourier transform $Q_{ij}(\mathbf{k}, \omega)$ of Eq. (17). If $F_{\mathbf{v}}(\mathbf{k}, \omega)$ is the spatial-temporal Fourier transform of the velocity fluctuations $\mathbf{v}$, then

$$Q_{ij}(\mathbf{k}, \omega) = |F_{\mathbf{v}}(\mathbf{k}, \omega)|^2 \, d\mathbf{k}\, d\omega. \tag{20}$$

The correlation function $Q_{ij}(\mathbf{r}, \tau)$ at $\tau = 0$ is the conventional spatial correlation coefficient $B_{\mathbf{v}}(\mathbf{r})$ with assumed isotropic spatial Fourier transform $F(\mathbf{k}) = F(k)$, and $E(k) = 4\pi k^2 F(k)$. Note that $Q_{ij}(\mathbf{k}, \omega)$ of Eq. (20) is a spectrum and the mean 'energy' (m^2/s^2 here) per unit $\mathbf{k}$ and ω is $Q_{ij}(\mathbf{k}, \omega)\, d\mathbf{k}\, d\omega$.

We are interested in the correlation of the velocities normal to the displacement $\mathbf{r}$, rather than those parallel, for the wavevector $\mathbf{k}$ (see [35]). The normal and longitudinal transforms are comparable so we will not explicitly separate them here. Importantly, the normal transform relates to shear (vortex) motion, and is the important contributor

in the conversion to sound at the surface. This conversion is described by the general equation

$$|H(\mathbf{k},\omega)|^2 = |F_{\mathbf{v}}(\mathbf{k},\omega)\, V(\mathbf{k},\omega)|^2, \tag{21}$$

where $V(\mathbf{k},\omega)$ is the transfer function for reflection of the *velocity* field for a plane wave with wavevector $\mathbf{k}$ and frequency ω, and $H(\mathbf{k},\omega)$ is the full Fourier transform of the reflected compressional (sound) wave velocity components. From Eqs. (20) and (21), the final outgoing energy spectrum (in terms of velocity squared) is

$$G(\mathbf{k},\omega) = |H(\mathbf{k},\omega)|^2\, d\mathbf{k}\, d\omega, = Q_{ij}(\mathbf{k},\omega)\, |V(\mathbf{k},\omega)|^2, \tag{22}$$

where we have regarded Q_{ij} as a source term. In this work, the velocity reflection coefficients V are obtained directly from any velocity or displacement potential formulation of multilayer reflection.

The main quantity of interest for us is the acoustic power of the noise radiated by a TBL. By integrating $G(\mathbf{k},\omega)\, d\mathbf{k}$ of Eq. (22) over all radiating values of source $\mathbf{k}$, and multiplying by ρc_l to convert the reflected velocity amplitudes to radiated acoustic power, we obtain the frequency based spectral density of radiated power w, per unit area of surface, ignoring all edge-related effects. As shown by Eq. (19), $c_s \ll c_l$, so only those wavevectors very close to normal produce propagating sound components in reflection (Snell's law applied to reflection for interconversion from c_s to c_l). The relevant values of source wavevectors $\mathbf{k}$ sit within a narrow cone of solid angle which is cut-off at a critical angle θ_c defined by

$$\sin\theta_c = c_s/c_l \approx U/c_l, \tag{23}$$

where θ is measured from the normal to the surface. For $\theta > \theta_c$ the reflected sound components are evanescent and do not radiate. The integral is therefore taken over all $k = \|\mathbf{k}\|$, θ, and polar angle ϕ, giving the following expression for the spectral density of TBL noise

$$\frac{dw}{d\omega} = \frac{\rho U}{2} \int_0^{\pi/2} T(\theta,\omega) \sin\theta\, d\theta \int_0^{\infty} E(k) R(\omega,k)\, dk, \tag{24}$$

where $T(\theta,\omega)$ is a conventional energy based reflection coefficient for shear–longitudinal wave transformation. In the specific case of $c_s \ll c_l$ ($M \ll 1$ here) the connection between an energy based T and the corresponding potential amplitude reflection coefficient V is

$$T(\theta,\omega) = \begin{cases} (c_s/c_l)|V(\theta,\omega)|^2, & \theta \le \theta_c \\ 0, & \theta > \theta_c \end{cases} \tag{25}$$

where c_s and c_l are assumed real, which leads to the factor of $\rho c_s = \rho U$ rather than ρc_l in Eq. (24). Note that V has been written as a function of θ as it is independent

of both ϕ and $k = \|\mathbf{k}\|$, and that the evanescent non-zero values of V for $\theta > \theta_c$ are excluded as they do not radiate.

Methods for calculating T or V are given, for example, by Refs. [11, 43, 44]. In this work T has been computed for multi-layered materials using the theory of Lévesque and Piché [11], as in [10]. Explicit approximate analytical expressions can be derived in simple cases, such as those used to derive Eq. (2), but general multilayered materials are more easily addressed with a numerical approach.

4 Numerical Results

In this section we present some results obtained by applying the proposed analytical framework. All data in Figs. 2–4 correspond to a TBL in water. The downstream distance is assumed $L = 50$ m, with flow velocity $U = 6$ m/s or $U = 12$ m/s. For illustrative purposes, Fig. 2 shows the spectrum of turbulent fluctuations in the TBL given by Eq. (15). This spectrum is used later in the correlation function, Eq. (17), and the radiated power calculation of Eq. (24). The important point is that in the model this spectrum is also affected by roughness (via drag coefficient, c_f). For $L = 50$ m, $U = 12$ m/s, the TBL thickness is about $\delta \approx 0.3$ m.

Next, we estimate the effect of underlying surface roughness on the shear-to-sound conversion efficiency represented by T of Eq. (25) for bare steel, 20 mm thick, backed by air. The results of these calculations are summarised in Fig. 3, spanning over four decades of non-dimensional frequency $\omega h/U$. The plot depicts the *change* in the θ-averaged value of T compared with T_s for a smooth surface of the same material, relative to the smooth-surface, expressed in dB (not the ratio of the rough surface T relative to the smooth surface T_s). This is simply a decibel measure of the increase in the efficiency of conversion induced by the roughness when referenced to the smooth surface. Zero dB therefore corresponds to an increase equal to that from the smooth

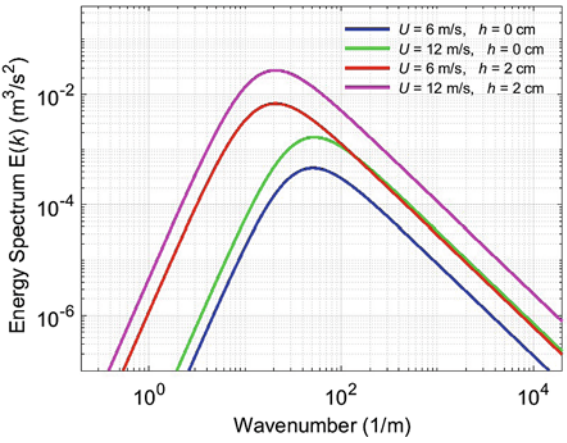

Fig. 2 Plot of the turbulence energy spectrum $E(k)$ for different parameters of a TBL over a rough surface in water, with $L = 50$ m (Colour online)

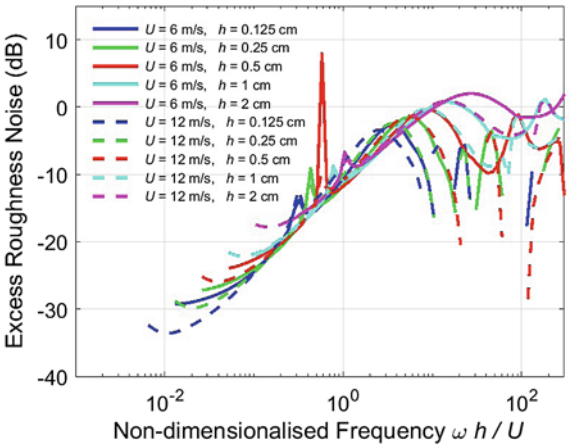

Fig. 3 The average increase in T of Eq. (25) (in comparison with smooth surface T_s) for a TBL over a steel surface in water, backed by air, where h is the effective roughness height (Colour online)

surface, and $-\infty$ dB to no change at all. Note that radiated power itself depends on both T, E and R in Eq. (24).

The results follow a general trend with some fine (and often non-monotonic) deviations. The general slope is an increase of approximately 10–15 dB per decade of frequency. A number of visible peaks are the result of resonances with the elastic structure of the underlying surface materials. These resonances are relatively small on a power plot but appear much larger when compared as differences from the reference, $h = 0$, case. They are difficult to explain in detail as they are produced by numerical simulation of multilayered materials, but some observations can be made. In particular, the peaks near $\omega h/U \approx 1$ come from change in the imaginary term of c_s with the roughening of the surface, and scale with frequency as the inverse of the square-root of the steel thickness, indicating bending wave effects. In contrast, the broad dips at higher frequencies scale as the inverse of the thickness, suggesting simple thickness interferences. Note also that this method of presenting data assumes that T increases with roughness. Conversely, decreases are negative and cannot be displayed on such a logarithmic plot. Apparent missing data on the plot is where some local decreases have occurred.

Finally, to demonstrate the capability of the method, we present in Fig. 4 examples of the *absolute* estimation of the spectral density of TBL noise from air-backed bare steel and rubber-coated steel with rough surfaces using Eq. (24). The steel is 20 mm thick and the generic rubber is 6 cm thick. The four curves correspond to flow velocity $U = 12$ m/s with two roughness heights. The Lagrangian correlation time given by $1/\tau_0 = K^{1/2}(k_e k^2)^{1/3}$ is used in these calculations. The Eulerian correlation time leads to similar results (not shown here).

The results presented above illustrate of the capability of the method. More extensive numerical data sets will be reported in further work.

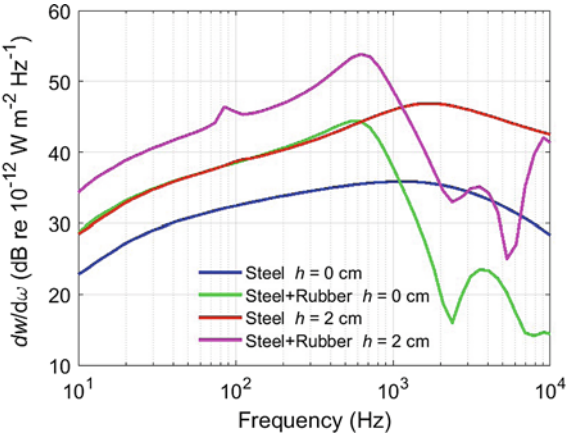

Fig. 4 The spectrum of TBL noise for the case of a steel surface with or without a rubber coating of 6 cm, backed by air, where h is the effective roughness height (Colour online)

5 Concluding Remarks

We have presented an analytical framework that allows estimations of flow noise generated by a TBL over an elastic (or impedance) surface that includes interface roughness. To illustrate the capability of our method we provided some quantitative estimation of the effect of elastic properties of an underlying surface and its roughness on the TBL noise. An improvement of the accuracy of the predictions can be achieved by refining the numerical constant in Eqs. (8) and (15). Our method is restricted to substantially subsonic flows and to materials with speed of elastic waves much greater than the velocity of the TBL flow. Under these conditions the proposed method is not specific to the simplest case of a TBL over a flat surface and can be extended to other flow conditions that include external pressure gradients, underlying surface curvature and change in materials properties of the fluid (such as polymer solutions [45]) and surfaces (such as hydrophobic coatings [46]). More rigorous validation of the proposed analytical framework including more specific estimation of the range of its validity will be reported in further publications.

References

1. W.K. Blake, *Mechanics of Flow-Induced Sound and Vibration*, 2nd edn. (Academic Press, 2017)
2. S.A.L. Glegg, W.J. Devenport, *Aeroacoustics of Low Mach Number Flows* (Academic Press, Oxford, 2017)
3. R.H. Kraichnan, Diffusion by a random velocity field. Phys. Fluids **13**(1), 22–31 (1970)
4. P. di Francescantonio, P. Ferrante, T. Deconinck, and C. Hirsch, "Assessment of SNGR method for robust and efficient simulations of flow generated noise," in *Proc. 19th AIAA/CEAS Aeroacoust. Conf., May 27-29, Berlin, Germany*, pp. 1–13, 2013

5. M. Dieste, G. Gabard, Random particle methods applied to broadband fan interaction noise. J Computat. Phys. **231**(24), 8133–8151 (2012)
6. M. Mesbah, J. Meyers, M. Baelmans, and W. Desmet, "Assessment of different parameters used in the SNGR method," in *Proc. ISMA (Int. Conf. Noise Vib. Eng.)*, pp. 389–402, 2004
7. W. Béchara, C. Bailly, P. Lafon, S.M. Candel, Stochastic approach to noise modeling for free turbulent flows. AIAA J. **32**(3), 455–463 (1994)
8. C. Bailly and D. Juvé, "A stochastic approach to compute subsonic noise using linearized Euler's equations," *AIAA Pap.*, no. 99-1872, 1999
9. M. Billson, M.-E. Eriksson, and L. Davidson, "Jet noise prediction using stochastic turbulence modeling," *AIAA Pap.*, no. 2003-3282, 2003
10. I. MacGillivray, A. Skvortsov, and P. Dylejko, "Flow noise estimation with the vibroelastic analogy: effect of material properties," in *FLINOVIA—Flow Induced Noise and Vibration Issues and Aspects–II* (E. Ciappi, S. D. Rosa, F. Franco, J.-L. Guyander, S. Hambric, R. C. K. Leung, and A. D. Hanford, eds.), pp. 289–305, Springer, 2018
11. D. Lévesque, L. Piché, A robust transfer matrix formulation for the ultrasonic response of multilayered absorbing media. J. Acoust. Soc. Am. **92**(1), 452–467 (1992)
12. W.W. Devenport, D. Grissom, N. Alexander, B. Smith, S. Glegg, Measurements of roughness noise. J. Sound Vib. **330**, 4250 (2011)
13. W. K. Blake and J. M. Anderson, "The acoustics of flow over rough elastic surfaces," in *FLINOVIA—Flow Induced Noise and Vibration Issues and Aspects–I* (E. Ciappi, S. D. Rosa, F. Franco, J.-L. Guyander, and S. Hambric, eds.), Springer, 2014
14. P. R. Donavan and W. K. Blake, "Measurement, prediction, and reduction of high-frequency aerodynamic noise generated and radiated from surfaces of various textures," in *FLINOVIA—Flow Induced Noise and Vibration Issues and Aspects–II* (E. Ciappi, S. D. Rosa, F. Franco, J.-L. Guyander, S. Hambric, R. C. K. Leung, and A. D. Hanford, eds.), pp. 147–154, Springer, 2019
15. J. Abshagen, D. Küter, and V. Nejedl, "Turbulent flow noise generation under sea conditions," in *FLINOVIA—Flow Induced Noise and Vibration Issues and Aspects–II* (E. Ciappi, S. D. Rosa, F. Franco, J.-L. Guyander, S. Hambric, R. C. K. Leung, and A. D. Hanford, eds.), pp. 325–338, Springer, 2019
16. T. Galib, R. Katz, S. Ko, B. Sandman, Measurements of turbulent pressure fluctuations using a buoyant vehicle coated with a thin elastomer layer. J. Acoust. Soc. Am. **96**(6), 3800–3803 (1994)
17. S.A.L. Glegg, W.J. Devenport, The far-field sound from rough-wall boundary layers. Proc. R. Soc. A **465**, 1717–1734 (2009)
18. Y. Liu, A. P. Dowling, and H.-C. Shin, "Effects of surface roughness on airframe noise," in *Proc. 12th AIAA/CEAS Aeroacoust. Conf.*, p. 2510, AIAA, 2006
19. P.D. Lysak, T.A. Brungart, Velocity spectrum model for turbulence ingestion noise from computational-fluid-dynamics calculations. AIAA J. **41**(9), 1827 (2003)
20. H. Schlichting, ed., *Boundary-Layer Theory*. McGraw-Hill Series, 1968
21. J. J. Allen, M. A. Shockling, G. J. Kunkel, and A. J. Smits, "Turbulent flow in smooth and rough pipes," *Philos. Trans. R. Soc. London, Ser. A*, vol. 365, no. 1852, pp. 699–714, 2007
22. K. Bhaganagar, J. Kim, G. Coleman, Effect of roughness on wall bounded turbulence. Flow Turbul. Combust. **72**, 463–492 (2004)
23. S.E. Belcher, N. Jerram, J.C.R. Hunt, Adjustment of a turbulent boundary layer to a canopy of roughness elements. J. Fluid Mech. **488**, 369–398 (2003)
24. R.J. Lowe, J.R. Koseff, S.G. Monismith, Oscillatory flow through submerged canopies: 1. velocity structure. J. Geophys. Res. **110**(C10016), 452–467 (2005)
25. D. Chung, L. Chan, M. MacDonald, N. Hutchins, A. Ooi, A fast direct numerical simulation method for characterising hydraulic roughness. J. Fluid Mech. **773**, 418–431 (2015)
26. K.A. Flack, M.P. Schultz, J.M. Barros, Y.C. Kim, Skin-friction behavior in the transitionally-rough regime. Int. J. Heat Fluid Flow **61**, 21–30 (2016)
27. I. Marusic, R. Mathis, N. Hutchins, Predictive model for wall-bounded turbulent flow. J. Acoust. Soc. Am. **329**(5988), 193–196 (2010)

28. S. Khan and B. Jayaraman, "Statistical structure and deviations from equilibrium in wavy channel turbulence," *Fluids*, vol. 4, no. 161, 2019
29. M. Hultmark, M. Vallikivi, S.C.C. Bailey, A.J. Smits, Logarithmic scaling of turbulence in smooth and rough wall pipe flow. J. Fluid Mech. **728**, 376–395 (2013)
30. Y. Wang, K. Zhao, X.-Y. Lu, Y.-B. Song, and G. J. Bennett, "Bio-inspired aerodynamic noise control: A bibliographic review," *Appl. Sci.*, vol. 9, no. 2224, 2019
31. C.F. Colebrook, Turbulent flow in pipes with particular reference to the transition region between the smooth and rough pipe laws. J. Inst. Civ. Eng. **I1**, 133–156 (1939)
32. C.F. Colebrook, T. Blench, H. Chatley, E. Essex, J. Finniecome, G. Lacey, J. Williamson, G. Macdonald, Correspondence. turbulent flow in pipes, with particular reference to the transition region between the smooth and rough pipe laws (includes plates). J. Inst. Civ. Eng. **12**(8), 393–422 (1939)
33. K. A. Flack and M. P. Schultz, "Roughness effects on wall-bounded turbulent flows," *Phys. Fluids*, vol. 26, no. 101305, 2014
34. L. Landau, E. Lifshitz, *Fluid Mechanics* (Elsevier, 1987)
35. A.S. Monin, A.M. Yaglom, *Statistical Fluid Mechanics* (Dover Publications, New York, 2007)
36. C.T. Goudar, J.R. Sonnad, Explicit friction factor correlation for turbulent flow in smooth pipes. Ind. Eng. Chem. Res. **42**, 2878–2880 (2003)
37. P. Rollmann, K. Spindler, Explicit representation of the implicit colebrook-white equation. Case Stud. Therm. Eng. **5**, 41–47 (2015)
38. R. Rubinstein, Y. Zhou, Turbulent time correlations and generation of acoustic waves by stellar or solar turbulent convection. Astrophys. J. **572**, 674–678 (2002)
39. R. Rubinstein and Y. Zhou, "Characterization of sound radiation by unresolved scales of motion in computational aeroacoustics," Tech. Rep. CR-1999-209688, NASA, 1999
40. S.B. Pope, *Turbulent Flows* (Cambridge University Press, 2000)
41. I. MacGillivray and A. Skvortsov, "Estimation of pressure pluctuations in a turbulent boundary layer based on vibro-elastic models," in *Proc. 43rd Int. Congress on Noise Control Eng. (INTERNOISE2014)*, pp. —, Nov. 2014
42. K. Naugolnykh, S. Rybak, Sound radiation from a turbulent boundary layer. Sov. Phys. Acoust. **26**(6), 502–504 (1980)
43. L. Brekhovskikh, *Waves In Layered Media* (Academic Press, New York, 1980)
44. P. Cervenka, P. Challande, A new efficient algorithm to compute the exact reflection and transmission factors for plane waves in layered absorbing media (liquids and solids). J. Acoust. Soc. Am. **89**(4), 1579–1589 (1991)
45. B. R. Elbing, M. Perlin, D. R. Dowling, and S. L. Ceccio, "Modification of the mean near-wall velocity profile of a high-reynolds number turbulent boundary layer with the injection of drag-reducing polymer solutions," *Phys. Fluids*, vol. 25, no. 085103, 2013
46. K. B. Golovin, J. W. Gose, M. Perlin, S. L. Ceccio, and A. Tuteja, "Bioinspired surfaces for turbulent drag reduction," *Philos. Trans. R. Soc. London, Ser. A*, vol. 374, no. 20160189, 2016

Numerical Methods for Vibration and Noise

Numerical Predictions of the Vibro-Acoustic Transmission Through the Side Window Subjected to Aerodynamics Loads

Dimitri Binet and François Van Herpe

Abstract The acoustic comfort level in modern car design mainly depends on the aerodynamic noise generated at high speed. This noise is characterized by a mid- and high- frequency spectrum and mainly radiates inside the passenger cabin through the different car glass surfaces. Predicting such noise can be done by coupling a Computational Fluid Dynamics (CFD) code solving the compressible turbulent flow with a vibro-acoustic simulation software. The simulation of the flow around the vehicle gives access to the wall pressure applied on the car glass surfaces, while the vibro-acoustic model takes this aerodynamic loading as excitation to predict the internal noise. In this paper, the vibro-acoustic frequency response of an existing Finite Element (FE) model is extended using a Statistical Energy Analysis (SEA) approach called Virtual SEA. In this approach, that simulates an experimental SEA process, the necessary information required to build the SEA matrix are extracted from the FE models. The evaluation of the injected power corresponding to the wall pressure field, which excites the Virtual SEA model, relies on the decomposition of the glass surfaces wall pressure into a turbulent and an acoustic contribution. Finally, the efficiency of the proposed methodology is demonstrated on an industrial car model, where numerical acoustic responses predicted by the Actran software are compared to experimental data measured in wind tunnel over a large frequency range.

D. Binet (✉)
Free Field Technologies, part of Hexagon, 4 rue du Professeur Pierre Vellas – Immeuble Jupiter – B10, 31300 Toulouse, France
e-mail: dimitri.binet@fft.be

F. V. Herpe
PSA, Centre Technique de Vélizy a Route de Gisy – Innovel Parc Sud, 78943 Velizy Villacoublay Cedex, France
e-mail: francois.vanherpe1@mpsa.com

E. Ciappi et al. (eds.), *Flinovia—Flow Induced Noise and Vibration Issues and Aspects-III*, https://doi.org/10.1007/978-3-030-64807-7_14

1 Introduction

Silence inside vehicles is an important issue for car manufacturers. For the acoustic comfort of the passengers, but also to facilitate intelligibility of voice commands and messages from human-machine interfaces that are developing to help the driver.

The three main sources of perceived noise in the passenger compartment are the engine, the rolling noise (contact between road and tyre) and aerodynamic noise. In this paper we focus on the last point.

The aerodynamic noise is generated by the turbulent air flow surrounding the vehicle. With conventional heat engine, it becomes predominant when travelling on motorways or peri-urban from 80 km/h and for frequencies greater than 400 Hz. On the other hand, new and quieter hybrid and electrical engines increase the risk of noise at low speed and low frequency as aerodynamic noise is not masked anymore.

However, the development of aero-acoustic design of vehicles is still often based on very expensive wind tunnel test. These tests require a lot of prototypes and can therefore only take place at the end of the process, where a new design solution can generate critical situations. For these reasons, PSA Group wishes to improve its noise computation system for the aero-dynamic noise in order to consider it earlier in the development process, during the design phase, and in order to decrease the number of wind tunnel tests.

The main path for the aero-dynamic noise is the vibro-acoustic transmission through the window subjected to aerodynamic loads. These phenomena can be estimated by coupling a Computational Fluid Dynamics (CFD) [1, 2] software which assesses the aerodynamic loads and a vibro-acoustic software (VA) which computes the sound pressure level radiated by the windows into the car.

At high frequencies, it is possible to use the Statistical Energy Analysis (SEA) [3]. In this paper we present the Virtual SEA approach based on the Finite Element (FE) model classically used in low and middle frequencies (0–4000 Hz). A feasibility study has been performed in 2011 and 2018 based only on the Finite Element modelling [1, 4].

Aerodynamic sources are computed by Power FLOW software. The Sound Pressure Level (SPL) at the driver's ear is computed by the Virtual SEA methodology thanks to Actran software and the numerical results are compared to the wind tunnel test.

2 Flow Simulation

The flow surrounding the car is computed based on the Lattice-Boltzmann (LBM) methods [1, 2, 4]. They are an alternative to the classical CFD methods, based on microscopic and mesoscopic kinematics equations contrary to the traditional macroscopic Navier Stokes equations. The flow simulation is the result of a simulation comprised of transient and steady phases to capture the pressure fluctuations of the acoustic component.

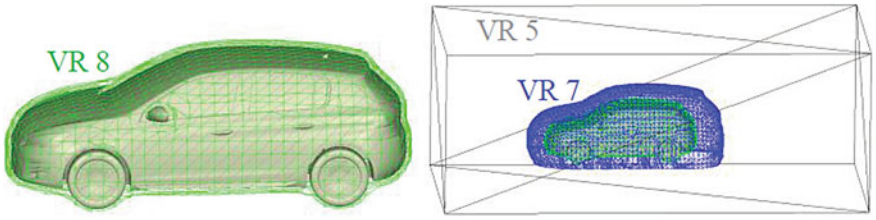

Fig. 1 Variables resolution area

Fig. 2 Maximal resolution areas

2.1 Mesh

The flow mesh is built around the exterior skin of the vehicle which is considered as a rigid wall. The mesh is composed of cubic elements (voxels) and surface elements (surfels) which are generated at the interface between the rigid body and the fluid flow. It is divided into different regions of variable resolution (VR). The size of the edge of a cubic element in a VR is twice of the next VR. For example, voxels size in the region 7 is equal to 8 mm, then 4 mm in the region 8, 2 mm in the region 9 etc. We used 11 variable resolution areas and the element size in the highest resolution area (VR11) is equal to 0.5 mm on the wing mirror and window pillar (Fig. 1).

Once the VR are defined, the mesh is automatically generated. In the case of the 308-model studied here the size of the fluid mesh is 225 million voxels and 17 million surfels (Fig. 2).

2.2 Results

To use the results of the flow simulation for a vibro-acoustic response, the Mach number is set as "same as experiments" in the numerical set-up [2]. It means that the flow speed (140 km/h) compared to the sound speed (343 m/s) is directly similar to the wind tunnel test. Two simulations are performed, with and without yaw angle (10°) (Fig. 3).

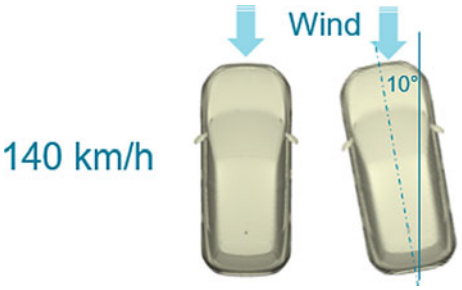

Fig. 3 Yaw angle

The turbulent wall pressure fluctuations are stored on the windshield and the front side windows with a space resolution equal to 1 mm (Fig. 4 and Table 1).

In order to use this data with Actran, results are stored in binary files under Ensight-gold format. There is one file per time step and for each window (leading to 14 627 files for each window at yaw angle 0° and 10 576 files for each window at yaw angle 10°). These spatio-temporal distributions of pressure will be used as the excitation in the Virtual SEA model.

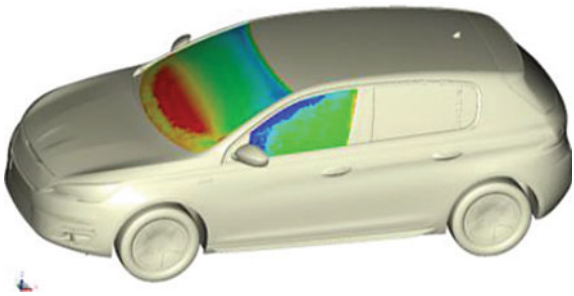

Fig. 4 Aerodynamic load—Turbulent wall pressure fluctuation

Table 1 Store data

Yaw angle	0°	10°
Number of time step	14 627	10 576
RAM Memory (Go)	131	99
Simulation time (s)	0.627	0.453
CPU Time (h)	61 539	49 680
Time step Δt (s)	4.28636×10^{-5}	
F_e (Hz)	23 329.8	

3 Vibro-Acoustic Computation

3.1 Theory

In this section the Statistical Energy Analysis is described along with the Virtual SEA and SmEdA approaches that are used to obtain the SEA model parameters, i.e. the coupling loss and damping loss factors. In the same time a new technology is used based on the pellicular modes.

3.1.1 Statistical Energy Analysis

Statistical Energy Analysis is an energy-based approach to assess the vibro-acoustic behavior of complex structures in the mid- and high frequency domain. It was first introduced in the 1960s by Lyon and Maidanik [5] and Smith [6]. The first step of the analysis is to decompose the complete system into a set of coupled subsystems that fulfill the SEA weak coupling condition, meaning the dissipated power of each subsystem is higher than the powers exchanged with others. Furthermore, the subsystems must have homogenous vibrational energy density and sufficient modal overlap. Then, the spatially and frequency band averaged energy of the subsystems can be estimated, and the power balance equation of each subsystem is written as: [3]

$$P_{in}^{i} = P_{diss}^{i} + \sum_{i \neq j} P_{c}^{i,j}. \tag{1}$$

The sum of the dissipated power P_{diss}^{i} in a subsystem and the exchanged powers with others $P_{c}^{i,j}$ is equal to the power injected by external loads to that subsystem, P_{in}^{i}. The dissipated power is given by

$$P_{diss}^{i} = \eta_i \omega E_i, \tag{2}$$

where η_i is the damping loss factor, ω is the center frequency of the considered frequency band and E_i is the subsystem energy. The power exchanged is assumed to be

$$P_{c}^{i,j} = \omega\left(\eta_{ij} E_i - \eta_{ji} E_j\right), \tag{3}$$

where η_{ij} and η_{ji} are the coupling loss factors. According to SEA theory, the reciprocity relation is given by

$$n_i \eta_{ij} = n_j \eta_{ji}, \tag{4}$$

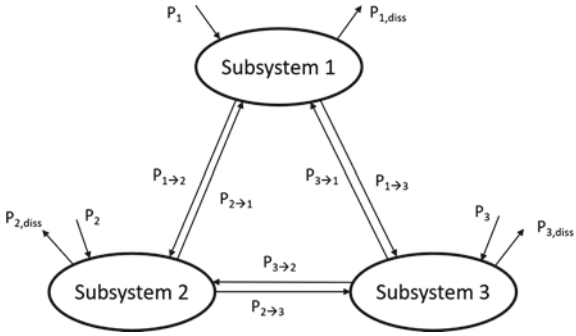

Fig. 5 Power balance of a 3-subsystem SEA model

in which n_i and n_j are the modal densities of the subsystems. Invoking the coupling power proportionality assumption that implies the coupling between any two subsystems is independent of the presence of other subsystems, the power balance equation for a general case can be written as [7]

$$P_{in}^{i} = \eta_i \omega E_i + \sum_{i \neq j} \omega\left(\eta_{ij} E_i - \eta_{ji} E_j\right), \tag{5}$$

or in matrix form

$$\boldsymbol{P} = \omega \boldsymbol{\eta} \boldsymbol{E}. \tag{6}$$

The most challenging part of the analysis is to obtain the coupling matrix containing the SEA model parameters. There are several methodologies in the literature for this purpose such as analytical SEA [8, 9], experimental SEA using the Power Injection Method (PIM) [10, 11] and Statistical modal Energy distribution Analysis (SmEdA). The last two are used by the Virtual SEA approach.

According to the SEA equation, the number of degrees of freedom is equal to the number of subsystems and independent from wavelength which allows affordable solution at high frequencies. Regarding output quantities, the energy content of subsystems is more suitable in the mid- and high frequency range than local responses. Figure 5 represents a simple SEA power balance model containing 3 subsystems as an example [12].

3.1.2 Virtual SEA

Virtual SEA performs the Power Injection Method (PIM) virtually in order to obtain the SEA model parameters (coupling loss and damping loss factors). It was first introduced by Gagliardini et al. [13] to use finite element computations to build an energy distribution model for the PIM. The energy distribution model is based on the eigenmodes, mass, and stiffness matrices of the model that can be obtained through

the eigen mode calculation. The PIM is then performed. Each subsystem is individually excited with uncorrelated random excitation, while the energetic response of all subsystem is stored. The following system of equations is obtained

$$\begin{bmatrix} P_{in}^1 & \cdots & 0 \\ \vdots & \ddots & \vdots \\ 0 & \cdots & P_{in}^i \end{bmatrix} = \omega\eta \begin{bmatrix} E_1^1 & \cdots & E_1^i \\ \vdots & \ddots & \vdots \\ E_i^1 & \cdots & E_i^i \end{bmatrix}. \tag{7}$$

The coupling matrix can be obtained by a simple matrix inversion and should approximate the SEA assumptions such as the reciprocity relation and the coupling power proportionality assumption as closely as possible. Once the SEA parameters are available, it allows to investigate the same model with different boundary conditions at low computational cost. Various types of loads can be applied as they are converted into injected powers according to Eq. 8, where F is the amplitude of the excitation force and Y is the mobility of the excited subsystem

$$P_{in} = \frac{1}{2}|F|^2 Re(Y). \tag{8}$$

3.1.3 SmEdA

The virtually performed PIM in Virtual SEA only provides coupling loss factors between subsystems that belong to the same physical object, either structure or fluid. The coupling between different physical objects is calculated by SmEdA introduced by Maxit et al. [14, 15]. In their work, Maxit et al. set out to describe the energy exchange between two subsystems, without the limitation of the energy equipartition assumption for the subsystem modes, that applies in classic SEA. The Coupling Loss Factor derived based on their model, depends on the interaction modal works of pairs of modes that belong to the two subsystems. Assuming the pth stress mode shape σ_p of the uncoupled-blocked fluid subsystems 1 and the qth displacement mode shape $\mathcal{W}_p$ of the uncoupled-free structure subsystem 2, the interaction modal work of this pair of modes is given by

$$\mathcal{W}_{pq} = \int_s \mathcal{W}_p \sigma_p n dS. \tag{9}$$

Herein, S is the surface between the two subsystems and n denotes the unit vector normal to it. Then, the expression for the CLF between the fluid and structure subsystems takes into account the interaction modal work terms of all the mode pairs that are resonant in the frequency range of interest according to Eq. (10).

$$\eta_{ij} = \frac{1}{N_i \omega_c} \sum_{p=1}^{N_i} \sum_{q=1}^{N_j} \left[\frac{\left(\mathcal{W}_{pq}\right)^2}{\omega_p^2 M_p M_q} \left(\frac{\Delta_p \omega_q^2 + \Delta_q \omega_p^2}{\left(\omega_p^2 - \omega_q^2\right)^2 + \left(\Delta_p + \Delta_q\right)\left(\Delta_p \omega_q^2 + \Delta_q \omega_p^2\right)} \right) \right], \tag{10}$$

where $\mathcal{W}_{pq}$ is the modal work of the pth and qth resonant mode pairs, N_i and N_j are the number of resonant modes in the frequency band with the center frequency ω_c, ω_p and ω_q are the natural frequencies, Δ_p and Δ_q are the modal damping bandwidths, M_p and M_q represent the modal mass of mode p and q.

3.1.4 Pellicular Modes

The pellicular modes [4, 16] correspond to a generalization of the mode concept on an arbitrary non-planar surface. For a rectangular planar section, they would correspond to classical sine and cosine functions. The same properties as the orthogonality are still valid. The pellicular modes provide a complete set of basis to decompose any signal available on this surface. Specifically, let us consider a surface Ω delimited by the contour $\partial\Omega$. The surface can be non-planar and the curvilinear orthonormal coordinates ξ_j define the position on this surface. The pellicular modes are defined by the two following conditions (11)

$$\begin{aligned} -\lambda_i^2 \phi^{\lambda_i} - c^2 \frac{\partial^2 \phi^{\lambda_i}}{\partial \xi_j \partial \xi_j} &= 0 \ \text{ in } \ \Omega, \\ \frac{\partial \phi^{\lambda_i}}{\partial \xi_j} n_j &= 0 \text{ in } \partial\Omega. \end{aligned} \tag{11}$$

The pellicular modes $\phi^{\lambda_i}\left(\underset{\xi}{\rightarrow}\right)$ are orthogonal on the surface. Equation (11) shows that given mode $\phi^{\lambda_i}\left(\underset{\xi}{\rightarrow}\right)$ corresponds to the natural acoustic mode for a frequency $\omega = \lambda_i$. The different pellicular modes are classified by increasing values of associated eigenvalues $\lambda_i : \lambda_i < \lambda_{i+1}$. For each frequency, the pressure field acting on the window will be decomposed in a basis of pellicular modes.

3.2 Studied Case Description

The studied case is based on a Peugeot 308 finite element model. In this model, the windshield, the front windows and the interior cavity are considered. The aerodynamic load is provided by CFD computation gives the turbulent wall pressure fluctuations on the windows. The vibro-acoustic response gives the SPL inside the car up to 10 kHz (Fig. 6).

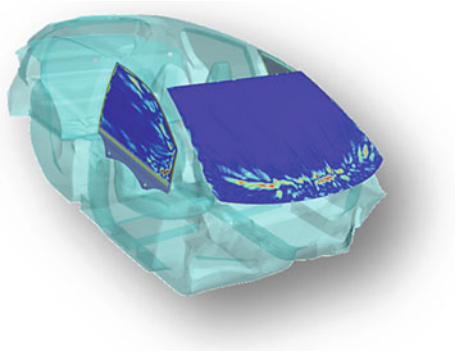

Fig. 6 Peugeot 308 FE model with aerodynamic load on the windows

3.3 FE Model

The vibro-acoustic model is divided in three parts, the interior cavity, the front side windows and the windshield. The inner cavity is meshed with a mesh size of 42.5 mm to respect the criteria of 4 quadratic elements per acoustic wavelength up to 2000 Hz. A vibro-acoustic coupling is realized with the windows and the windshield. The free faces of the cavity are considered as rigid if not coupled with the structure (Fig. 7).

Damping in the cavity is modelled thanks to reverberation time measurement T_R inside the passenger compartment with a complex sound speed (12)

$$c = c_0(1 + i\eta) \quad \text{with} \quad = \frac{13.8}{\omega T_R}. \tag{12}$$

The structure, in other words side windows and windshield, are meshed to respect 4 quadratic elements per bending wavelength up to 10 kHz. Thus, the mesh size is equal to 10 mm for the side windows and 8 mm for the windshield (Fig. 8).

Damping in the structure is modelled thanks to the Power Injection Method in measurement. The boundary condition of the structure is considered as clamped (Table 2).

As the number of modes becomes prohibitive after 2 kHz for the cavity (more than 100 000 modes to reach 10 kHz) pellicular modes are used to represent the cavity.

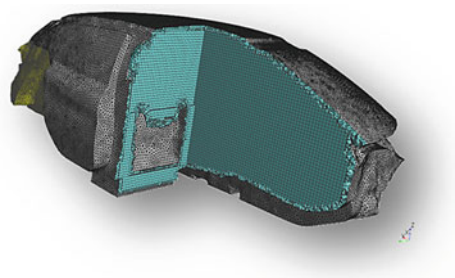

Fig. 7 Cavity mesh

Fig. 8 Structure mesh

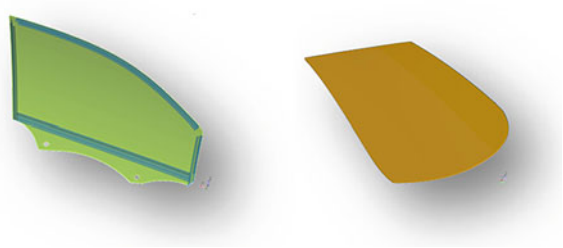

Table 2 FE model summary

Name		Number of nodes per part	Modal extraction
Cavity		1 173 123	2 kHz → 4 527 modes
Window left		33 183	10 kHz → 276 modes
Window right		33 183	10 kHz → 276 modes
Windshield	Upper glass	137 679	10 kHz → 1 212 modes
	PVB	137 679	
	Lower glass	137 679	

3.4 Computation Performance

Table 3 compares the computation time and the RAM consumption for each step. For aerodynamic loads, results are obtained in 18h45 min for the Direct Frequency Response (DFR) to reach 4 kHz whereas results are obtained in around 9 h with the Virtual SEA to reach 10 kHz.

Table 3 Computation time

Methodology	RAM	DMP/SMP	Computation time	Frequency
DFR	151 Gb	1/20	18 h 45 min	20 Hz–4 kHz
Modal extraction cavity	–	4/6	6 h 35 min	Up to 2 kHz
Modal extraction window side left	–	1/6	2 min	Up to 10 kHz
Modal extraction window side right	–	1/6	2 min	Up to 10 kHz
Modal extraction windshield	–	1/6	18 min	Up to 10 kHz
Virtual SEA	275 Gb	1/44	2 h 25 min	500 Hz–10 kHz

Fig. 9 Vehicle in the wind tunnel fitted with sleeve

4 Wind Tunnel Test

Tests have been performed at S2A aerodynamic and aero-acoustic wind tunnel. As the air flow between the ground and the chassis has a significant contribution for the aerodynamic load inside the vehicle cabin in low and middle frequencies but its radiation is not considered in the numerical modelling, the test vehicle is fitted with sleeve to block the air flow under the car.

Interface between the chassis and the openers, between the windows and the openers and between the windows and the chassis are taped to prevent leakage and thus only the windows contribution is measured. The SPL is evaluated in the vehicle at the passenger's ear using an acoustical head (Fig. 9).

5 Simulation and Test Comparisons

Figure 10 compares the SPL between the wind tunnel and Actran in third octave band at the driver's ears. The aerodynamics noise is generally perceived from 400 Hz thus the comparison is made between 500 Hz and 10 kHz.

Numerical results are really similar to the wind tunnel test. The slope around 7.5 dB/octave is well caught by the simulation up to 2500 Hz. Below 2500 Hz and for the yaw angle 0° a discrepancy about 2 dB occurs between the numerical prediction and measurements in S2A wind tunnel. For the yaw angle 10° the discrepancy is more significant around 4 dB due to the injected power. Indeed, for this configuration the injected power at low frequency is not correctly computed at the time this paper is being written (indeed the injected power is underestimated from the CFD probably due to the interpolation technique). At 3150 Hz a peak is observed in the wind tunnel test instead of 2500 Hz in the simulation. This difference of resonance frequency, side windows, is explained by the boundary condition in the simulation (perfectly

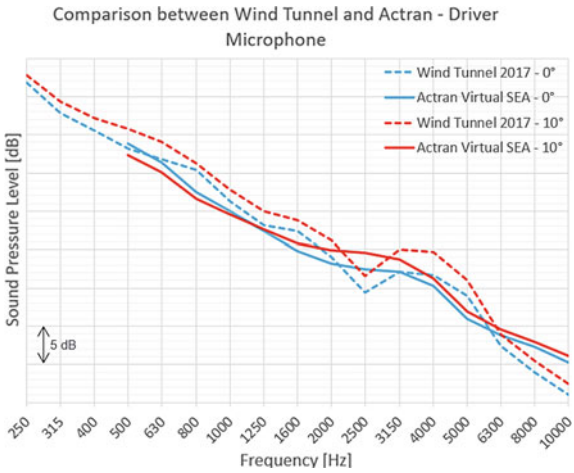

Fig. 10 SPL computed by Actran and measured at S2A for yaw angle 0° and 10°

clamped). After 3150 Hz, a discrepancy between the test and the simulation is around 4 dB.

The yaw angle effect, difference between the yaw angle 10° and 0°, is similar between the wind tunnel test and the simulation around 1–2 dB above 1250 Hz.

The discrepancies between the test and the simulation can be explained in part by the simplification of modelling, damping in the cavity and boundary conditions for the structure. Moreover, the FE model was scaled before being used. Nevertheless, the good correlation between tests and simulation has been demonstrated, hence showing the relevance of using simulation in the pre-design phase.

6 Conclusions

This paper shows a numerical methodology for the prediction of the windows contribution in the aerodynamic noise in the passenger compartment up to 10 kHz. In a first part, the turbulent flow surrounding the vehicle is simulated using CFD solution based on the Lattice-Boltzmann methodology. This steady computation catches the acoustic and turbulent components of pressure. The turbulent wall pressure fluctuations are the aerodynamic excitation in the vibro-acoustic Finite Element model.

The Virtual SEA method is based on the modal extraction of the Finite Element model for the cavity and the structure. Once the eigen values and mode shapes are computed, the Coupling Loss Factors and Damping Loss Factors are computed by Actran and thus the SPL inside the passenger compartment. At high frequencies, when the number of modes extraction becomes prohibitive a new technique is used called pellicular modes.

This numerical methodology was applied on Peugeot 308 and the results were compared to the wind tunnel test.

The correlation between simulation and test demonstrated that this methodology is relevant to evaluate the SPL inside the vehicle cabin. The remaining discrepancies can be explained by the modelling simplification, damping in the cavity and boundary conditions for the structure.

References

1. F. Van Herpe, D. d'Udekem, J. Jacqmot, R. Kouzaiha, Vibro-acoustic simulation of side windows and windshield excited by realistic CFD turbulent flows including car cavity, in *7th International Styrian Noise, Vibration & Harshness Congress* (2012). https://doi.org/10.4271/2012-01-1521
2. F. Van Herpe, S. Vergne, E. Gaudard, Wavenumber frequency analysis of the wall pressure fluctuations in the wake of a rear-view mirror using a lattice Boltzmann model, in *Proceedings of the Acoustics 2012 Nantes Conference, 11th Congrès Français d'Acoustique* (2012), pp. 1851–1856
3. P. Shorted, V. Cotoni, *Statistical Energy Analysis in Engineering Vibroacoustic Analysis: Methods and Applications* (John Wiley & Sons, Ltd., Chichester, 2016), pp. 339–383. ISBN: 978-1-119-95344-9
4. F. Van Herpe, D. Binet, Calcul de la réponse vibro-acoustique des vitrages automobiles à l'excitation aerodynamique par la méthode des éléments finis, in *Proceedings of the Acoustics 2018 Le Havre Conference, 14th Congrès Français d'Acoustique* (2018)
5. R.H. Lyon, G. Maidanik, Power flow between linearly coupled oscillators. J. Acoust. Soc. Am. **34**(5), 623–639 (1962)
6. P.W. Smith Jr., Response and radiation of structural modes excited by sound. J. Acoust. Soc. Am. **34**(5), 640–647 (1962)
7. Free Field Technologies, *Actran 2020 User's Guide*, vol. 1. Installation, Operations, Theory and Utilities (2020)
8. S. Preis, G. Borello, Prediction of light rail vehicle noise in running condition using SEA, in *INTER-NOISE and NOISE-CON Congress and Conference Proceedings*, vol. 253, no. 5. Institute of Noise Control Engineering (2016)
9. H. Dande, T. Wang, J. Maxon, J. Bouriez, SEA model development for cabin noise prediction of a large commercial business jet. SAE Technical Paper 2017-01-1764 (2017). https://doi.org/10.4271/2017-01-1764
10. P. Tathavadekar, R. de Alba Alvarez, M. Sanderson, R. Hadjit, Hybrid FEA-SEA modeling approach for vehicle transfer function. SAE Technical Paper 2015-01-2236 (2015). https://doi.org/10.4271/2015-01-2236
11. B. Martínez-Calvo, E. Roibas, M. Chimeno, P. Fajardo, et al., Development of FEM/BEM and SEA models from experimental results for structural elements with attached equipment. European Space Agency, (Special Publication) ESA SP. 691
12. H.A. Dande, T. Wang, J. Maxon, J. Bouriez, et al., Characterization of aircraft components for SEA modeling, in *INTER-NOISE and NOISE-CON Congress and Conference Proceedings*, vol. 254, no. 1. Institute of Noise Control Engineering (2017)
13. L. Gagliardini, L. Houillon, L. Petrinelli, G. Borello, Virtual SEA: mid-frequency structure-borne noise modeling based on finite element analysis. SAE Technical Paper 2003-01-1555 (2003). https://doi.org/10.4271/2003-01-1555
14. L. Maxit, J.-L. Guyader, Estimation of SEA coupling loss factors using a dual formulation and FEM modal information, part I: theory. J. Sound Vib. **239**(5), 907–930 (2001)
15. L. Maxit, J.-L. Guyader, Extension of SEA model to subsystems with non-uniform modal energy distribution. J. Sound Vib. **265**(2), 337–358 (2003)
16. Y. Detandt, D. Copiello, B. Ganty, A method to identify the acoustic contribution in pressure fluctuations acting on a realistic car's side window, in *Internoise* (2015)

Wave Finite Element Schemes for Vibrations and Noise Under Turbulent Boundary Layer Excitation

Fabrizio Errico, Francesco Franco, Sergio De Rosa, Giuseppe Petrone, and Mohamed Ichchou

Abstract In the framework of finite elements based methods, this work proposes two numerical approaches to deal with the vibrations and noise induced by a random excitation on periodic and homogeneous structural systems. First, a 1D Wave Finite Element scheme is developed to deal with flat, curved and tapered finite structures. A single substructure is modelled using finite elements and one-dimensional periodic links among nodes are applied to get the set of waves propagating along the periodicity direction. The set of waves is then used to calculate the Green transfer functions between a set of target degrees of freedom and a subset representing the loaded ones. A 2D approach is also developed in combination with a wavenumber-space load synthesis to simulate the sound transmission of infinite flat, curved and axisymmetric structures: both homogenised and complex periodic models are analysed. The proposed numerical approaches are validated with analytical, numerical and experimental results and under different load conditions. From the experimental point of view, the approach is validated comparing results in terms of transmission loss evaluated on aircraft fuselage panels under diffuse acoustic field excitation.

1 Introduction

Flow-induced vibrations are among the major causes of high noise levels for almost all modern transport means, especially in the aerospace sector [2, 4]. Reduced levels of cabin noise, which can be pursued by using dedicated predictive tools, are desirable both for comfort and health-related issues of the passengers [47, 53]. In the space industry, the flow-induced vibrations on missile and launchers' fairings may deteriorate a fragile payload, including electronic components of on-board equipments. Therefore, reboust and reliable predictive models are necessary in order to

F. Errico (✉) · M. Ichchou
Ecole Centrale de Lyon, 36 Avenue Guy de Collongue, Lyon, France
e-mail: fabrizio.errico@ec-lyon.fr

F. Franco · S. De Rosa · G. Petrone
Universitá di Napoli Federico II, Via Claudio 21, Napoli, Italy

E. Ciappi et al. (eds.), *Flinovia—Flow Induced Noise and Vibration Issues and Aspects-III*, https://doi.org/10.1007/978-3-030-64807-7_15

determine the vibration and noise levels of the structures, in the entire frequency spectrum, before the system gets operational.

Nowadays most of the methodological issues are associated with the complexity of the analytical modelling and the computational cost of the numerical simulations. For example, in terms of structural vibrations, some analytical and finite element based approach have been developed in the literature [13, 19, 27, 30, 32]. Most of the attention is placed on modal approaches with applications for simply-supported plates. For instance, De Rosa et al. [13] present both the exact and numerical procedures for the response of a simply-supported plate under a turbulent boundary layer excitation. Da Rocha [46] analyses the influence on the boundary layer induced vibrations of different TBL models, while Hambric et al. [30] studies the effects of the boundary conditions of a flat plate, identifying how the modal acceptance function changes with respect to the convective wavenumber peaks.

However, the main drawback, when using modal based approaches, is connected to the required number of the finite elements [27]; for most of industrially relevant applications, the convective wavelengths are much smaller than the structural ones, requiring finer mesh rules compared to the isolated structure. Some authors propose different methods to reduce the computational cost associated with this approach. A method of load approximation through equivalent deterministic forces, analysing the eigenvalues distributions of the load matrix for a general convective load distribution, is proposed in [12]. Scaled models or similitude approaches prove to be a feasible solution [8, 14]. Bonness et al. [6], on the other hand, propose a modelling approach using asymptotic approximations of the modal force matrix, that can remove any dependence of the structural mesh resolution [6]. Maxit [36] proposes the use of the wavenumber space to simulate random loads using uncorrelated wall plane waves. The randomization of load cases is required to avoid excessive computational cost [36].

More recently, Birgersson et al. [3] propose a spectral finite element method for the simulation of structural vibrations under distributed pressure fluctuations that Finnveden et al. [26], later validate with an experimental-numerical comparison.

When the noise radiation is targeted, energy approaches are often preferred to avoid the aero-acousto-elastic coupling issues. In the framework of the Statistical Energy Analysis (SEA), Ichchou et al. [31, 32], considering that spatially-correlated fluctuations can be represented by uncorrelated models at high-frequencies, propose an equivalent rain-on-the-roof load which approximates the real load correlation function, giving huge advantages to the calculation of the joint acceptance integrals.

Finnveden [25] uses a spectral finite element approach to get the modal densities and coupling loss factors of SEA subsystems loaded with stochastic excitations, as turbulent boundary layer. Similarly, Orrenius et al. [41, 42] propose an SEA-based approach using a single 2D periodic cell for the calculation of SEA parameters. Another efficient alternative in terms of computational cost, to the classic modal-based approaches, is the Transfer Matrix Method (TMM), generally used for the prediction of the propagation of monochromatic plane waves in planar and multi-layered structures of infinite extent [1]. This approach in particularly suitable for homogenised and infinite multi-layered structures, made up from a combination

of elastic, porous and fluid layers, using a representation based on the plane wave propagation in different media in terms of transfer matrices.

This Chapter proposes two wave-based finite element approaches for the simulation of flow-induced vibrations and noise respectively; flat, curved, homogenised and complex periodic structures are analysed. Mean-flow effects, thus considering the approximated effects of structural vibrations of the external fluid excitation, are also modelled.

2 Vibrations of Finite Structures (1D-WFE)

A single repetitive substructure in a one-dimensional periodic or homogeneous media is schematically represented in Fig. 1. In a finite-element framework, the dynamic stiffness equation of the unit-cell can be written as:

$$[\mathbf{K} + \omega\mathbf{B} - \omega^2\mathbf{M}]\mathbf{q} = \mathbf{D}\mathbf{q} = \mathbf{f} + \mathbf{e}, \tag{1}$$

where $\mathbf{q}$ are the vectors of nodal degrees of freedom, $\mathbf{f}$ and $\mathbf{e}$ are, respectively, internal and external forces applied to the cell; $\mathbf{D}$, $\mathbf{M}$ and $\mathbf{K}$ are the dynamic stiffness, the mass and stiffness matrices, respectively; $\mathbf{B}$ represents a damping model that can be viscous and/or structural ($\mathbf{K}$ being complex), as it is assumed here, for simplicity.

The idea is to move in a new base, made up by elastic waves propagating in the structure. These waves can be derived by imposing the periodic conditions to the unit cell (Bloch-Floquet conditions [5]). For one-dimensional systems, these periodic conditions are imposed considering the common hypernodes of two adjacent unit cells (see Fig. 1): displacements must agree and forces must balance. By separating the the left and right side of the unit cell, in the periodicity direction, the dynamic stiffness matrix can be written as:

$$\begin{bmatrix} \mathbf{D}_{LL} & \mathbf{D}_{LR} \\ \mathbf{D}_{RL} & \mathbf{D}_{RR} \end{bmatrix} \begin{Bmatrix} \mathbf{q}_L \\ \mathbf{q}_R \end{Bmatrix} = \begin{Bmatrix} \mathbf{F}_L \\ \mathbf{F}_R \end{Bmatrix}, \tag{2}$$

where L and R stand for the indices of the left and right side of the unit-cell, as in Fig. 1. Imposing continuity of displacements and equilibrium of forces at the interface between adjacent points (see Fig. 1), a transfer matrix ($\mathbf{T}$) linking the state vectors between adjacent cells can be derived as in Eq. 3 [35, 37, 38, 52].

$$[\mathbf{T}] = \begin{bmatrix} -\mathbf{D}_{LR}^{-1}\mathbf{D}_{LL} & \mathbf{D}_{LR}^{-1} \\ -\mathbf{D}_{RL} + \mathbf{D}_{RR}\mathbf{D}_{LR}^{-1}\mathbf{D}_{LL} & -\mathbf{D}_{RR}\mathbf{D}_{LR}^{-1} \end{bmatrix}. \tag{3}$$

The eigenvalues of the transfer matrix, which represent complex propagating constants, result in pairs corresponding to waves propagating in the arbitrary defined positive (+) and negative (–) direction [52]. The corresponding eigenvectors ($\boldsymbol{\phi}_j^{-,+}$)

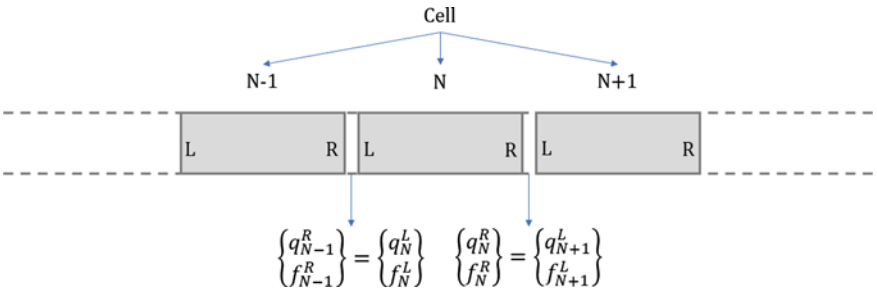

Fig. 1 Two adjacent elementary cells of a waveguide

represent the cross-sectional waveforms that propagate in the periodic structure. Every eigenvector can be partitioned, as in Eq. 4, into a sub-vector representing the displacements ($\mathbf{\Phi}_q^{+,-}$) and internal forces/moments distribution ($\mathbf{\Phi}_f^{+,-}$).

The selection of waves' direction is dependent on the magnitude of the propagation constants. If a wave propagates in the positive direction, its amplitude must decrease ($|\lambda_j^+| < 1$); vice-versa for reverse-going waves.

With this new wave base, one can move in a domain where the dynamics of the system is described in terms of wavemodes and waves' amplitudes [43, 44]. In particular, the following frequency-dependent relation holds:

$$\begin{Bmatrix} \mathbf{q}(x) \\ \mathbf{f}(x) \end{Bmatrix} = \begin{bmatrix} \mathbf{\Phi}_q^+ & \mathbf{\Phi}_q^- \\ \mathbf{\Phi}_f^+ & \mathbf{\Phi}_f^- \end{bmatrix} \begin{Bmatrix} \mathbf{a}^+(x) \\ \mathbf{a}^-(x) \end{Bmatrix}, \tag{4}$$

where $\mathbf{a}^{+,-}$ are the amplitudes of the set of waves. The filtering issues associated with the wave basis are deeply investigated in literature [22, 35, 38].

2.1 Curvature Simulation

The previously described approach is also applicable to curved structures, in fact, to simulate it in our unit-cell, the local reference of each grid point in the finite element model of the cell, as shown in Fig. 2, must be rotated with respect to the global one [21, 23]. Block diagonal matrices (**Rot**), assembled from rotation matrices for each node, can be pre and post multiplied to the original mass and stiffness matrices, in order to simulate the curvature. Each layer can have a different nature and even fluid-structure coupling at cell scale can be included if fluid layers are present [35]. Hence the following relations can be used to derive the FE matrices of the cell with simulated curvature:

$$\begin{aligned} \mathbf{M}_{curv} &= \mathbf{Rot}^T \mathbf{M} \mathbf{Rot} \\ \mathbf{K}_{curv} &= \mathbf{Rot}^T \mathbf{K} \mathbf{Rot}. \end{aligned} \tag{5}$$

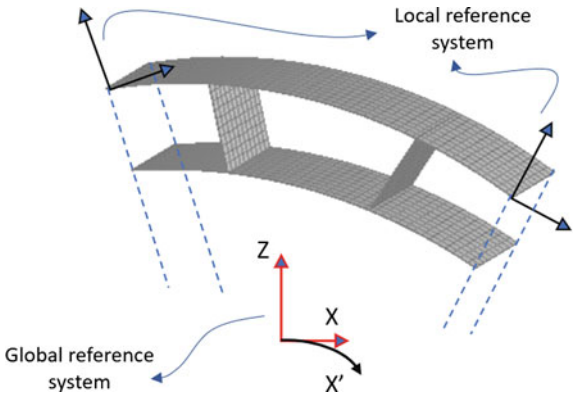

Fig. 2 The rotation of the global reference into the local one in each location and layer of the cell [23]

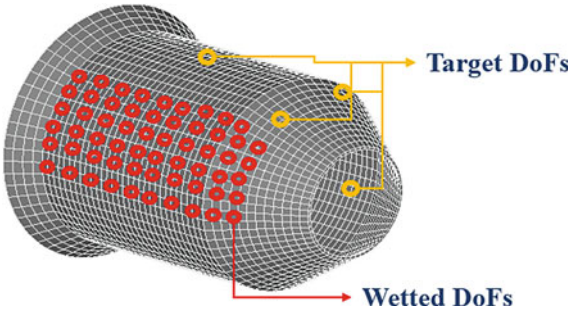

Fig. 3 Illustration of degrees of freedom distribution in a transfer matrix framework: target degrees of freedom and wetted/loaded ones

When the curvature is imposed, the wave propagation of the structure, which is studied from Eq. 3, is considered along the circumferential and axial direction of the structure and the waves represent circumferential and/or helical waves [21, 23].

2.2 *Transfer Functions Using Waves' Superposition*

The response to the random load can be calculated using a transfer matrix approach [21, 30]:

$$S_{vv}(x_i, x_j, \omega) = \boldsymbol{\Theta_v}^T(x_i, \omega)\mathbf{S}_{FF}(\omega)\boldsymbol{\Theta_v}(x_j, \omega), \tag{6}$$

where $\boldsymbol{\Theta_v}$ is the transfer matrix, $\mathbf{S}_{vv}$ is the matrix of the auto/cross spectral densities of the target quantity v (i.e. displacements) and $\mathbf{S}_{FF}$ is the load matrix [14]. The size of the transfer matrix $\boldsymbol{\Theta_v}$ is linked to the target DoFs and the fluid mesh (wetted surface); Fig. 3 shows an illustrative example. If, on the contrary, the excitation is distributed but deterministic, Eq. 7 can be used instead.

$$V(x_i, \omega) = \boldsymbol{\Theta_v}^T(x_i, \omega)\mathbf{P}_F(\omega), \tag{7}$$

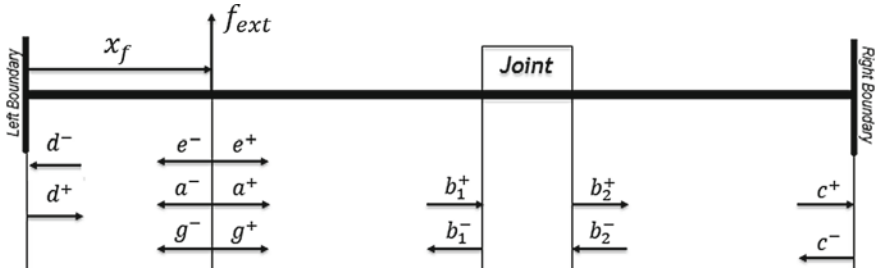

Fig. 4 Scheme of waves in a finite structure excited by point load

where V is the target quantity of interest, while $\mathbf{P}_F$ is the matrix describing the pressure load distribution.

Here, the assumption is made that the structural vibrations do not influence the pressure field outside, and analogously, the flow field have no effect on the structural dynamics.

The elements $\Theta_v^{i,j}$ are the Green transfer functions between the grid points i and j, and can be calculated using a WFE approach, as proposed here, and using the Maxwell-Betti theorem of reciprocity. With reference to Fig. 4, the vibrations in any point of the structure are calculated by superposition of the direct and reverberant wavefield.

At the point of application of the force, using the wave-base expansion in Eq. 4, the following equilibrium equation holds:

$$\begin{bmatrix} \mathbf{\Phi}_q^+ & -\mathbf{\Phi}_q^- \\ \mathbf{\Phi}_f^+ & -\mathbf{\Phi}_f^- \end{bmatrix} \begin{Bmatrix} \mathbf{e}^+ \\ \mathbf{e}^- \end{Bmatrix} = \begin{Bmatrix} \mathbf{0} \\ \mathbf{f}_{ext} \end{Bmatrix}. \tag{8}$$

The inversion of the wavemodes' matrix in Eq. 8 can lead to numerical errors and it is extensively discussed in [52].

At the same time, waves incident upon boundaries are reflected and transmitted. In Fig. 4 this is illustrated with $\mathbf{d}^{-,+}$ and $\mathbf{c}^{-,+}$, at the edges of the structure.

The dynamics at the border can be described using a matrix ($\mathbf{R}$) dependent on the type of constraint. Each boundary condition can always be described in the form [52]: $\mathbf{A}_1\mathbf{f} + \mathbf{A}_2\mathbf{q} = \mathbf{0}$. Substituting the wave base expansion for forces and displacements [22, 43]:

$$\begin{aligned} \mathbf{R}_{right} &= -\left(\mathbf{A}_1\mathbf{\Phi}_f^- + \mathbf{A}_2\mathbf{\Phi}_q^-\right)^{-1}\left(\mathbf{A}\mathbf{\Phi}_f^+ + \mathbf{A}_2\mathbf{\Phi}_q^+\right) \\ \mathbf{R}_{left} &= -\left(\mathbf{A}_1\mathbf{\Phi}_f^+ + \mathbf{A}_1\mathbf{\Phi}_q^+\right)^{-1}\left(\mathbf{A}_1\mathbf{\Phi}_f^- + \mathbf{A}_2\mathbf{\Phi}_q^-\right), \end{aligned} \tag{9}$$

where the matrices $\mathbf{A}_1$ and $\mathbf{A}_2$ change depending on the type of constrain [52].

Now, if some discontinuities, such as linear or complex joints, are reached by the waves, the scattering properties become largely impactive on the structural behaviour. In Fig. 4 this is illustrated with $\mathbf{b}_1^{-,+}$ and $\mathbf{b}_2^{-,+}$, at the edges of the joint. The scattering matrix $\mathbf{s}$ can be defined as:

$$\begin{Bmatrix} \mathbf{b}_1^- \\ \mathbf{b}_2^+ \end{Bmatrix} = \begin{bmatrix} \mathbf{s}_1 & \mathbf{s}_2 \\ \mathbf{s}_3 & \mathbf{s}_4 \end{bmatrix} \begin{Bmatrix} \mathbf{b}_1^+ \\ \mathbf{b}_2^- \end{Bmatrix} = \mathbf{s} \begin{Bmatrix} \mathbf{b}_1^+ \\ \mathbf{b}_2^-, \end{Bmatrix} \tag{10}$$

where the scattering matrix has been splinted in four matrices in Eq. 10: $\mathbf{s}_1$ and $\mathbf{s}_4$ represent transmission matrices, while $\mathbf{s}_2$ and $\mathbf{s}_3$ represent reflection ones.

Condensing the FE of the junction to the borders, one gets Eq. 11:

$$\mathbf{D}_J \, \mathbf{Q}_J = \mathbf{F}_J, \tag{11}$$

where $\mathbf{Q}_J$ and $\mathbf{F}_J$ are the vectors of displacements and nodal forces of the joint to its borders, which are in common with the two waveguides and can be thus expressed in wave base using Eq. 4:

$$\mathbf{Q}_J = \begin{bmatrix} \mathbf{\Phi}_q^{1,+}\mathbf{b}_1^+ + \mathbf{\Phi}_q^{1,-}\mathbf{b}_1^- \\ \mathbf{\Phi}_q^{2,+}\mathbf{b}_2^+ + \mathbf{\Phi}_q^{2,-}\mathbf{b}_2^- \end{bmatrix} \tag{12}$$

$$\mathbf{F}_J = \begin{bmatrix} \mathbf{\Phi}_f^{1,+}\mathbf{b}_1^+ + \mathbf{\Phi}_f^{1,-}\mathbf{b}_1^- \\ -\mathbf{\Phi}_f^{2,+}\mathbf{b}_2^+ - \mathbf{\Phi}_f^{2,-}\mathbf{b}_2^- \end{bmatrix}. \tag{13}$$

Substituting the previous equations in Eq. 11, the scattering matrix can be obtained:

$$\mathbf{s} = \left[-\mathbf{D}_J \begin{bmatrix} \mathbf{\Phi}_q^{1,-} & \mathbf{0} \\ \mathbf{0} & \mathbf{\Phi}_q^{2,+} \end{bmatrix} + \begin{bmatrix} \mathbf{\Phi}_f^{1,-} & \mathbf{0} \\ \mathbf{0} & -\mathbf{\Phi}_f^{2,+} \end{bmatrix} \right]^{-1} \left[\mathbf{D}_J \begin{bmatrix} \mathbf{\Phi}_q^{1,+} & \mathbf{0} \\ \mathbf{0} & \mathbf{\Phi}_q^{2,-} \end{bmatrix} - \begin{bmatrix} \mathbf{\Phi}_f^{1,+} & \mathbf{0} \\ \mathbf{0} & -\mathbf{\Phi}_f^{2,-} \end{bmatrix} \right]. \tag{14}$$

The inversion in Eq. 14 can cause numerical instabilities and the use of the left eigenvalues is required [40].

Using again Fig. 4 as reference we can evaluate the amplitude of waves in any point; here, the excitation location is considered as the reference point. At the excitation location, one can sum the incident and direct field:

$$\mathbf{a}^+ = \mathbf{e}^+ + \mathbf{g}^+; \qquad \mathbf{g}^- = \mathbf{e}^- + \mathbf{a}^-. \tag{15}$$

At boundaries, instead, the following reflection relations are valid (see Fig. 4):

$$\mathbf{c}^- = \mathbf{R}_{right}\mathbf{c}^+; \qquad \mathbf{d}^+ = \mathbf{R}_{left}\mathbf{d}^-. \tag{16}$$

At the same time, along the waveguide, the following propagation relations hold:

$$\mathbf{g}^+ = \mathbf{Tr}(x_f)\mathbf{d}^+; \quad \mathbf{d}^- = \mathbf{Tr}(x_f)\mathbf{g}^-; \quad \mathbf{a}^- = \mathbf{Tr}(L - x_f)\mathbf{c}^-; \quad \mathbf{c}^+ = \mathbf{Tr}(x_f)\mathbf{a}^+. \tag{17}$$

where **Tr** is the wave propagation matrix in a periodic framework (Bloch-Floquet conditions), that can be expressed as:

$$\mathbf{Tr}(x) = \mathrm{diag}\left(e^{-ik_1 x}, e^{-ik_2 x}, \ldots, e^{-ik_n x}\right). \tag{18}$$

Finally, the amplitudes of the waves can be calculated at a given response point by considering the excitation, reflection and propagation relations. First the scattering equation can be solved obtaining the values of the incoming and out-coming waves at the joint:

$$\mathbf{b}_2^+ = \left[\mathbf{I} - \mathbf{s}_4\mathbf{Tr}(L_2)\mathbf{R}_{left}\mathbf{Tr}(L_2)\right]^{-1}\left[\mathbf{s}_3\mathbf{Tr}(L_1 - x_f)\right]\mathbf{a}^+ \tag{19}$$

$$\mathbf{b}_1^- = \mathbf{s}_1\mathbf{Tr}(L_1 - x_f)\mathbf{a}^+ + \mathbf{s}_2\mathbf{Tr}(L_2)\mathbf{R}_{left}\mathbf{Tr}(L_2)\mathbf{b}_2^+, \tag{20}$$

with L_1 and L_2 the lengths of the first (left) and second (right) waveguide, x_f the position of the force. The following form of the wave amplitudes is derived, assuming, in this case, that the force is applied, for example, on the first waveguide:

$$\begin{aligned}\mathbf{a}^+ = \big[\mathbf{I} - \mathbf{Tr}(x_f)\mathbf{R}_{left}\mathbf{Tr}(x_f)\mathbf{Tr}(L_1 - x_f)\mathbf{s}_2\mathbf{Tr}(L_2)\mathbf{R}_{left}\mathbf{Tr}(L_2)\big[\mathbf{I}- \\ +\mathbf{s}_4\mathbf{Tr}(L_2)\mathbf{R}_{left}\mathbf{Tr}(L_2)\big]^{-1}\mathbf{s}_3\mathbf{Tr}(L_1 - x_f)- \\ +\mathbf{Tr}(x_f)\mathbf{R}_{left}\mathbf{Tr}(x_f)\mathbf{Tr}(L_1 - x_f)\mathbf{s}_1\mathbf{Tr}(L_1 - x_f)\big]^{-1} \\ \big[\mathbf{e}^+ + \mathbf{Tr}(x_f)\mathbf{R}_{left}\mathbf{Tr}(x_f)\mathbf{e}^-\big]\end{aligned} \tag{21}$$

$$\begin{aligned}\mathbf{a}^- = \mathbf{Tr}(L_1 - x_f)\big[\mathbf{s}_2\mathbf{Tr}(L_2)\mathbf{R}_{left}\mathbf{Tr}(L_2)\big[\mathbf{I} - \mathbf{s}_4\mathbf{Tr}(L_2)\mathbf{R}_{left}\mathbf{Tr}(L_2)\big]^{-1}\times \\ \mathbf{s}_3\mathbf{Tr}(L_1 - x_f) - \mathbf{s}_1\mathbf{Tr}(L_1 - x_f)\big]\mathbf{a}^+.\end{aligned} \tag{22}$$

Finally, the response in the reception point can be then calculated applying the propagation relations to the target distance [11, 21, 22, 43].

If curved or axisymmetric structures are considered, Fig. 5 becomes a reference, with equivalent considerations applicable, taking into account that no real boundaries are present, if impedance variations do not appear.

For example, with reference to the scheme in Fig. 5, the response in a target point can be expressed as:

$$\begin{aligned}\mathbf{a}^+ = \big[\mathbf{I} - \mathbf{Tr}(2\pi - \theta_1)\mathbf{s}_3\mathbf{Tr}(\theta_1) - \mathbf{Tr}(2\pi - \theta_1)\mathbf{s}_4\mathbf{Tr}(2\pi - \theta_1)\big[\mathbf{I} - \mathbf{Tr}(\theta_1)\mathbf{s}_2\mathbf{Tr}(\theta_1)\big]^{-1} \\ \mathbf{Tr}(\theta_1)\mathbf{s}_2\mathbf{Tr}(\theta_1)\big]^{-1}\big[\mathbf{e}^+ + \mathbf{Tr}(2\pi - \theta_1)\mathbf{s}_4\mathbf{Tr}(2\pi - \theta_1)\big[\mathbf{I} - \mathbf{Tr}(\theta_1)\mathbf{s}_2\mathbf{Tr}(\theta_1)\big]^{-1}\mathbf{e}^-\big]\end{aligned} \tag{23}$$

$$\mathbf{a}^- = \left[\mathbf{I} - \mathbf{Tr}(\theta_1)\mathbf{s}_2\mathbf{Tr}(\theta_1)\right]^{-1}\left[\mathbf{e}^- + \mathbf{Tr}(\theta_1)\mathbf{s}_1\mathbf{Tr}(\theta_1)\mathbf{a}^+\right] - \mathbf{e}^-. \tag{24}$$

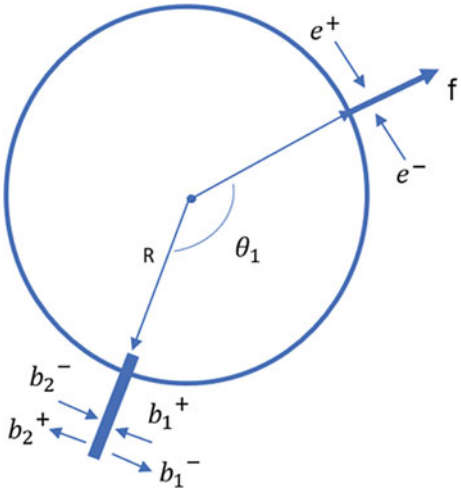

Fig. 5 Waves in an axial-symmetric jointed structure excited by a point load

Equations (23) and (24) represent the general solution when an impedance variation is also present on the circumferential wave-path. In the case that the axisymmetric structure is homogeneous, or simply there is no variation of impedance, Eqs. (23) and (24) remain the same, while the values of the $\mathbf{s}_J$ (J =1,…,4) matrices change in zeros and identity matrices since a full transmission must be simulated. For example, in the case of closed axisymmetric structures with no impedance variations, no scattering is present and assuming a $\Delta\theta>0$, the reverberant field is simply given by:

$$\mathbf{g}^{+} = \mathbf{Tr}(2\pi)\mathbf{b}^{+} \qquad \mathbf{g}^{-} = \mathbf{Tr}(2\pi - \Delta\theta)\mathbf{b}^{-}. \tag{25}$$

3 Sound Transmission of Infinite Structures (2D-WFE)

A 2D WFE approach is here proposed to target the wave propagation and the sound transmission in infinite periodic structures. With reference to Eq. 1 and Fig. 6, the periodicity conditions can be applied as follows:

$$\begin{bmatrix} \mathbf{q}_2 \\ \mathbf{q}_3 \\ \mathbf{q}_4 \end{bmatrix} = \begin{bmatrix} \mathbf{I}\lambda_X \\ \mathbf{I}\lambda_Y \\ \mathbf{I}\lambda_X\lambda_Y \end{bmatrix} \mathbf{q}_1 = \mathbf{\Lambda}\mathbf{q}_1, \tag{26}$$

with

$$\lambda_X = \mathrm{e}^{-\mathrm{i}k_X L_X}; \qquad \lambda_Y = \mathrm{e}^{-\mathrm{i}k_Y L_Y}, \tag{27}$$

where k_X and k_Y are the wavenumbers in the periodicity directions X and Y, L_X and L_Y the sizes of the cell in the same plane while $\mathbf{I}$ is the identity matrix. The dynamic

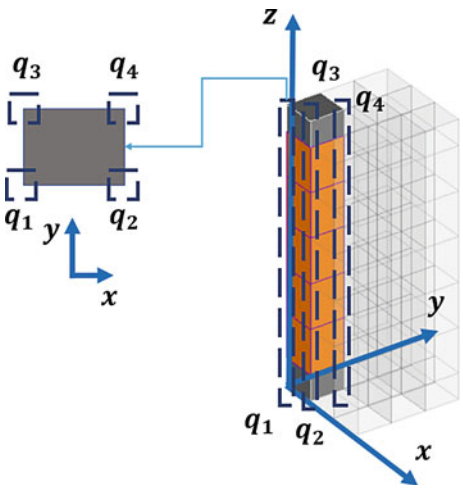

Fig. 6 Bi-dimensional unit cell model with in-plane periodicity

stiffness matrix of the reduced model can be derived by pre and post multiplying Eq. 1 with the 2D periodicity matrix $\mathbf{\Lambda}$:

$$\mathbf{\Lambda}^H[\mathbf{K} - \omega^2\mathbf{M}]\mathbf{\Lambda}\,\mathbf{q}_1 = \mathbf{\Lambda}^H\mathbf{\Lambda}\mathbf{f} + \mathbf{\Lambda}^H\mathbf{\Lambda}\mathbf{e}. \tag{28}$$

Modal order reduction becomes mandatory when fine meshes are employed; the internal degrees of freedom, which can be a consistent part of the unit cell degrees of freedom, are replaced by the modal participation factors for a relatively small subset of constrained cell modes [17, 23, 54].

3.1 One-Way Fluid-Structure Coupling

As said before, we assume here that the structural vibrations do not influence the pressure field outside, and analogously, the flow field have no effect on the structural dynamics. An infinite structure can separate two fluid domains which correspond to the excitation side (subscript 1; Fig. 7) and the radiation side (subscript 2; Fig. 7).

A forcing pressure wave can excite the structure and make it vibrating; it can be described as such, omitting the time harmonic dependence for simplicity:

- for a flat structure:

$$PW = p_I \mathrm{e}^{-\mathrm{i}(k_X X + k_Y Y - k_{Z,1} Z)}; \tag{29}$$

- for a curved/cylindrical structure:

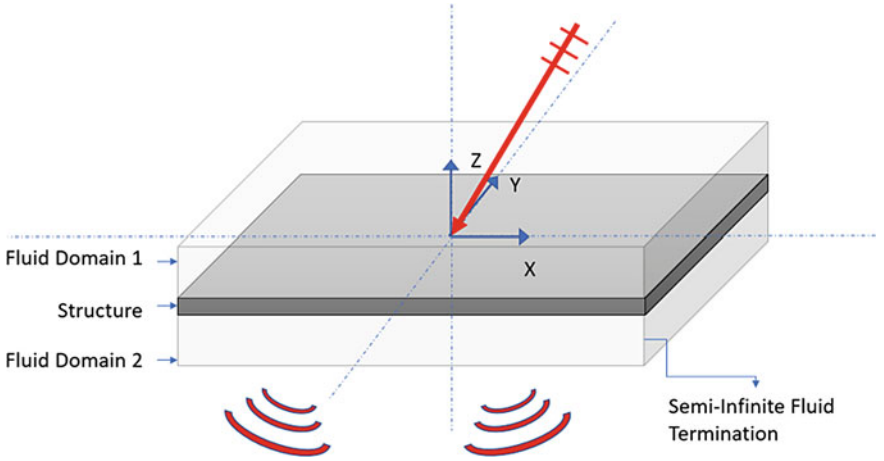

Fig. 7 Illustration of an infinite the structure excited by a plane wave and radiating sound

$$HW = p_I e^{-i(k_{X'}X' + k_Y Y - k_{Z',1}Z')} \approx p_I e^{-i(k_\theta \theta + k_Y Y - k_{Z',1}Z')}; \tag{30}$$

where, k_X, k_Y and k_Z are the wavenumbers of the plane wave along the global reference and $k_{X'}$ k_Y and $k_{Z'}$ are the projected components in the local reference as in Fig. 2, this local reference is coherent with the circumferential direction being $k_{X'}$ = k_θ x R, where R is the radius of curvature. The nodal forces, acting on the single cell, can be expressed using the sound pressure amplitudes and the nodal surfaces. Consistent nodal forces can be calculated as follows:

$$\mathbf{e}_1 = \mathbf{S} \cdot (\mathbf{p}_I + \mathbf{p}_R)\mathbf{w}_1 - \mathbf{S} \cdot \mathbf{p}_T \mathbf{w}_2, \tag{31}$$

where $\mathbf{S}$ is vector of the nodal areas, $\mathbf{w}_1$ and $\mathbf{w}_2$ are vectors of all zeros and ones in the position corresponding to the out-of-plane displacements degrees of freedom of the nodes belonging to the surfaces in contact with the flow (effective for the sound transmission), $\mathbf{p}_I$, $\mathbf{p}_R$ and $\mathbf{p}_T$ are the amplitudes of the excited, reflected and transmitted pressure waves, respectively. A link between pressure and displacements can be derived using the dynamic stiffness of the fluids, as follows [23]:

$$D_{f,1} = \frac{-i\rho_1\omega^2}{k_{Z,1}}; \qquad D_{f,2} = \frac{-i\rho_2\omega^2}{k_{Z,2}}, \tag{32}$$

where ρ_1 and ρ_2 are the fluid densities, $k_{Z,1}$ and $k_{Z,2}$ the wavenumber components in Z (i.e. out-of-plane) and $D_{f,1}$ and $D_{f,2}$ the dynamic stiffness of the fluid domains.

Exploiting the relationships of Eqs. 31 and 32 in Eq. 28, the final system equation becomes:

$$[\mathbf{D}_r + (D_{f,1}\mathbf{w}_1 + D_{f,2}\mathbf{w}_2)\mathbf{S}\mathbf{\Lambda}^H\mathbf{\Lambda}]\mathbf{q}_1 = 2p_I\mathbf{w}_1\mathbf{S}\mathbf{\Lambda}^H\mathbf{\Lambda}. \tag{33}$$

The sound transmission coefficient τ for each couple of wavenumbers k_X and k_Y, is derived by solving in $\mathbf{q}_1$ Eq. 33:

$$\tau(k_X, k_Y) = \frac{(k_{Z,2}/\rho_2)\mathbf{S}|(D_{f,2}\mathbf{w}_2\mathbf{q}_1)^2|}{(k_{Z,1}/\rho_1)\mathbf{S}|\mathbf{p}_I^2|}, \tag{34}$$

while the average velocity is given by:

$$v_{avg}(k_X, k_Y) = -\mathrm{i}\omega\mathbf{q}_1. \tag{35}$$

The results are valid for infinite structures, but can be re-scaled to include the effects of the finiteness of the structure [33, 45, 51].

3.2 Mean-Flow Effects

To remove the assumption of one-way coupling and simulate mean flow effects, on one side (or two) of an infinite structural domain, a specific aerodynamic theory has to be used to model the self excited aerodynamic components of the load.

Under the hypothesis of small disturbances, the aerodynamic pressure can be normally considered as made up of two components [16], as in Eq. (36): one is given by the pressure fluctuations for a rigid body (Δ_P^M); the second is dependent on the structural motion/elasticity (Δ_P^E). The following developments are connected to the second of these contributes; an illustration is given in Fig. 7.

$$\Delta_P = \Delta_P^M + \Delta_P^E; \qquad \mathbf{e} = \mathbf{e}^M + \mathbf{e}^E. \tag{36}$$

For sake of simplicity, the simplest aerodynamic theory (Piston Theory), valid from Mach > 1.5 [16, 48], is used for the following developments. With reference to Eqs. 28 and 36, the self-excited force terms can be written as a function of the convective and continuity derivative, [16, 18, 39, 48]:

$$\mathbf{e}^E = -\rho_0 a_0 \mathbf{A}_n \left(\frac{\partial \mathbf{w}}{\partial t} + U \frac{\partial \mathbf{w}}{\partial x} \right), \tag{37}$$

where $\mathbf{w}$ represents the vector of the out-of-plane displacements of the structural nodes belonging to the surfaces in contact with the flow (coordinate Z in Fig. 8), ρ_0 is the fluid density, a_0 the sound speed, $\mathbf{A}_n$ the nodal area vector and U the flow-speed. The out-of-plane displacements can be expressed by multiplying $\mathbf{q}$ for a matrix ($\boldsymbol{\epsilon}$) of 0 and 1 in the positions corresponding to the target degrees of freedom (i.e. the translations in Z).

For example, the matrix $\boldsymbol{\epsilon}$, can be built as such:

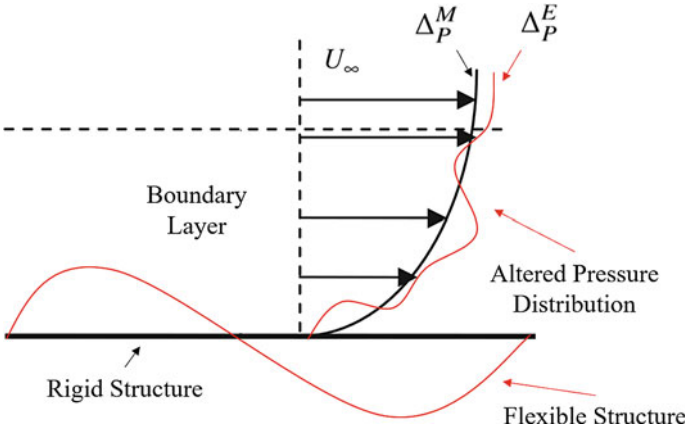

Fig. 8 An illustration on the effects of a flexible structure in terms of variation of pressure distribution in a turbulent boundary layer

$$\epsilon_{i,j} = \begin{cases} 1 & \text{if } \; j = 3; i = 1, N; \\ 0 & \text{else} \end{cases} \tag{38}$$

where i represents the number of nodes and j the nodal degree of freedom (3 corresponds to translation along Z). In a periodic structural framework, the spatial derivative in Eq. (37) is a function of the structural propagation constant (λ_x, assuming X as the flow direction), and can be expressed, using a simple numerical scheme for the first derivative, as follows:

$$\frac{\partial \mathbf{w}}{\partial x} = \mathbf{\Lambda} \left(\frac{\lambda_x - 1}{L_x} \right) \boldsymbol{\epsilon} \mathbf{q}_1. \tag{39}$$

The final dynamic stiffness equation can be derived, as in Eq. (40), substituting Eqs. (37) and (39) in Eq. (28).

$$\mathbf{\Lambda}^H \left[\mathbf{K} - \omega^2 \mathbf{M} - \mathrm{i}\omega\rho_0 a_0 \mathbf{A}_n \boldsymbol{\epsilon} + U\rho_0 a_0 \mathbf{A}_n \boldsymbol{\epsilon} \left(\frac{\lambda_x - 1}{L_x} \right) \right] \mathbf{\Lambda} \, \mathbf{q}_1 = \mathbf{\Lambda}^H \mathbf{\Lambda} \mathbf{f} = 0. \tag{40}$$

Additional damping and stiffness terms are observed in the new dynamic stiffness equation (Eq. (40)). The additional damping is proportional to the circular frequency, but, as discussed in [16], it is not a dominant term. A strong variation of the results of Eq. (28) versus the Eq. (40) ones, is given by the additional stiffness terms, which are proportional to the stream-wise elastic waves' propagation coefficient.

A detailed development is available in [20].

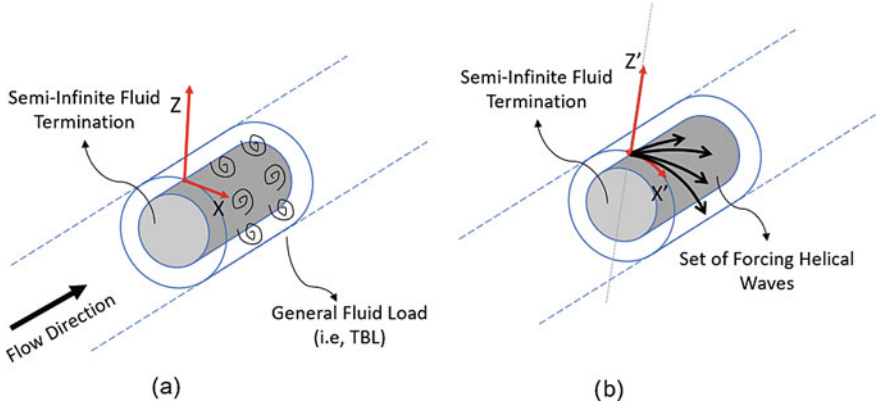

Fig. 9 Load sinthesys approach employed in this work: **a** Real phenomena; **b** Simulated equivalent conditions

3.3 Load Synthesis in Helical Waves

To simulate a general random excitation, a wavenumber synthesis approach is here proposed as in Fig. 9.

The idea is to assume a model of excitation and derive its unknown parameters imposing an analogy between its wavenumber spectra and the one of the real/physical (targeted) excitation. A finite sum of wall surface waves of unknown amplitude (A_j), number (N_W) and wavenumbers ($\bar{K}_j$) is considered:

$$P(\bar{X}) = \sum_{j=1}^{N_W} A_j \mathrm{e}^{-\mathrm{i}\bar{K}_j\bar{X}}, \tag{41}$$

where the harmonic dependence has been omitted and $\bar{X}$ stands for the surface coordinates (i.e. X–Y in Fig. 6). The unknown parameters of Eq. 41 are obtained with an analogy of the wavenumber spectra (ϕ_{PP} for the simulated load and Φ_{PP} the real one):

$$\begin{aligned}\phi_{PP}(\bar{K},\omega) = \Phi_{PP}(\bar{K},\omega) = \frac{1}{4\pi^2}\left(\sum_{j=1}^{N_W} A_j^2 \left[\frac{\mathrm{e}^{\mathrm{i}(\bar{K}_j-\bar{K})(\Delta\bar{X}_1-\Delta\bar{X}_2)}}{\mathrm{i}(\bar{K}_j-\bar{K})}\right]_{-\infty}^{+\infty}\right. \\ \left. + \sum_{j=1}^{N_W}\sum_{n=1;n\neq j}^{N_W} A_j A_n \left[\frac{\mathrm{e}^{\mathrm{i}(\bar{K}_j-\bar{K})(\Delta\bar{X}_1)}}{-\mathrm{i}(\bar{K}_j-\bar{K})}\right]_{-\infty}^{+\infty}\left[\frac{\mathrm{e}^{\mathrm{i}(\bar{K}_n-\bar{K})(\Delta\bar{X}_2)}}{-\mathrm{i}(\bar{K}_n-\bar{K})}\right]_{-\infty}^{+\infty}\right) = \\ = \int 4\pi^2 \frac{A_j^2}{\Delta\bar{K}_j}\delta(\bar{K}_j-\bar{K})\mathrm{d}\bar{K}_j + \int\int 8\pi^4 \frac{A_j A_n}{\Delta\bar{K}_j\Delta\bar{K}_n}\delta(\bar{K}_j-\bar{K})\delta(\bar{K}_n-\bar{K})\mathrm{d}\bar{K}_j\mathrm{d}\bar{K}_n,\end{aligned} \tag{42}$$

where δ is the Dirac functional and the auto/cross correlations are considered separately.

The $\delta(\bar{K}_j - \bar{K})\delta(\bar{K}_n - \bar{K})$ term in Eq. 42 is null being the indices j and n different.

For each couple k_X and k_Y, the synthesised load model can be written as:

$$P_W(X, Y, k_X, k_Y, \omega) = \sqrt{\frac{\Phi_{PP}(k_X, k_Y, \omega)\Delta k_X \Delta k_Y}{4\pi^2}} \mathrm{e}^{-\mathrm{i}(k_X X + k_Y Y)}. \tag{43}$$

The approach is applicable independently on the spatial correlation load and the reference. Finally, the total sound transmission coefficient will be given by an integration of all the k_X and k_Y contributes, as follows:

$$\tau_{TOT}(\omega) = \frac{\int\int \tau(k_X, k_Y) \times W_A(k_X, k_Y, \omega)\mathrm{d}k_X \mathrm{d}k_Y}{\int\int W_A(k_X, k_Y, \omega)\mathrm{d}k_X \mathrm{d}k_Y}, \tag{44}$$

where $W_A(k_X, k_Y,)$ represents the normalized amplitude function for the couple k_X, k_Y among the whole set of waves used for the load synthesis. The integration limits are not defined on a general basis but they are modified depending on the type of load to simulate; a dedicated study for TBL models is proposed in the next section. The final transmission loss is, by definition:

$$\mathrm{TL}(\omega) = -10 \log_{10}(\tau_{\mathrm{TOT}}(\omega)). \tag{45}$$

In the case of curved finite structures, some correction factors must be used [23, 28].

4 Results: Flow-Induced Vibrations

In this section, a validation is proposed for a flat and cylindrical structure under a turbulent boundary layer load; no-gradient effects are taken into account and the TBL is assumed to be fully developed.

First, a 3 mm-thick flat panel (0.36×0.20 m^2) is considered under a Corcos turbulent boundary layer model, in Fig. 10. The wavenumber spectra, Φ_{PP}, proposed by Corcos [10], is here reported for the sake of completeness assuming the directions X and Y as the stream-wise and cross-wise ones:

$$\Phi_{PP}(k_X, k_Y, \omega) = S_{pp}(\omega) \frac{4\alpha_X \alpha_Y}{\left[\alpha_Y^2 + \frac{U_c^2 k_Y^2}{\omega^2}\right]\left[\alpha_X^2 + \left(1 + \frac{U_c k_X}{\omega}\right)^2\right]}, \tag{46}$$

where U_c is the convective flow speed, S_{pp} is the single-point auto spectral density of the wall pressure distribution. The stream-wise and cross-wise correlation coefficients, α_X and α_Y, are assumed to be 0.15 and 0.77, respectively, in all the following test-cases.

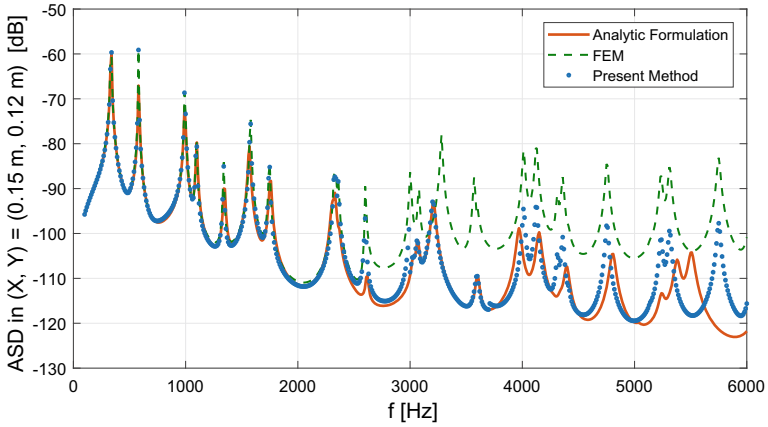

Fig. 10 Velocity auto spectral density in a grid point for a flat panel under TBL load [Reference: 1 m/s]

Table 1 Computation times for the vibrations of a flat panel under TBL load

Method	Aliasing (kHz)	Relative Time/Frequency
FEM	2	35
WFE	2	1

The panel has the following material properties: $E = 7.0\ 10^{10}$ Pa, $\rho = 2750\,\text{kg/m}^3$, $\nu = 0.33$ and 1% of structural damping. The analytical and FEM solutions are used as a reference [13]; simply supported boundary conditions are considered on the four sides of the panel.

The flexural aliasing frequency, which is the frequency where the adopted mesh becomes unable to simulate the fluid wavelength, is 2.0 kHz and the convective critical frequency 580 Hz. Considering Eq. 18, a variable size of the transfer matrix ($\boldsymbol{\Theta}_\nu$) can be employed in the periodicity direction [21], extending the accuracy of the numerical scheme over the standard aliasing frequency (for lumped-on-nodes approximations, as in this case). A comparison in terms of calculation time is given in Table 1, where the elapsed time is averaged in frequency band of analysis and normalised on the minimum one.

Then, a 0.6 m long cylinder, with a 0.4 m diameter and the same material as before, is used as a test-case under TBL excitation, using again a Corcos model [10], with an aliasing frequency 1250 Hz; a simple application of this model to a curved structure is still acceptable, if the stream-wise direction is parallel to the axis of rotation and the cross-wise is assumed to be the circumferential one [34]. The θWFE method (here named as a WFE version for curved structures, see Fig. 5) is used and compared with the FEM (Fig. 10).

The results show an excellent agreement in the whole frequency range and a computational cost comparison is given in Table 2.

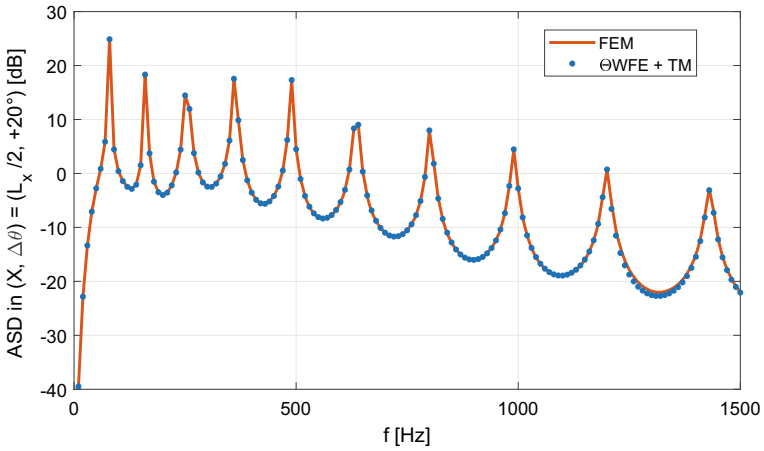

Fig. 11 Velocity auto spectral density in a grid point for a cylindrical shell under TBL load [Reference: 1 m/s]

Table 2 Computation times for the vibrations of a cylindrical shell under TBL load

Method	Aliasing (kHz)	Relative time/Frequency
FEM	1.25	287
θWFE	1.25	1

5 Results: Flow-Induced Noise

Here, the flow-induced transmission caused by a random excitation is considered, with a specific focus on turbulent boundary layer (TBL). The results, presented here for validation purposes, deal with flat panels and, with reference to the flow characteristics, no-gradient effects are taken into account and the TBL is assumed to be fully developed. In each of the following cases a 10-elements mesh per minimum wavelength (in the frequency band) is used for convergence purposes.

First, a 2mm-thick aluminium panel is studied, in Fig. 12, under a turbulent boundary layer modelled using the Corcos model [10] (U_c = 180 m/s; α_x = 0.125 and α_y = 0.78). The full FEM model is made using the same elements of the WFEM and is built by repeating the elementary cell along the two directions, up to achieve the size of the full panel. The results for the WFE approach are calculated in logarithmic scale (100 points), while the FEM solution is presented in third octaves. Given the assigned model, the aerodynamic coincidence (critical frequency) is 1.8 kHz while the acoustic one is 6 kHz. The results are scaled including approximated finite size effects, as proposed in [33].

A second test-case is also shown in Fig. 12. An honeycomb sandwich panel whose cell is modelled as an homogenised multi-layered panel is analysed under the same turbulent boundary layer. The panel has 1mm-thick aluminium skins and a 10mm-

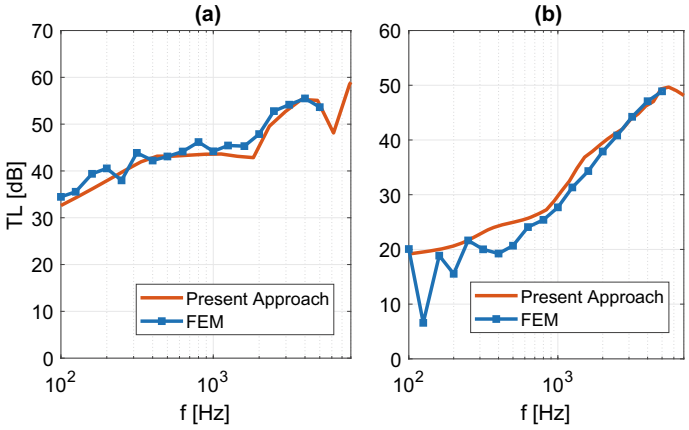

Fig. 12 The transmission loss under TBL excitation. Reference results calculated using the approach in [27]—**a** $0.5 \times 0.3\,\mathrm{m}^2$ isotropic plate; $U_c = 180\,\mathrm{m/s}$. **b** $0.82 \times 0.58\,\mathrm{m}^2$ sandwich plate; $U_c = 160\,\mathrm{m/s}$

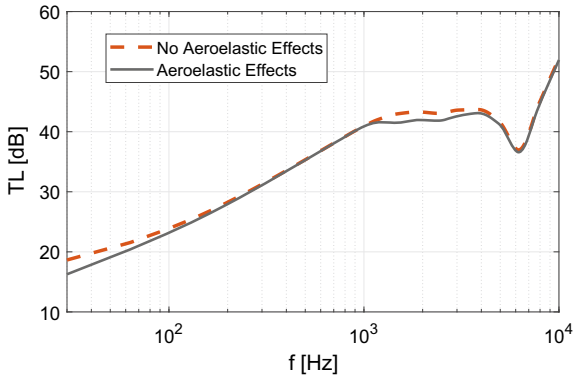

Fig. 13 Sound transmission under a supersonic turbulent boundary layer load (Mach 1.3) for a flat panel ($0.58 \times 0.4\,\mathrm{m}^2$)

thick core (E = 0.145 GPa, $\nu = 0.2$, $\rho = 110.4$ Kg/m^3). Both the aerodynamic and acoustic coincidences are described in frequency and the averaged amplitude values are properly identified.

In Fig. 13, the sound transmission loss of the same aluminium structure is simulated with and without aeroelastic effects. A supersonic flow is simulated (Mach 1.3) and a Cockburn-Robertson TBL model is used [9], being the most suited for this speeds. The supersonic flow is simulated since the mean flow effects are here presented for the Piston-Theory. Differences are observed in the low frequency region and also before the acoustic coincidence ($\approx$ 6 kHz). The drop caused by the critical aerodynamic frequency is hardly visible being close to the acoustic coincidence ($\approx$ 6.5 kHz).

5.1 Limits of the Integration

The presented numerical method, requires some care on convergence aspects.

First the cell must have a size coherent with a proper description of the structural wavelengths, at the maximum frequency of analysis. Here, at least 6 elements per (minimum) wavelength are used. In addition, the integration scheme in Eq. 44 must be carried out using a proper mesh in the wavenumber space, to describe the wavenumber spectrum of the excitation model of interest, at each frequency step. No general approach is available since, depending on the characteristics of the load, a coarser or finer meshing of the wavenumber space can be a good compromise solution between accuracy and calculation time.

In the work by Maxit [36], a specific case for a flat plate under turbulent boundary layer is investigated and some rules are given with respect to the wavenumber sampling of the load. In that case, it is suggested to take, as limits of integration, the maximum between the flexural wavenumber and the convective one, for the streamwise direction, and the maxim value of the structural bending wavenumber, for the cross-wise direction. These solutions, which are justified by the filtering effects of the structure, and thus represent an approximation of the total response, are not always applicable. In fact, when a complex media (i.e multi-layered, ribbed, curved, etc.) is analysed, some coupled bending wavemodes might arise in the frequency band of interest and these can be equally excited by the turbulent layer load. Moreover, to set the choice of the integration limits on maximum frequency of analysis, as in [36], is computationally inefficient. The convective wavenumbers, as the structural ones connected to dispersive waves, are frequency dependent and, therefore, if the wavenumber resolution is fixed (as in [36]), keeping large integration limits even in the lower frequency bands would induce a useless higher computational cost. On the other hand, with respect to the wavenumber sampling, a general rule, to identify the correct resolution, is not given and a trial-error approach is suggested before launching the simulations [36].

Nevertheless, the present developments can be considered as an evolution of the work done in [36] since they are in the same research line aiming at the same goal. In this framework, a study on different criteria based solely on the fluid operator, is conducted for two different turbulent boundary layer models: the Corcos model [10] and the Chase one [7]. Two approaches are initially followed: first the wavenumber space is sampled using a fixed number of points in k_X and k_Y, for each frequency; then a fixed wavenumber resolution is used.

5.1.1 Corcos TBL Model

Four integration domains are described in Table 3 and Fig. 14 and they are valid for each frequency step. The use of reduced integrations limits stands in using the advantage coming from the symmetry of the wavenumber spectra of some excitation models, as the Corcos one (which is also used in this study). Differently from [36],

Table 3 Integration limits in the wavenumber domain (see Fig. 14)

	I	II	III	IV
$k_{X,min}$ $[m^{-1}]$	0	$-1.9\ \omega\ /\ U_c$	0	$-1.9\ \omega\ /\ U_c$
$k_{X,max}$ $[m^{-1}]$	$1.9\ \omega\ /\ U_c$	$1.9\ \omega/U_c$	$1.9\ \omega\ /\ U_c$	$1.9\ \omega\ /\ U_c$
$k_{Y,min}$ $[m^{-1}]$	0	0	$-1.9\ \omega\ /\ U_c$	$-1.9\ \omega\ /\ U_c$
$k_{Y,max}$ $[m^{-1}]$	$1.9\ \omega\ /\ U_c$	$1.9\ \omega/U_c$	$1.9\ \omega\ /\ U_c$	$1.9\ \omega\ /\ U_c$

the scaling factor for the limits of integration is assumed to be 1.9 (Table 3). The results in Fig. 15 show the transmission loss for the same isotropic plate tested in Fig. 12a, when the wavenumber spectrum is sampled first with a coarse scheme (50 × 50 mesh) and then with a finer one (120 × 120 mesh). In using integration limits that exclude the lowest amplitude sector of the wavenumber spectrum of the load, which coincides with the reverse-stream-wise wavenumber components ($k_x \leq 0$; as Domain III; Table 3), the sound transmission levels are not affected. The integration of Eq. 44, being the ratio of equally weighted integrations, allows the use of symmetric domains (as Domain I or II; Table 3), with excellent accuracy even if coarse wavenumber meshes are used for the integration. On the contrary, when higher limits have to be imposed, a finer mesh is needed to avoid aliasing (see Domain IV in Fig. 15a). The computational cost in Fig. 15 is kept constant since the same mesh is used for each frequency.

It is worth to underline that, the use of Domain III is physically justified by the joint-acceptance of Corcos-like TBL models, which have a dominant amplitude of the spectra in the positive stream-wise direction, inducing dominant wavenumber components of the structural response in the positive k_x sector. Differently, the use of Domain I and II, derives from pure mathematical considerations on the form of the weighted integration in Eq. 44, which gives band-averaged sound transmission levels. In fact, for a purely structural response in weak coupling conditions, as in [13, 27, 30, 36], the use of these reduced domains as I and II (Fig. 14) would reduce the accuracy of the response, especially in the anti-resonance regions, due to an incomplete description of the single structural modes for the cutting of the negative-cross-wise structural wave components in the solution.

Differently, in Fig. 16, a fixed wavenumber resolution is kept. This approach increases, at each frequency step, the mesh size in the wavenumber domain and, thus, the computational cost of the integration, depending on the wavenumber limits of integration. In this case, thus, the integration over the domain I, II or III (Table 3) can speed up the total computation. In Fig. 16 it is observed how a finer resolution in the wavenumber domain gives a better accuracy, especially in the low frequency domain. This effect is physically justified by the enlargement of the boundaries of the convective region versus frequency. For a fixed wavenumber resolution, the smoother shape of the wavenumber spectrum, based on the model of Corcos, at higher frequencies, helps the predictive power of coarser resolutions.

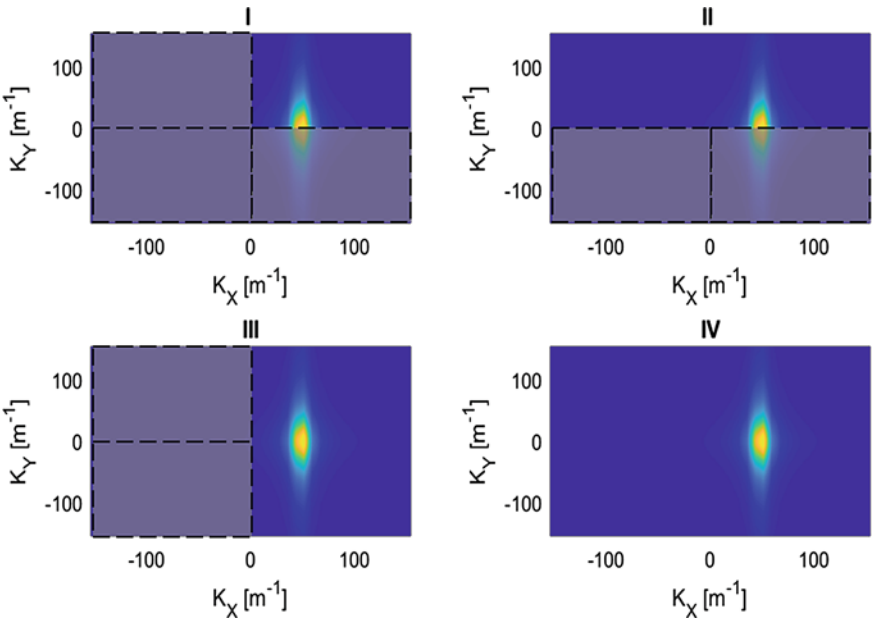

Fig. 14 The wavenumber spectra of a TBL load (Corcos: U_c = 130 m/s; f = 1 kHz). The four solutions correspond to the four integration tests performed with variable domains in Eq. 44

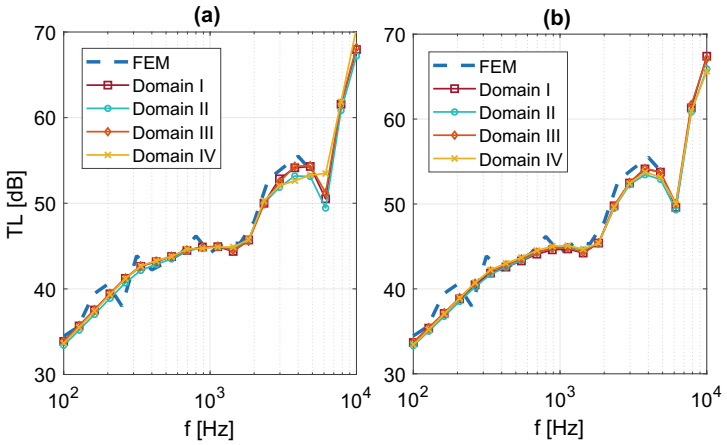

Fig. 15 The sound transmission of a flat isotropic panel loaded with TBL (Corcos: U_c = 190 m/s). The four integration domains is Fig. 14 are compared with a fixed mesh in the wavenumber domain. Mesh: **a** 50 × 50; **b** 120 × 120

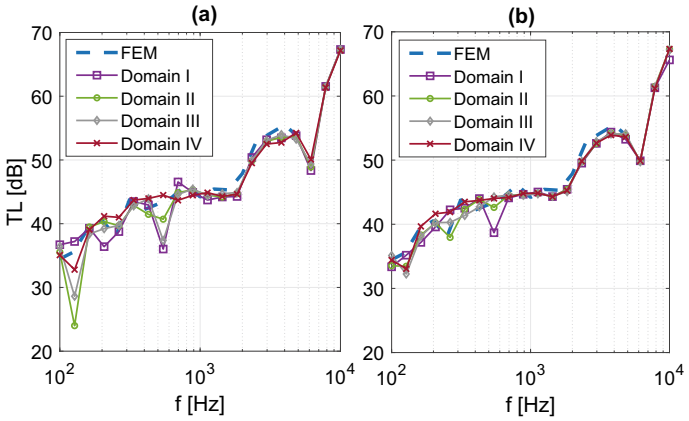

Fig. 16 The sound transmission of a flat isotropic panel loaded with TBL (Corcos: $U_c = 190$ m/s). The fours integration domains is Fig. 14 are compared with a fixed resolution in the wavenumber domain. Sampling: **a** Coarser; **b** Finer

5.1.2 Chase TBL Model

A similar investigation is conducted for the TBL model proposed by Chase, which, differently from the Corcos model, proposed a correlation function with un-separable variables [7, 29]. Differently from the model of Corcos, this model is dependent on the boundary layer thickness (δ), displacement thickness (δ^*) and the friction velocity (u_T). The Chase II formulation [29] implemented here, is a modified version of the original Chase model. A comparison of the normalised wavenumber spectrum, in the positive stream-wise wavenumber space, is presented in Fig. 17: the Chase model presents a narrower convective peak and lower relative amplitudes at high and low wavenumbers.

First, in Fig. 18a a comparison among fixed wavenumber meshes of finer sampling, is proposed. The critical frequency, for a convective velocity of 80 m/s, 380 Hz and is correctly captured in the TL curve. The sensitivity of the solutions is larger around the acoustic coincidence (6 kHz) since the Chase model (Chase II) is characterised by strong derivatives versus the cross-wise wavenumber components. Similarly, in Fig. 18b, the effect of the limits of integration are investigated using the domains described in Table 3. As for the Corcos model, the domain III (Table 3), physically justified by the form of the wavenumber spectrum of the Chase model, gives excellent results. Differently, enlarged domains as IV (Table 3), require finer meshes: in this case, in opposition to the case of Corcos, the effects are visible at higher frequencies.

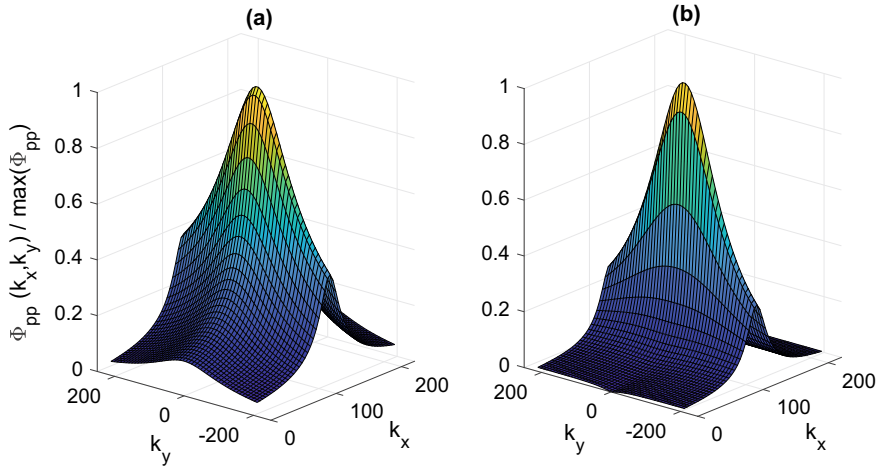

Fig. 17 Normalised wavenumber spectrum of the TBL model (f = 1.5 kHz; U_c = 80 m/s) **a** Corcos [10]; **b** Chase II [7]

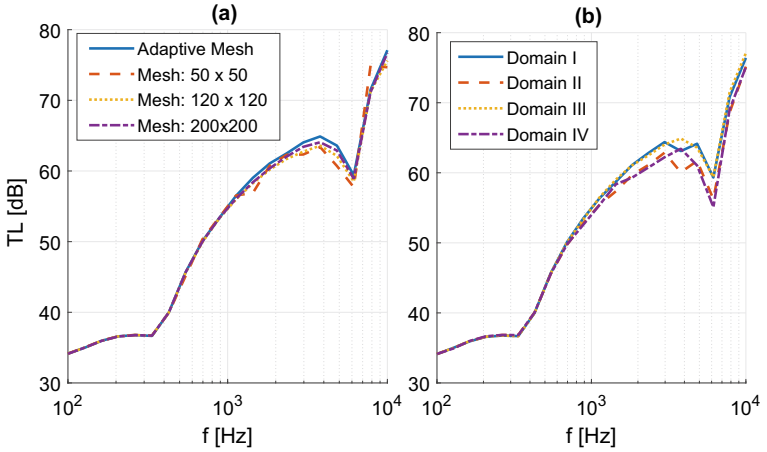

Fig. 18 The sound transmission of a flat isotropic panel loaded with TBL (Chase II: U_c = 80 m/s) **a** Comparison of mesh sizes; **b** Comparison of integration domains for a 100 × 100 mesh (Fig. 14). Flow data (see [29]): δ = 0.027 m; δ^* = 0.0018 m; u_T = 1.9 m/s

5.2 *The Influence of the Cross-Flow Components*

It is interesting to verify if the reduced cross-wise amplitude gradient of the wavenumber spectra, around the convective ridge region of the Corcos and Chase model, with respect to the stream-wise component, allows the use of larger sampling in the cross-flow direction. A simple example is reported in Fig. 19 where two computations are presented, with a fine stream-wise sampling and a larger cross-wise one and vice-

versa. A full integration domain is used (Domain IV; Table 3). The results demonstrate that, in the case of Corcos (Fig. 19a), the stream-wise resolution has a higher impact than the cross-wise one. Thus, a strong speed-up of the computation, can be achieved by using larger cross-wise sampling and a restricted integration domain, making use of the symmetry of the loading wavenumber spectra and the smoother decay of the convective region in the cross-wise direction. However, as shown in Figs. 15 and 16, some sensitivity and variations are observed below the aerodynamic coincidence, which is the frequency band where the structural bending wavenumber is higher than the convective one. In these frequency bands, an integration criterion, based solely on the load, might lead to a critical approximation, because the structural wavelength is lower than the convective one. On the other hand, a criterion based just on the excitation model has the advantage of not being case-dependent and not requiring an a-priori the knowledge of the structural filtering effects.

When the model of Chase (Fig. 19b) is used instead, the sensitivity of the solutions seems to be higher for the cross-wise wavenumber components. As said, this can be addressed to strong amplitude gradients of the model in the acoustic region, which lead to a deficient description, not in accordance with many experimental data, as discussed extensively by Graham [29]. The convective region, on the other hand, does not seem to be sensitive to directional sampling parameters and is always well described.

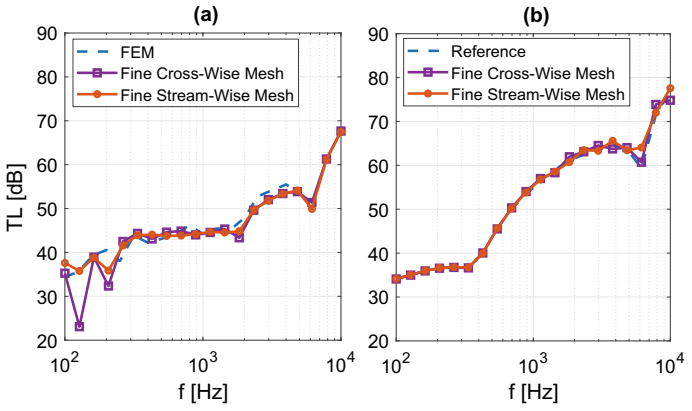

Fig. 19 The sound transmission of a flat isotropic panel loaded with TBL. The wavenumber sampling is studied for single stream-wise and cross-wise resolutions. TBL Model: **a** Corcos, U_c = 190 m/s; **b** Chase II, U_c = 80 m/s

5.3 A Comparison of Different TBL Models

Many works, dealing with flow-induced vibrations, compare the auto and cross correlation function of different TBL models [29]. Here, using the approach described in the present work, some of the most commonly used TBL models are compared in terms of induced noise on a flat isotropic plate. The choice of such a simple structural model is necessary to avoid filtering the effects and peculiarities of each single excitation model. The turbulent boundary models compared here are: Corcos [10], Chase [7], Cockburn–Robertson [9], Smolyakov–Tkachenko [49]. The same unitary auto spectral density is assumed for all the models, in order to evaluate the sensitivity to the cross-correlation model. The results here proposed, should be coherently scaled for the autospectra assumed in each TBL model, if the real transmission loss is the target.

In Fig. 20, the comparison shows how the Corcos model and the Cockburn-Robertson are in agreement almost in the whole frequency band. A higher transmission loss is observed, for the Cockburn-Robertson, around the aerodynamic coincidence, while a good agreement is evident among the other models. The Smolyakov-Tkachenko model, instead, seems the one that induces the highest sound transmission in the superconvective and subsonic frequency region, as in the subconvective one. On the other hand, with the modified Chase model (Chase II) a strong overestimation of the transmission loss, above the convective ridge is simulated. In that case, the drop starts critically before the other models and somewhat re-joins the others just before the aerodynamic coincidence. The results are also in accordance with the ones in [15] where the difference in the radiated power of a plate, associated to each TBL model, is investigated. In accordance to Fig. 20, in [15], the Corcos model induces a higher radiated sound power with respect to the Chase one, in the low frequency range.

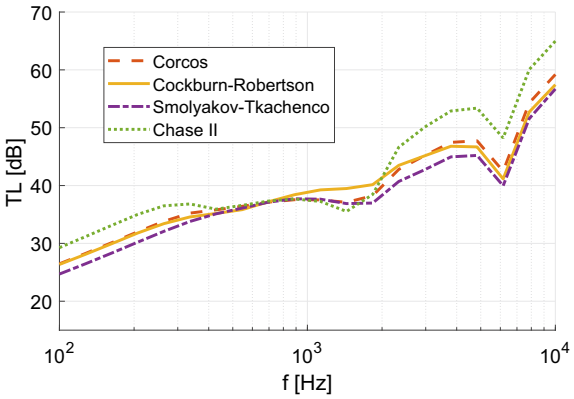

Fig. 20 A comparison of the sound transmission resulting from different of TBL models (U_c = 190 m/s). Flow data (see [29]): $\delta = 0.027$ m; $\delta^* = 0.0018$ m; $u_T = 1.9$ m/s; $\alpha = 0.125$; $\beta = 0.83$

It must be pointed out that each model might fit specific operational conditions and thus a preliminary study of the excitation environment to be simulated, might lead to a better choice in selecting the most adequate model. In respect to this, the status of the research is such that the models are not generally predictive: each of them works well for specific cases and frequency ranges.

6 Experimental Validation for Curved Structures

In this section a comparison with experimental data is performed on two different curved panels, under diffuse acoustic excitation.

The measurements are performed in coupled reverberant-anechoic rooms, following closely the standard (ISO 15186-1: 2000) [24]. The Schroeder frequency is 400 Hz and the acoustic excitation is generated using loudspeakers and white noise signal up to 5.0 kHz. The details of the experimental process are given in [24].

A composite and a stiffened panel are considered as in Fig. 21. The first is 1.54 m-long and 1.62 m-large, with a 0.94 m curvature, while the ribbed is made of aluminium and is 1.45 m-long and 1.70 m-large, with a 1.30 m curvature. Additional data on material and geometry are included in Tables 4 and 5.

The composite panel is modelled using 7 solid elements through-thickness; the curvature is simulated using the approach described in Eq. 5, with a ring frequency of

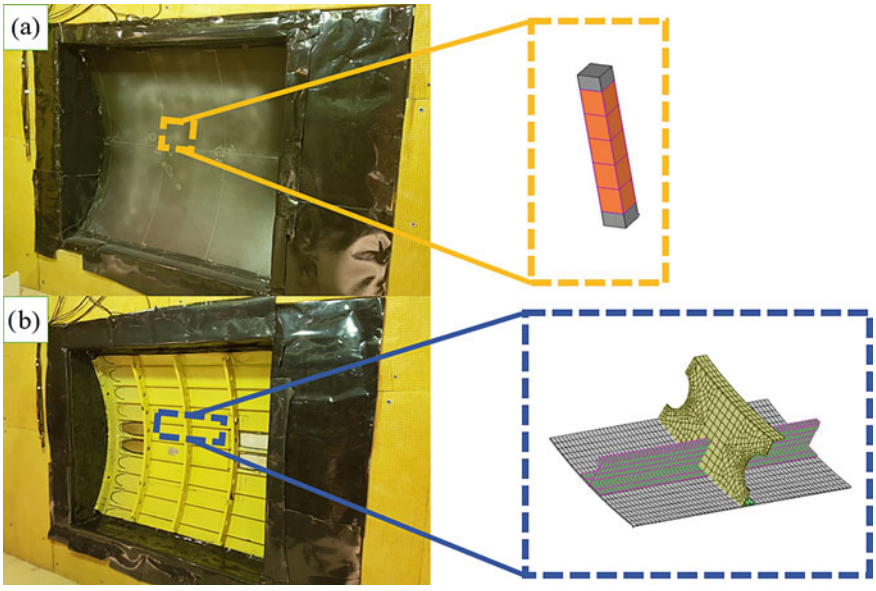

Fig. 21 The panels mounted in the testing facility [24]: **a** Thick sandwich panel with unit cell; **b** Ribbed fuselage panel with unit cell

Table 4 Curved composite panel: material data

	Skins	Core
E_1 (GPa)	46.0	0.01×10^{-3}
E_3 (GPa)	46.0	0.179
$G_{1,2}$ (GPa)	17.7	1.0×10^{-3}
$G_{1,3}$ (GPa)	17.7	26.0×10^{-3}
$G_{2,3}$ (GPa)	17.7	56.0×10^{-3}
$\nu_{1,2}$	0.3	0.45
$\nu_{1,3}$	0.3	0.01
ρ (kg/m^3)	1570	64
h (mm)	0.98	25.5

Table 5 Geometrical data of the curved fuselage panel

	Frames	Stringers	Skin
Thickness (mm)	1.8	1.2	1.2
Height (mm)	72	28	
Spacing (mm)	40.6	15.2	

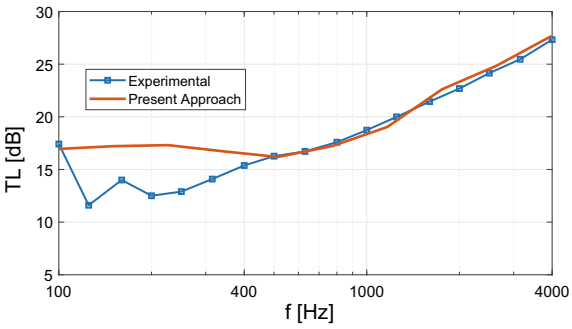

Fig. 22 The sound transmission loss for a curved composite panel under diffuse acoustic field load. Reference measurements from [24]

≈500 Hz. The load, which is a diffuse acoustic field is synthesised using Eq. 44. The agreement with measurements in Fig. 22 is excellent above the Schroeder frequency. The structural damping is simulated to be 3% in the whole frequency band (from measurements in [50]), to simulate the added damping from the installation; this is visible in the transmission loss measurements' drops being very smooth both at the ring frequency (≈500 Hz) and acoustic coincidence (≈1.5 kHz). Discrepancies in the lower frequency bands are confined below the cut-on frequency of the reverberant room.

The last and most complex validations are carried out on the ribbed fuselage panel in Fig. 21. The unit cell (illustrated in Fig. 21) is modelled using shell elements, while substructures as joints are not modelled. A modal order reduction scheme is employed

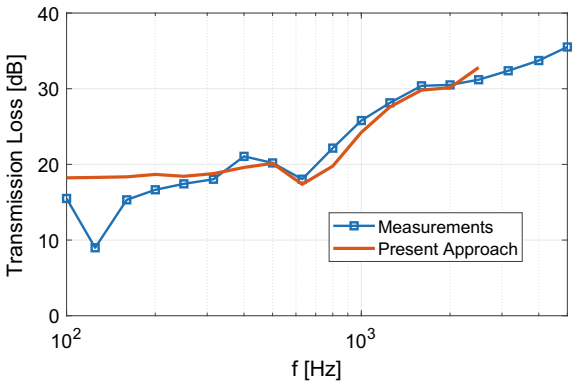

Fig. 23 The sound transmission loss for a ribbed fuselage panel under diffuse acoustic field load. Reference measurements from [24]; Numerical reference from [42]

(see [23]) to reduce the computational effort, still guaranteeing mesh convergence up to 3 kHz.

In Fig. 23, a good agreement with the present method is observed in the 0.3–2.5 kHz frequency band. The numerical solution agrees coherently with the measured data, above the Schroeder frequency. The ring frequency is ≈ 670 Hz and induces a dip in the transmission loss, which is well simulated too. This proves that the simulation of the curvature using Eq. 5 is still a good approximation even for large cell sizes. A pre-curvature of the cell finite element model is not needed unless extremely small radius of curvature are to be simulated.

7 Concluding Remarks

Two numerical approaches are developed and validated. These can be categorised by considering the wave propagation tracked in the structure: for structural vibrations a one-dimensional wave propagation is considered, while for the flow-induced noise a two-dimensional wave propagation is analysed.

For structural vibrations, the main achievements with respect to the previous literature, are linked to a reduced modelling complexity and the release of mesh constraints in the periodicity/homogeneity direction. This allows to keep the same accuracy of a standard finite element approach while reducing the computational cost of the calculation. The formulations developed are quite general and applicable for flat, curved and axisymmetric structures even in presence of impedance variations along the direction of wave propagation. Differently, the literature is limited to simple geometries and reduced frequency bands to constrain the computational cost.

In terms of flow-induced noise, the method is generally applicable independently on the curvature, load model and model homogeneity/heterogeneity. Validations are provided with numerical and experimental data for acoustic and aerodynamic load, for flat and curved structures. A real aircraft fuselage panels is also considered and

the results validated in terms of transmission loss. The method requires a simple FE modelling (unit cell) and provides accurate band-averaged results. The sensibility of the approach to meshing and wavenumber resolutions is also investigated.

The method allows also the introduction of mean-flow effects (aeroelastic coupling) at cell scale; this is only briefly introduced here.

However, some drawbacks are present in the developed methodologies. For example, in the 1D approach, the increasing number of operations for increasing number of target degrees of freedom. For what concerns the 2D approach, the increasing computational cost if a proper baffled window integration has to be calculated for finite size effects, and the required modal order reduction at cell scale if the model has too many internal degrees of freedom.

Acknowledgements This project has received funding from the European Union Horizon 2020 research and innovation programme under the Marie Sklodowska-Curie grant agreement No. 675441.

References

1. J. Allard, N. Atalla, Propagation of sound in porous media: modelling sound absorbing materials. Wiley (2009). https://doi.org/10.1002/9780470747339
2. W. Bhat, Flight test measurement of measurement of exterior turbulent boundary layer pressure fluctuations on boeing model 737 airplane. J. Sound Vib. **14**(4), 439–457 (1971)
3. F. Birgersson, N. Ferguson, S. Finnveden, Application of the spectral finite element method to turbulent boundary layer induced vibration of plates. J. Sound Vib. **259**(4), 873–891 (2003). https://doi.org/10.1006/jsvi.2002.5127, http://www.sciencedirect.com/science/article/pii/S0022460X02951278
4. D.E. Bishop, Cruise flight noise levels in a turbojet transport airplane. Noise Control **7**(2), 37–42 (1961). https://doi.org/10.1121/1.2369437
5. F. Bloch, Über die quantenmechanik der elektronen in kristallgittern. Zeitschrift für Physik **52**(7), 555–600 (1929). https://doi.org/10.1007/BF01339455
6. W.K. Bonness, J.B. Fahnline, P.D. Lysak, M.R. Shepherd, Modal forcing functions for structural vibration from turbulent boundary layer flow. J. Sound Vib. **395**, 224–239 (2017). https://doi.org/10.1016/j.jsv.2017.02.023, http://www.sciencedirect.com/science/article/pii/S0022460X17301177
7. D. Chase, Modelling the wavevector-frequency spectrum of turbulent boundary layer wall pressure. J. Sound Vib. **70**(1), 29–67 (1953). https://doi.org/10.1016/0022-460X(80)90553-2
8. E. Ciappi, F. Magionesi, S.D. Rosa, F. Franco, Analysis of the scaling laws for the turbulence driven panel responses. J. Fluids Struct. **32**, 90–103 (2012). https://doi.org/10.1016/j.jfluidstructs.2011.11.003
9. J. Cockburn, J. Robertson, Vibration response of spacecraft shrouds to in-flight fluctuating pressures. J. Sound Vib. **33**(4), 399–425 (1974). https://doi.org/10.1016/S0022-460X(74)80226-9
10. G. Corcos, Resolution of pressure in turbulence. J. Acoust. Soc. Am. **35**, 192–199 (1963). https://doi.org/10.1121/1.1918431
11. V. D'Alessandro, Investigation and assessment of the wave and finite element method for structural waveguides. PhD thesis, University of Naples Federico II (2014). http://www.fedoa.unina.it/9931/

12. S. De Rosa, F. Franco, E. Ciappi, A simplified method for the analysis of the stochastic response in discrete coordinates. J. Sound Vib. **339**, 359–375 (2015). https://doi.org/10.1016/j.jsv.2014.11.010
13. S. De Rosa, F. Franco, Exact and numerical responses of a plate under a turbulent boundary layer excitation. J. Fluids Struct **24**, 212–230 (2008). https://doi.org/10.1016/j.jfluidstructs.2007.07.007
14. S. De Rosa, F. Franco, A scaling procedure for the response of an isolated system with high modal overlap factor. Mech Syst Signal Process **22**, 1549–1565 (2008). https://doi.org/10.1016/j.ymssp.2008.01.007
15. S. De Rosa, F. Franco, D. Gaudino, Numerical investigations on the turbulence driven responses of a plate in the subcritical frequency range. Wind Struct. Int. J. **15**(3), 247–261 (2012)
16. E. Dowell, Aeroelasticity of plates and shells. *Mechanics: Dynamical Systems* (Springer, Netherlands, 1974). https://books.google.fr/books?id=qRpof4bV-VoC
17. C. Droz, J.P. Laine, M. Ichchou, G. Inquiete, A reduced formulation for the free-wave propagation analysis in composite structures. Compos. Struct. **113**, 134–144 (2014). https://doi.org/10.1016/j.compstruct.2014.03.017
18. E.H. Dowell, C. Ventres, Flutter of low aspect ratio plates. AIAA J. **8**(6), 1162–1164 (1970). https://doi.org/10.2514/3.5858
19. I. Elishakoff, *Probabilistic Method in Theory of Structures* (Wiley, New York, 1983). https://doi.org/10.2514/3.48790
20. F. Errico, S. De Rosa, F. Franco, G. Petrone, M. Ichchou, Aeroelastic effects on the wave propagation and sound transmission of plates and shells. AIAA J. **58**(5) (2019). https://doi.org/10.2514/1.J058722
21. Errico, F., Ichchou, M., De Rosa, S., Bareille, O., Franco, F.: The modelling of the flow-induced vibrations of periodic flat and axial-symmetric structures with a wave-based method. J. Sound Vib. **424**, 32–47 (2018). https://doi.org/10.1016/j.jsv.2018.03.012
22. F. Errico, M. Ichchou, S. De Rosa, O. Bareille, F. Franco, A WFE and hybrid FE/WFE technique for the forced response of stiffened cylinders. Adv. Aircr. Spacecr. Sci. Int. J. **5**(1), 1–16 (2018). https://doi.org/10.12989/aas.2018.5.1.0012
23. F. Errico, M. Ichchou, F. Franco, S. De Rosa, O. Bareille, C. Droz, Schemes for the sound transmission of flat, curved and axisymmetric structures excited by aerodynamic and acoustic sources. J. Sound Vib. **476**, 221–238 (2019). https://doi.org/10.1016/j.jsv.2019.05.041
24. F. Errico, G. Tufano, O. Robin, N. Guenfoud, M. Ichchou, N. Atalla, Simulating the sound transmission loss of complex curved panels with attached noise control materials using periodic cell wavemodes. Appl. Acoust. **156**, 21–28 (2019). https://doi.org/10.1016/j.apacoust.2019.06.027, http://www.sciencedirect.com/science/article/pii/S0003682X1930177X
25. S. Finnveden, Evaluation of modal density and group velocity by a finite element method. J. Sound Vib. **273**(1), 51–75 (2004). https://doi.org/10.1016/j.jsv.2003.04.004, http://www.sciencedirect.com/science/article/pii/S0022460X03008897
26. S. Finnveden, F. Birgersson, U. Ross, T. Kremer, A model of wall pressure correlation for prediction of turbulence-induced vibration. J. Fluids Struct. **20**(8), 1127–1143 (2005). https://doi.org/10.1016/j.jfluidstructs.2005.05.012, http://www.sciencedirect.com/science/article/pii/S0889974605000885
27. F. Franco, S. De Rosa, E. Ciappi, Numerical approximations on the predictive responses of plates under stochastic and convective loads. J. Fluids Struct. **42**, 296–312 (2013). https://doi.org/10.1016/j.jfluidstructs.2013.06.006
28. S. Ghinet, N. Atalla, H. Osman, Diffuse field transmission into infinite sandwich composite and laminate composite cylinders. J. Sound Vib. **289**, 745–778 (2006). https://doi.org/10.1016/j.jsv.2005.02.028
29. W. Graham, A comparison of models for the wavenumber-frequency spectrum of turbolent boundary layer pressures. J. Sound Vib. **206**(4), 541–565 (1997). https://doi.org/10.1006/jsvi.1997.1114
30. S. Hambric, Y. Hwang, W. Bonness, Vibrations of plates with clamped and free edges excited by low-speed turbulent boundary layer flow. J. Fluids Struct. **19**(1), 93–110 (2004). https://doi.org/10.1016/j.jfluidstructs.2003.09.002

31. M. Ichchou, O. Bareille, Y. Jacques, Energy predictions of turbulent boundary layer induced mid-high frequency structural vibrations. J.. Wind Eng. Ind. Aerodyn. **97**(2), 63–76 (2009). https://doi.org/10.1016/j.jweia.2008.11.001, http://www.sciencedirect.com/science/article/pii/S0167610508001761
32. M. Ichchou, B. Hiverniau, B. Troclet, Equivalent rain on the roof loads for random spatially correlated excitations in the mid frequency range. J. Sound Vib. **322**, 926–940 (2009). https://doi.org/10.1016/j.jsv.2008.11.050
33. F. Leppington, E. Broadbent, K. Heron, The acoustic radiation efficiency from rectangular plates. Proc. R. Soc. **382**, 245–271 (1982). https://doi.org/10.1098/rspa.1982.0100
34. Y. Li, Y. Zhang, D. Kennedy, Random vibration analysis of axially compressed cylindrical shells under turbulent boundary layer in a symplectic system. J. Sound Vib. **406**, 161–180 (2017). https://doi.org/10.1016/j.jsv.2017.06.018
35. E. Manconi, B.R. Mace, Modelling wave propagation in two dimensional structures using finite element analysis. J. Sound Vib. **318**(45)
36. L. Maxit, Simulation of the pressure field beneath a turbulent boundary layer using realisations of uncorrelated wall plane waves. J. Acoust. Soc. Am. **140**, 1268–1285 (2016)
37. J.M. Mencik, On the low- and mid-frequency forced response of elastic structures using wave finite elements with one-dimensional propagation. Comput. Struct. **88**, 674–689 (2010). https://doi.org/10.1016/j.compstruc.2010.02.006
38. J.M. Mencik, M. Ichchou, Wave finite elements in guided elastodynamics with internal fluid. Int. J. Solids Struct. **44**(7.8), 2148–2167 (2007). https://doi.org/10.1016/j.ijsolstr.2006.06.048
39. J. Miles, On the aerodynamic instability of thin panels. J. Aeronaut. Sci. **23**(8), 771–791 (1956)
40. G. Mitrou, N. Ferguson, J. Renno, Wave transmission through two-dimensional structures by the hybrid fe/wfe approach. J. Sound Vib. **389**, 484–501 (2017). https://doi.org/10.1016/j.jsv.2016.09.032, http://www.sciencedirect.com/science/article/pii/S0022460X16305004
41. U. Orrenius, V. Cotoni, A. Wareing, Analysis of sound transmission through aircraft fuselages excited by turbulent boundary layer or diffuse acoustic pressure fields, in *38th International Congress and Exposition on Noise Control Engineering 2009, INTER-NOISE 2009*, vol. 4 (2009), pp. 2637–2645
42. U. Orrenius, H. Liu, A. Wareing, S. Finnveden, V. Cotoni, Wave modelling in predictive vibro-acoustics: applications to rail vehicles and aircraft. Wave Motion **51**(4), 635–649 (2014). https://doi.org/10.1016/j.wavemoti.2013.11.007
43. J. Renno, B. Mace, Calculating the forced response of cylinders using the wave and finite element method. J. Sound Vib. **333**, 5340–5355 (2014). https://doi.org/10.1016/j.jsv.2014.04.042
44. J.M. Renno, B.R Mace, Vibration modelling of structural networks using a hybrid finite element/wave and finite element approach. Wave Motion **51**(4), 566–580 (2014). https://doi.org/10.1016/j.wavemoti.2013.09.001
45. D. Rhazi, N. Atalla, A simple method to account for finite size effects in the transfer matrix method. J. Acoust. Soc. Am. **127**(2), EL30–EL36 (2010). https://doi.org/10.1121/1.3280237
46. J. Rocha, Impact of the chosen turbulent flow empirical model on the prediction of sound radiation and vibration by aircraft panels. J. Sound Vib. **373**, 285–301 (2016). https://doi.org/10.1016/j.jsv.2016.03.026, http://www.sciencedirect.com/science/article/pii/S0022460X16300013
47. J.L.T. da Rocha, Coupled structural-acoustic analytical models for the prediction of turbulent boundary-layer-induced noise in aircraft cabins. PhD thesis, University of Victoria (2010)
48. W. Rodden, E. Farkas, H. Malcom, A. Kliszewski, Aerodynamic influence coefficients from supersonic strip theory: analytical development and computational procedure. Defense Technical Information Center (1962). https://books.google.fr/books?id=pBi5twAACAAJ
49. A. Smol'yakov, V. Tkachenko, Model of pseudosonic turbulent wall pressures and experimental data. Sov. Phys. Acoust. **37**(6), 627–631 (1991). https://doi.org/10.1121/1.4960516
50. G. Tufano, F. Errico, O. Robin, C. Droz, M. Ichchou, B. Pluymers, W. Desmet, N. Atalla, K-space analysis of complex large-scale meta-structures using the inhomogeneous wave correlation method. Mech. Syst. Signal Process. **135**, 106407 (2020). https://doi.org/10.1016/j.ymssp.2019.106407, http://www.sciencedirect.com/science/article/pii/S0888327019306284

51. M. Villot, C. Guigou, L. Gagliardini, Predicting the acoustical radiation of finite size multi-layered structures by applying spatial windowing on infinite structures. J. Sound Vib. **245**(3), 433–455 (2001). https://doi.org/10.1006/jsvi.2001.3592
52. Y. Waki, B. Mace, B., Brennan, M, Numerical issues concerning the wave and finite element method for free and forced vibrations of waveguides. J. Sound Vib. **327**, 92–108 (2009)
53. K. Waye, On the effects on environmental low frequency noise. Technical report, Department of Environmental Medicine, Goteborg University Publication (1995)
54. C. Zhou, J.P. Laine, M. Ichchou, A. Zine, Wave finite element method based on reduced model for one-dimensional periodic structures. Int. J. Appl. Mech. **7**(2), 32–47 (2015). https://doi.org/10.1142/S1758825115500180

A Hybrid UWPW-FEM Technique for Vibroacoustic Analysis of Panels Subject to a Turbulent Boundary Layer Excitation

Mahmoud Karimi, Laurent Maxit, Paul Croaker, Olivier Robin, Alex Skvortsov, Noureddine Atalla, and Nicole Kessissoglou

Abstract A hybrid uncorrelated wall plane wave (UWPW) and finite element method (FEM) technique is introduced to the predict vibroacoustic response of a panel under turbulent boundary layer (TBL) excitation. The spectrum of the wall pressure fluctuations is evaluated from the TBL parameters and by using semi-empirical models from literature. TBL parameters can be estimated by different means, using theoretical formula, Reynolds-averaged Navier Stokes (RANS) simulations or experimental data. The wall pressure field (WPF) underneath the TBL is then synthesized by realisations of uncorrelated wall plane waves. The FEM is employed to compute the structural and acoustic responses of the panel for each realisation of uncorre-

M. Karimi (✉)
Centre for Audio, Acoustics and Vibration, University of Technology Sydney, Sydney, Australia.
e-mail: Mahmoud.Karimi@uts.edu.au

L. Maxit
Univ Lyon, INSA Lyon, LVA, EA677, 69621 Villeurbanne, France
e-mail: Laurent.Maxit@insa-lyon.fr

P. Croaker · N. Kessissoglou
School of Mechanical and Manufacturing Engineering, The University of New South Wales, Sydney, Australia
e-mail: P.Croaker@unsw.edu.au

N. Kessissoglou
e-mail: N.Kessissoglou@unsw.edu.au

O. Robin · N. Atalla
Groupe d'Acoustique de l'Université de Sherbrooke, Université de Sherbrooke, Sherbrooke, J1K 2R1, Canada
e-mail: Olivier.Robin@USherbrooke.ca

N. Atalla
e-mail: Noureddine.Atalla@USherbrooke.ca

P. Croaker · A. Skvortsov
Maritime Division, Defence Science and Technology, Melbourne, Australia
e-mail: Alex.Skvortsov@dst.defence.gov.au

E. Ciappi et al. (eds.), *Flinovia—Flow Induced Noise and Vibration Issues and Aspects-III*, https://doi.org/10.1007/978-3-030-64807-7_16

lated wall plane waves. The responses are then obtained from an ensemble average of the different realisations. Selection criteria for cut-off wavenumber, mesh size and number of realisation are discussed. Two simply-supported baffled panels under TBL excitation are examined. Numerical results are compared with analytical results using the sensitivity functions of the panels, showing excellent agreement.

1 Introduction

Predicting the vibroacoustic responses of structures subject to random pressure fields is important in naval and aerospace industries. The correct prediction of the vibrational response is crucial to minimise structural fatigue as well as structure-borne radiating noise [1–3]. A large and growing body of literature has investigated the vibrational responses of plates excited by a turbulent flow field in air, including analytical models of infinite and finite plates [4, 5], numerical models [5–11], and from experiments [10]. Further, many researchers have investigated the vibroacoustic responses of planar structures excited by turbulent flow, for example, see Refs. [2–8, 12–26]. To predict the vibroacoustic response of a structure excited by a TBL, the turbulent pressure field should be obtained on the surface of the structure. This can be done using direct numerical simulation (DNS) or large eddy simulation (LES). However, these simulations are computationally very expensive. An alternative approach involves a steady-state RANS solution to predict the TBL parameters [27, 28]. Researchers have shown an increased interest in using RANS. This is due to its capabilities to predict TBL parameter mean values with good fidelity. These parameters can then be used as an input to analytical or semi-empirical models to predict the WPF under the TBL [29–31].

The vibroacoustic response of a structure excited by a TBL depends on the cross spectrum density (CSD) function of the wall pressure fluctuations. Therefore, to correctly describe the partial correlation of the excitation, a large number of frequency response functions needs to be obtained for the distributed points on the surface of structure [7, 9]. To describe the random WPF, a statistical model is required. The coupling between the statistical model and a deterministic numerical model of the structure represents a difficulty in the calculation process. In this work, a hybrid approach is proposed to overcome this difficulty by coupling the UWPW technique to simulate the WPF underneath a TBL and a deterministic method to model the structural-acoustic domain. A deterministic input load to the vibroacoustic solver based on the FEM is computed from each realisation of the WPF. The vibroacoustic response of the panel is then obtained from an ensemble average of the different panel responses. The major advantage of the UWPW technique is that it is a non-intrusive technique which produces deterministic loads. As such, any element-based numerical method can be used in conjunction with the UWPW technique to examine vibroacoustic response of the structure under TBL excitation. For example, the FEM as well as the boundary element method (BEM) can be employed to analyse structural and acoustic responses of the structure subject to a TBL excitation [11, 32, 33].

In this work, criteria for selecting calculation parameters in the hybrid UWPW-FEM technique such as cut-off wavenumber, mesh size and number of realisations are initially discussed. To demonstrate the hybrid technique, two case studies are considered corresponding to two different simply supported plates made of aluminium. The first case study only examines the vibrational response. Acoustic radiation from a panel is also studied in the second case study. Numerical results are compared with analytical results using sensitivity functions, showing excellent agreement. The analytical method is limited in its application to simple panels with simply supported boundary conditions. In contrast, the numerical method can be applied to complex structures with arbitrary boundary conditions.

2 Numerical Formulation

Figure 1 shows an elastic rectangular finite baffled panel excited by a turbulent flow field. It is assumed that the TBL is homogeneous, stationary and fully developed over the panel surface.

The UWPW technique recently introduced by Maxit [32] is used herein to simulate the pressure field beneath a TBL. The pressure beneath a TBL for the l^{th} realisation can be represented by a set of UWPWs at the q^{th} node, $\mathbf{x}^q = (x^q, y^q)$, of an FEM mesh as follows [11, 32, 34]

$$p^l_{\text{inc}}(\mathbf{x}^q, \omega) = \sum_{i=1}^{N_x} \sum_{j=1}^{N_y} \sqrt{\frac{\phi_{pp}(k^i_x, k^j_y, \omega)\delta k_x \delta k_y}{4\pi^2}} e^{\mathrm{i}(k^i_x x^q + k^j_y y^q + \varphi^l_{ij})}, \tag{1}$$

where ω is the angular frequency and φ is a random phase uniformly distributed in $[0\ 2\pi]$. Criteria for selecting the wavenumber resolutions δk_x, δk_y as well as the truncated numbers of plane waves N_x and N_y are discussed in Sect. 3. The CSD can be expressed in terms of the auto spectrum density (ASD) of the pressure field $\Psi_{pp}(\omega)$ and the normalized CSD of the pressure field $\tilde{\phi}_{pp}(\mathbf{k}, \omega)$ as follows [32, 35]

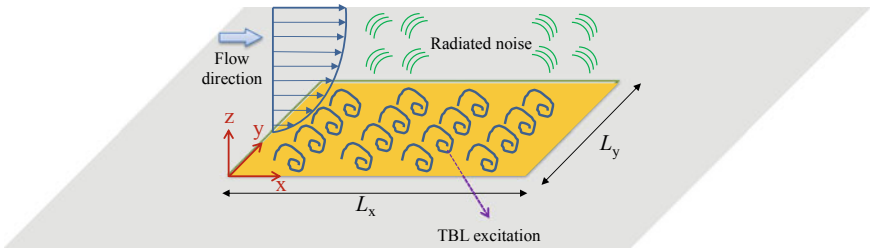

Fig. 1 An elastic baffled panel under TBL excitation

$$\phi_{pp}(\mathbf{k},\omega) = \Psi_{pp}(\omega)\left(\frac{U_c}{\omega}\right)^2 \tilde{\phi}_{pp}(\mathbf{k},\omega), \tag{2}$$

where U_c is the convective velocity. Using equation (1) as the deterministic load, the FEM is now implemented to simultaneously compute the l^{th} realisation of the structural displacement $\mathbf{u}^l$ and the radiated pressure $\mathbf{p}^l$ by solving the following fully coupled structural-acoustic equations [36]

$$\underbrace{\begin{bmatrix} -\omega^2\mathbf{M}_s + \mathbf{K}_s & -\mathbf{H}_{fs} \\ -\omega^2\rho_f c_f^2 \mathbf{H}_{fs}^{\mathrm{T}} & -\omega^2\mathbf{M}_f + \mathbf{K}_f \end{bmatrix}}_{\mathbf{A}} \begin{bmatrix} \mathbf{u}^l \\ \mathbf{p}^l \end{bmatrix} = \begin{bmatrix} \mathbf{f}_s^l \\ \mathbf{f}_f \end{bmatrix}, \tag{3}$$

where $\mathbf{K}$, $\mathbf{H}$ and $\mathbf{M}$ are respectively stiffness, coupling and mass matrices. Subscripts s and f respectively refer to the structure and fluid. $\mathbf{f}_s^l$ is the structural force vector corresponding to the l^{th} realisation of the TBL pressure field given by equation (1). $\mathbf{f}_f$ is the load from acoustic sources in the fluid domain, which is zero for the current case. After the inverse of the coefficient matrix $\mathbf{A}$ is obtained, the panel displacement response and radiated pressure can be computed for each realisation as follows

$$\begin{bmatrix} \mathbf{u}^l \\ \mathbf{p}^l \end{bmatrix} = \mathbf{A}^{-1} \begin{bmatrix} \mathbf{f}_s^l \\ \mathbf{0} \end{bmatrix}. \tag{4}$$

The ASD of the panel velocity S_{vv}, the cross spectrum between the sound pressure and the fluid particle velocity S_{pv_f} due to the TBL excitation are then calculated from the ensemble average of the different realisations by

$$S_{vv} = -\omega^2 \mathrm{E}\left[\mathbf{u}^l \mathbf{u}^{*l}\right]_l, \tag{5}$$

$$S_{pv_f} = \mathrm{E}\left[\mathbf{p}^l \mathbf{v}_\mathbf{f}^{*l}\right]_l, \tag{6}$$

where E[ ] represents the ensemble average of the realisations. The cross spectrum between the sound pressure and the fluid particle velocity can be used to determine the radiated sound power [33].

The computational steps for the proposed hybrid technique is illustrated in Fig. 2. First, an FEM mesh is created from the geometry of the structure. To estimate the TBL parameters over the surface of the structure for a given geometry and flow condition, a RANS simulation, theoretical formula or experimental data can be employed. The TBL parameters are then substituted into semi-empirical models to evaluate the CSD of the WPF. The deterministic WPF is synthesized using the UWPW technique. The WPF is then used as an input to the FEM solver to calculate the structural and acoustic responses. This

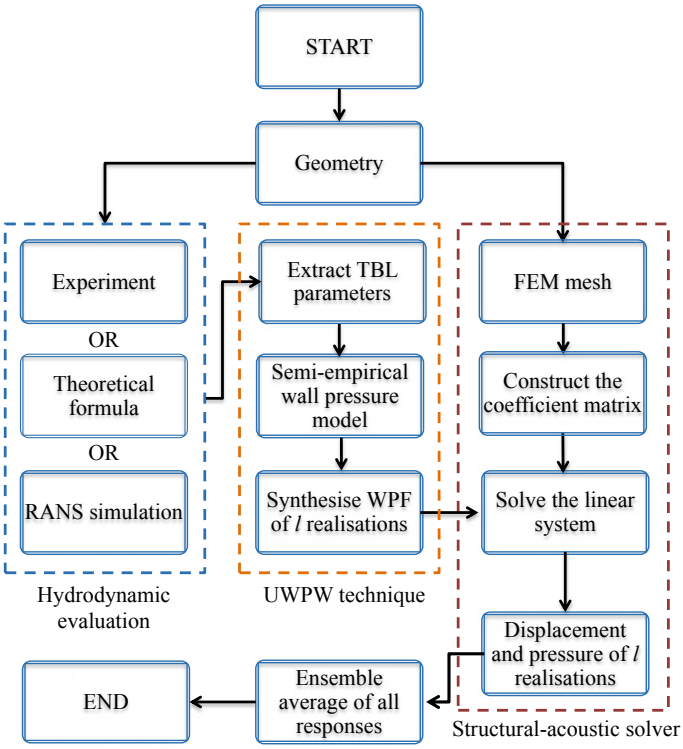

Fig. 2 Flowchart outlining the computational process of the hybrid UWPW-FEM technique

process is repeated for each realisation of the WPF. Finally, the vibroacoustic response of the system is obtained from an ensemble average of the different realisations of the WPFs at each frequency.

3 Selection of Calculation Parameters

3.1 Determination of Cut-Off Wavenumbers and Wavenumber Resolutions

To obtain the panel response, one needs to truncate the wavenumber domain in the x and y directions for Eq. (1). It was shown that in the vibrational response, for the frequencies of interest well above the aerodynamic coincidence frequency, the wavenumbers below or close to the flexural wavenumber of the plate are domi-

nant [7, 25, 32]. At the aerodynamic coincidence frequency, the flexural wavenumber $k_p = (\omega\sqrt{\rho_s h/D})^{1/2}$ equals the convective wavenumber $k_c = \omega/U_c$ and the TBL strongly excites the structure. D is the flexural rigidity, ρ_s is the density and h is the panel thickness. The aerodynamic coincidence frequency is given by $f_c = U_c^2\sqrt{\rho_s h/D}/(2\pi)$ [25]. Hence, a cut-off wavenumber of $2k_{p,\max}$ was used in both the streamwise and spanwise directions, where $k_{p,\max} = (\omega_{\max}\sqrt{\rho_s h/D})^{1/2}$ is the flexural wavenumber of the plate at the maximum frequency of interest, denoted by $\omega_{\max}$. This criterion was chosen based on the fact that for frequencies well above the aerodynamic frequency, the structural response of a panel excited by a TBL can be obtained by neglecting the effect of the convected ridge as confirmed in Refs. [11, 32]. The criterion defined here takes into account the effect of the convective ridge at lower frequencies as the cut-off wavenumber was defined as twice the flexural wavenumber at the highest frequency of interest. The validity of this criterion for evaluating the acoustic response of a panel excited by a TBL was recently examined by Karimi et al. [33]. It was shown that this criterion can be employed to predict the vibroacoustic response of a panel under a TBL excitation.

To represent the spatial variations in the wavenumber space of the wall pressure spectrum, a constant wavenumber resolution can be determined through a trial and error process [11, 32]. Alternatively, a frequency dependent increment in the wavenumber domain could be chosen similar to the work by Karimi et al. [34] for acoustic scattering prediction.

3.2 Criterion for the Mesh Size

The mesh size must be defined such that it enables us to properly describe the hydrodynamic field on the surface of structure. This requires taking into account the spatial distribution of the CSD function of the surface pressure. To synthesize the WPF, the Nyquist sampling theorem for space and wavenumber was adopted. The sampling wavenumber is given by [9]

$$k_s = \frac{2\pi}{\Delta h}, \tag{7}$$

where Δh is the element size. According to the Nyquist theorem, the sampling wavenumber must be at least twice the highest wavenumber of interest, that is, $k_s = 2k_{p,\max}$. Substituting this expression into equation (7), the mesh size is given by

$$\Delta h = \frac{\pi}{k_{p,\max}}. \tag{8}$$

Further, to properly resolve structural modes by considering the FEM mesh size requirement of at least 10 elements per wavelength, the grid size in the streamwise and spanwise directions can be defined as follows

$$\Delta x = \Delta y = \min\left\{\frac{\lambda_{p,\max}}{10}, \frac{\pi}{k_{p,\max}}\right\}, \tag{9}$$

where Δx, Δy are the element size in the x and y directions and $\lambda_{p,\max}$ is the flexural wavenumber of the plate at the maximum frequency of interest. Since $k_{p,\max} = 2\pi/\lambda_{p,\max}$, the mesh size criterion is given by $\Delta x = \Delta y = \lambda_{p,\max}/10$.

4 Verification of the UWPW-FEM Technique

To demonstrate the UWPW-FEM technique, two case studies comprising rectangular baffled panels with simply supported boundary conditions excited by a TBL are examined [11]. Dimensions and material properties of both panels are given in Table 1. The first case study investigates the vibrational response of panel A. The second case study examines the acoustic response of panel B. Numerical results obtained using the UWPW-FEM technique for the both panels are compared with analytical results. An analytical model based on sensitivity functions of the panel was used as a reference solution to verify the numerical method [11, 33]. The fluid density and the kinematic viscosity were set to 1.225 kg/m^3 and 1.5111×10^{-5} m^2/s, respectively. The simulations were conducted using Matlab on a desktop personal computer with 32 GB of RAM and a total of four physical cores. For the UWPW-FEM technique, the WPF was synthesized in Matlab and then imported as a load to the FEM model of the panel in the commercial software COMSOL Multiphysics (v5.3a) using Matlab LiveLink.

Table 1 Dimensions and material properties of the panels

Parameter	Panel A	Panel B
Young's modulus E (GPa)	70	68.9
Poisson's ratio ν	0.3	0.3
Density ρ_s (kg/m^3)	2700	2740
Length L_x (mm)	480	600
Width L_y (mm)	420	525
Thickness h (mm)	3.17	2.4
Damping loss factor η	0.005	0.01

Table 2 TBL parameters for Panel A at flow speeds of 40 m/s, 60 m/s and 80 m/s

Parameter	$U_\infty = 40$ m/s	$U_\infty = 60$ m/s	$U_\infty = 80$ m/s
TBL thickness δ (m)	0.0349	0.0322	0.0304
TBL displacement thickness δ^* (m)	0.0044	0.0041	0.0038
Wall shear stress τ (Pa)	2.5228	5.2341	8.7848

4.1 Synthetic Pressure Field

To obtain the WPF, the Goody model was used to evaluate the ASD function of the WPF [11, 37]. Note that $\Psi_{pp}(\omega)$ is a one-sided angular frequency spectrum. Hence $\Psi_{pp}(\omega)$ was multiplied by 2π to convert it to a one-sided cyclic frequency spectrum density $\Psi_{pp}(f)$. For the normalized CSD function, the Mellen model was employed [38]. The TBL parameters were calculated based on theoretical formula for a flat plate from literature and are given in Table 2 [11]. The convective velocity U_c was approximated as follows [11, 39]

$$U_c \cong U_\infty(0.59 + 0.3e^{-0.89\delta^*\omega/U_\infty}), \tag{10}$$

where U_∞ is the free flow velocity and δ^* is boundary layer displacement thickness. Employing the Goody and Mellen models, different realisations of the WPF were synthesized on the surface of panel A using Eq. (1). Figure 3 shows the visualization of two realisations of the surface pressure field at two discrete resonance frequencies corresponding to 177 Hz and 1005 Hz, for a flow speed of 40 m/s. Figure 3a shows that at low frequencies, a coarse mesh can resolve the waves as they have larger wavelengths. However, at higher frequencies, a finer mesh is needed to properly describe and synthesize the WPF for plane waves with short wavelengths (Fig. 3b). In this work, the criteria defined in Sect. 3.2 for the mesh size ensures that the plane waves with the shortest wavelength corresponding to the highest frequency of interest are adequately resolved.

4.2 Effect of the Number of Realisations

The number of realisations used in the calculation process has significant effect on the accuracy of the UWPW method. This effect has been investigated for acoustic scattering prediction [34], vibrational analysis of a panel [11] and acoustic radiation from a baffled panel [33]. In all of these cases, it was confirmed that 30 realisations is sufficient to obtain the response of the system with the maximum estimated error less than 1 dB for the frequency range considered. For example, the effect of the number of

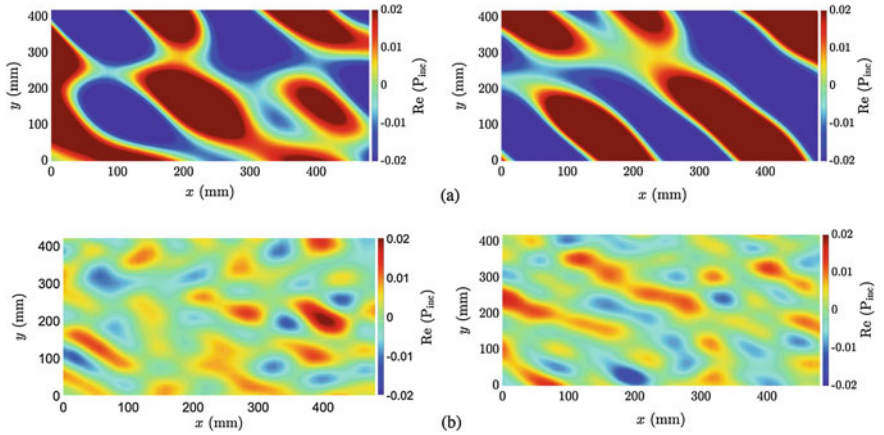

Fig. 3 Two realisations of the WPF (in Pascal) using the Mellen and Goody models for a flow speed of 40 m/s at (**a**) 177 Hz and (**b**) 1005 Hz

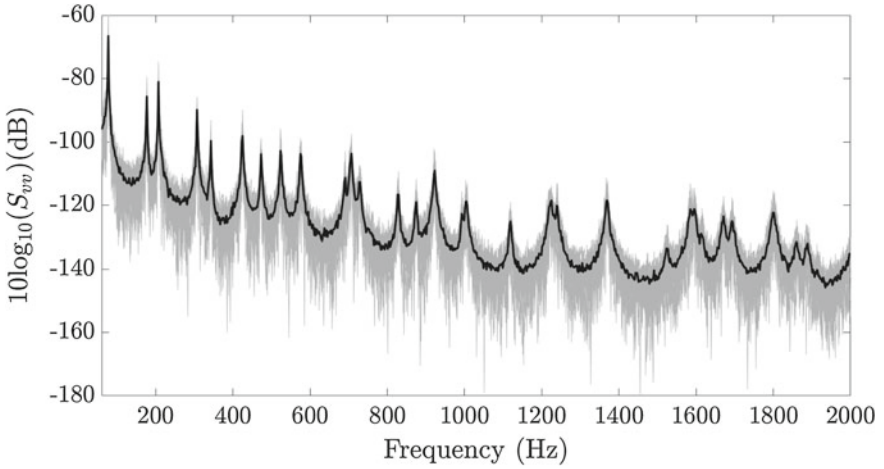

Fig. 4 ASD of the panel velocity predicted numerically using the UWPW-FEM technique for 30 realisations (grey lines), as well as predicted using the average of 30 realisations (black line), for a flow speed of 40 m/s (dB ref. 1 $(m/s)^2/Hz$)

realisations on the structural response of panel A excited by a TBL at a flow speed of 40 m/s is shown in Fig. 4. The spectral level predicted using 30 different realisations is shown in grey lines and the black line represents the predicted results by averaging of 30 realisations. Fig. 5 compares the velocity spectra obtained numerically using the average of 30 realisations with analytical results. The analytical solution described in Ref. [11] is provided as a reference solution. It can be observed from Figs. 4 and 5 that the numerical results become smoother and converge quickly towards the reference solution by increasing the number of realisations.

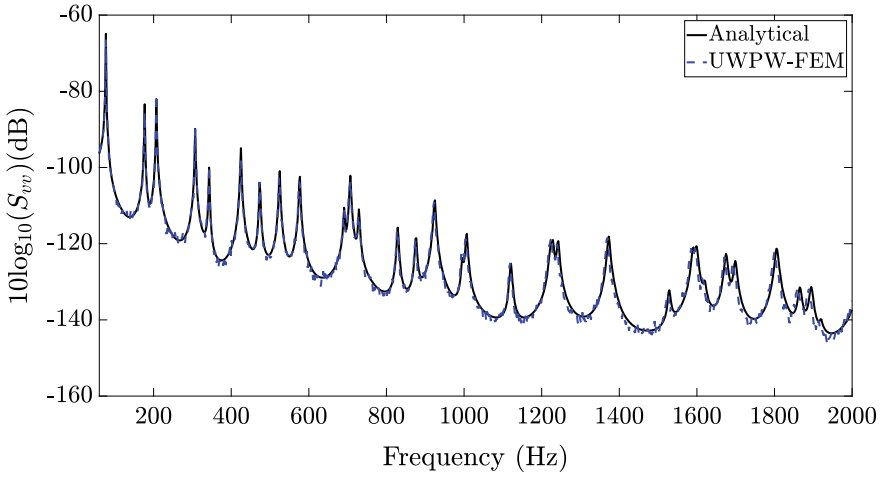

Fig. 5 ASD of the panel velocity predicted numerically using the UWPW-FEM technique by averaging of 30 realisations, as well as predicted analytically, for a flow speed of 40 m/s (dB ref. 1 $(\text{m/s})^2/\text{Hz}$)

4.3 Structural Response

To predict the panel responses, the synthesized WPF was applied as a load to the structural-acoustic solver. Figure 6 presents the predicted velocity spectra using the UWPW-FEM technique as well as the analytically calculated velocity spectra for panel A at flow speeds of 60 m/s and 80 m/s. The vibration of the panel was obtained at ($x = 0.3$ m, $y = 0.33$ m, $z = 0$ m) on the panel surface with respect to the coordinate system shown in Fig. 1. The numerical results are in excellent agreement with analytical results. As expected, with increasing flow speed, the magnitude of the vibrational response of the panel increases. For the parameters chosen here, the aerodynamic coincidence frequency is 66 Hz and 117 Hz for flow speeds of 60 m/s and 80 m/s, respectively.

4.4 Acoustic Response

The hybrid technique was applied to predict the acoustic response of panel B with simply-supported boundary conditions and excited by a TBL. The panel was tested in an anechoic wind tunnel at the Université de Sherbrooke [40]. The experiments were conducted at a free flow speed of 40 m/s. The wall pressure fluctuations of the turbulent flow generated over the baffle were measured by a flush-mounted microphone array as described in [25, 40]. The Mellen model was fitted to the measured WPF using the least square method to estimate the decay rates, α_x and α_y, and the

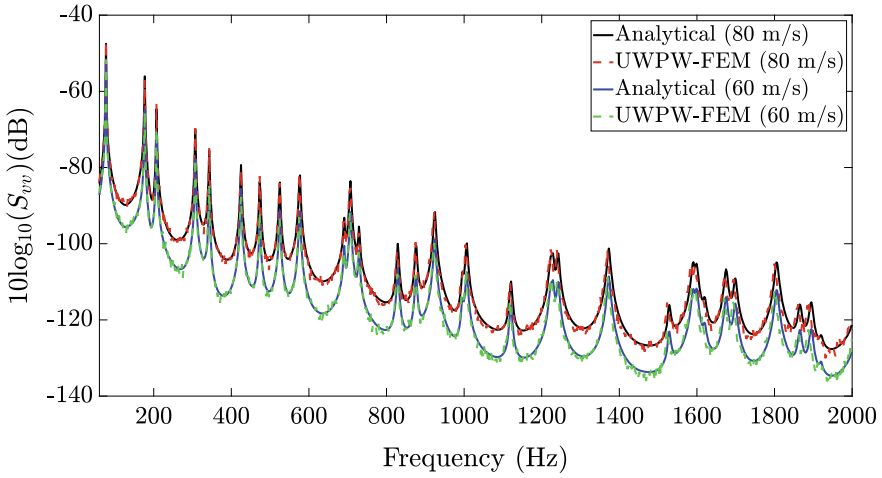

Fig. 6 ASD of the panel velocity for a simply supported plate predicted using the UWPW-FEM technique and analytical formulation, for flow speeds of 60 m/s and 80 m/s (dB ref. 1 $(\text{m/s})^2/\text{Hz}$)

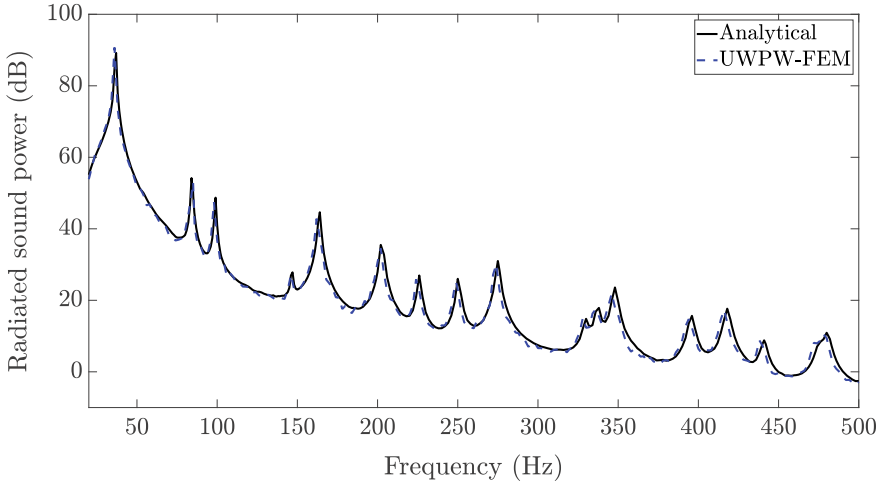

Fig. 7 Sound power spectrum level predicted using the UWPW-FEM technique and analytical formulation for flow speed of $U_\infty = 40$ m/s (dB ref. 1×10^{-12} W/Hz)

convective velocity U_c. The experimentally fitted Mellen model as well as the measured autospectrum of the WPF, presented in Ref. [33], were used for evaluation of the CSD function of the WPF. Numerical prediction of the acoustic power is compared with the analytical results in Fig. 7. It can be seen that numerical results are in excellent agreement with analytical results. Readers are referred to Refs. [11, 33] for detailed discussions on validation of the numerical results with experimental data.

5 Conclusions

An uncorrelated wall plane wave technique has been presented to deterministically synthesize the WPF underneath a TBL from the CSD of the WPF expressed in the frequency-wavenumber domain. The pressure field was then used as an input to an FEM solver to predict vibroacoustic responses of panels under TBL excitation. One of the main advantages of using the non-intrusive UWPW technique in the vibroacoustic solver is that the deterministic WPF is calculated at each FEM nodal point, and can be applied as an input to the FEM or other element-based approaches to evaluate the panel structural-acoustic response. Further, it was shown that the hybrid UWPW-FEM technique produced converged results using small number of realisations. An analytical method based on the sensitivity function was employed to verify the numerically obtained vibroacoustic results for two different simply-supported panels. It was shown that the hybrid UWPW-FEM technique can be confidently used to predict the vibroacoustic responses of panels excited by turbulent flow. Whilst the case studies presented here comprise simple panels with simply supported conditions, the proposed method can be applied to study the vibroacoustic responses of complex panels with arbitrary boundary conditions under TBL excitation. For example, the vibroacoustic response of a stiffened plate under TBL excitation has been recently analysed in Ref [33] using the hybrid UWPW-FEM technique. The technique is also well adapted for investigating the effects of design modifications. Once the WPF fields of the different realisations have been calculated, they can be applied to different panel models to study the influence of the design on the vibroacoustic response. Moreover, in the presence of complex flow conditions, a RANS simulation can be performed for more accurate calculation of the TBL parameters.

Acknowledgements This research was supported by the Australian Government through the Australian Research Council's Discovery Early Career Project funding scheme (project DE190101412).

References

1. R.C. Leibowitz, Vibroacoustic response of turbulence excited thin rectangular finite plates in heavy and light fluid media. J Sound Vib **40**(4), 441–495 (1975)
2. E. Ciappi, S. De Rosa, F. Franco, J.L. Guyader, and S.A. Hambric. *Flinovia - Flow Induced Noise and Vibration Issues and Aspects: A Focus on Measurement, Modeling, Simulation and Reproduction of the Flow Excitation and Flow Induced Response*. EBL-Schweitzer. Springer International Publishing Switzerland, 2014
3. E. Ciappi, S. De Rosa, F. Franco, J.L. Guyader, S.A. Hambric, R.C.K. Leung, A.D. Hanford, *Flinovia-Flow Induced Noise and Vibration Issues and Aspects-II: A Focus on Measurement, Modeling* (Springer International Publishing Switzerland, Simulation and Reproduction of the Flow Excitation and Flow Induced Response, 2018)
4. W. Strawderman, Turbulence-induced plate vibrations: an evaluation of finite and infinite plate models. J Acoust Soc Am **46**(5B), 1294–1307 (1969)
5. S. De Rosa, F. Franco, Exact and numerical responses of a plate under a turbulent boundary layer excitation. J Fluids Struct **24**(2), 212–230 (2008)

6. F. Birgersson, N.S. Ferguson, S. Finnveden, Application of the spectral finite element method to turbulent boundary layer induced vibration of plates. J Sound Vib **259**(4), 873–891 (2003)
7. S. Hambric, Y. Hwang, W. Bonness, Vibrations of plates with clamped and free edges excited by low-speed turbulent boundary layer flow. J Fluids Struct **19**(1), 93–110 (2004)
8. F. Birgersson and S. Finnveden. A spectral super element for modelling of plate vibration. Part 2: turbulence excitation. J Sound Vib, 287(1-2):315–328, 2005
9. C. Hong, K. Shin, Modeling of wall pressure fluctuations for finite element structural analysis. J Sound Vib **329**(10), 1673–1685 (2010)
10. E. Ciappi, S. De Rosa, F. Franco, P. Vitiello, M. Miozzi, On the dynamic behavior of composite panels under turbulent boundary layer excitations. J Sound Vib **364**, 77–109 (2016)
11. M. Karimi, P. Croaker, L. Maxit, O. Robin, A. Skvortsov, S. Marburg, N. Kessissoglou, A hybrid numerical approach to predict the vibrational responses of panels excited by a turbulent boundary layer. J Fluids Struct **92**, 102814 (2020)
12. W. Strawderman, R. Christman, Turbulence-induced plate vibrations: Some effects of fluid loading on finite and infinite plates. J Acoust Soc Am **52**(5B), 1537–1552 (1972)
13. H.G. Davies, Sound from turbulent-boundary-layer-excited panels. J Acoust Soc Am **49**(3B), 878–889 (1971)
14. G. Cousin, Sound from TBL-induced vibrations. In *4th AIAA/CEAS Aeroacoustics Conference*, page 2216, Toulouse, France, June 1998
15. F. Han, L. Mongeau, R. Bernhard, A model for the vibro-acoustic response of plates excited by complex flows. J Sound Vib **246**(5), 901–926 (2001)
16. C. Maury, P. Gardonio, S. Elliott, A wavenumber approach to modelling the response of a randomly excited panel, Part I: General theory. J Sound Vib **252**(1), 83–113 (2002)
17. C. Maury, P. Gardonio, S. Elliott, A wavenumber approach to modelling the response of a randomly excited panel, Part II: Application to aircraft panels excited by a turbulent boundary layer. J Sound Vib **252**(1), 115–139 (2002)
18. D. Mazzoni, An efficient approximation for the vibro-acoustic response of a turbulent boundary layer excited panel. J Sound Vib **264**(4), 951–971 (2003)
19. J. Park, L. Mongeau, T. Siegmund, An investigation of the flow-induced sound and vibration of viscoelastically supported rectangular plates: experiments and model verification. J Sound Vib **275**(1–2), 249–265 (2004)
20. E. Ciappi, F. Magionesi, S. De Rosa, F. Franco, Hydrodynamic and hydroelastic analyses of a plate excited by the turbulent boundary layer. J Fluids Struct **25**(2), 321–342 (2009)
21. B. Liu, Noise radiation of aircraft panels subjected to boundary layer pressure fluctuations. J Sound Vib **314**(3–5), 693–711 (2008)
22. B. Liu, L. Feng, A. Nilsson, M. Aversano, Predicted and measured plate velocities induced by turbulent boundary layers. J Sound Vib **331**(24), 5309–5325 (2012)
23. J. Rocha, Sound radiation and vibration of composite panels excited by turbulent flow: analytical prediction and analysis. Shock and Vibration **2014**, (2014)
24. C. Marchetto, L. Maxit, O. Robin, A. Berry, Vibroacoustic response of panels under diffuse acoustic field excitation from sensitivity functions and reciprocity principles. J Acoust Soc Am **141**(6), 4508–4521 (2017)
25. C. Marchetto, L. Maxit, O. Robin, A. Berry, Experimental prediction of the vibration response of panels under a turbulent boundary layer excitation from sensitivity functions. J Acoust Soc Am **143**(5), 2954–2964 (2018)
26. X. Zhao, B. AI, Z. Liu, and D. Li, A scaling procedure for panel vibro-acoustic response induced by turbulent boundary layer. J Sound Vib, 380:165–179, 2016
27. C. Bailly, P. Lafon, S. Candel, Subsonic and supersonic jet noise predictions from statistical source models. AIAA J **35**(11), 1688–1696 (1997)
28. L. Peltier, S. Hambric, Estimating turbulent-boundary-layer wall-pressure spectra from CFD RANS solutions. J Fluid Struct **23**(6), 920–937 (2007)
29. W.K. Blake, *Mechanics of flow-induced sound and vibration: Complex flow-structure interactions* (Academic Press, Applied Mathematics and Mechanics Series, 1986)

30. Y.T. Lee, W.K. Blake, T.M. Farabee, Modeling of wall pressure fluctuations based on time mean flow field. J Fluid Eng **127**(2), 233–240 (2005)
31. L. Chen, I.R. MacGillivray, Prediction of trailing edge noise based on Reynolds Averaged Navier Stokes solution. AIAA J **52**(12), 2673–2682 (2014)
32. L. Maxit, Simulation of the pressure field beneath a turbulent boundary layer using realizations of uncorrelated wall plane waves. J Acoust Soc Am **140**(2), 1268–1285 (2016)
33. M. Karimi, L. Maxit, P. Croaker, O. Robin, A. Skvortsov, S. Marburg, N. Atalla, N. Kessissoglou, Analytical and numerical prediction of acoustic radiation from a panel under turbulent boundary layer excitation. J Sound Vib (2020). https://doi.org/10.1016/j.jsv.2020.115372
34. M. Karimi, P. Croaker, A. Skvortsov, D. Moreau, N. Kessissoglou, Numerical prediction of turbulent boundary layer noise from a sharp-edged flat plate. Int J Numer Meth Fl **90**, 522–543 (2019)
35. W.R. Graham, A comparison of models for the wavenumber-frequency spectrum of turbulent boundary layer pressures. J Sound Vib **206**(4), 541–565 (1997)
36. P. Davidsson. *Structure-acoustic analysis; finite element modelling and reduction methods*. PhD thesis, Division of Structural Mechanics, LTH, Lund University, Lund, Sweden, 2004
37. M. Goody, Empirical spectral model of surface pressure fluctuations. AIAA J **42**, 1788–1793 (2004)
38. R. Mellen, Wave-vector filter analysis of turbulent flow. J Acoust Soc Am **95**(3), 1671–1673 (1994)
39. M.K. Bull, Wall-pressure fluctuations associated with subsonic turbulent boundary layer flow. J Fluid Mech **28**(4), 719–754 (1967)
40. M. Jenzri, O. Robin, N. Atalla, Vibration of and radiated acoustic power from a simply-supported panel excited by a turbulent boundary layer excitation at low Mach number. Noise Control Eng J **67**(4), 241–251 (2019)

Leveraging Flow-Induced Vibration for Manipulation of Airfoil Tonal Noise

Irsalan Arif, Garret C. Y. Lam, Randolph C. K. Leung, and Di Wu

Abstract A novel method for reduction in the airfoil tonal noise using flow-induced vibrations is explored by using a flush-mounted elastic panel over the suction surface of a NACA 0012 airfoil at low Reynolds number of 5×10^4. The fundamental aim of this approach is to reduce the airfoil tonal noise while maintaining laminar boundary layer over the airfoil with minimum or no penalty on the aerodynamic performance of the airfoil. Direct aeroacoustics simulation using conservation element and solution element method along with linear stability analysis is employed to study the aeroacoustic structural interaction between the flow field and elastic panel. Panel parameters are carefully selected to ensure that the natural frequency of panel in the presence of flow field coincides with the first dominant frequency of naturally evolving boundary layer disturbance on the airfoil suction surface. To gain further insight on the sensitivity of panel parameters on its vibration behavior and magnitude of reduction in tonal noise, a parametric study is also carried out. Contributions of panel density and thickness are found to be dominant in noise reduction. A maximum sound pressure level reduction of 2.74 dB is achieved for the current flow conditions through the proposed strategy.

I. Arif (✉) · G. C. Y. Lam · R. C. K. Leung · D. Wu
Department of Mechanical Engineering, The Hong Kong Polytechnic University, Hung Hom Kowloon, Hong Kong
e-mail: irsalan.arif@connect.polyu.hk

G. C. Y. Lam
e-mail: garret.lam.hk@connect.polyu.hk

R. C. K. Leung
e-mail: randolph.leung@polyu.edu.hk

D. Wu
e-mail: di.wu.wu@polyu.edu.hk

E. Ciappi et al. (eds.), *Flinovia—Flow Induced Noise and Vibration Issues and Aspects-III*, https://doi.org/10.1007/978-3-030-64807-7_17

Nomenculture

A	amplitude of pulse
a	speed of sound
C	panel structural damping coefficient
C_f	coefficient of friction
Cp	coefficient of pressure
c	airfoil chord
c_p	specific heat at constant pressure
D	panel bending stiffness
E	total energy
$\boldsymbol{F}, \boldsymbol{F_v}, \boldsymbol{G}, \boldsymbol{G_v}, \boldsymbol{U}$	flow flux conservation variables
$(f_{bl})_n$	harmonic of natural boundary layer instability
f	frequency
h	panel thickness
K	stiffness of foundation supporting the panel
k	thermal conductivity
L	panel length
M	Mach number
N	panel internal tensile stress
n	mode number
Pr	Prandtl number
p	pressure
q_x, q_y	heat flux
Re	Reynolds number based on airfoil chord
r	radius of pulse
T	panel external tension
t	time
u, v	velocity components along streamwise and transverse directions
w	panel vibration displacement
α	angle of attack
γ	specific heat ratio
ρ	density
$\tau_{xx}, \tau_{xy}, \tau_{yy}$	flow shear stresses
μ	viscosity

List of Acronyms

CFL	= Courant–Friedrichs–Lewy condition
EP	= elastic panel
NR	= non-resonating panel
RS	= Rigid airfoil
rad	= radius of curvature
SPL	= sound pressure level

Superscript

$'$ = perturbation
$\hat{}$ = dimensional quantities

Subscript

0	= freestream condition
$base$	= base flow
far	= far field
le	= leading edge
rms	= root mean square value
te	= trailing edge

1 Introduction

Airfoil self noise is one of the most undesirable phenomenon associated with its flight operations at various flow conditions. Research on the physical mechanism associated with airfoil self-noise generation and its underlying principles has received significant attention from aerospace and fluid mechanics community. Over the years, a number of attempts have been made to explore the mechanism of airfoil tonal noise generation for devices operating with low Reynolds number flow such as Micro Air Vehicles (MAV), wind turbines, and cooling fans etc. The earliest work on studying this phenomenon was carried out by Paterson et al. [1] with NACA 0012 and NACA 0018 airfoil in an open jet wind tunnel. They observed a ladder-like frequency structure of dominant frequency which varied with freestream velocity to the power of 0.8 locally. They attributed this phenomenon to vortex shedding at trailing edge. Later, Tam [2] claimed that a self-excited feedback loop exists between the airfoil trailing edge and some location in the airfoil wake which is responsible for airfoil tonal noise generation. Subsequently, Longhouse [3] proposed that the feedback loop exists between the airfoil trailing edge and some upstream location over the airfoil surface, whereas Arbey et al. [4] observed the existence of feedback loop between the airfoil trailing edge and the location of maximum velocity point on the airfoil surface. Nash et al. [5] performed experimental study with NACA 0012 in a closed wind tunnel and observed that only a single dominant tonal frequency exists without any ladder structure. It was claimed that feedback loop is not a necessary condition for tonal noise generation. Desquesnes et al. [6] carried out a detailed numerical investigation of a NACA 0012 airfoil and confirmed the existence of primary and secondary feedback loops. Furthermore, the most dominant frequency was found to be related to the most amplified boundary layer instability. Later, Jones et al. [7] and Fosas de Pando

et al. [8] also carried out numerical investigations to study the tonal noise phenomenon and boundary layer stability and receptivity mechanisms.

Although, a large amount of research have been carried out to enhance the understanding of the tonal noise generation mechanism, the study on its control and reduction is still being explored. Some of the recent passive methods include modifications on the airfoil trailing edge such as sawtooth [9, 10], serrations [11–13], porous trailing edge [14], flaplets [15] and leading edge modifications [16]. Application of porous trailing edge has been able to reduce the sound pressure level at low frequencies, however, the noise is adversely amplified at high frequencies [14]. Wang [17] applied perforations at trailing edge for noise reduction. However, the aerodynamic performance of the airfoil was severely affected. Hansen et al. [16] reduced the airfoil noise by using leading edge serrations which modified the boundary layer formation over the airfoil. As a collateral effect, the aerodynamic performance was degraded. Modifications in the airfoil geometry has resulted in appreciable noise reduction, however, there are certain limitations associated in their applicability such as manufacturing and performance degradation.

The present study aims to explore a novel approach for tonal noise reduction at low Reynolds number flows by applying a flush mounted elastic panel over the airfoil suction surface. Direct aeroacoustics simulation (DAS) using Conservation Element and Solution Element (CE/SE) along with linear stability analysis (LSA) is employed to study the aeroacoustic-structural interaction between the flow field and elastic panel. The panel is designed in such a way that it weakens the unsteady flow fluctuations within the boundary layer before they scatter as acoustic noise with trailing edge interactions. The panel aims to leverage flow energy absorption by fluid-structure interaction to suppress the flow instabilities and even weaken the acoustic feedback loop. Furthermore, the study also investigates the panel design parameters and their dependence on tonal noise reduction or amplification. In this regard, a parametric study is also carried out to analyze the sensitivity of panel parameters reducing the boundary layer instabilities and subsequent tonal noise reduction.

2 Research Methodology

2.1 Direct Aeroacoustic Simulation

Direct aeroacoustic simulation (DAS) is employed in the present study due to its capability to accurately capture flow and acoustic features. DAS solves unsteady compressible Navier-Stokes (N-S) equations and equation of state simultaneously. Its applicability in aeroacoustic research has been validated by a number of researches including jet flows, cavity and duct flow [18, 19]. To solve the unsteady N-S equations, Conservation Element and Solution Element (CE/SE) method is adopted. CE/SE is a multidimensional method for solving conservation laws with high resolution [20]. Since its inception, it has been successfully applied to simulate various

physical problem including shock interaction, jet noise and acoustic wave propagation [18, 21, 22]. The two dimensional N-S equations in dimensionless strong conservative form can be written as:

$$\frac{\partial \mathbf{U}}{\partial t} + \frac{\partial \left(\mathbf{F} - \mathbf{F}_v\right)}{\partial x} + \frac{\partial \left(\mathbf{G} - \mathbf{G}_v\right)}{\partial y} = 0, \tag{1}$$

The above equation is normalized by reference density, velocity, viscosity, temperature, specific heat at constant pressure c_p in free stream flow and reference chord length. The speed of sound is defined by $\hat{a}_0 = (\gamma \hat{R} \hat{T}_0)^{1/2}$, where $\gamma = 1.4$ and the specific gas constant for air $\hat{R} = 287.058 J/(kgK)$. Re, M and Pr can be calculated by:

$$Re = \hat{\rho}_0 \hat{U}_0 \hat{c}_0 / \hat{\mu}_0;\ M = \hat{U}_0 / \hat{a}_0;\ Pr = \hat{c}_{p,0} \hat{\mu}_0 / \hat{k}_0 = 0.71.$$

where k_0 is reference thermal conductivity. In Eq 1, $\boldsymbol{U}$, $\boldsymbol{F}$ and $\boldsymbol{G}$ are given by:

$$\begin{aligned}
\boldsymbol{U} &= [\rho \quad \rho u \quad \rho v \quad \rho E]^T; \\
\boldsymbol{F} &= [\rho u \quad \rho u^2 + p \quad \rho u v \quad (\rho E + p) u]^T; \\
\boldsymbol{G} &= [\rho v \quad \rho u v \quad \rho v^2 + p \quad (\rho E + p) v]^T.
\end{aligned}$$

The flux vectors $\boldsymbol{F_v}$ and $\boldsymbol{G_v}$ are defined by:

$$\begin{aligned}
\boldsymbol{F}_v &= (1/Re)[0 \quad \tau_{xx} \quad \tau_{xy} \quad \tau_{xx} u + \tau_{xy} v - q_x]^T; \\
\boldsymbol{G}_v &= (1/Re)[0 \quad \tau_{xy} \quad \tau_{yy} \quad \tau_{xy} u + \tau_{yy} v - q_y]^T.
\end{aligned}$$

where τ_{xx}, τ_{xy} and τ_{yy} are defined by:

$$\tau_{xx} = \left(\frac{4}{3}\frac{\partial u}{\partial x} - \frac{2}{3}\frac{\partial v}{\partial y}\right)\mu;\ \tau_{xx} = \left(\frac{4}{3}\frac{\partial v}{\partial y} - \frac{2}{3}\frac{\partial u}{\partial x}\right)\mu;\ \tau_{xy} = \left(\frac{\partial u}{\partial x} - \frac{\partial v}{\partial y}\right)\mu.$$

The total energy E and pressure p are defined as:

$$E = p/\rho(\gamma - 1) + (u^2 + v^2)/2;\ p = \rho T/(\gamma M^2).$$

and thermal fluxes are calculated by:

$$q_x = \left[\mu/(\gamma - 1) Pr M^2\right](\partial T/\partial x)\,,\ q_y = \left[\mu/(\gamma - 1) Pr M^2\right](\partial T/\partial y)\,.$$

2.2 Linear Stability Analysis

Linear Stability Analysis (LSA) is widely used in studying the boundary layer instabilities and its transition as it can effectively analyze stability response of boundary layer [23, 24]. For the present study, we also employed LSA to analyze the stability

characteristics of boundary layer over the airfoil surface at low Reynolds number. An infinitesimal perturbation in the flow field is introduced near the leading edge of airfoil which could lead to tonal noise generation due to scattering of boundary layer instabilities at the trailing edge of the airfoil. For an unstable boundary layer, the perturbation introduced would lead to growing instabilities convecting downstream, resulting in stronger noise generation [7]. This approach opens up the possibility of even conducting the parametric study for panel design due to its lower computational time as compared to DAS.

One of the most classical method for employing LSA is by using Orr-Sommerfeld equation. However, it is only limited to parallel flows which is not appropriate for our current study due to presence of complex non-parallel flow over an the airfoil. Hence, a modified two-dimensional linear stability analysis using forced N-S equations is employed which circumvent the limitation of parallel flows only [7, 25]. In this approach, the normalized two-dimensional compressible N-S equations with a constant forcing $\boldsymbol{S}$ may be written in strong conservative form as:

$$\frac{\partial \boldsymbol{U}}{\partial t} + \frac{\partial (\boldsymbol{F} - \boldsymbol{F_v})}{\partial x} + \frac{\partial (\boldsymbol{G} - \boldsymbol{G_v})}{\partial y} = \boldsymbol{S} \tag{2}$$

Given a base flow for Eq. 2, we introduce an infinitesimal perturbation to start the LSA calculation. We may write $\boldsymbol{U}(x, y, t) = \boldsymbol{U}_{base}(x, y) + \boldsymbol{U'}(x, y, t)$ and take the forcing term derived from spatial gradients of the base flow, so Eq. (2) becomes:

$$\frac{\partial (\boldsymbol{U}_{base} + \boldsymbol{U'})}{\partial t} + \left(\frac{\partial (\boldsymbol{F} - \boldsymbol{F_v})}{\partial x} + \frac{\partial (\boldsymbol{G} - \boldsymbol{G_v})}{\partial y} \right)_{base} + \left(\frac{\partial (\boldsymbol{F} - \boldsymbol{F_v})}{\partial x} + \frac{\partial (\boldsymbol{G} - \boldsymbol{G_v})}{\partial y} \right)' = \boldsymbol{S} = \left(\frac{\partial (\boldsymbol{F} - \boldsymbol{F_v})}{\partial x} + \frac{\partial (\boldsymbol{G} - \boldsymbol{G_v})}{\partial y} \right)_{base} \tag{3}$$

Assuming no modification to the flow field to maintain the initial condition as a reference state, the behavior of small perturbations introduced to the solution of Eq. 3 can be traced to illustrate linear stability behaviors. The final form of equation with small perturbations can be written as:

$$\frac{\partial \left(\boldsymbol{U}_{base} + \boldsymbol{U'} \right)}{\partial t} + \left(\frac{\partial (\boldsymbol{F} - \boldsymbol{F_v})}{\partial x} + \frac{\partial (\boldsymbol{G} - \boldsymbol{G_v})}{\partial y} \right)' = 0 \tag{4}$$

Since the base flow is steady, i.e. $\partial \boldsymbol{U}_{base}/\partial t = 0$, Eq. 4 becomes,

$$\frac{\partial \boldsymbol{U'}}{\partial t} + \left(\frac{\partial (\boldsymbol{F} - \boldsymbol{F_v})}{\partial x} + \frac{\partial (\boldsymbol{G} - \boldsymbol{G_v})}{\partial y} \right)' = 0, \tag{5}$$

The flow fluctuation equation (Eq. 5) is then solved by the CE/SE method. A weak Gaussian pulse is introduced just ahead of the airfoil leading edge which can generate a weak disturbance over the airfoil surface and convects towards trailing edge. The introduced pulse is defined as:

$$u(x, y) = -\frac{A}{\rho_{base}(x, y)} \frac{(y - y_0)}{r} \exp\left(-\frac{(x - x_0)^2 + (y - y_0)^2}{r^2}\right)$$
$$v(x, y) = \frac{A}{\rho_{base}(x, y)} \frac{(x - x_0)}{r} \exp\left(-\frac{(x - x_0)^2 + (y - y_0)^2}{r^2}\right) \quad (6)$$

where, A and r are the amplitude and radius of pulse respectively. A very small amplitude of 10^{-5} is chosen which does not alter the overall flow characteristics. The proposed LSA can effectively capture the hydrodynamic instabilities within the boundary layer and subsequent acoustic propagation and boundary layer receptivity to acoustic disturbances [7]. However, an established base flow is required as an initial condition for the analysis [25]. For the present study, we used time averaged solution as the base flow for LSA. The time averaged solution was obtained from DAS of the rigid airfoil [26]. Quality of time averaged solution as a base flow was evaluated by LSA without any perturbation and the deviation from its initial state was checked. A negligible deviation of order 10^{-10} was observed which is five orders of magnitude weaker than the pulse excitation amplitude. Hence, the time averaged solution can be confidently selected as base flow for our study.

2.3 Numerical Setup

Numerical analysis of flow at low Reynolds Number of 5×10^4 around a NACA 0012 airfoil at $\alpha = 5°$ is analyzed for the present study due to availability of extensive literature [6, 7, 27]. Also, at this flow condition the boundary layer tends to be laminar over the airfoil and is found to be unstable due to acoustic feedback loop [7]. Hence, the existing condition can provide an opportunity to design and implement elastic panel over the airfoil suction surface for possible tonal noise reduction. The schematic of computational domain is shown in Fig. 1 where the airfoil trailing edge is located at $(x, y) = (1, 0)$. The domain is set as a rectangular box with a length of $6c$ and width of $6.5c$. Flow is allowed to swipe through the whole domain from left and bottom boundary at an angle of 5°. A buffer zone is used around the boundaries of domain to suppress any numerical reflections. No-slip boundary condition is used for the airfoil surface and a buffer zone of width 1.5 surrounding the physical domain is set to eliminate any possible erroneous numerical reflection. All domain boundaries adopt non-reflecting boundary condition except the inlet boundaries to allow the flux from the interior fluid domain to exit into the exterior of the domain smoothly [28]. The pulse is introduced at a location of $(x, y) = (-0.015, -0.01)$. A small time step size of 10^{-5} is set to maintain the $CFL \leq 1$. Mesh size at different locations around the airfoil is shown in Fig. 1b–d. Details of mesh sizes are listed in Table 1.

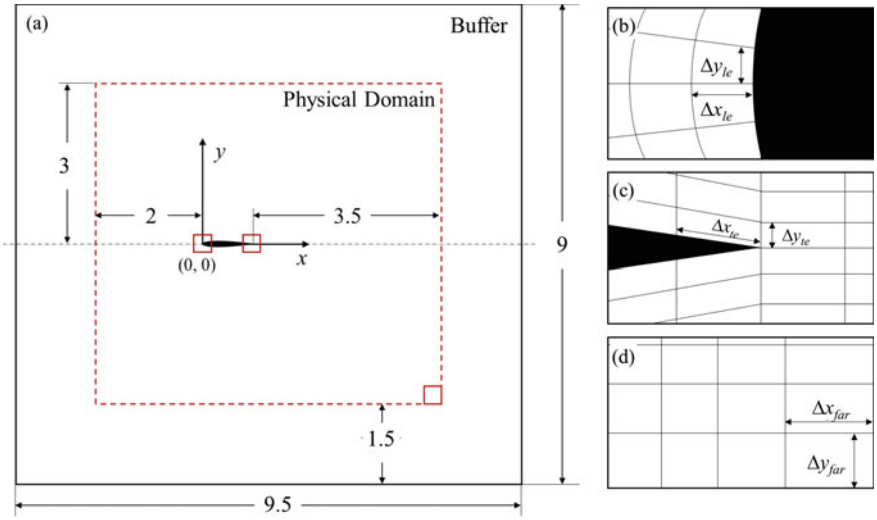

Fig. 1 Schematic sketch of computational domain and definition of mesh parameters

Table 1 Mesh parameters

Δx_{le}	Δy_{le}	Δx_{te}	Δy_{te}	Δx_{far}	Δy_{far}
5×10^{-4}	6×10^{-4}	9×10^{-4}	6×10^{-4}	1×10^{-2}	1×10^{-2}

3 DAS of Rigid Airfoil

DAS of rigid airfoil is initially analyzed to ascertain important flow features including laminar separation bubble, scattering of flow instabilities at trailing edge, and acoustic wave propagation. Furthermore, it would also allow us to establish base flow solution for subsequent stability analysis. The coefficient of pressure Cp for both both suction and pressure surface based on time-averaged solution are plotted in Fig. 2 along with the results of Jones et al. [7]. A strong adverse pressure gradient can be observed near the leading edge of suction surface. The Cp values remains stable from $x = 0.2 - 0.45c$ which is followed by a rapid transition from $x = 0.44 - 0.6c$.

Coefficient of friction C_f plot based on time-averaged solution for suction surface of the airfoil is shown in Fig. 3. The separation and reattachment point can be identified where C_f crosses zero. The separation of laminar boundary layer over the suction surface occurs at $0.18c$ and the flow reattaches at $0.58c$. Hence, a laminar separation bubble of a length $0.4c$ is observed at the selected flow conditions.

Spectral plot of transverse velocity fluctuations over the airfoil suction surface at $x = 0.9c$ is analyzed and shown in Fig. 4. From FFT plot, the first dominant non-dimensional frequency is found to be 3.37 whereas its second and third harmonics appear at 6.6 and 10 respectively which are in close agreement with Jones et al. [7].

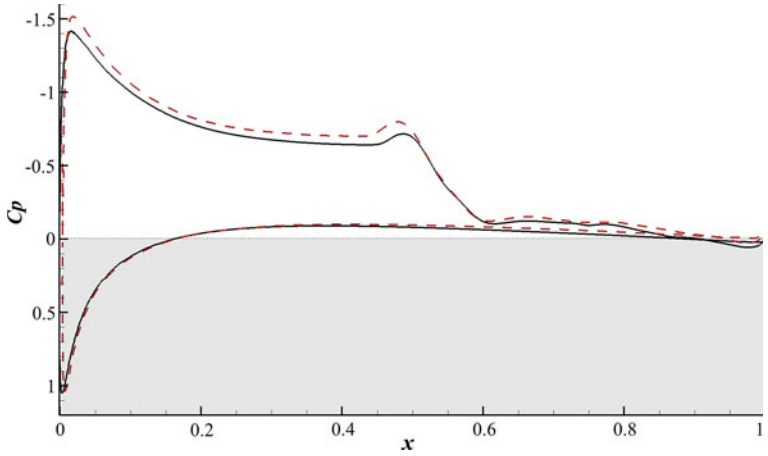

Fig. 2 Distribution of Cp on airfoil. –, CE/SE result, - - , Jones et al. [7]

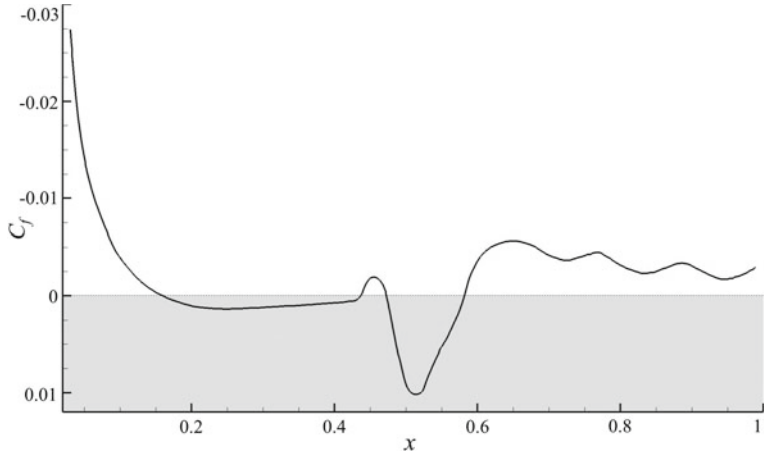

Fig. 3 Distribution of C_f on airfoil suction surface

Since, the first dominant frequency of naturally evolving boundary layer disturbance on the airfoil suction surface is 3.37, therefore, the natural frequency of elastic panel should take a similar value in order to initiate a resonance condition.

4 Panel Design

To study the aeroacoustic-structural interaction, a thin elastic panel is analyzed for present work. The panel dynamics is governed by the dimensionless equation [29]:

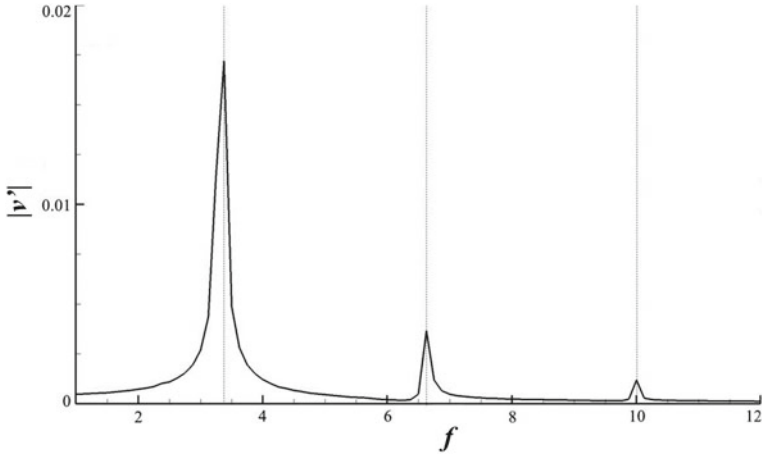

Fig. 4 Spectra of transverse fluctuations over the airfoil suction surface at $x = 0.9c$

$$D_{EP}\frac{\partial^4 w}{\partial x^4} - (T_{EP} + N_{EP})\frac{\partial^2 w}{\partial x^2} + \rho_{EP} h_{EP}\frac{\partial^2 w}{\partial t^2} + C_{EP}\frac{\partial w}{\partial t} + K_{EP} w = p_{ex}, \quad (7)$$

where p_{ex} is the net pressure across the panel. For a panel with membrane like dynamical properties, structural damping and bending stiffness can be neglected. The panel dynamics equation is coupled with N-S equation in a monolithic manner [30], which are then solved by CE/SE method. The methodology is fully validated with a series of benchmark aeroacoustic-structural interaction problems and is proven to accurately resolve aeroacoustic-structural coupling of various complexity over a long solution time [30].

4.1 Panel Location

An elastic panel similar to a thin membrane is designed to manipulate fluid-structure interactions for tonal noise reduction. One of the most important requirements for the implementation of this approach is to ascertain the panel location over the airfoil suction surface. In order to evaluate the optimum location of panel, the transverse velocity at the first $(f_{bl})_0$ and second $(f_{bl})_1$ dominant frequencies, i.e, 3.37 and 6.6 along the airfoil chord are plotted as shown in Fig. 5. It can be observed that the amplitude of the transverse velocity fluctuations starts to grow at $x > 0.27c$. A significant growth is observed at $x \sim 0.4 - 0.45c$. For $(f_{bl})_0$, a maximum growth rate is achieved at a location of $x \sim 0.45 - 0.55c$ and subsequently decreases to a smaller amplitude from $x \sim 0.57c$. For $(f_{bl})_1$, magnitude of growth is much smaller than first dominant frequency. Furthermore, the velocity fluctuations magnitude for both frequencies reach its maximum within the separation bubble over the suction surface

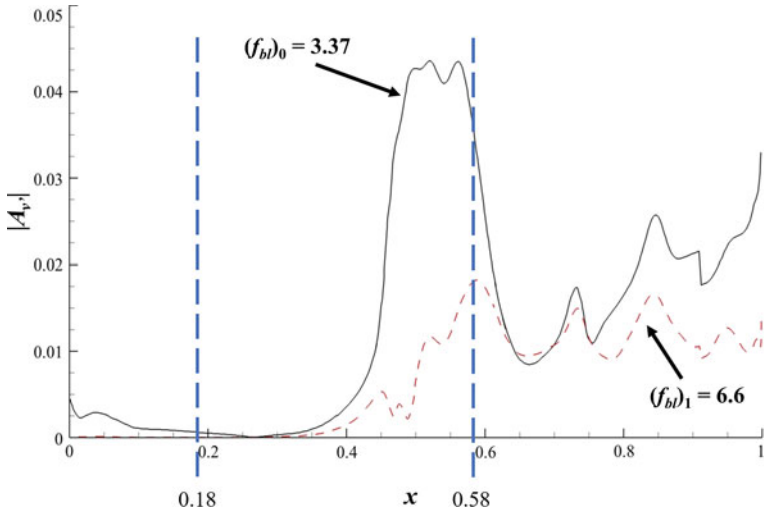

Fig. 5 Spatial growth of flow instability over the airfoil suction surface. The two blue dashed lines show the extent of separation bubble

of the airfoil which confirms the presence of Tollmien–Schlichting instability waves within the laminar boundary layer. Hence, applying an elastic panel at a location of maximum amplitude may lead to significant reduction in boundary layer instabilities. Therefore, the leading edge of elastic panel is set at $x = 0.4c$ for the present study with an aim to reduce the boundary layer instabilities just at the onset of growth of magnitude of velocity fluctuations.

4.2 Panel Length

The proposed approach aims to maintain the laminar boundary layer over the airfoil with minimum or no penalty on the airfoil aerodynamics. Therefore, the length of panel is required to be minimal so that the radius of curvature over the airfoil suction surface is not affected. Keeping in view this limitation, the length of panel is chosen to be only $0.05c$ and the curvature radius is calculated by:

$$rad\,(x) = \left(1 + \left(\frac{dy}{dx}\right)^2\right)^{\frac{3}{2}} / \left(\left|\frac{d^2y}{dx^2}\right|\right) \tag{8}$$

where $y = y\,(x)$ is the function of NACA 0012 geometry. It is observed that the ratio between panel size and local curvature radius is less than 1.5% which is quite small and part of the airfoil surface at that location can be replaced by flexible panel.

Table 2 Elastic panel configurations

Case	Material	Density	Tension	Thickness
NR	Steel (Non-Resonating)	6367.34	4.023	0.0090
ST1	Steel	6367.34	0.7249	0.0090
ST2			1.4339	0.0079
AL1	Aluminium	2212.24	0.5696	0.0090
AL2			1.4339	0.0057
CF1	Carbon Fiber	1469.38	0.3784	0.0090
CF2			1.4339	0.0086

4.3 Material Properties

In order to analyze the effect of panel material properties on tonal noise reduction a parametric study is conducted. We selected three different panel materials namely Steel (ST), Aluminium (AL), and Carbon Fiber (CF). For each material, thickness and tension are changed simultaneously in a way that the natural frequency of the panel coincides with the flow dominant frequency to achieve a resonance condition. The panel natural frequency in the presence of flow can be evaluated by [31, 32]:

$$(f_{EP})_n = \frac{n}{2L_{EP}}\sqrt{\frac{T_{EP}}{\rho_{EP}h_{EP}}}\Bigg/\sqrt{1+\frac{L_{EP}}{\pi n \rho_{EP}h_{EP}}}\,. \tag{9}$$

A non-resonating panel (NR) is also chosen for the present study to analyze and compare the effect of panel resonance in tonal noise reduction. Hence a total of seven different combinations were selected for the present study. All the panel parameters are chosen in non-dimensional form. Details of selected parameters are shown in Table 2.

5 Results and Discussion

LSA results for all seven cases are evaluated and compared with the rigid airfoil to study the effectiveness of elastic panel in tonal noise reduction and its dependence on panel properties. The following section is divided into three subsections, where the effect of panel properties for each material is discussed and subsequently a comparative analysis is presented.

5.1 Steel

For both ST1 and ST2 cases, the acoustic scattering due to hydrodynamic fluctuations are analyzed. Transverse velocity fluctuations near the airfoil suction surface trailing edge at three locations, i.e. $0.8c$, $0.9c$ and $0.99c$ for each case is evaluated as shown in Fig. 6. It is observed that the amplitude of transverse velocity fluctuations are reduced for ST1, ST2 and NR cases as compared to RS. Also, the difference in magnitude of fluctuations between ST and RS cases increases along the chord. Hence, it can be seen that the resonating panel is more effective than the non-resonating panel in reducing flow instabilities. Furthermore, the velocity fluctuations plot reveals that the reduction in flow instabilities for ST1 is much higher than ST2 for all three locations.

To evaluate the overall tonal noise reduction, pressure fluctuations around the airfoil at a radius of 2 chord lengths are calculated. Hence, an azimuth map of pressure fluctuations around the airfoil is plotted as shown in Fig. 7. It is evident that a significant pressure reduction all around the airfoil is achieved with the help of an elastic panel. The reduction in magnitude of pressure fluctuation is non uniform around the airfoil and a maximum reduction is achieved at an angle of 168° for ST1, ST2 and NR cases. Based on pressure fluctuations, the reduction in sound pressure level (SPL) can be calculated by:

$$\Delta SPL_{reduction} = 20 \times log_{10}\left(\frac{p'_{rms,EP}}{p'_{rms,RS}}\right) \tag{10}$$

The SPL reduction achieved for ST1 and ST2 cases are plotted and compared with NR case as shown in Fig. 7. A significant sound reduction is observed for both ST1 and ST2 cases as compared to the non-resonating case NR. An average reduction of 2.74 dB and 2.69 dB in SPL for ST1 and ST2 is observed respectively, whereas an average reduction of 1.27 dB is observed for NR. Hence, the overall effectiveness of ST1 case is slightly better than ST2 case in terms of SPL reduction.

5.2 Aluminium

For the case of aluminium panel, a similar methodology is adopted as discussed in previous section. Once again, reduction in velocity fluctuations at all three locations near the airfoil trailing edge is observed for AL1 and AL2 cases. Azimuth plot of pressure fluctuations for all cases are shown in Fig. 8. A significant pressure reduction is observed for AL1 case as compared to AL2 and NR cases. SPL reduction for AL1 and AL2 cases are plotted and compared with NR case in Fig. 8. An average reduction of 2.54 dB and 1.67 dB in SPL is achieved for AL1 and AL2 respectively as compared to 1.27 dB for NR case. Hence, the overall effectiveness of AL1 is much higher than AL2 and NR cases in terms of SPL reduction.

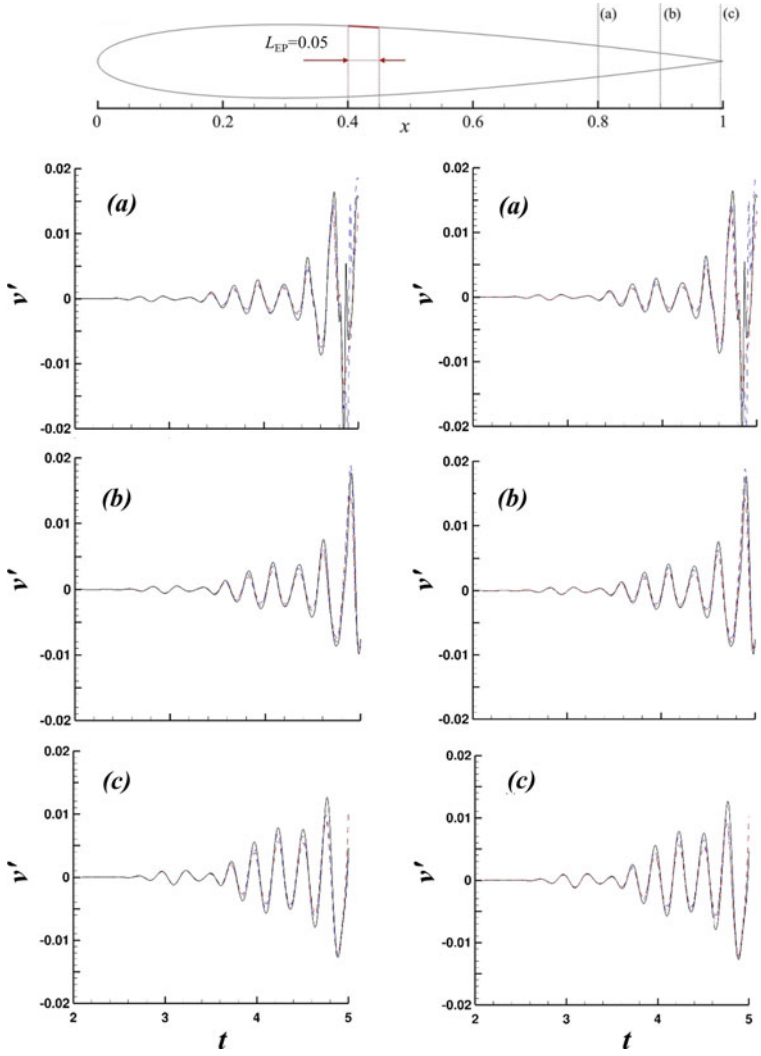

Fig. 6 Comparison of v' time histories at locations 0.8 (first row), 0.9 (second row) and 0.99 (third row). Left column, ST1; Right column, ST2. - - -, ST1/ST2; - - -, NR; —, RS

5.3 Carbon Fiber

For carbon fiber panel, a similar procedure is adopted. Reduction in magnitude of velocity fluctuations near the airfoil trailing edge was observed for both CF1 and CF2 cases with respect to RS case. Pressure fluctuations around the airfoil is shown in Fig. 9. A significant reduction is observed for CF1 case as compared to CF2 and NR cases. SPL plot reveals an average reduction of 2.37 dB and 1.67 dB for CF1

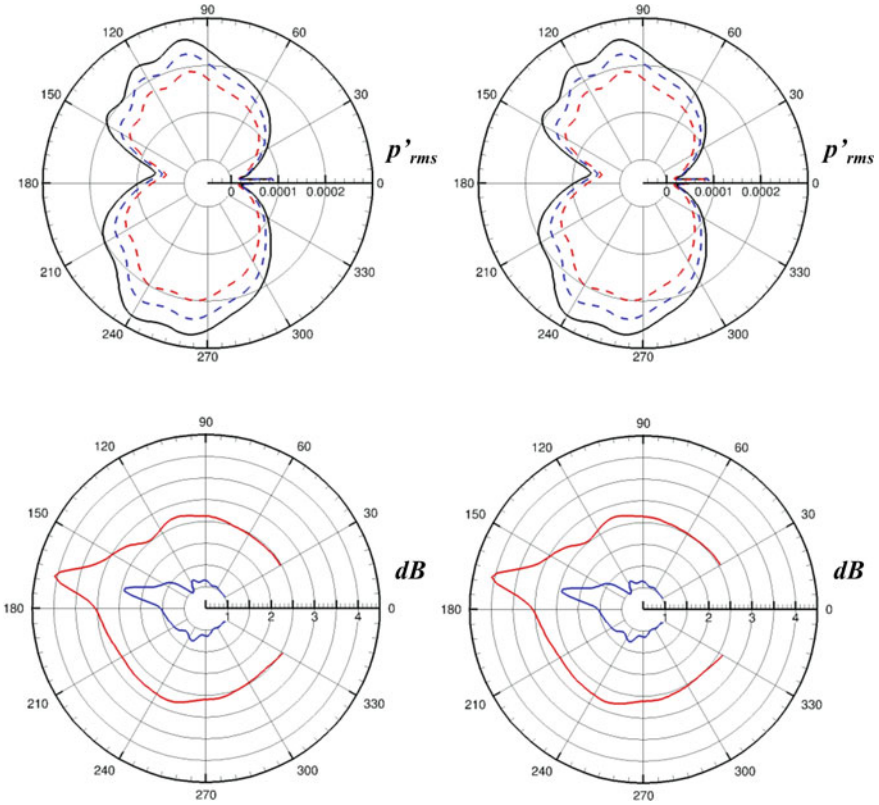

Fig. 7 Azimuthal p'_{rms} comparison and SPL reduction. Left column, ST1; Right column, ST2.- - -, ST1/ST2; - - -, NR; —, RS

and CF2 respectively in Fig. 9. The overall effectiveness of CF1 is found to be better than CF2 and NR cases.

5.4 Comparative Analysis

In the previous section, effect of panel material and properties were evaluated which revealed some significant insights. It is evident that both the resonating and non-resonating elastic panel are able to reduce sound pressure level all around the airfoil. Hence, the approach of using elastic panel to reduce flow instabilities seems quite feasible. However, a noticeable difference in magnitude of SPL reduction is observed for resonating and non-resonating panel, where the former is observed to effectively reduce noise level much better than its counterpart of non-resonating panel in each case. A comparative plot of pressure fluctuations for all seven cases are shown in

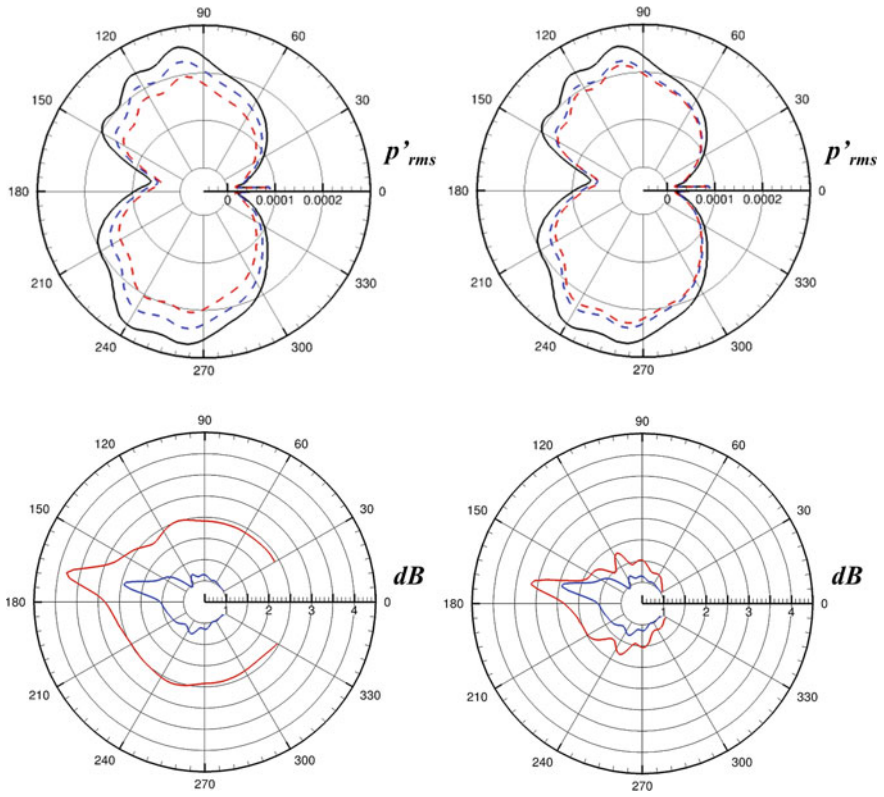

Fig. 8 Azimuthal p'_{rms} comparison and SPL reduction. Left column, AL1; Right column, AL2.- - -, AL1/AL2; - - -, NR; —, RS

Fig. 10. It is observed that the material with low density is less effective in tonal noise reduction when the panel thickness is kept constant. Furthermore, for a selected material, an increase in panel thickness favorably enhances the panel performance in noise reduction as shown in previous section. However, an increase in panel tension adversely affects its performance in terms of noise reduction. Hence, an elastic panel with high density and thickness but low tension is preferred for effective tonal noise reduction, provided that a resonance condition is achieved in the presence of flow.

6 Conclusions

A novel approach of using elastic panel mounted on the suction surface of an airfoil is explored. Linear stability analysis is employed to predict the noise generation using elastic panel over a NACA 0012 airfoil at low Re. A parametric study is also carried

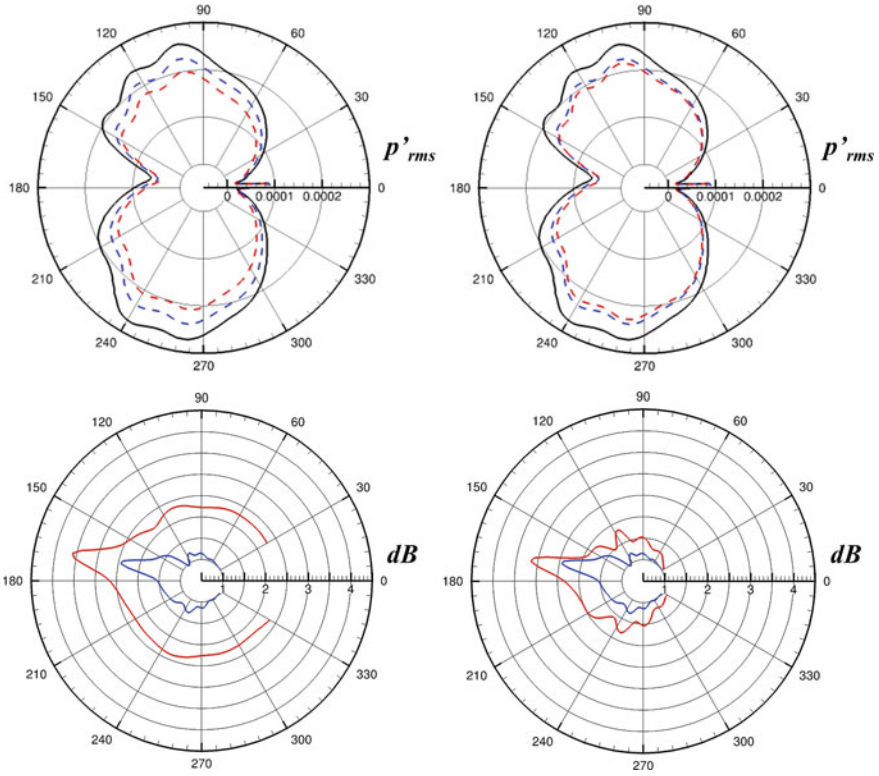

Fig. 9 Azimuthal p'_{rms} comparison and SPL reduction. Left column, CF1; Right column, CF2.- - -, CF1/CF2; - - -, NR; —, RS

out to analyze the effect of panel parameters in reducing the airfoil tonal noise. Results revealed that the panel efficiency in tonal noise reduction is significantly increased by ensuring a resonance condition between flow dominant frequency and panel natural frequency. Furthermore, a thick elastic panel with high density and low tension is the best candidate for tonal noise reduction.

Acknowledgements The authors gratefully acknowledge the support given by the Central Research Grant of the Hong Kong Polytechnic University (PolyU) under grant no. G-YBGF. The third author acknowledges the support from a research donation from the Philip K. H. Wong Foundation under grant no. 5-ZH1X. The first and fourth authors gratefully acknowledge the support with research studentship tenable at Department of Mechanical Engineering, PolyU.

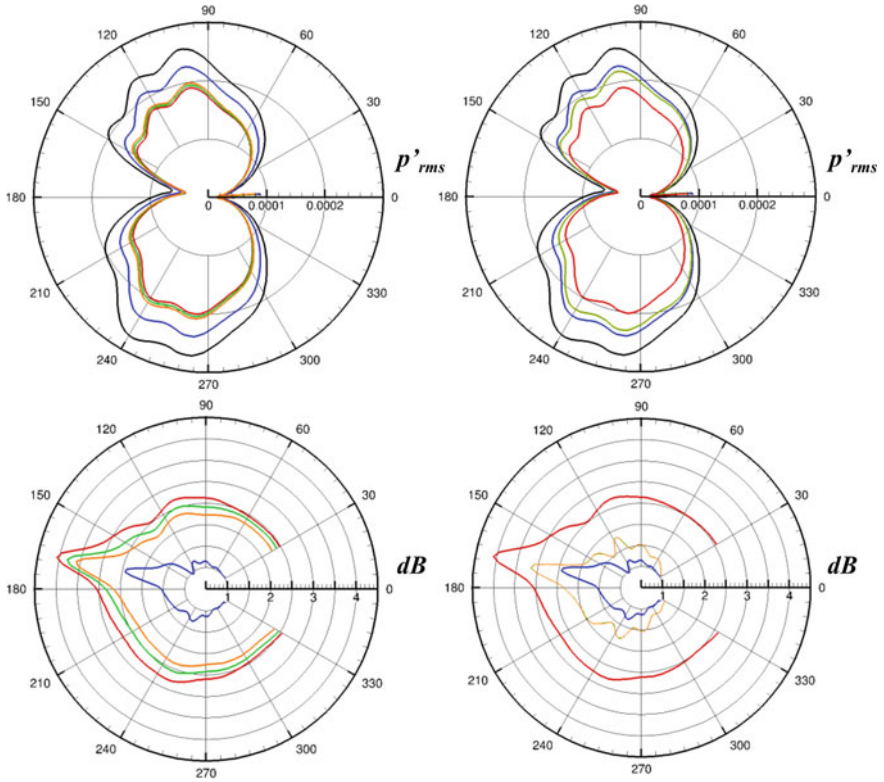

Fig. 10 Azimuthal p'_{rms} comparison and SPL reduction. Left column (ST1, AL1, CF1); Right column (ST2, AL2, CF2). - - -, ST1/ST2; - - -, AL1/AL2; - - -, CF1/CF2; - - -, NR; —, RS

References

1. R.W. Paterson, P.G. Vogt, M.R. Fink, C.L. Munch, Vortex noise of isolated airfoils. J. Aircraft **10**(5), 296–302 (1973)
2. C.K. Tam, Discrete tones of isolated airfoils. J. Acoustic. Soc. Am. **55**(6), 1173–1177 (1974)
3. R.E. Longhouse, Vortex shedding noise of low tip speed, axial flow fans. J. Sound Vibrat. **53**(1), 25–46 (1977)
4. H. Arbey, J. Bataille, Noise generated by airfoil profiles placed in a uniform laminar flow. J. Fluid Mech. **134**, 33–47 (1983)
5. E.C. Nash, M.V. Lowson, A. McAlpine, Boundary-layer instability noise on aerofoils. J. Fluid Mech. **382**, 27–61 (1999)
6. G. Desquesnes, M. Terracol, P. Sagaut, Numerical investigation of the tone noise mechanism over laminar airfoils. J. Fluid Mech. **591**, 155–182 (2007)
7. L. Jones, R. Sandberg, N. Sandham, Stability and receptivity characteristics of a laminar separation bubble on an aerofoil. J. Fluid Mech. **648**, 257–296 (2010)
8. M. Fosas de Pando,P.J. Schmid, D. Sipp, A global analysis of tonal noise in flows around aerofoils. J. Fluid Mech. 754, 5–38 (2014)
9. K. Braun, N. Van der Borg, A. Dassen, F. Doorenspleet, Gordner, A., Ocker, J., Parchen, Serrated trailing edge noise. In: European Wind Energy Conference. pp. 180–183 (1999)

10. M.S. Howe, Noise produced by a sawtooth trailing edge. J. Acoustic. Soc. Am. **90**(1), 482–487 (1991)
11. S. Oerlemans, M. Fisher, T. Maeder, K. Kögler, Reduction of wind turbine noise using optimized airfoils and trailing-edge serrations. AIAA J. **47**(6), 1470–1481 (2009)
12. M. Gruber, P. Joseph, T.P. Chong, Experimental investigation of airfoil self noise and turbulent wake reduction by the use of trailing edge serrations. In: *16th AIAA/CEAS aeroacoustics conference*. pp. 3803–3825 (2010)
13. D.J. Moreau, C.J. Doolan, Noise-reduction mechanism of a flat-plate serrated trailing edge. AIAA J. **51**(10), 2513–2522 (2013)
14. T. Geyer, E. Sarradj, C. Fritzsche, Measurement of the noise generation at the trailing edge of porous airfoils. Experiments Fluids **48**(2), 291–308 (2010)
15. E. Talboys, T.F. Geyer, C. Brücker, An aeroacoustic investigation into the effect of self-oscillating trailing edge flaplets. J. Fluids Struct. pp. 2–11 (2019)
16. K. Hansen, C. Doolan, R. Kelso, Reduction of flow induced airfoil tonal noise using leading edge sinusoidal modifications. Acoustics Australia **40**(3), 1–6 (2012)
17. X. Wang, S. Chang, P., Jorgenson, Numerical simulation of aeroacoustic field in a 2D cascade involving a downstream moving grid using the space-time CE/SE method. Computational Fluid Dynamics pp. 157–169 (2000)
18. G.C.Y. Lam, R.C.K. Leung, K.H. Seid, S.K. Tang, Validation of CE/SE scheme for low mach number direct aeroacoustic simulation. Int. J. Nonlinear Sci. Numeric. Simulat. **15**(2), 157–169 (2014)
19. X. Gloerfelt, C. Bailly, D. Juvé, Direct computation of the noise radiated by a subsonic cavity flow and application of integral methods. J. Sound Vibrat. **266**(1), 119–146 (2003)
20. S.C. Chang, The method of space-time conservation element and solution element-a new approach for solving the Navier-Stokes and Euler equations. J. Computat. Phys. **119**, 295–324 (1995)
21. B.S. Venkatachari, G.C. Cheng, B.K. Soni, S. Chang, Validation and verification of courant number insensitive conservation element and solution element method for transient viscous flow simulations. Math. Comput. Simulat. **78**(5–6), 653–670 (2008)
22. C. Loh, L. Hultgren, P. Jorgenson, Near field screech noise computation for an underexpanded supersonic jet by the conservation element and solution element method. In: 7th AIAA/CEAS Aeroacoustics Conference and Exhibit, pp. 2252–2262 (2001)
23. P. Huerre, P.A. Monkewitz, Local and global instabilities in spatially developing flows. Ann. Rev. Fluid Mech. **22**(1), 473–537 (1990)
24. L.M. Mack, Linear stability theory and the problem of supersonic boundary-layer transition. AIAA J. **13**(3), 278–289 (1975)
25. L.E. Jones, R.D. Sandberg, Numerical analysis of tonal airfoil self-noise and acoustic feedback-loops. J. Sound Vibrat. **330**(25), 6137–6152 (2011)
26. D. Wu, G.C.Y. Lam, R.C.K. Leung, An attempt to reduce airfoil tonal noise using fluid-structure interaction. In: 2018 AIAA/CEAS Aeroacoustics Conference. pp. 3790–3816 (2018)
27. J.H. Almutairi, L.E. Jones, N.D. Sandham, Intermittent bursting of a laminar separation bubble on an airfoil. AIAA J. **48**(2), 414–426 (2010)
28. C. Loh, On a non-reflecting boundary condition for hyperbolic conservation laws. In: 16th AIAA Computational Fluid Dynamics Conference. p. 3975 (2003)
29. E.H. Dowell, E.H., Aeroelasticity of plates and shells, vol. 1. Springer Science & Business Media (1974)
30. H.K.H. Fan, R.C.K. Leung, G.C.Y. Lam, Y. Aurégan, X. Dai, Numerical coupling strategy for resolving in-duct elastic panel aeroacoustic/structural interaction. AIAA Journal **56**(12), 5033–5040 (2018)
31. R.D. Blevins, *Formulas for natural frequency and mode shape* (Van Nostrand Reinhold, New York, 1979)
32. I. Arif, Lam, G.C.Y., Leung, R.C.K., D. Wu, Leveraging surface aeroacoustic-structural interaction for airfoil tonal noise reduction—a parametric study. In: 25th AIAA/CEAS Aeroacoustics Conference. pp. 2758–2773 (2019)

Broadband Aerodynamic Noise Simulation Using Synthetic Turbulence Methods

Xin Zhang and Siyang Zhong

Abstract Turbulence generated broadband noise is an important source of noise that can be found in many applications. The characteristics of noise are defined by a combination of turbulence statistics, flow and geometry, imposing challenges in developing efficient and robust prediction methods. Direct simulations of flow governing equations are currently too costly for design optimisation. An efficient strategy is to solve governing equations such as the full or linearized Euler equations with a synthetic turbulence model, which reproduces main turbulence statistics, therefore capturing the physics of noise generation and sound propagation. In this paper, synthetic turbulence methods for aeroacoustics, especially those suitable for the broadband noise simulations of leading edge noise problems, are introduced. Examples are provided, together with progresses made in tackling the challenges of computational aeroacoustics for transonic flows and far-field noise computation.

Keywords Synthetic turbulence · Computational aeroacoustics · Leading edge noise

1 Introduction

Turbulence generated broadband noise can be found in many applications such as turbofan engines, contra-rotating open rotors, cooling fans, wind turbines, etc. There exist a number of sources of broadband noise, e.g. scattering of turbulence off the trailing edge of a wing, tip vortex breakdown, etc. Numerical simulations based on the state-of-the-art computational aeroacoustics methods are promising solutions with the increasing computer power. The requirement of precursory computation

X. Zhang (✉) · S. Zhong
Department of Mechanical and Aerospace Engineering, The Hong Kong University of Science and Technology, Clear Water Bay, Kowloon, Hong Kong SAR, China
e-mail: aexzhang@ust.hk

S. Zhong
e-mail: zhongsy@ust.hk

HKUST ShenZhen Research Institute, Shenzhen, China

E. Ciappi et al. (eds.), *Flinovia—Flow Induced Noise and Vibration Issues and Aspects-III*, https://doi.org/10.1007/978-3-030-64807-7_18

to initiate turbulence flow is a long-standing problem in turbulent flow simulations using computational fluid dynamics (CFD) [1]. With different precursory computation setups, the simulation outcomes can differ, as nonlinear processes are involved in amplifying the initial differences in the flow variables. A direct approach is to invest in expensive computations to capture the laminar-to-turbulence transition process, and recycle computations to arrive at a fully developed inflow turbulence. Alternatively, an efficient simulation approach is to inject synthetic turbulence into the flow field to initialize the turbulence simulation; a synthetic turbulence method introduces fluctuations to the mean flow field to approximate the turbulence statistics [2]. The synthetic turbulence methods for aeroacoustics are the focus of this paper. Specifically, this paper will focus on broadband airfoil-turbulence interaction noise simulation using synthetic turbulence methods [3].

The airfoil-turbulence interaction is a major source of broadband noise in many applications, e.g. turbofan engines [4, 5], contra rotating open rotors (CRORs), etc. In general, the rotating fan blades generate turbulent wakes behind the trailing edges of the rotating blades, which in themselves are acoustically inefficient. However, the turbulence convected through the background mean flow can experience significant distortion, which can lead to interaction noise with downstream aerodynamic surfaces. These noise sources can be found in turbofan engines fan-OGV (outlet guide vanes) section or at the aft blades of CROR. Similar processes can occur if the ingested turbulence [6, 7] or the oncoming boundary layer flow [4] interacts with the fan blades in an aero-engine. In evaluating the leading edge noise, a widely used noise prediction method is based on Amiet's flat plate solution [3, 8], in which the mean flow is assumed to be uniform and the acoustic response is caused by the transverse velocity fluctuations, i.e. in the direction normal to the flat plate. Experimental studies [9–13] and simulations based on computational aeroacoustics (CAA) [14–20] have been conducted on the impact of geometry, background mean flow and turbulence statistics on noise generation and sound propagation. A good understanding of the physical problem has been obtained and many physics-based predication methods are developed based on the Amiet solution. High-fidelity CAA simulations, though, can still play an important role in simulating both the resulting near-field noise generation process and far-field directivity, providing physical insights into the noise generation process. High-fidelity CAA can also be used to validate the accuracy of analytical solutions, to assess their underlying assumptions [21, 22], and to improve physics-based prediction models.

To capture the key physics of interaction noise, a synthetic turbulence method is often employed in CAA simulations as an efficient and robust approach in solving either the full or the linearized Euler equations [23]. With this method the flow field is decomposed into mean flow and fluctuation components. The mean flow can then be solved either by the Euler equations or the averaged solutions of the Navier-Stokes equations; whereas the random velocity fluctuations can be represented by a synthetic turbulence model to reproduce the desired statistics. In a turbulent flow field, the fluctuations may contain vortical (the main component of the turbulence), entropy and acoustic velocity modes [24]. The acoustic and vortical velocity modes can be

converted to one another due to the interactive aeroacoustic processes [25]. Under the assumption of slowly varying mean flow and small amplitude of velocity fluctuations [26], the turbulence could be regarded as frozen, such that the motion of the turbulent eddies is characterized by the convection process of the background mean flow [27]. The conversion of the turbulence (vortical mode) to the acoustic waves usually appears at abrupt variations or discontinuities in the flow and geometry, such as near the leading edge of an airfoil. The role of the synthetic turbulence is to generate the vortical velocities numerically, and to reproduce the key turbulence statistics of the flow field. In direct numerical simulations (DNS) and large eddy simulations (LES), synthetic turbulence is one of the means to initialize the random fluctuations with deterministic coherent structures [1]. In CAA simulations, the synthesized turbulence should be divergence-free to avoid the appearance of non-physical and spurious noise sources. As will be seen in the following analysis, in uniform mean flows where the synthetic turbulence is introduced in CAA simulations, the frozen turbulence, divergence-free velocity and spurious noise-free properties are rigorously valid. In this case, the linearized Euler equations that govern the fluctuation variations are

$$\begin{aligned} \frac{D\rho'}{Dt} + \rho_0 \nabla \cdot \boldsymbol{u'} &= 0, \\ \frac{D\boldsymbol{u'}}{\boldsymbol{Dt}} + \frac{\nabla p'}{\rho_0} &= 0, \\ \frac{Dp'}{Dt} + \gamma p_0 \nabla \cdot \boldsymbol{u'} &= 0, \end{aligned} \tag{1}$$

where ρ, $\boldsymbol{u}$ and p are the density, velocity and pressure respectively, and $D/Dt = \partial/\partial t + \boldsymbol{u}_0 \cdot \nabla$ is the substantial derivative. The subscript of $(\cdot)_0$ refers to the background mean flow, whereas the superscript $(\cdot)'$ denotes the fluctuation properties. To model the vortical components, it is required that $\rho' = p' = 0$, which is achieved when $\nabla \cdot \boldsymbol{u'} = 0$ (divergence-free condition). The linearized momentum equation is then reduced to $D\boldsymbol{u'}/Dt = 0$, suggesting that the frozen turbulence, divergence-free velocity fluctuation and non-spurious noise generation properties are valid simultaneously.

In the remaining part of the paper, Sect. 2 reviews the synthetic turbulence methods for CAA and their recent developments. Section 3 gives several examples of applying the synthetic turbulence technique to various aeroacoustics problems relating to the airfoil-turbulence interaction. Lastly, a summary is produced in Sect. 4.

2 Development of Synthetic Turbulence Methods for CAA

In this section, a review of the existing synthetic turbulence methods is given. Different methods are classified into Fourier modes superposition, synthetic eddy and digital filter, based on their numerical implementation strategies.

2.1 Fourier Modes Superposition Methods

Fourier modes superposition is the most direct method to synthesize turbulence, in which the fluctuating velocity field is represented by a summation of weighted sinusoidal functions in space and time. These weighting factors are determined by the turbulence energy spectra, and the turbulent kinetic energy is computed by the overall amplitude [1]. For the fluctuation at each wavenumber $\boldsymbol{k}$, which is also known as a harmonic gust, the velocity components in a two-dimensional (2D) domain are

$$\left\{ \begin{array}{l} u_1(\boldsymbol{x}, t) \\ u_2(\boldsymbol{x}, t) \end{array} \right\} = \left\{ \begin{array}{l} A_1 \\ A_2 \end{array} \right\} \cos(\omega t - k_1 x_1 - k_2 x_2 + \phi), \tag{2}$$

where ϕ is the phase, $\omega = k_1 U_\infty$ since the turbulence is frozen (assume the mean flow has a speed U_∞ and the direction is in the x_1-direction) and $A_1 k_1 + A_2 k_2 = 0$ due to the divergence-free property. An early study of using Fourier modes to generate the homogeneous isotropic Gaussian energy spectrum turbulence was made by Kraichnan [28], which was then extended to the von Kármán spectrum turbulence by Karweit et al. [29], by adjusting the amplitude of each mode. For three-dimensional (3D) problems, Smirnov et al. [30] and Huang et al. [31] reproduced the velocity correlation tensor of isotropic and anisotropic turbulence, whereas Battern et al. [32] calculated the modal amplitude by performing Cholesky decomposition of the Reynolds stress tensor. For CAA simulations, a stochastic noise generation and sound radiation method was developed by Bechara et al. [33] to study jet noise problems by solving the linearized Euler equations, and the temporal variation of the velocity fluctuations was later introduced by Bailly et al. [34] to account for the convection of the turbulent eddies. One-component Fourier method was employed by Clair et al. [14] to study airfoil interaction noise produced by the transverse velocity disturbances (perpendicular to the airfoil surface). Gill et al. [15, 19] developed a method to take into account velocity fluctuations in other directions, besides studying various flow and geometrical parameters.

Usually, the velocity fluctuation of each Fourier mode appears in the whole computational domain. However, for many practical problems, the main sound generating physical process often occurs in confined regions, such as the leading edge of a wing or a rotor blade. To isolate the key aeroacoustic mechanisms in different regions, Zhong et al. [35] developed a local gust injection method whereby a profile function is introduced that allows gradual decay of velocity fluctuations away from the region

of interest, and the flow variables are varied accordingly to ensure the divergence-free property.

Although the Fourier mode method is direct and easy to implement, it can incur a high computational cost when used for broadband noise simulations, as a large number of modes and phase variations are required to remove the pseudo-periodic property caused by the discretized sinusoidal treatment [36].

2.2 Synthetic Eddy Method

A synthetic eddy method employs multiple, superimposed elementary eddies to model the target turbulence spectra. The discrete eddies are distributed in space, typically at locations upstream of aerodynamic objects such as wings or rotor blades. The combination of eddies is made to reproduce necessary velocity distributions, which then yield desired random velocity fluctuations. By using the synthetic eddy method, Jarrin et al. [2, 37] reproduced the target Reynolds stress tensor for LES. For CAA simulations, the target is to produce divergence-free eddies. A common approach is to compute the curl of a vector potential function that often displays the Gaussian distribution [38]. Another possible distribution that can be used is the Mexican hat function [39]. To simulate realistic turbulence energy spectra, elementary eddies with various length scales are typically superimposed, leading to the general formulation for the divergence-free synthetic eddy method [39]

$$\boldsymbol{\psi}(\boldsymbol{x}, t) = \sum_{i=1}^{N_e} A_i \boldsymbol{\psi}_{\boldsymbol{i}}(\boldsymbol{x}, t),$$

$$\boldsymbol{u}'(\boldsymbol{x}, t) = \nabla \times \boldsymbol{\psi}(\boldsymbol{x}, t), \tag{3}$$

where $\boldsymbol{\psi}_{\boldsymbol{i}}$ is the time varying potential of the elementary eddy. In a numerical implementation, the number of the eddies N_e, the properties of the eddy $\boldsymbol{\psi}_{\boldsymbol{i}}$ and the amplitude of the eddy A_i could influence the simulation accuracy. For interaction noise problems, Kim and Haeri [39] reconstructed the 3D von Kármán energy spectrum with more than 15 eddies, and the parameters of the eddies were obtained by optimization using genetic algorithms.

2.3 Digital Filter Method

The continuous velocity fluctuations can also be produced by a digital filter method, in which filters are applied to white noise to produce target velocity fluctuations. The main idea is to design filters that are characterized by the key turbulence statistics. An early digital filter method was proposed by Careta et al. [40], in which the

velocity fluctuations are governed by the stochastic Langevin equation, where the coefficients that affect the white-noise evolution are directly linked to the turbulence structure. However, many digital filter methods designed for CFD simulations are not divergence-free [41, 42] and are therefore not suitable for CAA simulations. This problem was overcome by the random particle-mesh (RPM) method proposed by Ewert [43] and Ewert et al. [44]. In the RPM method, the velocity fluctuations are computed as the curl of the stream function, which is the convolution of a spatial filter and white noise [36], as shown below

$$\begin{aligned} \boldsymbol{\psi}(\boldsymbol{x}, t) &= \int_V G(\boldsymbol{x} - \boldsymbol{y}) \mathcal{U}(\boldsymbol{y}, t) \mathrm{d}\boldsymbol{y}, \\ \boldsymbol{u'}(\boldsymbol{x}, t) &= \nabla \times \boldsymbol{\psi}(\boldsymbol{x}, t), \end{aligned} \tag{4}$$

where $\mathcal{U}$ and G represent the white noise and the digital filter respectively, the latter is determined by the turbulence correlation function in the wavenumber space. For isotropic turbulence with a Gaussian energy spectrum, the formulation and realization of G are simple. In a CAA computation, superposition of several Gaussian filters is employed to realize non-Gaussian [45] or anisotropic [46] turbulence. For 2D problems, Dieste and Gabard [47] derived direct filters for isotropic turbulence with either a Liepmann or a von Kármán energy spectrum to study the airfoil-turbulence interaction noise. The resultant velocity profiles may have abrupt variation in the filter center because the spectrum decay algebraically at large wavenumbers. Therefore, they developed interpolations of the filters to deal with the associated singularities.

In the RPM method, the integral in Eq. (4) needs to be numerically implemented [43] for all filters used in superposition treatment. An extension to reduce the number of parametric constraints was made by Gea-Aguilera et al. [36]. For frozen turbulence in a 2D domain, the random velocity fluctuations of the isotropic Gaussian turbulence with zero mean and standard deviation Δ_e are explicitly represented as

$$\begin{aligned} u'_{x,p}(x, t) &= \epsilon_p(t) \Delta_e \frac{\partial}{\partial y} G\big(x - x_p\big) \\ u'_{y,p}(x, t) &= -\epsilon_p(t) \Delta_e \frac{\partial}{\partial x} G\big(x - x_p\big), \end{aligned} \tag{5}$$

where x_p is the location of the center of the p-th eddy in the computational domain. When the eddies are introduced into the domain, ϵ_p is randomly set as $+1$ or -1 such that the velocities are randomly varying in both space and time. The numerical implementation of the filter method is similar to the synthetic eddy method, where velocity fluctuations are introduced, and no spatial integrations are performed as in the RPM method. The eddies are determined by the filter $G(\boldsymbol{x} - \boldsymbol{y})$ based on the turbulence energy spectra. For isotropic energy turbulence, $G_p = G\big(x - x_p\big) \propto \exp\Big(-\pi \big|x - x_p\big|^2 / 2\Lambda^2\Big)$, where Λ is the turbulence integral length scale. The accuracy of the synthetic turbulence method can be evaluated through examining the 1D turbulence energy spectra $E_{ij}(k_x)$

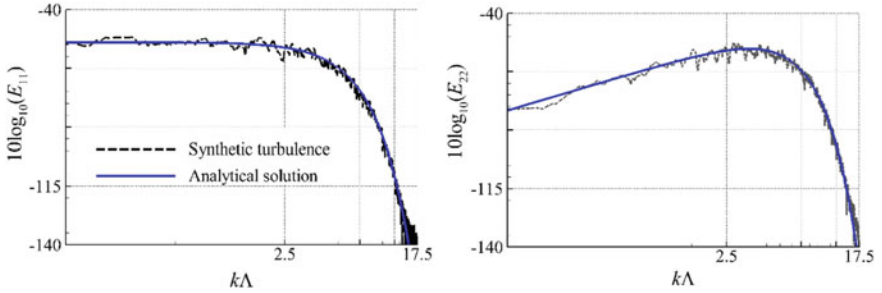

Fig. 1 Energy spectra produced by an advanced digital filter [36], for a background mean flow at a Mach number of 0.5, and a turbulence integral length scale Λ of 0.1. The analytical solutions are the target isotropic Gaussian energy spectrum

$$E_{ij}(k_x) = 2\int_{-\infty}^{\infty} \Phi_{ij}(k_x, k_y)dk_y,$$

where $\Phi_{ij}(k)$ is the turbulence velocity spectra, which is linked to the energy spectra $E(k)$, where for isotropic turbulence, $\Phi_{ij}(k) = E(k)/\pi k\left(\delta_{ij} - k_i k_j/k^2\right)$ [48]. An example of using a synthetic turbulence method to reproduce the isotropic Gaussian energy spectra is shown in Fig. 1.

For general turbulence spectra, a superposition of multiple Gaussian eddies (typically more than 5) is also needed for the advanced digital filter approach [36]. Before the numerical simulations, optimizations of the eddy parameters are needed. To avoid ad hoc calculation of specific flow speed dependent coefficients, Shen and Zhang [49] developed a generalized filter for anisotropic turbulence, based on the homogeneous axisymmetric turbulence proposed by Kerschen and Gliebe [50]. It produces the Liepmann spectrum in the case of isotropic turbulence [51]. This method differs from previous approaches. Only one eddy (or filter) is needed in the numerical implementation, and the model coefficients are independent of Mach number. It is suitable to produce the turbulence statistics in many practical applications. By linking to the turbulence velocity spectrum tensor, the anisotropic turbulence filter in the wavenumber space is determined as

$$\hat{G}(k) = \frac{l_a^{0.5} l_t^2 u'_{rms}}{2\pi^{2.5}\left(1 + l_a^2 k_a^2 + l_t^2 k_t^2\right)^{1.5}} \tag{6}$$

where $k_a = k_x$ and $k_t = \sqrt{k_y^2 + k_z^2}$ are the axial and tangential wavenumbers, l_a and l_t are the corresponding turbulence length scales. In the spatial domain, the anisotropic filter is given as

$$G(r) = \int_{-\infty}^{\infty} \int_{0}^{\infty} \int_{0}^{2\pi} \hat{G}(\boldsymbol{k}) e^{i(k_a r_a + k_t \sigma_n \cos\theta)} k_t \mathrm{d}\theta \mathrm{d}k_t \mathrm{d}k_a = \frac{2u'_{rms} K_0(\xi)}{\pi^{1.5} l_a^{0.5}}, \tag{7}$$

where r_a is the projection of r in the x-direction, and $\sigma = \sqrt{r^2 - r_a^2}$ is the projection in the tangential direction, $\xi_n = \sqrt{(r_a/l_a)^2 + (\sigma/l_t)^2}$ and K_0 is the 0^{th} order modified Bessel function of the second kind. In simulations, various eddies are introduced in the computational domain at different locations $\boldsymbol{x_p}$, at which only one filter described in Eq. (7) is needed, and the induced velocity fluctuations are

$$\begin{aligned}
u'_p(x,\ t) &= \left(\epsilon_{p,z} \frac{\partial G(r_p)}{\partial y} - \epsilon_{p,y} \frac{\partial G(r_p)}{\partial z} \right) \sqrt{\Delta_x \Delta_y \Delta_z} \\
v'_p(x,t) &= \left(\epsilon_{p,x} \frac{\partial G(r_p)}{\partial z} - \epsilon_{p,z} \frac{\partial G(r_p)}{\partial x} \right) \sqrt{\Delta_x \Delta_y \Delta_z} \\
v'_p(x,t) &= \left(\epsilon_{p,x} \frac{\partial G(r_p)}{\partial z} - \epsilon_{p,z} \frac{\partial G(r_p)}{\partial x} \right) \sqrt{\Delta_x \Delta_y \Delta_z}
\end{aligned} \tag{8}$$

where $\epsilon_{p,x}(t)$, $\epsilon_{p,y}(t)$ and $\epsilon_{p,z}(t)$ take values of ± 1 randomly at each time step to introduce the p-th eddy to ensure the velocities are random in both space and time. The parameters Δ_x, Δ_y and Δ_z are the vortex separation distances in each direction. The subscript $(\cdot)_p$ denotes the variables for the p-th eddy in the computational domain. An example of turbulent flow field is shown in Fig. 2.

3 CAA Examples and Challenges

A useful application of using synthetic turbulence in CAA is to study the noise generated by airfoil-turbulence interaction. High-fidelity CAA simulations can effectively examine the influence of local aerodynamic flow, geometry and anisotropic turbulence, whereas these factors are often omitted in analytical solutions [3] due to mathematical simplifications and restricted physical assumptions. In this section, recent CAA studies of anisotropic turbulence effect, cascade noise, leading edge serration and transonic flow effect are reviewed. The related issue and challenge in computing far-field directivities and proposed solutions are outlined.

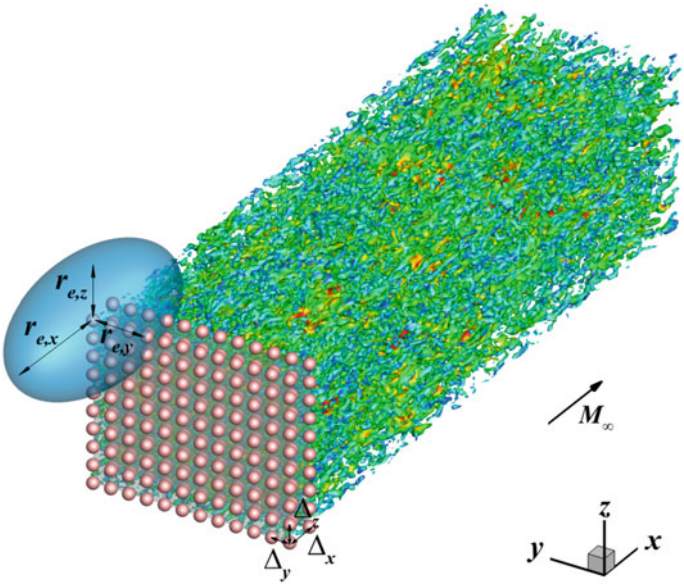

Fig. 2 A turbulence field obtained by the direct anisotropic filter method [49]. The dots are the locations to introduce the eddies. The Mach number is $M_\infty = 0.6$ and the iso-contours of the constant Q-criterion are shown

3.1 Effects of Anisotropic Turbulence on Airfoil Leading Edge Noise

Anisotropic turbulence, of which the integral length scales differ in various directions [52], can be commonly found in aero-engine applications, e.g. fan-OGV interaction. In the wake region downstream of the fan rotor of turbofan engines, the ratio of streamwise-to-transverse integral length scales is often higher than one [4, 5]. The variation in the integral length scales changes the turbulence spectra, and therefore alters the acoustic responses of OGV, located downstream of the fan [53]. For turbulence stretched in the axial direction, more turbulent kinetic energy is contained in the low wavenumber component, making the maximum noise level appear in the low-frequency range [53, 54]. The noise variation was attributed to "energy re-distribution" of anisotropic turbulence by Gea-Aguilera et al. [55]. For isotropic turbulence, the airfoil-turbulence interaction noise is insensitive to the angle of attack of airfoil [10, 12]. For anisotropic turbulence, there is an increase in noise with the angle of attack of the airfoil, suggesting that additional noise is produced by the airfoil incidence [10]. Consequently, the noise prediction can be sensitive to the input turbulence spectra [54, 56].

A study of the anisotropic turbulence on the airfoil leading edge noise was conducted by Gea-Aguilera et al. [57]. In the study, anisotropic Gaussian eddies were employed as the elementary filters, and a total of 5 eddies with optimized

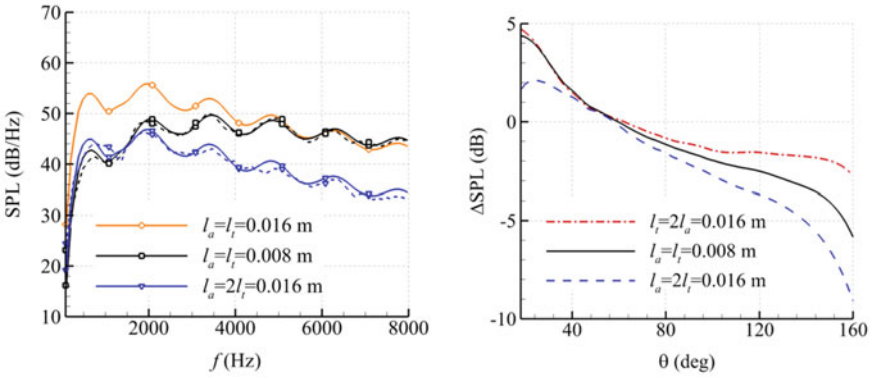

Fig. 3 Left: Far-field noise spectra of a NACA0001 airfoil leading edge noise at an observation angle of 90° (above the airfoil) [49]. The simulated results (dashed lines) are compared with the analytical flat plate solutions (solid lines) [3]. Right: Overall noise reduction of a NACA0012 airfoil interacting with anisotropic turbulence. ΔSPL is defined as $OASPL_{plate} - OASPL_{airfoil}$

parameters were superimposed (at each location to introduce turbulence) to realize the target homogeneous axisymmetric turbulence (anisotropic). Airfoil parameters such as thickness, angle of attack and camber were investigated, and the noise variation was compared with the flat plate analytical solution [3]. Similar computational simulations were also made by Shen and Zhang based on the direct anisotropic filter method [49]. Figure 3 shows the noise prediction results at Mach number $M_\infty = 0.5$, for a thin NACA0001 airfoil. Variations in the turbulence integral scales can result in different acoustic spectra, but the results are consistent with the flat plate solution, as shown in Fig. 3 (Left). For a NACA0012 airfoil, an increase in the thickness of airfoil leads to a noise reduction in the high-frequency range, which is more pronounced in the downstream direction (low observer angle). However, the sound level of the NACA0012 airfoil is higher in the upstream direction, as shown in Fig. 3 (Right) that $\Delta SPL < 0$ at high observer angles (higher than 60° for this case).

For the NACA0012 airfoil, the increase of noise level in the upstream direction is more pronounced for turbulence stretched in the flow direction, in which case the turbulence kinetic energy is mainly contained by the streamwise fluctuations. Using both numerical and analytical methods, Zhong and Zhang [58] showed that the noise increase was caused by the coupling of streamwise fluctuations with the non-uniform mean flows in the near field. In the CAA studies, the 1D turbulence kinetic energy $E_{22}(k_1)$ was kept unchanged to ensure that the noise induced by the transverse disturbance distortion remained constant. On the other hand, $E_{11}(k_1)$ was changed (via adjustment of the integral length scales) to highlight the impact of streamwise fluctuations. As a result, more noise was produced in the upstream direction with a thicker airfoil, at a higher flow Mach number and a larger ratio l_a/l_t (larger value means more streamwise fluctuations). An illustration of the impact of the anisotropic turbulence on the sound generation is shown in Fig. 4. It is shown that the sound produced in the upstream direction is higher if the turbulence is stretched

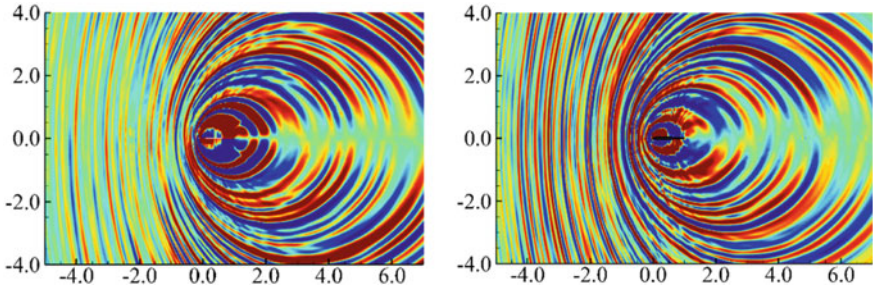

Fig. 4 Instantaneous sound pressure distribution for the airfoils interacting with anisotropic turbulence [58]. The flow Mach number is $M_\infty = 0.8$. (Left) NACA0002 airfoil and $l_a/l_t = 0.5$; (Right) NACA0006 airfoil and $l_a/l_t = 2.0$

in the streamwise direction, and the effect is more profound for the thicker airfoils since the non-uniformity of the flow is more significant.

The theoretical analysis [58] to study the influence of the streamwise fluctuation was based on the acoustic analogy by recasting the flow governing equations in the form of an inhomogeneous convected wave equation. To solve the equation, an approximation of the equivalent source was made by using turbulence components only, as the amplitudes of sound are low. The coupling of the near-field non-uniform mean flow with the streamwise fluctuations is more acoustically efficient than the transverse disturbances. Also, the equivalent sources yield higher noise radiation at high observer angles. The analysis explains the findings in the numerical simulations. Also, a correction to the Amiet's flat plate solution based on the analysis (to account for the non-uniform flow effect) was proposed in that study. The accuracy of the corrected solution is observably improved in the upstream direction, especially for the larger l_a/l_t cases, as shown in Fig. 5.

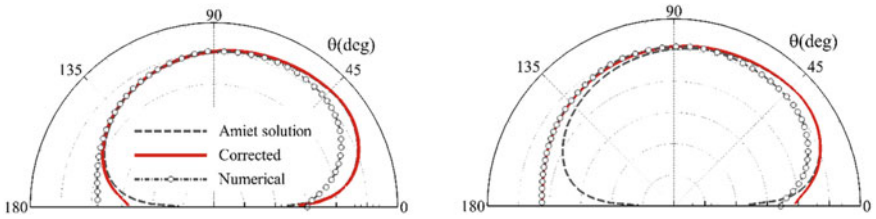

Fig. 5 Correction of the sound radiation patterns of a NACA0012 airfoil interacting with anisotropic turbulences in a non-uniform mean flow [58]. The Mach number is 0.5. The ratio of streamwise/transverse integral length scales are $l_a/l_t = 0.5$ (Left) and $l_a/l_t = 2$ (Right)

3.2 Fan-Wake Modelling and Cascade-Turbulence Interaction Noise

Many leading-edge noise studies were conducted for isolated airfoils, and their aeroacoustic features have been well understood. For practical aero-engine applications, the propagation of sound can be scattered by the solid surfaces of the fan cascade, and the noise properties can be significantly altered. A challenge of studying the cascade interaction noise is to model the turbulent fan wake. Early studies modelled the interaction of cascade with the harmonic gusts [59, 60]. In many physics-based models based on analytical solutions, the underlying assumptions are flat plate geometry, uniform mean flow, and homogeneous and isotropic turbulence [61]. In practice, the wake turbulence shed from the fan blades is unsteady and non-uniform due to the rotating motion of the fan. The modelling of the turbulent wake can play a large role in defining the resulting noise spectra [62, 63]. An approach to model the variation is based on the cyclostationary assumption, in which the turbulent kinetic energy varies as [64, 65]

$$K_W(y,t) = u'^2_{rms,b} + u'^2_{rms,w} \sum_{n=-\infty}^{\infty} \exp\left(-\ln 2 \frac{(y - V(t + nT_W))}{h_w^2}\right), \tag{9}$$

where $u_{rms,b}$ is the root-mean-square fluctuation velocity of the background turbulence, $u_{rms,w}$ is the maximum value in the wake region, h_w is the half-width, V is speed of the airfoil cascade movement and T_w is the period of the fan wakes. Using this approach, the turbulence length scales can also be changed spatially and temporally as in Eq. (9). This could then be used in conjunction with the synthetic turbulence to consider the varying turbulent kinetic energy and integral length scales in the flow field. At each time step of a CAA computation, the eddies are placed in the upstream injection plane, and they will be convected downstream by the background mean flow. Empirical parameters are introduced in the cyclostationary approach, through which one can control the turbulence distribution in the computational domain. When K_W and the turbulence integral length scale are set as constants, the turbulence will be the common homogeneous turbulence often employed for isolated airfoil studies. Figure 5 shows an example of using the cyclostationary synthetic turbulence to study the noise generated in a cascade. Through a systematic CAA investigation, Gea-Aguilera et al. [65] showed that the broadband noise is mainly influenced by the circumferentially averaged spectrum perceived by the cascade. The airfoil thickness can reduce the sound, especially in the high-frequency range, and the periodic airfoil blades distribution could lead to cut-off modes of the sound propagation.

An alternative approach to model the turbulent wake cast by rotating fan is to implement a moving/sliding mesh in the CAA solvers [67]. In the moving part of the CAA grids, the synthetic turbulence that reproduces the target turbulence statistics is introduced at fixed locations to mimic the fan wake. The CAA grids move during the numerical computation at the rotating speed of the fan. At different time steps, the relative positions of grids (to introduce the turbulent fluctuations) to the downstream

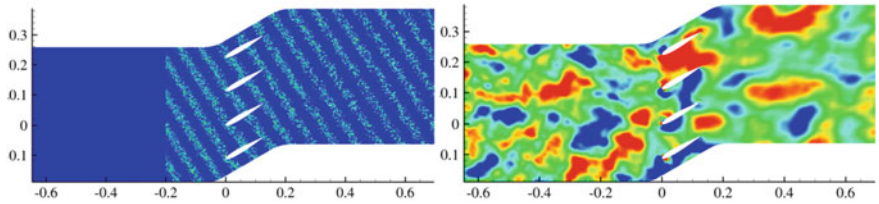

Fig. 6 Simulation of the turbulence-cascade interaction noise using cyclostationary method. Left: vorticity distribution. Right: sound pressure distribution [66]

blades are changed, leading to spatial and temporal variations of the modelled wake turbulence. The flow data at the interface between the moving and the stationary grids are exchanged via a high-order interpolation [67]. An illustration of the wake realization using the moving mesh approach at different time steps is shown in Fig. 6. In this method, there are no empirical parameters to control the wake profile. Also, the effect of relative motion between the fan blades (with moving grid) and OGV cascade (stationary grid) on the blockage of broadband noise propagation in the upstream direction [68] can be investigated numerically if the blades are considered in the computation.

3.3 Airfoil-Turbulence Interaction Noise in Transonic Flow

Most studies on airfoil-turbulence interaction noise were conducted at subsonic speeds. In situations such as contra rotating open rotors, locally supersonic flows can be generated around the tips of rotor blades at high rotating speeds [69, 70]. The supersonic flow may also be generated at the tips of aero-engine fan blades, the flow becomes more complex as the ingested turbulence and boundary layer turbulence on the internal wall of any ducted fan, such as the casing of the turbofan engine, interact with the supersonic flow [6]. A schematic of the noise mechanisms in a transonic flow is shown in Fig. 7. For a typical transonic airfoil-turbulence interaction problem, a locally supersonic region can appear on the surface of airfoil and is terminated by a shock, producing process rich in aeroacoustic features such as turbulence-shock interaction, turbulence-airfoil interaction, sound scattering by shock waves, oscillation of shock waves anchored on the surface [35], etc. In previous studies of the shock-turbulence interaction problem, normal and infinite shocks were assumed [71]. Evers [72] and Evers and Peake [73] developed an analytical solution for transonic flow based on the small disturbance theory for thin airfoils and predicted noise generation in the downstream direction. For general cases with more complex geometrical and flow features, achieving accurate analytical solutions can be challenging. CAA simulations using synthetic turbulence could potentially offer better solutions to the problem.

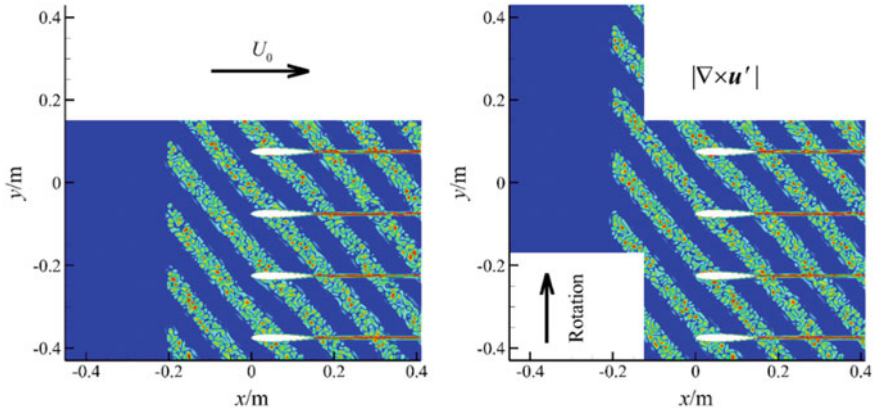

Fig. 7 Schematic of the fan wake modelling using the moving mesh method

A systematic CAA investigation of airfoil interacting with oncoming turbulence at transonic speeds was conducted by Zhong et al. [35]. A localized artificial diffusivity scheme [75] was implemented in the CAA solver [76, 77] for shock capturing, and the synthetic turbulence was introduced upstream of airfoil in the computational domain where the background flow is uniform. Based on single-frequency Fourier mode computations, it was found that the noise radiation pattern of a transonic airfoil contains more radiation peaks in both the upstream and the downstream directions than those in subsonic flows. By placing equivalent acoustic sources on the surface of airfoil, similar radiation patterns were found, suggesting that the radiation peaks are likely caused by the interference of the direct radiation and the sound scattering by shocks. As a result, for leading edge noise problem with shocks, the near-field sound distribution become irregular, accompanied by noise produced in both the upstream and the downstream directions, as shown in Fig. 8 (Left). In cases of oncoming high

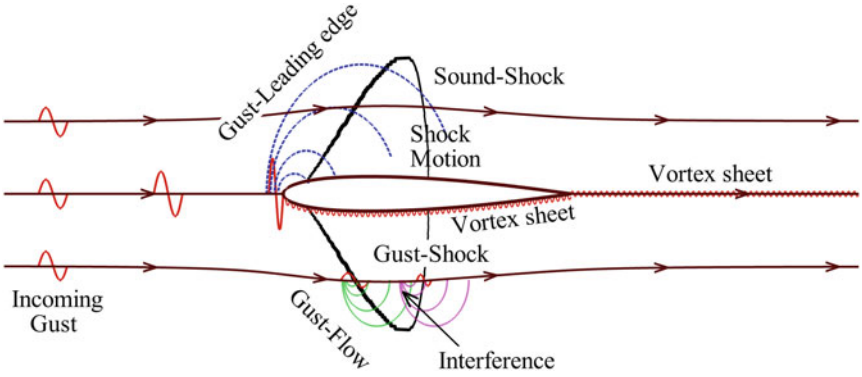

Fig. 8 Schematic of the aeroacoustic physics of airfoil-turbulence/gust interaction noise in a transonic flow [74]

intensity turbulence or gusts, the shocks may experience local oscillation due to the nonlinear aerodynamic process. Then, the sound radiation in the near field can be significantly altered as shown in Fig. 8 (Right).

A systematic CAA study of geometry effect on the interaction noise in transonic flows was conducted by Zhong et al. [78]. It showed that in transonic flows, the effect of the thickness of the airfoil on noise reduction is not as significant as in subsonic flows. This is the result of different noise mechanisms, where the noise generated by non-uniform mean flow and shock-turbulence interaction can compensate the thickness-induced noise reduction. However, the thickness is still the most influential parameter as it alters the shock patterns and sound radiation. As for the angle of attack, it changes the acoustic response of a single-frequency harmonic gust. The overall effect, though, is relatively small for isotropic turbulence because of the symmetric turbulence velocity. In addition, the far-field directivities and overall sound pressure levels vary with the airfoil camber in transonic flows, but the effect is not as significant as the thickness.

3.4 Effects of Leading-Edge Serrations

Experimental [79, 80] and analytical [81, 82] studies have demonstrated that leading-edge serration on a wing can reduce the turbulence interaction broadband noise compared with a conventional straight-edged wing. The aerodynamic performance of a wing with a serrated leading edge can be improved as the onset of flow separation is delayed [83, 84], suggesting that the leading edge serration can be a promising noise reduction solution. Investigations of the noise reduction mechanism and parametric studies for optimal design are nevertheless still required. For numerical simulations, single-frequency studies using a harmonic gust [85] and broadband noise studies based on synthetic turbulence [55, 86] have been conducted, showing that size and the length scales of the eddies relative to the serration are the influential parameters. Particularly, Gea-Aguilera et al. [55] systematically studied the distortion and the resultant noise production of different anisotropic turbulence interacting with a wing with a serrated leading edge and a NACA0012 airfoil profile. The vorticity of the synthetic turbulence in 3D and the pressure distribution on the surface of the wing are shown in Fig. 9. The CAA simulation shows that the mean flow gradient in the root region of the serration is more impactful than that in the peak region. The study has also confirmed that the turbulence length scale in the spanwise direction is more influential than in other directions, this might be due to the variation of spanwise coherence of the turbulence. The implication is that for different turbulent flow fields with similar turbulence kinetic energy, the properties of the noise generation are sensitive the ratio of the turbulence length scale and the size of serration.

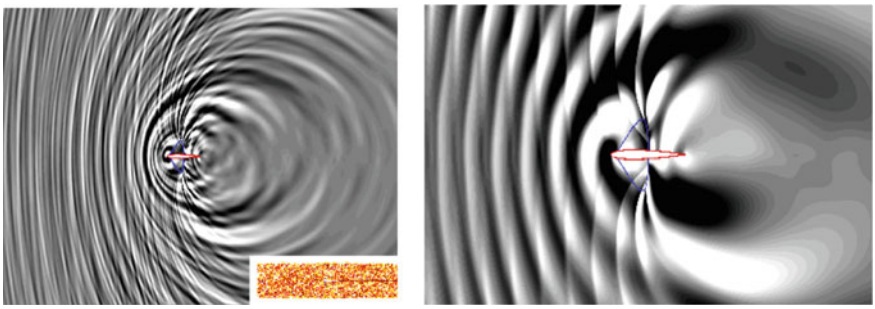

Fig. 9 CAA study of the turbulence-airfoil interaction in transonic flows with shocks. Left: broadband simulation using synthetic turbulence (with the vorticity distribution in the right bottom corner). Right: single-frequency simulation with shock oscillation [35]

3.5 Computation of the Far-Field Directivities

The broadband noise simulation using CAA faces challenges aside from realizing correct turbulence properties. Usually, the far-field directivities are obtained through an integral solution of the Ffowcs-Williams and Hawkings (FW-H) equation [87], which in turn is derived from the flow governing equations [88]. Of various elements of the integral solution, the volume integral part is often omitted as it is acoustically inefficient but computationally expensive. However, for broadband noise problems where there exists turbulence in the flow field, the location of the integration surface could significantly affect the noise prediction without considering the volume integral parts.

Often in a CAA computation, the integration surface is placed on the solid aerodynamic surface. This can produce errors in predictions as the influence of the non-uniform flows in the near field is not accounted for. Moreover, this method is invalid for transonic flow due to the likely presence of shock waves in the flow field. However, if an off-body permeable integration surface is used, the computation can suffer from spurious wave contamination arises from the passage of the non-acoustical turbulent eddies through the integration surface. The errors can be eliminated by including the volume integral terms in the computation [89], but the procedure is computationally expensive.

To compute acoustic far-field directivity in the presence of vortical disturbances in the flow field effectively and accurately, Zhong and Zhang developed an improved sound extrapolation method [90] in seeking an integral solution of acoustic governing equations. In calculating the equivalent sources collected on the integration surface, the vortical components are filtered by additional operations, based on the divergence-free and frozen turbulence properties. Only the acoustic components on the permeable integration surface are then used in the far-field directivity computation. The integration surface should be placed at a sufficiently large distance from the non-uniform mean flow region to yield an accurate far-field noise prediction. Figure 10 shows an example of far-field directivity computation of a thin NACA0001 airfoil interacting

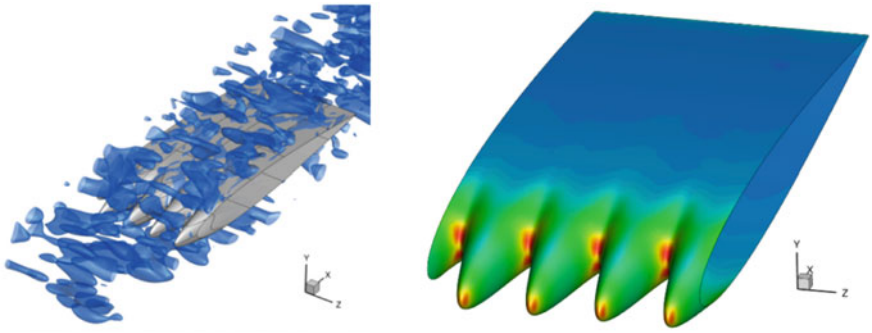

Fig. 10 Anisotropic turbulence interacting with a wing with serrated leading edge. (Left) the iso-surfaces of the turbulence stretched in the spanwise direction; (Right) the root-mean-squire pressure fluctuations on the surface of the wing [55]

with a harmonic gust, where the permeable integration surface is indicated by the black dashed line. If the Farassat Formulation 1A of the integral solution of the FW-H equation is used [91], incorrect far-field directivity due to spurious wave contamination is produced. In contrast, the new sound extrapolation method matched well with the Amiet's flat plate analytical solution [3].

Further extensions to the sound extrapolation method was also made by Zhong and Zhang [92], to treat more general turbulent flows. The key idea is to filter out the non-acoustic components of the turbulent flow by applying a convection operator to the locally convecting turbulence fluctuations. A third-order wave equation, sharing similarity with Lilley's acoustic analogy [93], was proposed and solved to compute the acoustic far-field directivities. The method was tested for various aeroacoustic problems including the turbulence-airfoil interaction noise, vortex shedding noise from cylinders, airfoil trailing edges noise and co-flowing jet noise; generally good

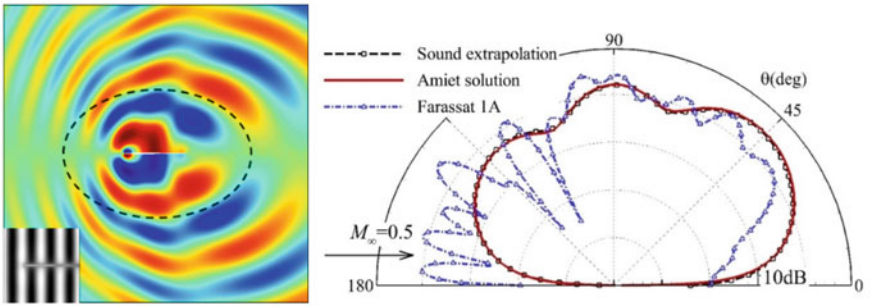

Fig. 11 Example of the far-field directivity of the airfoil gust interaction noise. The thin NACA0002 airfoil is studied at $M_\infty = 0.5$ and the wavelength of the single-frequency harmonic mode is 0.5 of the chord. The black dashed line indicates the location of the off-body integration surface. The result obtained by the sound extrapolation method [90] is compared with the Amiet's flat plate solution [3] and the Farassat Formulation 1A [91] of the FW-H equation [87]

results were obtained. On top of this development, work on the frequency-domain formulation [94] has also been carried out, this formulation offers comparable performance with the multi-surface averaging FW-H method at a reduced computational cost [94].

4 Summary

CAA simulations of leading edge noise problems based on synthetic turbulence methods are reviewed, with focus on typical broadband noise problems such as the airfoil-turbulence interaction noise that can be found in turbofan aero-engines and contra rotating open rotors. The swirling and highly turbulent flows have various length and time scales and the resultant sound fields are rich in aeroacoustic features. The problems include varying geometries, non-uniform flow and acoustic physics due to the possible appearance of shocks at transonic speeds. These call for comprehensive examinations and validation of available analytical predictive models, which tend to over-simplify the problems.

For typical leading-edge noise problems, high-fidelity simulations using the full Navier-Stokes equations for aeroacoustic problems are computationally expensive. Moreover, it is often desirable to study specific noise generation mechanisms in isolation, which has been proven difficult using a full solution of Navier-Stokes equations. Instead CAA simulations of either the full or the linearized Euler equations with synthetic turbulence modelling, to reproduce the turbulence statistics such as the energy spectra and two-point correlation tensors are effective for many practical problems.

For CAA simulations, synthetic turbulence should be divergence-free to avoid the appearance of spurious noise sources. Usually, the synthetic turbulence can be realized by either Fourier modes summation, synthetic eddy superposition or through using digital filters in convolution with random noise signals, the suitability of which is highly depending on the problem of interest. The Fourier mode-based methods are mathematically straightforward but computationally expensive for calculating the continuous anisotropic turbulence. Many of the earlier synthetic eddy and digital filter methods require semi-empirical coefficients (often Mach number dependent) of various elementary eddies/filters to reproduce an arbitrary turbulence spectrum. Recent development of using a single direct anisotropic digital filter has been proposed for generic axisymmetric turbulence.

This paper provides examples of broadband noise simulation using CAA with synthetic turbulence, including the effect of anisotropic turbulence, leading serration, fan-wake modelling, airfoil cascade interaction noise and transonic flow. The proposed synthetic turbulence method is not limited to the above applications, it can also be applied in other CAA problems such as airframe noise [43] and more general CFD studies [1]. For future CAA studies, synthetic turbulence method in sheared mean flows will need to be developed, and the applications in 3D problems will also be important.

Acknowledgements The authors wish to thank Dr Fernando Gea-Aguilera, Dr Zhen Shen and Mr. Wei Ying for their help during the preparation of the article. The work is supported by the National Science Foundation of China (11772282) and the Hong Kong Research Grants Council (16203817).

References

1. X.H. Wu, Inflow turbulence generation methods. Annu. Rev. Fluid Mech. **49**, 23–49 (2017)
2. N. Jarrin, S. Benhamadouche, D. Laurence, R. Prosser, A synthetic-eddy-method for generating inflow conditions for large-eddy simulations. Int. J. Heat Fluid Flow **27**, 585–593 (2006)
3. R.K. Amiet, Acoustic radiation from an airfoil in a turbulent stream. J. Sound Vib. **41**(4), 407–420 (1975)
4. U. W. Ganz, P. D. Joppa, T. J. Patten and D. F. Scharpf, "Boeing 18-inch fan rig broadband noise test," *NASA Tech. Rep. CR-1998-208704,* 1998
5. G. G. Podboy, M. J. Krupar, S. M. Helland and C. E. Hughes, "Steady and unsteady flow field measyrements within a NASA 22-inch fan model," *AIAA Paper 2002–1033,* 2002
6. R. Mani and K. Bekofske, "Experimental and theoretical studies of subsonic fan noise," *NASA Tech. Rep. CR-2660,* 1976
7. R. A. Kantola and R. E. Warren, "Reduction of rotor-turbulence interaction noise in static fan noise testing," *AIAA Paper 79-0656,* 1979
8. R.K. Amiet, High frequency thin-airfoil theory for subsonic flow. AIAA J. **14**(8), 1076–1082 (1976)
9. R. W. Paterson and R. K. Amiet, "Acoustic radiation and surface pressure characteristics of an airfoil due to incident turbulence," *NASA Tech. Rep. CR-2733,* 1976
10. W.J. Devenport, J.K. Staubs, S.A. Glegg, Sound radiation from real airfoils in turbulence. J. Sound Vib. **17**, 3470–3483 (2010)
11. S. Oerlemans and P. Migliore, "Aeroacoustic wind tunnel tests of wind turbine airfoils," *AIAA Paper 2004-3042,* 2004
12. S. Moreau, M. Roger and V. Jurdic, "Effect of angle of attack and airfoil shape on turbulence-interaction noise," *AIAA Paper 2005-2973,* 2005
13. P. Chaitanya, J. Gill, S. Narayanan, P. Joseph, C. Vanderwel, X. Zhang and G. B., "Aerofoil geometry effects on turbulence interaction noise," *AIAA 2015-2830*
14. V. Clair, C. Polacsek, T. Le Garrec, G. Reboul, M. Gruber, P. Joseph, Experimental and numerical investigation of turbulence-airfoil noise reduction using wavy edge. AIAA J. **51**(11), 2695–2713 (2013)
15. J. Gill, X. Zhang, P. Joseph, Single velocity-component modeling of leading edge turbulence interaction noise. J. Acoust. Soc. Am. **137**(6), 3209–3220 (2015)
16. H.M. Atassi, M. Dusey, C.M. Davis, Acoustic radiation from a thin airfoil in non-uniform subsonic flows. AIAA J. **31**(1), 12–19 (1993)
17. J. Scott and H. M. Atassi, "Numerical solutions of the linearised Euler equations for unsteady vortical flows around lifting airfoils," *AIAA Paper 90-0694,* 1990
18. D.P. Lockard, P.J. Morris, Radiated noise from airfoils in realistic mean flows. AIAA J. **36**(6), 907–914 (1998)
19. J. Gill, X. Zhang, P. Joseph, Symmetric airfoil geometry effects on leading edge noise. J. Acoust. Soc. Am. **134**(4), 2669–2680 (2013)
20. F. Gea-Aguilera, X. Zhang, X. X. Chen, J. Gill and T. Node-Langlois, "Synthetic turbulence methods for leading edge noise predictions," *AIAA Paper 2015-2670,* 2015
21. S.Y. Zhong, X. Zhang, B. Peng, X. Huang, An analytical correction to Amiet's solution of airfoil leading-edge noise in non-uniform mean flows. J. Fluid Mech. **882**, A29 (2020)
22. S.Y. Zhong, H.B. Jiang, W. Ying, X. Zhang, X. Huang, An efficient computation of cascade-gust interaction noise based on a hybrid analytical and boundary element method. J. Sound Vib. **461**, 114911 (2019)

23. X. Zhang, Aircraft noise and its nearfield propagation computations. Acta Mech. Sinica **28**(4), 960–977 (2012)
24. L.S.G. Kovasznay, Turbulence in supersonic flow. J. Aero. Sci. **20**, 657–682 (1953)
25. B.-T. Chu, L.S.G. Kovasznay, Non-linear interactions in a viscous heat-conducting compressible gas. J. Fluid Mech. **3**, 494–514 (1958)
26. C.C. Lin, On Taylor's hypothesis and the acceleration terms in the Navier-Stokes equations. Quart. Appl. Math. **10**(4), 295–306 (1953)
27. G.I. Taylor, The spectrum of turbulence. Proc. R. Soc. A. **164**(919), 476–490 (1938)
28. R.H. Kraichnan, Diffusion by a random velocity field. Phys. Fluids **13**(1), 22–31 (1970)
29. M. Karweit, P. Blanc-Benon, D. Juve, G. Comte-Bellot, Simulation of the propagation of an acoustic wave through a turbulent velocity field: a study of phase variance. J. Acoust. Soc. Am. **89**(1), 52–62 (1991)
30. A. Smirnov, S. Shi, I. Celik, Random flow generation technique for large eddy simulations and particle-dynamics modeling. J. Fluid Engineering **123**(2), 359–371 (2001)
31. S.H. Huang, Q.S. Li, J.R. Wu, A general inflow turbulence generator for large eddy simulation. J. Wind Eng. Indust. Aero. **98**(10–11), 600–617 (2010)
32. P. Batten, U. Goldberg, S. Chakravarthy, Interfacing statistical turbulence closures with large-eddy simulation. AIAA J. **42**(3), 485–492 (2004)
33. W. Bachara, C. Bailly, P. Lafon, S.M. Candel, Stochastic approach to noise modeling for free turbulent flows. AIAA J. **32**(3), 455–463 (1994)
34. C. Bailly, P. Lafon and S. Candel, "Computation of noise generation and propagation for free and confined turbulent flows," *AIAA Paper 96-1732,* 1996
35. S.Y. Zhong, X. Zhang, J. Gill, R. Fattah, Y.H. Sun, A numerical investigation of the airfoil-gust interaction noise in transonic flows: acoustic processes. J. Sound Vib. **425**, 239–256 (2018)
36. F. Gea-Aguilera, J. Gill, X. Zhang, Synthetic turbulence methods for computational aeroacoustic simulations of leading edge noise. Computer Fluids **157**(3), 240–252 (2017)
37. N. Jarrin, R. Prosser, J.C. Uribe, S. Benhamadouche, D. Laurence, Reconstruction of turbulent fluctuations for hybrid RANS/LES simulations using a synthetic eddy method. Int. H. Heat Fluid Flow **30**(3), 435–442 (2009)
38. A. Sescu, R. Hixon, Toward low-noise synthetic turbulent inflow conditions for aeroacoustic calculations. Int. J. Num. Method Fluids **73**(12), 1001–1010 (2013)
39. J.W. Kim, S. Haeri, An advanced synthetic eddy method for the computation of airfoil-turbulence interaction noise. J. Comput. Phys. **287**, 1–17 (2015)
40. A. Sescu, F. Sagues, J.M. Sancho, Stochastic generation of homogeneous isotropic turbulence with well defined spectra. Phys. Rev. E **48**(3), 2279–2287 (1993)
41. M. Klein, A. Sadiki, J. Janicka, A digital filter based generation of inflow data for spatially developing direct numerical or large eddy simulations. J. Comput. Phys. **186**(2), 652–665 (2003)
42. L. di Mare, M. Klein, W.P. Jones, J. Janicka, Synthetic turbulence inflow conditions for large eddy simulation. Phys. Fluids **18**(2), 025107 (2006)
43. R. Ewert, Broadband slat noise prediction based on CAA and stochastic sound sources from a fast random particle-mesh (RPM) method. Comput. Fluids **37**(4), 369–387 (2008)
44. R. Ewert, J. Dierke, J. Siebert, A. Neifeld, C. Appel, M. Siefert, O. Kornow, CAA broadband noise prediction for aeroacoustic design. J. Sound Vib. **330**(17), 4139–4160 (2011)
45. A. Wohlbrandt, N. Hu, S. Guerin, R. Ewert, Analytical reconstruction of isotropic turbulence spectra based on the Gaussian transform. Comput. Fluids **132**, 46–50 (2016)
46. M. Siefert and R. Ewert, "Sweeping sound generation in het realised with a random particle mesh method," *AIAA Paper 2009-3369,* 2009
47. M. Dieste, G. Gabard, Random particle methods applied to broadband fan interaction noise. J. Comput. Phys. **231**(24), 8133–8151 (2012)
48. S. B. Pope, Turbulent flows, Cambridge University Press, 2000
49. Z. Shen, X. Zhang, Direct anisotropic filter method of generating synthetic turbulence applied to turbulence-airfoil interaction noise prediction. J. Sound Vib. **458**, 544–564 (2019)

50. E.J. Kerschen, P.R. Gliebe, Noise caused by the interaction of a rotor with anisotropic turbulence. AIAA J. **19**(6), 717–723 (1981)
51. H. W. Liepmann, J. Laufer and K. Liepmann, "On the spectrum of isotropic turbulence," *NACA Tech. Rep. TN-2473,* 1951
52. H. M. Atassi and M. M. Logue, "Fan broadband noise in anisotropic turbulence," *AIAA 2009-3148,* 2009
53. H. Posson, S. Moreau, M. Roger, Broadband noise prediction of fan outlet guide vane using a cascade response function. J. Sound Vib. **330**(25), 6153–6183 (2011)
54. F. Gea-Aguilera, J. Gill, D. Angland and X. Zhang, "Wavy leading edge airfoils interacting with anisotropic turbulence," *AIAA Paper 2017-3370,* 2017
55. S.M. Grace, Fan broadband interaction noise modeling using a low-order method. J. Sound Vib. **346**, 402–423 (2015)
56. F. Gea-Aguilera, J. Gill, X. Zhang, X. X. Chen and T. Node-Langlois, "Leading edge noise predictions using anisotropic synthetic turbulence," *AIAA Paper 2016-2840,* 2016
57. S.Y. Zhong, X. Zhang, On the effect of streamwise disturbance on the airfoil-turbulence interaction noise. J. Acoust. Soc. Am. **145**(4), 2530–2539 (2019)
58. M. D. Dahl, "Third computational aeroacoustics (CAA) workshop on benchmark problems," *NASA Tech. Rep. CP-2000-209790,* 2000
59. P. Chaitanya, J. Coupland and P. Joseph, "Airfoil geometry effects on turbulence interaction noise in cascades," *AIAA Paper 2016-2738,* 2016
60. M. Nallasamy, E. Envia, Computation of rotor wake turbulence noise. J. Sound Vib. **282**(3–5), 649–678 (2005)
61. H. Ju, R. Mani, M. Vysohlid, A. Sharma, Investigation of fan-wake/outlet-guide-vane interaction broadband noise. AIAA J. **53**(12), 3534–3550 (2015)
62. A.M. Wohlbrandt, C. Kissner, S. Guerin, Impact of cyclostationarity on fan broadband noise prediction. J. Sound Vib. **420**, 142–164 (2018)
63. V. Jurdic, P. Joseph, J. Antoni, Investigation of rotor wake turbulence through cyclostationary spactral analysis. AIAA J. **47**, 2022–2030 (2009)
64. F. Gea-Aguilera, J. Gill, X. Zhang, On the effects of fan wake modelling and vane design on cascade noise. J. Sound Vib. **459**, 114859 (2019)
65. F. Gea-Aguilera, J. Gill, X. Zhang and T. Node-Langlois, "Turbulence-cascade interaction noise using an advanced digital filter method," *23 Int. Congress Sound Vib.,* 2016
66. R. Fattah and X. Zhang, "A hybrid high-order sliding mesh interface for finite difference schemes," *24th Int. Congress Sound Vib.,* 2017
67. S. Kaji, T. Okazaki, Propagation of sound waves through a blade row. I analysis based on the semi-actor disk theory. J. Sound Vib. **11**, 339–353 (1970)
68. J. Gill, "Roadband noise generation of a contra-rotating open rotor blade," *PhD thesis, University of Southampton,* 2015
69. A. M. Hall, O. V. Atassi, J. Gilson and R. Reba, "Effects of leading edge thickness on high-speed airfoil-turbulence interaction noise," *AIAA Paper 2011-2861,* 2011
70. F. K. Moore, "Unsteady oblique interaction of a shock wave with a plane disturbance," *NASA Report 1165,* 1953
71. I. Evers, Gust-shock interaction in transonic small-disturnance flow. AIAA J. **39**(1), 29–36 (2001)
72. I. Evers, N. Peale, Noise generation by high-frequency gust interacting with an airfoil in transonic flow. J. Fluid Mech. **411**, 91–130 (2000)
73. S. Y. Zhong, "An analytical and computational aeroacoustics investigation of gust-airfoil interaction noise," *PhD thesis, The Hong Kong Universtiy of Science and Technology,* 2018
74. A.W. Cook, Artificial fluid properties for large-eddy simulation of compressible turbulent mixing. Phys. Fluids **19**(5), 1–9 (2007)
75. X. Zhang, X.X. Chen, C.L. Morfey, P.A. Nelson, Computation of spinning modal radiation from an unflanged duct. AIAA J. **42**(9), 1795–1801 (2004)
76. Z.K. Ma, X. Zhang, Numerical investigation of broadband slat noise attenuation with acoustic liner treatment. AIAA J. **47**(12), 2812–2820 (2009)

77. S.Y. Zhong, X. Zhang, J. Gill, R. Fattah, Y.H. Sun, Geometry effect on the airfoil-gust interaction noise in transonic flows. Aero. Sci. Tech. **92**, 181–191 (2019)
78. P. Chaitanya, S. Narayanan, P. Joseph and J. W. Kim, "Leading edge serration geometries for significantly enhanced leading edge noise reduction," *AIAA Paper 2016-2736,* 2016
79. P. Chaitanya, P. Joseph, S. Narayanan, C. Vanderwel, J. Turner, J.W. Kim, B. Ganapathisubramani, Performance and mechanism of sinusoidal leading edge serrations for the reduction of turbulence-aerofoil interaction noise. J. Fluid Mech. **818**, 435–464 (2017)
80. J. Mathews and N. Peake, "Noise generation by turbulence interacting with an aerofoil with a serrated leading edge," *AIAA Paper 2015-2204,* 2015
81. L.J. Ayton, J.W. Kim, An analytic solution for the noise generated by gust-aerofoil interaction for plates with serrated leading edges. J. Fluid Mech. **853**, 515–536 (2018)
82. D.S. Miklosovic, M.M. Murray, L.E. Howle, F.E. Fish, Leading edge tubercles delay stall on humpback whale (Megaptera Novaeangliae) flippers. Phys. Fluid **16**(5), 39–32 (2004)
83. E.A. van Nierop, S. Blben, M.P. Brenner, How bumps on whale flippers delay stall: an aerodynamic model. Phys. Rev. Lett. **100**, 054502 (2008)
84. A.S.H. Lau, S. Haeri, J.W. Kim, The effect of wavy leading edge on aerofoil-gust interaction noise. J. Sound Vib. **332**(24), 6234–6253 (2013)
85. J. Turner, J. W. Kim, P. Chaitanya and P. Joseph, "Towards understanding aerofoils with dual-frequency wavy leading edges interacting with vortical disturbances," *AIAA Paper 2016-2951,* 2016
86. J.E. Ffowcs-Williams, D.L. Hawkings, Sound generation by turbulence and surfaces in arbitrary motion. Proc. R. Soc. A. **264**(1151), 321–342 (1969)
87. J. Lighthill, On sound generated aerodynamically. I. General theory. Proc. R. Soc. A. **211**, 546–587 (1952)
88. G. Rahier, M. Huet, J. Prieur, Additional terms for the use of Ffowcs-Williams and Hawkings surface integrals in turbulent flows. Comput. Fluids **120**, 158–172 (2015)
89. S.Y. Zhong, X. Zhang, A sound extrapolation method for aeroacoustics far-field prediction in presence of vortical waves. J. Fluid Mech. **820**, 424–450 (2017)
90. F. Farassat, G.P. Succi, A review of propeller discrete frequency noise prediction technology with emphasis on two current methods for time domain calculations. J. Sound Vib. **71**(3), 399–419 (1980)
91. S.Y. Zhong, X. Zhang, A generalized sound extrapolation method for turbulent flows. Proc. R. Soc. A. **474**, 20170614 (2018)
92. G. Lilley, "Appendix: generation of sound in a mixing region. Fourth monthly progress report on contract F-33615-71-C-1663," *Lockheed Aircraft Co.,* 1971
93. S.Y. Zhong, X. Zhang, On the frequency domain formulation of the generalized sound extrapolation method. J. Acoust. Soc. Am. **144**(1), 24–31 (2018)
94. S.Y. Zhong, X. Zhang, X. Huang, A comparison of acoustic far-field prediction methods for turbulent flows. Int. J. Aeroacoustics **18**(6–7), 579–595 (2019)